Bernd M. Ohnesorge
Thomas G. Flohr
Christoph R. Becker
Andreas Knez
Maximilian F. Reiser

Multi-slice and Dual-source CT in Cardiac Imaging

Principles – Protocols – Indications – Outlook

Second Edition

CD-ROM
INCLUDED

Springer

Ohnesorge · Flohr · Becker · Knez · Reiser

Multi-slice and Dual-source CT in Cardiac Imaging

Principles – Protocols – Indications – Outlook

Second Edition

Bernd M. Ohnesorge · Thomas G. Flohr
Christoph R. Becker · Andreas Knez
Maximilian F. Reiser

Multi-slice and Dual-source CT in Cardiac Imaging

Principles – Protocols – Indications – Outlook

Second Edition

With 316 Figures in 673 Separate Illustrations in Color and 26 Tables

Springer

Bernd M. Ohnesorge, PhD
President Siemens Medical Solutions Group, China
7, Wangjing Zhonghuan Nanlu
Chaoyang District, Beijing 100102, P.R. China

Thomas G. Flohr, PhD
Head of CT Physics and Applications Development
Siemens Medical Solutions, Division CT
Siemensstrasse 1, 91301 Forchheim, Germany

Christoph R. Becker, MD
Section Head CT, Department of Clinical Radiology
University of Munich, Klinikum Grosshadern
Marchioninistrasse 15, 81377 Munich, Germany

Andreas Knez, MD
Section Head Imaging, Department of Cardiology
University of Munich, Klinikum Grosshadern
Marchioninistrasse 15, 81377 Munich, Germany

Maximilian F. Reiser, MD
Medical Director, Department of Clinical Radiology
University of Munich, Klinikum Grosshadern
Marchioninistrasse 15, 81377 Munich, Germany

Library of Congress Control Number: 2006933722

ISBN 3-540-25523-0 Springer Berlin Heidelberg New York
ISBN 978-3-540-25523-9 Springer Berlin Heidelberg New York

Springer is part of Springer Science+Business Media

http//www.springer.com

Printed in Germany

Medical Editor: Dr. Ute Heilmann, Heidelberg
Desk Editor: Dörte Mennecke-Bühler, Heidelberg
Production Editor: Kurt Teichmann, Mauer
Cover-Design: Frido Steinen-Broo, eStudio Calmar, Spain
Typesetting: Verlagsservice Teichmann, Mauer

Printed on acid-free paper – 21/3151xq – 5 4 3 2 1 0

Preface to the Second Edition

Despite worldwide efforts to assess and control cardiovascular risk factors, cardiac diseases and in particular coronary artery disease (CAD) are still the foremost causes of death in the developed countries of Western Europe, North America and Asia and are becoming increasingly common in Eastern Europe and the developing world (Deanfield 2001). Approximately one in five deaths is currently related to cardiac disease in Europe and the US. Nearly 500,000 deaths caused by CAD are reported every year in the US, over 600,000 in Europe, 170,000 of these in Germany alone. Over 12 million US citizens have a history of CAD, while every year 1.1 million US and 300,000 German citizens suffer a coronary attack and more than 40% will die as a result of these attacks. Every second patient dies without prior symptoms and, in most cases, myocardial infarction occurs without warning. Once a blockage of the coronary arteries has occurred, death may ensue within a few minutes, even before hospitalization is possible. These alarming statistics highlight an acute need for tools to diagnose cardiac and coronary artery disease. Presently, the gold-standard modality for diagnosis of CAD is invasive selective coronary angiography. More than 2.5 million diagnostic coronary angiograms are performed every year in Europe and the US, but about 40% of them are not followed by subsequent interventional or surgical treatment and are conducted only for the purpose of ruling out CAD (Windecker 1999). These data show the significant need for and importance of reliable non-invasive imaging for early and preventive diagnosis of CAD and other cardiac diseases.

Since its introduction by G. Hounsfield in 1972, X-ray computed tomography (CT) has become a reliable and widely used non-invasive imaging modality for vascular diagnosis, starting in the early 1990s with the advent of spiral CT. The reliability, simplicity and reproducibility of CT scanning could have made it a very interesting modality for non-invasive cardiac diagnosis. However, at that time imaging the heart and coronary arteries was not possible with general purpose CT scanners due to the high demands in terms of spatial and temporal resolution. As a result of dedicated development in cardiac CT scanning electron beam CT (EBCT) was introduced in 1984. With non-mechanical control and movement of the X-ray source, fixed detector system and ECG-correlated sequential scanning EBCT enabled extremely short image acquisition times to virtually freeze cardiac motion. However, the limited application spectrum of EBCT in general purpose use and in cardiac imaging has restricted distribution of the technology. The general purpose mechanical single-slice CT systems

with sub-second rotation and ECG-correlated scanning that were introduced in 1994 have challenged EBCT in the domain of cardiac imaging. The early results were promising, but restrictions in spatial and temporal resolution have limited the application to cardiac work. In 1998 mechanical multi-slice CT systems with simultaneous acquisition of four slices were introduced by all major CT manufacturers. For the first time these scanners enabled ECG-correlated multi-slice acquisition at considerably faster volume coverage and higher spatial and temporal resolution for cardiac applications compared to single-slice scanners. Since then multi-slice technology has become standard for general purpose CT diagnosis with over 10,000 multi-slice CT scanners installed to date. Within just 5 years major performance advances have taken place in terms of enhancing the number of slices acquired per rotation from 4 to 8, from 8 to 16 and now even up to 64. With the recent introduction of dual-source CT a new development is under way that will further enhance the reliability and expand the spectrum of CT in cardiac imaging in the near future (Flohr 2006; Scheffel 2006).

This book presents and discusses the technical concepts, the spectrum of clinical applications and the future developments of multi-slice CT in cardiac imaging based on the experience of internationally leading clinical institutions. It promises to serve as a comprehensive piece of literature that covers all aspects from the technical principles of CT acquisition and image evaluation all the way to clinical indications and potential pitfalls of multi-slice cardiac CT imaging. The first edition that appeared in early 2002 outlined the basic technical concepts and early clinical experience with one specific 4-slice CT scanner from a single vendor (SOMATOM Volume Zoom, Siemens, Germany), using special cardiac imaging test software (HeartView, Siemens, Germany) that had been evaluated in various recognized academic clinical institutions. Since the publication of the first edition multi-slice cardiac CT has attracted great interest among radiologists and cardiologists and advanced CT imaging products have become available from all major CT manufacturers based on common acquisition and reconstruction principles. The keen interest in the first edition of our book, combined with the extremely fast technical development in terms of both slices per rotation and rotation speed, as well as the increasing clinical acceptance of multi-slice cardiac CT in radiology and cardiology, have motivated us to publish this new and entirely reworked second edition. We received many highly constructive recommendations from readers, reviewers and clinical experts which have helped to further broaden the spectrum and improve the quality of this book and, as a result, we have tried to incorporate as many of these aspects as possible.

In this second edition we discuss the technological principles of general purpose and cardiac multi-slice CT based on the new state-the-art CT scanners with simultaneous acquisition of at least 16 and up to 64 slices per rotation. On the basis of these technical principles we have put emphasis on the discussion of scan and examination protocols from 4- to 16- and 64-slice CT and incorporated an extensive analysis of drawbacks and advantages of the various technology levels for certain clinical applications. Efficient postprocessing of the acquired thin-slice image data has become an integral part

of successful cardiac CT examinations and we have therefore extended the relevant section of the first edition to give an extensive overview of the various available techniques, including a chapter dedicated to their clinical usefulness.

A completely new section has been added to this second edition to provide the reader a comprehensive overview of the most recent clinical experience and recommendations. In this section world-renowned clinical experts from Europe and the US share their experience with the most relevant clinical applications and indications of multi-slice cardiac CT. The reader also has the opportunity to learn more about some initial "hands-on" experience by means of representative 64-slice case studies based on CT image data sets included on the attached CD-ROM. Although the editors and guest authors are most familiar with the equipment from one particular vendor and the related cardiac CT imaging software, the introduction to technical principles and the discussion of clinical applications is also valid for equipment from other manufacturers. With regard to system and hardware design concepts and scan protocols special attention has been paid to potential differences between currently available CT scanner products from the different CT vendors. To allow newcomers to the field and readers without extensive experience in CT imaging or cardiac diagnosis a quick ramp-up, we have included chapters that address the fundamental principles of CT, as well as an introduction to cardiac anatomy and the most relevant cardiac diseases.

In the final section we discuss remaining limitations of the latest multi-slice CT scanners in cardiac imaging and present future directions in terms of scanner technology and clinical applications. In this section we will introduce, for the first time, the technical concept of and initial experiences with a new dual-source CT system which provides significant enhancements in terms of temporal resolution compared to conventional multi-slice CT scanners and which may soon represent the CT technology of choice for cardiac applications.

Interdisciplinary collaboration between radiology and cardiology is particularly important for the successful implementation of this new method in a clinical environment and the editors would like to thank Dr. A. Knez, Dr. A. Leber, Dr. A. Becker and Prof. G. Steinbeck from the Department of Cardiology at the University of Munich, Klinikum Grosshadern, for their unflagging support. A global network of numerous world-leading institutions has been established for the early testing of new applications and protocols for multi-slice cardiac CT and for the evaluation of its use in clinical practice. The open exchange of experience and ideas has contributed substantially to the comprehensive spectrum of information included in this book. Thus, the editors would like to express their special thanks to the extraordinary support from this edition's guest authors, Dr. Roman Fischbach, Dr. Kai-Uwe Jürgens, Prof. Walter Heindel, Dr. Koen Nieman, Dr. Nico Mollet, Dr. Filippo Cademartiri, Prof. Pim de Feyter, Dr. Stephan Achenbach, Dr. Stephen Schröder, Dr. Axel Küttner, Dr. Andreas Kopp, Prof. Claus Claussen, Dr. Jean-Francois Paul, Dr. Steffen Fröhner, Dr. Jürgen Willmann, Dr. Bernd Wintersperger, Dr. Konstantin Nikoalou, Dr. Michael Poon, Dr. C. Learra and Dr. Uwe-Joseph Schöpf, for their extremely valuable contributions of outstanding

quality. The editors would also like to thank Dr. Katharina Anders, Dr. Ullrich Baum, Prof. Werner Bautz (University of Erlangen), Dr. Joachim Wildberger, Dr. Andreas Mahnken, Prof. R. Günther, Prof. Matheijs Oudkerk (University of Groningen), Dr. Stephan Martinoff, Dr. Jörg Hausleiter (German Heart Center Munich), Prof. Schmidt, Prof. Kerber (Rhön-Klinikum, Bad Neustadt), Prof. Rick White (Cleveland Clinic), Dr. Cynthia McCollough, Dr. Joel Fletcher, Dr. David Hough (Mayo Clinic Rochester), Prof. Geoffrey Rubin, Prof. Gary Glazer (Stanford University), Dr. Udo Hofmann, Dr. Thomas Brady (MGH, Boston), Prof. Martine Remy-Jardin, Prof. Jaque Remy (University of Lille), Prof. Kunihiko Fukuda (Jikei University, Tokyo), Prof. Sato (Nihon University, Tokyo), Prof. Sim (Sarawak Heart Center, Kuching), Mrs. Karin Barthel, Mrs. Heike Theesen, Mrs. Sigi Scheuerer, Mr. Andreas Blaha, Mrs. Dominique Sandner, Mrs. Loke-Gie Haw, Dr. Karl Stierstdorfer, Dr. Herbert Bruder, Dr. Reiner Raupach, Dr. Lars Hofmann and Dr. Tobias Seyfarth (Siemens Medical Solutions) for their support and contributions to this work and to related clinical and technical studies.

This book aims to highlight that multi-slice cardiac CT has arrived in clinical practice and has the potential to become a reliable and widely available tool for non-invasive cardiac and coronary diagnosis in day-to-day patient care. With this second edition of the book "Multi-slice and Dual-source CT in Cardiac Imaging" we hope to make a valuable and significant contribution to the education of radiologists, cardiologists, technologists and physicists on this new, upcoming and exciting clinical tool, covering a broad spectrum from comprehensive overviews of the basics for newcomers to the introduction of new imaging protocols using the latest technology and new clinical applications for experienced users and researchers.

Forchheim, Beijing — Bernd M. Ohnesorge, Thomas G. Flohr

Munich — Christoph R. Becker, Andreas Knez, Maximilian F. Reiser

Deanfield JE, Mason RP, Nissen SE, Williams BW (2001) Coronary artery disease: from managing risk factors to treating complications. Clin Cardiol 24[Suppl I Intn'l]

Windecker S et al (1999) Interventional cardiology in Europe 1995. Eur Heart J 20:484–495

Scheffel H, Alkadhi H, Leschka S, et al (2006) Diagnostic accuracy of dual-source CT coronary angiography: first experience in a high pre-test probability population without heart rate control. Eur Radiol (in press)

Flohr T, McCollough C, Ohnesorge B, et al (2006) First performance evaluation of a dual source CT (DSCT) system. Eur Radiol 16:256–268

Contents

1 Introduction

Bernd Ohnesorge 1

1.1 **Basic Principles of CT Imaging** 1
1.2 **Established Imaging Modalities for Cardiac Imaging** 3
1.2.1 Invasive Imaging 3
1.2.2 Non-invasive Imaging 8
1.3 **Clinical Goals for CT in the Diagnosis of Cardiac and Thoracic Diseases** 11
1.3.1 Coronary Artery Disease 11
1.3.2 Other Cardiac Diseases 13
1.3.3 Diseases of the Thoracic Vessels 14
1.4 **The History and Evolution of CT in Cardiac Imaging** 14
1.4.1 Principles and Applications of Electron-Beam CT 14
1.4.2 Cardiac Imaging with Conventional Mechanical CT 17
References 20

2 Cardiac and Cardiothoracic Anatomy in CT

Roman Fischbach 23

2.1 **Topography** 23
2.2 **Standard Views** 24
2.3 **Coronary Arteries and Veins** 30
2.4 **Pericardium** 32
2.5 **Cardiac Chambers** 33
2.6 **Cardiac Valves** 34
2.7 **Great Vessels** 35
References 39

3 Multi-slice CT Technology

Thomas Flohr and Bernd Ohnesorge 41

3.1 **Evolution from 1 to 64 Slices** 41
3.2 **Principles of Multi-slice CT System Design** 45

3.3 **Multi-slice CT Acquisition and Reconstruction for Body Imaging** *52*
3.3.1 Definition of the Pitch 52
3.3.2 The Cone-Angle Problem in Multi-slice CT 53
3.3.3 Multi-slice Spiral Reconstruction Neglecting the Cone-Beam Geometry 54
3.3.4 Multi-slice Spiral Reconstruction with Cone-Beam Algorithms ... 58
References 67

4 Principles of Multi-slice Cardiac CT Imaging
Bernd Ohnesorge and Thomas Flohr 71

4.1 **Basic Performance Requirements for CT Imaging of the Heart** 71
4.2 **CT Imaging with Optimized Temporal Resolution: The Principle of Half-Scan Reconstruction** 73
4.3 **Prospectively ECG-Triggered Multi-slice CT** 76
4.4 **Retrospectively ECG-Gated Multi-slice CT** 79
4.4.1 Multi-slice Cardiac Spiral Reconstruction 81
4.4.2 ECG-Gated Multi-slice Spiral Acquisition 83
4.4.3 Segmented Cardiac Reconstruction Algorithms 88
4.4.4 Cardiac Cone-Beam Reconstruction Algorithms 97
4.4.5 ECG-Gated Spiral Scanning with Increased Volume Speed 101
4.5 **Synchronization with the ECG and Cardiac Motion** 106
4.5.1 ECG-Based Phase Selection 106
4.5.2 The Pros and Cons of ECG Gating and ECG Triggering 108
4.5.3 Alternative Cardiac-Motion Gating Approaches 110
4.6 **Radiation Exposure Considerations** 113
4.6.1 Principles of Radiation Dose Measurement in CT 113
4.6.2 Radiation Exposure for Selected Cardiac Examination Protocols .. 117
4.6.3 Exposure Reduction with ECG-Gated Tube-Current Modulation .. 119
4.6.4 Optimization for Different Patient Sizes 121
4.6.5 Optimization of Contrast-to-Noise Ratio 123
References 124

5 Clinical Examination Protocols with 4- to 64-Slice CT
Bernd Ohnesorge 127

5.1 **Quantification of Coronary Artery Calcification** 127
5.2 **CT Angiography of the Cardiac Anatomy and Coronary Arteries** 133
5.3 **Cardiac Function Imaging** 141
5.4 **Cardiothoracic Examination Protocols** 144
References 148

6 Image Visualization and Post-processing Techniques

Thomas Flohr and Bernd Ohnesorge 151

6.1 **Trans-axial Image Slices** 151
6.2 **Multi-planar Reformation** 153
6.3 **Maximum-Intensity Projection** 154
6.4 **Volume-Rendering Technique** 157
6.5 **Vessel Segmentation and Vessel Analysis** 162
6.6 **Four-Dimensional Visualization and Functional Parameter Assessment** 165
6.7 **Myocardial Perfusion Evaluation** 169
6.8 **Quantification of Coronary Calcification** 171
References 176

7 Clinical Indications

7.1 **Current and Future Clinical Potential**

Christoph Becker and Andreas Knez 179

7.1.1 Cardiac Multi-slice CT Technique 179
7.1.2 Coronary Calcium Screening 180
7.1.3 Coronary CT Angiography 182
7.1.4 Non-coronary Applications 189
References 190

7.2 **Risk Assessment with Coronary Artery Calcium Screening**

Roman Fischbach 192

7.2.1 Introduction 192
7.2.2 Methods of Coronary Artery Calcification Quantification 192
7.2.3 Multi-slice CT Examination Technique 195
7.2.4 Clinical Applications of Coronary Calcium Measurement 197
7.2.5 Further Clinical Applications of Calcium Scanning 200
7.2.6 Conclusion 202
References 203

7.3 **Detection and Exclusion of Coronary Artery Stenosis**

Koen Nieman, N. Mollet, F. Cademartiri, and F. de Feyter 205

7.3.1 Introduction 205
7.3.2 Diagnostic Performance of 4-Slice CT 205
7.3.3 Diagnostic Performance of 16-Slice CT 206
7.3.4 Diagnostic Performance of 64-Slice CT 207

7.3.5 Image Processing and Analysis 208
7.3.6 Discussion 208
References 212

7.4 **Assessment and Interpretation of Atherosclerotic Coronary Plaques**
Stephan Achenbach. 192

7.4.1 Clinical Background 214
7.4.2 Clinical Concepts 215
7.4.3 Visualization of Coronary Atherosclerotic Plaques 215
7.4.4 Visualization of Non-calcified Plaques by Multi-slice CT. 215
7.4.5 Perspective. 219
References 221

7.5 **Coronary CT Angiography in Patients with Chest Pain**
Axel Küttner and Stephen Schröder 224

7.5.1 Clinical Background 224
7.5.2 Methods and Protocols 225
7.5.3 Results in a Representative Patient Population. 226
7.5.4 Discussion 228
References 230

7.6 **Evaluation of Coronary Artery Bypass Grafts**
Axel Küttner and Andreas Kopp 232

7.6.1 Clinical Background 232
7.6.2 Protocol to Assess Graft Patency and Native Vessels with Multi-slice CT. 233
7.6.3 Results in a Representative Patient Population. 235
7.6.4 Conclusion. 237
References 238

7.7 **Patency Control of Coronary Stents**
Koen Nieman, N. Mollet, F. Candemartiry, and F. de Feyter. 239

7.7.1 Introduction 239
7.7.2 CT Imaging Characteristics of Stents 239
7.7.3 Post-processing and Analysis. 240
7.7.4 In Vivo Coronary Stent Imaging 241
7.7.5 Conclusion. 242
References 244

7.8 **Evaluation of the Coronary Anomaly, Fistula, Aneurysm, and Dissection**
Steffen Fröhner . . . 245

7.8.1 Introduction . . . 245
7.8.2 Anomalies of the Coronary Arteries . . . 245
7.8.3 Coronary Artery Fistulas . . . 246
7.8.4 Myocardial Bridges . . . 251
7.8.5 Coronary Aneurysms . . . 254
7.8.6 Coronary Dissection . . . 254
7.8.7 Coronary Vasculitis . . . 256
7.8.8 Conclusion . . . 256
References *256*

7.9 **Diagnosis of Congenital Heart Disease in Adults and Children**
Jean-François Paul . . . 258

7.9.1 Introduction . . . 258
7.9.2 Technical Aspects and Imaging Protocols . . . 258
7.9.3 Clinical Indications . . . 261
7.9.4 Improvements with 64-Slice CT . . . 263
7.9.5 Conclusion . . . 263
References . . . 265

7.10 **Evaluation of Ventricular Function Parameters**
Kai Uwe Jürgens and Roman Fischbach . . . 266

7.10.1 Introduction . . . 266
7.10.2 Determination of Cardiac Function Parameters with Multi-slice CT . . . 267
7.10.3 Data Acquisition and Image Reconstruction . . . 269
7.10.4 Image Analysis . . . 270
7.10.5 Limitations . . . 270
7.10.6 Clinical Considerations . . . 272
7.10.7 Summary and Outlook . . . 277
References . . . 279

7.11 **Imaging and Diagnosis of Cardiac Valves**
Jürgen Willmann . . . 281

7.11.1 Introduction . . . 281
7.11.2 Technical Considerations . . . 281
7.11.3 Valvular Morphology . . . 282
7.11.4 Valvular Disease . . . 283

7.11.5 Limitations 285
7.11.6 Conclusion 286
References 286

7.12 **Visualization of Cardiac Tumors and Masses**
Bernd Wintersperger 290

7.12.1 Introduction 288
7.12.2 Imaging Techniques 290
7.12.3 Epidemiology of Cardiac Masses and Clinical Application of CT . . 290
7.12.4 Conclusion 293
References 295

7.13 **Imaging of the Pulmonary Veins in Patients with Atrial Fibrillation**
Michael Poon and C. Learra 296

7.13.1 Introduction 296
7.13.2 Pharmacological Treatment Options 297
7.13.3 Non-pharmacological Treatment of Atrial Fibrillation: Catheter Ablation 298
7.13.4 The Role of Imaging in the Era of Catheter Ablation of the Pulmonary Veins 299
7.13.5 Multi-slice CT Imaging of the Pulmonary Veins and Left Atrium 299
7.13.6 The Role of Multi-slice CT in Catheter Ablation of Afib 302
7.13.7 Conclusions 303
References 305

7.14 **Potential of Myocardial Perfusion and Viability Studies**
Konstantin Nikolaou and Bernd Wintersperger 307

7.14.1 Introduction 307
7.14.2 Principles of Myocardial Perfusion Assessment 307
7.14.3 Technical Considerations of Multi-slice CT 308
7.14.4 Study Data on Myocardial Perfusion Imaging Using Multi-slice CT 308
7.14.5 Assessment of Myocardial Viability with Multi-Slice CT 310
7.14.6 Conclusion 313
References 315

7.15 **Cardiothoracic Multi-Slice CT in the Emergency Department**
Uwe-Joseph Schöpf 317

7.15.1 ECG-Gated Multi-Slice CT Scanning of the Chest 317

7.15.2 Patients with Equivocal Chest Pain in the Emergency Department . . . 320
7.15.3 64-Slice CT as a Triage Tool in the Emergency Department . . . 320
References . . . 324

8 Future Technical Developments in Cardiac CT
Bernd Ohnesorge . . . 327

8.1 **Limitations and Pitfalls with Today's Multi-slice CT** . . . 327
8.1.1 Temporal Resolution . . . 327
8.1.2 Volume Coverage . . . 328
8.1.3 Spatial Resolution and Signal-to-Noise Ratio . . . 329
8.1.4 Radiation Exposure . . . 331
8.2 **A Future for Electron-Beam CT?** . . . 332
8.3 **Future Possibilities with Area Detector CT** . . . 334
8.4 **New Frontiers with Dual-Source CT** . . . 335
8.4.1 Dual-Source CT: System Concept and Design . . . 338
8.4.2 Dual-Source CT: Cardiac Scanning Principles and Techniques . . . 339
8.4.3 Dual-Source CT: System Performance Evaluation . . . 342
8.4.4 Dual-Source CT: Clinical Scan Protocols and Preliminary Clinical Results . . . 347
References . . . 357

Subject Index . . . 359

Contributors

Stephan Achenbach, MD
University of Erlangen
Medizinische Klinik II mit Poliklinik,
Abteilung für Klinische Kardiologie
Ulmenweg 18
91054 Erlangen, Germany

F. Cademartiri, MD
Erasmus Medical Center
Thoraxcenter
Department of Radiology
Dr. Molewaterplein 40
3015 GD Rotterdam, The Netherlands

P. De Feyter, MD
Erasmus Medical Center
Thoraxcenter
Department of Radiology
Dr. Molewaterplein 40
3015 GD Rotterdam, The Netherlands

Roman Fischbach, MD
University of Münster
Institut für Klinische Radiologie
Röntgendiagnostik
Albert-Schweitzer-Str. 33
48149 Münster, Germany

Steffen Fröhner, MD
Rhön Klinkum Bad Neustadt
Herz- und Gefäßklinik Bad Neustadt
Institut für Diagnostische und
Interventionelle Radiologie
Salzburger Leite 1
97616 Bad Neustadt/Saale, Germany

Kai Uwe Jürgens, MD
University of Münster
Institut für Klinische Radiologie
Röntgendiagnostik
Albert-Schweitzer-Str. 33
48149 Münster, Germany

Andreas Kopp, MD
University of Tübingen
Abt. für Radioloogische Diagnostik
Hoppe-Seyler-Str. 9
72076 Tübingen, Germany

Axel Küttner, MD
University of Erlangen
Abteilung für Klinische Radiologie
Ulmenweg 18
91054 Erlangen, Germany

C. Learra, MD
Mount Sinai School of Medicine,
Department of Cardiology
1 Gustave L. Levy Place
New York, 10029
USA

N. Mollet, MD
Erasmus Medical Center
Thoraxcenter
Department of Radiology
Dr. Molewaterplein 40
3015 GD Rotterdam, The Netherlands

Koen Nieman, MD
Erasmus Medical Center
Thoraxcenter
Department of Radiology
Dr. Molewaterplein 40
3015 GD Rotterdam, The Netherlands

Konstantin Nikolaou, MD
University of Munich, Klinikum Grosshadern
Marchioninistrasse 15
81377 München, Germany

Jean-François Paul, MD
Hôpital Marie-Lannelongue, Paris
Centre Chirurgical Marie Lannelongue
133, avenue de la Résistance
92350 Le Plessis Robinson, France

Michael Poon, MD
Cabrini Hospital, Cabrini Medical Center
227 East 19th Street
New York, NY 10003, USA
and
Mount Sinai School of Medicine
Department of Cardiology
1 Gustave L. Levy Place
New York, 10029, USA

Uwe-Joseph Schöpf, MD
Medical University of South Carolina, Charleston
169 Ashley Avenue
Charleston, SC 29425, USA

Stephen Schröder, MD
University of Tübingen
Abt. für Klinische Kardiologie
Hoppe-Seyler-Str. 9
72076 Tübingen, Germany

Jürgen Willmann, MD
University Hospital Zürich
Institute of Diagnostic Radiology
Rämistrasse 100
8091 Zürich, Switzerland

Bernd Wintersperger, MD
University of Munich, Klinikum Grosshadern
Institut für Klinische Radiologie
Marchioninistrasse 15
81377 München, Germany

Introduction

1

Bernd Ohnesorge

Contents

1.1 **Basic Principles of CT Imaging** *1*
1.2 **Established Imaging Modalities for Cardiac Imaging** *3*
1.2.1 Invasive Imaging *3*
1.2.2 Non-invasive Imaging *8*
1.3 **Clinical Goals for CT in the Diagnosis of Cardiac and Thoracic Diseases** *11*
1.3.1 Coronary Artery Disease *11*
1.3.2 Other Cardiac Diseases *13*
1.3.3 Diseases of the Thoracic Vessels *14*
1.4 **The History and Evolution of CT in Cardiac Imaging** *14*
1.4.1 Principles and Applications of Electron-Beam CT *14*
1.4.2 Cardiac Imaging with Conventional Mechanical CT *17*
References *20*

1.1 Basic Principles of CT Imaging

In 1979, G. Hounsfield and A.M. Cormack received the Nobel Prize for their significant contributions to the development of computed axial tomography. Using computer reconstruction techniques, Hounsfield demonstrated that the internal structures of an object could be reconstructed based on the attenuation pattern of an X-ray beam that had passed through the object at different angles. In 1971, Hounsfield had constructed the first CT scanner that could image the brain (Hounsfield 1972). Cormack's contribution was the development of fast signal-processing algorithms that allowed for computer-based CT image reconstruction according to the mathematical fundaments published by Johann Radon in 1917. The first commercially available CT scanners were introduced in 1972 for brain imaging and in 1974 for body imaging (Fig. 1.1).

The basic principles in the acquisition of cross-sectional image slices with newer single-slice CT scanners are shown in Figures 1.2 and 1.3. X-rays emitted by the X-ray source in the form of a fan beam pass through the cross-section of the patient, who is located within the scan field of view (Fig. 1.2). The patient's anatomical structures attenuate these X-rays before they are registered by a detector array, which typically consists of 500–1000 detector elements in a row, located on the opposite side. Each of the detector elements measures the X-ray intensity of an attenuated ray that has passed through the object. The electrical intensity signals from the detector are converted by analog-digital converters (ADC) into digital data, which are fed into a computer. These intensity signals (I) are transformed using an "absorption equation" (Eq. 1.1) into attenuation values for each detector element and for every angular position of the X-ray source.

$$\ln\left(\frac{I}{I_0}\right) = -\int_L \mu(x,y)\,dl \qquad (1.1)$$

In Eq. (1.1), I_0 represents the intensity of the unattenuated X-ray either in air or before entering the object.The natural logarithm (ln) of the ratio (I/I_0) is equivalent to the accumulation of the X-ray attenuation coefficients along a line through the object that is determined by the path of the X-ray. The integration path (L) corresponds to the path of the X-ray through the two-dimensional X-ray absorption distribution $\mu(x, y)$ of the object, while x and y represent the spatial coordinates within the image plane (Fig. 1.2). The attenuation values of all detector ele-

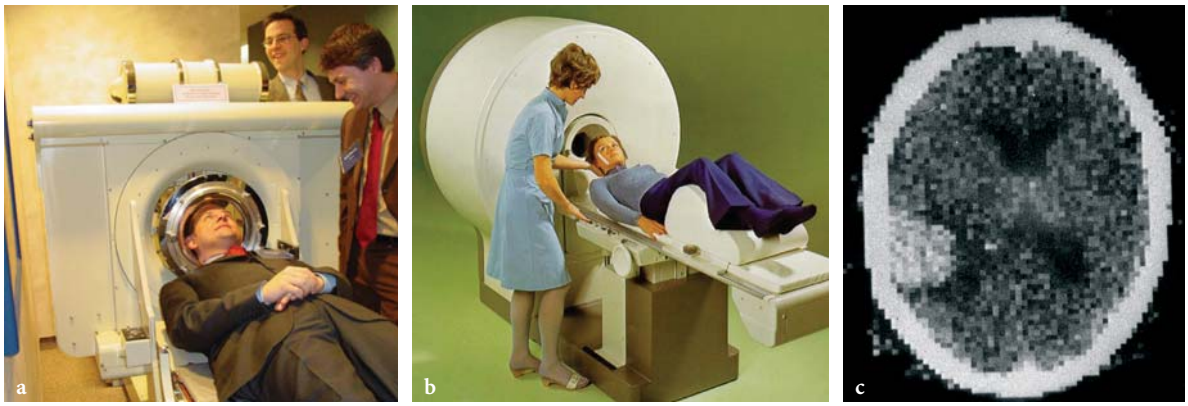

Fig. 1.1a–c. The first clinical CT scanners were introduced in 1972. **a** One of the earliest scanners, constructed by G. Hounsfield, can still be seen at the Mayo Clinic in Rochester, Minnesota (USA). **b, c** The first commercial CT scanners dedicated to brain imaging (e.g., Siemens Siretom, 1974) were able to acquire images of the brain with an image matrix of 64×64 pixels in 7 min scan time per slice

ments of the detector array generate an attenuation profile of the object for a considered angular position of the X-ray source and the detector array. This attenuation profile is called a "projection".

A large number of different projections (~1000–2000 per rotation) are generated by continuous mechanical movement of both the X-ray tube and the detector array around the patient (Fig. 1.2). These projection data serve as the basis for computation of the X-ray attenuation distribution of the patient's morphology in the cross-section representing the image slice (Kak and Slaney 1984). Most modern reconstruction techniques use "filtered back-projection" algorithms for reconstruction of transaxial slices based on parallel-beam geometry (Kak and Slaney 1988). This requires numerical transformation of the acquired fan-beam projection data into parallel-beam projections prior to image reconstruction (Fig. 1.3). During filtered back-projection, the "reconstruction kernel" represents a high-pass filter for the projections and it determines both sharpness and noise appearance within the image plane.

The reconstructed cross-sectional image slices are represented by a pixel matrix (usually 512×512 pixels), with each pixel representing the X-ray attenuation coefficient of the underlying anatomy. The X-ray attenuation coefficients of each pixel are transformed into Hounsfield units (HUs) (Fig. 1.2), ranging from –1024 to 3071, and these serve as the basis for displaying the images in either gray-scale or color-scale.

$$HU(x,y) = 1000 \cdot \frac{\mu(x,y) - \mu_{water}}{\mu_{water}} \qquad (1.2)$$

In Eq. (1.2), μ_{water} represents the X-ray attenuation coefficient of water. Typical HU values of usual anatomical structures are: –1000 HU for air, –100 to –50 HU for fatty tissue, 0 HU for water, 30–70 HU for blood and muscle tissue, 130–500 HU for calcifications, 200–500 HU for contrast-enhanced blood, and 500–1500 HU for bone (Fig. 1.4). The width of the individual detector elements, the size of the focal spot, and the number of projections per rotation determine the spatial resolution in the image plane. The thickness of the fan beam in the patient's longitudinal direction determines the slice-thickness and thus the spatial resolution in the longitudinal direction. The detector array of conventional CT scanners usually generates only one slice per rotation, as the detector supports only one row of detector elements. Modern CT scanners, called multi-slice CT scanners, are equipped with detector arrays consisting of parallel detector rows that are adjacent in the longitudinal direction and thus have the capability of acquiring multiple slices and a larger amount of object volume in one rotation.

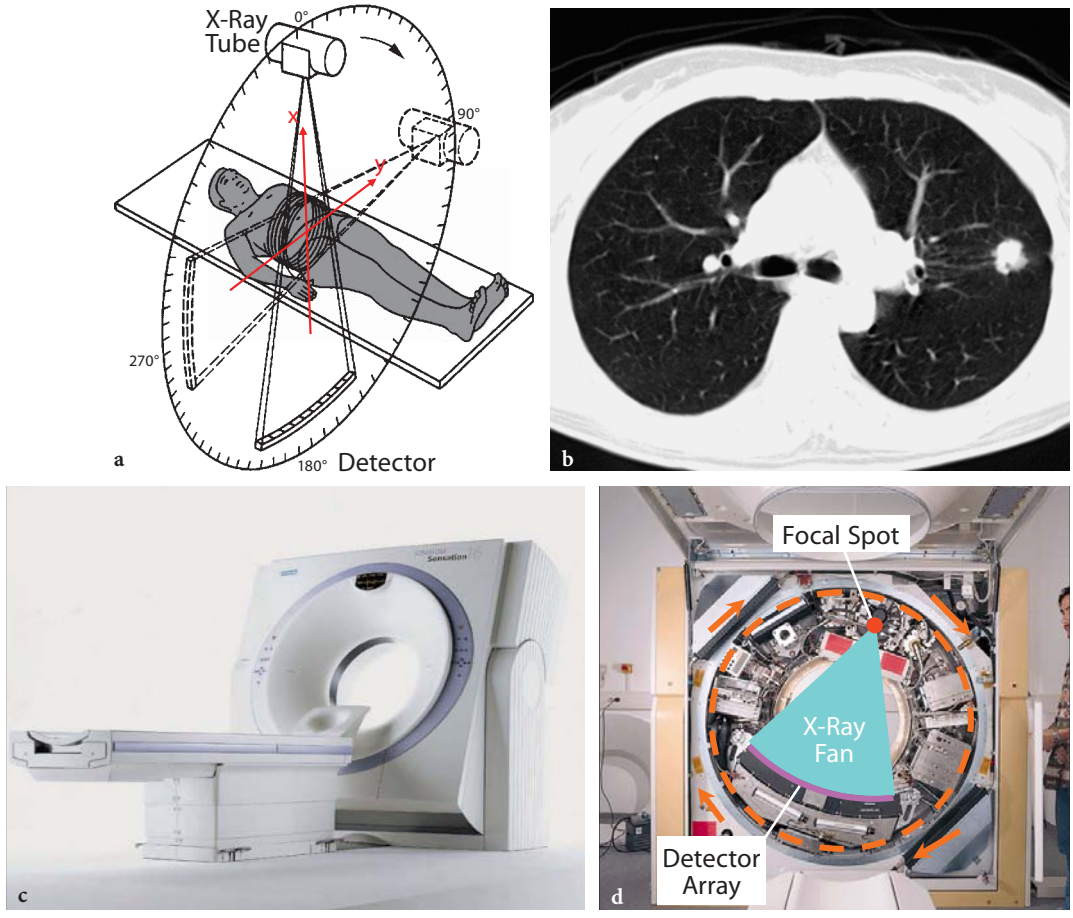

Fig. 1.2a–d. **a** X-rays emitted by the X-ray tube in the form of a fan beam pass through the cross-section of the patient, who is located within the scan field of view. The image plane is defined with the two spatial coordinates x and y. **b** Projections are acquired from 1000–2000 different positions of the X-ray source to construct a cross-sectional image of the scanned anatomy, e.g., of the chest. Within the chest, the lung tissue, which has low attenuation, is displayed in dark shades; the bronchi, mediastinum, lung lesions, and the ribs have high attenuation and appear as bright areas. Within the CT system (**c**), the tube and detector are mounted on a fast-rotating mechanical system, called a gantry (**d**)

1.2 Established Imaging Modalities for Cardiac Imaging

Various invasive and non-invasive imaging techniques are in use for cardiac diagnosis, with the goal of visualizing the anatomical structures of the heart (Fig. 1.5) and obtaining information about cardiac function by means of monitoring cardiac motion and the blood supply of the heart muscles. The potential role of CT imaging as a new modality in the management of patients with known or suspected cardiac disease derives from limitations in the clinical application of techniques that are currently established in clinical routine and their shortcomings in terms of economic efficacy.

1.2.1 Invasive Imaging

Selective coronary angiography (CA) is considered to be the gold standard in the diagnosis of the coro-

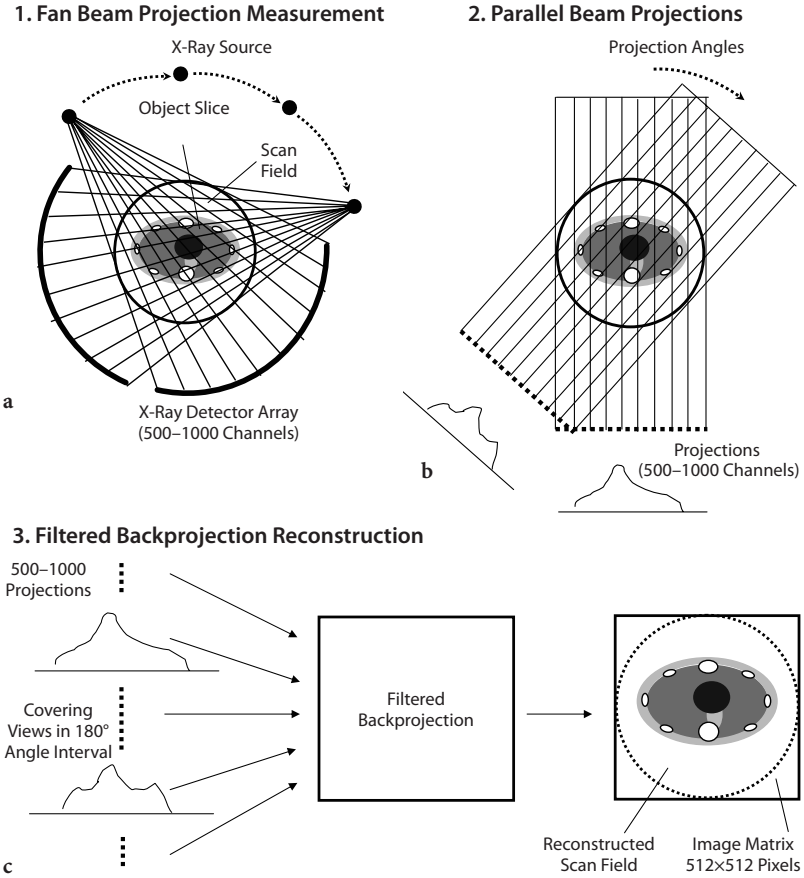

Fig. 1.3a–c. Fan-beam projections typically consist of 500–1000 individual data points that belong to individual ray projections. **a** A large number of fan-beam projections are generated for different angular positions of the measurement system, which consists of an X-ray source and an X-ray detector array. **b** For most reconstruction algorithms, the measured fan-beam projections are rearranged to parallel-beam projections by 2-dimensional interpolation algorithms. The minimum acquisition time per slice is achieved using only 180° of parallel-beam projections (typically 500–1000 parallel beam projections per 180°), which is the minimum number of projections required for reconstruction of the slice. **c** Final computation of the slice is done using a so-called back-projection of the filtered parallel-beam projections

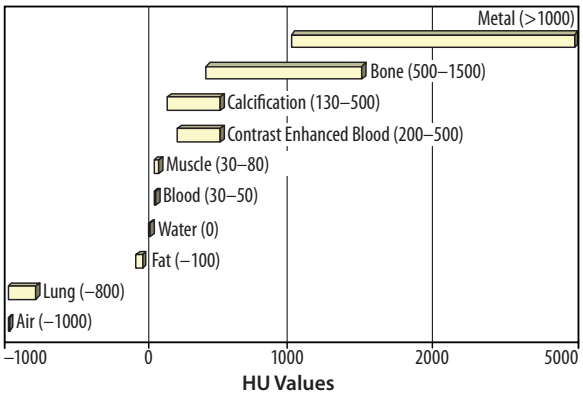

Fig. 1.4. Typical attenuation values of body structures and other objects, measured in Hounsfield units (HUs)

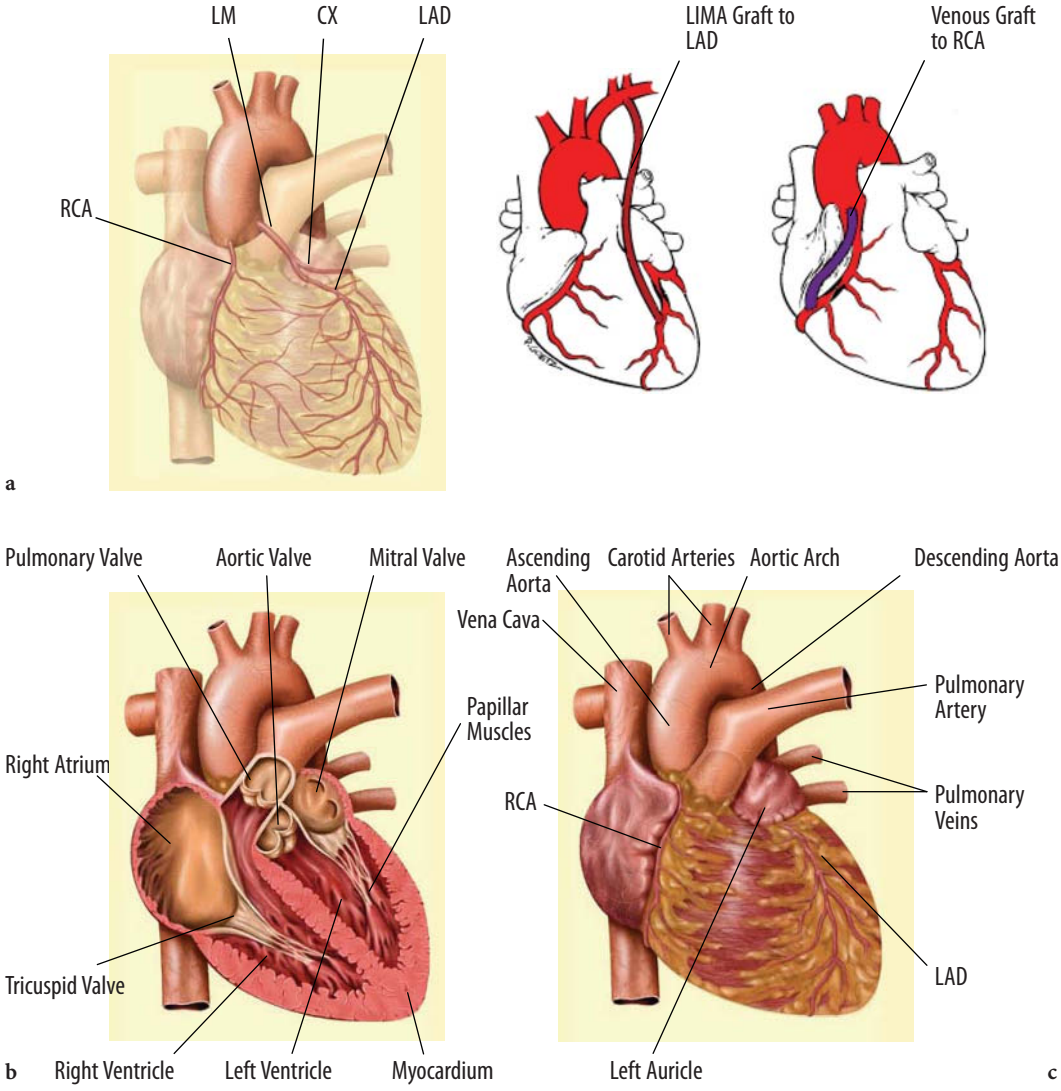

Fig. 1.5. a The coronary artery tree and the coronary segments according to AHA nomenclature: left main trunk (LM, AHA segment 5), left anterior descending (LAD, 6–10), circumflex (CX, 11–12), and right (RCA, 1–4) coronary arteries. A venous coronary bypass graft that originates from the ascending aorta supplies the peripheral LAD. Also shown is the general cardiac morphology, including the cardiac chambers and the cardiac valves (**b**), and the great thoracic vessels: ascending, transversal, and descending aorta and the pulmonary vessels (**c**). (Illustrations kindly provided by BayerVital AG, Leverkusen, Germany: www.cardio.bayer.com)

nary artery lumen. A catheter is inserted into the arterial system through a peripheral artery (Judkins technique) and moved along the aorta into the origins of the coronary arteries. Contrast agent is then administered through the catheter into the coronary arteries and its distribution is imaged in several views with planar X-ray technique in order to identify narrowing of the vessel lumen. The maximum resolution that can be achieved in 2D projections is about 0.15 mm, with a temporal resolution of about 20 ms (Fig. 1.6). Advanced image-analysis tools employ quantitative coronary analysis (QCA) to provide quantitative information regarding narrowing of the coronary artery lumen (Fig. 1.7). Basic cardiac function parameters (i.e., ejection fraction) and the size of the ventricle during diastole and systole can be derived after the administration of contrast agent into the ventricle. For patients with suspected coronary artery disease (CAD), the diagnostic procedure can be combined with PTCA or insertion of a stent in the same session. Although evaluation of the vessel wall and of coronary plaques is not possible, CA is currently the standard technique to detect and evaluate coronary artery stenosis and is the basis for decision-making regarding further work-up. Recent technological advances in CA using the bi-plane technique and flat-panel detectors have contributed to further enhancing image quality and performance. For example, the newest catheter angiography systems provide 3D modeling of the coronary arteries based on simultaneous acquisition of two projections of the same artery (Fig. 1.8). However, the invasiveness, with its subsequent complications (Harrison 1995), the considerable amount of X-ray radiation (3–6 mSv on average) (Leung 1996), and the fact that hospitalization of the patient is usually required are persisting limitations of CA. In addition, CA-related complications include myocardial infarction, stroke, and peripheral embolism, with a risk that is estimated to be below 1% (Rees 2004). Therefore, there is great interest in exploring new, non-invasive imaging modalities with less X-ray radiation, less direct interaction of the physician, and less hospital time for the patient.

Evaluation of the vessel wall and of atherosclerotic plaques has become feasible with the advent of intravascular ultrasound (IVUS) (Ziada 1999). IVUS of the coronary arteries allows assessment of the lumen diameter and the dimension of the plaque (Nair 2002). Plaque morphology can be evaluated in terms of lipid content and the presence of fibrous and calcified material (Fig. 1.9). However, IVUS has not yet been established as a clinically routine tool because of its high degree of invasiveness, restriction to proximal coronary segments, and high costs.

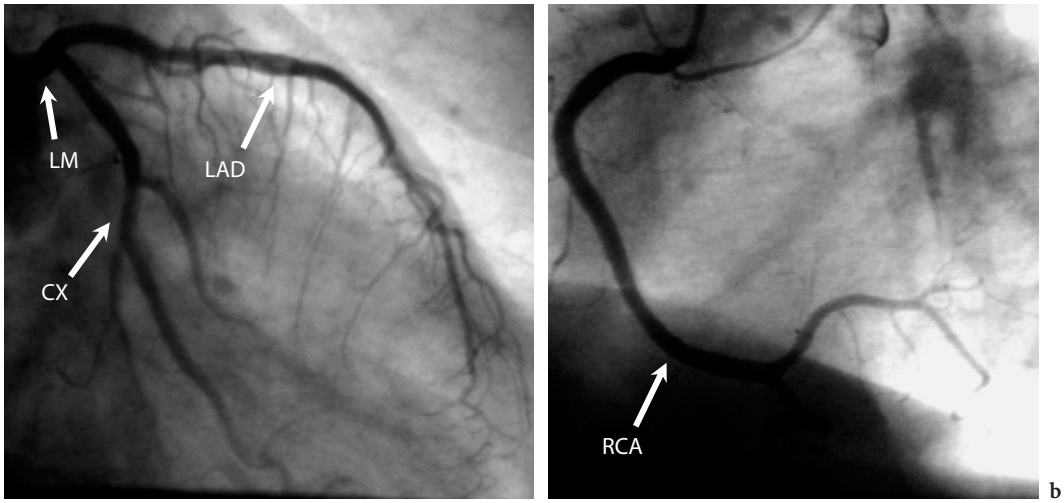

Fig. 1.6a, b. Selective coronary angiography in two planes. **a** Left coronary tree (*LM, LAD, CX*) in a RAO/30-view and **b** *RCA* in RAO/30-view. (Images courtesy of Klinikum Grosshadern, Munich, Germany)

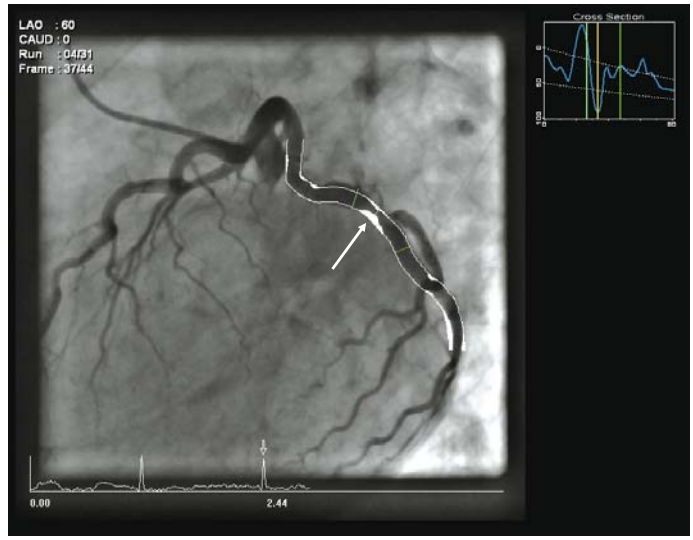

Fig. 1.7. Selective coronary angiography: the left coronary tree (*LM, LAD, CX*) in LAO/60-view. Quantitative coronary analysis (QCA) reveals a high-grade stenosis in the CX coronary artery (*arrow*). (Images courtesy of the Department of Cardiology, University Hospital Münster, Germany)

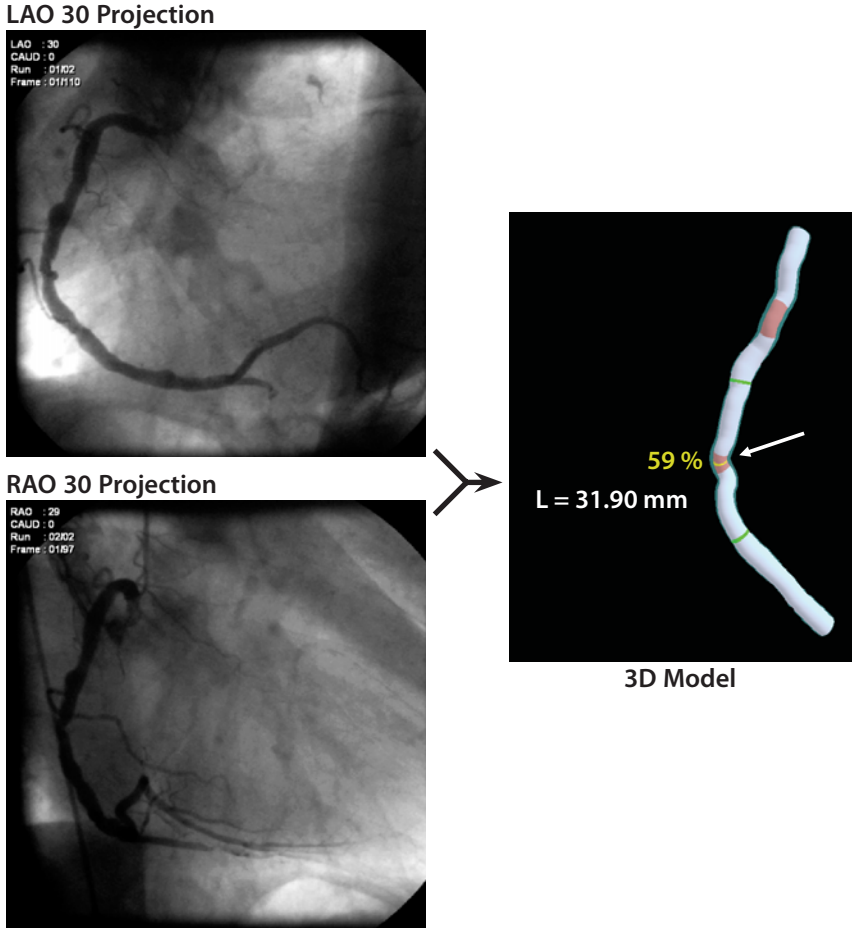

Fig. 1.8. Selective coronary angiography of the RCA. A 3D model was produced based on two simultaneously generated projections in LAD/30-view and RAO/30-view. The model reveals a 50% stenosis in the RCA (*arrow*) that could not be clearly depicted in 2D projections. (Images courtesy of the Department of Cardiology, University Hospital Münster, Germany)

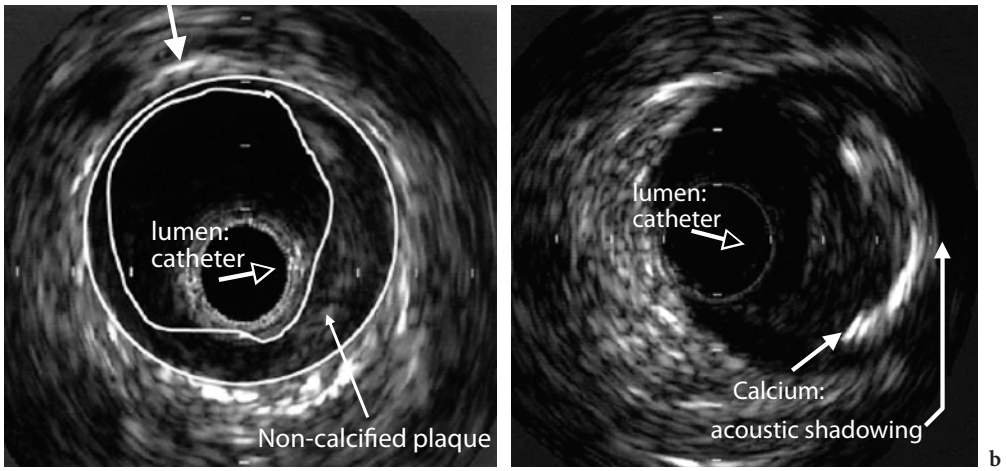

Fig. 1.9a, b. Cross-sectional intravascular ultrasound (IVUS) images of a left coronary artery showing non-calcified atherosclerotic wall change (**a**) and a calcified plaque causing elimination of the ultrasound signal (**b**). (Images courtesy of Klinikum Grosshadern, Munich, Germany)

1.2.2 Non-invasive Imaging

The non-invasive cardiac imaging tools routinely employed today are echocardiography, nuclear imaging, and magnetic resonance imaging.

Echocardiography (cardiac ultrasound) is used to assess the shape and thickness of the cardiac walls and heart valves. Cardiac function can be evaluated in terms of wall motion, and cardiac blood flow assessment is possible with Doppler sonography techniques. The presence of atherosclerotic disease can be determined in the carotid arteries and great thoracic vessels; however, imaging of the coronary arteries and detection of coronary plaques and stenosis is not yet possible.

Nuclear imaging is used to evaluate cardiac function, myocardial perfusion, and myocardial viability. Single photon emission CT (SPECT) uses the radioactive γ-isotope thallium-201 to mark areas of normal and reduced perfusion in the myocardium. Positron emission tomography (PET) uses β-isotopes to depict areas of normal and reduced metabolism in order to identify and differentiate viable and necrotic myocardium. To date, nuclear imaging techniques are restricted to functional and perfusion information and cannot be used to assess cardiac and coronary artery morphology (Fig. 1.10). With the development of new high-resolution detectors and radionuclides, PET may also become useful in the identification of plaques in larger vessels. The combination of CT technology with PET or SPECT can potentially provide information regarding cardiac morphology and function with one non-invasive imaging modality. These new approaches have been the focus of growing interest in the fields of radiology and cardiology and will be addressed elsewhere in this volume.

Magnetic resonance imaging (MRI) is routinely used for neuro-imaging, body imaging, and non-invasive diagnosis of the vascular system. The capabilities of MRI in the different areas of cardiac diagnosis have been studied intensively throughout the last 20 years (Crooks 1984; Higgins 1989; Kim 2001). Dedicated scan sequences have been developed for ECG-correlated imaging, and the high temporal resolution, down to 20–50 ms, allows for true 4D imaging of the heart. MRI is increasingly being used to evaluate cardiac morphology, cardiac function, myocardial perfusion, and myocardial viability (Figs. 1.11, 1.12) (Kim 2004). Initial studies have shown very promising results in the practicability of

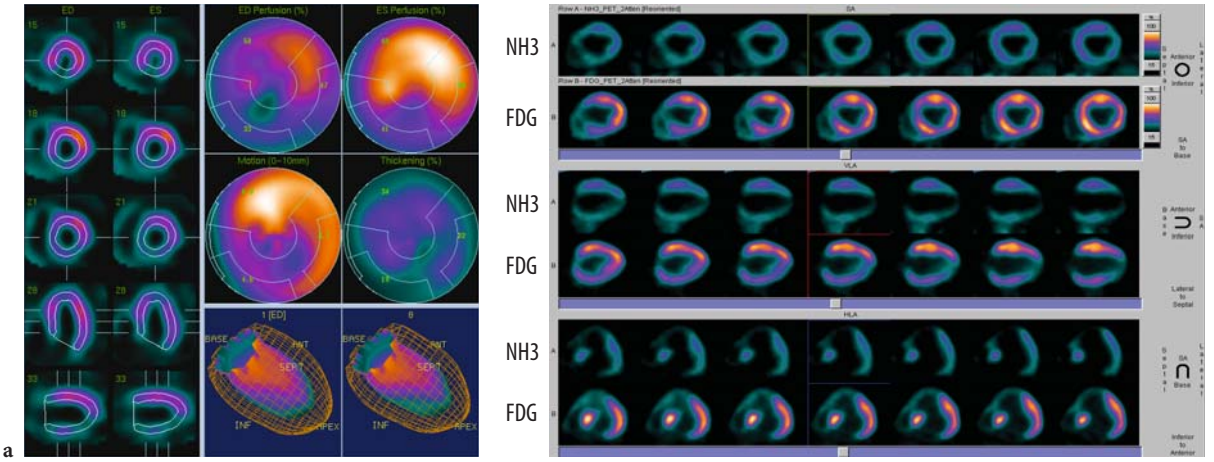

Fig. 1.10. a Cardiac SPECT study displayed in short-axis view, long-axis view, bulls-eye plot, and 3D model reveals an inferio-apical infarction with moderate peri-infarct ischemia. **b** Cardiac PET study with FDG and NH3 tracer radionuclides demonstrates a myocardial infraction of the posterior wall with a large area of necrotic myocardium. (Images courtesy of: **a** Page-Campbell Cardiology, Nashville, USA and **b** Cleveland Clinic Foundation, USA)

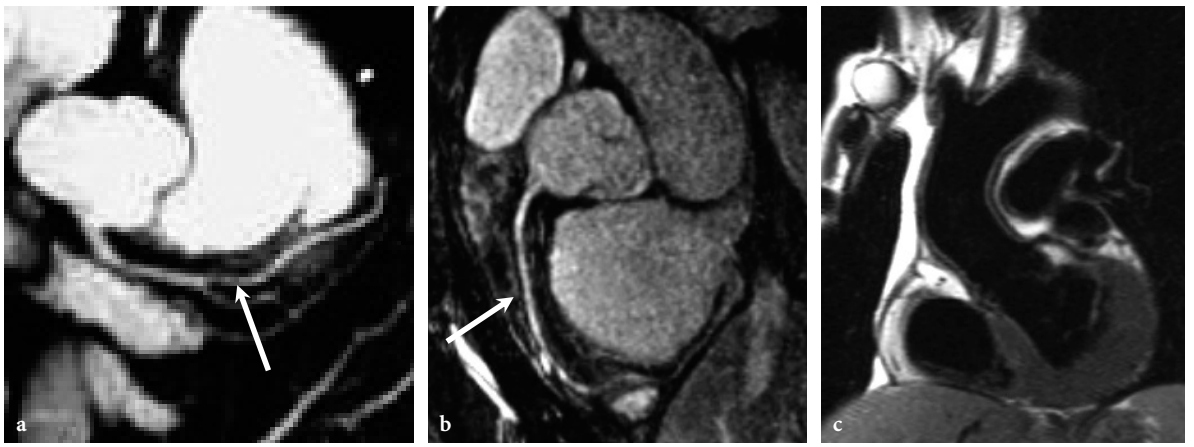

Fig. 1.11. Cardiac MRI of the left coronary artery (LCA) (**a**) and RCA (**b**) with 2D-breath-hold bright-blood technique (**c**) and of the general cardiac morphology, showing arteritis in the ascending aorta, with the TRUE-FISP black-blood technique. (Images courtesy of the MRI division, Siemens, Erlangen, Germany)

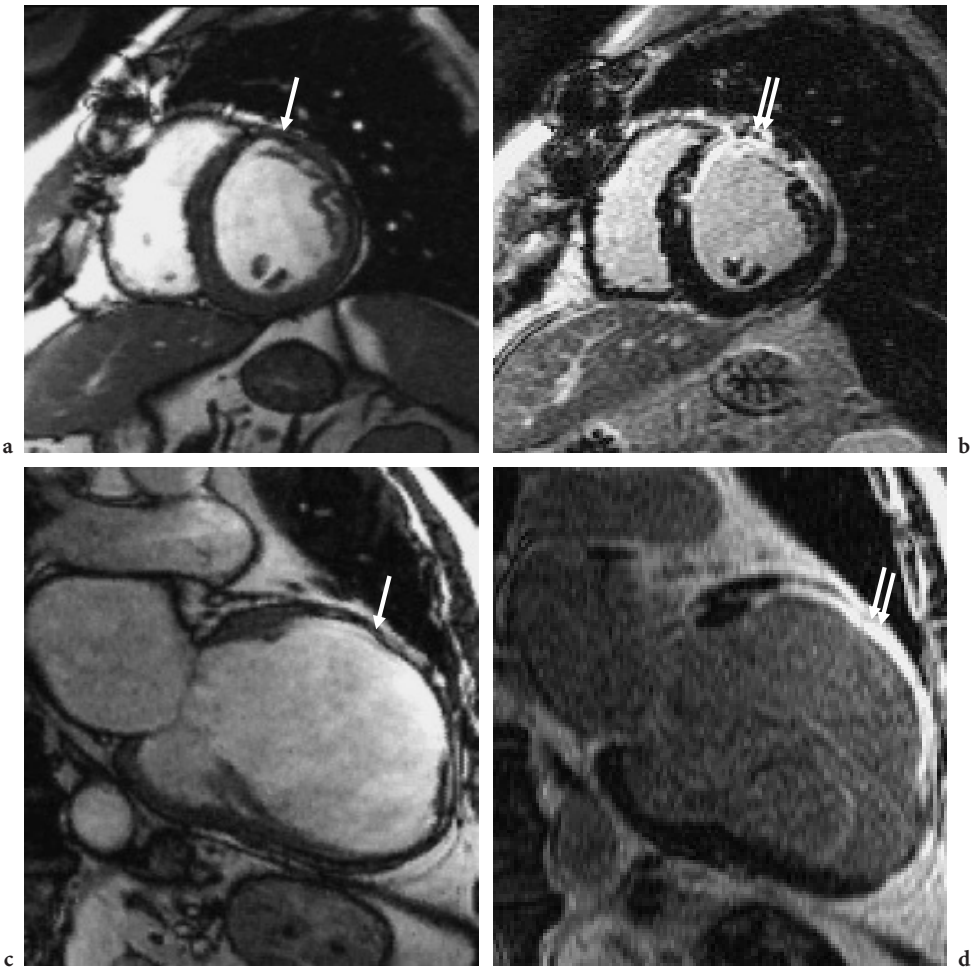

Fig. 1.12. a, b TRUE-FISP cine and **c, d** delayed enhancement studies of a patient after myocardial infarction, as visualized in short-axis (**a, c**) and long-axis (**b, d**) views. The cine study clearly demonstrates thinning of the myocardium (*arrow*), while the delayed enhancement study reveals strong enhancement, which indicates infarcted tissue that will likely not benefit from revascularization (*double arrow*). (Images courtesy of the MRI division, Siemens, Erlangen, Germany)

MRI for monitoring coronary artery stenosis (Post 1996) and coronary bypass grafts (White 1988; Wintersperger 1998). However, the 3D spatial resolution that can be achieved within reasonable examination times with today's technology does not yet allow for reliable evaluation of the coronary arteries (Wielopolski 1998; Kim 2001). The development of new contrast agents together with on-going improvements in MRI technology may fill this gap within a few years. Theoretically, MRI shows advantages over CT, as no radiation exposure is required, very good resolution of soft tissue in atherosclerotic plaques can be achieved (Halliburton 1996; Fayad 2000; Corti 2002), and evaluation of dynamic processes is possible. Nonetheless, the long overall examination times and the shortcomings of MRI with respect to the spatial resolution needed to evaluate the coronary arteries have limited the application of MRI technology in the management of patients with suspected coronary disease.

1.3 Clinical Goals for CT in the Diagnosis of Cardiac and Thoracic Diseases

General-purpose CT imaging is frequently used for non-invasive angiographic diagnosis of abdominal, thoracic, cerebral, and peripheral vessels, i.e., where image quality is not substantially influenced by cardiac motion or vessel pulsation. Dedicated cardiac CT acquisition techniques are needed for the diagnosis of cardiac and cardiovascular diseases where extensive cardiac motion is present. Here, the major fields of interest are the diagnosis of: (1) cardiac pathology, with special focus on coronary artery disease, and (2) thoracic vessel segments that show substantial pulsation.

1.3.1 Coronary Artery Disease

The coronary arteries are small vessels, with a lumen diameter of ≤4 mm. They originate from the ascending aorta and cover the heart with a complex 3D shape to supply the myocardium with blood and oxygen (Fig. 1.5a). The close proximity of the coronary arteries to the heart muscles results in their strong movement during the cardiac cycle. Thus, CT imaging of the coronary arteries, including the vessel walls, requires maximum performance in terms of 3D spatial resolution and temporal resolution. Diseases of the coronary arteries present as a reduction of blood supply to the heart muscle, which affects its function. Therefore, dedicated cardiac CT acquisition protocols are needed that eliminate cardiac motion in order to facilitate the diagnosis of cardiac morphology and to visualize heart function during different phases of the cardiac cycle.

In western societies, CAD is one of the leading causes of death, accounting for about 20% of all deaths in Germany (Loewel 1999) and 25% of all deaths in USA (Jones and Eaton 1994). About 50% of CAD patients die after an acute myocardial infarction without prior symptoms (Anzai 1994). The main risk factors to develop CAD are age, sex (men are at higher risk than women), high blood pressure, high blood lipid level, smoking, diabetes, overweight, family history, lack of exercise, and mental stress (Assmann 1999). CAD is the symptomatic presentation of coronary atherosclerosis, which causes narrowing of the coronary vessel lumen by the adherence of lipid-rich, fibrous, or calcified plaques to the vascular walls. The reduction in blood and oxygen supply causes ischemia in the myocardium. The patient perceives this as an attack of chest pain (angina pectoris) and, in advanced stages, as acute myocardial infarction, with necrotic changes of the heart muscle if the coronary vessels are severely obstructed or totally occluded.

The pathological process of developing atherosclerosis is most likely triggered by injury of the endothelial cells, leading to an inflammatory reaction and deposits of fat on the surface of the intima (Wyngaarden 1996). Due to the accumulation of defense cells, smooth muscle cells, and deposits of fat, the atherosclerotic plaque continuously grows. In its later stages, atherosclerosis may be characterized by lipid plaques with extracellular lipid and a fibrous cap, fibrous plaques, calcified plaques, and complex thrombotic lesions subsequent to rupture (Stary 1995). Fibrous plaques, calcified plaques, and complex lesions may cause substantial stenosis of the coronary arteries, leading to ischemia and reduced function of the heart muscle. By contrast, lipid plaques are usually non-stenotic, but they may rupture (Pasterkamp 2000) and form a thrombotic occlusion, resulting in an immediate coronary event (Fig. 1.13).

Significant coronary stenosis can be treated with interventional procedures. During percutaneous transluminal coronary angioplasty (PTCA), the stenosis is dilated via an inflatable balloon that is inserted into the coronary artery through a catheter. In addition, metal stents can be inserted during dilation to maintain patency, thus reducing the risk of restenosis. Alternatively, a stenosis can be bridged via coronary bypass surgery. In this procedure, a peripheral leg vein is removed and connected proximally to the ascending aorta (venous graft) and distally to the affected coronary artery beyond the obstruction. The internal mammary artery is employed for arterial bypass grafts (IMA grafts). The grafts are connected to the coronary bed distal to the site of the narrowed lumen to allow blood flow into the undersupplied area downstream.

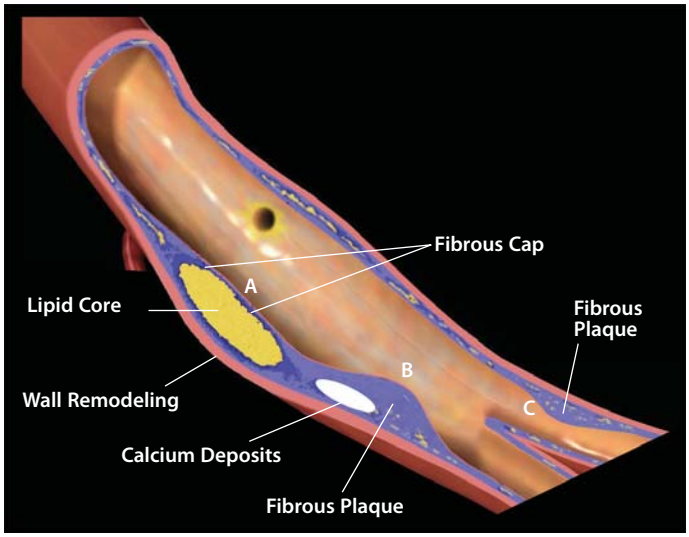

Fig. 1.13. The different compositions of coronary atherosclerotic plaques: (*A*) non-stenotic non-calcified lesion with large lipid core, thin fibrous cap, and remodeling of the wall, which makes it prone to rupture; (*B*) stenotic stable fibrous lesion with calcified deposit; (*C*) stenotic stable fibrous lesion

The goal of CAD diagnosis with non-invasive CT imaging is to identify the location and degree of coronary stenosis, both of which may be hemodynamically relevant in terms of perfusion and viability of the myocardium, cardiac function, and coronary blood flow. Moreover, beyond the assessment of the coronary lumen, evaluation of the vessel walls and atherosclerotic plaques (i.e., identification of rupture-prone lipid plaques) may offer very important information about the prognosis of the patient, with possible consequences for treatment. It has been demonstrated that the majority of acute coronary events occur at the site of angiographically non-significant lesions (Virmani 2000; Deanfield 2001). In addition, the presence of atherosclerotic plaque does not necessarily correspond to lumen narrowing due to remodeling mechanisms of the vessel wall (Glagov 1987). The use of non-invasive imaging to identify "vulnerable patients" in the intermediate risk group has been proposed by a leading international expert panel and the American Association for Eradication of Heart Attack (Naghavi 2003). Analysis of atherosclerotic plaques, however, requires a high-performance imaging system in order to distinguish slight density differences in small lesions. Non-invasive CT imaging may also be very useful for follow-up diagnosis after PTCA, stenting, or bypass surgery, as it allows the early detection of occlusion and restenosis.

Electron-beam CT (EBCT) and CT have proven to be very sensitive methods for detecting sites of coronary artery calcification (Agatston 1990; Shemesh 1995; Becker 1999), which are markers of coronary atherosclerosis. The finding of such sites confirms the presence of atherosclerosis; and indeed, the amount of coronary calcium has been shown to correlate with both the presence of risk factors of CAD (Wong 1995) and the total burden of atherosclerotic plaque (O'Rouke 2000). Both EBCT and CT may thus be useful in assessing the presence of obstructive CAD and the probability of an individual being at risk to eventually suffer a myocardial event. Although the absence of coronary calcium is a strong indicator for the absence of obstructive CAD, the presence of coronary calcification does not necessarily correlate with the presence of obstructive CAD (O'Rouke 2000). Thus, a role for coronary calcium measurements in the prediction and diagnosis of CAD has yet to be proven and it remains controversially discussed in the scientific community (Wexler 1996; O'Rouke 2000). However, measurement of coronary calcification to detect the regression or progression of atherosclerosis and CAD based on changing amounts of calcium appears to be promising (O'Rouke 2000). Nonetheless, this application requires greater accuracy and reproducibility than has yet been achieved with EBCT. It has been recently suggested that coronary artery calcifica-

tion represents an independent emerging risk factor (Assmann 2004) and that the finding of advanced calcified and non-calcified atherosclerotic lesions in the coronary arteries may justify more aggressive treatment of patients at intermediate risk (Assmann 2003). Therefore, the measurement of coronary calcification, at least in intermediate-risk patients, may develop into a viable application for CT in preventive cardiology (Fig. 1.14).

1.3.2 Other Cardiac Diseases

Besides the coronary arterial tree and CAD-related disease, other cardiac structures, such as the cardiac chambers, cardiac valves, myocardium, and epicardium, are important targets in the diagnosis of cardiac diseases that may cause reduced cardiac output and reduced blood flow (Fig. 1.5b). In these cases, the imaged anatomy is usually larger in size so that the requirements for spatial resolution are less critical than in coronary artery imaging. However, there is still a need for dedicated cardiac CT acquisition protocols with sufficient spatial 3D resolution and the ability to eliminate cardiac motion, and which allow for imaging the heart in different phases of the cardiac cycle.

As a consequence of CAD or other heart diseases, the heart chambers may be enlarged and the contractility of the heart may be reduced (cardiac insufficiency). In addition to reduced cardiac output, the reduced pump function of the ventricles and of the atria (e.g., atrial fibrillation) may lead to the development of a wall thrombus, which can embolize into the general or cerebral circulation. Another frequent cause of reduced cardiac output is stenosis or functional defects of the cardiac valves subsequent to valve scarring or malformation. Inflammatory diseases of the myocardium (myocarditis) and pericardium (pericarditis) can lead to reduced contraction of the cardiac muscles. The affected areas show reduced

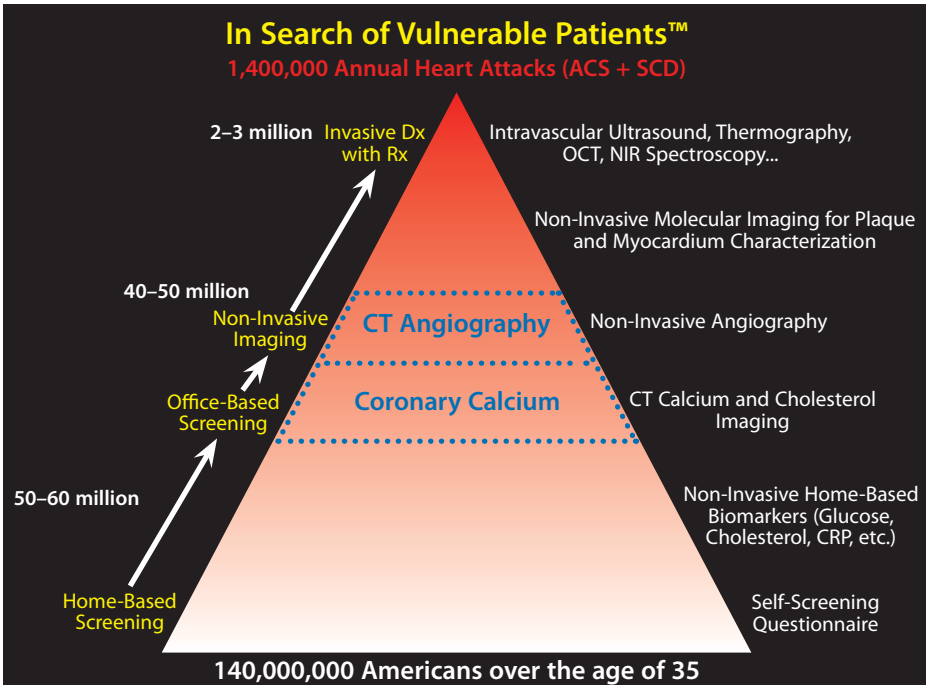

Fig. 1.14. The "vulnerable patient" pyramid proposes the use of coronary calcium quantification by CT and non-invasive CT angiography for the identification of patients at intermediate risk of a heart attack, as determined by general risk scoring methods such as Framingham or PROCAM

perfusion and may develop necrosis, discharges of fluid, and heavy calcification (Harrison 1995). After heart transplantation, the coronary arteries and cardiac muscle are often sites of an intense immune reaction. This may lead to the rapid development of coronary atherosclerosis and calcification of the myocardium – processes that can be monitored by imaging techniques (Barbier 1994). Finally, the detection and diagnosis of congenital heart disease in adults or children, such as malformation of the coronary arteries, cardiac valves, or the origins of the great vessels are important applications of non-invasive imaging.

Acute heart failure related to electrophysiological (EP) defects is an increasingly important cause of morbidity and mortality in industrialized nations. The usual treatment methods include pacemaker insertion and ablation of the pulmonary veins or cardiac chambers. Non-invasive CT imaging can be useful in visualizing cardiac anatomy related to the EP system, such as the cardiac venous system, the cardiac atria, and the pulmonary veins, and for the planning of subsequent EP-related interventions.

1.3.3 Diseases of the Thoracic Vessels

The elasticity of the great thoracic vessels is essential to maintaining constant blood flow throughout the cardiac cycle (Fig. 1.5c). Motion artifacts caused by transmitted cardiac pulsation frequently degrade thoracic CT studies in patients with acute chest pain. Thus, diagnosis will no doubt benefit from dedicated cardiac CT acquisition techniques that suppress cardiac motion.

The extremely high pulsation forces acting on the aorta can result in diseases of the vessel wall, such as dissections and aneurysms. The assessment or exclusion of dissections and the evaluation of aneurysms are particularly difficult in the ascending aorta due to strong vessel pulsation. A typical diagnostic pitfall is an artifactual intimal flap, which in the ascending aorta resembles dissection (Loubeyre 1997). Distortion of paracardiac lung segments by cardiac pulsation often precludes the confident exclusion of small peripheral pulmonary emboli in segmental and subsegmental arteries (Schöpf 2000) and an accurate assessment of pulmonary nodules.

1.4 The History and Evolution of CT in Cardiac Imaging

Since its introduction in 1972, X-ray CT has become a robust and frequently used non-invasive imaging modality for contrast-enhanced angiographic vascular diagnosis (Kalender 1990; Rubin 1993). Due to rapid cardiac motion and limitations in scan speed, temporal resolution, and volume coverage, CT imaging of the heart and coronary arteries continues to be a challenging field of research and development.

1.4.1 Principles and Applications of Electron-Beam CT

In order to achieve the very short image acquisition times that are needed to virtually freeze cardiac motion, fourth-generation CT systems with fixed detector arrays and non-mechanical movement of the X-ray source have been developed. This so-called electron-beam CT (EBCT) technology was first introduced and used in clinical trials in 1982 (Boyd 1982). An X-ray fan beam is emitted from a tungsten anode ring, fixed in space, that is hit by an electron beam. The electron beam is electromagnetically controlled and sweeps continuously over the target ring, thereby covering the X-ray source positions that are required for reconstruction of axial slices (Fig. 1.15a). The anode ring and the detector ring have to cover an angle of about 270° in order to acquire a complete fan-beam data set for image reconstruction within a 500-mm scan field of view. The anode ring and the detector ring are located in adjacent planes and the emitted X-ray fan beams are tilted by a cone angle that may produce artifacts with high-contrast structures. The housing of the electron gun limits the movement of the patient table and thus the scan range. To cover the cardiac anatomy, ECG-synchronized sequential single-slice scans with a 50- to 100-ms exposure time at a fix-beam current of about 640 mA are used, providing an exposure of 32–64 mAs per slice (Stanford 1992). Synchronization of the acquisition with the movement of the heart is achieved

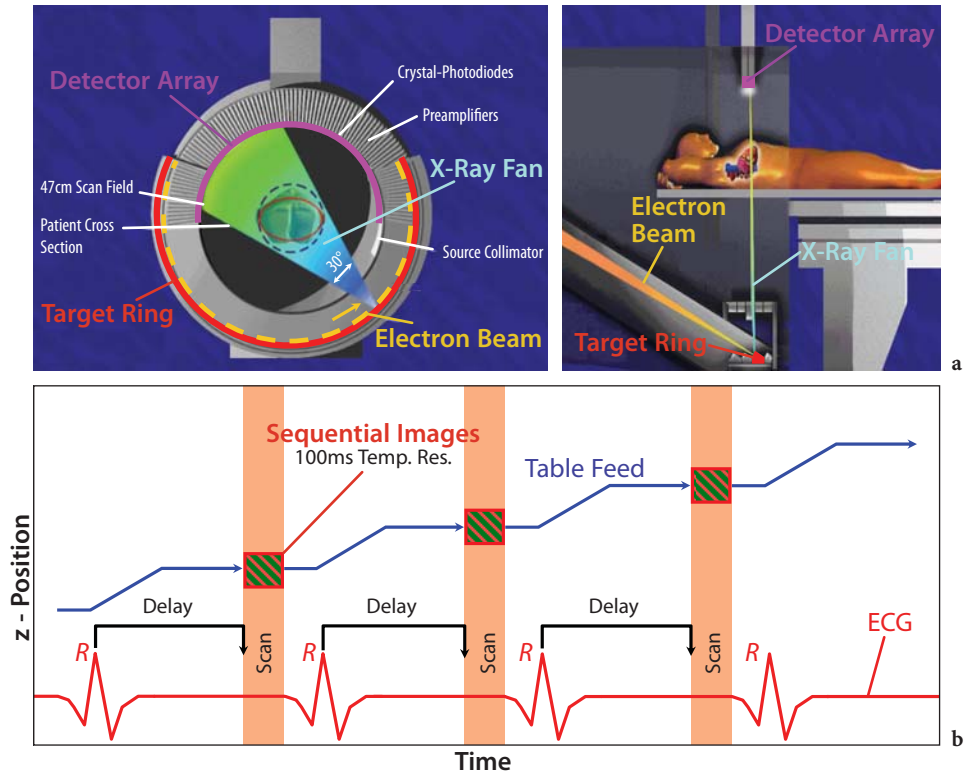

Fig. 1.15. a The electron-beam CT acquisition system and **b** the principle behind prospectively ECG-triggered sequential scanning. EBCT with prospective ECG-triggering can acquire one slice for every heartbeat, with a 50- to 100-ms temporal resolution. (Imatron C-150, Imatron, South San Francisco, USA and Evolution XP, Siemens, Forchheim, Germany)

using ECG information and provides phase-consistent slices during phases of low cardiac motion. For sequential imaging with EBCT, a prospective trigger is derived from the ECG trace to initiate the CT scan with a specific user-selectable delay time after the R-wave (Fig. 1.15b). The delay time is calculated from a given phase parameter (e.g., a percentage of the RR-interval time as the delay after an R-wave) for each cardiac cycle and is individually based on a prospective estimation of the RR intervals. Usually, the delay is defined such that the scans are acquired during the diastolic phase of the heart, when motion of the cardiac chambers and the coronary arteries is at a minimum (Achenbach 2000a; He 2001). High image-noise due to the very short exposure time limits the image quality, while single-slice acquisition restricts the longitudinal resolution. The typical voxel sizes of 0.8×0.8×3 mm are the product of an in-plane resolution up to 7 lp/cm and a 3-mm slice-width, with typical scan times of 25–40 s for a 12-cm volume. Higher longitudinal resolution with overlapping slice acquisition and thinner slices (down to 1.5 mm slice-width) is possible, but often clinically not feasible due to the long scan times and increased image noise.

The major clinical applications of EBCT are the detection and quantification ("scoring") of coronary artery calcification (Agatston 1990; Arad 1996; Becker 1999; Rumberger and Kaufmann 2003) (Fig. 1.16a) and CT angiography (CTA) of the coronary arteries (Achenbach 1998a; Achenbach 1998b; Budoff 1999; Ooijen 2000) (Fig. 1.16b, c). Current limitations of EBCT imaging include the limited reproducibility of coronary calcium quan-

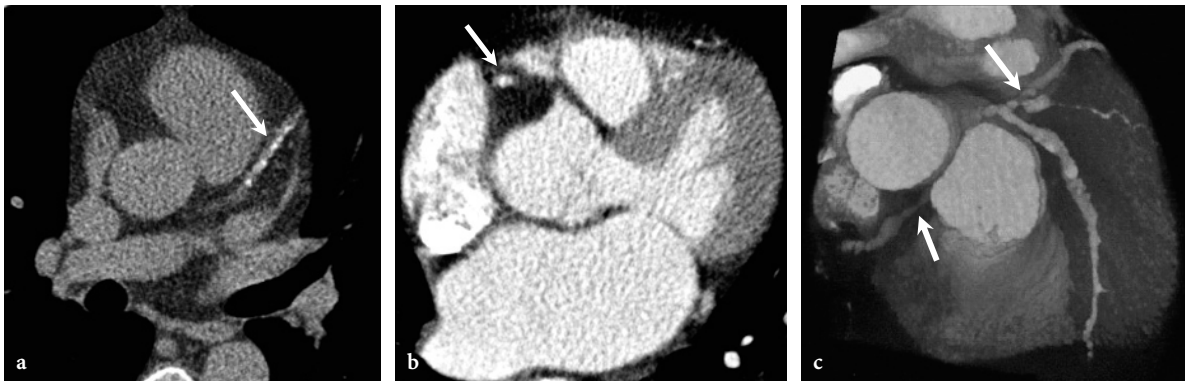

Fig. 1.16. Electron-beam CT acquisition allows the display of coronary calcification in a transaxial image planes and **b**, **c** coronary CT angiography. Transaxial image slices of coronary CT angiography by EBCT are compromised due to limited signal-to-noise-ratio (**b**). 3D display (3D volume rendering) for visualization of the coronary arteries is possible in selected cases (**c**). Severe LAD and RCA stenoses (*arrows* in **c**) can be detected in proximal coronary segments. (Images courtesy of (**a**, **b**) Klinikum Grosshadern, Munich, Germany and (**c**) Erasmus University Rotterdam, Netherlands)

tification, the limited ability to detect non-calcified atherosclerotic plaques due to the compromised signal-to-noise-ratio, and the limited spatial resolution of 3D visualizations of the coronary arteries (Flamm 1998; Leber 2003). Because of the restriction to axial, non-spiral scanning in ECG-synchronized cardiac investigations, acquisition of 3D volume images using EBCT can only provide limited *z*-resolution within a single breath-hold scan. In addition to scans of the cardiac anatomy, EBCT offers acquisition modes for cardiac function and cardiac perfusion imaging. The system includes four target rings and two detector rings for simultaneous scanning of eight slices. A volume of 64 mm can be covered with low in-plane spatial resolution and an 8-mm slice-width (Rumberger 1989). These applications are rarely used because of the high radiation exposure and limited extra information they provide compared to other, established non-invasive imaging modalities for this purpose, such as MRI, SPECT, and PET.

On-going development efforts have been carried out since the early 1990s for EBCT-based systems, and increased beam currents, increased in-plane resolution, and increased body-scan ranges have been achieved by altering the construction of the electron gun. Special reconstruction algorithms were developed for continuous volume acquisition (Weisser 1999) and scatter artifact elimination (Ohnesorge 1999). Recently, new EBCT detector developments have been introduced that allow for simultaneous acquisition of two detector slices with a slice-width down to 1.5 mm and an increased in-plane spatial resolution up to 9 lp/cm that is provided by finer sampling of the elements.

However, increased spatial resolution in the longitudinal direction within reasonable breath-hold times can only be provided with a multiple stationary detector ring at equivalent in-plane resolution for simultaneous ECG-synchronized acquisition of multiple slices. EBCT-based multi-slice detector concepts featuring four or more detector slices will be accompanied by substantially increased hardware costs and the increased impact of cone-beam geometry problems, as the additional detector rings have to be moved even further away from the plane of the X-ray source. Furthermore, new, advanced reconstruction algorithms will be needed that reduce the cone-beam-induced artifacts and allow for ECG-gated reconstruction from non-helical continuous acquisition, such as provided by the stationary partial detector and anode rings. An electron-beam current significantly higher than 640 mA is needed to improve contrast resolution at lower image noise and to support slice collimations thinner than 3 mm at an appropriate contrast-to-noise ratio. The realization

of higher electron-beam currents, however, remains a technical challenge with regard to the power-supply requirements and anode heat development.

In conclusion, EBCT may undergo further technological improvement in the future. Significant research and development efforts and, most likely, substantially higher hardware costs will be necessary to considerably enhance the performance of EBCT in cardiac imaging. However, all major CT manufacturers currently are focusing on the technological enhancement of mechanical multi-slice CT systems, as EBCT-based systems may not be able to catch up with mechanical multi-slice CT as applied to general vascular and body imaging. It is therefore likely that the distribution of EBCT technology will always be limited to dedicated cardiac imaging centers.

1.4.2 Cardiac Imaging with Conventional Mechanical CT

The advantages in acquisition geometry and the ability of continuous spiral scanning confer conventional mechanical CT systems with superior general image quality and spatial resolution compared to EBCT. However, temporal resolution, which is one of the most important parameters for cardiac imaging, depends on the system rotation time, which should be as fast as possible but is nonetheless limited by mechanical forces.

Preliminary cardiac imaging results with mechanical CT using a 2-s rotation, third-generation scanner (Lackner 1981) were reported in 1981. Scan data segments of a single slice were collected from several heartbeats in corresponding phases of the cardiac cycle using ECG information. Images were obtained with an effective temporal resolution of about 0.5 s, and acquisition of the data segments was controlled by a foot switch in the scan room. Since the collection of data from several cardiac cycles requires desynchronization of the heartbeat and rotation of the measurement system, the scanner rotation speed was selected individually and controlled interactively according to the patient's heart rate. This technique allowed for acquisition of a few thick slices without the coverage of larger volumes, thus enabling a coarse diagnosis of large cardiac structures (Fig. 1.17). Application in clinical

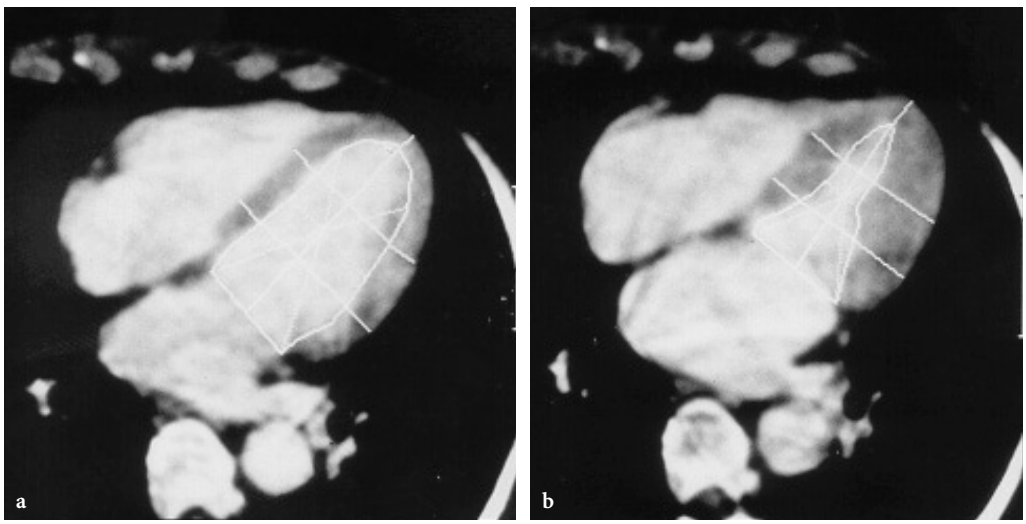

Fig. 1.17. Cardiac CT images acquired in 1981 on a mechanical CT scanner with a 2.0-s rotation speed. Images were generated in the diastolic and systolic phases of the cardiac cycle to demonstrate cardiac motion. Scan data segments of a single slice were collected from several heartbeats in corresponding phases of the cardiac cycle using ECG information. (Images courtesy of Siemens Medical Solutions, CT Division, Forchheim, Germany)

routine, however, was very limited due to the need for intensive user interaction and the lack of standardized scan protocols.

With the advent of sub-second rotation combined with ECG-synchronized scanning, mechanical single-slice CT with spiral capability and superior general image quality has challenged EBCT in the domain of cardiac imaging. Early promising results were achieved in 1997 and were based on systems with a 0.75-s rotation time and prospectively ECG-triggered or retrospectively ECG-gated (Fig. 1.18) acquisition. Partial scan techniques (Parker 1982) combined with new ECG-correlated acquisition techniques yielded a temporal resolution of 500-ms (Becker 1999; Schöpf 1999; Becker 2000). However, ECG-triggered single-slice acquisition (Fig. 1.18a) did not allow for imaging of the entire heart in a single breath-hold with higher longitudinal resolution. Scan times were about 60 s with voxel sizes of about 0.6×0.6×3 mm. Sub-second mechanical spiral CT systems offer the new cardiac acquisition technique of retrospectively ECG-gated spiral scanning (Woodhouse 1997; Kachelriess 1998; Carr 1999; Bahner 1999). A continuous spiral scan with slow table-feed is acquired with the ECG signal recorded simultaneously. The acquired scan data are selected for image reconstruction with respect to a pre-defined phase of the cardiac cycle. Similar to ECG-triggered sequential scanning, a specific R-wave delay time defines the starting point of data to be used for image reconstruction (Fig. 1.18b).

The initial clinical studies clearly demonstrated the ability of ECG-triggered single-slice CT to detect coronary artery calcification (Becker 1999) and basic cardiac morphology (Fig. 1.19). However, it was also shown that a single-slice spiral CT system hardly allows for continuous ECG-gated volume

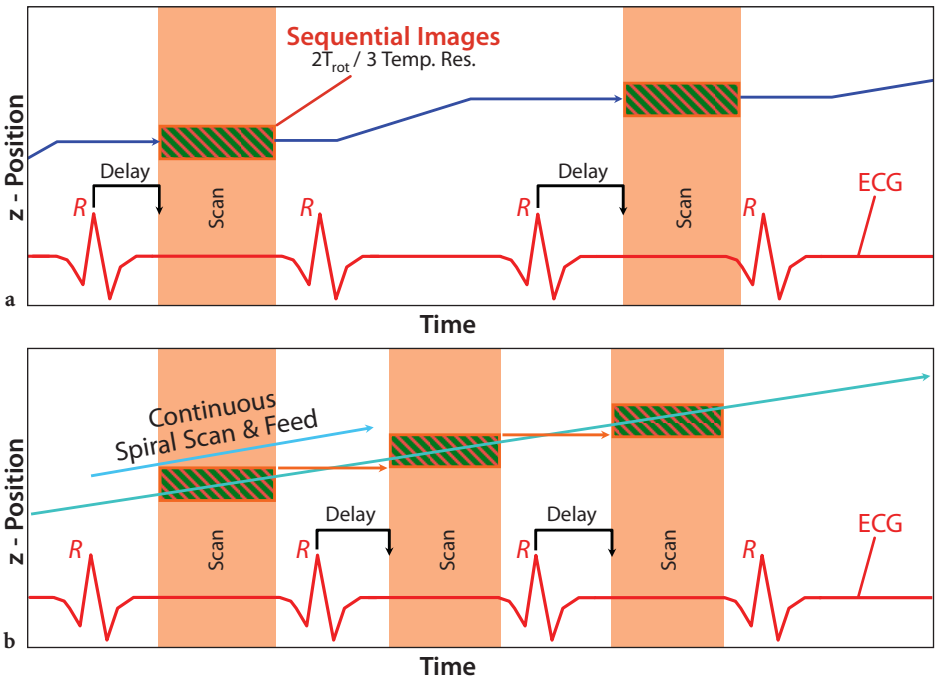

Fig. 1.18. a Sequential volume coverage with prospectively ECG-triggered single-slice scanning and **b** coverage with retrospectively ECG-gated single-slice spiral scanning. Mechanical CT with 0.75-s rotation and prospective ECG-triggering can acquire one slice during every second heartbeat, with a 500-ms acquisition time. With retrospective ECG-gating, images can be reconstructed at every heartbeat with a temporal resolution equal to half the rotation time

coverage with overlapping slice acquisition of the entire heart with reasonable longitudinal resolution within reasonable scan times.

The introduction of mechanical multi-slice CT systems, in 1998, with simultaneous acquisition of four slices and an increased rotation speed up to 0.5 s per rotation, opened new horizons for general-purpose CT imaging and new opportunities in cardiac CT imaging. These scanners allow for considerably faster coverage of the heart volume and at higher temporal resolution than obtained with single-slice scanning. The increased scan speed allows for thinner collimated slice widths (i.e., 1 mm), thus increasing the z-resolution of ECG-correlated examinations of the heart. For the first time, multi-slice CT scanners with four slices can cover the heart in a single breath-hold and with a temporal resolution of about 250 ms, which essentially freezes cardiac motion (Ohnesorge 2000; Nieman 2001). Despite all these promising advances, some challenges did remain for ECG-gated multi-slice CT examinations of the heart and the coronary arteries with 4-slice detectors: adequate visualization of calcified and smaller coronary artery segments and examination of patients with higher heart rates as well as those who cannot adequately hold their breath for at least 30 s.

With the newest generation of multi-slice CT systems, offering simultaneous acquisition of 16 and, more recently, up to 64 sub-millimeter slices as well as gantry rotation times as low as 0.33 s, both axial and temporal resolution have been further improved, while examination times have been considerably reduced (Küttner 2004) (Fig. 1.20). This new performance level together with ongoing fast technical developments (Fig. 1.21) has the potential to establish multi-slice CT as a clinical tool for cardiac imaging.

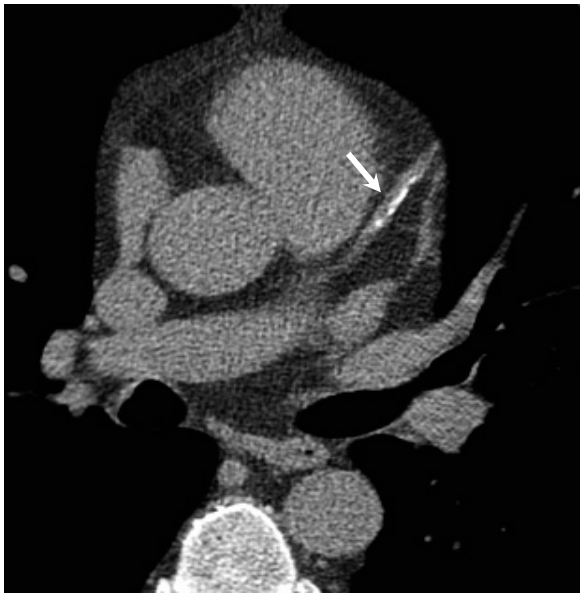

Fig. 1.19. Transaxial image display of coronary calcification in LAD using ECG-triggered acquisition with subsecond single-slice mechanical CT. (Images by courtesy of Klinikum Grosshadern, Munich, Germany)

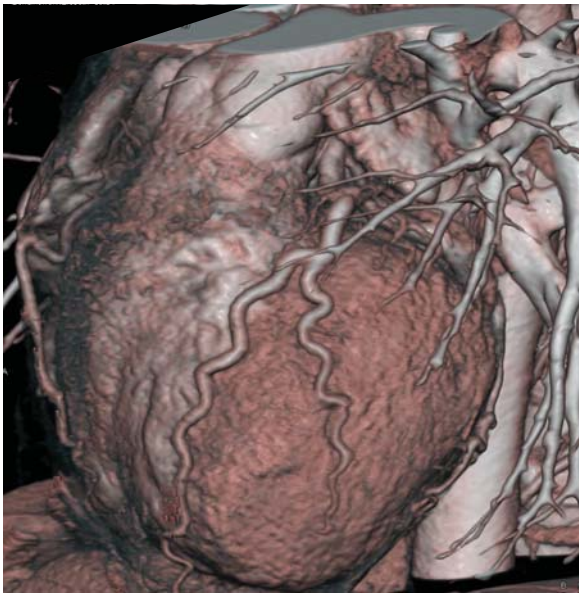

Fig. 1.20. 3D volume rendering of a coronary CT angiography examination using the latest 64-slice CT generation with 0.4-mm voxel resolution and 0.33-s rotation time. The entire heart could be covered in a 9-s breath-hold (SOMATOM Sensation 64, Siemens, Forchheim, Germany). (Image courtesy of University of Erlangen, Germany)

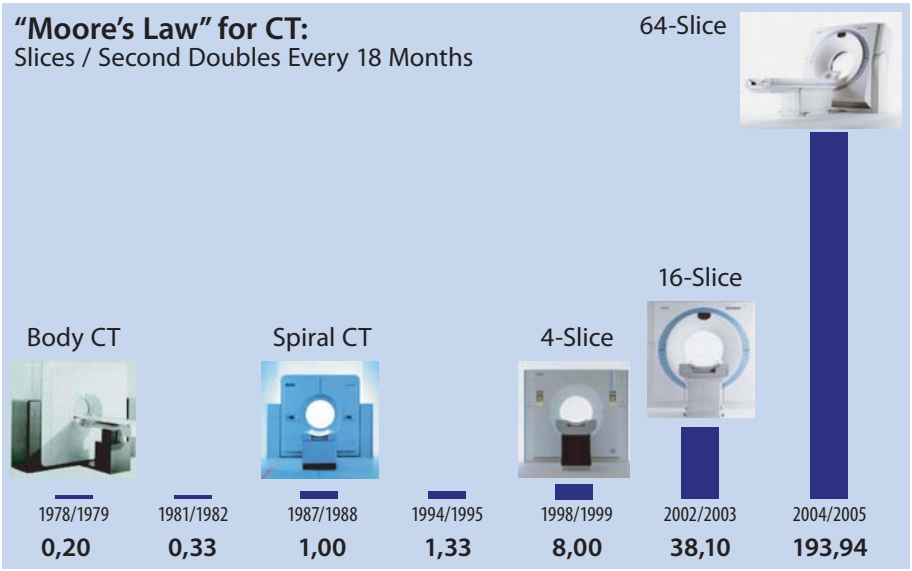

Fig. 1.21. The increased performance of CT since the introduction of multi-slice CT technology in 1998. CT acquisition performance, measured in slices per second, has doubled almost every 18 months and has currently reached nearly 200 slices per second with the latest 64-slice CT scanners

References

Achenbach S, Moshage W, Ropers D, Bachmann K (1998a). Curved multiplanar reconstructions for the evaluation of contrast-enhanced electron-beam CT of the coronary arteries. AJR 170:895–899.

Achenbach S, Moshage W, Ropers D, Nössen J, Daniel WG (1998b). Value of electron-beam computed tomography for the non-invasive detection of high-grade coronary artery stenoses and occlusions. N Engl J Med 339:1964–71.

Achenbach S, Ropers D, Holle J, Muschiol G, Daniel WG, Moshage W (2000a). In-plane coronary arterial motion velocity: measurement with electron-beam CT. Radiology 216:457–463.

Agatston AS, Janowitz WR, Hildner FJ, Zusmer NR, Viamonte M, Detrano R (1990). Quantification of coronary artery calcium using ultrafast computed tomography. J Am Coll Cardiol 15:827–832.

Anzai et al (1994). Effect of short-term prognosis and left-ventricular function of angina pectoris prior to first Q-wave anterior wall acute myocardial infarction. Am J Cardiol 74(8):755–759.

Arad Y, Spadaro M, Goodman KG et al (1996). Prediction of coronary events with electron beam computed tomography: 19-month follow-up of 1173 asymptomatic subjects. Circulation 93:1951–1953.

Assmann G, Carmena R, Cullen P et al (1999). Coronary heart disease: reducing the risk, a worldwide view. Circulation 100:1930–1938.

Assmann G, Cullen P, Schulte H (2002). Simple scoring scheme for calculating the risk of acute coronary events based on the 10-year-follow-up of the prospective cardiovascular Münster (PROCAM) study. Circulation 105:310–315.

Assmann G, et al (2003). International Task Force for Prevention of Coronary Heart Disease in Cooperation with the International Atherosclerosis Society. pocket guide to prevention of coronary heart disease. www.chd-taskforce.com and www.athero.org, January 2003.

Assmann G, Cullen P, Fruchart JC, Greten H et al (2004). Implications of emerging risk factors for therapeutic interventions. Consensus statement of the International Task Force for Prevention of Coronary Heart Disease, Munich, August 2004. www.chd-taskforce.com.

Bahner ML, Böse J, Lutz A, Wallschläger H, Regn J, van Kaick G. (1999). Retrospectively ECG-gated spiral CT of the heart and lung. Eur Radiol 9:106–109.

Barbier M, Bowler T, Ludman PA, Mitchell AG, Wood D, Yacoub M (1994). Ultrafast computed tomography scanning for detection of coronary disease in cardiac transplant recipients. Am J Cardiol 71:941–944

Becker CR, Knez A, Jakobs TF, Becker A, Schöpf UJ, Brüning R, Haberl R, Reiser MF (1999). Detection and quantification of coronary artery calcification with electron-beam and conventional CT. Eur Radiol 9:620–624.

Becker CR, Jakobs TF, Aydemir S, Becker A, Knez A, Schöpf UJ, Brüning R, Haberl R, Reiser MF (2000). Helical and single-slice conventional CT versus electron beam CT for the quantification of coronary artery calcification. AJR 174:543–547.

Boyd DP, Lipton MJ (1982). Cardiac computed tomography. Proceedings of the IEEE 71:298–307

Budoff MJ, Georgiou D, Brody A et al (1996). Ultrafast computed tomography as a diagnostic modality in the detection of coronary artery disease : a multicenter study.Circulation 93: 898–904.

Budoff MJ, Oudiz RJ, Zalace CP, Bakhsheshi H, Goldberg SL, French WJ, RAmi TG, Brundage BH (1999) Intravenous three-dimensional coronary angiography using contrast enhanced electron beam computed tomography. Am.J.Cardiol. 83: 840–845

Carr JJ, Crouse JR, Goff DC Jr, et al (2000). Evaluation of subsecond gated helical CT for quantification of coronary artrey calcium and comparison with electron beam CT. AJR 174:915–921.

Corti R, Fuster V, Fayad ZA, et al (2002). Lipid lowering by Simvastatin induces regression of human atherosclerotic lesions. Two-years follow-up by high-resolution noninvasive magnetic resonance imaging. Circulation 106:2884–2887.

Crooks LE, Barker B, Chang H, et al (1984). Magnetic resonance imaging strategies for the heart. Radiology 153:459.

Deanfield JE, Mason RP, Nissen SE, Williams BW (2001). Coronary artery disease: from managing risk factors to treating complications. Clin Cardiol 24 (Suppl I Intn'l). Fayad ZA, Fuster V, Fallon JT (2000) Noninvasive in vivo human coronary artery lumen and wall imaging using black-blood magnetic resonance imaging. Circulation 102:506–510.

Flamm SD (1998). Coronary artery calcium screening: ready for prime time ?. Radiology 208:571–572.

Glagov S, Weisenberg E, Zarins C, et al (1987). Compensatory enlargement of human atherosclerotic coronary arteries. N Engl J Med 316:1371–1375.

Halliburton SS, Paschal CB (1996). Atherosclerotic plaque components in human aortas contrasted by ex vivo imaging using fast spin-echo magnetic resonance imaging and spiral computed tomography. Invest Radiol 31(11):724–728.

Harrison TR (1995) Harrison's principles of internal medicine. Textbook 13th Edition, Chapter, 192, Page 1162–1168.

He S, Dai R, Chen Y, Bai H (2001). Optimal electrocardiographically triggered phase for reducing motion artifact at electron beam CT in the coronary artery. Acad Radiol 8:48–56.

Higgins CB, Holt W, Pflugfelder P, et al (1988). Functional evaluation of the heart with magnetic resonance imaging. Magn Reson Med 6:121–139.

Hounsfied GN (1973). Computerized transverse axial scanning tomography: Part I, description of the system. Br J Radiol 46:1016–1022.

Janowitz WR, Agatston AS, Viamonte Jr J (1991). Comparison of serial quantitative evaluation of calcified coronary artery plaque by ultrafast computed tomography in persons with and without obstructive coronary artery disease. Am J Cardiol 68–1-6.

Jones PH, Eaton CB (1994). Cost-benefit analysis of walking to prevent coronary heart disease. Archives of Family Medicine 3(8):703–710.

Kachelrieß M, Kalender WA (1998). Electrocardiogram-correlated image reconstruction from subsecond spiral computed tomography scans of the heart. Med Phys 25: 2417–2431.

Kak AC, Slaney M (1984). Principles of computerized tomographic imaging. IEEE Press New York, pp. 77–86.

Kak AC, Slaney M (1988). Principles of computerized tomographic imaging. IEEE Press New York, pp. 49–112.

Kalender W, Seissler W, Klotz E, Vock P (1990). Spiral volumetric CT with single-breath-hold technique, continuous transport and continuous scanner rotation. Radiology 176, 181–183.

Kalender W (1995). Thin-section three-dimensional spiral CT: is isotropic imaging possible? Radiology 197:578–580.

Kim WYK, Danias PG, Stuber M, Wanning WJ, et al (2001). Coronary magnetic resonance angiography for the detection of coronary stenoses. New Engl J Med 345(26), 1863–1869.

Kim R, et al (2004). MR to predict wall motion recovery. New Engl J Med Feb 2004

Küttner A, Wildberger J, Anders K, et al (2004). A new frontier in non-invasive cardiac imaging: first clinical experience using 64-slice MDCT Technology. Fortschr Röntgenstr 176, 1810–1816.

Lackner K, Thurn P (1981). Computed tomography of the heart: ECG-gated and continuous scans. Radiology 140:413–420.

Leber AW, Knez A, Becker C, et al (2003). Non-invasive intravenous coronary angiography using electron-beam tomography and multi-slice computed tomography. Heart 89:&33–639.

Leung KC, Martin CJ. (1996). Effective doses for coronary angiography. Br J Radiol 69:426–431.

Liang Y, Kruger RA. (1993). Dual-slice spiral versus single-slice spiral scanning: Comparison of the physical performance of two computed tomography scanners. Med. Phys. 23:205–220.

Loewel H, Engel S, Hoermann A, Gostomzyk J, Bolte HD, Keil U (1999). Akuter Herzinfarkt und plötzlicher Herztod aus epidemiologischer Sicht. Intensivmed 36:652–661.

Loubeyre P, Angelie E, Grozel F, Abidi H, Minh VA (1997). Spiral CT artifact that simulates aortic dissection: image reconstruction with use of 180 degrees and 360 degrees linear-interpolation algorithms. Radiology 205:153–157.

Naghavi M, Libby P, Falk E, et al (2003a). From vulnerable plaque to vulnerable patient – a call for new definitions and risk assessment strategies. Part I. Circulation 108:1664–1672.

Naghavi M, Libby P, Falk E, et al (2003b). From vulnerable plaque to vulnerable patient – a call for new definitions and risk assessment strategies. Part II. Circulation 108:1772–1778.

Nair A, Kuban BD, Tuzcu EM, Schönhagen P, Nissen SE, Vincent DG (2002). Coronary plaque classification with intravascular ultrasound radiofrequency data analysis. Circulation 106:2200–2206.

Niemann K, Oudkerk M, Rensing BJ, van Ooijen P, Munne A, van Geuns RJ, de Feyter P (2001). Coronary angiography with multi-slice computed tomography. Lancet 357:599–603.

Ohnesorge B, Flohr T, Klingenbeck-Regn K (1999). Efficient object scatter correction for third and fourth generation CT scanners. Eur Radiol 9:563–569.

Ohnesorge B, Flohr T, Becker C R, Kopp A F, Knez A Baum U, Klingenbeck-Regn K, Reiser MF (2000). Cardiac imaging by means of electrocardiographically gated multisection spiral CT: initial experience. Radiology 217:564–571.

Ooijen van PMA, Oudkerk, M, Geuns van RJM, Rensing BJ, de Feyter PJ (2000). Coronary artery fly-through using electron beam computed tomography. Circulation 102:e6-e10.

O'Rouke RA, Brundage BH, Frölicher VF, et al (2000). ACC/AHA expert consensus document on EBCT for the diagnosis and prognosis of coronary artery disease. Circulation 102:126–140.

Parker DL (1982). Optimal short scan convolution reconstruction for fanbeam CT. Med Phys 9(2):254–257.

Pasterkamp G, Falk E, Woutman H, Borst C (2000). Techniques characterizing the coronary atherosclerotic plaque: influence on clinical descision making ? J Am Coll Cardiol 36(1):13–21.

Post JC, van Rossum AC, Hofmann MB, Valk J, Visser CA (1996). Three-dimensional respiratory-gated MR angiography of coronary arteries: comparison with conventional coronary angiography. Am J Roentgenol 166:1399–1404.

Rees MR, Zijlstra F, Reiber JHC, Roelandt JRTC, et al (2004). Invasive coronary imaging. In: Oudkerk et al. (eds) Medical radiology diagnostic imaging – coronary radiology. Springer Berlin, Heidelberg, New York. pp.25–40.

Rubin GD, Dake MD, Napel SA (1993) Three-dimensional spiral CT angiography of the abdomen: initial clinical experience. Radiology 186: 147–152

Rubin GD, Dake MD, Napel S (1994). Spiral CT of renal artery stenosis: comparison of three-dimensional rendering techniques. Radiology 190: 181–189.

Rumberger JA, Weiss RM, Feiring AJ, Stanford W, Karim R, Marcus ML (1989). Patterns of regional diastolic function in the normal human left ventricle: an ultrafast computed tomographic study. J Am Coll Cardiol 14:119–126.

Rumberger JA, Kaufmann L (2003). A rosetta stone for coronary calcium risk stratification. Agatston, volume and mass scores in 11490 individuals. Am J Roentgenol 181:743–748.

Schöpf UJ, Becker CR, Brüning RD, Helmberger A, Stäbler A, Leimeister P, Reiser MF (1999). Electrocardiographically gated thin-section CT of the lung. Radiology 212:649–654.

Schöpf UJ, Helmberger T, Holzknecht N, Kang DS, Brüning RD, Aydemir S, Becker CR, Mühling O, Knez A, Haberl R, Reiser MF (2000). Segmental and subsegmental pulmonary arteries: evaluation with electron beam CT versus spiral CT. Radiology 214:433–439.

Shemesh J, Apter S, Rozenman J, et al (1995). Calcification of coronary arteries: detection and quantification with double helix CT. Radiology 197:779–783.

Stanford W, Rumberger J (1992) Ultrafast computed tomography in cardiac imaging: principles and practice. Futura Publishing Company New York.

Stary HC, Chandler AB, Dinsmore RE, Fuster V, Glagov S, Insull Jr W, Rosenfeld ME, Schwartz CJ, Wagner WD, Wissler RW (1995). A definition of advanced types of atherosclerotic lesions and a histological classification of atherosclerosis. Circulation 92:1355–1374.

Stehling MK, Turner R, Mansfield P (1991). Echo-Planar imaging: magnetic resonance imaging in a fraction of a second. Science 254: 43–50.

Virmani R, Kolodgie FD, Burke AP et al (2000). Lessons from sudden coronary death. A comprehensive morphological classification scheme for atherosclerotic lesions. Arterioscler Thromb Vasc Biol 20:1262–1275.

Weisser G, Lehmann K-J, Scheck R, Coppenrath E, Fehrentz D, Georgi M (1998). Performance of electron-beam CT: continuous volume scan in comparison to spiral CT. Der Radiologe 38:993–998.

Wexler L, Brundage B, Crouse J, et al (1996). Coronary artery calcification: pathophysiology, epidemiology, imaging methods and clinical implications: a statement for health professionals from the AHA Writing Group. Circulation 94:1175–1192.

White RD, Pflugfelder PW, Lipton MJ, Higgins CB (1988). Coronary artery bypass grafts: evaluation of patency with CINE MR imaging. Am J Roentgenol 150:1271–1274.

Wielopolski PA, van Geuns RJM, de Feyter PJ, Oudkerk M (1998). Coronary arteries. Eur Radiol. 8:873–885.

Windecker S et al (1999). Interventional Cardiology in Europe 1995. European Heart Journal 20:484–495.

Wintersperger B, Engelmann M, v. Smekal, et al (1998). Patency of coronary bypass grafts: assessment with breath-hold contrast-enhanced MR-angiography. Radiology 208:345–351.

Wong ND, Vo A, Abrahamson D (1994). Detection of coronary artery calcium by ultrafast computed tomography and its relation to clinical evidence of coronary artery disease. Am J Cardiol 73:223–227.

Wong ND, Detrano RC, Abrahamson D, Tobis JM, Gardin JM (1995). Coronary artery screening by electron beam computed tomography: facts, controversy and future. Circulation 92:632–636.

Woodhouse CE, Janowitz WR, Viamonte M (1997). Coronary arteries: retrospective cardiac gating technique to reduce cardiac motion artifact at spiral CT. Radiology 204:566–569.

Wyngaarden, Smith, Bennet (1996). Cecil, textbook of medicine. 19th Edition, Part VI, Chapter 47. Saunder, Philadlphia.

Ziada K, Kapadia S, Tuzcu EM, Nissen S (1999). The current status of intravascular ultrasound imaging. Curr Prob Cardiol 24:541–566.

Cardiac and Cardiothoracic Anatomy in CT

2

Roman Fischbach

Contents

2.1 **Topography** *23*
2.2 **Standard Views** *24*
2.3 **Coronary Arteries and Veins** *30*
2.4 **Pericardium** *32*
2.5 **Cardiac Chambers** *33*
2.6 **Cardiac Valves** *34*
2.7 **Great Vessels** *35*
References *39*

Modern cross-sectional imaging techniques such as echocardiography, magnetic resonance imaging (MRI), and multi-slice CT provide high-resolution visualization of cardiac morphology and function (Ooijen 2004). All of these modalities permit imaging of the heart in 2D and, at least to some extent, in 3D. While transthoracic echocardiography is dependent on an acoustic window, which sometimes permits imaging in every desired plane, MRI can be performed in any orientation. Multi-slice CT of the heart relies on an axial data acquisition; however, the high-resolution spiral data sets obtained with modern systems allow for display of small anatomical structures of the heart (Fig. 1.5) and for reformation in virtually any imaging plane. This chapter will introduce cardiac and cardiothoracic anatomy, as displayed by new multi-slice high-resolution CT scanners based on standard 2-dimensional views, which have been established with cardiac catheterization (Bittl 1997), echocardiography, and cardiac MRI and based on 3-dimensional surface reconstructions. The image data used for illustration have primarily been acquired with 4- and 16-slice CT with 0.5-s and 0.42-s rotation time, respectively. Of course, the described anatomical relations are also true for data obtained from multi-slice CT with more than 16-slices or from dual-source CT.

2.1 Topography

The human body can be viewed in three standard anatomic planes, which are oriented perpendicular to each other: sagittal, coronal, and transverse. These planes are aligned with the thoracic midline structures, the aorta and esophagus. In contrast, the heart is oriented obliquely in the chest and therefore imaging in standard anatomic planes is suboptimal to visualize cardiac anatomy and pathology (Edward 1984a, Edwards 1984b). The heart's three standard planes are its vertical and horizontal long axis and its so-called short axis. These cardiac axes are tilted against the standard anatomic planes, as shown in (Fig. 2.1).

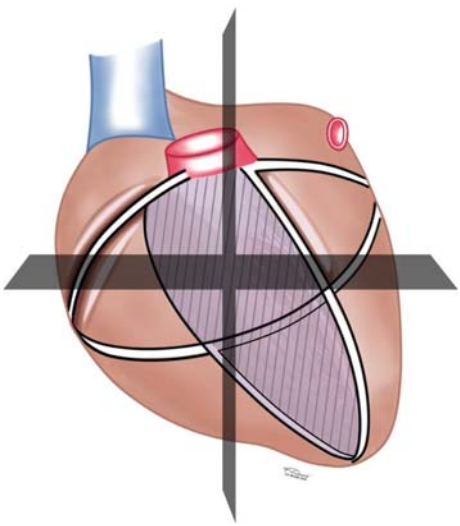

Fig. 2.1. Orientation of the vertical long axis and the short axis of the heart in relation to the standard anatomic planes of the body

The apex of the heart points to the left while the base of the heart is oriented dorsally and to the right, when viewed from above (Fig. 2.2). The right atrium and the right ventricle are to the right and anterior, and the left ventricle and left atrium are located to the left and posterior. A groove between atrium and ventricle marks the cardiac base. The right coronary artery (RCA) courses within the adipose tissue of the right atrioventricular groove. The left atrioventricular groove contains the left circumflex artery and great coronary vein. The interventricular septum, which separates right and left ventricles, is marked by less prominent indentations, the anterior and inferior interventricular grooves. The left anterior descending (LAD) coronary artery follows the anterior interventricular groove and the posterior descending artery courses along the inferior (posterior) interventricular groove (Fig. 2.2). Atrioventricular and interventricular grooves meet at the inferior base of the heart, the cardiac crux.

2.2 Standard Views

Even though the axial plane is not optimal for visualization of cardiac anatomy, it is the primary imaging plane in CT and usually gives a good overview of cardiac and coronary anatomy (Fig. 2.3). The angulations of the standard views for cardiac imaging correspond to the axis from base to apex and are oriented either parallel (horizontal or vertical long axis) or perpendicular (short axis) to this plane (Figs. 2.4–2.6).

Vertical Long Axis. The vertical long axis or two-chamber view is easily produced from the axial plane. It corresponds to a vertical plane through the cardiac apex and the middle of the mitral valve plane into the left atrium (Fig. 2.4) and is similar to the right anterior oblique view used with fluoroscopy or left ventriculography. The vertical long axis view displays the left ventricular inflow tract with the left atrium and the

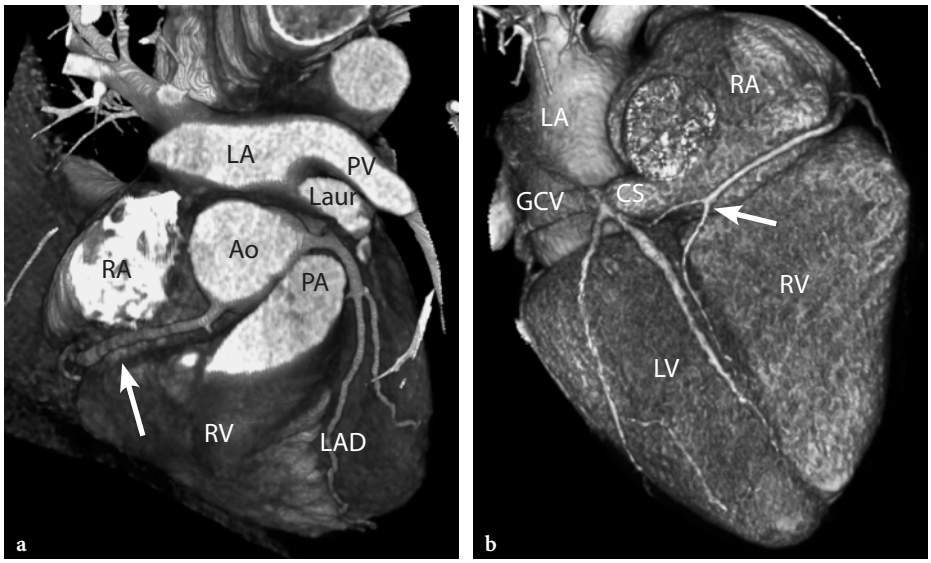

Fig. 2.2a, b. Three-dimensional display of the heart. **a** *Arrow* indicates right atrioventricular groove and right coronary artery. **b** Great cardiac vein (*GCV*) and posterior interventricular vein at the inferior aspect of the heart. The right coronary artery (RCA) bifurcates slightly proximal of the cardiac crux (*arrow* in **b**). *LA* left atrium, *RA* right atrium, *Ao* aorta, *PV* pulmonary vein, *Laur* left auricle, *PA* pulmonary artery, *D1* first diagonal branch, *RV* right ventricle, *LAD* left anterior descending coronary artery, *LV* left ventricle, *CS* coronary sinus

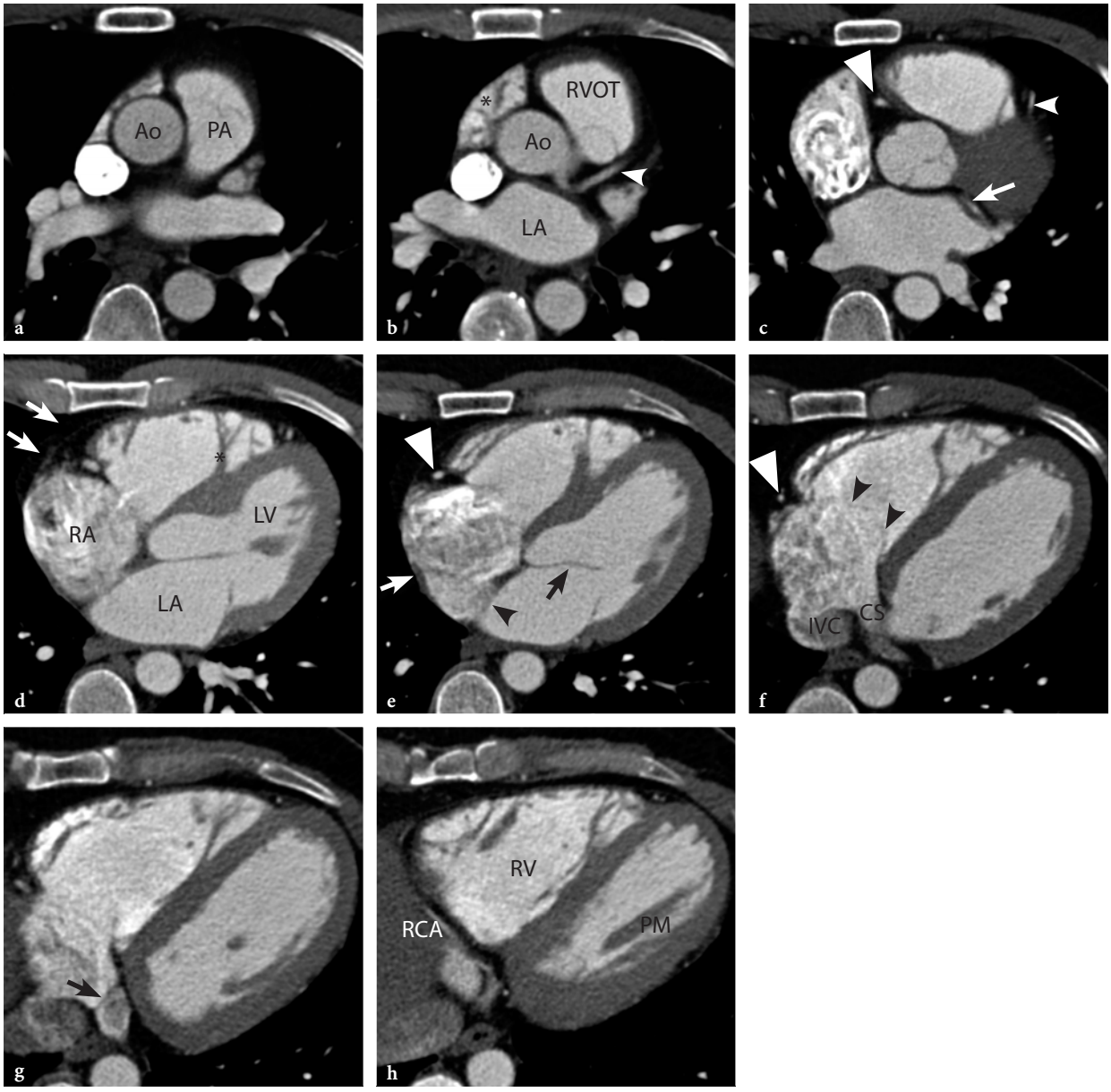

Fig. 2.3a–h. Axial anatomy of the heart in the craniocaudal direction. Visualization starts above the origin of the coronary arteries and displays the ascending aorta and pulmonary artery (*Ao* and *PA*, respectively, in **a**). The right atrial appendage (∗ in **b**) shows pronounced trabeculation. The LAD passes between the pulmonary trunk and the left atrial appendage and follows the anterior interventricular groove (*small white arrowhead* in **b** and **c**) down to the apex. The *RCA* (*large arrowhead* in **c**, **e**, and **f**) is depicted in the right atrioventricular groove, and the left circumflex artery is seen as a small vessel in the left atrioventricular groove (*small arrow* in **c**). The pericardium is identified as a thin tissue band (*small white arrows* in **d**). The mitral valve is well-delineated (*black arrow* in **e**) while the tricuspid valve is only faintly shown (*black arrowheads* in **f**). Also, separation of the right and left atria can be visualized (*black arrowhead* in **e**). The crista terminalis is seen in the right atrium (*white arrow* in **e**) and a small ridge at the orifice of the coronary sinus marks the thebesian valve (*black arrow* in **g**). Visualization of a slice at the apex of the heart reveals the distal segments of the *RCA* (**h**). *RVOT* Right ventricular outflow tract, *IVC* inferior vena cava, *PM* papillary muscle

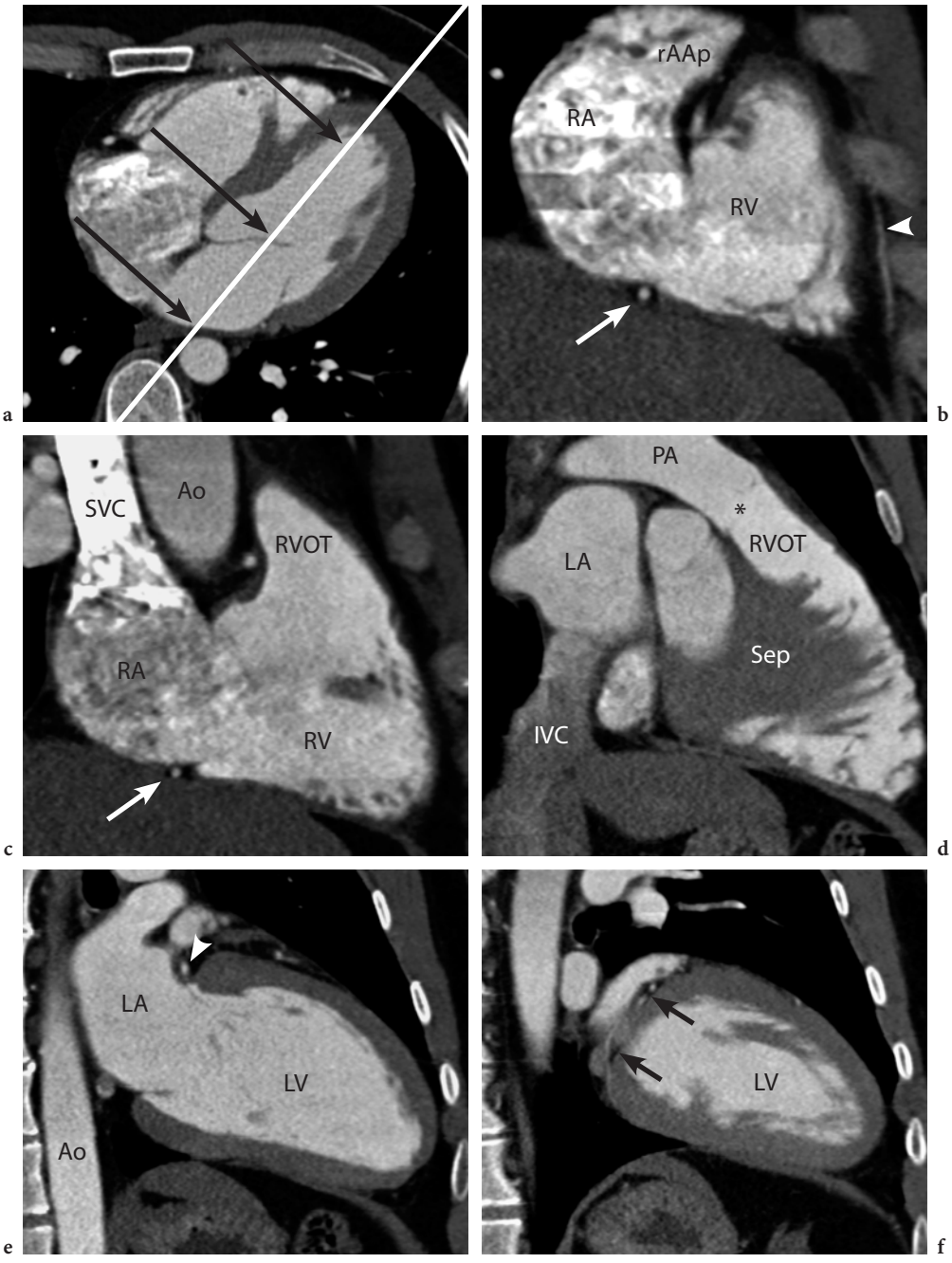

Fig. 2.4a–f. Vertical long axis views of the heart. **a** Vertical long axis orientation is shown as a line from the cardiac apex through the middle of the mitral valve plane. The tubular configuration of the *RA* and the more triangular shape of the RV are well-appreciated. Note the smooth appearance of the *RVOT* as opposed to the trabeculated inferior portion of the *RV* and the marked thinning of the left ventricular myocardium at the apex. *White arrow* in **b** and **c** *RCA*, *white arrowhead* in **e** left circumflex coronary artery, *black arrows* in **f** left atrioventricular groove, *white arrowhead* in **b** internal mammary artery. *rAAp* right atrial appendage, *SVC* superior vena cava, *Sep* septum

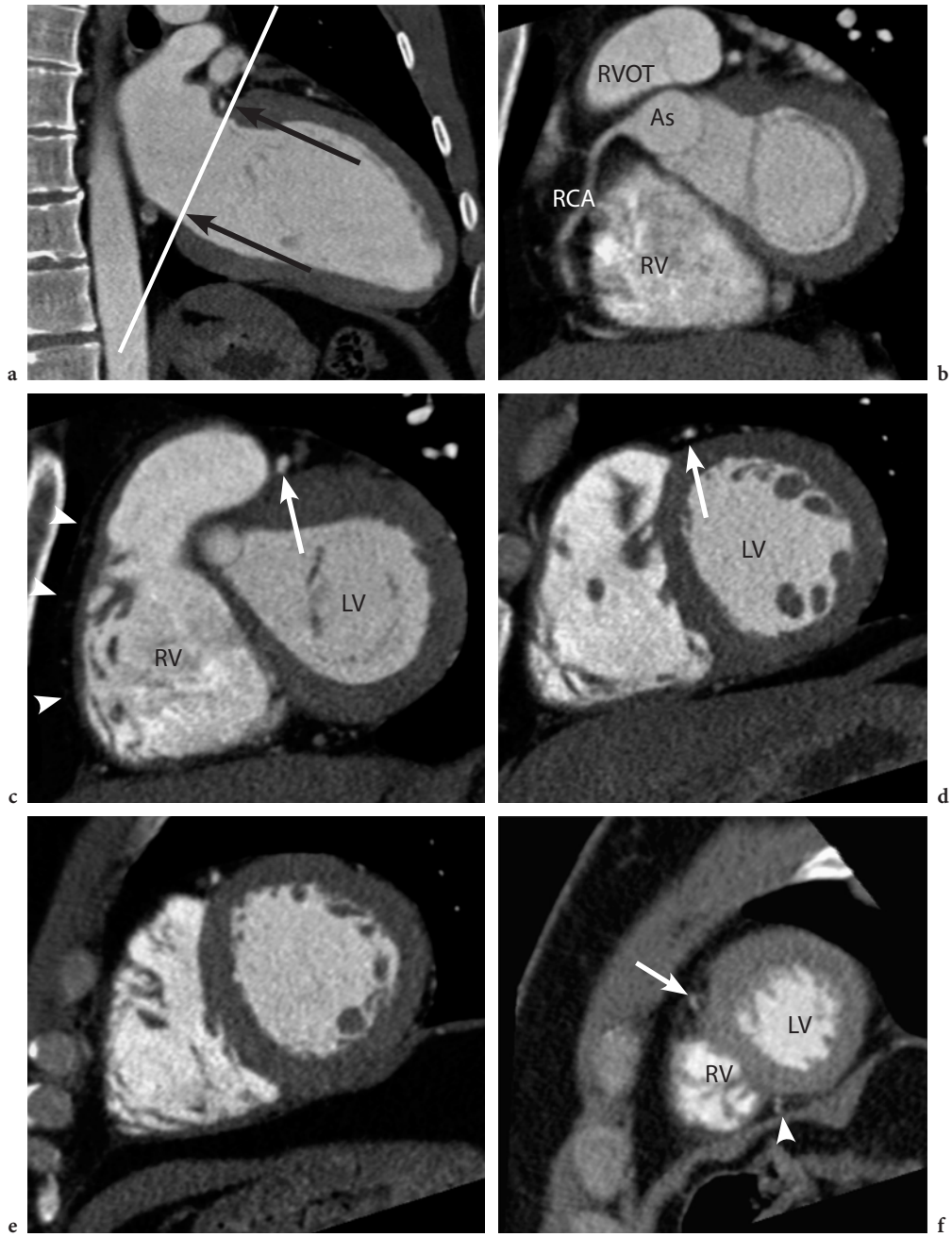

Fig. 2.5a–f. Short axis view of the heart. **a** Short axis orientation as planned from a vertical long axis view. The mitral valve is depicted as a thin soft-tissue structure in the left ventricular lumen in (**c**). Note the round configuration of the left ventricular cavity. *White arrow* (in **c**, **d**, and **f**) *LAD*, *white arrowhead* (in **f**) posterior descending artery. The *RCA* has an orientation parallel to the cardiac base and its descending segments are well-seen in this orientation. Note the anterior pericardium (*arrowheads* in **c**). *As* aortic sinus

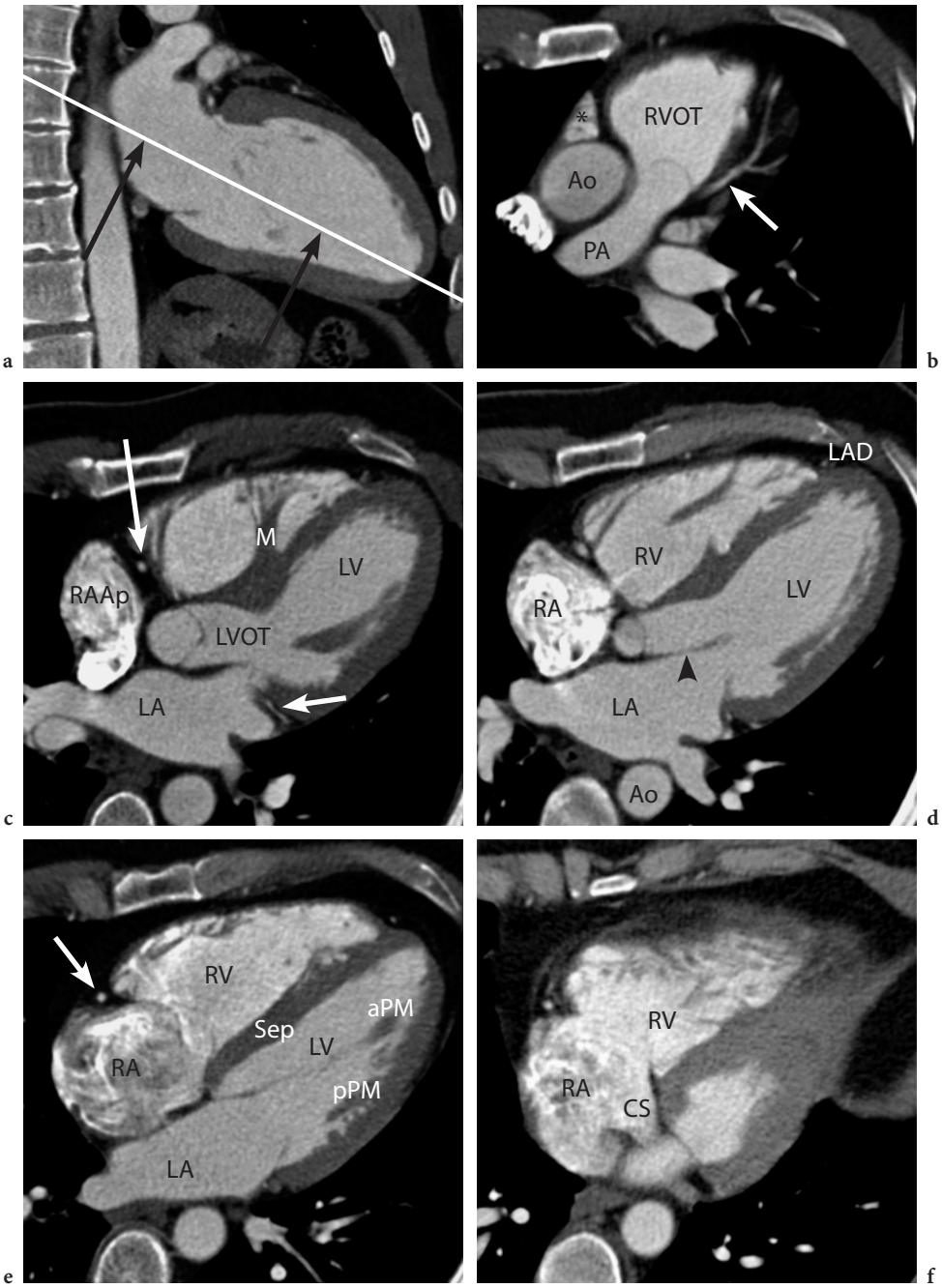

Fig. 2.6a–f. Horizontal long axis views of the heart. **a** Horizontal long axis orientation as planned from a vertical long axis view. Note the S-shape of the interventricular septum and the thin membranous part of the septum close to the cardiac base. The different coronary arteries can be delineated: *LAD* (*arrow* in **b**), *RCA* (*long arrow* in **c** and **e**), and *LCx* (*short arrow* in **c**). The moderator band (*M*) is well seen in the apical *RV* in (**c**). The anterior mitral valve leaflet (*white arrow* in **d**) forms part of the left ventricular outflow tract (*LVOT*)

mitral valve as well as parts of the left outflow tract; the right outflow tract is obliquely depicted. This view is particularly well-suited to delineate the configuration of the left ventricle and to assess the contraction of the anterior and inferior segments of the left ventricular myocardium. A vertical long axis view adapted to the course of the LAD along the anterior interventricular groove can be used to depict the LAD in almost its entirety. Maximum-intensity projection (MIP) images in this orientation also give an overview of the obtuse marginal branches of the left circumflex artery and the descending segment of the RCA.

Short Axis. The short axis view is oriented perpendicular to the vertical long axis and is parallel with the mitral valve plane and the cardiac base (Fig. 2.5). The short axis therefore has a double-oblique angulation to account for the dorsoventral and medioleftlateral tilt of the heart. Due to the alignment of the short axis view with the atrioventricular grooves, it can be used to display the RCA down to the cardiac crux, the posterolateral branches of the distal RCA, and the left circumflex coronary artery in its course in the left atrioventricular groove. The inferior facet of the right ventricle is parallel with the diaphragm and thus the transverse plane has a sharp angle (also called the acute margin), with the anterior free wall and the outflow tract of the right ventricle giving the right ventricle an almost triangular shape in this view. The left ventricle has a circular aspect on short axis view. Right and left ventricular motion can also be visualized with the short axis view and it is the basis for volumetric measurements used in global ventricular function evaluation.

Horizontal Long Axis. The horizontal long axis corresponds to a tilted plane from cardiac apex through the middle of the mitral valve plane to the cardiac base. It is perpendicular to the vertical long axis and displays both ventricles and atria in their largest diameters. This view is a frontal view onto the heart from the anterior aspect directed to the inferior wall and thus gives a good overview of the size and configuration of both ventricles. It can be used to delineate the mitral and tricuspid valves. As shown in Figure 2.6, the horizontal long axis imaging plane displays the left main coronary artery and the LAD with its diagonal branches. The RCA, like the proximal left circumflex coronary artery, is depicted in an orthogonal cut plane.

Left Ventricular Outflow Tract. In addition to the standard cardiac planes, several other views are used to depict motion or special anatomic or pathologic features. The left ventricular outflow tract (LVOT) view delineates the left inflow and outflow tracts and is useful to assess motion of the mitral and aortic valves or septum changes in hypertrophic obstructive cardiomyopathy. The LVOT view can be planned on a coronal view by tilting the imaging plane according to the ascending aorta (Fig. 2.7).

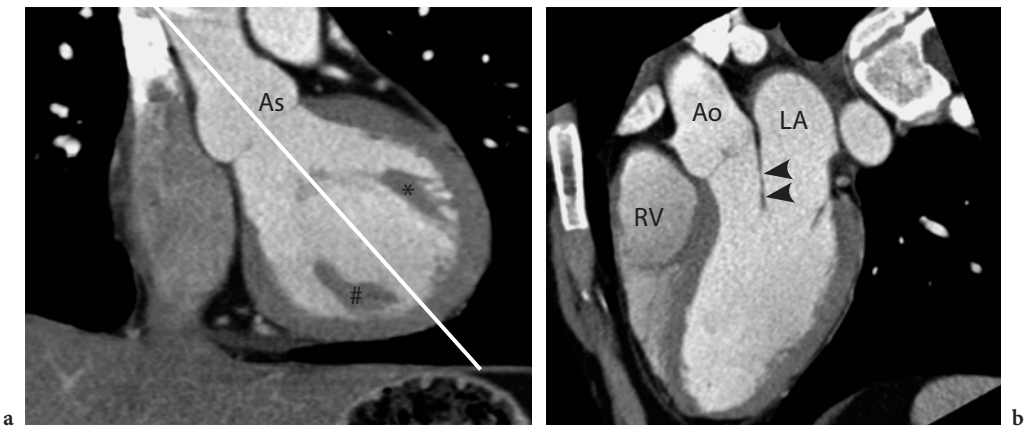

a b

Fig. 2.7a, b. Left ventricular outflow tract view as planned from a true coronal view. Note the bulging of the aortic sinus (*As*) and the aortic valve in closed position (**a**). The anterior mitral valve leaflet is well-depicted (*black arrowheads* in **b**) with its relation to the *LV* inflow and outflow tracts

2.3 Coronary Arteries and Veins

This section gives an overview of the relevant anatomy for coronary artery angiography with CT. Figure 2.8 provides a schematic overview of the coronary artery anatomy and Table 2.1 summarizes the segmental nomenclature of the major coronary vessels according to AHA recommendations (Scanlon 1999) For a more detailed description of coronary artery anatomy, including its many variations, the reader is referred to the literature (Mc Alpine 1975).

Right Coronary Artery. The right and left coronary arteries arise from the right and left aortic sinus. The RCA arises from the aorta slightly caudal from the origin of the left coronary artery. The RCA takes its course down the right atrioventricular groove toward the cardiac crux, where it usually bifurcates into the posterior descending artery (PDA) and the right posterolateral ventricular (PLV) branches (Fig. 2.2b). The artery that crosses the cardiac crux and gives rise to the PDA represents the dominant coronary artery. In most people (>70%), the PDA arises from the distal RCA and supplies the inferior portion of the ventricular septum. Right PLV branches supply the inferior left ventricular wall and the inferior papillary muscle. A left dominance is found in 10% of persons, with the PDA arising from the left circumflex coronary artery. In this case, the RCA remains a very small vessel and terminates before it reaches the cardiac crux. In 20% of human hearts, there is an equal coronary distribution, so that the PDA arises from the RCA but the left coronary artery supplies the inferior segments of the left ventricle.

In a majority of people (50–60%), the first branch of the RCA is the conus artery. It passes upward and anteriorly to supply the right ventricular outflow tract. Otherwise, the conus artery arises as a separate vessel from the right aortic sinus just above the right coronary ostium. This vessel can be depicted with short axis MIP images (Fig. 2.9a). The second RCA branch in 60% of human hearts is the sinoatrial node artery. This vessel is rather tiny, but can be identified in a significant number of CT reformations as a vessel that courses dorsally toward the

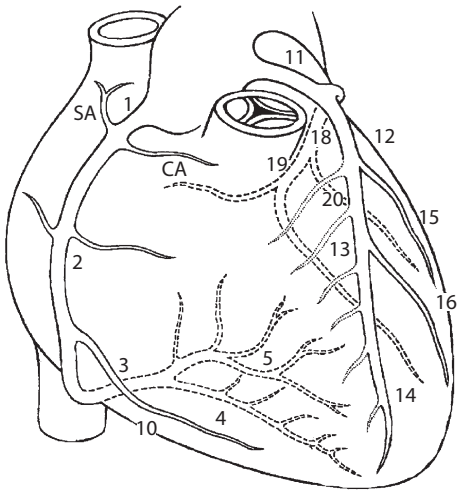

Fig. 2.8. Coronary artery anatomy and segmental classification as summarized in Table 2.1

Table 2.1. Coronary artery segments and corresponding anatomic names

Segment		Anatomic name and location
AHA 1999	AHA 1976	
1	1	RCA, proximal segment
2	2	RCA, middle segment
3	3	RCA, distal segment
4	4	PDA, right posterior descending artery
6		Right posterolateral branch
10		Acute marginal branch
11	5	LM, left main coronary artery
12	6	LAD, proximal segment
13	7	LAD, middle segment
14	8	LAD, distal segment
15	9	First diagonal branch
16	10	Second diagonal branch
18	11	LCx, proximal segment
19	13	LCx, middle/distal segment
20	12	First obtuse marginal branch
21		Second obtuse marginal branch
22		Third obtuse marginal branch
24	14	First left posterolateral branch
27	15	Left posterolateral descending artery
28		Ramus intermedius

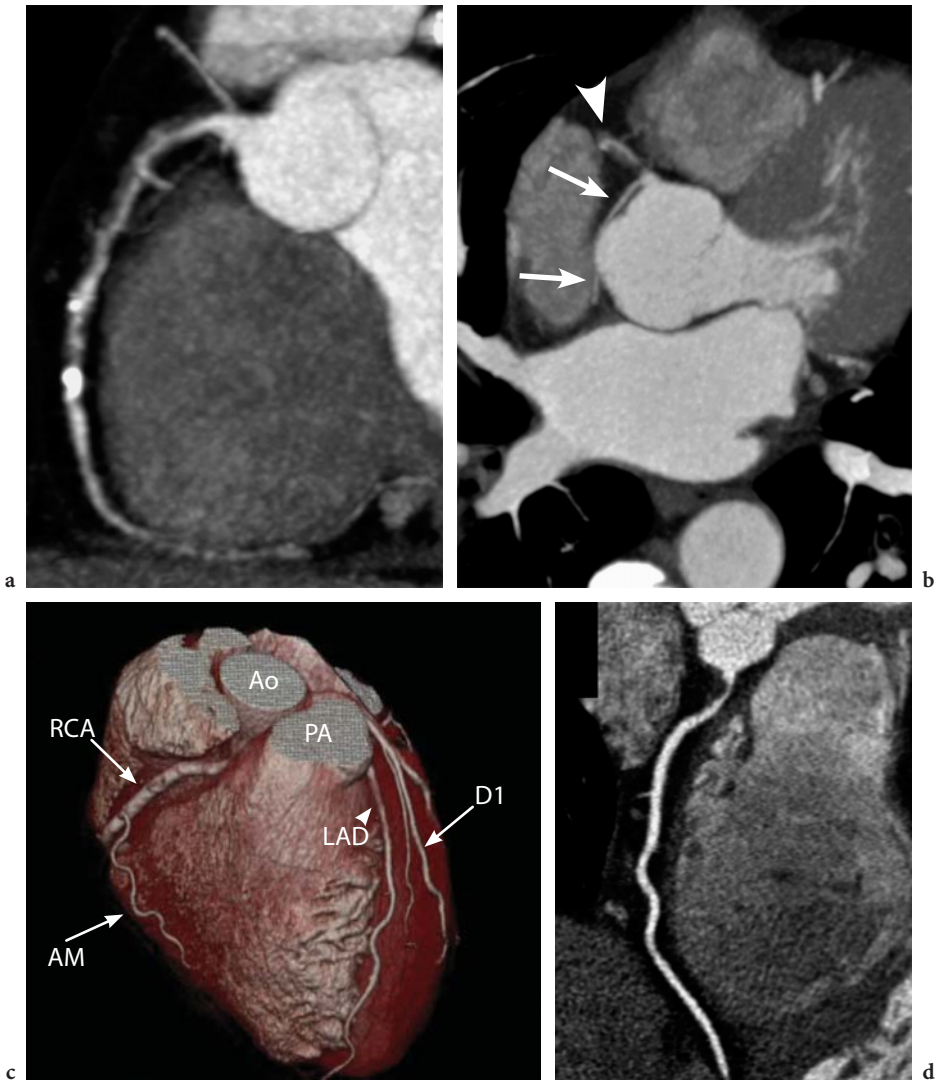

Fig. 2.9. a Right coronary artery displayed with curved maximum intensity projection (MIP) over its entire course. The conus artery is seen as the first branch of the RCA (*arrowhead* in **b**). The sinus node artery passes between the *Ao* and right atrial appendage (*arrows* in **b**). Proximal and middle segment including the acute marginal branch (*AM*) in 3D display is shown in (**c**). Curved multiplanar reformation (MPR) allows display of all four main segments in one view (**d**)

lateromedial aspect of the right atrium (Fig. 2.9b). Several marginal (or right ventricular) branches supply the anterior free wall of the right ventricle. The right ventricular branch originates from the middle RCA segment (Fig. 2.9c). The largest marginal branch usually travels along the acute margin from base to apex and thus is called the acute marginal branch. Despite the tortuous course of the RCA, the entire vessel can be displayed in one view using curved multiplanar reformations (Fig. 2.9d).

Left Coronary Artery. The left main coronary artery takes a short course along the epicardium, between the pulmonary trunk and left atrium. It then divides

into the LAD and the left circumflex (LCx) arteries. A third artery, the intermediate artery, may also arise at this division, thus forming a trifurcation in 20–30% of hearts (Figs. 2.9c, 2.10). This ramus intermedius is analogous to a diagonal branch and it usually supplies the anterolateral free wall.

The LAD passes down the cardiac midline along the anterior interventricular groove to the cardiac apex. Its major branches are the septal and diagonal branches. The septal branches, which supply the anterior and apical septum, vary in size, but they are rarely identified on CT. There is a wide variability in the number and size of the diagonal branches. Unlike the septal branches, one to three diagonal branches, which supply the anterior left ventricular free wall, are usually well seen on CT (Figs. 2.9c, 2.11).

The left circumflex artery follows the left atrioventricular groove and gives off one to three large obtuse marginal branches. The distal LCx beyond the obtuse marginal branch tends to be a rather small vessel that is difficult to delineate on CT. The LCx and its obtuse marginal branches supply the lateral left ventricular wall. This artery commonly terminates beyond its large obtuse marginal branch. The length and caliber of the LCx coronary artery varies with the caliber and distribution of the right coronary artery, as described above.

Coronary Veins. The coronary venous circulation comprises the cardiac veins, coronary sinus, and thebesian veins (venae cordis minimae). The great cardiac vein courses in the anterior interventricular groove along the LAD and then follows the LCx coronary artery in the left atrioventricular groove. The great cardiac vein and the left posterior and middle cardiac veins drain into the coronary sinus (Fig. 2.2b). The coronary sinus drains the coronary blood into the right atrium.

2.4 Pericardium

The parietal pericardium is a fibrous sac that envelops the heart and attaches onto the great vessels. The visceral pericardium forms the serous inner lining of the fibrous pericardium as well as the outer lining of the heart and great vessels. The pericardium is usually seen as single thin layer of a soft-tissue-density structure (Fig. 2.3d). It contains the epicardial coronary arteries and veins, autonomic nerves, lymphatics, and adipose tissue. The junctions between the visceral and parietal pericardium lie along the

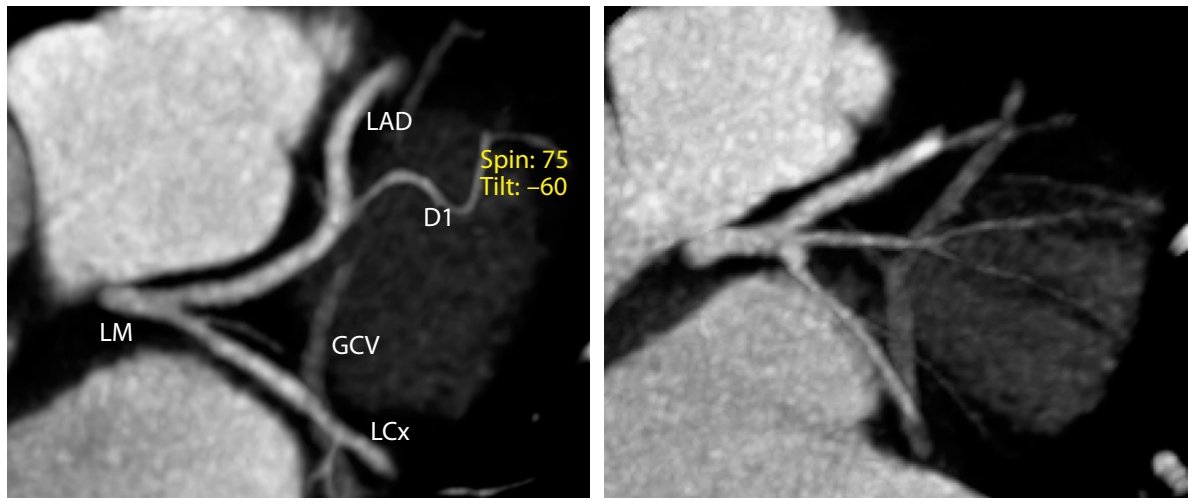

Fig. 2.10a, b. Normal left coronary artery. The left main coronary artery (*LM*) bifurcates and gives off the *LAD* and left circumflex (*LCx*) coronary arteries. An intermediate ramus is depicted in **b**. The *GCV* is seen adjacent to the *LAD* (**a**) and in the atrioventricular groove (**b**)

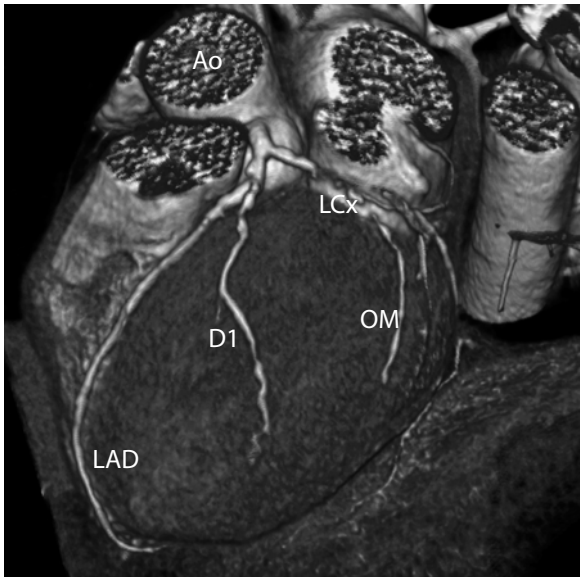

Fig. 2.11. Three-dimensional display of the left coronary system. Note a proximal occlusion of the *LCx* artery. *OM* Obtuse marginal branch

great vessels and form the pericardial reflections. Almost the entire ascending aorta and main pulmonary artery as well as portions of both venae cavae and all four pulmonary veins are intrapericardial.

2.5 Cardiac Chambers

Right Atrium. The right atrium has a tubular shape and with its smooth-walled posterior portion forms an almost straight continuation of the upper and inferior venae cavae. The posterior component that receives the venae cavae and the coronary sinus is separated by a prominent muscle ridge, the crista terminalis (Fig. 2.3e), from a muscular anterior region from which the right atrial appendage emanates. The right atrial appendage lies in close proximity to the right aortic sinus and overlies the proximal right atrioventricular groove and the RCA.

Right Ventricle. The right ventricle occupies the sternocostal surface of the heart. It is made up of inlet and trabecular outflow components. The myocardium of the right ventricular free wall ranges between 1 and 3 mm in CT and is much thinner than that of the left ventricle. The inlet portion extends from the tricuspid annulus to the insertions of the three papillary muscles. A trabecular zone extends beyond the attachments of the papillary muscles toward the ventricular apex. There, an intracavitary muscle, the moderator band, forms a prominent trabecular structure that connects the septum with the anterior tricuspid papillary muscle (Fig. 2.3d). The right outflow tract, or conus, is a smooth-walled muscular subpulmonary channel.

Left Atrium. The left atrium is dorsally located and collects the blood from the valveless pulmonary veins. Anterolaterally, the left atrial appendage overlies the LCx coronary artery and sometimes the left main coronary artery. The left atrial appendage is tubular in shape and less trabeculated than the right atrial appendage. The atrial septum consists of the interatrial and atrioventricular regions. The interatrial portion is characterized by the fossa ovalis, a shallow depression at the position of the former foramen ovale, which is usually not delineated with CT.

Left Ventricle. The left ventricle has an inlet component and a subaortic outflow component. The interventricular septum bulges towards the right ventricle, which results in the round configuration of the left ventricular cavity seen on short axis views (Fig. 2.5). The left ventricular free wall is normally thickest toward the base, where it measures between 6 and 12 mm, and thinnest toward the apex, where it averages only 1–2 mm in thickness (Fig. 2.4). The trabeculae of the left ventricle are more densely packed than those of the right ventricle, which result in a rather smooth appearance of the left ventricular cavity. The two papillary muscles are distinct soft-tissue structures seen in the cavity of the left ventricle. The anterior papillary muscle attaches to the anterior leaflet of the mitral valve, while the inferior muscle extends to the posterior leaflet. The ventricular septum may be divided into the muscular septum and a short membranous portion at the base. The membranous septum lies beneath the right and posterior aortic cusps and contacts the mitral and

tricuspid annuli. The septum has a slightly S-shaped configuration due to the different orientations of the infundibular and ventricular components, which is well-appreciated on images in the axial plane or the horizontal long axis view. The majority of clinically significant ventricular septal defects involve the membranous septum.

The left ventricle can be divided into specific segments with reference to the long axis and short axis views (Cerqueira 2002). The location of a segment along the long axis is defined as basal, mid-cavity, and apical. In the short axis view, the basal and mid-cavity slices are further subdivided into six equal segments: anterior, anteroseptal, inferoseptal, inferior, inferolateral, and anterolateral. The appropriate names for each segment are the combination of the long axis location and the circumferential position, e.g., basal anteroseptal or mid-inferolateral. The apical slices are dived into only four segments, the apical anterior, apical septal, apical inferior, and apical lateral segments. The apical cap, which represents the left ventricular myocardium of the extreme tip of the left ventricle, is called the apex. Using this scheme, the left ventricular myocardium can be divided into 17 segments, which are used for bulls-eye plots of the left ventricular myocardium (Fig. 2.12). Although there is tremendous variability in the coronary artery blood supply to myocardial segments, individual segments have been assigned to specific coronary artery territories. The LAD usually supplies the anterior and anteroseptal segments, the RCA is assigned to the inferior and inferolateral segments, while the LCx supplies the anterolateral and inferolateral segments. The apex may derive its supply from any of the three vessels.

2.6 Cardiac Valves

The four cardiac valves are anchored to fibrous rings, which comprise their annuli at the base of the heart. The annuli join to form the fibrous skeleton of the heart. The aortic valve is located centrally, and its fibrous ring extensions abut each of the other three valves (Fig. 2.13).

Tricuspid Valve. The tricuspid valve consists of the anterior, septal, and posterior leaflets. The anterior leaflet is the largest and forms an intracavitary separation of the inflow and outflow tracts of the right ventricle. The septal leaflet has many direct chordal attachments to the ventricular septum, and the posterior leaflet is usually the smallest. The tricuspid valve is a rather thin structure and, due to either small attenuation differences between blood

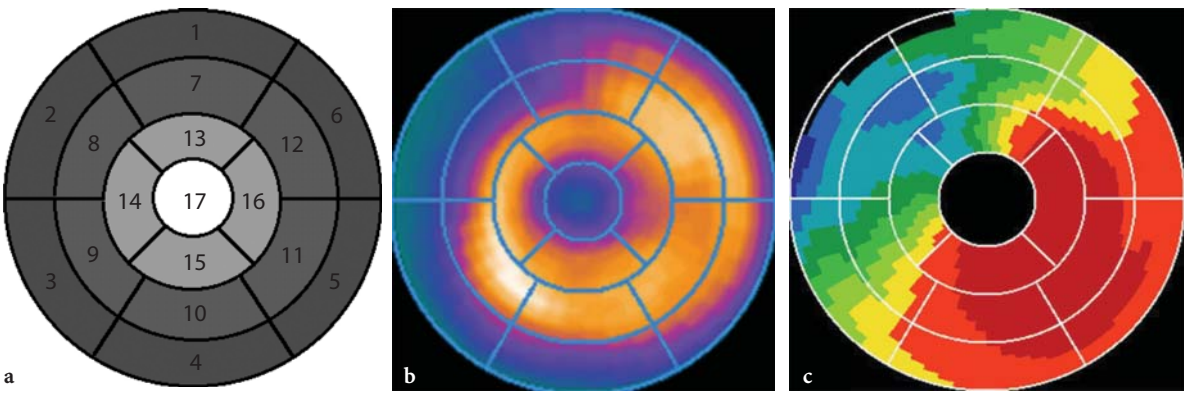

Fig. 2.12. a Bulls-eye plot of the left ventricle segments. *1* basal anterior, *2* basal anteroseptal, *3* basal inferior, *4* basal inferior, *5* basal inferolateral, *6* basal anterolateral, *7* mid-anterior, *8* mid-anteroseptal, *9* mid-inferior, *10* mid-inferior, *11* mid-inferolateral, *12* mid-anterolateral, *13* apical anterior, *14* apical septal, *15* apical inferior, *16* apical inferior, *17* apex. **b**, **c** Examples of color coded bulls-eye plots. **b** PET perfusion study, **c** MR regional ejection fraction

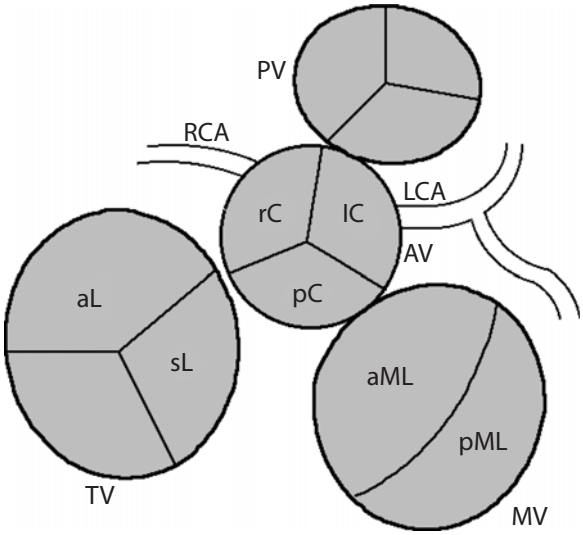

Fig. 2.13. Anatomy of the cardiac base and cardiac valves. The aortic valve (*AV*) is centrally located. The coronary arteries rise at the right (*rC*) and left (*lC*) aortic cusps. The posterior cusp is the non-coronary cusp. *TV* Tricuspid valve with anterior (*aL*) and septal (*sL*) leaflets. *MV* Mitral valve with anterior (*aML*) and posterior (*pML*) leaflets. *LCA* Left coronary artery

and valve tissue or streak artifacts related to high-density contrast agent in the right atrium, it is rarely well-delineated on CT images (Fig. 2.3f).

Mitral Valve. In contrast to the other cardiac valves, the mitral valve has only two leaflets. The anterior leaflet is large and semicircular, and, like the anterior tricuspid leaflet, it partially separates the ventricular inflow and outflow tracts. Unlike its right-sided counterpart, the mitral valve leaflets are usually well-depicted on CT. Beneath the two mitral commissures – the separations of the leaflets – lie the anterior and inferior papillary muscles, which arise from the left ventricular free wall. Commissural chords arise from each papillary muscle and extend in a fan-like array to insert into both leaflets adjacent to the commissures.

Aortic Valve. The aortic valve comprises the annulus, cusps, and commissures and, like the pulmonary valve, has no tensor apparatus. The left, right, and posterior half-moon-shaped (semilunar) aortic cusps form pocket-like tissue flaps. The commissures between the cusps reach the level of the aortic sinotubular junction, where the sinus and tubular portions of the ascending aorta meet. The components of the aortic valve are well-visualized by CT and may be depicted in open and closed positions with appropriate reconstructions. There is a close relation between the mitral valve and the aortic valve as the intervalvular fibrosa at the level of the left and posterior aortic cusps is merged with the anterior mitral leaflet.

2.7 Great Vessels

Vena Cava. The right and left subclavian veins merge with the corresponding internal jugular veins to form the right and left brachiocephalic veins. The left brachiocephalic vein is longer than its right-sided counterpart and travels anterior to the aortic arch and the ascending aorta until it merges with the right brachiocephalic vein to form the superior vena cava. The superior vena cava lies anterior to the right pulmonary artery and receives the azygos vein posteriorly before it drains into the right atrium (Fig. 2.14). A left superior vena cava may persist. This vessel then usually drains into the coronary sinus (Fig. 2.15a).

Pulmonary Artery. The pulmonary trunk arises from the conus of the right ventricle and ascends obliquely ventral and then to the left of the ascending aorta (Fig. 2.15b). It bifurcates near the undersurface of the aortic arch into right and left branches. The left pulmonary artery courses over the left bronchus, whereas the right pulmonary artery, which is longer and slightly larger than the left, travels horizontally beneath the aortic arch and ventral to the right bronchus. At the root of the lung, it divides into the upper lobe artery and the intermediate artery. The upper lobe artery divides into the apical and posterior segmental branches and the anterior branch. The intermediate artery, or interlobar trunk, gives rise to the middle lobe artery and the segment artery of the apical seg-

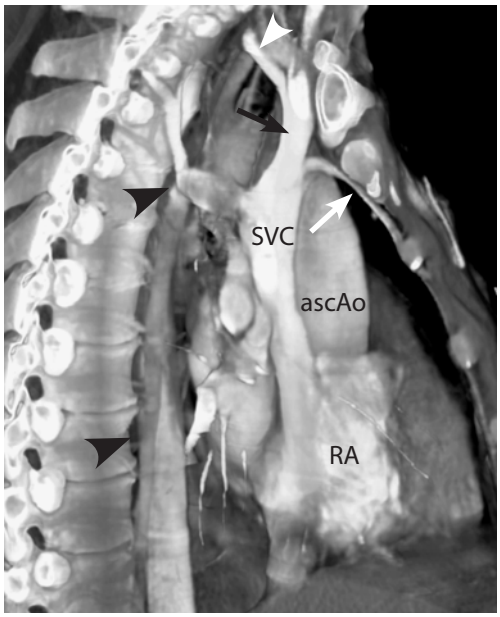

Fig. 2.14. Anatomy of the superior vena cava. The internal jugular (*white arrowhead*) and right subclavian veins form the short right brachocephalic vein (*black arrow*). The azygos vein (*black arrowheads*) courses over the right bronchus and drains into the SVC from posterior. Note the right internal mammary vein (*white arrow*) draining into the cranial vena cava

ment of the right lower lobe. The continuation of the intermediate artery divides into the four basal segment arteries. The left pulmonary artery gives rise to the apical and posterior arteries of the apicoposterior segment and the anterior segment artery of the left upper lobe. The lingular artery and the superior segmental artery of the lower lobe arise from the interlobular portion of the left pulmonary artery. The remainder of the artery divides into the four basal segment arteries.

Pulmonary Veins. In conventional normal anatomy, single right and left superior and inferior pulmonary veins drain into the left atrium (Fig. 2.16). Their orifices lie on the posterior aspects of the left atrial cavity and are well-visualized using 3D volume-rendering technique (Lacomis 2003). A large atriovenous junction is created when upper and lower lobe veins merge proximal to the left atrium. This variant is found more frequently on the left than on the right. Accessory pulmonary veins with independent junctions with the left atrium are seen more frequently on the right (Fig. 2.17). A vein that drains into a structure other than the left atrium is termed an anomalous pulmonary vein. With the

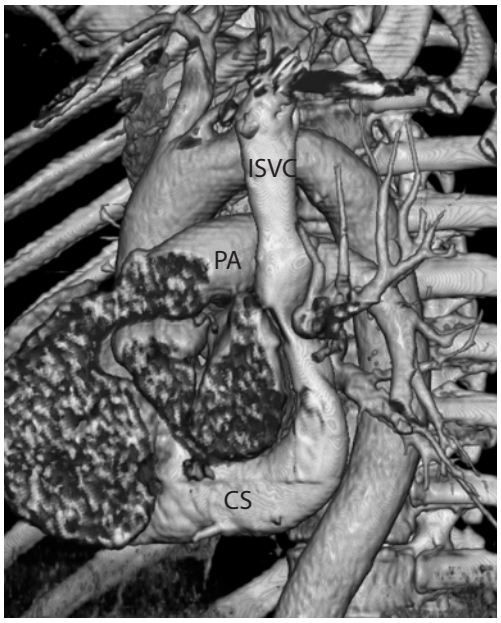

a

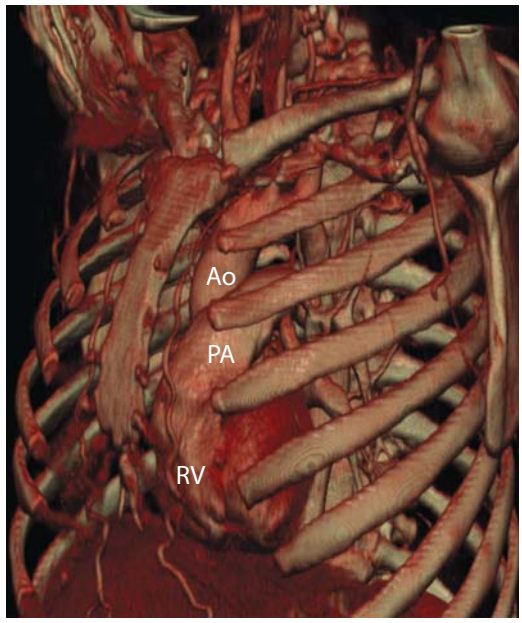

b

Fig. 2.15. 3D volume-rendering displays of a persistent left-sided vena cava draining into the enlarged coronary sinus and **b** the *PA* originating from the conus of the *RV*

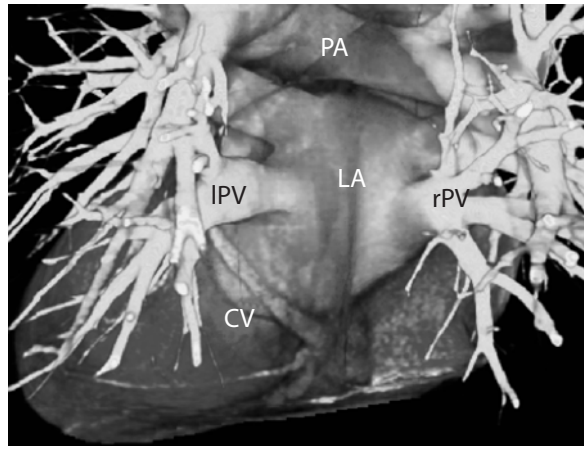

Fig. 2.16. Pulmonary venous anatomy as seen from a left posterior view. Single inferior and superior pulmonary veins are seen on the left and right. *lpV*, *rPV* Left and right pulmonary veins, *CV* coronary vein

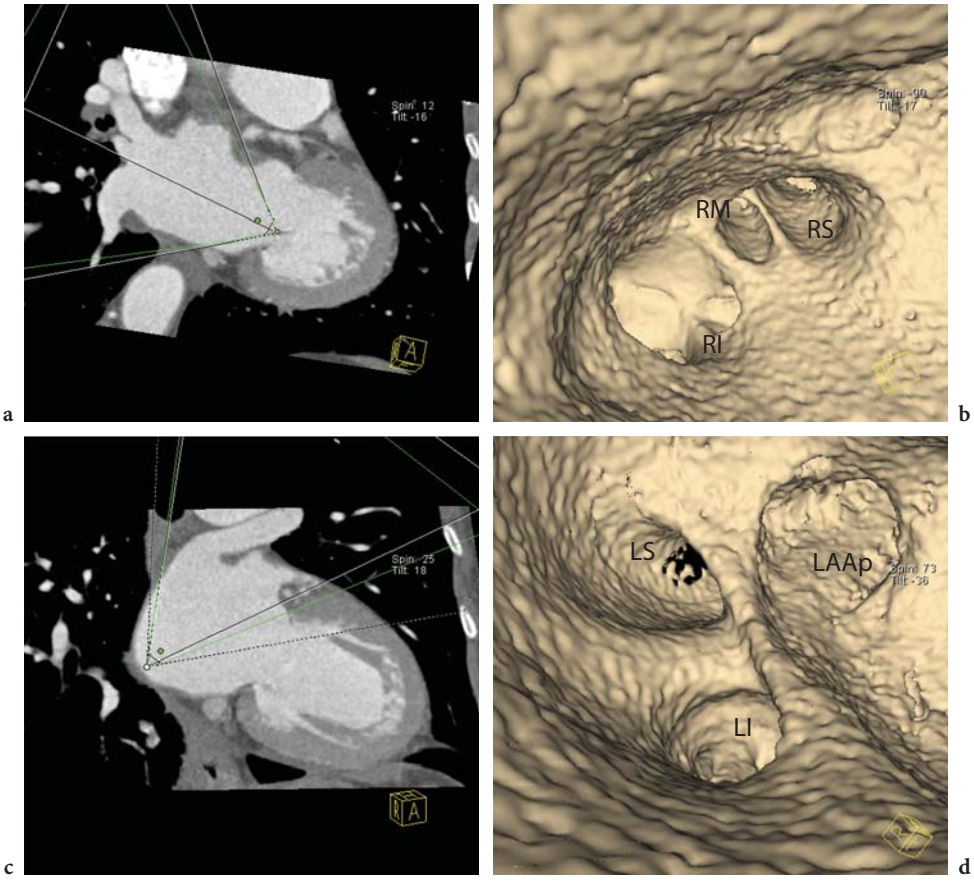

Fig. 2.17a–d. Endocardial views and corresponding reference images of the LA with pulmonary ostia. **a**, **b** A small intervenous saddle separates the accessory right middle vein from the right superior vein. *RI* Right inferior vein. **c**, **d** On the left, the superior and inferior veins are depicted with the adjacent orifice of the left atrial appendage (*LAAp*)

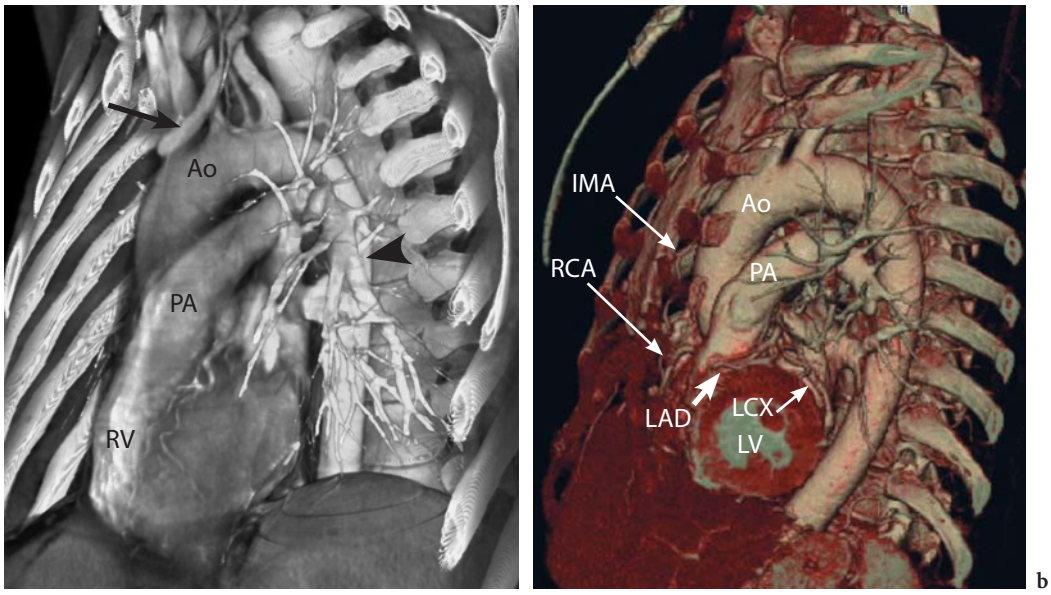

a b

Fig. 2.18. a 3D volume rendering of the thoracic vessels from an ECG-gated spiral *CT*. The left brachiocephalic vein passes ventral to the aortic arch to drain into the SVC. The aortic arch gives off the brachiocephalic trunk, the left common carotid, and subclavian arteries, and a variant left vertebral artery. The *PA* ascends from the RVOT and rises ventral to the ascending aorta to bifurcate underneath the aortic arch. The left *PA* branches (*arrow*) are posterior to the left PVs. **b** An ECG-gated spiral scan of the chest using the latest 64-slice CT scanners reveals the great thoracic vessels, the internal mammary arteries (*IMA*), the greater cardiac anatomy, and the coronary arteries from the same scan

evolution of pulmonary vein ablation therapy for atrial fibrillation, precise demonstration of pulmonary vein anatomy is becoming increasingly important. Virtual endoscopic views can easily be generated to display pulmonary vein anatomy as seen from the left atrium (Fig. 2.17) and may help to guide catheter ablation.

Aorta. The thoracic aorta arises at the level of the aortic valve and is divided into three segments: ascending aorta, aortic arch, and descending thoracic aorta. The ascending aorta is about 3 cm in diameter and consists of sinus and tubular portions, which are demarcated by the sinotubular junction. The entire ascending aorta is covered by the visceral pericardium. The aortic arch travels over the left main bronchus and the right pulmonary artery and gives rise to the brachiocephalic (innominate), the left common carotid, and the left subclavian arteries. In about 10% of persons, the innominate and left common carotid share a common ostium; in 5%, the left vertebral artery arises directly from the aortic arch in between the left common carotid and the left subclavian artery instead of from the subclavian artery (Fig. 2.18a). The remnant of the ductus arteriosus botalli, which, when patent, connects the proximal left pulmonary artery with the aortic arch, forms the ductal artery ligament. The descending thoracic aorta lies adjacent to the left atrium and the vertebral column. An ECG-gated scan of the entire chest using the latest 64-slice CT scanners enables display of the great thoracic vessels, the greater cardiac anatomy, and the coronary arteries from a single scan (Fig. 2.18b).

Abbreviations used in figure legends	
aL	Anterior leaflet
AM	Acute marginal branch
aML	Anterior mitral valve leaflet
Ao	Aorta
As	Aortic sinus
AV	Aortic valve
CS	Coronary sinus
CV	Coronary vein
D1	First diagonal branch
GCV	Great coronary vein
IMA	Internal mammary arteries
IVC	Inferior vena cava
LA	Left atrium
LAAp	Left atrial appendage
LAD	Left anterior descending artery
Laur	Left auricle
lC	Left aortic cusp
LCA	Left coronary artery
LCx	Left circumflex coronary artery
lPV	Left pulmonary vein
LV	Left ventricle
LVOT	Left ventricular outflow tract
M	Moderator band
MV	Mitral valve
OM	Obtuse marginal branch
PA	Pulmonary artery
PM	Papillary muscle
pML	Posterior mitral valve leaflet
PV	Pulmonary vein
RA	Right atrium
rAAp	Right atrial appendage
rC	Right aortic cusp
RCA	Right coronary artery
RI	Right inferior vein
rPV	Right pulmonary vein
RV	Right ventricle
RVOT	Right ventricular outflow tract
Sep	Septum
sL	Septal leaflet
SVC	Superior vena cava
TV	Tricuspid valve

References

Bittl JA, Levin DC (1997). Coronary arteriography. In: Braunwald E (ed) Heart disease – a text book of cardiovascular medicine. Vol. 1. Saunders, Philadelphia, 240–272

Cerqueira MD, Weissman NJ, Dilsizian V, Jacobs AK, Kaul S, Laskey WK, Pennell DJ, Rumberger JA, Ryan T, Verani MS. Standardized myocardial segmentation and nomenclature for tomographic imaging of the heart: a statement for healthcare professionals from the Cardiac Imaging Committee of the Council on Clinical Cardiology of the American Heart Association. Circulation 2002; 105:539–542

Edwards W (1984a). Anatomic basis for tomographic analysis of the heart at autopsy. Cardiol Clin 2:485–506

Edwards W (1984b). Anatomy of the cardiovascular system. In: Clinical Medicine. Philadelphia: Harper & Row

Lacomis JM, Wigginton W, Fuhrman C, Schwartzman D, Armfield DR, Pealer KM (2003). Multi-detector row CT of the left atrium and pulmonary veins before radio-frequency catheter ablation for atrial fibrillation. Radiographics 23 Spec No:S35–48; discussion S48–50

McAlpine W (1975). Heart and coronary arteries: An anatomic atlas for radiologic diagnosis and surgical treatment. Springer, New York

Ooijen van PM, Sablayrolles JL, Ligabue G, Zijlstra F (2004). Coronary anatomy. In: Oudkerk (ed) Coronary radiology. Springer, Berlin Heidelberg, New York. pp.1–23

Scanlon P, Faxon D, et al (1999). ACC/AHA guidelines for coronary angiography. A report of the American College of Cardiology/American Heart Association Task Force on Practice Guidelines. J Am Coll Cardiol; 33:1756–1824

Multi-slice CT Technology

3

Thomas Flohr and Bernd Ohnesorge

Contents

3.1 **Evolution from 1 to 64 Slices** *41*

3.2 **Principles of Multi-slice CT System Design** *45*

3.3 **Multi-slice CT Acquisition and Reconstruction for Body Imaging** *52*
3.3.1 Definition of the Pitch *52*
3.3.2 The Cone-Angle Problem in Multi-slice CT *53*
3.3.3 Multi-slice Spiral Reconstruction Neglecting the Cone-Beam Geometry *54*
3.3.3.1 180° and 360° Multi-slice Linear Interpolation *54*
3.3.3.2 z-Filter Approaches *56*
3.3.4 Multi-slice Spiral Reconstruction with Cone-Beam Algorithms *58*
3.3.4.1 Overview of Cone-Beam Reconstruction Algorithms *58*
3.3.4.2 3D Filtered Back-Projection *58*
3.3.4.3 Adaptive Multiple Plane Reconstruction *59*
3.3.4.4 Weighted Hyperplane Reconstruction *61*
3.3.4.5 Double z-Sampling *62*

References *67*

3.1 Evolution from 1 to 64 Slices

Computed tomography (CT) was introduced in the early 1970s and has revolutionized not only diagnostic radiology, but also the entire practice of medicine. In the early 1990s, the introduction of spiral CT constituted a further evolutionary step in the development and ongoing refinement of CT imaging techniques (Kalender 1990, Crawford 1990). Until then, the examination volume had to be covered by subsequent axial scans in a «step-and-shoot» mode, the so-called sequence-scan technique. Consequently, axial scanning required long examination times because of the inter-scan delays necessary to move the table incrementally from one scan position to the next, and it was prone to misregistration of anatomical details due to the potential movement of relevant anatomical structures between two scans, e. g., by patient motion, breathing, or swallowing. With spiral CT, the patient table is continuously translated while scan data are acquired. The prerequisite for the success of spiral scanning was the introduction of slip-ring gantries, which eliminated the need to rewind the gantry after each rotation and enabled continuous data acquisition during multiple rotations. For the first time, volume data could be acquired without the danger of misregistration or double-registration of anatomical details. Images could be reconstructed at any position along the patient axis (longitudinal axis), and overlapping image reconstruction could be used to improve longitudinal resolution. Volume data became the very basis for applications such as CT angiography (Rubin 1995), which has revolutionized non-invasive assessment of vascular disease. The ability to acquire volume data also paved the way for the development of 3D image-processing techniques, such as multi-planar reformations (MPR), maximum intensity projections (MIP), surface-shaded displays (SSD), and volume-rendering techniques (VRT) (Napel 1993). These have become vital components of medical imaging today.

Ideally, volume data are of high spatial resolution and isotropic in nature, i.e., the data element («voxel») of each image is of equal dimensions in all three spatial axes, and forms the basis for image display in arbitrarily oriented imaging planes. For most clinical scenarios, however, single-slice spiral

CT with 1-s gantry rotation time is unable to fulfill these prerequisites. To avoid motion artifacts and to optimally use the contrast bolus, spiral CT body examinations need to be completed within a certain timeframe of, ordinarily, one patient breath-hold (25–30 s). If a large scan range, such as the entire thorax or abdomen (30 cm), has to be covered with single-slice spiral CT within a single breath-hold, a thick collimation of 5–8 mm must be used. While the in-plane resolution of a CT image depends on the system geometry and on the reconstruction kernel selected by the user, the longitudinal (z-) resolution is determined by the collimated slice width and the spiral interpolation algorithm. A thick collimation of 5–8 mm results in a considerable mismatch between the longitudinal resolution and the in-plane resolution, which is usually 0.5–0.7 mm depending on the reconstruction kernel. Thus, with single-slice spiral CT, the ideal of isotropic resolution can only be achieved for very limited scan ranges (Kalender 1995).

Strategies to achieve more substantial volume coverage with improved longitudinal resolution have included the simultaneous acquisition of more than one slice at a time and a reduction of the gantry rotation time. Interestingly, the very first medical CT scanners were 2-slice systems, such as the EMI head scanner, introduced in 1972, or the Siemens SIRETOM, introduced in 1974. With the advent of whole-body fan-beam CT systems for general radiology, 2-slice acquisition was no longer used. Apart from a dedicated 2-slice system for cardiac applications, the IMATRON C-100, introduced in 1984, the first step towards multi-slice acquisition in general radiology was a 2-slice CT scanner introduced in 1993 (Elscint TWIN) (Liang 1996). In 1998, all major CT manufacturers introduced multi-slice CT (MSCT) systems, which typically offered simultaneous acquisition of 4 slices at a rotation time of down to 0.5 s. This was a considerable improvement in scan speed and longitudinal resolution and offered better utilization of the available X-ray power (Klingenbeck 1999, McCollough 1999, Ohnesorge 1999, Hu 2000). These developments were quickly recognized as revolutionary improvements that would eventually enable users to do real isotropic 3D imaging. Consequently, all vendors pushed towards more and more slices, turning the number of slices into the most important performance characteristic of a CT scanner. Figure 3.1 shows the performance of new CT systems, measured by the number of slices per rotation, at the time of their market introduction. Interestingly, analogous to "Moore's Law" in the computer industry, the increase in the number of slices has been exponential, approximately doubling every 18 months.

Simultaneous acquisition of N slices results in an N-fold increase in speed if all other parameters, such as slice thickness, are unchanged. This increased performance of multi-slice CT compared to single-slice CT allowed for the optimization of a variety of clinical protocols. The examination time for standard protocols could be significantly reduced, which proved to be of immediate clinical benefit for the quick and comprehensive assessment of trauma victims and non-cooperative patients. Alternatively, the scan range that could be covered within a certain scan time was extended by a factor of N, which is relevant for oncological staging or for CT angiography with extended coverage, for example, of the lower extremities (Rubin 2001). The most important clinical benefit, however, proved to be the ability to scan a given anatomic volume within a given scan time with substantially reduced slice width, at N-times-increased longitudinal resolution. This way, for many clinical applications, the goal of isotropic resolution was within reach with 4-slice CT systems. Examinations of the entire thorax (Schoepf 2001) or

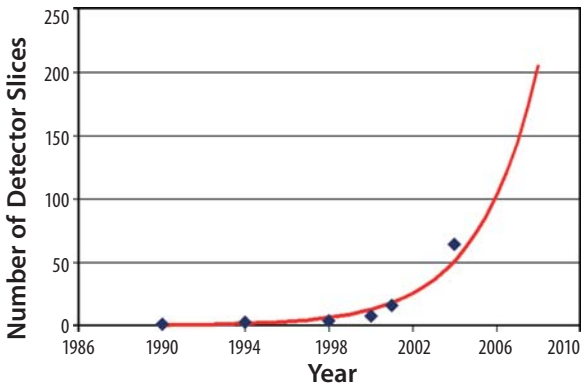

Fig. 3.1. The number of slices of new CT scanners at the time of market introduction. Performance in terms of slice number doubles about every 18 months

abdomen (Klingenbeck 1999) could now routinely be performed with a collimated slice width of 1 mm or 1.25 mm. Multi-slice CT also expanded into areas previously considered beyond the scope of conventional spiral CT scanners, such as routine vascular diagnosis (Ohnesorge 2001, Schoepf 2003), high-resolution low dose CT of the lung (Swensen 2002), virtual CT colonography (Macari 2002, Wessling 2003), and cardiac imaging with the addition of ECG gating capability. The introduction of 4-slice CT with a gantry rotation time of 0.5 s and dedicated image-reconstruction approaches represented a breakthrough for mechanical CT in cardiac imaging. The temporal resolution for the acquisition of an image was improved to 250 ms and less (Kachelriess 2000, Ohnesorge 2000), sufficient for motion-free imaging of the heart in the mid- to end-diastolic phase at slow to moderate heart rates (Hong 2001). With four simultaneously acquired slices, coverage of the entire heart volume with thin slices and ECG-gating within a single breath-hold became feasible, enabling non-invasive visualization of the cardiac morphology and coronary arteries (Ohnesorge 2000, Achenbach 2000, Knez 2000, Nieman 2001).

Despite all these promising advances, clinical challenges and limitations remained for 4-slice CT systems. True isotropic resolution for routine applications had not yet been achieved, since a longitudinal resolution of about 1 mm does not fully match the in-plane resolution of about 0.5–0.7 mm in a routine scan of the chest or abdomen. For large volumes, such as CT angiography of lower-extremity run-off (Rubin 2001), thicker (i.e. 2.5 mm) collimated slices had to be chosen to complete the scan within a reasonable timeframe. Scan times were often too long to allow image acquisition during pure arterial phase. For CT angiography of the circle of Willis, for instance, a scan range of about 100 mm must be covered (Villablanca 2002). With 4-slice CT, at a collimated slice width of 1 mm, a pitch of 1.5, and 0.5.s gantry rotation time, this volume can be covered in a scan time of about 9 s, which is not fast enough to avoid venous overlay assuming a cerebral circulation time of less than 5 s. For ECG-gated coronary CT angiography, stents or severely calcified arteries constituted a diagnostic dilemma, mainly due to partial volume artifacts as a consequence of insufficient longitudinal resolution (Nieman 2001). For patients with higher heart rates, careful selection of separate reconstruction intervals for different coronary arteries has been mandatory (Kopp 2001). The breath-hold time of about 40 s required to cover the entire heart volume (~12 cm) with 4-slice CT is almost impossible for patients with manifest heart disease to comply with.

As a next step, the introduction of an 8-slice CT system in 2000 enabled shorter scan times, but did not yet provide improved longitudinal resolution (thinnest collimation 8 × 1.25 mm). The latter was achieved with the introduction of 16-slice CT (Flohr 2002a, Flohr 2002b), which made it possible to routinely acquire substantial anatomic volumes with isotropic sub-millimeter spatial resolution. Improved longitudinal resolution goes hand in hand with the considerably reduced scan times that enable high-quality examinations in severely debilitated and severely dyspneic patients (Fig. 3.2). Clinical practice suggests the potential of 16-slice CT angiography to replace interventional catheter angiography in the evaluation of carotid artery stenosis (Lell 2002). For patients with suspicion of ischemic stroke, both the status of the vessels supplying the brain and the location of the intracranial occlusion can be assessed in the same examination (Ertl-Wagner 2002). Additional brain-perfusion CT permits differentiation of irreversibly damaged brain tissue from reversibly impaired tissue at risk (Tomandl 2003). Examining the entire thorax (350 mm) with sub-millimeter collimation requires a scan time of approximately 11 s. Due to the short breath-hold time, central and peripheral pulmonary embolism can be reliably and accurately diagnosed (Remy-Jardin 2002, Schoepf 2003). Whole-body angiographic studies with sub-millimeter resolution in a single breath-hold are also possible with 16-slice CT. Compared to invasive angiography, the same morphological information is obtained (Wintersperger 2002a, Wintersperger 2002b). ECG-gated cardiac scanning with 16-slice CT systems benefits from both improved temporal resolution achieved by gantry rotation times down to 0.375 s and improved spatial resolution (Nieman 2002). As a consequence of the increased robustness of the technology, characterization and classification of coronary plaques are becoming feasible even in the presence of calcifications (Ropers 2003).

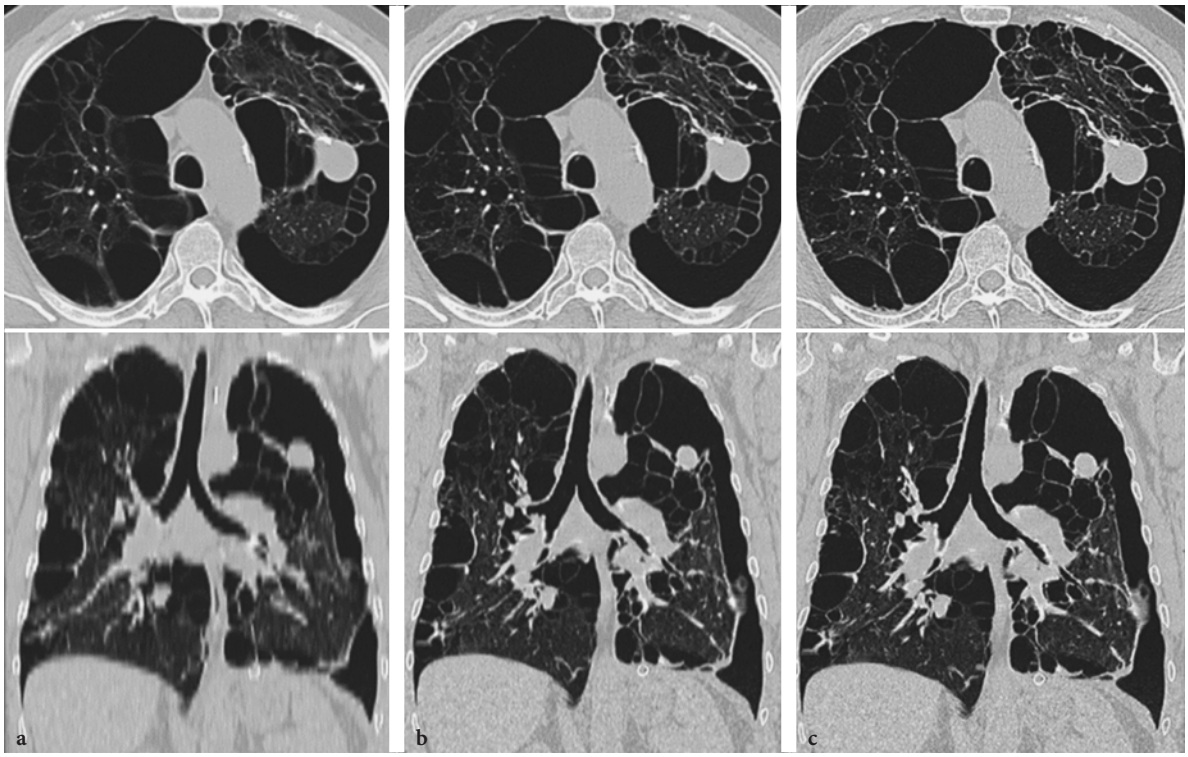

Fig. 3.2a–c. Case study consisting of axial slices and coronal multi-planar reformations (MPRs) of a thorax examination illustrating the clinical performance of a single-slice CT (7-mm slices, 30 s), **b** 4-slice CT (1.25-mm slices, 30 s) and **c** 16-slice CT (0.75-mm slices, 10 s). The difference in diagnostic image quality is most obvious in the MPRs. The single-slice and 4-slice images were synthesized from the 16-slice CT data. (Case courtesy of the Medical University of South Carolina, Charleston, USA)

Currently, the race for more slices is on-going. In 2004, all major CT manufacturers introduced the next generation of multi-slice CT systems, with 32, 40, and even 64 simultaneously acquired slices, which brought about a further leap in volume coverage speed. Whereas most of the scanners increase the number of acquired slices by increasing the number of the detector rows, some of the new scanners use additional refined z-sampling techniques with a periodic motion of the focal spot in the z-direction (z-flying focal spot). This so-called double z-sampling technique can further enhance longitudinal resolution and image quality in clinical routine (Flohr 2003). With gantry rotation times down to 0.33 s, temporal resolution for ECG-gated examinations is again markedly improved. The progress in longitudinal spatial resolution from 4-slice to 64-slice CT can best be demonstrated with a z-resolution phantom, which consists of a Lucite plate with rows of cylindrical holes of different diameters aligned in the z-direction. The 4-slice CT scanner with 4 × 1-mm collimation can resolve 0.8-mm objects. With 16 × 0.75-mm collimation, 0.6-mm objects can be delineated. The latest 64-slice CT scanner technology using 0.6-mm collimation and double z-sampling can routinely resolve 0.4mm objects, as demonstrated in Figure 3.3.

The most recent generation of CT systems will make CT angiographic examinations with sub-millimeter resolution feasible in the pure arterial phase even for extended anatomical ranges. CT angiography of the carotid arteries and the circle of Willis with 64 × 0.6-mm slice, 0.375-s rotation time, and pitch 1.5 requires only 5 s for a scan range of 350 mm, as shown in the clinical example in Figure 3.4. Whole-body sub-millimeter CT angiography with a 1500-mm scan range, 64 × 0.6-mm slice, 0.375-s rotation

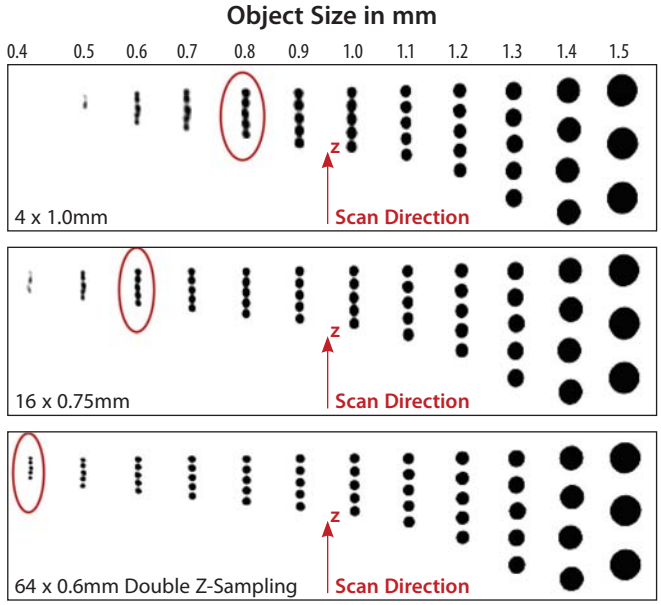

Fig. 3.3. Spatial resolution in the longitudinal (z-) direction for different multi-slice CT scanner technologies. A special resolution phantom containing cylindrical air-filled holes of different defined diameters in a Lucite plate was used. Whereas 16-slice CT scanners can resolve objects approximately 0.6 mm in size in the longitudinal direction, the latest 64-slice CT scanners employing "double z-sampling" techniques can resolve objects down to 0.4 mm size in this direction

time, and pitch of 1.2–1.4 will be completed in only 22–25 s (Fig. 3.5). Cardiac scanning will again benefit both from increased spatial and temporal resolution, facilitating the successful integration of CT coronary angiography into routine clinical algorithms. The improved temporal resolution obtained with a gantry rotation time of 0.33 s has the potential to increase clinical robustness at higher heart rates, thereby significantly reducing the number of patients requiring heart-rate control.

Table 3.1 shows examples of scan protocols for different generations of CT scanners for illustration. Very useful up-to-date information regarding multi-detector row CT is also readily available on the Internet, for example, at the UK MDA CT website (www.medical-devices.gov.uk or at www.ctisus.org).

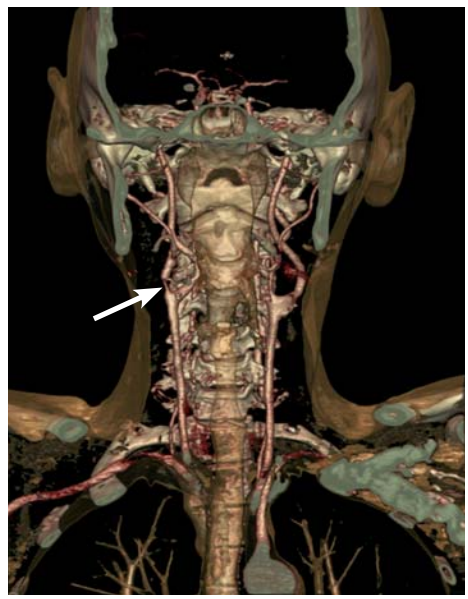

Fig. 3.4. Clinical example of a CT angiography of the carotid arteries and the circle of Willis in 3D volume-rendering display to illustrate the performance of the new 64-slice CT scanners with z-flying focal spot. Scan parameters: 120 kV, 150 effective mAs, 0.6-mm collimation, 0.375-s gantry rotation time, pitch 1.4, scan time 6 s for 350-mm scan range. The arrow indicates a severe carotid artery stenosis. (Case courtesy of the University of Erlangen, Germany)

3.2 Principles of Multi-slice CT System Design

The fundamental demands on a modern multi-slice CT scanner for large-volume coverage can be summed up in the following two requirements:

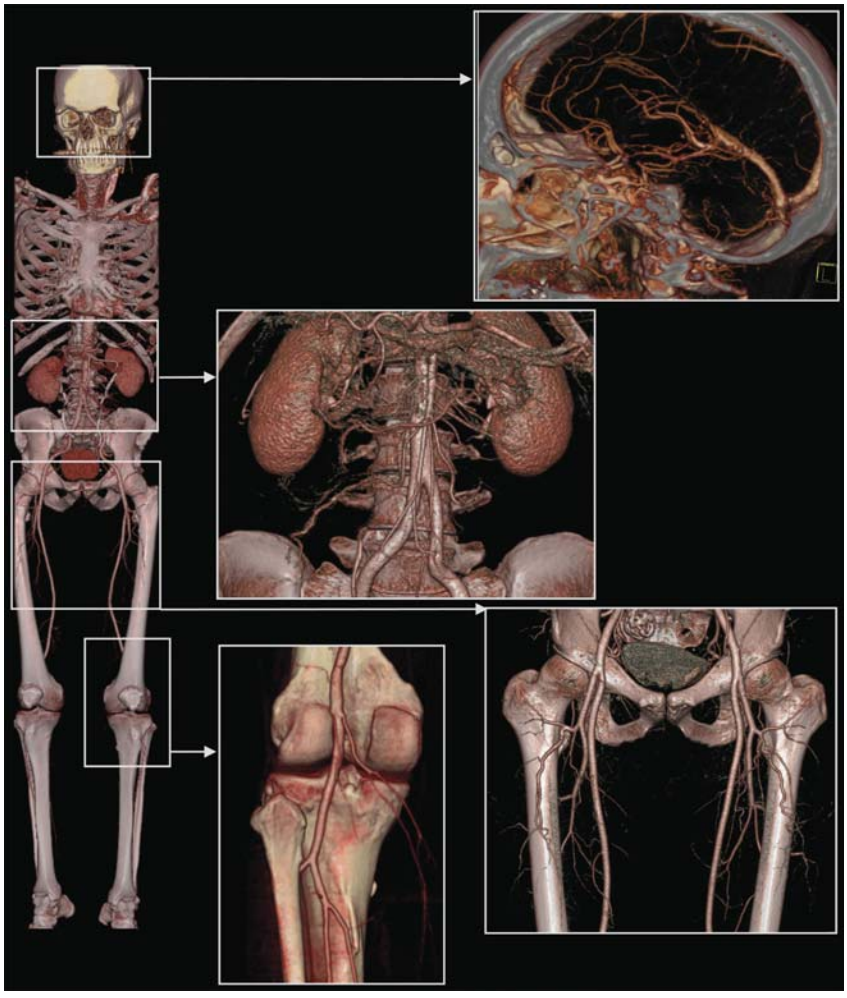

Fig. 3.5. Example of a whole-body CT angiography examination using a 64-slice CT with z-flying focal spot. Blow-up displays of the individual anatomical regions demonstrate the uncompromised regional resolution. Scan parameters: 120 kV, 150 effective mAs, 0.6 mm collimation, 0.375-s gantry rotation time, pitch 1.4, scan time 24 s for 1570-mm scan range. (Case courtesy of the University of Erlangen and the University of Tübingen, Germany)

Table 3.1. Scan protocols for thorax scans for different generations of CT scanners. With older single-slice CT scanners, users had to trade-off longitudinal resolution in favor of scan speed

	Collimation	Rotation time	Typical scan time for 35-cm range
Single-slice spiral (1992)	e.g., 1 mm	e.g., 0.75 s	175 s
	e.g., 10 mm	e.g., 0.75 s	17.5 s
Four slice (1998)	e.g., 4 × 1 mm	e.g., 0.5 s	29 s
16-slice (2001)	e.g., 16 × 0.75 mm	e.g., 0.5 s	10 s
64-slice (2003)	e.g., 64×0.6-mm sampled at 0.3 mm	e.g., 0.33 s	5 s

1. Continuous data acquisition (the possibility to reconstruct images at any *z* position)
2. Ability to scan a long range in a short time without compromising longitudinal (*z*) resolution

The first requirement calls for a spiral acquisition. The breakthrough in multi-slice spiral CT brought about in 1998 was due to the fact that it was able to fulfill the second requirement: maximum z resolution is defined by the longitudinal detector pixel size alone rather than by a combination of spiral pitch and detector collimation as in single-slice spiral scanners. Moreover, multi-slice spiral scanners provide the new feature of allowing the z-resolution to be specified in the image-reconstruction step, i.e., after the scan has been done.

The technical challenges of multi-slice CT are manifold: A detector capable of measuring several thousand channels at a time has to be built; the data have to be transferred to the image-reconstruction system, and a suitable reconstruction algorithm has to be provided.

The basic system components of a modern "third-generation" CT system are shown in Figure 2.2. Third-generation CT scanners employ a "rotate/rotate" geometry, in which both the X-ray tube and the detector rotate about the patient (Fig. 2.2d). In a multi-slice CT system, the detector comprises many rows of 700 and more detector elements that cover a scan field of view (SFOV) of usually 50 cm. The X-ray attenuation of the object is measured by the individual detector elements. Each measurement value is characterized by: (1) its projection angle α, i. e., the angular coordinate of the line connecting the center of the detector and the focal spot of the X-ray tube; (2) the fan angle β, i. e., the angle between each individual detector element and this center-line; and (3) the slice-index m. All measurement values acquired at the same angular position of the measurement system, that is, at the same α, are called a projection of view. Typically, 1000 projections are measured during each 360° rotation. An alternative set of variables characterizing the measurement rays is θ, b, and m, where θ is the azimuthal angle and b denotes the distance of a ray from the iso-center (Fig. 3.6). α and β are used when projection data are in the form of fan-beam projections, θ and b are used to label rays when projection data are in the form of parallel projections. Most modern CT scanners use "rebinning", which is an interpolation of the measured fan-beam data to parallel data, since parallel geometry simplifies image reconstruction.

The overall performance of a CT system depends on several key components. These include the X-ray source; a high-powered generator, detector, and detector electronics; data transmission systems (slip-rings); and the computer system for image reconstruction and manipulation.

State-of-the-art X-ray tube/generator combinations provide a peak power of 60–100 kW, usually at various user-selectable voltages, e. g., 80, 100, 120, and 140 kV. Different clinical applications require different X-ray spectra and hence different kV settings for optimum image quality and/or best possible signal-to-noise ratio at the lowest radiation dose. As an example, CT angiographic examinations generally benefit from a lower tube voltage (Schöpf 2003). In a conventional tube design, an anode plate that is typically 160–220 mm in diameter rotates in a vacuum housing (Fig. 3.7a). The heat-storage capacity of the anode plate and tube housing – measured in mega heat units (MHU)–determines the performance level: the bigger the anode plate is, the larger the heat-storage capacity, and the more scan-seconds can be delivered until the anode plate reaches its temperature limit. Typically, a conventional state-of-the-art X-ray tube has a heat-storage capacity of 5–9 MHU, realized by thick graphite layers attached to

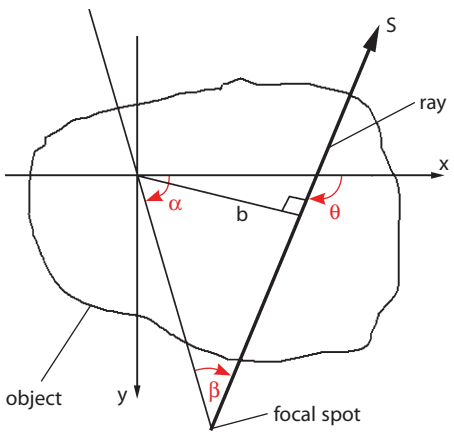

Fig. 3.6. Definition of variables used to characterize the measurement rays of a CT scanner. A parallel projection is obtained by assembling rays from several fan-beam projections

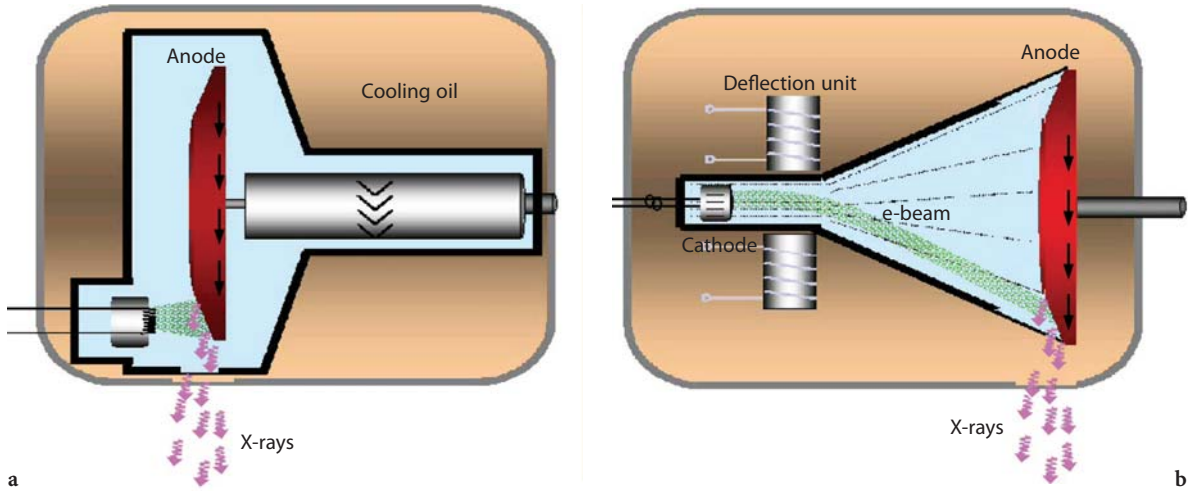

Fig. 3.7. A conventional X-ray tube (**a**) and a rotating-envelope tube (**b**). The electrons emitted by the cathode are represented by green lines, the X-rays generated in the anode are depicted as purple arrows. In a conventional X-ray tube, the anode plate rotates in a vacuum housing. Heat is mainly dissipated via thermal radiation. In a rotating-envelope tube, the anode plate constitutes an outer wall of the tube housing and is in direct contact with the cooling oil. Heat is effectively dissipated via thermal conduction, and the cooling rate is significantly increased. Rotating-envelope tubes have no moving parts and no bearings in the vacuum

the backside of the anode plate. The heat produced in the anode during X-ray emission is mainly dissipated via thermal radiation, with only a small percentage released via thermal conduction (Fig. 3.7a). The moderate heat dissipation rates of 0.5–1.8 MHU/min usually limit the rate at which scans can be repeated as well as the maximum available power for each scan. Constructive efforts aim at increasing both the heat-storage capacity and the heat-dissipation rate, e.g., by increasing the anode diameter, using circular grooves in the anode support to increase the contact area for improved cooling, or by employing special liquid-metal vacuum bearings that allow for faster anode rotation. An alternative design is the so-called rotating-envelope tube, as illustrated in Figures 3.7b and 3.8. The anode plate constitutes an outer wall of the rotating tube housing; it is therefore in direct contact with the cooling oil and can be effectively cooled by thermal conduction. In this way, a very high heat-dissipation rate of 5 MHU/min is achieved, eliminating the need for heat storage in the anode, which consequently has a heat-storage capacity close to zero. Due to the rapid cooling of the anode, rotating-envelope tubes can perform high-power scans in rapid succession. With rotating-envelope tubes, up to five full-power 10-s spirals are possible within 100 s (Schardt 2004). Ultimately, the performance of both conventional and rotating-envelope tubes is limited by the maximum heat dissipation of the CT system itself. Since there are no moving parts and no bearings in the vacuum, the tube design can be small and compact (anode diameter 12 cm) so that it

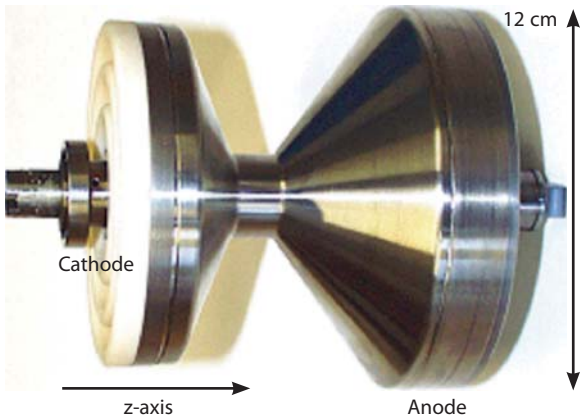

Fig. 3.8. A rotating-envelope X-ray tube (STRATON tube, Siemens, Forchheim, Germany). The tube design is very compact; the anode diameter is only 12 cm

has the potential to better withstand the high gravitational forces associated with gantry rotation times of < 0.4 s. Due to the central rotating cathode, permanent electromagnetic deflection of the electron beam is needed to position and shape the focal spot on the anode. Versatile electromagnetic deflection is a prerequisite for the flying focal spot in the z-direction that has been used in most of the recent 64-slice CT-systems.

With the increasing number of detector rows and decreasing gantry rotation times, the data-transmission systems of multi-slice CT scanners must be capable of handling significant data rates. A 4-slice CT-system with 0.5-s rotation time roughly generates 1000 × 700 × 4 × 2 Bytes = 5.6 MB of data per rotation, corresponding to 11.2 MB/s; a 16-slice CT-scanner with the same rotation time generates 45 MB/s, and a 64-slice CT-system can produce up to 180–200 MB/s. This stream of data is a challenge for data transmission off the rotating part of the gantry and for real-time data processing in the subsequent image-reconstruction systems. In modern CT systems, contactless transmission technology is generally used for data transfer; that is, either laser transmission or electromagnetic transmission with coupling between a rotating transmission ring antenna and a stationary receiving antenna. In the image-reconstruction, computer images are reconstructed at a rate of up to 40 images/s using special array processors.

Modern CT systems generally use solid-state detectors. Each detector element consists of a radiation-sensitive solid-state material (such as cadmium tungstate, gadolinium-oxide, or gadolinium oxisulfide with suitable dopings), which converts the absorbed X-rays into visible light. The light is then detected by a silicon photodiode. The resulting electrical current is amplified and converted into a digital signal. Key requirements for a suitable detector material are good detection efficiency and very short afterglow time to enable the fast gantry rotation speeds that are essential for ECG-gated cardiac imaging. Gas detectors, such as the xenon detectors used in previous generations of single-slice CT systems, have meanwhile become obsolete due to their limited detection efficiency.

A CT detector must provide different slice widths to adjust the optimum scan speed, longitudinal resolution, and image noise for each application. With a single-slice CT detector, different collimated slice widths are obtained by pre-patient collimation of the X-ray beam (Fig. 3.9). Figure 3.9 shows a very elementary model of a 2-slice CT detector consisting of two detector rows generating 2 slices per rotation. Different slice widths are obtained by pre-patient collimation as the detector is separated midway along the z-extent of the X-ray beam.

For acquisition of more than 2 slices per rotation, this simple design principle must be replaced by a more flexible one, in which the number of detector

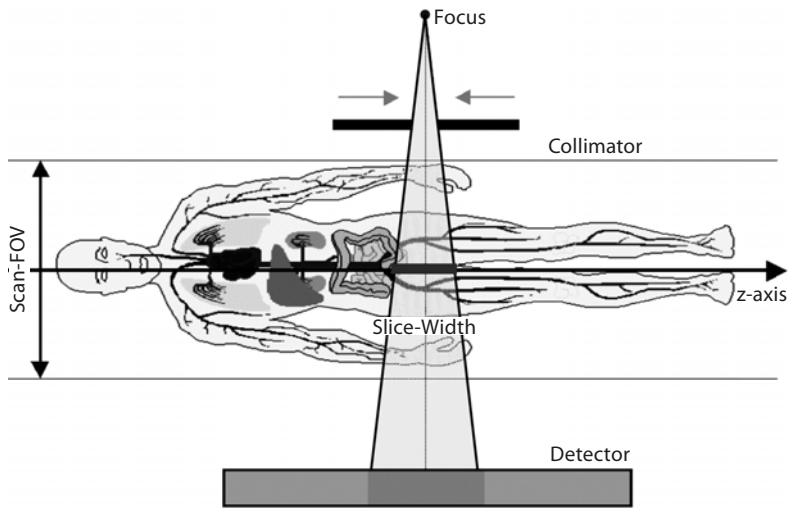

Fig. 3.9. Pre-patient collimation of the X-ray beam to obtain different collimated slice widths with a single-slice CT detector or a dual-slice CT detector

rows is greater than the number of simultaneously acquired slices. In order to be able to select different slice widths, several detector rows are electronically combined into a smaller number of slices according to the selected beam collimation and the desired slice width.

For the 4-slice CT systems introduced in 1998, two detector types have been commonly used. The fixed array detector consists of detector elements with equal sizes in the longitudinal direction. A representative example for this scanner type has 16 detector rows, each of them defining a collimated slice width in the center of rotation of 1.25 mm (Hu 1999, Hu 2000, McCollough 1999). The total coverage in the longitudinal direction is 20 mm at iso-center; due to geometric magnification, the actual detector is about twice as wide. By pre-patient collimation and combination of the signals of the individual detector rows, the following slice widths (measured at iso-center) are realized: 4 × 1.25, 4 × 2.5, 4 × 3.75, and 4 × 5 mm (Fig. 3.10a). The same detector design can be used for an 8-slice version of this system, with collimated slice widths of 8 × 1.25 and 8 × 2.5 mm.

A different approach uses an adaptive array detector design, which comprises detector rows with different sizes in the longitudinal direction. Scanners of this type have eight detector rows that can be combined to yield different slice-collimation settings (Klingenbeck 1999, Ohnesorge 1999). Slice widths in the longitudinal direction range from 1 to 5 mm (at iso-center) and allow for the following collimated slice widths: 2 × 0.5, 4 × 1, 4 × 2.5, 4 × 5, 2 × 8, and 2 × 10 mm (Fig. 3.10b).

The selection of the collimated slice width determines the intrinsic longitudinal resolution of a scan. In a ""step-and-shoot"" axial mode, any multiple of the collimated width of one detector slice can be obtained by adding the detector signals during image reconstruction. In a spiral mode, the effective slice width – which is usually defined as the full width at half maximum (FWHM) of the spiral slice sensitivity profile (SSP) – is adjusted independently in the spiral interpolation process during image reconstruction. Hence, from the same data set, both narrow slices for high-resolution detail or 3D post-processing and wide slices for better contrast resolution or quick review and filming may be derived.

The established 16-slice CT systems generally have adaptive array detectors. One representative example for this scanner type uses 24 detector rows (Flohr 2002). The 16 central rows define a 0.75-mm collimated slice width at iso-center; the four outer rows on both sides define a 1.5-mm collimated slice width (Fig. 3.10c). The total coverage in the longitudinal direction is 24 mm at iso-center. By appropriate combination of the signals of the individual detector rows, either 12 or 16 slices, each with a collimated slice width of 0.75 mm or 1.5 mm, can be acquired simultaneously. Most commercially available 16-slice CT scanners use similar detector designs, partly with different collimation settings (e.g., 16 × 0.625 mm/16 × 1.25 mm or 16 × 0.5 mm/16 × 1mm/16 × 2 mm collimated slice width).

In 2004, the latest generation of multi-slice CT systems providing more than 16 slices, up to 64 slices per rotation, was introduced. One of the new scanners employs an adaptive array detector with a total of 40 detector rows and a special double z-sampling technique that doubles the number of slices acquired per rotation. The 32 central detector rows of this scanner define a 0.6-mm collimated slice width at iso-center; the four outer rows on both sides define a 1-mm collimated slice width (Fig. 3.10d). When all 40 detector rows are illuminated, the total coverage in the longitudinal direction is 28.8 mm. Using a periodic motion of the focal spot in the z-direction (z-flying focal spot), two subsequent 32-slice readings with a collimated slice width of 0.6 mm are slightly shifted in the z-direction and combined to yield one 64-slice projection with a sampling distance of 0.3 mm at iso-center. With this double z-sampling technique, 64 overlapping 0.6-mm slices per rotation are acquired. Alternatively, 24 slices, each with a 1.2-mm slice width, can be obtained to provide the full longitudinal detector coverage of 28.8 mm.

Another 40-slice system design provides 40 slices based on an adaptive array detector design with 40 × 0.625-mm or 32 × 1.25-mm collimation, with a coverage of 40 mm at iso-center (Fig. 3.10e). Other recently introduced 64-slice scanners employ fixed array detectors with 64 detector rows, with a thinnest collimated slice width of 0.5–0.625 mm, thus providing a total volume coverage of 32–40 mm (Fig. 3.10f). A direct comparison of the two different 64-slice detec-

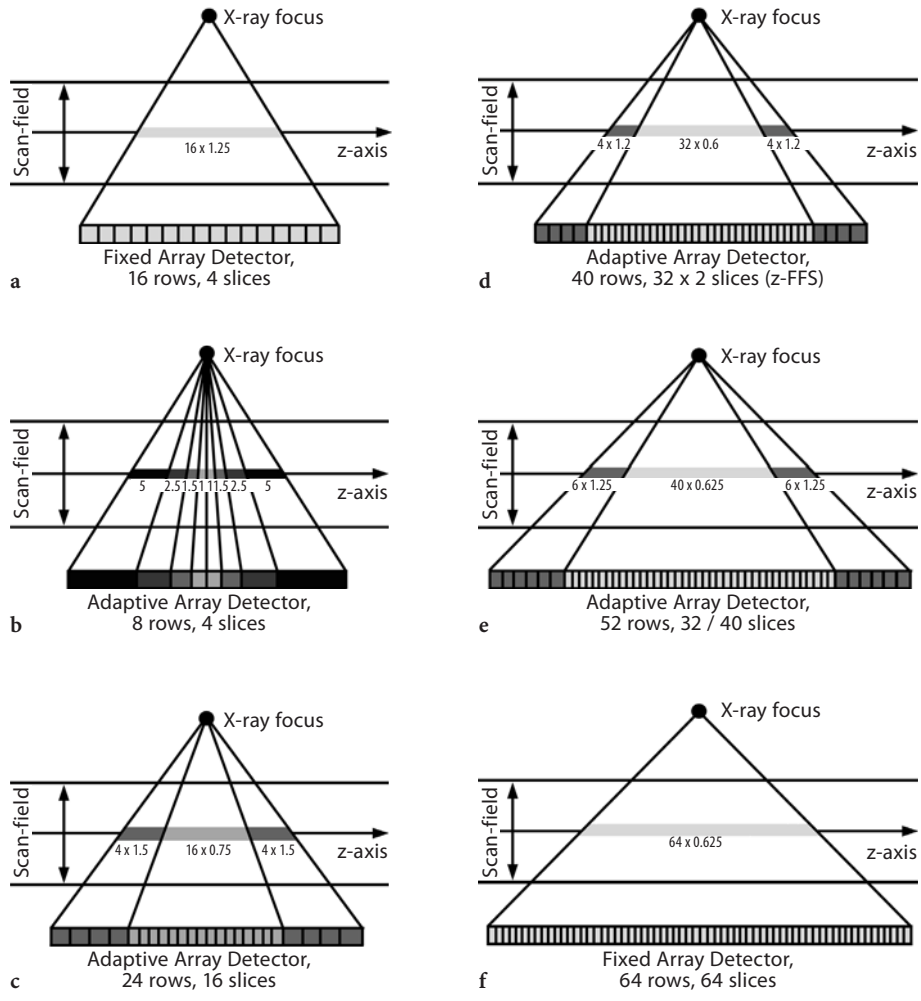

Fig. 3.10a–f. Examples of fixed array detectors and adaptive array detectors used in commercially available multi-slice CT systems. **a** Fixed array detector of a 4- to 8-slice CT scanner, GE LightSpeed Plus and Ultra; **b** adaptive array detector of a 4-slice CT scanner (Siemens SOMATOM Sensation 4 and Philips MX 8000); **c** adaptive array detector of a 16-slice CT scanner (Siemens SOMATOM Sensation 16 and Philips MX 8000 IDT); **d** adaptive array detector of a 64-slice CT scanner employing double z-sampling technique (Siemens SOMATOM Sensation 64); **e** adaptive array detector of a 40-slice CT scanner (Philips Brilliance 40); **f** fixed array detector of a 64-slice CT scanner using 64 detector rows (GE LightSpeed VCT and Philips Brilliance 64)

tor designs with 32 rows and double z-sampling vs. straight 64-row geometry is shown in Figure 3.11a–c. Whereas the straight 64-row concept can acquire four times more volume per rotation with sub-millimeter slices than the previous 16-slice CT scanners, double z-sampling can still allows the acquisition of two times more volume per rotation but also twice the amount of data per volume. This results in improved resolution and image quality compared to previous 16-slice CT scanners. Figure 3.11d shows a representative example of a detector module of a 64-slice CT scanner that employs the double z-sampling technique. Each module consists of 40 × 16 detector pixels and the corresponding electronics. The anti-scatter collimators are diagonally cut to open the view of the detector ceramics.

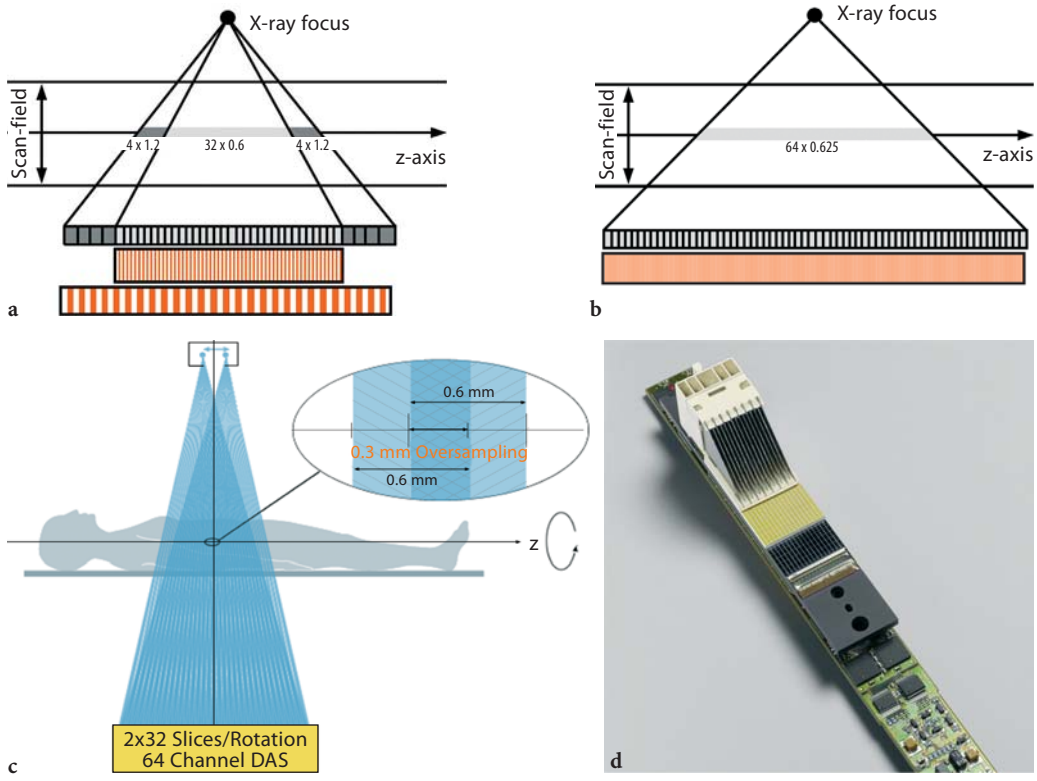

Fig. 3.11. Direct comparison of two different 64-slice detector designs shows that the 32-row design with double z-sampling (**a**) acquires double the amount of data per volume compared to a straight 64-row geometry (**b**). The double z-sampling technique with 0.6-mm detector collimation provides data samples at 0.3-mm sampling distance in the z-direction (**c**). A detector module of a 64-slice CT scanner using the double z-sampling technique (Siemens SOMATOM Sensation 64) is shown in (**d**). Each module consists of 40 × 16 detector pixels with the corresponding electronics. The anti-scatter collimators are diagonally cut to open the view on the detector ceramics (*yellow*)

3.3 Multi-slice CT Acquisition and Reconstruction for Body Imaging

With the advent of multi-slice CT, axial sequential scanning ("step-and-shoot" scanning) has remained in use only for few clinical applications, such as standard head scanning, high-resolution lung scanning, perfusion CT, and interventional applications. A detailed theoretical description to predict the performance of multi-slice CT in sequential mode can be found in (Hsieh 2001). However, spiral (or "helical") scanning is the method of choice for the vast majority of multi-slice CT examinations.

3.3.1 Definition of the Pitch

An important parameter to characterize a spiral/helical scan is the pitch. According to IEC (International Electrotechnical Commission 2002) specifications, the pitch is given by:

pitch = table feed per rotation / total width of the collimated beam (3.1)

This definition holds for single-slice CT and for multi-slice CT. It shows whether data acquisi-

tion occurs with gaps (pitch > 1) or with overlap (pitch < 1) in the longitudinal direction. For a 4-slice CT scanner with 4 × 1-mm collimation and a table-feed of 6 mm per rotation, pitch = 6/(4 × 1) = 6/4=1.5. With 16 × 0.75-mm collimation and a table-feed of 18 mm/rotation, pitch = 18/(16 × 0.75) = 18/12=1.5, too. In the early days of 4-slice CT, the term "detector pitch" was additionally introduced, and it accounts for the width of one single slice in the denominator. For a beam collimation of 4 × 1 mm, the beam consists of four sub-beams, each 1-mm wide at the center of rotation. With 6-mm table-feed per rotation, the detector pitch is pitch_{vol} = 6/1=6. For the sake of clarity, the detector pitch should no longer be used.

3.3.2 The Cone-Angle Problem in Multi-slice CT

The 2D image-reconstruction approaches used in commercially available, single-slice CT scanners require that all measurement rays contributing to an image run in a plane perpendicular to the patient's longitudinal axis. In multi-slice CT systems, this requirement is violated. For illustration of the cone-beam effect, Figure 3.12 shows the geometry of a 4-slice scanner in an exaggerated manner. The measurement rays are tilted by the so-called cone-angle with respect to the center plane. The cone-angle is largest for the slices at the outer edges of the detector and it increases with an increasing number of detector rows if their width is kept constant. As a first approximation, the cone-angle is neglected in multi-slice CT reconstruction approaches. Then, the measurement rays are treated as if they travel perpendicular to the z-axis, and modified two-dimensional image-reconstruction algorithms are used. The data, however, are then inconsistent, and cone-beam artifacts will be produced. These are most pronounced at high-contrast structures and increase with increasing distance of the object from the iso-center. Typical sources of cone-beam artifacts in medical images are the ribs or the pelvic bones (Fig. 3.13).

It has been demonstrated that cone-beam artifacts can be tolerated if the slice blurring δS does not exceed the half-slice collimation $SW_{coll}/2$

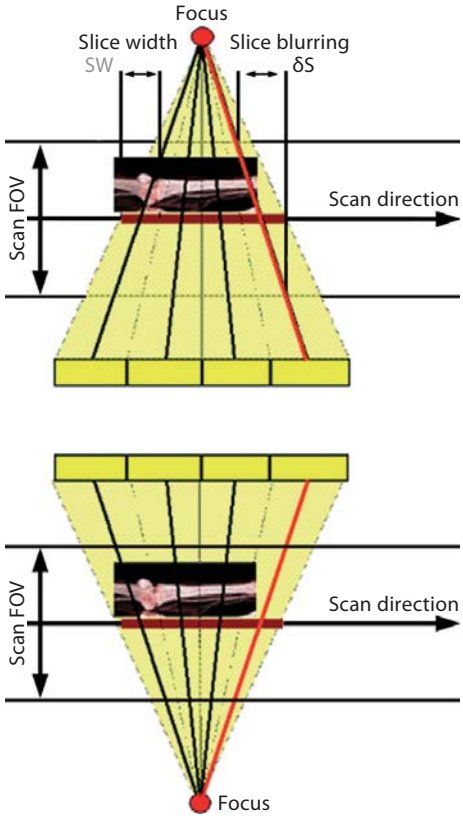

Fig. 3.12. Geometry of a 4-slice CT scanner demonstrating the cone-angle problem: the measurement rays are tilted by the so-called cone-angle with respect to the center plane. Top and bottom Two different view angles in an axial scan that are shifted by 180° so that the positions of X-ray tube and detector are interchanged. With a single-slice CT system, identical measurement values would be acquired whereas with a multi-slice CT system, different measurement values are acquired

(Klingenbeck 1999, Ohnesorge 1999, Ohnesorge 2001) (for definitions, see Fig. 3.12). This condition holds generally true if the maximum number N of simultaneously acquired slices does not significantly exceed N = 4 (Saito 1998). As a consequence, the image-reconstruction approaches of all commercially available CT-systems with 4–6 slices, and of some with even more slices, neglect the cone-angle of the measurement rays and either extend 180° or 360° single-slice spiral interpolation techniques to multi-slice spiral scanning (180° or 360° multi-slice

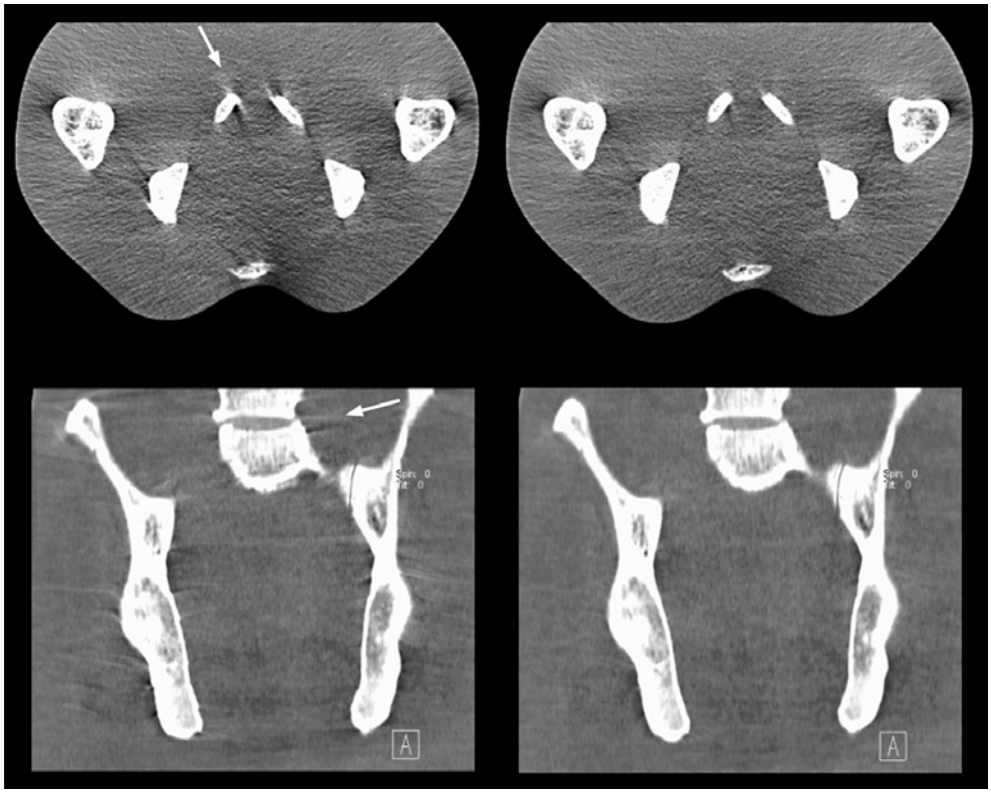

Fig. 3.13. Typical cone-beam artifacts demonstrated for a CT system with 16 × 1.5-mm collimation. Axial slice (*top*) and MPR (*bottom*) for a spiral scan of a pelvic phantom at pitch 1. Left Conventional multi-slice spiral reconstruction neglecting the cone-angle of the measurement rays. Cone beam-artifacts at the pelvic bones are indicated by *arrows*. Right Cone-beam reconstruction adaptive multiple plane reconstruction (AMPR). Cone-beam artifacts are suppressed

linear interpolation; see Hu 1999) or they introduce generalized z-filter approaches (Taguchi 1998, Schaller 2000). While these approaches are fully adequate for 4–6 slice CT scanners, they will lead to artifacts and image-quality degradation if applied to spiral scanning with 16 and more slices. In this context, ECG-gated cardiac scanning requires special attention. The heart is usually sufficiently centered and does not contain extended high-contrast structures that could be the source of cone-beam artifacts. Indeed, adequate results without cone correction are obtained for cardiac scanning with 16 slices; only with 64 slices do cone-beam reconstruction approaches also become mandatory for ECG-gated spiral CT (Flohr 2003) (Fig. 3.14).

3.3.3 Multi-slice Spiral Reconstruction Neglecting the Cone-Beam Geometry

3.3.3.1 180° and 360° Multi-slice Linear Interpolation

The 360° and 180° linear interpolation (LI) single-slice spiral reconstruction approaches can be extended to multi-detector row spiral scanning in a straightforward way (Hu 1999, Schaller 2000, Hsieh 2003). Both 360° and 180° multi-slice linear interpolation (MLI) are characterized by a projection-wise linear interpolation between two rays on either side of the image plane. The cone-angle of

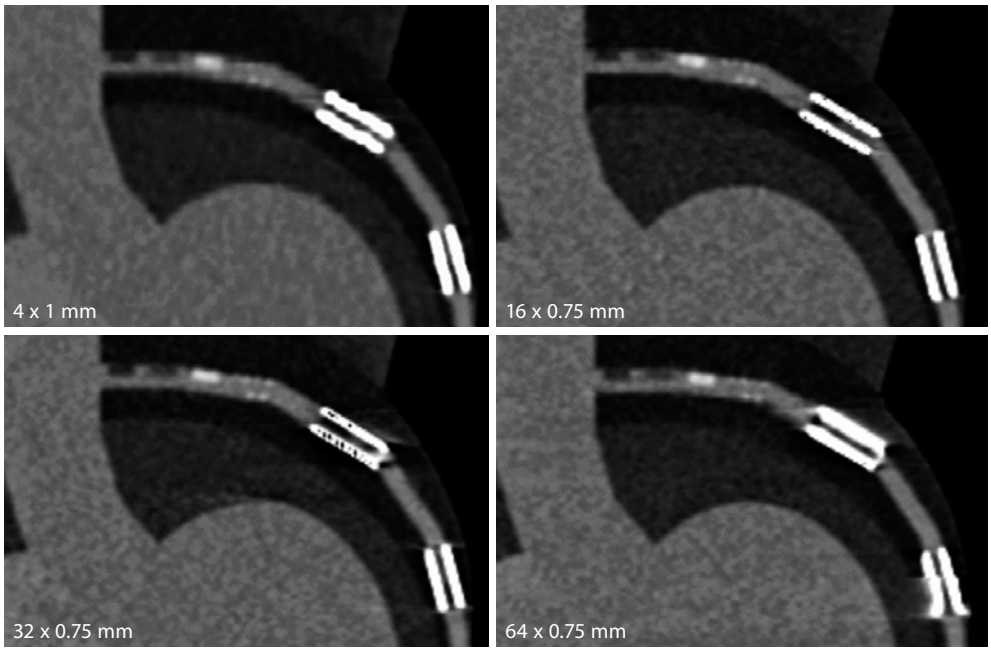

Fig. 3.14. Cone-beam artifacts in cardiac CT. MPRs along the left anterior descending (LAD) coronary artery of an anthropomorphic heart phantom for virtual scanner geometries with collimations of 4 × 1, 16 × 0.75, 32 × 0.75, and 64 × 0.75 mm. ECG-gated reconstruction neglecting the cone-angle of the measurement rays. Deviating from general radiology applications, the MPRs show no significant cone-beam artifacts for up to 16 slices. For 32 slices, the MPRs begin to suffer from such artifacts; see the stents in the LAD. For 64 slices, MPRs show severe cone-beam artifacts

the measurement rays is not taken into account. In the 360° MLI spiral reconstruction approach, either rays measured at the same projection angle by different detector rows or rays measured in consecutive rotations of the scanner (i.e., 360° apart) are used for spiral interpolation. In the 180° MLI spiral reconstruction approach, both direct and complementary rays are considered. At iso-center, direct and complementary rays interleave in the z-direction for selected pitch values. In this way, the distance between measured samples is significantly reduced and equals half the collimated slice width, SW_{coll}, which results in the desired narrow SSPs. Appropriate pitch values are 0.75 for 4-slice scanning (Hu 1999) and 0.5625 or 0.9375 for 16-slice scanning (Hsieh 2003). Figure 3.15 schematically illustrates 180° and 360° MLI for the example of a 4-slice CT scanner.

In general, scanners relying on 180° or 360° MLI techniques and extensions thereof provide selected discrete pitch values to the user – such as 0.75 and 1.5 for 4-slice scanning (Hu 1999), or 0.5625, 0.9375, 1.375, and 1.75 for 16-slice scanning (Hsieh 2003). The user has to be aware of pitch-dependent effective slice widths (s). For low-pitch scanning (at pitch = 0.75 using 4 slices and at pitch = 0.5625 or 0.9375 using 16 slices), SW ~ SW_{coll}, and for a collimated 1.25-mm slice the resulting effective slice width stays at 1.25 mm. The narrow SSP, however, is achieved by a 180° MLI reconstruction using conjugate interpolation at the price of increased image noise (Hu 1999, Hsieh 2003). For high-pitch scanning (at p = 1.5 using 4 slices and at pitch = 1.375 or 1.75 using 16 slices), SW ~ 1.27SW_{coll}, and a collimated 1.25-mm slice results in an effective 1.5- to 1.6-mm slice. When comparing dose and image noise for different pitch values, widening of the SSP has to be taken into account. To obtain the same image noise as in an axial scan with the same collimated slice width, 0.73–1.68 times the dose depending on the spiral

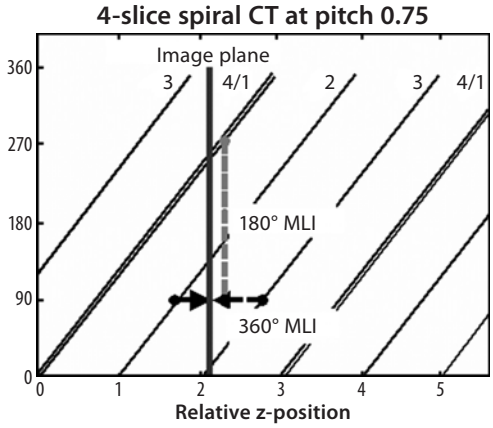

Fig. 3.15. Schematic illustration of 180° and 360° multi-slice linear interpolation (*MLI*) for a 4-slice CT system at pitch 0.75. The projection angle of the central channels of the 4 detector rows (in degrees) is indicated as a function of their relative z-positions (in multiples of the collimated slice width). In a full rotation (*360°*), the detector travels three collimated slice widths, and the z-positions that were sampled by detector row 4 are now again sampled by detector row 1. For *360° MLI*, rays measured at the same projection angle are used; these may be either taken from subsequent rotations or from different detector rows in the same rotation. For the projection angle indicated in this example (*90°*), data from detector rows 2 and 3 are used, and the sampling distance equals the collimated slice width (*two dark arrows*). For *180° MLI*, complementary rays from opposite directions are used; these are shifted by 180° in the center of rotation. In this example, the direct interpolation partner from row 3 at *90°* is replaced by a complementary one from row 1 and row 4 at *270°* (*dashed light-gray line*). The sampling distance is now half the collimated slice width, which results in the desired narrow slice sensitivity profile

pitch is required, with the lowest dose at the highest pitch (Hsieh 2003). Some manufacturers provide a semi-automatic adaptation of the mA value to keep the image noise constant if the pitch is changed. When selecting the scan protocol for a particular application, scanning at low pitch optimizes image quality and longitudinal resolution at a given collimation, yet at the expense of increased dose of radiation to the patient. To reduce patient dose, high pitch values should be chosen

3.3.3.2 z-Filter Approaches

In a z-filter multi-slice spiral reconstruction (Taguchi 1998, Schaller 2000), the spiral interpolation for each projection angle is no longer restricted to the two rays in closest proximity to the image plane. Instead, all direct and complementary rays within a selectable distance from the image plane contribute to the image. The weighting function for the rays is selectable, which allows adjustment of both the functional form and the FWHM of the spiral SSP. Still, the cone-angle is neglected. A representative example for a z-filter approach is the adaptive axial interpolation (Schaller 2000), which is illustrated in Figure 3.16. Another example is the MUSCOT algorithm (Taguchi 1998). With z-filtering, the system can trade-off z-axis resolution (SSP) for image noise (which directly correlates with required dose). With

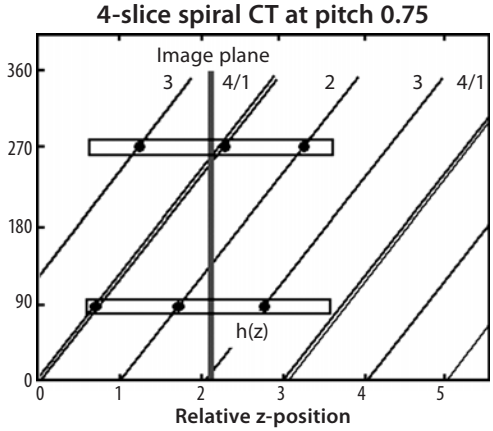

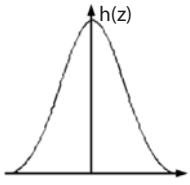

Fig. 3.16. A z-filter reconstruction (adaptive axial interpolation) for a 4-slice CT system at pitch 0.75 (similar to Fig. 3.14). Contributions from all projections at corresponding or opposite projection angles within a selectable distance from the image plane are used, as indicated by the two boxes at 90° and 270°. The weight of the contribution depends on the distance of the respective measurement ray from the image plane. The weighting function *h(z)* (*right*) is selectable

the adaptive axial interpolation, the spiral pitch is freely selectable in the range 0.5–2.0, and the same effective slice width, defined as the FWHM of the spiral SSP, is generated at all pitch values (Klingenbeck 1999, Schaller 2000, Fuchs 2000). Therefore, longitudinal resolution is independent of the pitch, deviating from single-slice spiral CT and from multi-slice CT relying on 180°and 360°MLI (Hu 1999, Hsieh 2003). Figure 3.17 shows the SSPs of the 2-mm slice (for 4 × 1-mm collimation) and MPRs of a spiral z-resolution phantom for selected pitch values. As a consequence of the pitch-independent spiral slice width, the image noise for fixed mA (fixed tube current) would decrease with decreasing pitch due to the increasingly overlapping spiral acquisition. Instead, the user selects an "effective" mAs value, and the tube current (mA) is then automatically adapted to the pitch of the spiral scan to compensate for dose accumulation. The dose for fixed effective mAs is independent of the spiral pitch and equals the dose of an axial scan with the same mAs.

In conclusion, when using z-filter multi-slice spiral reconstruction approaches, changing the pitch in multi-slice CT does not change the radiation dose to the patient, which is not the case in single-slice spiral CT. Accordingly, using higher pitch in multi-slice CT does not result in dose reduction, which is an important practical consideration with CT systems, in particular those applying adaptive axial interpolation reconstruction algorithms.

The intrinsic resolution of a multi-slice spiral CT scan is determined by the choice of collimation, e.g., 4 × 1 or 4 × 2.5-mm. With z-filtering, retrospective reconstruction of images with different slice widths from the same CT raw data set is possible. Only slice widths equal to or larger than the collimation of one slice can be obtained. In many cases, both thick slices for initial viewing and filming and thin slices

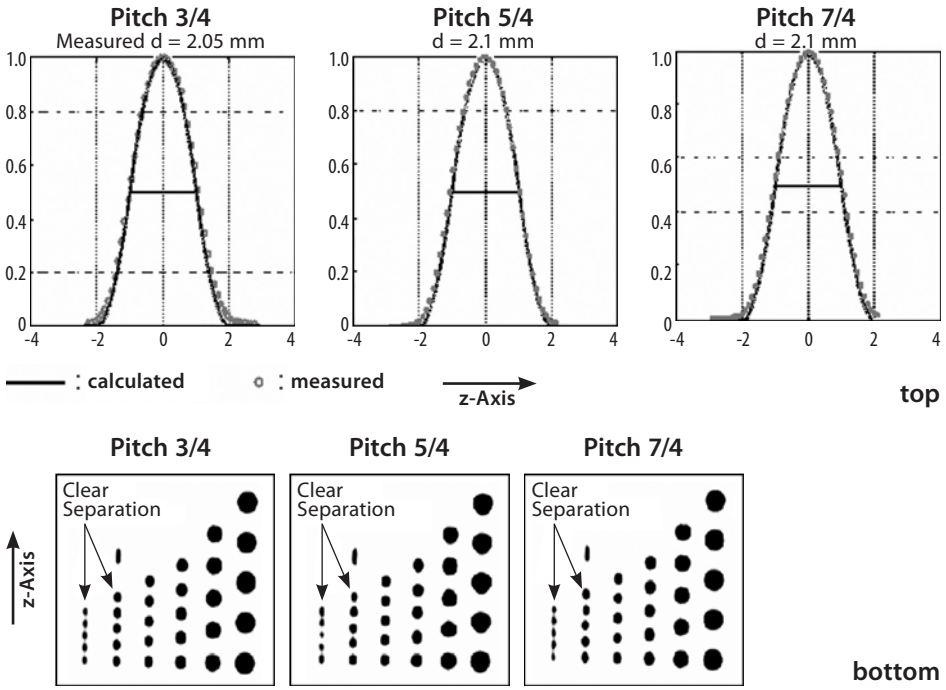

Fig. 3.17. Adaptive axial interpolation for a 4-slice CT-system. Top Slice sensitivity profiles (SSPs) of the 2-mm slice (for 4 × 1-mm collimation) at selected pitch values. The functional forms of the SSPs, and hence the slice widths, are independent of the pitch. Bottom MPRs of a spiral z-resolution phantom scanned with 2-mm slice width show clear separation of the 1.5- and 2-mm cylinders for all pitch values as a consequence of the pitch-independent SSPs

for detail diagnosis or as an input for advanced 3D post-processing are routinely reconstructed. For a 1.25-mm spiral slice width reconstructed from a 4 × 1-mm collimation, only a factor 0.61–0.69 of the dose is required to maintain the image noise of an axial scan at the same collimation, depending only slightly on the spiral pitch (Fuchs 2000). In contrast to 180° and 360° MLI, image noise is therefore practically independent of the pitch at constant dose.

For optimum image quality, a narrow collimation relative to the desired slice width is preferable (Schaller 2000). Except for a minor dose increase due to the different relative contributions of the penumbra zones of the dose profile, scanning at narrow collimation does not result in a higher radiation dose to the patient, as long as the effective mAs is kept constant. Narrow collimation scanning should therefore be the protocol of choice for all applications that require 3D post-processing as part of the clinical evaluation. In the clinical management of uncooperative patients or trauma victims, or for protocols such as routine oncological staging, the use of wider collimation can be considered. Optimal suppression of spiral artifacts is achieved by using narrow collimation relative to the desired slice width and by reducing the spiral pitch. In general, more challenging clinical protocols, such as examinations of the spine and base of the skull, rely on a combination of narrow collimation and low pitch.

Some manufacturers who use z-filter approaches do not provide completely free selection of the spiral pitch, but recommend a selection of fixed pitch values aimed at optimizing the z-sampling scheme and reducing spiral artifacts, such as pitch 0.625, 0.75, 0.875, 1.125, 1.25, 1.375, and 1.5 for 4-slice scanning (Taguchi 1998).

3.3.4 Multi-slice Spiral Reconstruction with Cone-Beam Algorithms

3.3.4.1 Overview of Cone-Beam Reconstruction Algorithms

For CT scanners with 16 and more slices, modified reconstruction approaches accounting for the cone-beam geometry of the measurement rays have to be considered. All commercially available multi-slice CT systems providing cone-beam reconstruction rely on approximate algorithms. Although these algorithms are theoretically not exact, image artifacts may be controlled for moderate cone-angle and moderate number of simultaneously acquired slices and kept at a level tolerable for medical CT. Some manufacturers extend the Feldkamp algorithm (Feldkamp 1984, Grass 2000), an approximate 3D filtered back-projection reconstruction originally introduced for axial scanning, to multi-slice spiral scanning (Wang 1993, Schaller 1998, Hein 2003). Other manufacturers use variations and extensions of nutating slice algorithms (Larson 1998, Turbell 1999, Proksa 2000, Kachelriess 2000, Bruder 2000), which split the 3D reconstruction task into a series of conventional 2D reconstructions on tilted intermediate image planes. Representative examples are the adaptive multiple plane reconstruction (AMPR) (Schaller 2001, Flohr 2003) and the weighted hyperplane reconstruction (WHR) (Hsieh 2001, Hsieh 2003).

3.3.4.2 3D Filtered Back-Projection

An example of a 3D convolution-back-projection reconstruction is the true cone-beam tomography (TCOT) algorithm implemented in some of the newer 16-slice and 32-slice scanners. In this approach, the measurement rays undergo a filter operation (convolution) in the fan-angle direction and are then back-projected into a 3D volume along the lines of measurement, thus accounting for their cone-beam geometry. To reconstruct a pixel i located at the co-ordinates (x_i, y_i) on the image plane of interest (Fig. 3.6), the ray that passes from the X-ray source through the pixel to the detector array is selected for each projection angle (Hein 2003). The filtered detector values for all ray sums passing through the pixel for all views are summed up and normalized to create the final reconstructed image. However, 3D back-projection is computationally demanding and requires dedicated hardware to achieve acceptable image-reconstruction times.

Recently, it has been shown that the choice of the proper direction along which the data should be fil-

tered is of critical importance for the image quality achieved with 3D filtered back-projection (Stierstorfer 2004). If the fan-beam projections are filtered along the fan-angle direction β, as proposed in the original Wang algorithm (Wang 1993), severe artifacts appear for larger cone angles. Filtering of the data in the direction of the spiral tangent can markedly improve image quality. A good approximation is filtering of the data in the p-direction after rebinning to parallel geometry.

3.3.4.3 Adaptive Multiple Plane Reconstruction

The AMPR-approach (Schaller 2001, Flohr 2003) is an extension and generalization of advanced single-slice rebinning (ASSR) (Larson 1998, Kachelriess 2000). AMPR allows for free selection of the spiral pitch with optimized dose utilization, which is beneficial for medical applications. With ASSR, a partial scan interval (~ 240° of scan data) is used for image reconstruction. The image planes are no longer perpendicular to the patient axis; instead, they are tilted to match the spiral path of the focal spot (Fig. 3.18a). For every view angle in this partial scan interval, the focal spot is positioned in or nearby the image plane, i.e., measurement rays running in or very close to the image plane are available. These conditions need to be fulfilled for a standard 2D reconstruction. In a final z-reformation step, the traditional axial images are calculated by an interpolation between the tilted original image planes. ASSR encounters its limitations when the spiral pitch is reduced to make use of the overlapping spiral acquisition and the resulting dose accumulation When a range of projection angles much larger than π (in parallel geometry) for an image are used, it becomes impossible to optimally fit the image plane to the spiral path. The AMPR algorithm (Schaller 2001, Flohr 2003) addresses this problem: instead of using all available data for one single image, the data are distributed to several partial images on double-oblique image planes, which are individually adapted to the spiral path and fan out like the pages of a book (Fig. 3.18b). To ensure full use of the dose, both the number of partial images (the number of "pages" in the book) and the length of the data interval per image depend on the spiral pitch (Fig. 3.19a). The final axial (or arbitrarily oriented) images are calculated by a z-

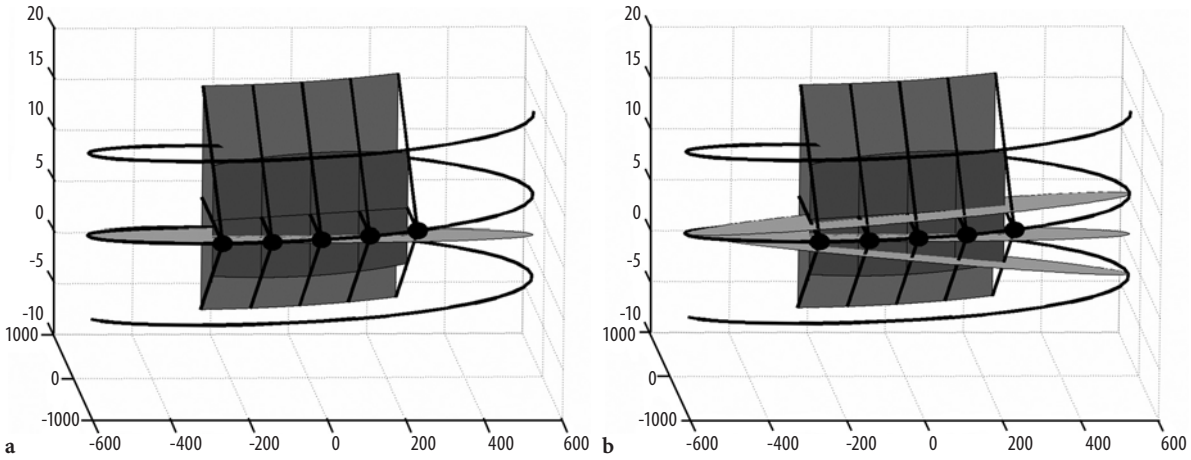

Fig. 3.18. The advanced single-slice rebinning (ASSR) (**a**) and AMPR (**b**) approaches. **a** In the ASSR approach, the image plane is attached to the focus at reference projection angle $\theta_r = 0$ (*left side*). It is tilted by an angle γ around the x-axis. A parallel projection at projection angle $\theta = \pi/2$ is indicated. The dots represent the focus positions for selected rays within this parallel projection. The reconstruction plane optimally fits the spiral path in a projection angle range $[-\pi/2, \pi/2]$. **b** The AMPR approach for a 16 slice detector at pitch = 0.75 using the same perspective as in **a**. Three double-oblique image planes are attached to the focus at reference projection angle $\theta_r = 0$ (*left side*). The three image planes fan out like the pages of a book. A parallel projection at projection angle $\theta = \pi/2$ is indicated

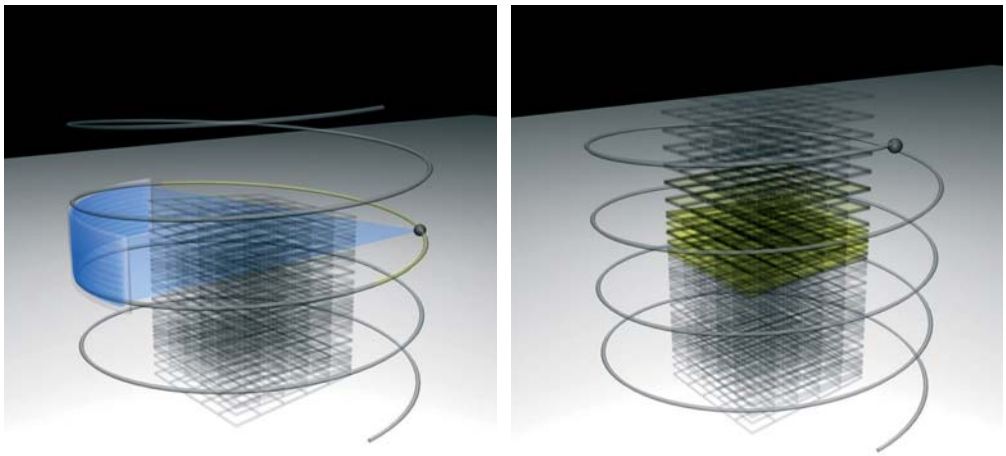

a b

Fig. 3.19a, b. Adaptive multiple plane reconstruction AMPR. **a** Multi-slice spiral data are divided into overlapping pitch-dependent segments. As an intermediate step for each of these segments, partial images are reconstructed on double-oblique image planes that are adapted to the local curvature of the spiral and open like the pages of a book. **b** The resulting images on axial planes are generated via z-reformatting, similar to MPR post-processing

interpolation between the tilted partial image planes (Fig. 3.19b). The shape and the width of the z-interpolation functions are selectable. Different SSPs and different slice widths can therefore be adjusted, so that z-axis resolution (SSP) can be traded off with image noise. The spiral pitch is freely selectable and slice width, and consequently z-axis resolution, are independent of the pitch. The concepts of effective mAs and automatic adaptation of the tube current to the pitch also apply to AMPR.

With the AMPR approach, good image quality is obtained for all pitch values between 0.5 and 1.5 (Flohr 2002). Figure 3.20 shows an axial slice and a MPR of an anthropomorphic thorax phantom. Scan data for 16×0.75-mm collimation at pitch 1 was reconstructed with 1-mm slice width, using z-filtering (top), the AMPR algorithm (center), and 3D back-projection (bottom). If the cone-angle is neglected, artifacts are created for high-contrast objects and geometric distortions occur, particularly in MPRs (top). Both AMPR (center) and 3D back-projection (bottom) restore the spatial integrity of high-contrast objects, reduce cone-beam artifacts, and are fully equivalent for 16-slice scanning. Recent studies have demonstrated the adequacy of extended versions of AMPR for medical CT systems with up to 64 rows (Stierstorfer 2002). The remaining artifacts shown in Figure 3.20 are spiral interpolation artifacts ("windmill" artifacts), as opposed to cone-beam artifacts. Windmill artifacts are not related to the cone-beam geometry but result from the finite width of the detector rows, which thus requires interpolation between them for image reconstruction. Hence, they occur independently of the reconstruction approach. They are exaggerated in the mathematical phantom shown and can be reduced by either decreasing the pitch and/or increasing the reconstruction slice width relative to the collimation.

Multi-slice spiral scanning using AMPR is characterized by the same key properties as adaptive axial interpolation, as discussed above for z-filter reconstruction. Thus, all recommendations regarding the selection of collimation and pitch that were discussed above also apply for AMPR. In particular, changing the pitch does not change the radiation exposure to the patient, and using higher pitch does not result in dose saving. Narrow collimation scanning should be performed whenever possible.

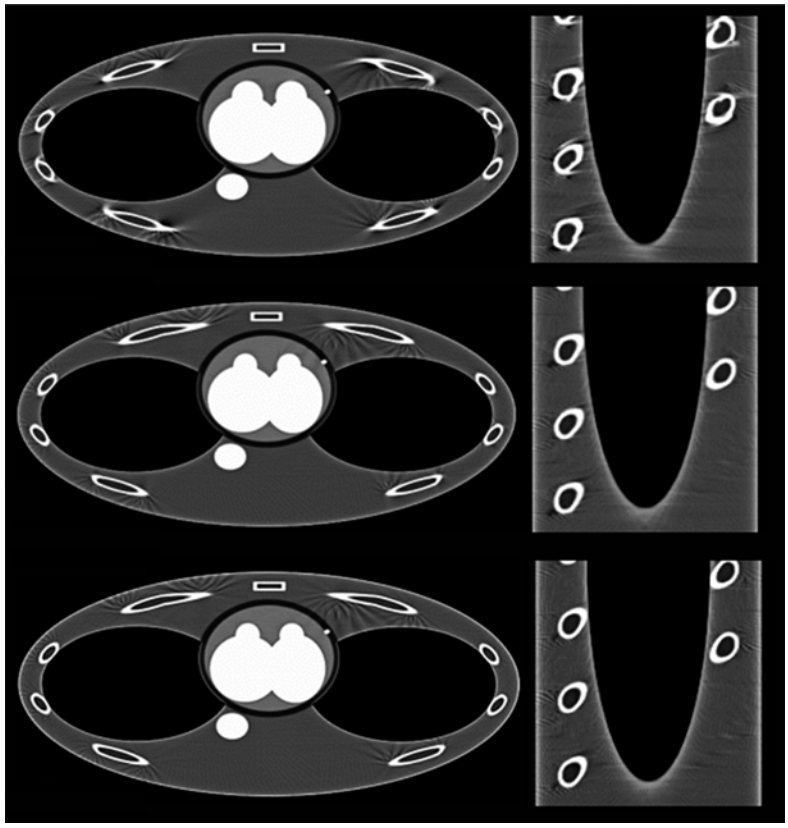

Fig. 3.20. Axial slice and MPR of an anthropomorphic thorax phantom. Scan data for 16 × 0.75-mm collimation at pitch 1 was reconstructed with 1-mm slice width and z-filtering, neglecting the cone-angle of the measurement rays (*top*), with the AMPR algorithm (*center*), and with 3D back-projection with optimized filter direction (*bottom*). Neglecting the cone-angle leads to artifacts for high-contrast objects, particularly in MPRs (*top*). Both AMPR (*center*) and 3D back-projection (*bottom*) reduce cone-beam artifacts and are fully equivalent for 16-slice scanning

3.3.4.4 Weighted Hyperplane Reconstruction

The concepts used in WHR, (described in Hsieh 2001, Hsieh 2003) are related to those used in AMPR, yet are derived in a different way. Similar to AMPR, 3D reconstruction is split into a series of 2D reconstructions. Instead of reconstructing traditional axial slices, convex hyper planes are proposed as the region of reconstruction. The increasing spiral overlap with decreasing pitch is handled by introducing subsets of detector rows, which are sufficient to reconstruct an image at a given pitch value. At pitch = 0.5625 with a 16-slice scanner, the data collected by detector rows 1–9 form a complete projection data set. Similarly, projections from detector rows 2–10 can be used to reconstruct another image at the same z-position; projections from detector rows 3–11 yield a third image, and so on. In a way, these "sub-images" are related to the "book pages" of AMPR. The final image is based on a weighted average of the sub-images. In Hsieh (2003), good image quality for a 16-slice CT system is demonstrated using the WHR approach.

3.3.4.5 Double z-Sampling

In 2004, a new concept for multi-slice spiral scanning was introduced that makes use of a periodic motion of the focal spot in the longitudinal direction to improve data sampling along the z-axis (Flohr 2004). By permanent electromagnetic deflection of the electron beam in a rotating-envelope X-ray tube (see above), the focal spot is wobbled between two different positions on the anode plate. Due to the anode angle of typically 7–9° this translates into motion both in the radial direction and the z-direction (Fig. 3.21). The radial motion is a side-effect that has to be taken care of by the image-reconstruction algorithms, most favorably in the "rebinning" procedure, which is the interpolation of the measured fan-beam data to parallel geometry. The amplitude of the periodic z-motion is adjusted such that two subsequent readings are shifted by half a collimated slice width in the patient's longitudinal direction (Fig. 3.22). Therefore, the measurement rays of two subsequent detector read-outs with collimated slice width SW_{coll} interleave in the z-direction, and every two N-slice readings are combined to one 2N-slice projection with a sampling distance of $SW_{coll}/2$ (Fig. 3.22).

The most recent multi-slice CT system using double z-sampling has a detector that provides 32 collimated 0.6-mm slices. Two subsequent 32-slice detector read-outs are combined to one 64-slice projection with a sampling distance of 0.3 mm at iso-center. With this technique, 64 overlapping 0.6-mm slices per rotation are acquired. The sampling scheme is identical to that of a 64 × 0.3-mm detector, and the AMPR algorithm is used for image reconstruction. In this way, spatial resolution in the longitudinal direction is increased, thus providing a measurable longitudinal spatial resolution of 0.33 mm, and objects below 0.4 mm in diameter can be routinely resolved at any pitch (Fig. 3.23). Another, clinically even more relevant benefit of double z-sampling is the suppression of spiral windmill artifacts at any pitch (Fig. 3.24, 3.25). Double z-sampling provides a sampling distance of $SW_{coll}/2$ independent of the pitch. The improved sampling along the z-direction is not restricted to the iso-center, but is maintained over a wide range of the SFOV. Longitudinal resolution is therefore not severely degraded for off-center objects. This is a major difference in approaches that attempt to improve longitudinal resolution by the choice of optimized small pitch values, so that data acquired in different rotations interleave in the z-direction. In this case, a sampling distance of $SW_{coll}/2$ is achieved close to iso-center only.

In conclusion, 16- and 64-slice spiral scanning with cone-beam reconstruction techniques enables scanning of large scan ranges with sub-millimeter resolution and superb image quality. The ability to provide sub-millimeter volume coverage repre-

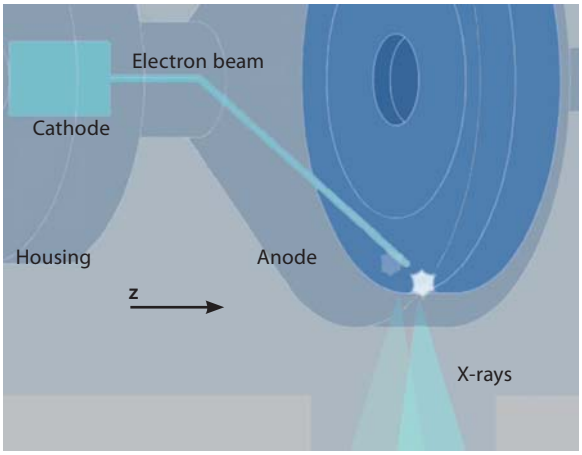

Fig. 3.21. A rotating-envelope X-ray tube (Siemens STRATON, Forchheim, Germany) with z-flying focal spot technique. The entire tube housing rotates in an oil bath. The anode plate is in direct contact with the cooling oil. The central cathode also rotates, and permanent electromagnetic deflection of the electron beam is needed to control the position and the shape of the focal spot. The electromagnetic deflection unit can be used to switch the focal spot between two different positions on the anode plate (indicated by two asterisks). Due to the anode angle of typically 7–9°, this translates into a motion both in the radial direction and the z-direction

sents a significant performance enhancement over 4-slice CT systems. The latest 64-slice CT scanners even allow for coverage of arbitrarily large scan ranges without compromising on spatial resolution. Therefore, 16-slice CT scanners and, even more, 64-slice CT scanners are very well-suited for angiographic applications in all body regions (Figs. 3.26–3.28), which represents one of the most rapidly emerging applications. The use of the latest 16- and 64-slice CT scanners in cardiac applications requires special ECG-gated scan and reconstruction techniques, which will be introduced in the following chapters.

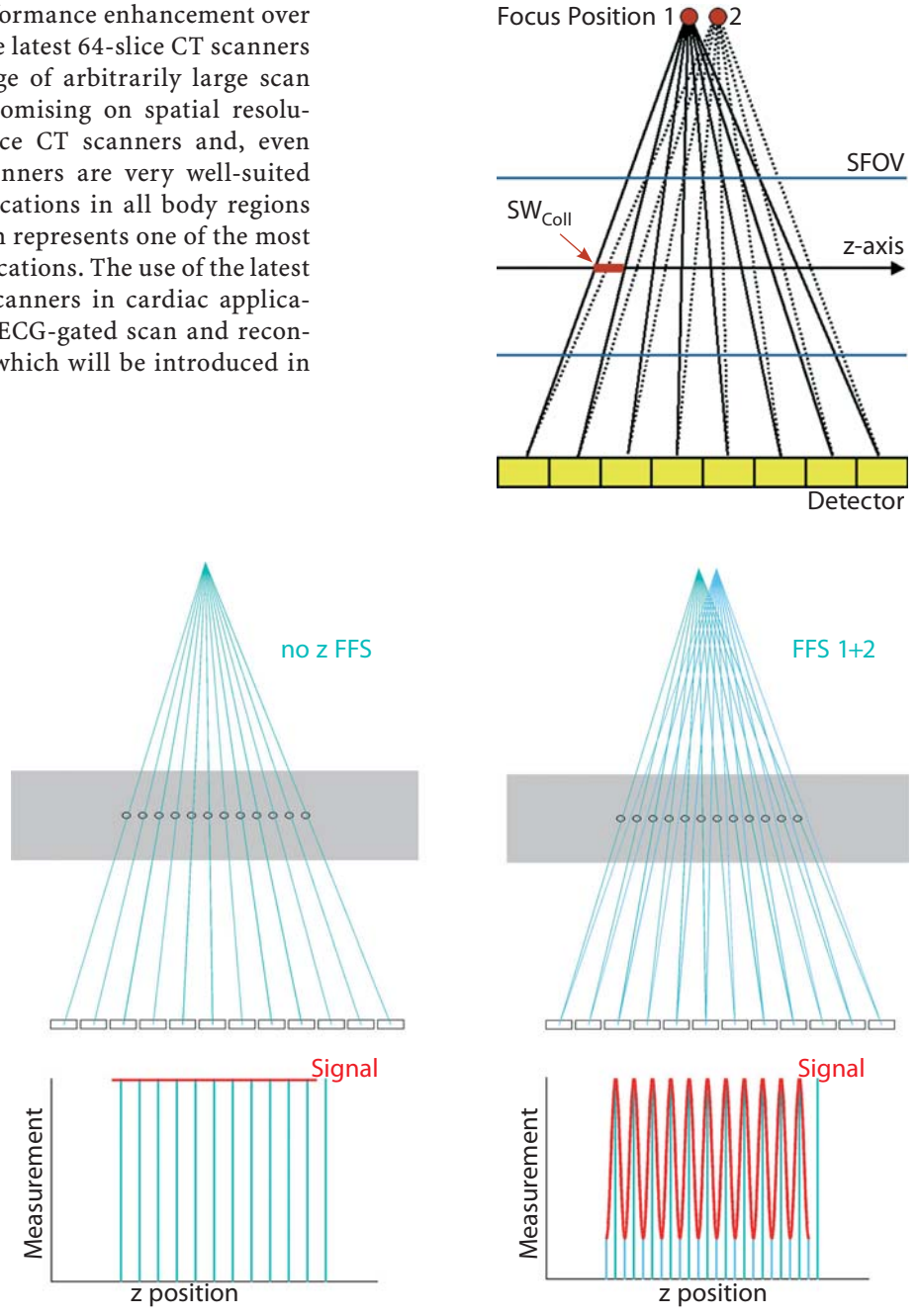

Fig. 3.22a, b. Principle of improved z-sampling with the z-flying focal spot technique. **a** Due to a periodic motion of the focal spot in the z-direction, two subsequent N-slice readings are shifted by half a collimated slice width (SWcoll/2) at iso-center and can be interleaved to one 2N-slice projection. Improved z-sampling is not only achieved at iso-center, but maintained over a wide range of the SFOV. The simultaneous radial motion of the focal spot in an actual X-ray tube has been omitted to simplify the drawing. **b** The improved z-sampling with the z-flying focal spot technique provides consistent resolution of smaller objects due to a finer sampling scheme

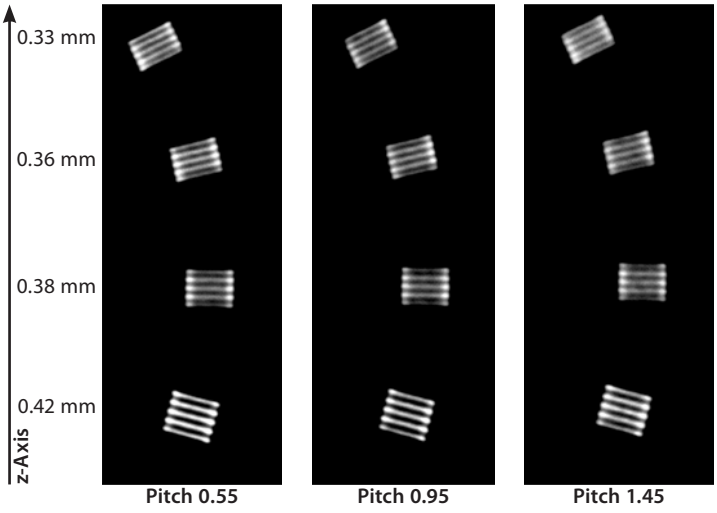

Fig. 3.23. Demonstration of spatial resolution at iso-center for the evaluated 64-slice CT scanner (SOMATOM Sensation 64, Siemens, Forchheim, Germany). The bar patterns of the high-resolution insert of the CATPHAN (computer-assisted tomography phantom, standardized for contrast and resolution measurements) have been aligned in the longitudinal direction (at iso-center). Scan data have been acquired with 64 × 0.6-mm slices using the z-flying focal spot and a sharp body reconstruction kernel (B70). Independent of the pitch, the bar patterns down to 0.33 mm bar diameter are visible

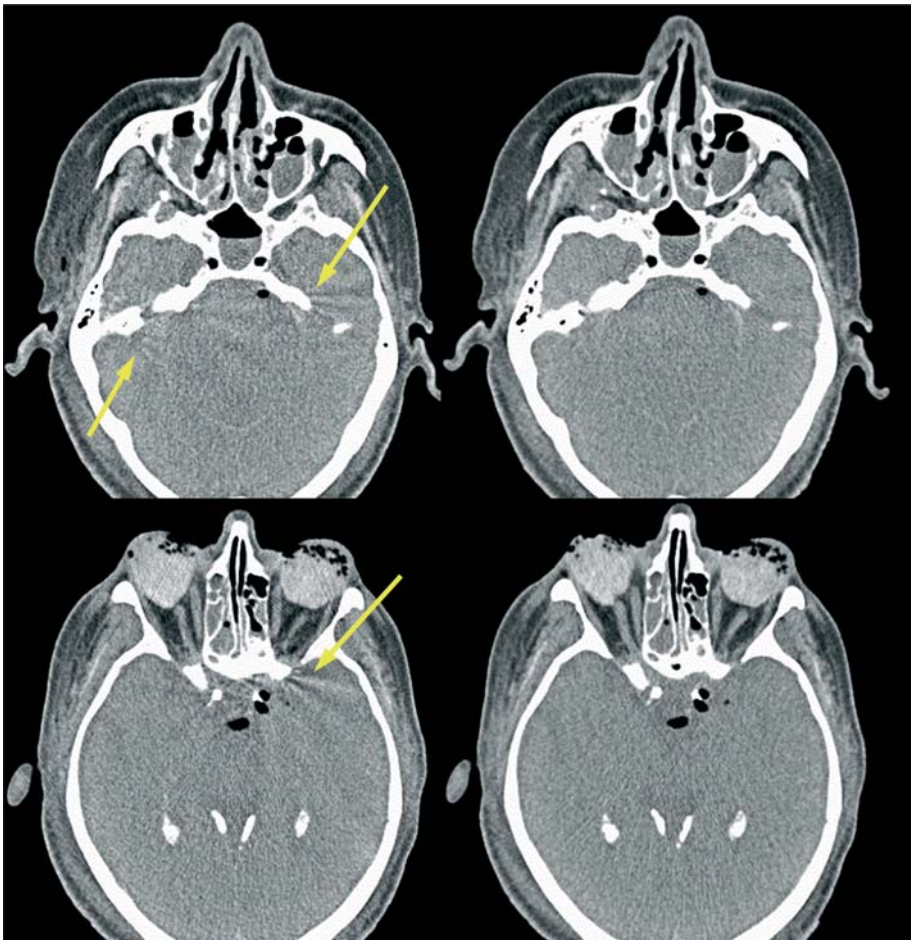

Fig. 3.24. Reduction of spiral artifacts with the z-flying focal spot technique. Left Head specimen scanned with 32 × 0.6-mm collimation at pitch 1.4, without z-flying focal spot. Right Head specimen scanned at the same pitch with 64 × 0.6-mm slices using the z-flying focal spot technique. Due to the improved longitudinal sampling, spiral interpolation artifacts (the windmill structures indicated by the arrows) are suppressed without degradation of z-axis resolution

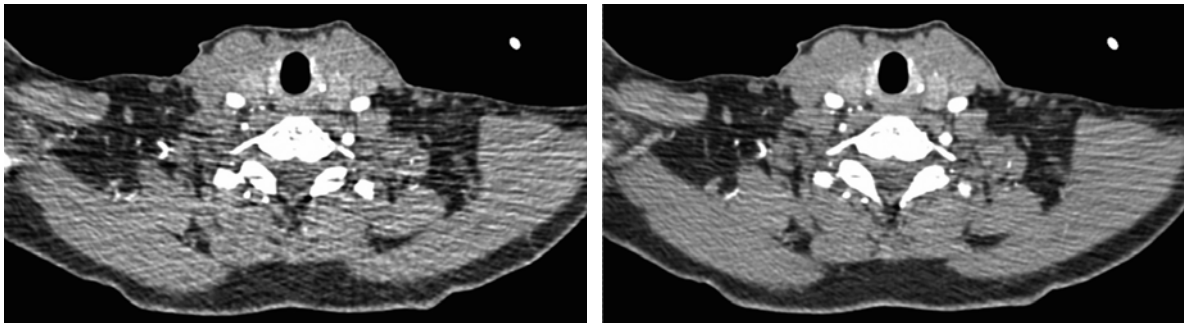

Fig. 3.25. Reduction of spiral artifacts with the z-flying focal spot technique. Left Axial slice at the level of the shoulder scanned with 32 × 0.6-mm collimation at pitch 1.4, without z-flying focal spot. Right The same patient and the same z-position scanned with the same pitch with 64 × 0.6-mm slices using the z-flying focal spot technique. Due to the improved longitudinal sampling, spiral interpolation artifacts that appear as pronounced streaks propagating from left to right are suppressed without degradation of z-axis resolution

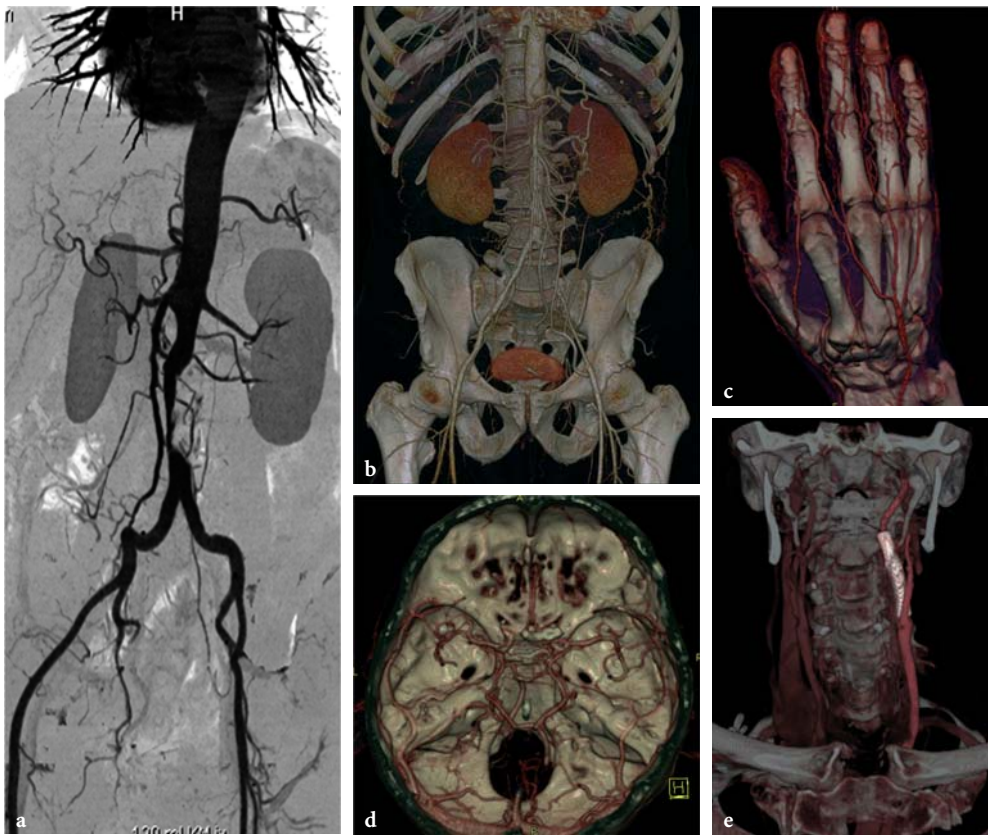

Fig. 3.26a–e. Case examples of 16-slice CT angiography examinations using a CT scanner with 16 × 0.75-mm collimation. High-resolution CT angiography of the aorta and iliac arteries with a 1200-mm scan range, visualized in an angiographic-type maximum intensity projections (MIP) display (**a**) and volume-rendering technique (**b**). CT angiography examinations of the digital arteries (**c**), the carotid arteries with an inserted stent (**d**), and the cerebral vessels (**e**). (Case courtesy of **a**, **b** the University of Tübingen, Germany, and **c–e** the University of Munich, Grosshadern Clinic, Germany)

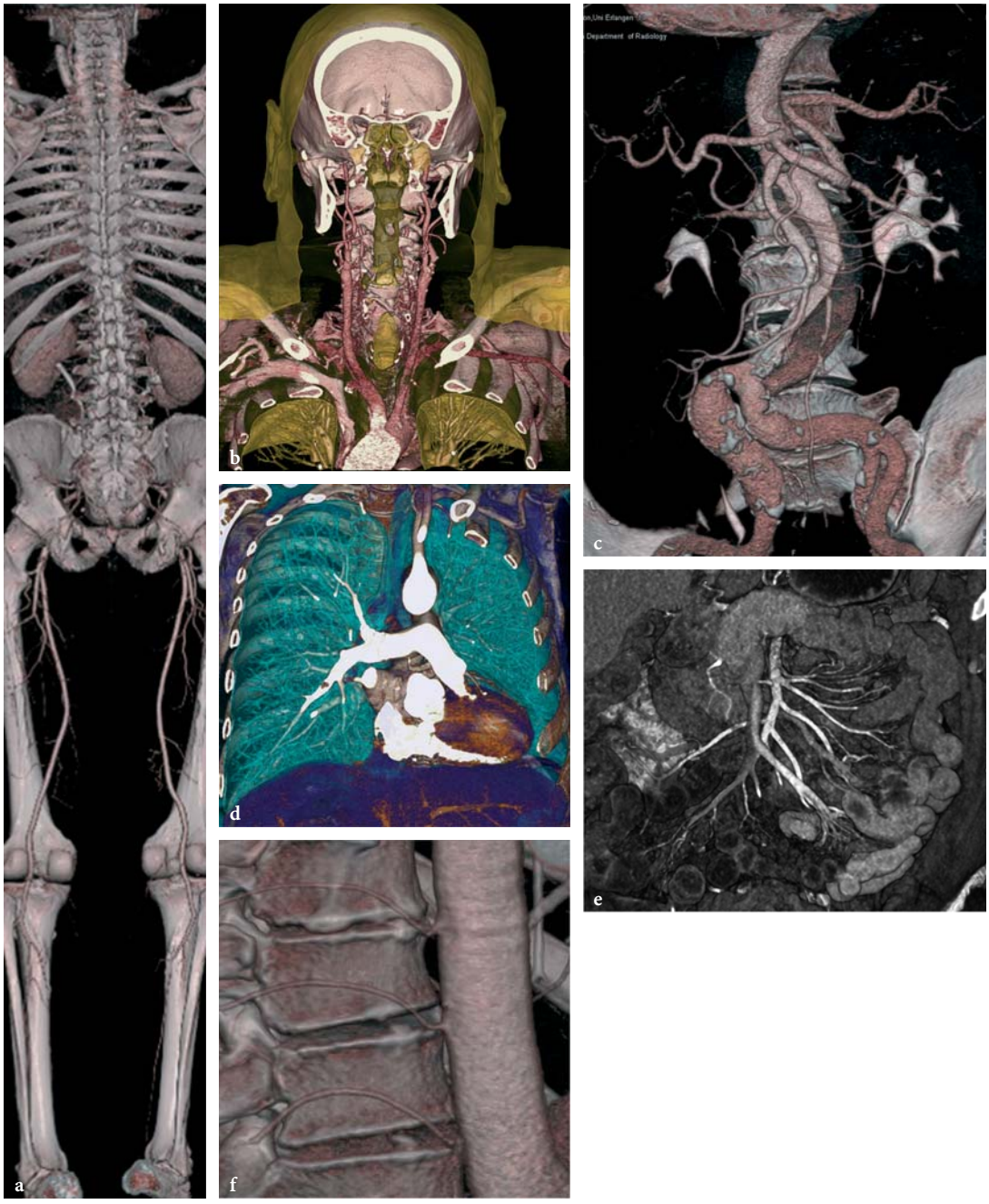

Fig. 3.27a–f. Case examples of 64-slice CT angiography examinations using a CT scanner with 0.6-mm collimation and double z-sampling technique. Whole-body CT angiography examination with 0.4-mm resolution and 1570-mm scan range (**a**). Pure arterial-phase carotid artery examination in 5-s scan time (**b**). CT angiography of a dissection of the abdominal aorta with excellent visualization of calcifications and small-caliber abdominal vessels (**c**). Detection of pulmonary embolism in a patient with chest pain within a breath-hold time of 5 s (**d**). CT angiography of the mesenteric arteries in a patient with acute bowel ischemia (**e**). Display of small vessels with calibers of < 1 mm originating from the thoracic aorta perpendicular to the scan axis (**f**). (Cases courtesy of the University of Erlangen, Germany)

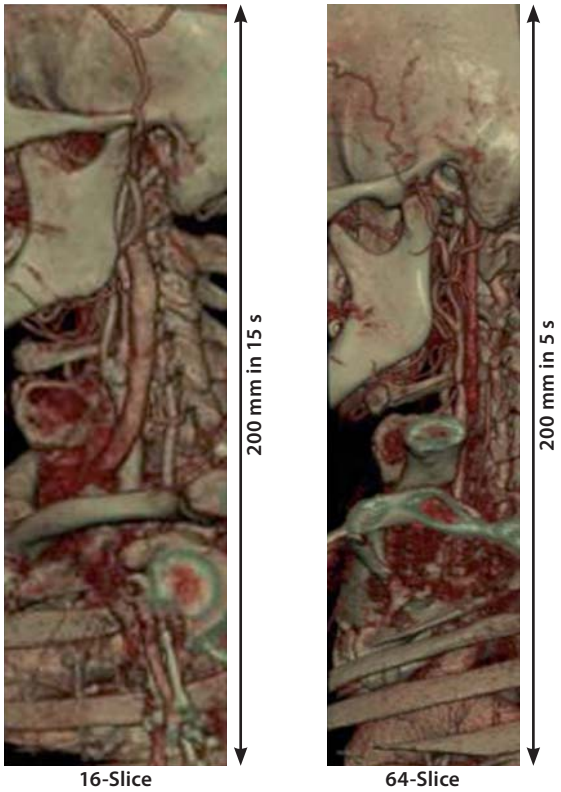

Fig. 3.28. Direct comparison of a CT angiography of the carotid arteries in the same patient, performed with a 16-slice CT at 0.75-mm collimation and with a 64-slice CT using 0.6-mm collimation and double z-sampling technique. Image quality can be greatly improved using 64-slice CT and with significantly shorter scan times due to the absence of strong venous overlap. (Case courtesy of the University of Munich, Grosshadern Clinic, Germany)

References

Achenbach S, Ulzheimer S, Baum U et al (2000). Noninvasive coronary angiography by retrospectively ECG-gated multislice spiral CT. Circulation 102:2823–2828

Becker C, Knez A, Ohnesorge B, Schöpf U, Reiser MF (2000). Imaging of non-calcified coronary plaques using helical CT with retrospective EKG gating. AJR 175:423–424

Bruder H, Kachelrieß M, Schaller S, Stierstorfer K, Flohr T (2000). Single-slice rebinning reconstruction in spiral cone-beam computed tomography. IEEE Trans Med Imag 19(9): 873–887

Crawford CR, King KF (1990). Computed tomography scanning with simultaneous patient translation. Med Phys 17: 967–982

Ertl-Wagner B, Hoffmann RT, Brüning R, Dichgans M, Reiser MF (2002). Supraaortale Gefäßdiagnostik mit dem 16-Zeilen-Multidetektor-Spiral-CT. Untersuchungsprotokoll und erste Erfahrungen. Radiologe 42:728–732

Feldkamp LA, Davis LC, and Kress JW (1984). Practical cone-beam algorithm. J Opt Soc Am A1 612–619

Flohr T, Stierstorfer K, Bruder H, Simon J, Schaller S (2002a). New Technical developments in multislice CT. Part 1: Approaching isotropic resolution with sub-mm 16-slice Scanning, Röfo Fortschr Geb Rontgenstr Neuen Bildgeb Verfahr. 174:839–845

Flohr T, Bruder H, Stierstorfer K, Simon J, Schaller S, Ohnesorge B (2002b). New technical developments in multislice CT. Part 2: Sub-millimeter 16-slice scanning and increased gantry rotation speed for cardiac imaging. Röfo Fortschr Geb Rontgenstr Neuen bildgeb verfahr 174:1022–1027

Flohr T, Stierstorfer K, Bruder H, Simon J, Polacin A, Schaller S (2003a). Image reconstruction and image quality evaluation for a 16-slice CT scanner. Med Phys 30 (5): 832–845

Flohr T, Ohnesorge B, Bruder H, Stierstorfer K, Simon J, Suess C, Schaller S (2003b). Image reconstruction and performance evaluation for ECG-gated spiral scanning with a 16-slice CT system. Med Phys 30(10): 2650–2662

Flohr T, Bruder H, Stierstorfer K, Schaller S (2003c). Evaluation of approaches to reduce spiral artifacts in multi-slice spiral CT (abstract). Abstracts of the 89th scientific assembly and annual meeting of the RSNA 2003, 567

Flohr T, Stierstorfer K, Raupach R, Ulzheimer S, Bruder H (2004). Performance evaluation of a 64-slice CT-system with z-flying focal spot. Röfo Fortschr Geb Rontgenstr Neuen Bildgeb Verfahr 176:1803–1810

Fuchs T, Krause J, Schaller S, Flohr T, Kalender WA (2000). Spiral interpolation algorithms for multislice spiral CT. Part 2. Measurement and evaluation of slice sensitivity profiles and noise at a clinical multislice system. IEEE Trans Med Imag 19(9): 835–847

Grass M, Köhler T, Proksa R (2000). 3D cone-beam CT reconstruction for circular trajectories. Phys Med Biol 45(2):329–347

Hein I, Taguchi K, Silver MD, Kazarna M, Mori I (2003). Feldkamp-based cone-beam reconstruction for gantry-tilted helical multi-slice CT. Med Phys 30(12), 3233–3242

Hong C, Becker C R, Huber A, Schoepf U J, Ohnesorge B, Knez A, Brüning R, Reiser MF (2001). ECG-gated reconstructed multi-detector row CT coronary angiography: effect of varying trigger delay on image quality. Radiology 220: 712–717

Hu H (1999). Multi-slice helical CT: Scan and reconstruction. Med Phys 26(1):5–18

Hu H, He HD, Foley WD, Fox SH (2000). Four multidetector-row helical CT: image quality and volume coverage speed. Radiology 215: 55–62

Hsieh J (2001a). Investigation of the slice sensitivity profile for step-and-shoot mode multi-slice computed tomography. Med Phys 28: 491–500

Hsieh J, Toth TL, Simoni P, Grekowicz B, Slack CC, Seidenschnur GE (2001b). A generalized helical reconstruction

algorithm for multi-slice CT. Abstracts of the 87th Scientific Assembly and Annual Meeting of the RSNA 2001 271

Hsieh J (2003a). Analytical models for multi-slice helical CT performance parameters. Med Phys 30(2): 169–178

Hsieh J, Grekowicz B, Simoni P, Thibault JB, Joshi MC, Dutta S, Williams EC, Shaughnessy C, Sainath P (2003b). Convolution reconstruction algorithm for multi-slice helical CT. In: Proc. SPIE Int Symp Med Imag 2003

Kachelrieß M, Schaller S, Kalender WA (2000a). Advanced single-slice rebinning in cone-beam spiral CT. Med Phys 27: 754–772

Kachelriess M, Ulzheimer S, Kalender W (2000b). ECG-correlated image reconstruction from subsecond multi-slice spiral CT scans of the heart. Med Phys 27: 1881–1902

Kalender W, Seissler W, Klotz E, Vock P (1990). Spiral volumetric CT with single-breath-hold technique, continuous transport and continuous scanner rotation. Radiology 176: 181–183

Kalender W (1995). Thin-section three-dimensional spiral CT: is isotropic imaging possible? Radiology 197: 578–580

Klingenbeck-Regn K, Schaller S, Flohr T, Ohnesorge B, Kopp AF, Baum U (1999). Subsecond multi-slice computed tomography: basics and applications. EJR 31:110–124

Knez A, Becker C, Leber A, Ohnesorge B, Reiser MF, Haberl R (2000). Non-invasive assessment of coronary artery stenoses with multidetector helical computed tomography. Circulation 101: e221-e222

Kopp A, Schröder S, Küttner A et al (2001). Coronary arteries: retrospectively ecg-gated multidetector row CT angiography with selective optimization of the image reconstruction window. Radiology 221: 683–688

Larson G, Ruth C, Crawford C (1998). Nutating slice CT image reconstruction. US Patent Application WO 98/44847, filed 8 April, 1998

Lell M, Wildberger J, Heuschmid M, Flohr T, Stierstorfer K, Fellner F, Lang W, Bautz W, Baum U (2002). CT-Angiographie der A. carotis: Erste Erfahrungen mit einem 16-Schicht-Spiral-CT – CT-angiography of the carotid artery: First results with a novel 16-slice-spiral-CT scanner, Röfo Fortschr Geb Rontgenstr Neuen Bildgeb Verfahr 174: 1165–1169

Liang Y, Kruger RA (1996). Dual-slice spiral versus single-slice spiral scanning: comparison of the physical performance of two computed tomography scanners. Med Phys 23(2): 205–220

Macari, M, Bini MJ, Xue X, et al (2002). Colorectal neoplasms: prospective comparison of thin-section low-dose multi–detector row CT colonography and conventional colonoscopy for detection. Radiology 224:383–392

McCollough CH, Zink FE (1999). Performance evaluation of a multi-slice CT system. Med Phys 26:2223–2230

Nieman K, Oudkerk M, Rensing B, van Oijen P, Munne A, van Geuns R, de Feyter P (2001). Coronary angiography with multi-slice coputed tomography. The Lancet 357: 599–603

Nieman K, Cademartiri F, Lemos PA, Raaijmakers R, Pattynama PMT, de Feyter PJ (2002). Reliable noninvasive coronary angiography with fast submillimeter multislice spiral computed tomography. Circulation 106; 2051–2054

Ohnesorge B, Flohr T, Schaller S, Klingenbeck-Regn K, Becker C, Schöpf U J, Brüning R, Reiser MF (1999). Technische Grundlagen und Anwendungen der Mehrschicht-CT (German). Radiologe 39:923–931

Ohnesorge B, Flohr T, Becker C, Kopp A, Schoepf U, Baum U, Knez A, Klingenbeck-Regn K, Reiser MF (2000). Cardiac imaging by means of electro-cardiographically gated multisection spiral CT – initial experience. Radiology 217:564–571

Ohnesorge B, Kopp AF, Becker CR, Knez A, Schröder S, Flohr T (2001). Technical aspects of cardiovascular and cardiac diagnosis with CT. In: Topol E and Lanzer P, Theory and practise of cardiovascular medicine II. Chap. 15:121–130. Springer Verlag Berlin, Heidelberg

Proksa R, Koehler T, Grass M, Timmer J (2000). The n-PI Method for helical cone-beam CT. IEEE Trans Med Imag 19:848 – 863

Remy-Jardin J, Tillie-Leblond I, Szapiro D et al (2002). CT angiography of pulmonary embolism in patents with underlying respiratory disease: impact of multi-slice CT on image quality and negative predictive value. Eur Radiol 12: 1971–1978

Ropers D, Baum U, Pohle K, et al (2003). Detection of coronary artery stenoses with thin-slice multi-detector row spiral computed tomography and multiplanar reconstruction. Circulation 107:664–6

Rubin GD, Dake MD, Semba CP (1995). Current status of three-dimensional spiral CT scanning for imaging the vasculature. Radiol Clin North Am 33(1): 51–70 (Review)

Rubin GD, Schmidt AJ, Logan LJ, Sofilos MC (2001). Multidetector row CT angiography of lower extremity arterial inflow and runoff: initial experience. Radiology 221(1): 146–58

Saito Y, Suzuki T (1998). Evaluation of the performance of multi-slice CT system in non-helical scanning, Abstracts of the 84th Scientific Assembly and Annual Meeting of the RSNA 1998, 578

Schaller S (1998). Practical image reconstruction for cone-beam computed tomography, PhD-Thesis University Erlangen Nürnberg, Germany

Schaller S, Flohr T, Klingenbeck K, Krause J, Fuchs T, Kalender WA (2000). Spiral interpolation algorithm for multi-slice spiral CT. Part I: Theory. IEEE Trans Med Imag 19(9): 822–834

Schaller S, Stierstorfer K, Bruder H, Kachelrieß M, Flohr T (2001). Novel approximate approach for high-quality image reconstruction in helical cone beam CT at arbitrary pitch. In: Proc SPIE Int Symp Med Imag 4322:113–127

Schardt P, Kutschera W, Knüpfer W (2004). Technical design and performance evaluation of a new rotation envelope tube concept in X-ray computed tomography. Med Phys 31:2699–2706

Schöpf U J, Bruening R D, Hong C, Eibel R, Aydemir S, Crispin A, Becker C, Reiser MF (2001). Multislice helical CT of focal and diffuse lung disease: comprehensive diagnosis with reconstruction of contiguous and high-resolution CT sections from a single thin-collimation scan. AJR Am J Roentgenol 177(1):179–84

Schoepf UJ, Becker CR, Hofmann LK, Das M, Flohr T, Ohnesorge BM (2003). Multislice CT angiography. Eur Radiol 13:1946–1961

Schroeder S, Kopp A, Baumbach A, Meisner C, Kuettner A, Georg C, Ohnesorge B, Herdeg C, Claussen C, Karsch K (2001a). Noninvasive detection and evaluation of atherosclerotic coronary plaques with multi-slice computed tomography. JACC 37(5): 1430–1435

Schroeder S, Flohr T, Kopp A F, Meisner C, Kuettner A, Herdeg C, Baumbach A, Ohnesorge B (2001b). Accuracy of density measurements within plaques located in artificial coronary arteries by X-Ray multislice CT: results of a phantom study. JCAT 25(6): 900–906

Stierstorfer K, Flohr T, Bruder H (2002). Segmented multiple plane reconstruction- a novel approximate reconstruction scheme for multi-slice spiral CT. Phys Med Biol 47:2571–2581

Stierstorfer K, Rauscher R, Boese J, Bruder H, Schaller S, Flohr T (2004). Weighted FBP- a simple approximate 3D FBP algorithm for multi-slice spiral CT with good dose usage for arbitrary pitch. Phys Med Biol 49:2209–2218

Swensen SJ (2002). CT screening for lung cancer. AJR 179:833–836

Taguchi T, Aradate H (1998). Algorithm for image reconstruction in multi-slice helical CT. Med Phys 25(4): 550–561

Tomandl BF, Klotz E, Handschu R, Stemper B, Reinhardt F, Huk WJ, Eberhardt KE, Fateh-Moghadem S (2003). Comprehensive imaging of ischemic stroke with multisection CT. RadioGraphics 23(3):565–592

Turbell H, Danielsson PE (1999). An improved PI-method for reconstruction from helical cone beam projections. In: IEEE Medical Imaging Conference, Seattle

Villablanca J P, Lahan R, Hooshi P, Lim S, Duckwiler G, Patel A, Sayre J, Martin N, Frazee J, Bentson J, Vinuela F (2002). Detection and characterization of very small cerebral aneurysms by using 2D and 3D helical CT angiography. AJNR Am J Neuroradiol 23(7):1187–98

Wang G, Lin T, Cheng P (1993). A general cone-beam reconstruction algorithm. IEEE Trans Med Imag 12, 486–496

Wessling J, Fischbach R, Meier N, et al (2003). CT colonography: protocol optimization with multi-detector row CT – study in an anthropomorphic colon phantom. Radiology 228:753–759

Wintersperger B, Helmberger T, Herzog P, Jakobs T, Waggershauser T, Becker C, Reiser MF (2002a). Hochaufgelöste abdominelle Übersichtsangiographie mit einem 16-Detektorzeilen-CT-System – New abdominal CT angiography protocol on a 16 detector-row CT scanner. Radiologe 42: 722–727

Wintersperger B, Herzog P, Jakobs T, Reiser MF, Becker C. Initial experience with the clinical use of a 16 detector row CT system (2002b). Crit Rev Comput Tomogr 43:283–316

Principles of Multi-slice Cardiac CT Imaging

4

Bernd Ohnesorge and Thomas Flohr

Contents

4.1 **Basic Performance Requirements for CT Imaging of the Heart** *71*

4.2 **CT Imaging with Optimized Temporal Resolution: The Principle of Half-Scan Reconstruction** *73*

4.3 **Prospectively ECG-Triggered Multi-slice CT** *76*

4.4 **Retrospectively ECG-Gated Multi-slice CT** *79*
4.4.1 Multi-slice Cardiac Spiral Reconstruction *81*
4.4.2 ECG-Gated Multi-slice Spiral Acquisition *83*
4.4.3 Segmented Cardiac Reconstruction Algorithms *88*
4.4.4 Cardiac Cone-Beam Reconstruction Algorithms *97*
4.4.5 ECG-Gated Spiral Scanning with Increased Volume Speed *101*

4.5 **Synchronization with the ECG and Cardiac Motion** *106*
4.5.1 ECG-Based Phase Selection *106*
4.5.2 The Pros and Cons of ECG Gating and ECG Triggering *108*
4.5.3 Alternative Cardiac-Motion Gating Approaches *110*

4.6 **Radiation Exposure Considerations** *113*
4.6.1 Principles of Radiation Dose Measurement in CT *113*
4.6.2 Radiation Exposure for Selected Cardiac Examination Protocols *117*
4.6.3 Exposure Reduction with ECG-Gated Tube-Current Modulation *119*
4.6.4 Optimization for Different Patient Sizes *121*
4.6.5 Optimization of Contrast-to-Noise Ratio *123*

References *124*

4.1 Basic Performance Requirements for CT Imaging of the Heart

To virtually freeze cardiac motion and avoid motion-artifacts, very short exposure times are needed for the acquisition of transaxial slices. High temporal resolution is particularly important for imaging the coronary arteries, as they are located very close to the heart muscles and show strong movement during the cardiac cycle. Due to the very complex 3D motion pattern of the heart, the intensity of movement varies for different cardiac anatomies and different coronary vessels, and within the cardiac cycle. The strongest movement is present during contraction of the atria and ventricles in systole. The short end-systolic rest phase is followed by a continuous-filling phase of the ventricles during diastole that slows down towards mid- and end-diastole. This motion pattern can be measured by the dislocation of the left ventricular wall, the aortic valve flaps, and the different segments of the coronary arteries in representative transaxial planes (Fig. 4.1a) (Achenbach 2000). The least amount of movement of the major cardiac anatomy and the coronary arteries, and thus the least amount of dislocation over time, is observed in end-systole and mid- to end-diastole of the cardiac cycle (Fig. 4.1a). While the duration of the end-systolic phase (approximately 100–150 ms) is more or less independent of the present heart rate (and the related RR-interval time), the duration of the phase with the least cardiac motion during diastole narrows with increasing heart rate (Fig. 4.1b). For low heart rates, the end-systolic phase is much shorter than the diastolic rest phase, but the difference decreases with increasing heart rate. For

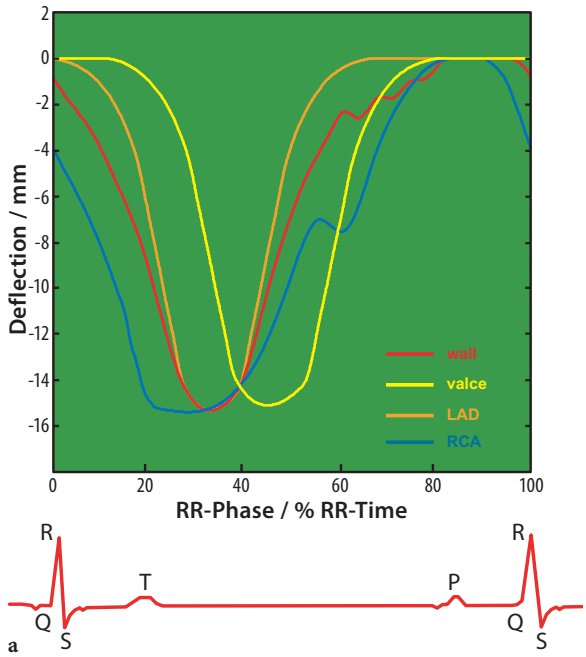

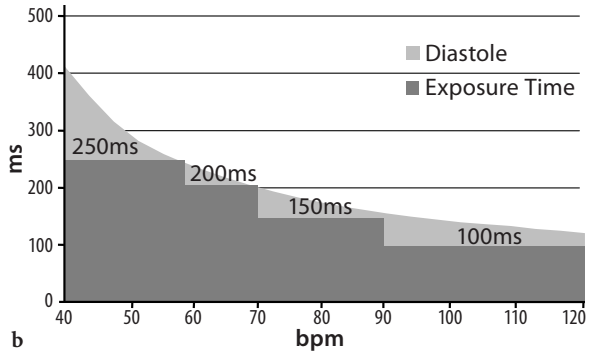

Fig. 4.1. a Cardiac motion during the different phases of the cardiac cycle (Achenbach 2000). Rest phases of the myocardial wall and the coronary arteries can be observed during diastolic filling and during end-systole. **b** The duration of the phase of lowest cardiac motion, during the diastolic rest phase, depends on heart rate. For clinically usual heart rates up to 90 bpm, a temporal resolution of about 150 ms is needed for motion-free imaging during the diastolic rest phase, whereas a 100-ms temporal resolution is feasible for imaging during the cardiac rest phases at heart rates above 100 bpm

higher heart rates, the diastolic rest phase can be even shorter than the end-systolic rest phase.

The cardiac anatomy should be imaged during those phases of cardiac cycle in which there is the least movement; that is, when the least blurring due to motion artifacts is to be expected. Thus, image acquisition and reconstruction need to be synchronized as accurately as possible to the movement of the heart, i.e., by using ECG information that is recorded in parallel to the CT scan acquisition. Since the fastest gantry rotation speeds of today's multislice CT scanners are between 0.5 s up to 0.33 s per rotation, imaging of the heart is usually performed during the diastolic rest phase of the cardiac cycle, as the achievable temporal resolution is usually not sufficient to reliably eliminate cardiac motion during other phases of the cardiac cycle. However, with CT gantry rotation speeds becoming even faster, imaging in the end-systolic rest phase may also become feasible.

According to a rough estimation, a temporal resolution of about 250 ms is appropriate for motion-free imaging in the diastolic rest phase up to a heart rate of about 60 bpm, about 200 ms up to a heart rate of 70 bpm, and approximately 150 ms for clinically usual heart rates up to 90 bpm (Fig. 4.1b). It can be expected that a temporal resolution of about 100 ms is sufficient for imaging the heart during the diastolic or end-systolic rest phase also at high heart rates (Achenbach 2000). Image acquisition during other phases of the cardiac cycle (e.g., systole) with rapid cardiac motion is needed for evaluation of cardiac function. Motion-free imaging during phases other than the diastolic and end-systolic rest phases requires a temporal resolution of about 50 ms (Stehling 1991) and is usually not possible with state-of-the-art CT systems. Thus, only the larger cardiac anatomy or cardiac anatomy with low motion amplitudes should be assessed during phases of high cardiac motion.

Many structures of the cardiac morphology, especially the coronary arteries and the cardiac valves including the valve flaps, represent small and complex 3D structures that require very high and, at best, sub-millimeter isotropic spatial resolution with longitudinal resolution close or equal to in-plane resolution. The most proximal coronary segments and the distal segments of the right coronary artery (RCA) are directed parallel to the image plane, while the middle segments are directed

perpendicular to the image plane. The lumen diameter of the main segments of the coronary artery tree ranges from 4 mm (left main coronary artery) down to about 1 mm (peripheral left main coronary artery and circumflex). Detection and quantification of coronary stenosis with the ability to differentiate a 20% change in the diameter of the vessel lumen for the larger-caliber vessels represents a viable goal for cardiac CT imaging. To achieve this, CT systems need to provide a spatial resolution in all three dimensions (isotropic) of at least 0.5 mm for visualization of the main coronary vessels and of smaller branches. Thus, in-plane and through-plane resolution significantly below 1 mm are needed to assess the main coronary segments, including narrowing and plaques. Less spatial resolution is sufficient for assessment of the larger cardiac anatomy, such as the myocardium and the cardiac chambers. However, scans should a priori be acquired at best possible spatial resolution, as lower spatial resolution can be generated via data post-processing.

In addition to high spatial resolution, sufficient contrast-to-noise ratio is important to resolve small and low-contrast structures, such as atherosclerotic coronary plaques, with different attenuation properties. Appropriate low-contrast resolution has to be provided with limited radiation exposure at the shortest possible exposure time. For most cardiac applications, appropriate contrast enhancement of the cardiac vessels and the cardiac anatomy is achieved with peripheral injection of contrast agent and optimized timing of the bolus. Sufficient contrast enhancement is particularly important for imaging the distal coronary segments, as they are located very close to the myocardium and are separated from it only by a thin layer of epicardial fat. Only the assessment of cardiac and coronary calcification is possible without administration of contrast agents.

Scan acquisition within a single and short breath-hold time is mandatory for minimizing the amount of contrast material needed for vascular enhancement and to avoid respiratory artifacts. Breath-hold times of 20 s or less are appropriate for stable patients but 10 s or less are preferable for less stable, dyspneic patients. Ideally, a complete data set of the entire heart anatomy would be acquired within a single phase of the cardiac cycle without patient movement, but CT technology today, and presumably in the near future, does not provide sufficient detector width to cover the entire heart volume within a single heartbeat. Instead, images at consecutive z-positions that continuously cover the heart volume need to be generated from data acquired in different cardiac cycles. A virtually «frozen» cardiac volume can only be produced by phase-consistent synchronization of the acquisition to the movement of the heart using simultaneously recorded ECG information. A reasonably stable sinus rhythm without rapid arrhythmic changes provides the best 3D images of the cardiac anatomy. Functional information can be derived if cardiac volume images can be generated in different phases of the cardiac cycle, e.g., as a basis for quantitative evaluation.

Cardiac imaging is obviously a highly demanding application for CT, since the temporal, spatial, contrast resolutions as well as scan time have to be optimized simultaneously, and radiation exposure has to be limited to levels of related imaging modalities, such as invasive diagnostic coronary angiography or nuclear imaging studies. These conflicting performance requirements have to be fulfilled and optimized for the particular application at the same time and within the same cardiac scan protocol. Optimization of one performance cornerstone alone (e.g., high temporal resolution, low radiation exposure) by trading-off other important parameters (e.g., spatial and contrast resolutions) may not lead to clinically useful results.

4.2 CT Imaging with Optimized Temporal Resolution: The Principle of Half-Scan Reconstruction

For motion-free imaging of the heart, data have to be acquired during phases of the cardiac cycle with little cardiac motion and with as high as possible temporal resolution. In the first place, temporal resolution of an axial CT slice is determined by the exposure time associated with the scan data used for reconstruction of that CT slice. Therefore, scan techniques and reconstruction algorithms need

to be developed that use a minimum amount of scan data while maintaining high image quality. In modern 3rd-generation CT systems with fan-beam geometry, the minimum amount of scan data needed for reconstruction of axial slices is a so-called partial scan (Parker 1982). Depending on the exact system geometry and its dimensions, a partial-scan fan-beam data set has to cover a projection-angle interval α_P (angle interval between tube positions at the start and end points of tube rotation) of 180° plus the breadth of the X-ray fan: $\alpha_P = \pi + \beta_f$. The breadth of the X-ray fan-beam β_f depends strongly on the diameter of the scan field of view (usually 50 cm) and the distances of the focal spot and detector from the center of the scan field of view. The equation $\alpha_P = \pi + \beta_f$ states that a minimum data segment of 180° has to be available for every fan angle β. As a consequence, a partial rotation usually covers about two-thirds of a rotation (≈240°) (Fig. 4.2a). Conventional partial-scan reconstruction techniques based on fan-beam geometry (Parker 1982) make use of all acquired data even if more data than the minimum angle of 180° are available for a fan angle β. These techniques produce a temporal resolution equal to the partial-scan acquisition time (≈two-thirds of the rotation time).

Better temporal resolution can be achieved with special reconstruction algorithms that use the minimum required amount of scan data. These algorithms, referred to as "half-scan" reconstruction, can be best explained using parallel-beam geometry. To this end, the fan-beam geometry of the partial-scan data set is transformed to parallel-beam

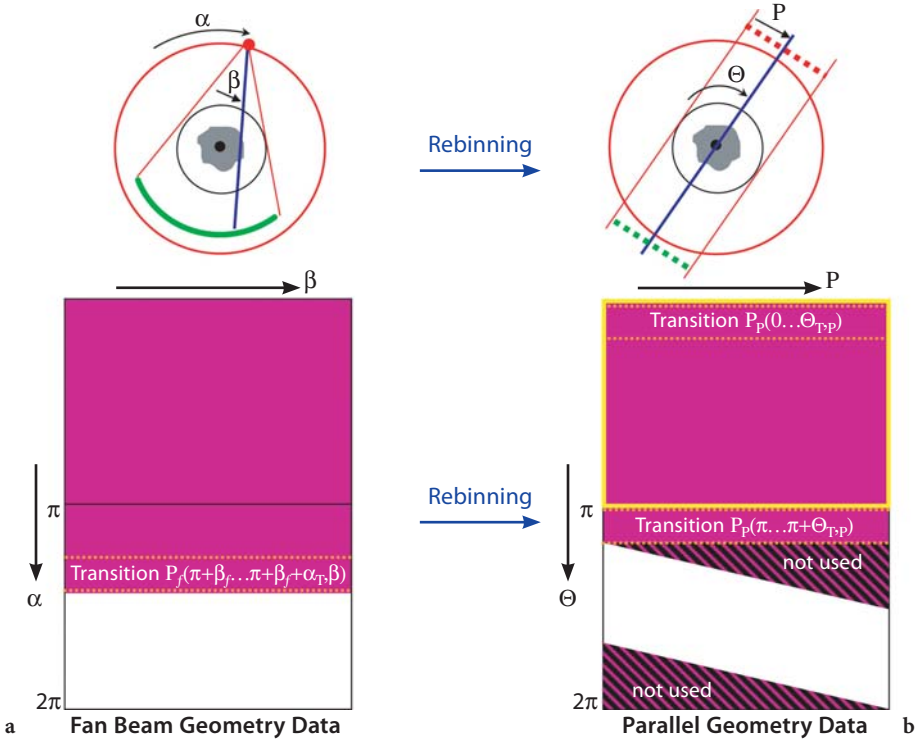

Fig. 4.2a, b. Principle of "half-scan" image reconstruction based on parallel-beam scan data. Scan data acquired in fan-beam geometry (**a**) with fan-beam projection angle α and fan-ray angle β is transformed into parallel-beam geometry (**b**) with parallel-beam projection angle Θ and parallel-ray position p using the "rebinning" technique and 2D interpolations. Acquired fan-beam data that form incomplete parallel projections are omitted during reconstruction. A data transition range enables smooth transition weighing for reduction of artifacts due to data inconsistencies

geometry using "rebinning" techniques (Kak 1988). The rebinning of a partial-scan fan-beam data set provides 180° of complete parallel projections, including chunks of incomplete parallel projections that consist of redundant data. Fan-beam data are described by angle α of the tube position and angle β of a certain ray within the fan-beam projection (Fig. 4.2a). Correspondingly, parallel data can be identified with angle Θ for the projection angle and position p of the rays within the parallel-beam projection (Fig. 4.2b). Fan-beam data $P_f(\alpha,\beta)$ are transformed into parallel-beam data $P_p(\Theta,p)$ based on:

$$P_p(\Theta,p) = P_f(\alpha+\beta-\pi/2, R_F \sin\beta) \text{ for } \Theta = 0\ldots\pi,\quad p = -D/2\ldots D/2 \qquad (4.1)$$

R_F represents the distance of the X-ray source to the center of rotation of the measurement system, and D the diameter of the scan field of view. As all projection data are digitally processed and therefore digitally sampled, continuous transformation requires simple interpolation procedures. The geometrical transformation is illustrated in Figure 4.2. An image can be reconstructed from parallel projections that cover a parallel-projection angle range of 180°. If the extra data sectors with incomplete parallel projections are omitted during reconstruction (Fig. 4.2b), temporal resolution is improved.

However, half-scan reconstruction is prone to streak-type artifacts due to inconsistencies of the projections $P_p(0,p)$ and $P_p(\pi,p)$ at the beginning and end of the data set that may be produced by object motion between the acquisition of these projections. This effect can be substantially reduced by acquisition of a slightly extended range of fan-beam projections $\alpha_P = \pi + \beta_f + \alpha_T$. The additional projection range α_T transforms into an extra range of parallel-beam projections $\Theta_T = \alpha_T$ for smooth transition weighting of the projections at the start and end of the parallel-beam data set:

$$P'_p(\Theta,p) = W(\Theta)\, P_p(\Theta,p) + (1- W(\Theta))\, P_p(\Theta+\pi,p') \text{ for } \Theta = 0\ldots\Theta_T,\ p = -D/2\ldots D/2 \qquad (4.2)$$

$$P'_p(\Theta,p) = P_p(\Theta,p) \text{ for } \Theta = \Theta_T\ldots\pi,\ p = -D/2\ldots D/2$$

p' = -p represents the so-called complementary ray.

The function $W(\Theta)$ [e.g. $W(\Theta) = \sin^2(\pi\Theta/2\Theta_T)$] represents a smooth, monotone transition between 0 and 1 within the angle range $0\ldots\Theta_T$. We used a transition range of $\Theta_T = 28°$ with a total scan angle of $\alpha_P = 260°$. This type of transition weighting does not affect temporal resolution but can effectively suppress streak-artifacts in a reconstruction of the parallel-beam data set $P'_p(\Theta,p)$.

The temporal resolution that is present at a particular position within the scan field of view is determined by the temporal window of the data that contributes to the reconstruction of that particular image point. The temporal resolution is represented by time sensitivity profiles (Hu 2000) that vary with position in the scan field of view (similar to slice sensitivity profiles for spiral reconstruction). We used the full-width at half maximum (FWHM) of the time sensitivity profile as a measure to determine the distribution of the temporal resolution within the scan field of view produced by our reconstruction algorithm. The temporal resolution equals half the rotation time in a centered region of the scan field of view (e.g. 250 ms for 500-ms rotation time, 200 ms for 400-ms rotation time, and 165 ms for 330-ms rotation time). It shows an approximately linear decrease between the edges of the scan field of view, with a gradient that is perpendicular to the connection line of the start and end position of the source (Fig. 4.3a). Different temporal data windows visualized by the paths of different image points within the fan-beam data set (Fig. 4.3b) can qualitatively explain the different temporal resolutions within the scan field.

In all modern multi-slice CT scanners, the half-scan reconstruction technique is the method of choice for image reconstruction in cardiac applications. In clinical applications, the heart should be sufficiently centered within the scan field of view in order to maintain a consistent and stable temporal resolution of about half the rotation time. It is not possible to make clinical use of the areas with better temporal resolution within the scan field of view because the start and end positions of the X-ray source vary strongly for individual slices during ECG-synchronized acquisition and, as they depend on the patient's heart rate, can therefore not be fixed.

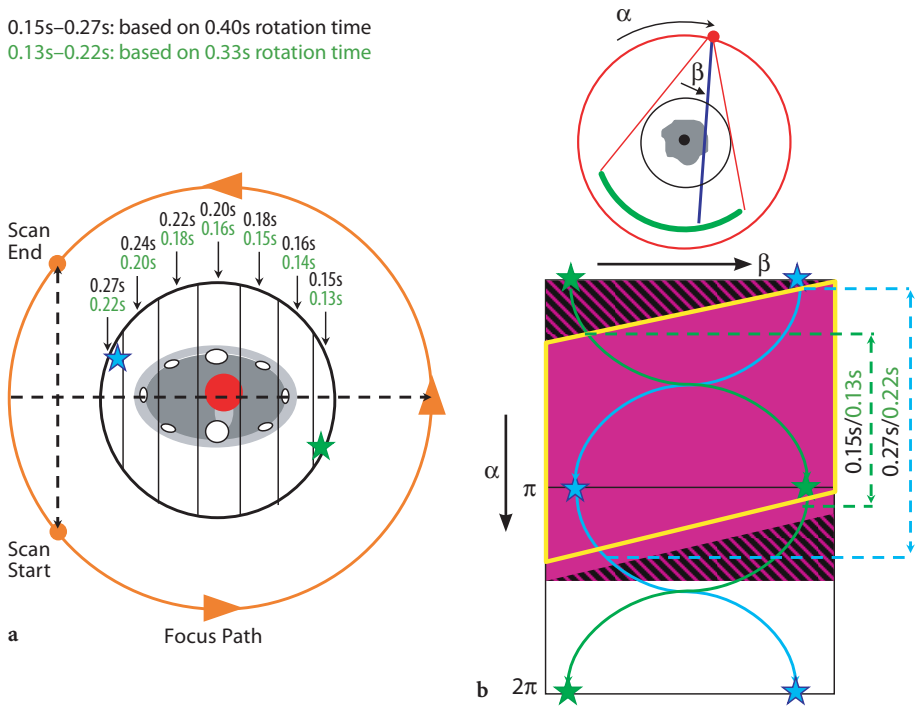

Fig. 4.3a, b. Display of a spatially variable temporal resolution after half-scan reconstruction within the scan field of view (examples given for 400- and 330-ms rotation times). **a** Temporal resolution increases continuously between the edges of the scan field of view with a gradient that is perpendicular to the line connecting the source start and source end positions. **b** This situation can be explained by temporal data windows of different widths within the acquired fan-beam data set that contribute to image points at different locations during image reconstruction (**b**)

4.3 Prospectively ECG-Triggered Multi-slice CT

Prospective ECG triggering is an established method to synchronize sequential CT scanning using the partial-scan technique to the motion of the heart in order to acquire data in a certain phase of the cardiac cycle, preferably in the diastolic phase, when cardiac motion is minimal.

For ECG-triggered sequential imaging, a prospective trigger is derived from the ECG trace to initiate the CT scan with a certain, user-selectable delay time after the R-wave. For best temporal resolution, a partial scan is acquired that is reconstructed with the half-scan algorithm described above. After every scan, the table moves by the width of the acquired scan range in the z-direction towards the next scan position in order to provide gap-less volume coverage. The delay time for scan acquisition after an R-wave is calculated from a given phase parameter (e.g., a percentage of the RR-interval time as delay after an R-wave) for each cardiac cycle and is individually based on a prospective estimation of the RR-intervals. Usually, the delay is defined such that the scans are acquired during the diastolic phase of the heart.

Prospectively ECG-triggered sequential scanning has already been used with electron-beam (EBCT) (Stanford 1992) and mechanical single-slice CT (Becker 1999). In both techniques, single slices are acquired in consecutive heartbeats within equivalent phases of the cardiac cycle. The total scan time is related to the heart rate of the patient and is often too long for volume coverage with thin slices within a single breath-hold. Multi-slice CT scanners can

acquire multiple slices within one heartbeat. Thus, they offer shorter scan times that can be beneficial for clinical applications.

The first generation of multi-slice CT scanners, introduced in 1998, allowed for simultaneous acquisition of up to four adjacent slices per prospective ECG trigger for sequential coverage of the heart volume (Fig. 4.4a). Newer, multi-slice CT scanners acquire up to 16 slices simultaneously per heart beat and provide shorter rotation times and shorter acquisition windows per heart cycle (Fig. 4.4b). The latest generation of multi-slice CT scanners, with up to 64 slices per rotation, often do not use the maximum possible amount of slices. The maximum number of simultaneously acquired slices in sequential scan mode of such scanners is usually limited to 24–32 slices, due to increasing cone-beam artifacts that cannot easily be compensated by sequential scanning. With an increasing number of slices, more scan volume can be covered with every individual scan. This translates either into a significantly shorter acquisition time for the total scan range or the ability to acquire a given scan range with thinner slices in comfortable breathhold times (Fig. 4.4b).

The concept of coverage of the entire heart with sequential ECG-triggered scans is illustrated in Figure 4.5. The exact scan time for such coverage heart depends on the patient's individual heart rate, as the RR-interval time determines the time between the individual scans. In this regard, an additional technical effect has to be considered. As the patient table has to move by the distance covered by multiple slices in between the scans, a certain technical delay time (so-called scan-cycle time) has to be taken into consideration before a following scan can be initiated. The minimum scan-cycle time between two consecutive ECG-triggered scans depends on the table-feed between the two scans and on the acquisition time of one scan. Usual scan-cycle times of modern multi-slice CT scanners are in the range of 0.8–1.5 s; thus, one heart beat has to be skipped in between every scan for usual clinical examinations at heart rates between 50 and 90 bpm with RR-interval times between 0.7 and 1.2 s. In the example of a 16-slice scanner presented in Figure 4.5, the entire heart is scanned within the time of 15 heart beats and reconstructed from data that are acquired during eight heart beats.

The two different filter techniques that are commonly used for prospective estimation of the position of the following R-wave are mean filtering (e.g., 3 previous RR-intervals) and median filtering (e.g., 5 previous RR-intervals). The median filter approach shows increased robustness for patients with moderate arrhythmia due to the fact that single extra beats are eliminated.

To diagnose dynamic processes, ECG-triggered acquisition can also be done without table-feed in between the scans. The same volume is then acquired in corresponding phases of consecutive heartbeats. As no table-feed is needed, the scan-cycle time is reduced and scans can usually be acquired within every heart beat for normal heart rates (scan-cycle time 0.5–0.8 s).

Prospectively ECG-triggered multi-slice CT acquisition results in significantly faster volume coverage than obtained with ECG-triggered acquisition with single-slice mechanical CT or EBCT. The acquisition of a small volume with each triggered scan reduces the probability of misregistration of lesions that can occur due to significant motion of the heart in the z-direction. With 4-slice CT and a collimated slice-width of 4 × 2.5 mm, the complete heart can be scanned within a comfortable single breath-hold of 15–20 s. With this performance, prospective ECG triggering is feasible for quantification of coronary calcification (Fig. 4.6a) and CT angiographic imaging of larger cardiac and cardiothoracic anatomy, such as the myocardium, cardiac valves, thoracic aorta, and proximal segments of coronary bypass grafts (Fig. 4.6b). With modern 16- and 64-slice CT, breath-hold times of ECG-triggered acquisition can be further reduced and the use of thin collimation becomes feasible. The increased rotation speed of up to 0.33 s per rotation provides increased temporal resolution up to 165 ms for significantly improved robustness compared to 4- and 8-slice CT, also at higher heart rates. Furthermore, with 16- and 64-slice CT scanners prospective ECG-triggered scanning can be used for quantification of coronary calcification (Fig. 4.6c) as well as examination of the general cardiac anatomy and coronary bypass grafts (Fig. 4.6d). However, the quality of contrast-enhanced imaging of smaller cardiac anatomy and the coronary arteries with ECG triggering is limited, since the longitudinal spatial resolution

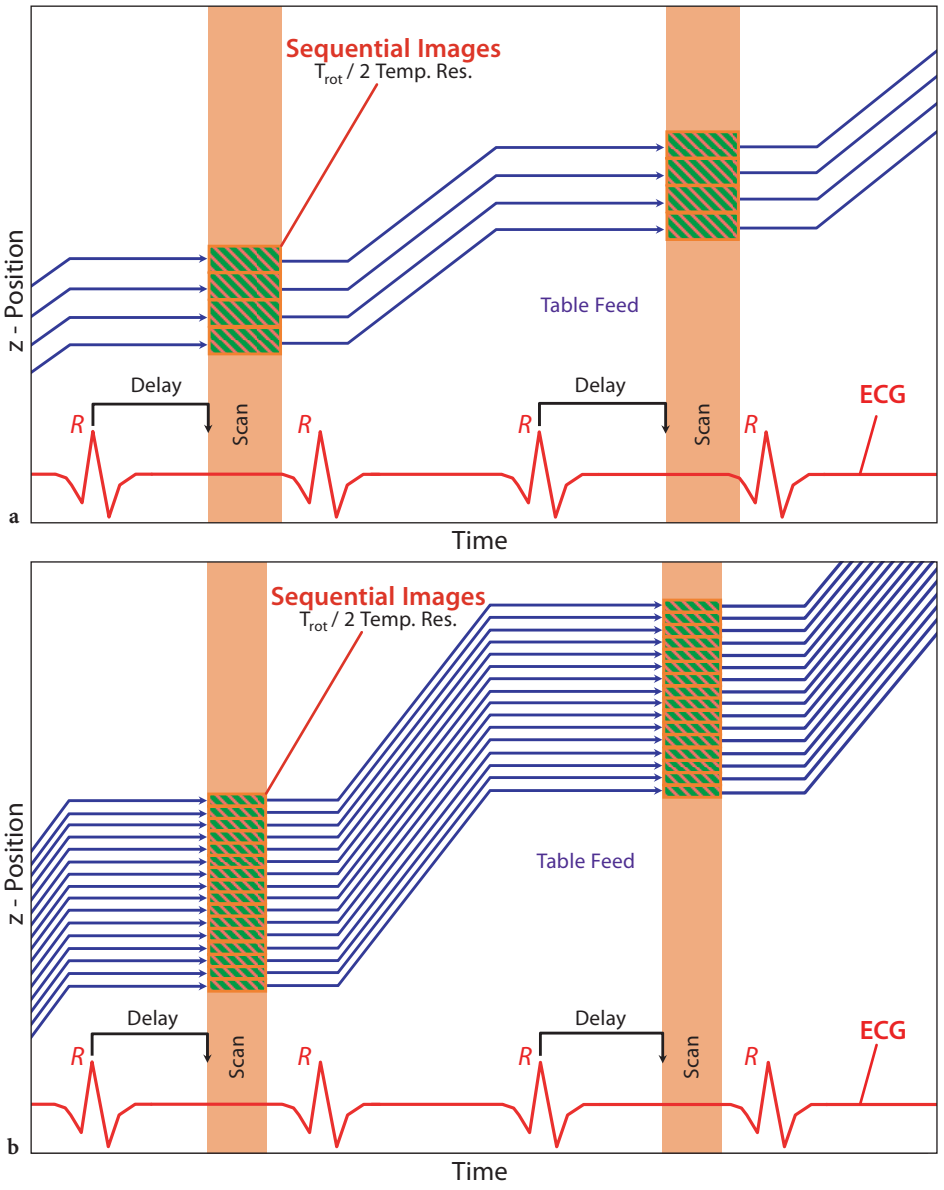

Fig. 4.4a, b. Sequential volume coverage with prospectively ECG-triggered 4-slice (**a**) and 16-slice (**b**) acquisition. Four and 16 adjacent images, respectively, with a slice thickness depending on the collimation (hatched blocks) are acquired at a time with $T_{rot}/2$ temporal resolution. Due to the limitation of the scan-cycle time, a scan can be acquired every other heart cycle for usual heart rates. Faster volume coverage and thinner slices are provided by 16-slice CT

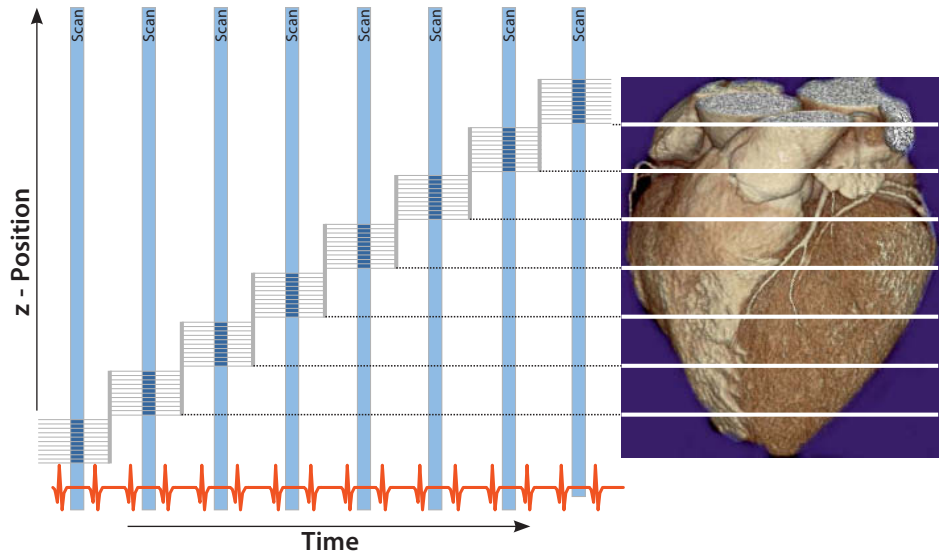

Fig. 4.5. Prospectively ECG-triggered scan coverage of the heart with a 16-slice CT scanner and 0.5-s rotation time. In the example, 16 slices with a total coverage of 16 mm (detector collimation 16 × 1 mm) are acquired with every individual scan. The entire scan range of 128 mm is scanned within the time of 15 heart beats, based on data acquired during eight heart beats. With the given heart rate of 60 bpm and the scan cycle time of about 1.5 s, scan data are acquired with every second heart beat

is compromised by the purely sequential, non-overlapping slice acquisition. In addition, small changes in heart rate during the scan can cause acquisition in inconsistent heart phases and thus inconsistent volume coverage, resulting in artifacts at the intersections of adjacent image stacks.

4.4 Retrospectively ECG-Gated Multi-slice CT

Spiral CT acquisition with continuous table movement represented a very important step towards true volumetric imaging with mechanical CT. With spiral scanning, a true 3D data set can be acquired that consists of overlapping transaxial image slices (Kalender 1995). Additional advantages of spiral CT acquisition compared to sequential CT scanning are considerably improved spatial z-resolution, faster scan speed, and larger volume coverage. ECG-triggered acquisition techniques are limited to sequential scan modes and cannot be applied to spiral scanning.

Retrospectively ECG-gated spiral scanning is an attempt to synchronize the reconstruction of a continuous spiral scan to the movement of the heart by using an ECG trace that is recorded simultaneously. The acquired scan data are selected for image reconstruction with respect to a pre-defined cardiac phase with a certain temporal relation to the onset of the R-waves that defines the start point of data used for image reconstruction.

Although retrospectively ECG-gated spiral scanning was introduced for sub-second single-slice spiral CT systems, its feasibility in clinical routine could not be demonstrated due to various limitations. To obtain the best temporal resolution, partial-scan-based reconstruction techniques are applied to the spiral scan data (Kachelriess 1998, Bahner 1999). However, no spiral interpolation algorithms could be used for retrospectively ECG-gated single-slice CT and data inconsistencies due to table movement and spiral artifacts were very common in transaxial slices. Slow table-feed is a precondition

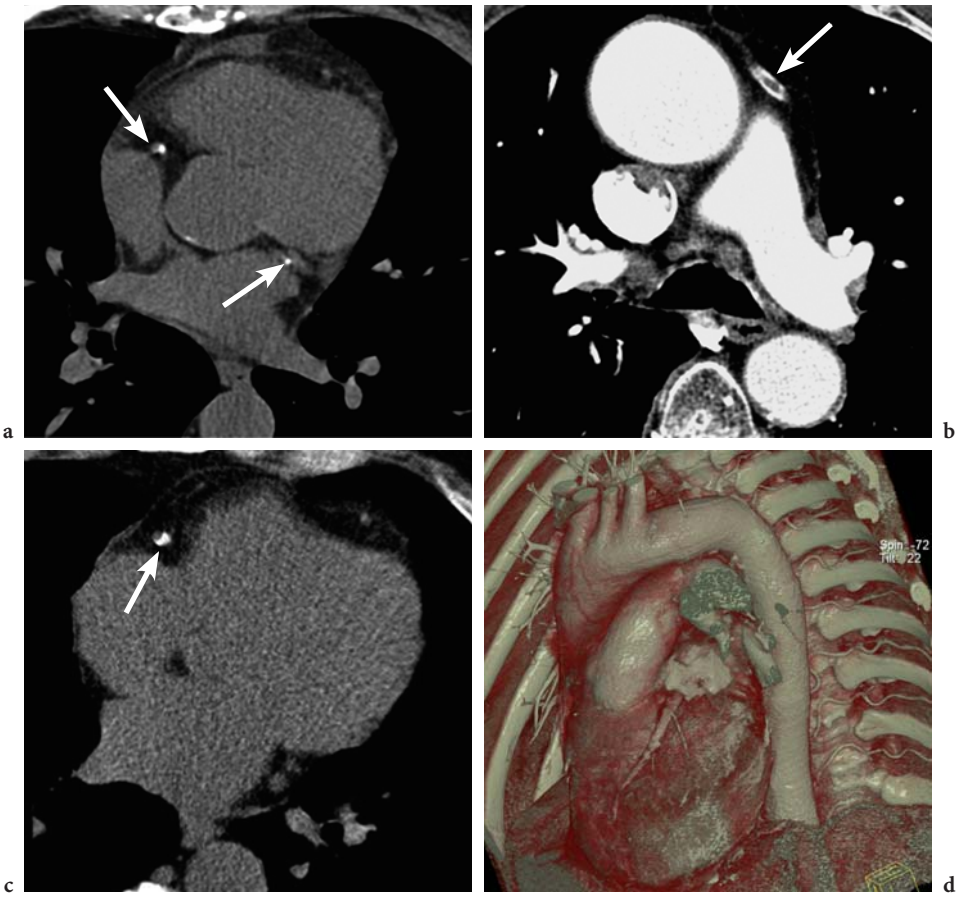

Fig. 4.6a–d. Case examples acquired with prospectively ECG-triggered 4-slice CT with a 0.5-s rotation time (**a**, **b**) and 64-slice CT with a 0.33-s rotation time (**c**, **d**). With ECG-triggered 4-slice CT, 4 × 2.5-mm collimation, 120 kV, and 100 mA tube current, coronary calcifications in the circumflex and right coronary arteries can be detected with high sensitivity and high signal-to-noise ratio (*arrows* in **a**). Cardiac morphology and bypass patency can be evaluated with contrast-enhanced scanning using 4×2.5-mm collimation, 120 kV, and 200 mA tube current. In the example, a coronary bypass occlusion can be appreciated in the transaxial slices (*arrow* in **b**). With ECG-triggered 64-slice CT, 3- and 1.2-mm-thick slices can be generated from a 30 × 0.6-mm collimation setting. ECG-triggered 64-slice CT with 3-mm slices, 120 kV, and 126 mA tube current is used for coronary calcium quantification (*arrow* in **c**). For contrast enhanced imaging of the cardiothoracic morphology, ECG-triggered 64-slice CT with 1.2-mm slices, 120 kV, and 250 mA can be used (**d**). Based on the fast rotation of 0.33 s and the underlying thin-slice scan acquisition with 0.6-mm collimation, 64-slice CT scanners have advantages in image resolution and image quality at higher heart rates. (Images courtesy of (**a**, **d**) University of Erlangen, Germany and (**b**,**c**) Klinikum Grosshadern, Munich, Germany)

for continuous and consistent volume coverage of the beating heart in all phases of the cardiac cycle, including diastole. Thus, single-slice systems hardly allow for continuous ECG-gated volume coverage with overlapping slice acquisition of the entire heart and reasonable longitudinal resolution within reasonable scan times. Retrospective ECG gating can improve the robustness of ECG synchronization against arrhythmia during the scan. However, single-slice acquisition produces a direct relation of the positions of the reconstructed slices and heart rate, including arrhythmia. For a given spiral table-feed, images with high overlap can be reconstructed for high heart rates; for low heart rates, gaps may be produced such that no fix reconstruction increment can be used.

Retrospectively ECG-gated multi-slice spiral scanning has the potential to provide an isotropic, 3D image data set of the complete cardiac volume without gaps and which can be acquired with a single breath-hold spiral acquisition. For ECG-gated reconstruction of scan data with continuous table-feed, dedicated multi-slice spiral reconstruction algorithms are needed that are optimized with respect to temporal resolution, spiral artifact reduction, and volume coverage. Such algorithms require certain pre-conditions of the scan data acquisition. Therefore, we will explain the technical principles of cardiac image reconstruction algorithms in the first section of this chapter before introducing the related acquisition techniques.

4.4.1 Multi-slice Cardiac Spiral Reconstruction

Multi-slice cardiac spiral reconstruction techniques allow for the reconstruction of overlapping images with fixed and heart-rate-independent image increments at arbitrary z-positions and during any given phase of the cardiac cycle. These algorithms consist of two major steps and combine the previously described half-scan reconstruction for optimized temporal resolution with a multi-slice spiral weighting algorithm that compensates for table movement and provides well-defined slice sensitivity profiles. A representative example of these algorithms that also served as the basis for today's algorithms is the so-called multi-slice cardiac volume reconstruction (MSCV) algorithm; (Ohnesorge 2000a), which is explained in detail below.

During the first step of the MSCV algorithm, so-called multi-slice spiral weighting, a "single-slice" partial-scan data segment is generated for each image using a partial rotation of the multi-slice spiral scan that covers the pertinent z-position. For each projection angle α within the multi-slice data segment, a linear interpolation is performed between the data of those two detector slices that are in closest proximity to the desired image plane z_{ima}. In contrast to standard multi-slice interpolation techniques (Klingenbeck 1999, Taguchi 1998, Hu 1999, Schaller 2000), each projection is treated independently. As a representative example, the spiral interpolation scheme for a 4-slice CT system, including the calculation of the spiral interpolation weights for some representative projection angles, is illustrated in Figure 4.7. The presented approach is also used for today's CT scanners with more than four slices and can easily be extended to 16- and 64-slice scanner geometry. With increasing scan time t and increasing projection angle α, the detector slices travel along the z-axis relative to the patient table. The z-position is normalized to the collimated slice width of one detector slice (SW_{coll}). Each multi-slice fan-beam projection $P_{f,M}(\alpha_q,\beta_m,n)$ consists of N sub-projections corresponding to the N detector slices that are measured at the same focus (source) position. (α_q: projection angle of fan-beam projection q, β_m: the angle of a ray m within the fan relative to the central ray, n: detector slice n = 0,1,2,3 for the example of N = 4 detector slices). For reconstructing an image at a given z-position z_{ima}, the single-slice projections $P_f(\alpha_q,\beta_m)$ are calculated by linear interpolation of those sub-projections within the multi-slice projection $P_{f,M}(\alpha_q,\beta_m,n)$ that are closest to the image z-position z_{ima} for a given projection angle α_q (Eq. 4.3a). The interpolation weights are determined according to the distances $d(\alpha_q,n)$ of the sub-projections that are considered for reconstruction with z-positions $z_f(\alpha_q,n)$ to the image position z_{ima} (Eqs. 4.3b,c).

$$P_f(\alpha_q,\beta_m)=\sum_{n=0}^{n=3} w(\alpha_q,n)\cdot P_{f,M}(\alpha_q,\beta_m,n) \tag{4.3a}$$

$$w(\alpha_q,n)=\begin{cases} 1-\left|d(\alpha_q,n)\right| & , \quad \left|d(\alpha_q,n)\right|\le SW_{coll} \\ 0 & , \quad \left|d(\alpha_q,n)\right|> SW_{coll} \end{cases} \tag{4.3b}$$

with

$$d(\alpha_q,n)=z_{ima}-z_f(\alpha_q,n) \tag{4.3c}$$

A sole partial rotation of the multi-slice spiral scan can provide single-slice partial-scan data segments with linearly interpolated projections to reconstruct images that continuously cover a limited z-range. That z-range can be extended if projections of single-slice partial-scan data segments are generated with nearest-neighbor interpolation if two interpolation partners for linear interpolation are not available (Eq. 4.4).

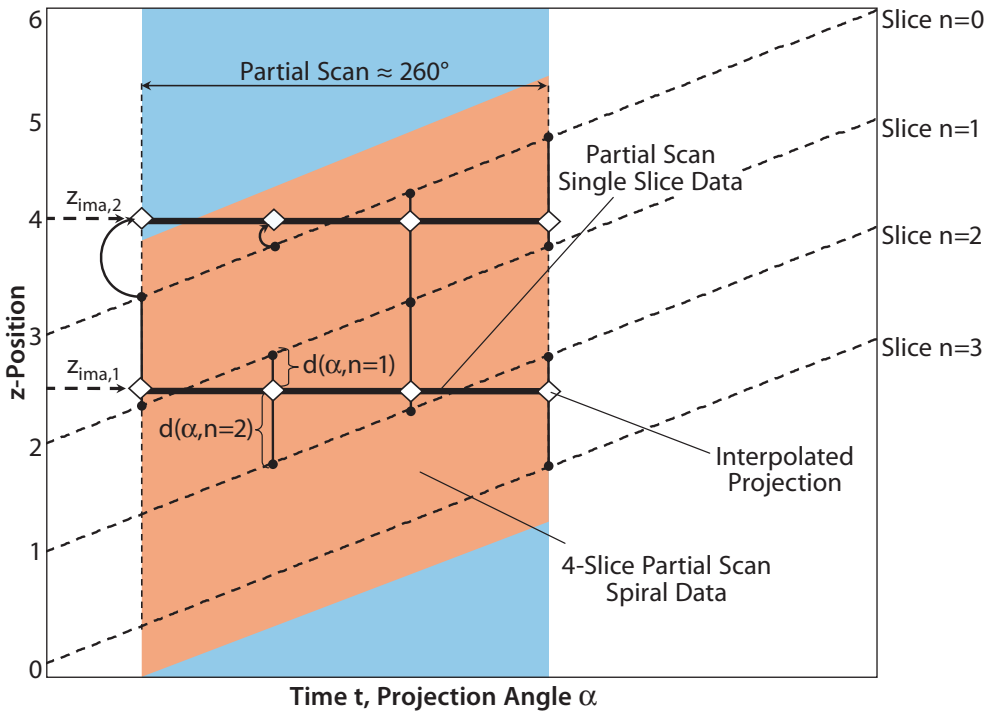

Fig. 4.7. Generation of a single-slice partial-scan fan-beam data set from multi-slice fan-beam projections acquired in a spiral scan with the MSCV algorithm. • Projections used for interpolation, ◊ interpolated projections. Continuous table movement is compensated for by linear interpolation within multi-slice fan beam projections in order to generate single-slice partial-scan data for image z-positions

$$P_f(\alpha_q,\beta_m)=\begin{cases}P_{f,M}(\alpha_q,\beta_m,3) & , \quad z_{ima}\le z_f(\alpha_q,3)\\ P_{f,M}(\alpha_q,\beta_m,0) & , \quad z_{ima}\ge z_f(\alpha_q,0)\end{cases} \qquad (4.4)$$

Of course, nearest-neighbor interpolation may not be performed if the distances of the image z-position and the nearest measured sub-projection are too large. A reasonable limitation is to allow that a maximum of 50% of the projections within a single-slice partial-scan data segment may be generated by using the projection of the nearest detector slice only. This situation is shown for image position $z_{ima,2}$ in Figure 4.7.

Special attention has to be paid to the slice sensitivity profiles (SSPs) as an important parameter of image quality in spiral CT. SSPs produced by the spiral weighting scheme of the MSCV algorithm have been evaluated according to measurements with a gold-plate phantom and based on theoretical calculations in Flohr (1999). In this study, the SSPs and resulting slice widths were assessed for different collimated slice widths and different image positions. In a first-order approximation, MSCV provides a constant, pitch-independent relation (Eq. 4.5) of the collimated slice width (SW_{coll}) of one detector slice to the FWHM of the SSP representing the slice width (SW) of the reconstructed image.

$$SW \approx 1.3\ SW_{coll} \qquad (4.5)$$

Dependent on the weighting scheme that is present for a particular slice, the FWHM may vary between 1.1 SW_{coll} and 1.5 SW_{coll} (Flohr 2001). Slices that are generated in the center of the multi-slice partial scan (Fig. 4.7, $z_{ima,1}$) show symmetric profiles. However, at boundary positions (Fig. 4.7, $z_{ima,2}$), where projections may be generated with nearest-neighbor interpolation, slices show moderate shifts of the center position on the order of 10%.

MSCV also allows for retrospective generation of thicker slices for a certain collimated slice width SW_{coll} than given by Eq. 4.5, and it can be performed in a separate reconstruction using the same scan data. During the multi-slice spiral weighting step, up to three single-slice partial-scan data segments are generated for each image z-position z_{ima} at closely adjacent z-positions $z_{ima}-\delta z$, z_{ima} and $z_{ima} + \delta z$ (δz is a small distance in the z-direction) (Fig. 4.8). The weighted sum of these data segments before performing the partial-scan reconstruction step results in the reconstruction of a thicker slice at the desired position z_{ima}. Table 4.1 contains the appropriate parameters for reconstruction of the slice widths $SW = 1.5SW_{coll}$, $SW = 2SW_{coll}$, and $SW = 3SW_{coll}$. This technique is suited for reconstruction of images with reduced image noise for improved low-contrast resolution at the expense of reduced z-resolution.

Further advanced weighting schemes for multi-slice cardiac spiral reconstruction using 16- and 64-slice CT scanners have recently been developed (Flohr 2003). In those generalized weighting schemes, spiral interpolation functions are used that involve more than only the two detector slices in closest proximity to the desired z-position z_{ima}. The slice width can be controlled by the shape of the interpolation function (Fig. 4.9). For reconstruction of wide slices relative to the collimation SW_{coll}, trapezoidal weighting functions are used that provide well-defined SSPs almost rectangular in shape, which help to reduce partial-volume artifacts. The parameters a= 0.4, 0.5, and 0.6 determine the width of the weighting function (Flohr 2003). With edge-enhancing weighting functions, the usual slice-broadening by linear trapezoidal weighting functions can be avoided and slice widths can be generated that are equal to the collimated slice width SW_{coll}. Figure 4.10a, b shows the SSPs that are generated for a 16-slice CT scanner for different heart rates and using different weighting functions. Different slice widths can be provided, and it can be demonstrated that the SSPs are largely independent from the heart rate. The smallest reconstructed slice width, measured by means of FWHM, using an edge-enhancing weighting function shows slice broadening of less than 10% compared to the collimated slice width. Based on the generalized weighting scheme, equivalent reconstructed slice widths can also be generated based on different collimation settings (Fig. 4.10c). However, SSPs that are based on thinner collimation are better defined and closer to the ideal rectangular shape, thus minimizing spiral artifacts.

Multi-slice cardiac spiral weighting generates partial-scan data segments for all required image z-positions z_{ima} in arbitrary image increments. Usually, the selected increments are smaller that the reconstructed slice width in order to enhance z-axis resolution. The following, second step of the MSCV algorithm performs the previously described single-slice half-scan reconstruction (see Sect. 4.2) of the partial-scan fan-beam data at each image position z_{ima}. According to the sequential half-scan reconstruction, the temporal resolution in the center of the scan field of view equals half the rotation time. The time sensitivity profiles are spatially variable depending on the start and end positions of the tube for acquisition of the considered multi-slice partial-scan data set.

4.4.2 ECG-Gated Multi-slice Spiral Acquisition

For retrospectively ECG-gated reconstruction, each image is reconstructed using a multi-slice partial-scan data segment with an arbitrary temporal rela-

Table 4.1. Target positions for generating segments for the reconstruction of thicker slices

Slice width	$SW = 1.3SW_{coll}$	$SW = 1.5SW_{coll}$	$SW = 2SW_{coll}$	$SW = 3SW_{coll}$
z-positions for segments	z_{ima}	$z_{ima} + 0.25\ SW_{coll}$	$z_{ima} + 0.5\ SW_{coll}$	$z_{ima} + SW_{coll}$
		$z_{ima} - 0.25\ SW_{coll}$	$z_{ima} - 0.5\ SW_{coll}$	z_{ima}
				$z_{ima} - SW_{coll}$

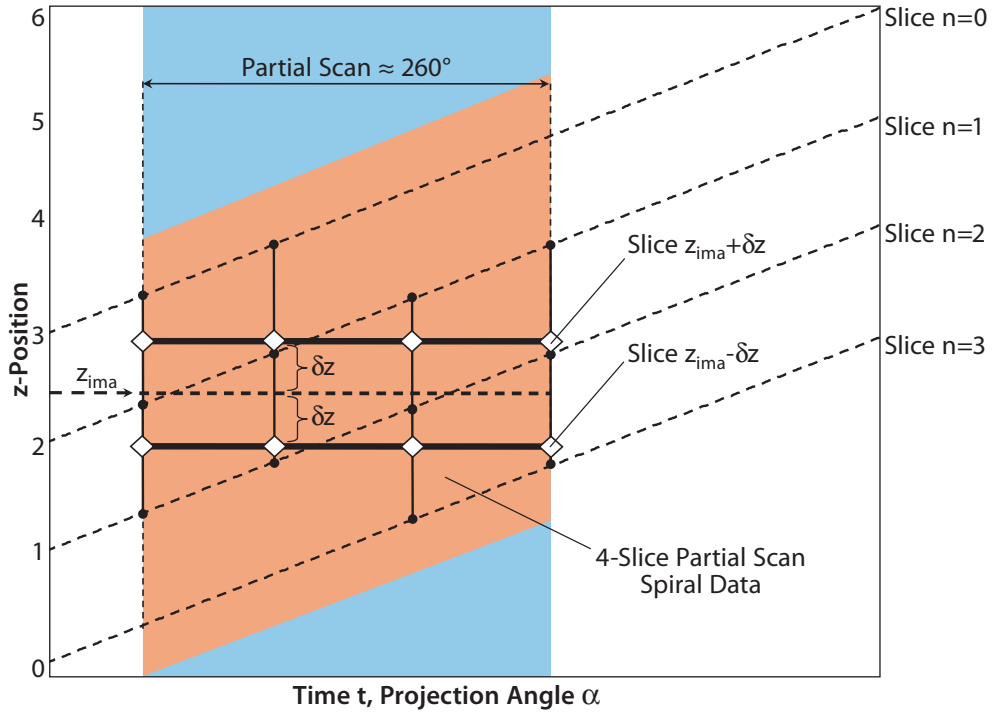

Fig. 4.8. Reconstruction of thicker slice-width with the MSCV algorithm by combining closely adjacent single-slice partial-scan fan-beam data sets. The ratio between the collimation and slice thickness determines the distance and number of adjacent data sets that have be used

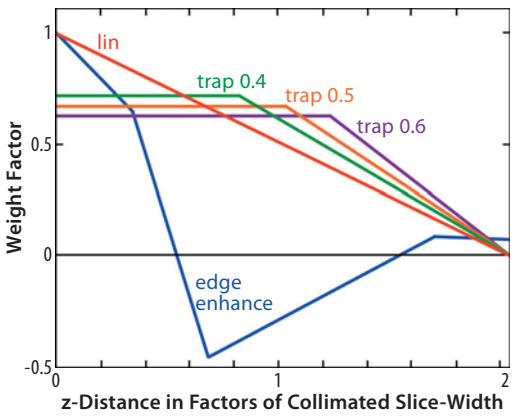

Fig. 4.9. Interpolation functions for a generalized cardiac spiral weighting approach. Trapezoidal weighting functions are used to generate wider slices with well-defined, rectangular-shaped slice sensitivity profiles (SSPs). Edge-enhancing weighting functions are used to generate thin slices with minimal slice-broadening compared to the collimated slice width

tion to the R-wave of the ECG trace. Image reconstruction during different heart phases is feasible by shifting the start point of image reconstruction relative to the R-wave. For a given start position, a stack of images at different z-positions covering a small sub-volume of the heart can be reconstructed owing to multi-slice data acquisition. Figure 4.11 shows how the cardiac volume is successively covered with stacks of axial images (shaded stacks) reconstructed in consecutive heart cycles. Each stack that is reconstructed in one heart cycle covers a certain portion of cardiac anatomy. The maximum extension of these image stacks in the z-direction is determined by extension of the multi-slice detector, which can consist of from 4 to 64 individual detector rows. All image stacks are reconstructed at identical time points during the cardiac cycle. The detector rows travel along the z-axis relative to the patient table. The slope of the detector position lines represents

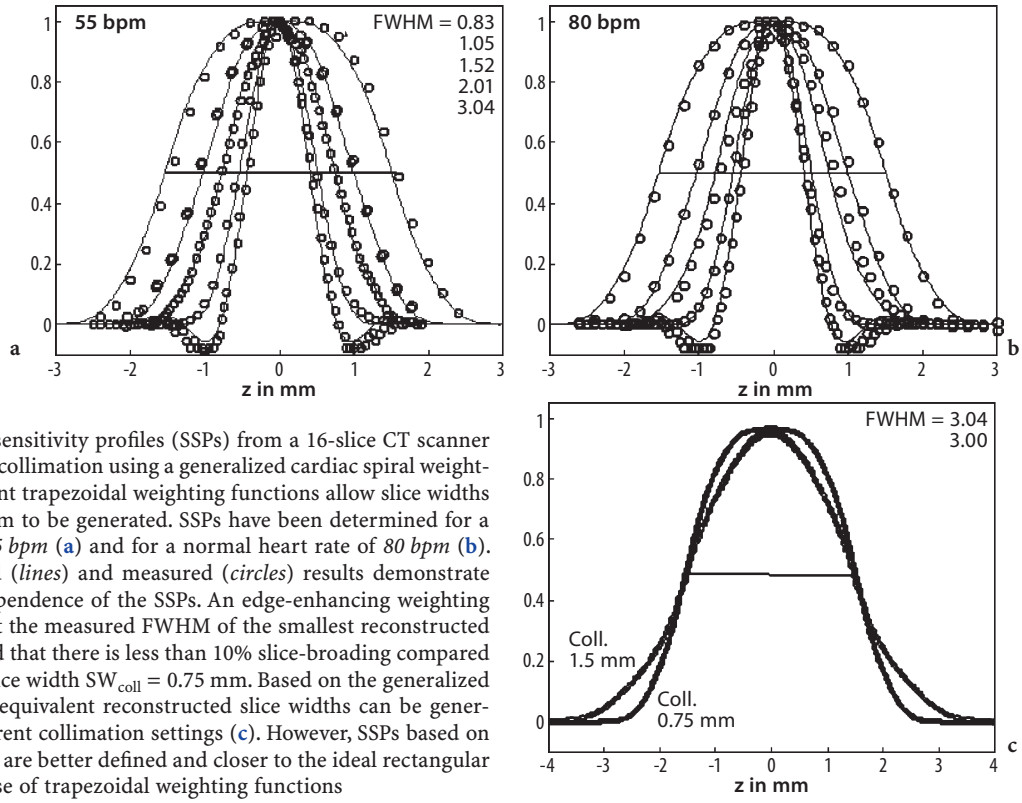

Fig. 4.10a–c. Slice sensitivity profiles (SSPs) from a 16-slice CT scanner with 16 × 0.75-mm collimation using a generalized cardiac spiral weighting scheme. Different trapezoidal weighting functions allow slice widths between 1 and 3 mm to be generated. SSPs have been determined for a low heart rate of *55 bpm* (**a**) and for a normal heart rate of *80 bpm* (**b**). Both the calculated (*lines*) and measured (*circles*) results demonstrate the heart-rate independence of the SSPs. An edge-enhancing weighting function shows that the measured FWHM of the smallest reconstructed slice is 0.83 mm and that there is less than 10% slice-broading compared to the collimated slice width SW_{coll} = 0.75 mm. Based on the generalized weighting scheme, equivalent reconstructed slice widths can be generated based on different collimation settings (**c**). However, SSPs based on thinner collimation are better defined and closer to the ideal rectangular shape, due to the use of trapezoidal weighting functions

the pitch, which needs to be properly limited to allow for continuous volume coverage. In the shown example, an ECG gating approach was used with a delay that results in image reconstruction during the diastolic phase (shaded stacks). The hatched bars represent image stacks reconstructed from the same spiral data set, but in a different heart phase with a different delay parameter that, in turn, results in image reconstruction during the systolic phase. The entire heart volume can be reconstructed in both heart phases and in any other selected heart phase without gaps. Thus, a multi-phase reconstruction for true functional volume imaging of the moving heart can be generated from various 3D images with incrementally shifted delay parameters.

In each stack, single-slice partial-scan data segments are generated equidistantly spaced in the z-direction depending on the selected image reconstruction increment. Continuous volume coverage can only be achieved when the spiral pitch is appropriately limited by the heart rate. In order to achieve full-volume coverage, the image stacks reconstructed in subsequent heart cycles must cover all z-positions. If the pitch is too high, volume gaps between image stacks that are reconstructed using data from different heart cycles are present (Fig. 4.12). The pitch is limited by the patient's heart cycle time (RR-interval time), as every z-position of the heart has to be covered by a detector slice at every time during one entire heart cycle. Consequently, the table may not move more than approximately the width of the multi-slice detector within one heartbeat. According to Eq. 4.6, the table feed is restricted to N-1 single slice widths of a detector with N detector slices within the time interval $T_{RR} + T_Q$, where T_{RR} represents the RR-interval time for the present heart rate, T_{rot} the full rotation time (between 330 ms and 500 ms), and T_Q the partial scan time of a 240–260°

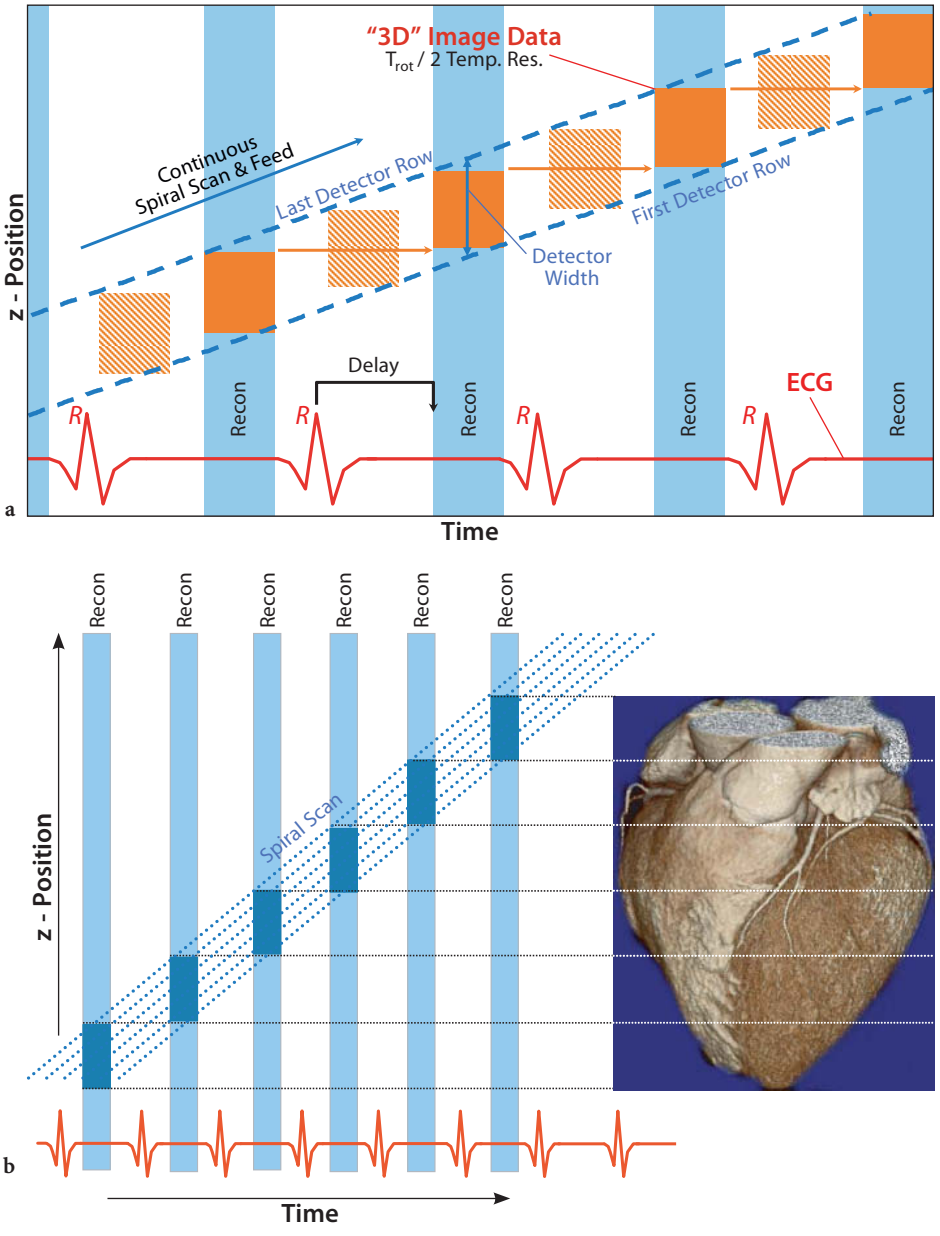

Fig. 4.11. a A scan with continuous table feed and continuous exposure is acquired for retrospectively ECG-gated multi-slice spiral scanning. **b** Stacks of overlapping images can be reconstructed with $T_{rot}/2$ temporal resolution in every cardiac cycle with the MSCV algorithm. The individual stacks cover certain portions of the cardiac anatomy. Continuous 3D images can be reconstructed in different phases of the cardiac cycle by selection of the data ranges with certain phase relations to the R-waves

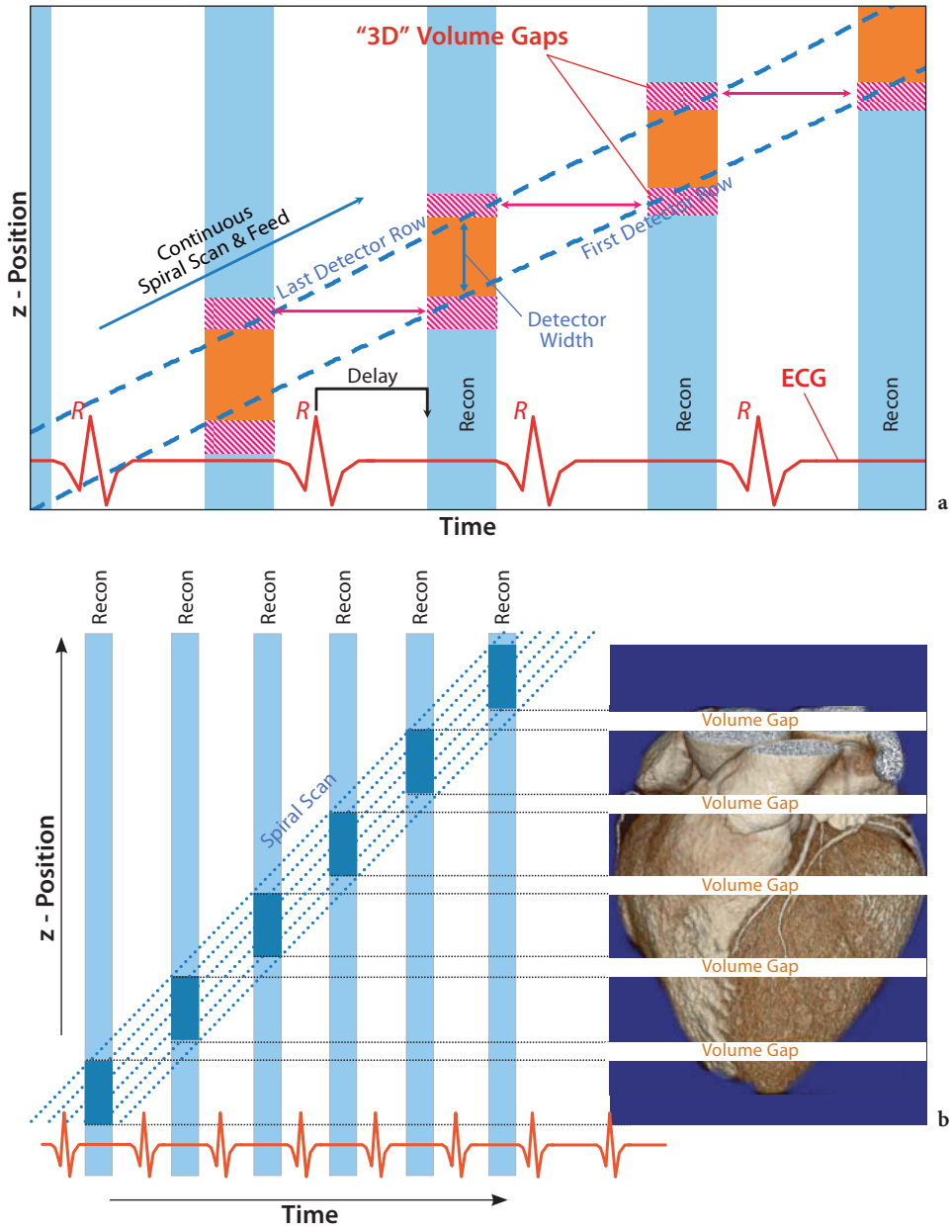

Fig. 4.12. a ECG-gated cardiac spiral examination with a multi-slice CT scanner at a pitch that is too high for the given heart rate. Continuous coverage of the heart volume is no longer possible. Volume gaps are present (hatched segments) between the image stacks that can be reconstructed in each cardiac cycle. **b** The gaps result in missing cardiac anatomy that could not be covered by the scan

partial rotation (e.g., T_Q = 360 ms for T_{rot} = 500 ms and T_Q= 238 ms for T_{rot}= 330 ms).

$$pitch \leq [(N\text{-}1)\ T_{rot}/(T_{RR}+T_Q)]\ /\ N \qquad (4.6)$$

N represents the number of illuminated detector slices, each with collimated slice width SW_{coll}. Based on Eq. 4.6, spiral weighting can be performed with two interpolation partners for all projections within the partial-scan data set if the interpolation function covers two detector widths (Fig. 4.9). If the interpolation function covers four detector widths (Fig. 4.9), at least three interpolation partners are available for all projections within the partial-scan data set. For example, with a heart rate of 60 bpm (T_{RR} = 1000 ms), N = 16, T_{rot} = 370 ms and T_Q = 267 ms (e.g., SOMATOM Sensation 16, Siemens), Eq. 4.6 reveals a pitch limit of about 0.27. The maximum pitch depends on the number of illuminated detector slices and rotation time. With N = 32, T_{rot} = 330 ms and T_Q = 238 ms (e.g., SOMATOM Sensation 64, Siemens) the maximum pitch for a heart rate of 60 bpm is reduced to 0.258. However, due to the larger width of the detector with N = 32 detector rows, a significantly increased volume coverage speed is still present compared to the scanner with N = 16 detector rows.

Scan speed can be increased for faster volume coverage by allowing that up to 50% of the interpolated projections are generated with nearest-neighbor interpolation at the edges of the image stacks. With this approach, the heart-rate-dependent spiral pitch is independent of the number of detector rows and is restricted according to Eq. 4.7. For example, with a heart rate of 60 bpm (T_{RR} = 1000 ms), N = 16, T_{rot}=370 ms, and T_Q = 267 ms, the pitch can be increased from pitch = 0.27, according to Eq. 4.6, to pitch = 0.37, according to Eq. 4.7.

$$pitch \leq T_{rot}/T_{RR} \qquad (4.7)$$

Scan protocols with pitch limitations according to Eq. 4.7 have been in use with 4-slice CT systems due to their limited volume coverage speed. With an increasing number of available detector rows (16 and even up to 64), most modern CT scanners use scan protocols with pitch limitations according to Eq. 4.6, due to significant image-quality advantages related to higher-quality SSPs.

The spiral pitch has to be selected prior to the scan and cannot be modified during the scan if the heart rate changes. Substantial drops in heart rate during the scan can produce local volume gaps. Therefore, the maximum heart cycle time (for the minimum heart rate) that is expected during the spiral scan should be used for calculation of the pitch for an individual patient. For modern 16- and 64-slice CT scanners, a spiral pitch of about 0.25 is feasible for most clinical applications, as the entire range of clinically relevant heart rates ≥45 bpm can be covered and the heart volume can be scanned with the thinnest available slices within a single breath-hold (e.g., 12 cm in 15 s with N = 16, T_{rot} = 370 ms, and SW_{coll} = 0.75 mm).

Retrospectively ECG-gated spiral scanning with 4-slice CT scanners (Ohnesorge 2000a) offered, for the first time, continuous volume imaging for quantification of coronary calcification (Fig. 4.13a) and high-resolution CT angiographic scanning of the coronary arteries (Fig. 4.13b). Moreover, assessment of cardiac function became possible by reusing the same scan data that had been acquired for evaluation of cardiac and coronary morphologies (Fig. 4.13c). The introduction of 16- and 64-slice CT technology and rotation times down to 0.33 s have significantly enhanced spatial and temporal resolution as well as volume-coverage speed (Fig. 4.14), but the basic principles of cardiac scan acquisition and image reconstruction have remained the same since the appearance of the first 4-slice CT scanners. The significant improvement of spatial resolution from 4- to 16-slice and from 16- to 64-slice CT scanners is demonstrated in Figure 4.15. The application spectrum and clinical experience in cardiac and coronary imaging using the presented ECG-gated multi-slice spiral CT acquisition and reconstruction techniques will be presented separately, in detail, in the clinical application section.

4.4.3 Segmented Cardiac Reconstruction Algorithms

Conventional cardiac spiral reconstruction algorithms provide a continuous volume image of the heart with a temporal resolution equal to half the rotation time (T_{rot}/2) of the individual slices. How-

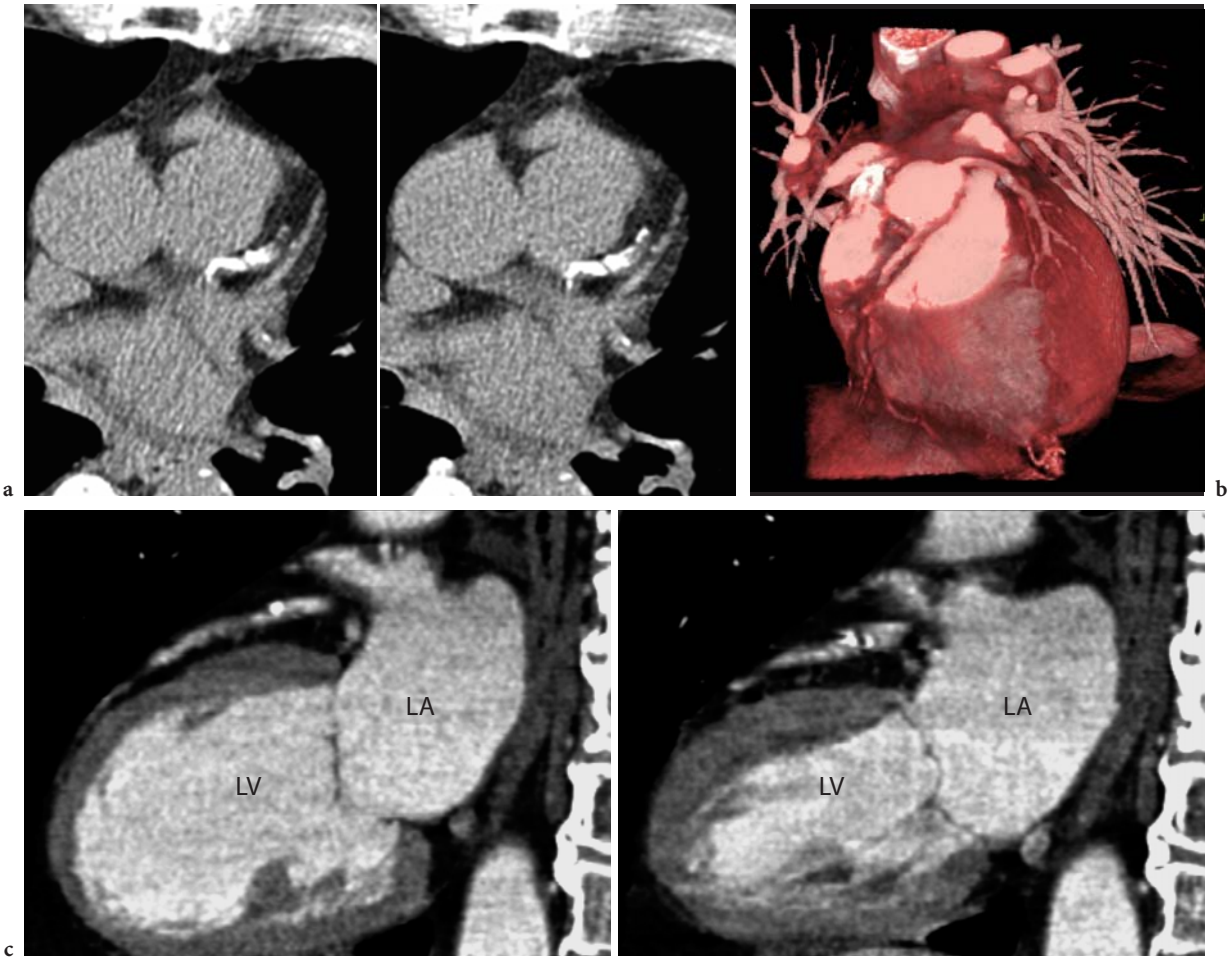

Fig. 4.13a–c. Case examples obtained with retrospectively ECG-gated 4-slice spiral CT scans with 0.5-s rotation time. **a** Coronary calcification of the left main and left descending coronary arteries can be identified with high longitudinal resolution. Image reconstruction with overlapping increments enables more accurate evaluation of the calcified plaque morphology in the z-direction. **b** The main coronary segments can be evaluated in a 3D reconstruction of a contrast-enhanced coronary CT angiography examination using volume-rendering technique. **c** Reconstruction of the same data set in end-diastole and end-systole allows for functional evaluation, e.g., of the left atrium (*LA*) and left ventricle (*LV*). Volume changes in the *LA* and *LV* and in mitral valve movement can be assessed. (Images courtesy of (**a**) University of Tübingen, Germany, and (**b**, **c**) Klinikum Grosshadern, Munich, Germany)

ever, the resulting temporal resolution with today's available minimum rotation times down to 330 ms may not be sufficient for motion-free imaging of the heart at high heart rates (Fig. 4.1) or for imaging the heart in phases with rapid cardiac motion. With unchanged rotation time, the temporal resolution can be improved by using scan data from more than one heart cycle for reconstruction of an image ("segmented reconstruction") (Lackner 1981, Kachelriess 1998, Bruder 1999, Hu 2000, Kachelriess 2000, Flohr 2001). The temporal resolution can be improved up to $T_{rot}/(2S)$ by using scan data of S subsequent heart cycles for image reconstruction, but at the expense of reduced volume-coverage speed or loss of resolution. To maintain good longitudinal resolution and thin-slice images, every z-position of

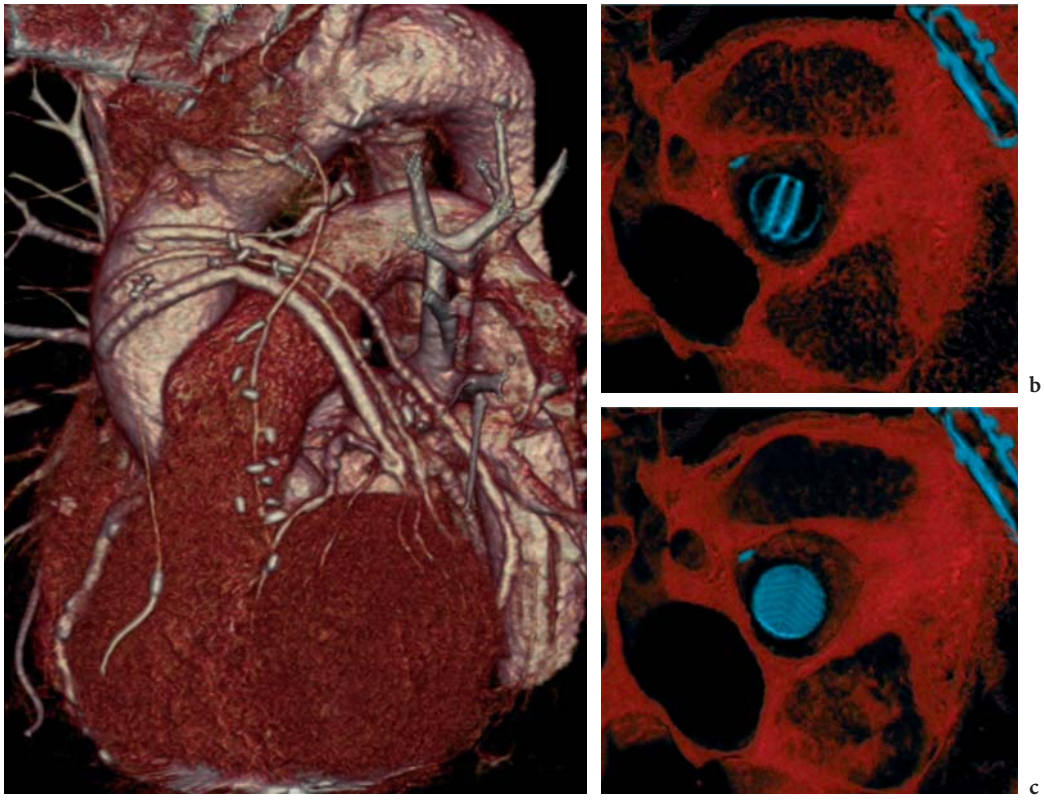

Fig. 4.14a–c. Case examples obtained with retrospectively ECG-gated 64-slice spiral examinations. **a** The coronary artery tree can be visualized with significantly increased spatial resolution and examined with significantly reduced breath-hold time and increased volume coverage compared to 4-slice CT. Reconstruction of the same data set in end-diastole and end-systole allows for functional evaluation of the cardiac chambers and of the cardiac valves. In the example, aortic-valve replacement can be visualized in the open (**b**, systole) and closed (**c**, diastole) positions. The reduced rotation time of 0.33 s allows for improved image quality also in systolic phase, when there is rapid cardiac motion. (Images courtesy of Jankharia Heart Scan Center, Bombay, India)

the heart has to be seen by a detector slice at every time during the S heart cycles. As a consequence, the larger the value of S and the lower the patient's heart rate, the more the spiral pitch has to be reduced. If the pitch is too high, there will be z-positions that are not covered by a detector slice in the desired phase of the cardiac cycle. To obtain images at these z-positions, far-reaching interpolations have to be performed, which may degrade the SSP and reduce z-resolution (Kachelriess 1998, Kachelriess 2000). If the selected spiral pitch is sufficiently small for continuous and gap-less volume coverage, the resulting increase in scan time usually needs to be compensated by thicker slice collimation and thus reduced spatial z-resolution. Moreover, a reduction of the spiral pitch also correlates with a significant increase of radiation exposure. Improved temporal resolution alone, at the expense of reduced longitudinal resolution and increased radiation exposure, may degrade the overall diagnostic quality of studies at low heart rates due to blurring of small anatomical details.

Heart-rate-adaptive algorithms were developed that provide adequately improved temporal resolution by using segmented reconstruction techniques that maintain high z-resolution at the same

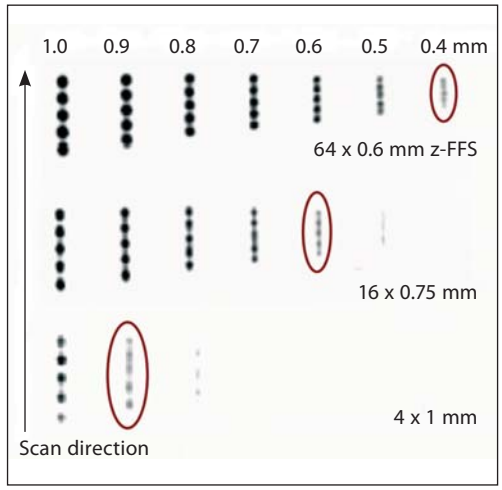

a

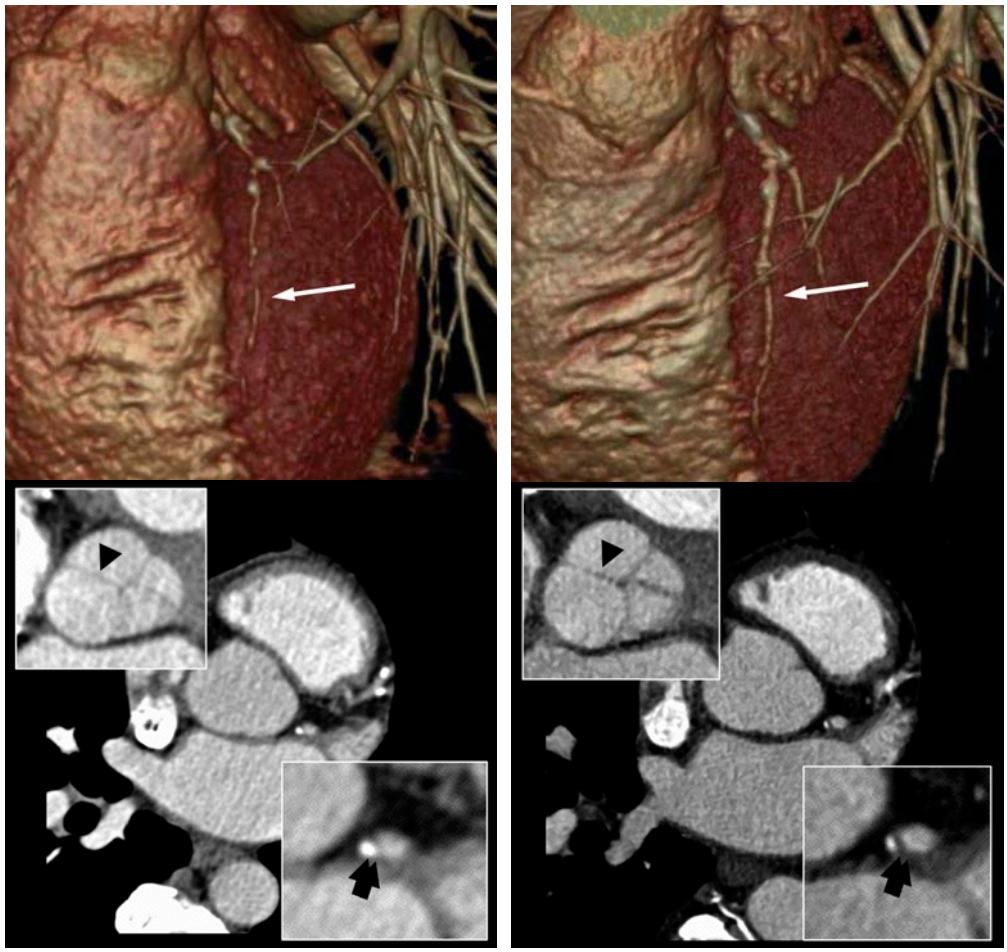

b c

Fig. 4.15. a z-resolution phantom measurements for 4-, 16- and 64-slice CT scanners with ECG-gated spiral acquisition and reconstruction. The resting resolution phantom includes air-filled spheres 0.4–3.0 mm in diameter that can be visualized with multi-planar (MPR) cuts along the scan direction. The thinner collimation of 16-slice CT than of 4-slice CT provides an increase in z-resolution from about 0.9 mm with 4-slice CT to about 0.6 mm with 16-slice CT. Further reduced slice collimation combined with double z-sampling technique (using a z-flying focal spot, z-FFS) enables a further increase of z-resolution for 64-slice CT to about 0.4 mm. Direct comparison of an examination of the same patient with 4-slice (**b**) and 64-slice (**c**) CT demonstrates the enhanced spatial resolution of 64-slice CT and its improved visualization of small cardiac structures, such as the flaps of the aortic valve (*arrowheads* in **b** and **c**), and of complex coronary lesions (*double arrows* in **b** and **c**). Also, small-caliber distal coronary artery segments that could not be visualized with 4-slice CT (*arrow* in **b**) can be visualized with 64-slice CT (*arrow* in **c**)

time. A representative example of these algorithms is the adaptive cardiac volume (ACV) reconstruction technique, which can use data from up to three consecutive heart cycles (Ohnesorge 2001, Flohr 2001). Depending on the patient's heart rate during the scan, a variable number of heart cycles is used for image reconstruction, ranging from S = 1 heart cycle at low heart rates (temporal resolution $T_{rot}/2$) up to S = 3 heart cycles at high pulse rates [temporal resolution heart-rate-dependent up to $T_{rot}/(2S)$]. With this adaptive approach, narrow SSPs may be obtained at adequate temporal resolution for a wide range of clinically relevant heart rates. A spiral pitch can be used that is sufficient to scan the complete heart with thin slices within a short single breathhold and with only a moderate increase of radiation exposure.

If scan data are used for the reconstruction of an image that is acquired in S > 1 subsequent heart cycles, every z-position of the heart has to be covered by a detector slice at every time during the S heart cycles. Thus, spiral pitch is not only limited by the heart rate but also by the number of heart cycles S used for reconstruction. If the table moves too quickly, interpolation between data acquired at a larger distance from the image plane can degrade the SSPs (Kachelriess 2000). As an extension of Eq. 4.7, the spiral pitch is limited by the minimum RR-interval time T_{RR} during the scan, according to Eq. 4.8, in order to maintain a reasonable quality of the SSPs.

$$pitch \leq \frac{1}{N}\left(\frac{N-1}{S}+1\right)\frac{T_{rot}}{T_{RR}} \qquad (4.8)$$

S is the number of subsequent heart cycles that are used for image reconstruction. The maximum pitch as a function of heart rate and number S of consecutive heart cycles used for reconstruction (S = 1, 2, 3) is shown in Fig. 4.16 for the example of a 16-slice CT scanner with 0.37-s rotation time. Reasonably fast volume coverage of the heart within one breathhold and thin slices can be achieved with pitch = 0.2. According to Eq. 4.8, pitch = 0.2 implies that image reconstruction should be restricted to using data from S = 1 heart cycle only for moderate heart rates <63 bpm. For heart rates ≥3 bpm, S = 2 heart cycles may be used and S = 3 heart cycles for heart rates ≥95 bpm. For other pitch values, different heart-rate thresholds are implied.

Adaptive-segmented reconstruction algorithms automatically adapt the number of consecutive heart cycles used for image reconstruction according to the momentary heart rate of the patient during the scan (Fig. 4.17). These algorithms are extensions to single-segment methods that are limited to the use of one heart cycle only. Both major processing steps of single-segment algorithms, multi-slice spiral weighting and half-scan reconstruction, are also used for adaptive-segmented algorithms. During multi-slice spiral weighting, single-slice partial-scan data segments are generated from partial-scan data segments that are divided into S = 1, 2 or 3 sub-segments (depending on the heart rate), resulting in a temporal resolution of up to $T_{rot}/(2S)$. S = 1 sub-segment is used for low heart rates and reconstruction is performed with the conventional single-segment algorithm. At higher heart rates, the partial-scan data segment is divided into S = 2 or 3 sub-segments to improve temporal resolution. Thus, multi-slice spiral data from two or three consecutive heart cycles, respectively, contributes to the single-slice partial-scan data segment. Each sub-segment is generated using data from one heart cycle only. Equivalent to single-segment algorithms, a linear interpolation is performed for each projection angle α_n within each sub-segment j (j = 0...S-1) between the data of those two detector slices that are in closest proximity to the desired image plane. The interpolation produces S single-slice sub-segments located at the same z-position z_{ima} (Fig. 4.18) that can be assembled to a complete single-slice partial-scan data segment for image reconstruction. A certain overlap between the sub-segments can be taken into account to allow for smooth transition weighting, which reduces image artifacts due to data inconsistencies. For data consistency during image reconstruction, the sub-segments have to be picked at identical time points within the heart cycle, when the beating heart is exactly in the same relative phase position. The time points are determined by a certain distance relation to the R-waves. Data inconsistency due to arrhythmic heart rates or irregular heart movement in consecutive heart cycles will result in degraded temporal resolution and substantial spatial blurring of moving structures.

Similar to the single-segment algorithms, the second step of adaptive-segmented algorithms per-

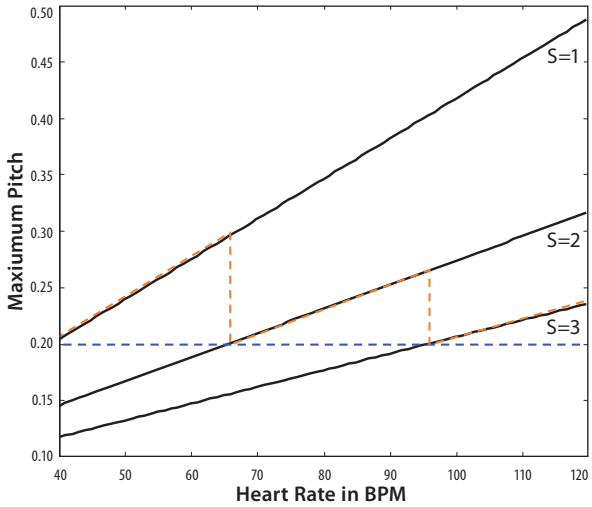

Fig. 4.16. Maximum spiral pitch as a function of heart rate and the number S (S = 1, 2, 3) of used data segments from consecutive cardiac cycles for the example of a 16-slice CT scanner with 0.37-s rotation time. Exceeding the spiral pitch limitation for a certain heart rate results in volume gaps. Minimum heart rates for use of S = 2 and S = 3 segments are shown for a pitch of 0.2, which allows for reasonably fast volume coverage with thin-slice collimation. Other pitch values imply different heart-rate thresholds. A pitch of 0.2 enables gap-less volume reconstruction for 16- and 64-slice CT scanners for all heart rates > 40 bpm

forms the previously described single-slice half-scan reconstruction of the partial-scan fan-beam data that are generated for each image position z_{ima}. The different data sub-segments from S individual heart cycles are transformed independent of the parallel-beam geometry and are appended as parallel-beam projections.

Adaptive-segmented reconstruction with S > 1 sub-segments only allows for improved temporal resolution if the patient's heart rate and the rotation time of the scanner are appropriately de-synchronized. In a situation of optimal de-synchronization, the projection angles of the start- and end projections of the sub-segments fit together and form a complete partial-scan data segment that contains 180° parallel projections after rebinning to parallel geometry (Fig. 4.19a). The partial-scan interval may then be divided into S sub-segments of equal size, and each sub-segment covers a temporal data interval $T_{rot}/4$ for S = 2 or $T_{rot}/6$ for S = 3 within the same relative heart phase. However, if heart rate and scanner rotation are synchronous, the same heart phase always corresponds to the same projection-angle segment, and a partial-scan interval cannot be divided into smaller sub-segments. As a conse-

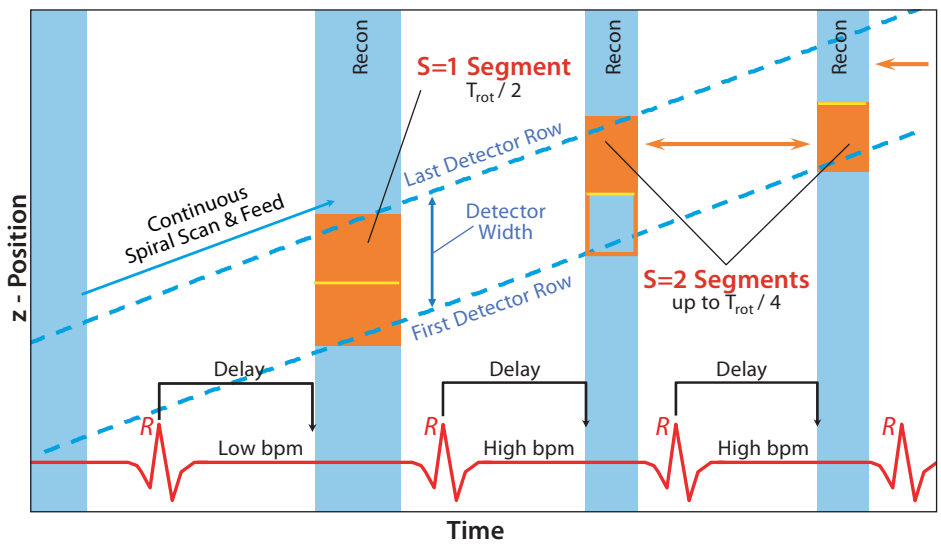

Fig. 4.17. Retrospectively ECG-gated multi-slice spiral reconstruction using adaptive-segmented reconstruction with up to S = 2 segments. Reconstruction with S = 1 segment ($T_{rot}/2$ temporal resolution) is performed for low heart rates (e.g., ≤ 63 bpm). S = 2 segments (up to $T_{rot}/4$ temporal resolution) are used for higher heart rates (e.g., > 63 bpm)

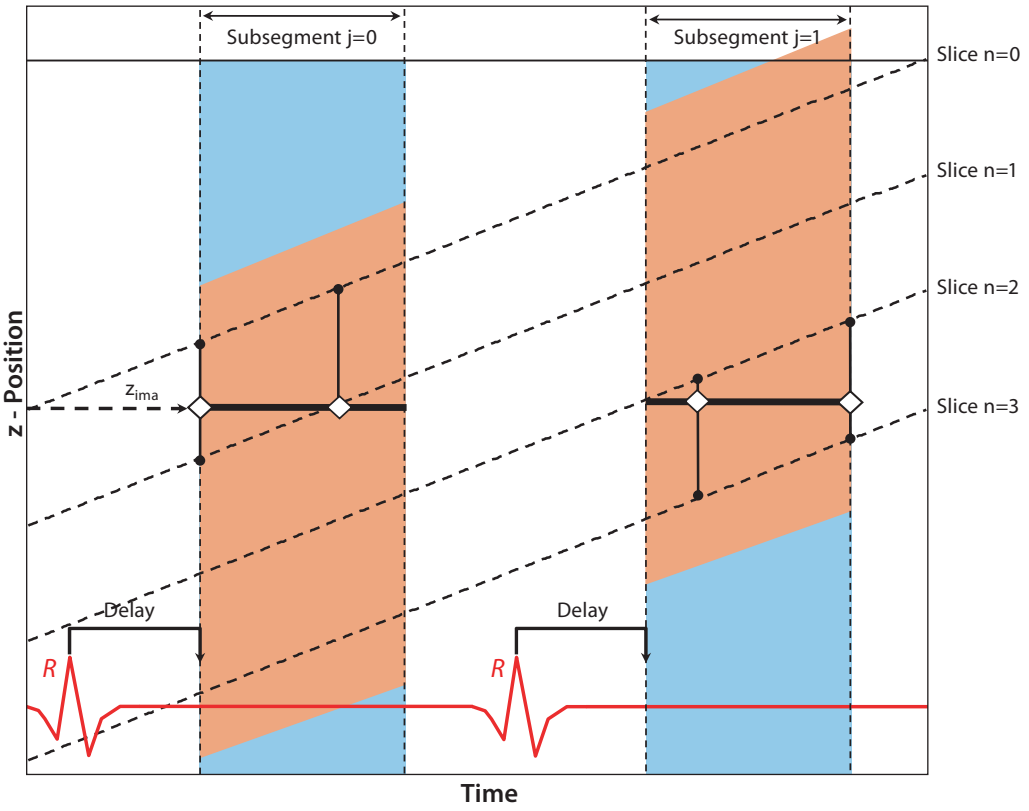

Fig. 4.18. Generation of a single-slice partial-scan fan-beam data set from multi-slice fan-beam projections acquired in a spiral scan with adaptive-segmented reconstruction. • Projections used for interpolation, ◊ interpolated projections. Single-slice data segments are generated in consecutive cardiac cycles by linear interpolation at specific image z-positions. The individual data segments are combined into a single-slice partial-scan data set for image reconstruction at the considered z-position

quence, no better temporal resolution than $T_{rot}/2$ is possible. In a situation with partially de-synchronized heart rate and rotation, the partial-scan interval may be divided into S sub-segments of different size, each covering temporal data intervals between $T_{rot}/2$ and $T_{rot}/2S$. The sub-segment with the longest temporal data interval then determines the temporal resolution of the image (Fig. 4.19b). Segmented reconstruction techniques assume that all anatomy is exactly located in the same position in equivalent phases during the cardiac cycle. Slight shifts of the cardiac anatomy from one heart cycle to the next produce inconsistent scan data and may result in image artifacts (Fig. 4.20). Generally, adaptive-segmented reconstruction algorithms generate images with temporal resolution in the interval [$T_{rot}/2$, $T_{rot}/2S$], depending on the relation of rotation time and patient heart rate. During the same scan, temporal resolution can vary with changing heart rate as the rotation time is fixed. The relationship between temporal resolution and rotation time and heart rate is demonstrated in Figure 4.21 for different rotation times between 0.5 s and 0.33 s and up to S = 2 segments. Figure 4.22 shows the temporal resolution as a function of heart rate for a 64-slice CT scanner with 0.33-s rotation time and up to S = 4 segments. The temporal resolution is calculated as the FWHM of the time sensitivity profiles in the center of the scan field of view. Although excellent temporal resolution can be achieved for certain heart rates, for others the heart cycle and scanner rotation are perfectly synchronized and the temporal resolution

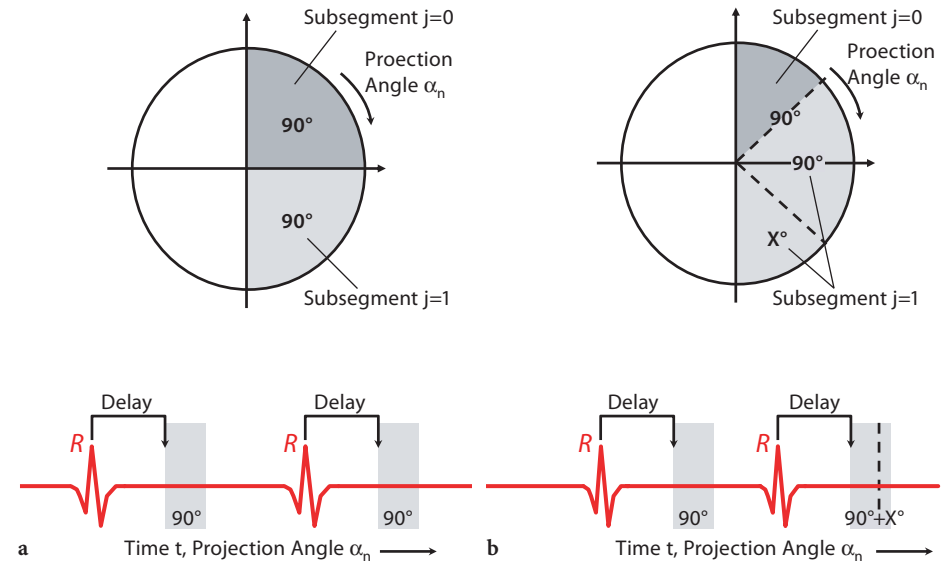

Fig. 4.19. a For segmented reconstruction with S = 2 segments and optimal de-synchronization of heart rate and system rotation, the sub-segments form a complete partial-scan data segment without overlap and with temporal resolution $T_{rot}/4$. **b** For only partially de-synchronized heart rate and system rotation, the sub-segment with the longest temporal data interval determines the temporal resolution of the image

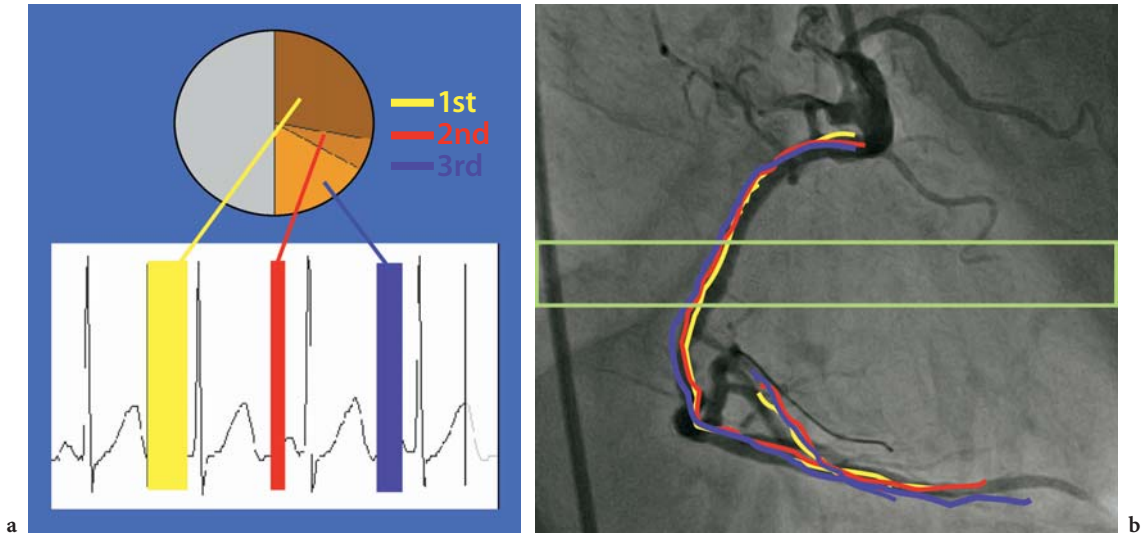

Fig. 4.20a, b. Segmented reconstruction with S = 3 segments. The segments have different temporal widths for the given rotation time and heart rate. **a** Sub-segment 1, with the longest temporal data interval, determines the temporal resolution of the image. However, the coronary anatomy may be located at slightly shifted positions during consecutive heart cycles, which may result in data inconsistencies and blurring artifacts. **b** In the example, coronary angiography shows the slightly shifted location of the center line of the right coronary artery in three consecutive heart cycles

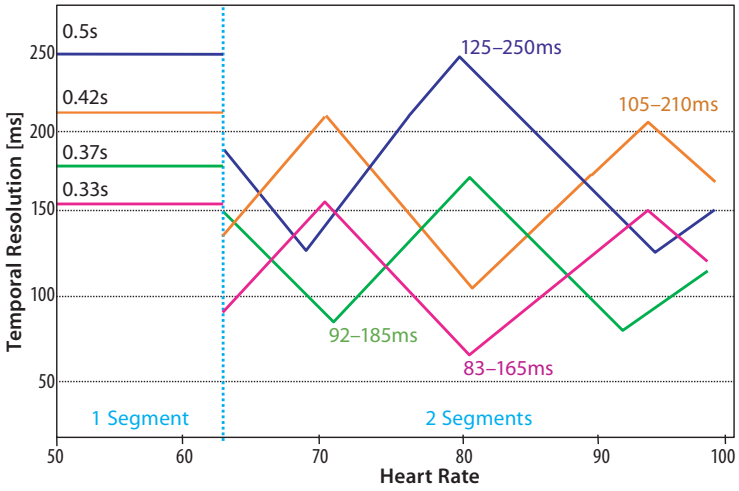

Fig. 4.21. Demonstration of temporal resolution as a function of heart rate and rotation time for adaptive-segmented reconstruction using up to S = 2 segments. The heart rate threshold for switching from S = 1 to S = 2 segments is set to 63 bpm. Temporal resolution is strongly heart rate dependent within the interval [$T_{rot}/2$, $T_{rot}/2S$]. The very different locations of maxima and minima for different rotation speeds suggest that heart-rate-dependent selection of rotation speed might be feasible only in patients with stable and predictable heart rate. Reconstruction with S = 1 segment can also be used for higher heart rates. The temporal resolution then remains constant at $T_{rot}/2$, independent of heart rate

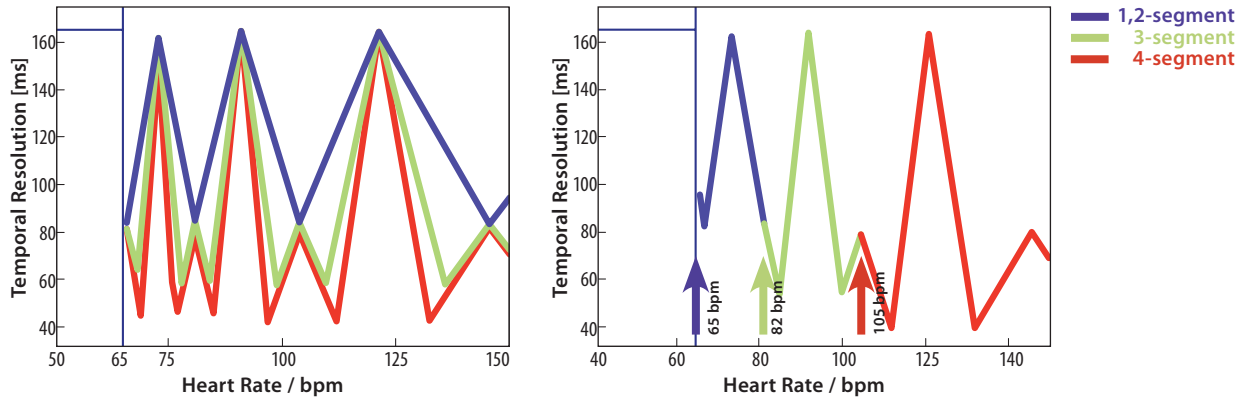

Fig. 4.22. Temporal resolution as a function of heart rate for adaptive-segmented reconstruction with up to S = 4 segments using a 0.33-s rotation time. With S = 4, temporal resolution can be increased to $T_{rot}/8$ only for certain heart rates. With S = 4 segments, temporal resolution changes significantly with only small changes in heart rate. The locations of maxima and minima are strongly dependent on rotation time. Temporal resolution may be difficult to predict in clinical conditions – given the very strong variation of temporal resolution with heart rate and rotation speed – when using S = 3, or S = 4 segments for reconstruction

of $T_{rot}/2$ may not be improved by using data from multiple heart cycles. Image quality improvements with adaptive-segmented reconstruction techniques can be demonstrated in patients with higher heart rates. A direct comparison of single-segment reconstruction and reconstruction with S = 2 segments can reveal significantly improved delineation of coronary calcifications in a patient with a heart rate of 76 bpm (Fig. 4.23).

Image quality and resolution along the scan direction provided by segmented reconstruction algorithms have been assessed with a longitudinal resolution phantom that included air-filled spheres with diameters ranging from 0.4 to 3 mm (Flohr 2001, Flohr 2003). It could be demonstrated that adaptive-segmented reconstruction can provide stable longitudinal resolution without a considerable influence of heart rate (Fig. 4.24).

The possible image quality improvements of segmented reconstruction algorithms compared to single-segment reconstruction can be demonstrated in examinations of patients with high heart rates

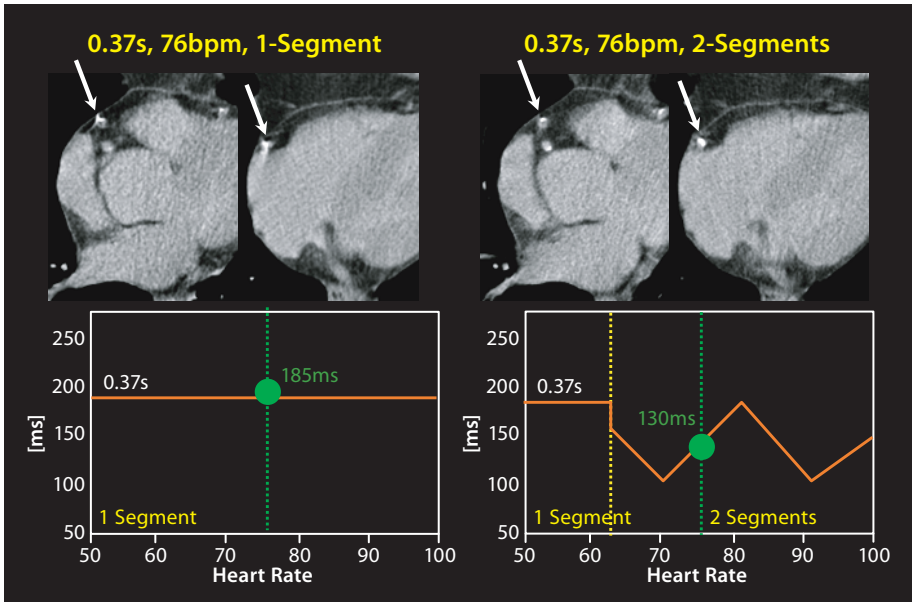

Fig. 4.23. Case example of a 16-slice CT cardiac examination that demonstrates the improvement of image quality with adaptive segmented vs. single-segment reconstruction at higher heart rate. A coronary calcium scan was performed in a patient with 76 bpm during the scan with: 16 × 1.5-mm collimation, 0.37-s rotation, reconstruction in diastole at 55% of the RR-interval. Coronary calcifications in the left anterior descending and right coronary arteries (*arrows*) are depicted with considerably less motion using adaptive-segmented reconstruction (*right, S = 2 segments,* 130-ms temporal resolution) compared to single-segment reconstruction (*left, S = 1 segment,* 185-ms temporal resolution). (Case courtesy of Tübingen University, Germany)

(Fig. 4.25) or for reconstruction of images in phases of the cardiac cycle with rapid cardiac motion (Fig. 4.26). However, cardiac anatomy can be located at slightly shifted positions even in equivalent phases during the cardiac cycle. Due to these inconsistencies, segmented reconstruction techniques may produce degraded image quality compared to single-segment reconstruction, despite higher temporal resolution (Fig. 4.27). To achieve most robust cardiac image quality with the lowest possible radiation exposure, single-segment reconstruction techniques combined with fast rotation speeds are usually preferred in clinical practice. The use of segmented reconstruction techniques is limited to special clinical situations, such as patients with either very high heart rates or stable and predictable heart rates, and for reconstruction of the larger cardiac anatomy during phases with rapid cardiac motion in order to analyze cardiac function.

4.4.4 Cardiac Cone-Beam Reconstruction Algorithms

The cardiac image reconstruction algorithms introduced thus far were designed for multi-slice CT systems with only a limited number of detector rows, and did not take into account the conical shape of the X-ray beam in the axial direction. As demonstrated in Chapter 3, cone-beam reconstruction algorithms are mandatory for general-purpose CT scanning with eight and more detector slices to avoid severe image artifacts. The severity of cone-beam-induced artifacts depends on the number of simultaneously acquired slices, on the width of each slice, and on the distance of a considered object from the center of the scan field of view. Cone-beam artifacts are most pronounced at high contrast boundaries; thus, typical sources of cone-beam artifacts are the ribs, pelvic bones, and bronchi. Since the heart is

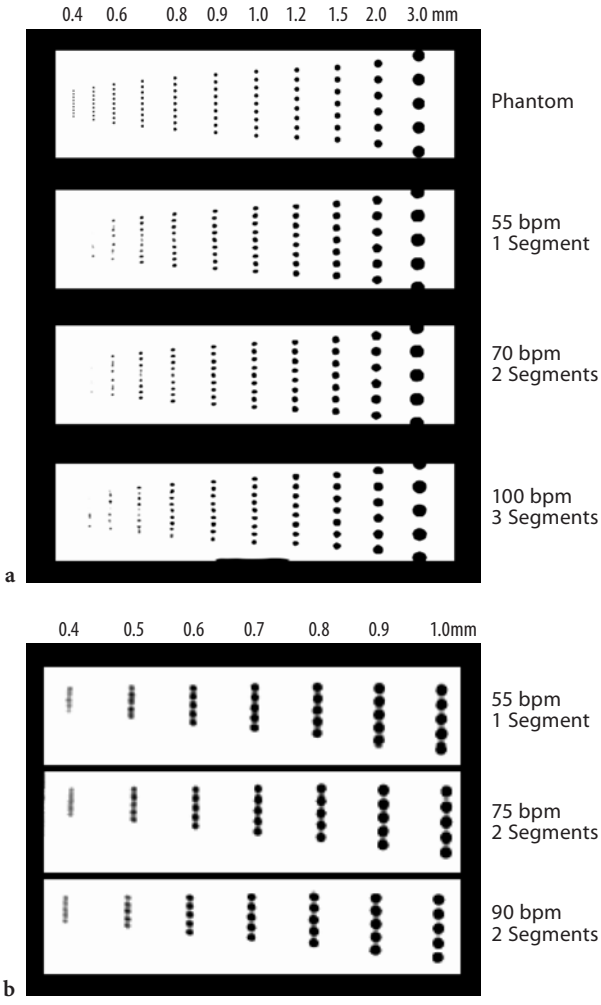

Fig. 4.24a, b. Investigation of the influence of heart rate on image quality and resolution in the scan direction with 16-slice (**a**) and 64-slice (**b**) CT using a resting longitudinal resolution phantom (see Figs. 4.3 and 4.15) and simulated ECG signals with different heart rates that control the adaptive-segmented reconstruction. The 16-slice CT scans were acquired with 0.75-mm collimation, 0.37-s rotation, pitch 0.2, 0.75-mm slice width, and 0.5-mm increments. A longitudinal resolution of 0.6 mm can be achieved for all anticipated heart rates. The 64-slice CT scans were acquired with 0.6-mm collimation (using double z-sampling technique), 0.33-s rotation, pitch 0.2, 0.6-mm slice width, and 0.3-mm increments. A longitudinal resolution of 0.4-mm can be achieved for all anticipated heart rates. In 16-slice and 64-slice CT phantom tests, image quality is largely independent of both heart rate and the number of segments used for reconstruction

Fig. 4.25a–c. Case examples of a 64-slice CT scanner with 0.6-mm collimation and 0.33-s rotation time. The figure shows the improved image quality of cardiac and coronary CT angiography examinations with adaptive-segmented vs. single-segment reconstruction at higher heart rate. The patient's heart rate was between 106 and 110 bpm during the scan. Images were reconstructed at 35% of the RR-interval. Motion artifacts are present in the images based on single-segment reconstruction with 165-ms temporal resolution (**a**, *arrows*). Two segments can increase temporal resolution from 165 ms to about 90 ms using adaptive segmented reconstruction, and motion artifacts can be largely eliminated (**b**). Three segments allow a further improvement in temporal resolution to 70 ms, but image quality is compromised due to the combination of data from three consecutive heart beats (**c**). (Cases courtesy of Klinikum Grosshadern, University of Munich, Germany)

usually centered and does not contain large high-contrast structures, cone-beam artifacts are largely negligible for CT scanners up to 16 slices (Flohr 2003). However, cardiac cone-beam reconstruction algorithms gain importance for CT scanners with a higher number (32 or 64) of detector slices as well as for ECG-gated examinations of the chest and diagnosis of anatomy that is located at a larger distance from the center of the scan field of view. The cardiac cone-beam reconstruction algorithms in use today (Bruder 2001, Bruder 2002) represent extensions of those in use for general-purpose multi-slice spiral reconstruction and have been successfully tested for the latest multi-slice CT scanners with 32 and up to 64 detector slices.

Similar to cone-beam reconstruction techniques in multi-slice body CT imaging, cardiac cone-beam reconstruction techniques generate double-oblique image stacks (so-called booklets) that are individually adapted and optimally fitted to the spiral path. In a second step, these booklets are reformatted to a set of overlapping trans-axial images (Fig. 4.28). For single-segment reconstruction, one booklet is used for reconstruction and reformation in each heart cycle. Data segments that cover 180° of parallel-beam projections are employed for the generation of these booklets, leading to a temporal resolution of the images within the booklet of half of the rotation time of the scanner. In the case of segmented

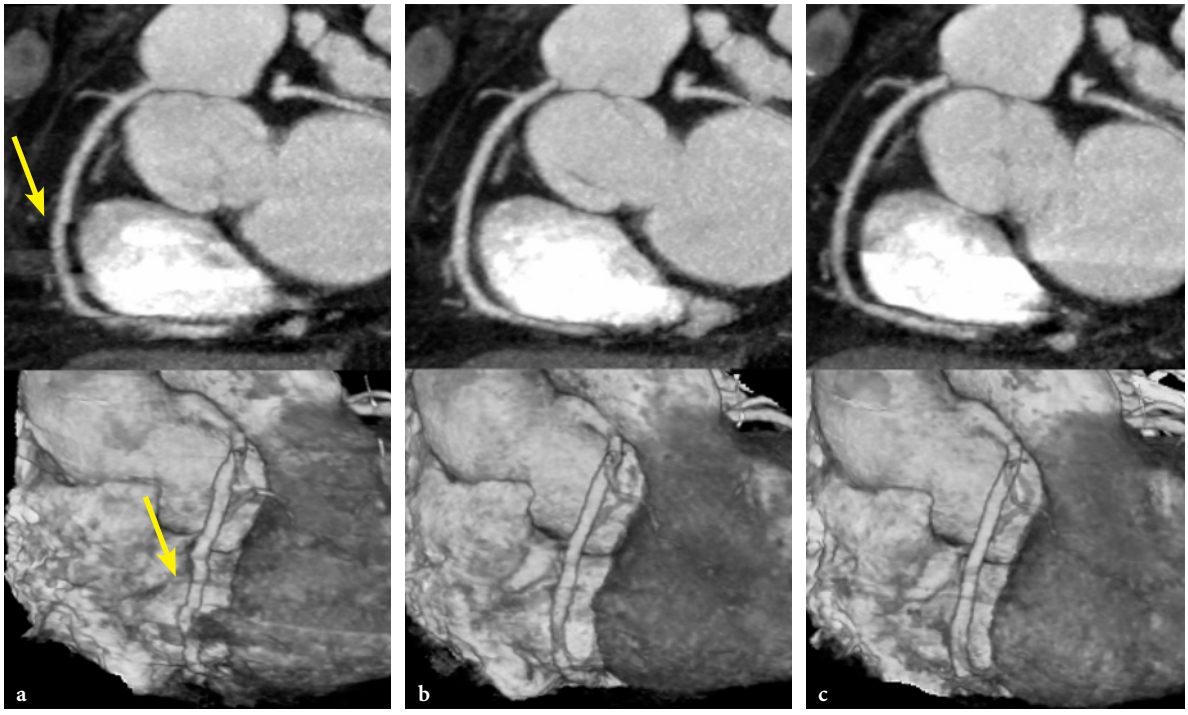

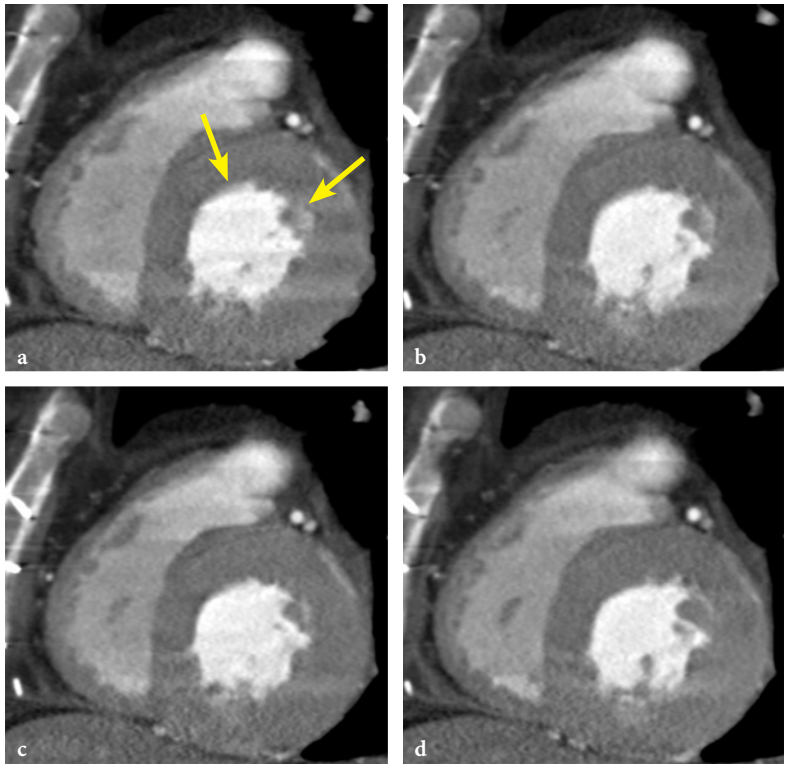

Fig. 4.26a–d. Case example of a cardiac CT angiography examination for a patient with a heart rate of 100–107 bpm using a 64-slice CT scanner with 64 × 0.6-mm slices and 0.33-s rotation time. Images are reconstructed during the systolic phase with a relative delay of 25% of the RR-interval, and MPRs are generated in the short heart axis. With single-segment reconstruction and a temporal resolution of 165-ms, motion artifacts are present (**a**, *arrows*). Adaptive-segmented reconstruction with 2 (**b**), 3 (**c**), and 4 (**d**) segments improves temporal resolution up to 60 ms, and cardiac anatomy can be visualized during phases of rapid cardiac motion. A substantial image quality improvement takes place when using two segments instead of one. Further image quality improvements are only minor when using more than two segments. (Cases courtesy of Klinikum Grosshadern, University of Munich, Germany)

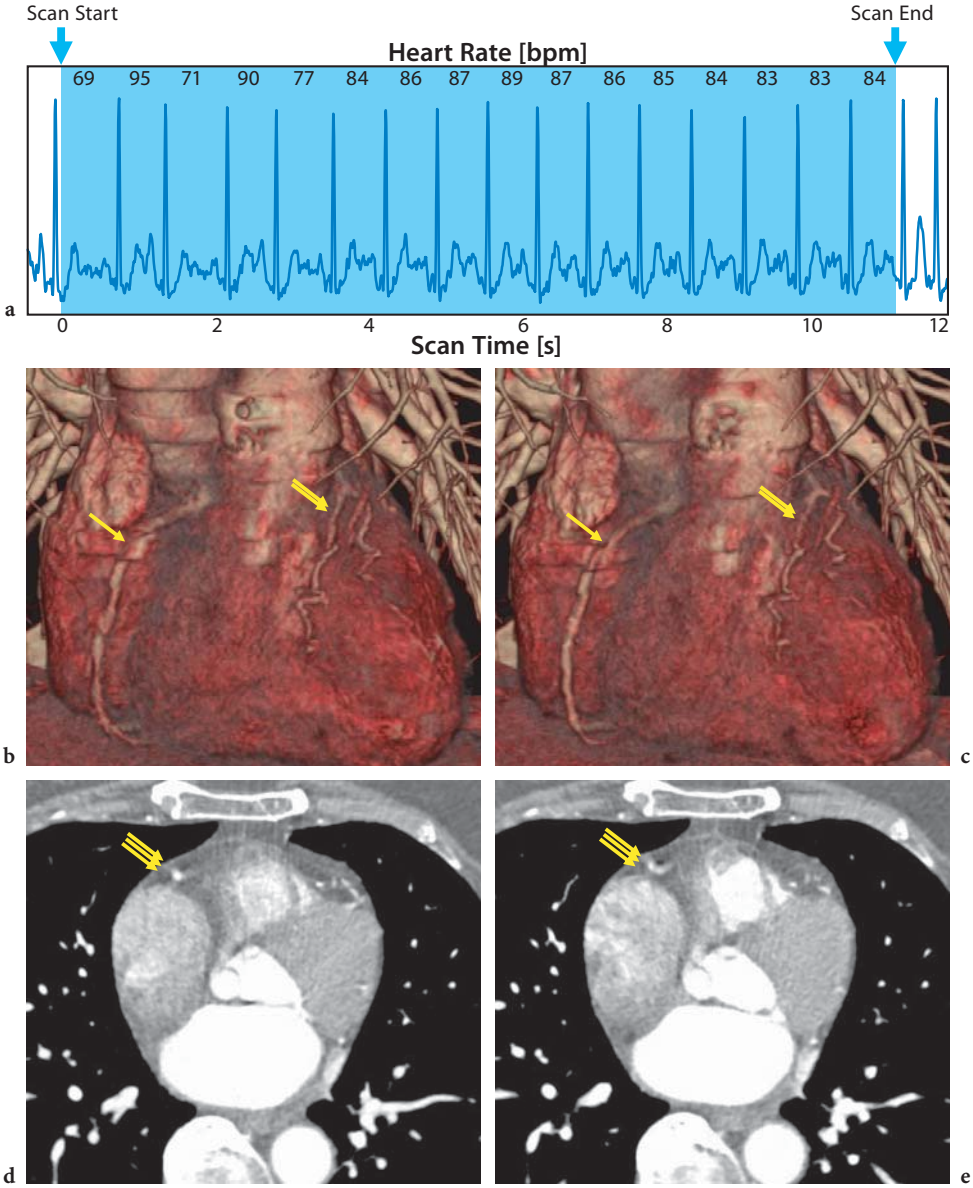

Fig. 4.27a–e. Case example of a cardiac CT angiography using a 64-slice CT scanner with 64 × 0.6-mm slices and 0.33-s rotation time. **a** The patient had a varying heart rate between 69 and 95 bpm during the scan. The *arrows* in a point to the scan start and to the scan end, and illustrate the scan time interval of about 11 s. **b**, **d** Images were reconstructed with a relative delay of 45% of the RR-interval using single-segment reconstruction with 165-ms temporal resolution. **c**, **e** Three-segment reconstruction with increased temporal resolution between 55 and 165 ms depending on heart rate. Despite the higher effective temporal resolution of 3-segment reconstruction, motion artifacts are still present (*arrows*). In some segments, even better image quality is achieved with single-segment reconstruction (*double arrows, triple arrows*) due to beat-to-beat data inconsistencies with 3-segment reconstruction in the presence of heart-rate changes. (Cases courtesy of Klinikum Grosshadern, University of Munich, Germany)

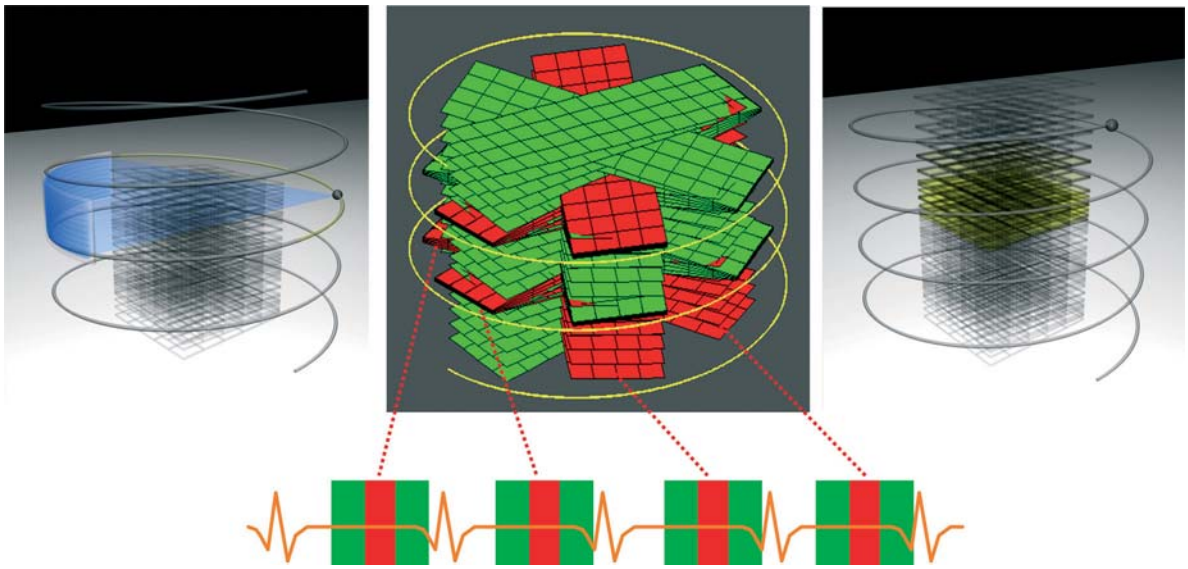

Fig. 4.28. The principle of cardiac cone-beam reconstruction with generation of individual double-oblique image stacks (so-called booklets) in each heart cycle that are subsequently reformatted to overlapping transaxial image slices

cardiac reconstruction data, segments from consecutive heart cycles that cover less than 180° of parallel-beam projections are used for image formation. Segmented cardiac cone-beam reconstruction algorithms permit reconstruction of image booklets from data segments covering less than 180°; however, these do not represent complete CT images due to truncation of the projection segments. The incomplete CT images from individual heart cycles are separately reformatted and subsequently combined to complete axial CT images containing contributions from multiple consecutive heart cycles that add up to a total parallel projection interval of 180°.

The elimination of cone-beam artifacts in cardiac CT images has been demonstrated in phantom studies using data from multi-slice CT scanners with up to 64 individual detector rows (Bruder 2002) (Fig. 4.29). Cardiac cone-beam reconstruction algorithms have also demonstrated considerable image quality improvements in ECG-gated cardiac studies with latest 64-slice CT scanners, in particular for the diagnosis of peripheral thoracic anatomy located further from the center of the scan field of view (Fig. 4.30).

4.4.5 ECG-Gated Spiral Scanning with Increased Volume Speed

Both ECG-triggered sequential scanning and ECG-gated spiral scanning require substantially slower scan speeds than conventional multi-slice spiral scanning without ECG-gating. Normal ECG-triggered or ECG-gated scan techniques using the present 4- and 16-slice CT scanners cannot provide thin-slice coverage of the entire chest anatomy with a scan range of about 350 mm within a short single breath-hold. However, thoracic CT studies are frequently degraded by motion artifacts caused by transmitted cardiac pulsation (Loubeyre 1997, Schöpf 2000) and elimination of motion artifacts via ECG synchronization may substantially improve diagnostic quality. Although the latest 32- and 64-slice CT scanners are capable of covering the entire chest with ECG-gated scan protocols in about 15–20 s, a further reduction of breath-hold time remains feasible.

Scan speed can be increased with a modified ECG-gated spiral acquisition technique that enables image reconstruction with high temporal resolution by the use of higher pitch values (Flohr 2002). The

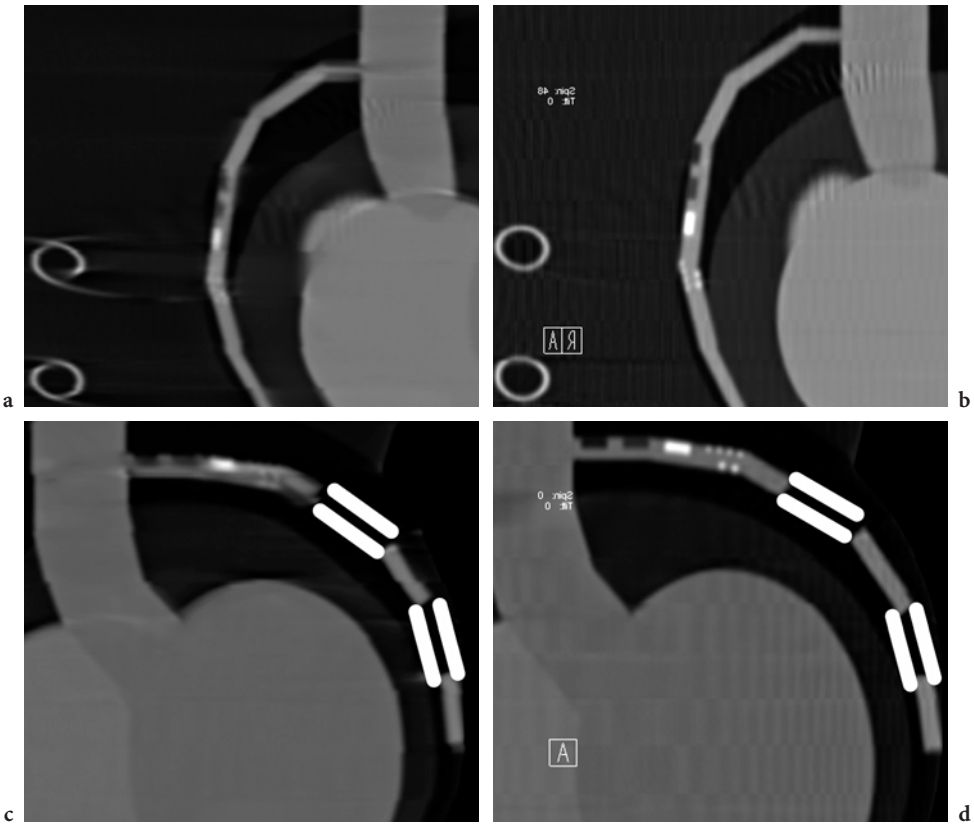

Fig. 4.29a–d. Evaluation of cardiac cone-beam reconstruction algorithms using an anthropomorphic heart phantom. CT data were generated for a multi-slice CT scanner with 64 × 0.625-mm collimation (40-mm coverage per rotation, no z-flying focal spot) and reconstructed using cardiac reconstruction algorithms without (**a**, **c**) and with (**b**, **d**) cone-beam correction. Due to the larger volume coverage per rotation, images without cardiac cone-beam reconstruction demonstrate significant cone-beam artifacts in the heart and in the periphery. These can be eliminated using cardiac cone-beam reconstruction

limitation of the spiral pitch for ECG-gated multi-slice spiral scanning results is a consequence of the phase-consistent coverage of the heart volume, i.e., data may only be used during identical relative time points within the cardiac cycle. The spiral pitch can be increased by allowing images that are part of the same continuous volume to be reconstructed with half-scan reconstruction algorithms but in different phases of the cardiac cycle. In this approach, data have to be excluded from image reconstruction acquired during phases of high cardiac motion (i.e., systole). The data windows that are excluded from reconstruction during the different cardiac cycles may be positioned relative to the onset of the R-waves with a certain temporal relation (Fig. 4.31). A stack of images with a given increment is reconstructed during each cardiac cycle and combined to form a volume image data set. For each image, an interpolated partial-scan data segment is generated with the previously described single-segment cardiac spiral reconstruction approach. Thus, the temporal resolution of each individual image is equal to half of the rotation time. The data segments selected for reconstruction of individual slices are shifted equidistantly in time within the heart cycle. Pulsation artifacts are usually most severe during the systolic phase of cardiac contraction. Therefore, to eliminate image degradation due to systolic pulsation, scan

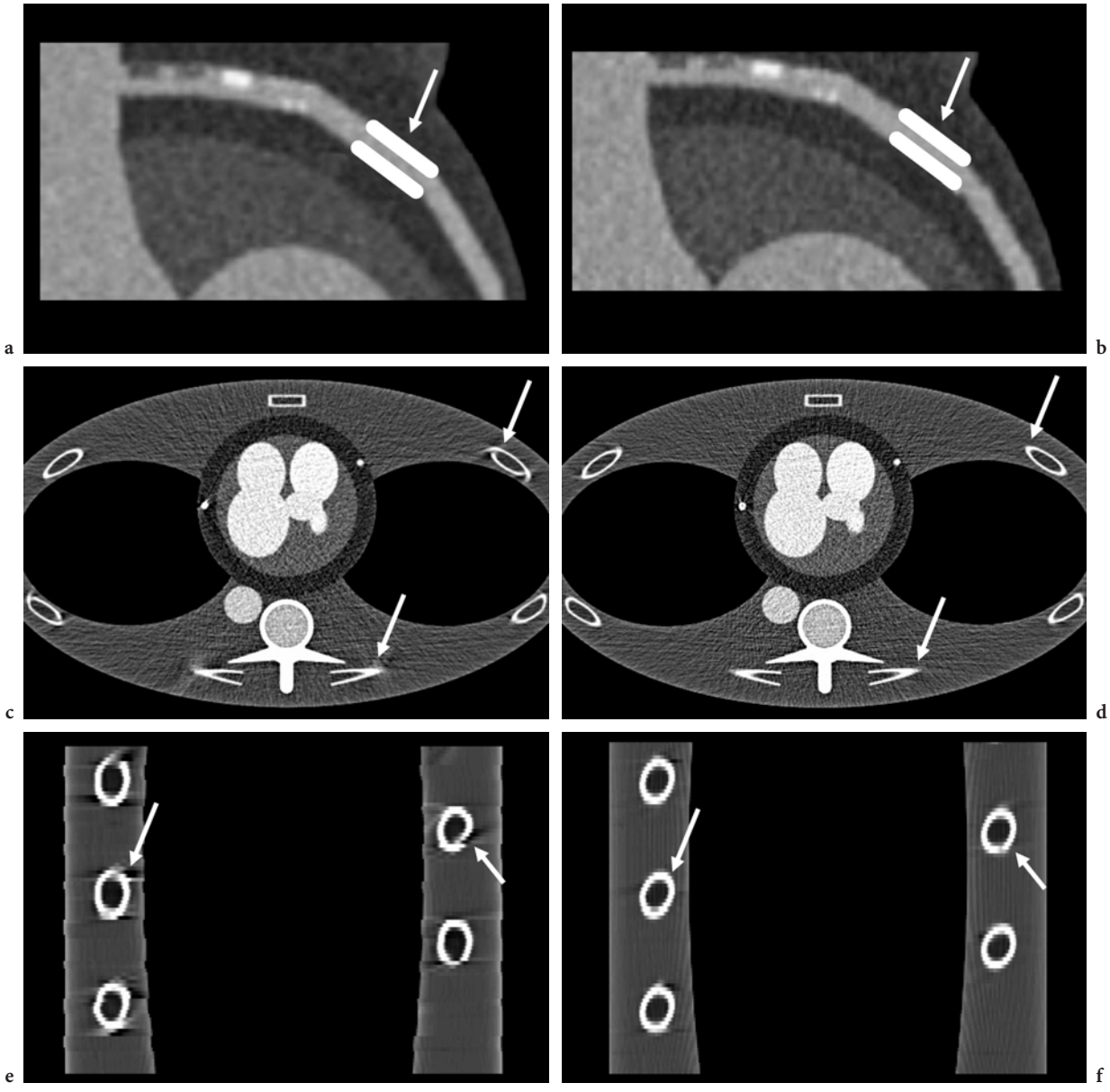

Fig. 4.30a–f. Demonstration of image-quality improvements using cardiac cone-beam reconstruction techniques with a 64-slice CT scanner. CT data were acquired in a chest phantom for a 64-slice CT scanner with 32 × 0.6-mm collimation (19.2-mm coverage per rotation, with z-flying focal spot) and reconstructed using cardiac reconstruction algorithms without (**a**, **c**, **e**) and with (**b**, **d**, **f**) cone-beam correction. Due to the limited volume coverage per rotation, images can be reconstructed without cone-beam reconstruction to display the cardiac anatomy, and cone-beam artifacts are negligible (*arrows* in **a** and **b**). However, such artifacts are present in the periphery of the scan field of view (*arrows* in **c** and **e**) and cardiac cone-beam reconstruction is required to reduce artifacts, in particular for the peripheral thoracic anatomy (*arrows* in **d** and **f**)

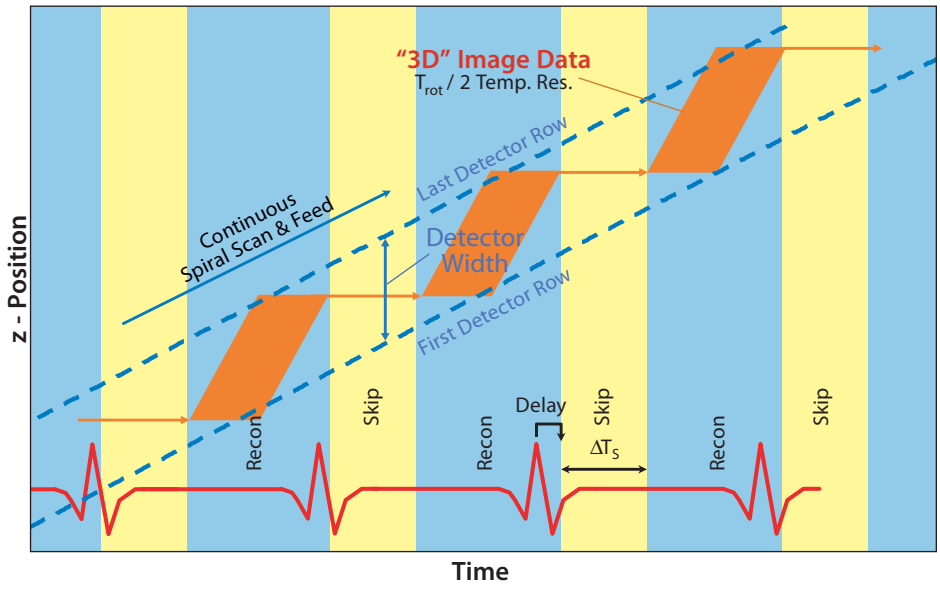

Fig. 4.31. Volume coverage with fast ECG-gated spiral acquisition using increased pitch. Stacks of overlapping images can be reconstructed with $T_{rot}/2$ temporal resolution in every cardiac cycle. Data ranges acquired during phases with fastest cardiac motion are omitted for reconstruction of 3D volume image data. The omitted temporal range is defined with an adjustable width ΔT_S and an adjustable phase related to the onset of the R-wave

data acquired during this phase of cardiac contraction is omitted within a temporal window of fixed width ΔT_S. This window is defined within the cardiac cycle with a fixed temporal relation to the onset of the R-wave. Continuous volume coverage requires that the image stacks that are reconstructed in consecutive heart cycles overlap in the z-direction. Thus, the spiral pitch is restricted to a value given by the fixed temporal width ΔT_S of the data window that is omitted during image reconstruction (Eq. 4.9). Here, the pitch limitation is independent of heart rate.

$$pitch \leq \frac{N-1}{N} \cdot \frac{T_{rot}}{\Delta T_S + T_{rot}/2} \qquad (4.9)$$

N represents the number of slices and T_{rot} is the scanner rotation time. It has been shown that values between ΔT_S 400 ms and ΔT_S 500 ms are a reasonable approximation for the duration of the phase of strongest cardiac pulsation. The resulting pitch values between 0.5 and 0.6 allow the entire thorax to be covered with thin slices within a single breath-hold. As an example, a modern 16-slice CT scanner can cover a 350-mm scan range with 16 × 0.75-mm collimation, 0.37-s rotation, and a pitch of 0.5 in a breath-hold time of 22 s. Examples of examinations of the thoracic aorta are shown in Figs. 4.32 and 4.33. Direct comparison of conventional non-gated spiral reconstruction and ECG-gated reconstruction of the same scan data demonstrates a substantial improvement with the latter technique, since motion artifacts can be largely eliminated.

With the advent of 32- and 64-slice CT scanners, thin-slice ECG-gated coverage of the entire chest has also become feasible with regular ECG-gated cardiac scan protocols. Based on a usual pitch value of 0.2, which can provide gap-less volume coverage for a heart rate down to about 40 bpm, a 350-mm scan range can be covered within a breath-hold time of 10–20 s. For patients with heart rate of 60 bpm and above during the scan, the pitch can be increased to values of about 0.3, thus providing a 50% increase in volume coverage speed. Cardiac cone-beam reconstruction algorithms become increasingly important for ECG-gated scanning of the cardiothoracic anatomy with 32- and 64-slice CT scanners, since large portions of the thoracic anatomy are located

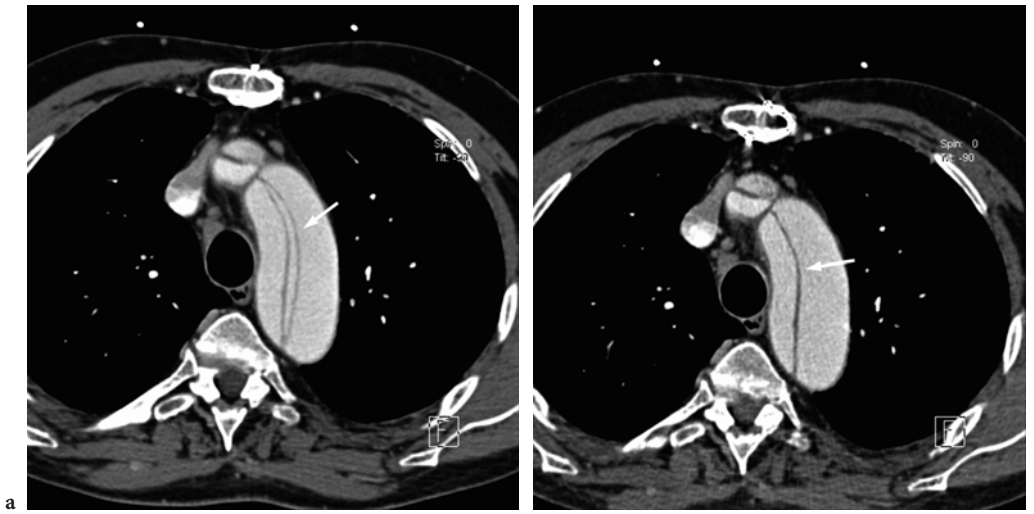

Fig. 4.32a, b. Fast ECG-gated spiral acquisition with a 4-slice CT scanner for evaluation of the thoracic aorta: comparison with multi-slice spiral reconstruction using a standard algorithm. **a** With standard reconstruction, considerable pulsation artifacts that produce a double contour are visible. **b** The intimal flap of a type-A dissection can be evaluated free of pulsation artifacts on a corresponding transverse section using fast ECG gating. Scan and reconstruction parameters: 4 × 1-mm collimation, 0.5-s rotation, 120 kV, 300 mA/200 mAs, pitch 0.6, 1.25-mm slice-width, 0.8-mm image increments, window of omitted data has width ΔT_S = 400 ms and starts 0 ms after onset of the R-wave. (Images courtesy of the University of Tübingen, Germany)

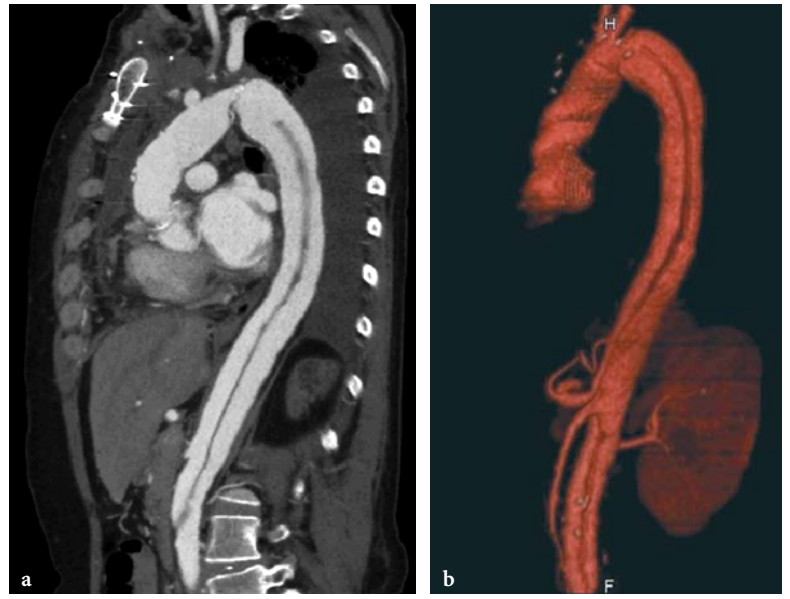

Fig. 4.33a, b. Case study of a CT angiography examination of the thoracic and abdominal aorta using a 16-slice CT scanner with 16 × 0.75-mm collimation and 0.37-s rotation time and fast ECG gating. In the conventional non-gated technique, the displayed scan range of 500 mm can be scanned in 10 s with a pitch of 1.5 but pulsation artifacts may be present. With a fast ECG-gated spiral protocol and pitch 0.5, the scan time is increased to 30 s but pulsation artifacts are largely eliminated. In the presented case, fast ECG-gated acquisition demonstrates an aortic dissection (type B) free of motion over its entire course in sagittal MPR (**a**) and volume-rendering technique (**b**) (Case by courtesy of University Hospital Graz, Austria)

at greater distance to the center of the scan field of view and thus are subject to cone-beam artifacts.

4.5 Synchronization with the ECG and Cardiac Motion

4.5.1 ECG-Based Phase Selection

With both prospective ECG triggering and retrospective ECG gating, the starting points of data acquisition or the start points of data selection for reconstruction have to be defined within each cardiac cycle during the acquisition. These start points are determined relative to the R-waves of the ECG-signal by a phase parameter. The following phase-selection strategies can be used (Fig. 4.34).

- Relative delay: A temporal delay T_{del} relative to the onset of the previous R-wave is used for determining the start point of the ECG-triggered acquisition or the start point of the reconstruction data interval. The delay time T_{del} is determined individually for each heart cycle as a given percentage δ_{RR} of the RR-interval time T_{RR}. For ECG triggering, the RR-interval times have to be prospectively estimated based on the prior RR-interval times.
- Absolute delay: Fixed delay times T_{del} after onset of the R-wave define the start point of the ECG-triggered acquisition or the start point of the reconstruction data interval.
- Absolute reverse: Fixed times T_{rev} prior to the onset of the next R-wave define the start point of the ECG-triggered acquisition or the start point of the reconstruction data interval. For ECG triggering, the position of the next R-wave has to be prospectively estimated based on the prior RR-interval times.

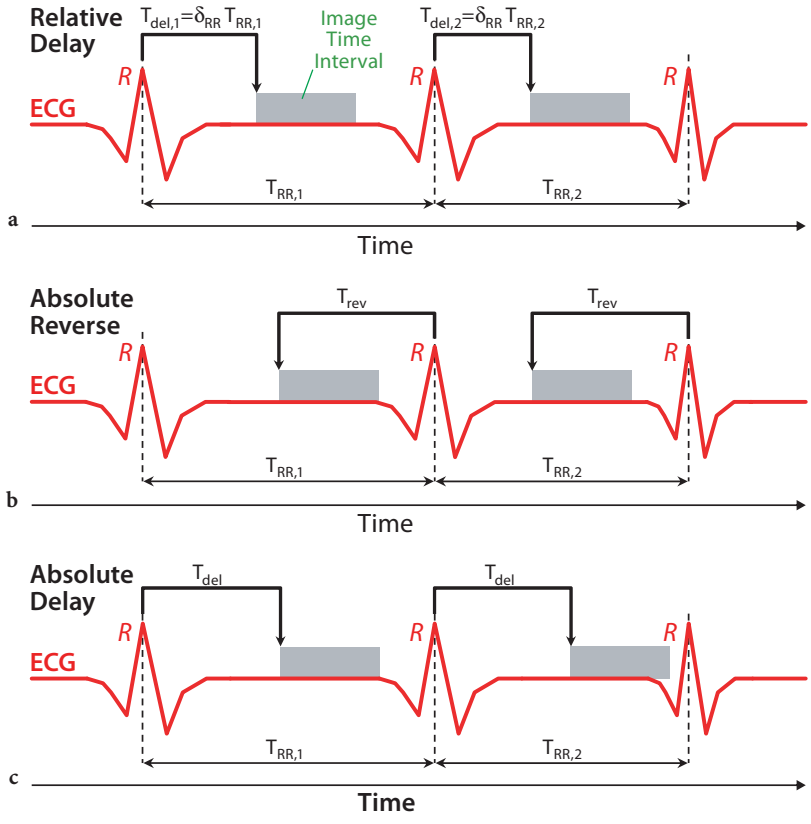

Fig. 4.34a–c. Phase definition for ECG triggering and ECG gating by selection of the start point of the temporal data interval within every heart cycle. The following different phase-definition strategies are used. **a** Relative delay: delay time after the previous R-wave, determined as a fraction δ_{RR} of the RR-interval. **b** Absolute reverse: constant interval T_{rev} prior to the next R-wave. c Absolute delay: constant delay time T_{del} after the previous R-wave

Different approaches are in use in clinical practice today depending on the clinical application. For motion-free imaging of small anatomical structures (i.e., coronary arteries) in diastolic phase, with least cardiac motion, the relative delay and absolute reverse approaches are most frequently used. Cardiac image quality greatly depends on the cardiac phase selected for image reconstruction (Fig. 4.35), as cardiac motion varies widely during different phases within the cardiac cycle (Fig. 4.1). Cardiac image reconstruction is usually performed during phases of least cardiac motion – usually between mid-diastole and end-diastole of the cardiac cycle. Within the ECG trace, end-diastole is usually represented by the onset of the P-wave. For the latest 64-slice CT scanners, which provide higher temporal resolution, cardiac image reconstruction can also be feasible during end-systole. The latter represents a shorter phase of low cardiac motion and is marked within the ECG trace by the onset of the T-wave. Despite intensive research to standardize phase selection for cardiac image reconstruction, heart-rate-dependent and patient-individualized optimization usually remain necessary to obtain the best possible results (Hong 2001a, Kopp 2002).

For functional imaging with retrospective ECG gating, images need to be reconstructed in phases of maximum and minimum filling of the ventricles (end-diastole and end-systole). End-diastolic reconstruction is feasible with the absolute reverse approach, while the absolute delay approach allows for most consistent reconstruction in end-systolic phase.

A regular heart rate without significant and sudden heart rate changes during the scan is usually a pre-requisite for diagnostic image quality for examinations of small cardiac and coronary anatomy. A strongly irregular heart rate may result in substantial data mis-registration and image artifacts, thus leading to results that cannot be used diagnostically (Fig. 4.36). However, retrospective ECG gating allows for viewing and analysis of the ECG signal after the end of the scan, and data are available during all phases of the cardiac cycle. This offers the possibility of retrospectively modifying synchronization of the ECG trace and data reconstruction. Interactive editing of R-peak positions that are detected inappropriately or represent irregular heart beats can have a positive impact on phase consistency and image quality in patients with irregular

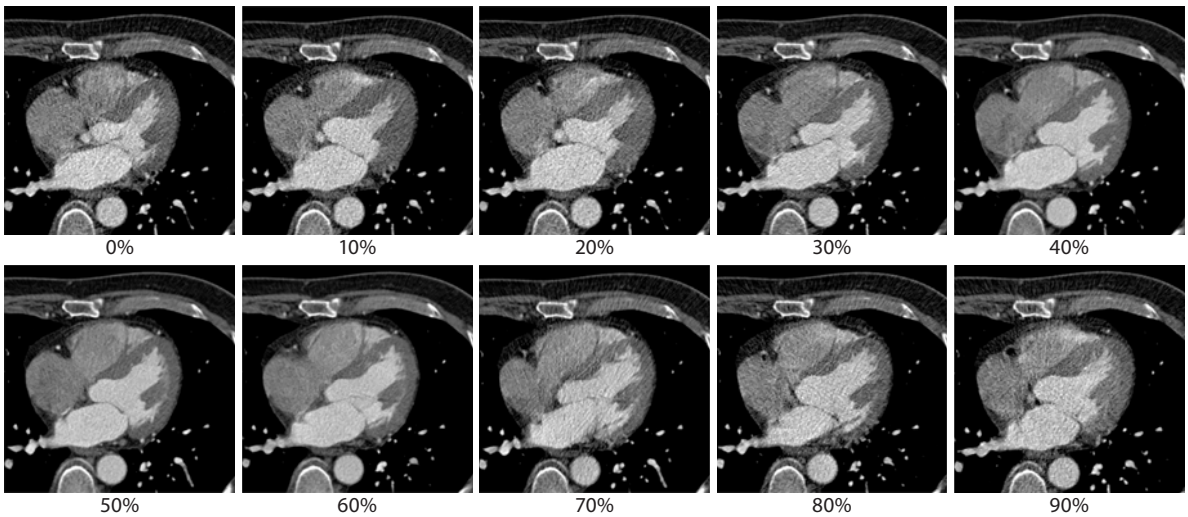

Fig. 4.35. Cardiac image reconstruction of data acquired with a 64-slice CT scanner with 0.33-s rotation time in different phases of the cardiac cycle using the relative-delay approach. Images were reconstructed with single-segment reconstruction, thus providing a temporal resolution of 165 ms. Image quality largely depends on the selected phase of the cardiac cycle. The best image quality can be obtained in mid-diastolic phase (δ_{RR} = 50%) and end-systolic phase (δ_{RR} = 30%)

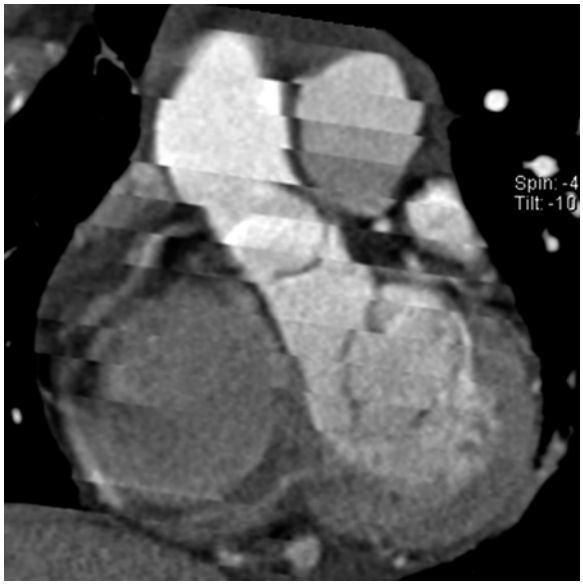

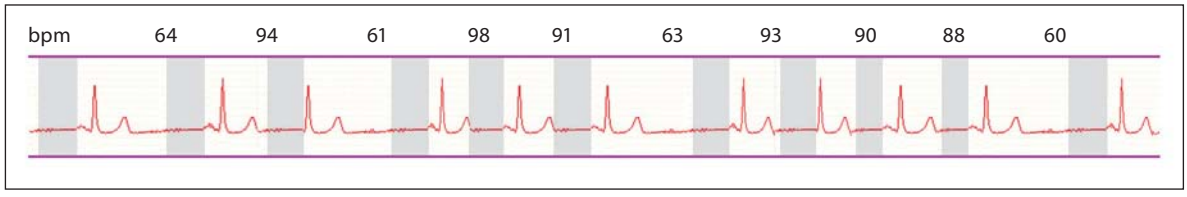

Fig. 4.36. Case example of a patient scanned with a 16-slice CT scanner with 16 × 0.75-mm collimation and 0.42-s rotation time. The patient had a strongly irregular heart rate that changed between 60 and 98 bpm during the scan. Although the quality of the individual image stacks reconstructed from individual heart beats is acceptable, the image quality of 3D reformats is heavily compromised due to misalignment of the image stacks for consecutive cardiac cycles. (Case courtesy of Münster University, Germany)

heart beats (Fig. 4.37). Also, individual adjustment of the image-time interval positions – independent of the position that is determined by the ECG-gating parameter – may be useful in patients with substantial arrhythmias.

4.5.2 The Pros and Cons of ECG Gating and ECG Triggering

Retrospectively ECG-gated spiral scanning with single-slice CT systems featuring sub-second rotation has been tested for coronary artery and cardiac-function imaging in clinical trials but serious limitations have been discovered (Mochizuki 2000). With the advent of multi-slice acquisition, ECG-gated spiral scanning has become feasible, and with significant advantages over prospective ECG triggering that are important for clinical applications.

- ECG-gated spiral scanning provides continuous volume coverage and better spatial resolution in the patients' longitudinal direction, as images can be reconstructed with arbitrary, overlapping slice increments. ECG-triggered sequential scanning is usually restricted to scanning with non-overlapping adjacent slices or slice increments with only small overlap. The scan time to cover the heart volume is thus directly proportional to the slice increment.
- Retrospective analysis of the ECG results in less sensitivity to heart-rate changes during the scan. The ECG trace can be retrospectively analyzed and extra-systolic beats can be eliminated for reconstruction. With prospective ECG triggering, estimation of the next RR-interval may be incorrect when heart-rate changes are present (e.g., arrhythmia, Vasalva maneuver) and scans may be placed in inconsistent heart phases. In that case, even slices with high temporal resolu-

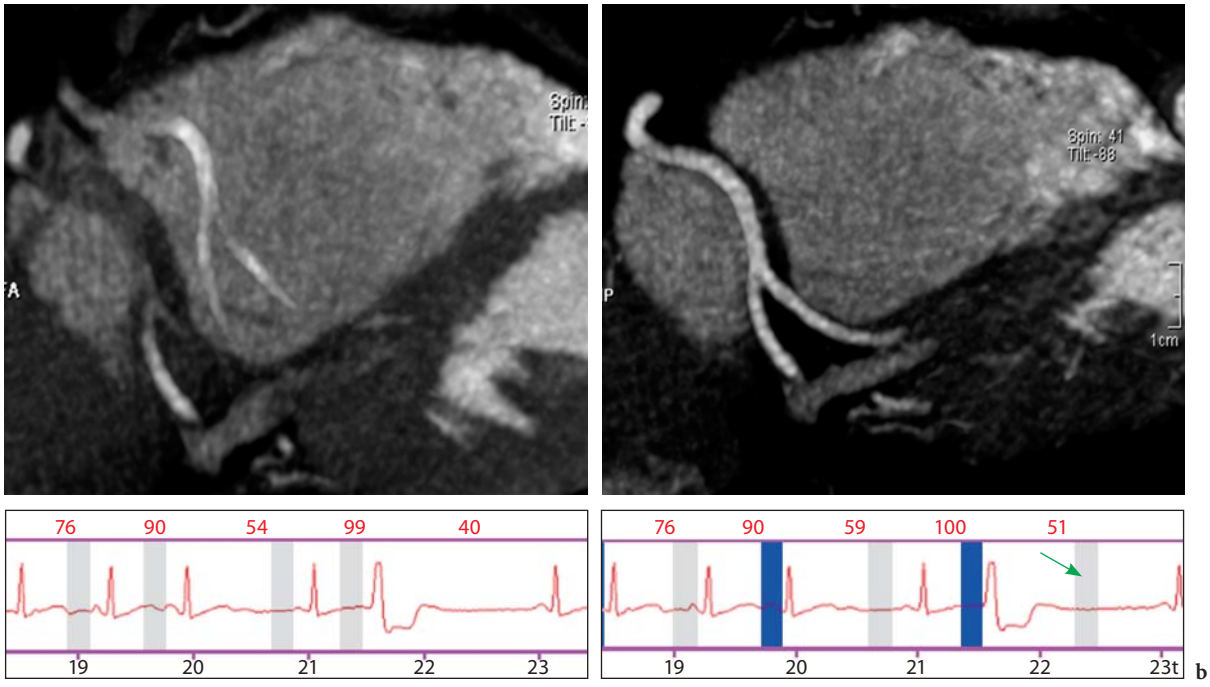

a b

Fig. 4.37a, b. Case example of a patient scanned with a 64-slice CT scanner. The patient had extra-systolic beats during the scan. The scan was acquired using a slice acquisition of 64 × 0.6 mm and a rotation time of 0.33 s. Misregistration artifacts can be strongly reduced and the diagnostic quality of the study restored via interactive elimination of the extra heart beats before image reconstruction. In this case, an extra-systolic beat strongly compromises visualization of the distal right coronary artery (**a**). After interactive elimination of those reconstruction intervals affected by the extra-systolic beat (*blue bars*) and manual introduction of alternative image reconstruction intervals (*gray bars, green arrow*), image quality could be fully restored (**b**). (Case courtesy of New York University, USA)

tion that are free of motion artifacts cannot be used for continuous 3D image data sets.

- ECG-gated spiral scanning provides faster volume coverage than ECG-triggered sequential scanning because spiral scan data can be acquired continuously and images can be reconstructed in every cardiac cycle. Relatively long travel distances and travel times of the table are present for multi-slice acquisition in between two consecutive scans. This limits the scan-cycle time (minimum time in between the start of two consecutive scans), and ECG-triggered scans can often be obtained only in every second heart beat for patients with higher heart rates.
- ECG-gated spiral acquisition allows for imaging in a complete cardiac cycle using the same scan data set, thus providing information on cardiac function. ECG-triggered acquisition targets only one specific phase of the cardiac cycle and requires additional examinations with new breath-hold levels and additional contrast agent to cover more phases of the cardiac cycle.

During ECG-gated spiral imaging of the heart, data are acquired with small spiral pitch (pitch << number of slices, i.e., overlapping acquisition) and continuous X-ray exposure. Thus, ECG-gated spiral acquisition requires a higher patient dose of radiation than ECG-triggered sequential acquisition for comparable signal-to-noise ratio. All spiral data can be used for image reconstruction in different cardiac phases and no data have to be omitted. However, if only one dedicated cardiac phase (i.e., diastolic phase) needs to be targeted by retrospec-

tive data selection, the specific requirements of the clinical application should indicate whether ECG-triggered sequential scanning with less radiation exposure could provide sufficient performance and image quality. Newer developments enable a reduction of radiation exposure during retrospectively ECG-gated scanning. The goal of these techniques is to maintain the important benefits of ECG-gated spiral scanning but to reduce X-ray radiation exposure to levels comparable to those of ECG-triggered sequential acquisition, as will be explained in a later chapter.

4.5.3 Alternative Cardiac-Motion Gating Approaches

Phase selection of ECG-synchronized CT scans is usually performed with respect to the temporal position of the R-waves. The R-wave can be easily detected from the patient's ECG due to its high signal amplitudes. Cardiac image reconstruction is frequently carried out during end-systole and end-diastole, which are the phases of the cardiac cycle with the least cardiac motion and which determine minimum and the maximum left ventricular volumes. For R-wave-based ECG-synchronization, end-systole and end-diastole have to be estimated with appropriate phase parameters relative to the R-wave. More advanced ECG-gating techniques that determine the location of the end-systolic phase based on the detection of the T-wave and the end-diastolic phase based on the detection of the P-wave are under investigation. However, given the small signal amplitudes, reliable detection of the T-waves and P-waves requires advanced software-based algorithms, which themselves are currently under development. Nonetheless, the first promising results were obtained in a clinical study that obtained better results with cardiac image reconstruction in end-diastole based on P-wave gating, compared to reconstruction in diastole with a relative delay in relation to the R-wave (Sato 2003) (Fig. 4.38).

It should be kept in mind that the ECG is only an indirect measure of cardiac motion. In some cases, such as in patients with atrial fibrillation or with extra-systoles, the electrical stimulation does not directly correspond to the real motion of the heart. Therefore, motion-detection algorithms have been investigated that have the potential to directly measure cardiac motion from the acquired scan data.

The first cardiac-motion detection algorithm to be clinically investigated (Ohnesorge 1999) used the opposite parallel-beam projections $P_p(\Theta,p)$ and $P_p(\Theta-\pi,p)$ in a fixed image plane measured at a projection angle with a 180° shift. In a static object, the signal difference between two opposite parallel-beam projections measured in the same plane equals zero. If the object is moving, the magnitude of the signal difference can be used to measure the displacement of a particular anatomical structure and the amount of movement that occurs between measurements of the two opposite projections, i.e., within the time of a half rotation of the system (Fig. 4.39). For example, the sum of the absolute values of the individual signal differences of all complementary rays in the considered opposite projections $\Sigma_p|P_p(\Theta,p)-P_p(\Theta-\pi,p)|$ can be used as an indicator for the displacement and motion of an anatomical structure at the point in time when the projection $P_p(\Theta,p)$ was measured. With this approach, it could be demonstrated that the derived signal difference correlates with both the displacement and the motion of the heart during the cardiac cycle (Fig. 4.39). However, the accuracy and consistency of the signal for reproducible detection of equivalent phases in consecutive cardiac cycle is limited, so that use of the algorithm is restricted to assessing the presence or absence of cardiac motion in patients with irregular heart beats during the scan, and therefore as input information for interactive editing of the recorded ECG.

A more recent approach, the so-called Kymogram algorithm (Kachelriess 2002), derives cardiac motion from projection data based on the calculation of the "center of mass" of the scanned fan-beam projections (m_{COM}) and the center of mass of the object in the considered image plane. The center of mass $m_{COM,q}$ of a fan-beam projection $P_f(\alpha_q,\beta_m)$ is determined by the ray at angle β_m within the projection such that the sum of the signals on both sides of that ray is equivalent (Eq. 4.10). The center of mass of the object in the considered image plane can be determined by the point of intersection of the rays that determine the centers of mass in two closely adjacent projections (Fig. 4.40).

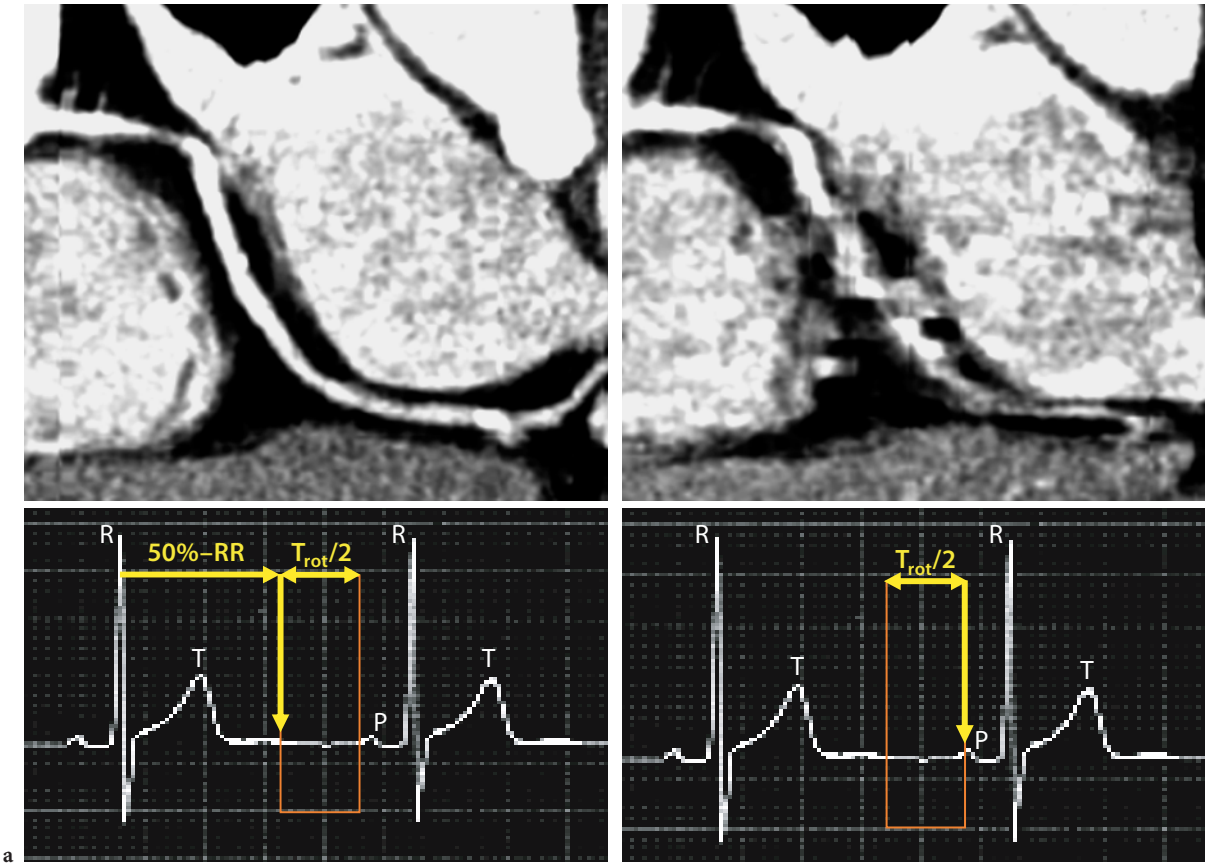

a b

Fig. 4.38a, b. Cardiac image quality obtained by a 4-slice CT scanner with 0.5-s rotation time in end-diastole based on R-wave- and P-wave-gated image reconstruction. **a** During P-wave gating, the end of the image reconstruction window is positioned on the P-wave. **b** During R-wave gating, the start of the image reconstruction window is positioned at 50% of the RR-interval. P-wave-gated reconstruction yields superior image quality compared to R-wave-gated reconstruction due to more consistent phase selection

$$\sum_{m=0}^{m=m_{COM;q}-1} P_f(\alpha_q,\beta_m) = \sum_{m=m_{COM;q}+1}^{m=M-1} P_f(\alpha_q,\beta_m) \qquad (4.10)$$

The center of mass changes its position with changing static anatomy from image plane to image plane and with changing positions of an anatomical structure due to motion. After subtracting the function of the center of mass for different slice positions, the variation of the center of mass over time represents a measure of cardiac motion. The resulting function of the variation of the center of mass over time is called the Kymogram (Fig. 4.41). Kachelriess (2002) demonstrated that peaks of the Kymogram often correlate to the position of R-waves in ECGs recorded during the scans of patients with regular heart rates, and that Kymogram-gated cardiac image reconstruction could yield results comparable to those obtained with ECG-gated image reconstruction (Fig. 4.42a). However, further clinical studies have demonstrated that Kymogram-gated image reconstruction results in inferior image quality compared to ECG-gated image reconstruction under clinical conditions, in both patients with regular heart rates and in those with irregular heart rates (Fig. 4.42b), (Fischbach 2004).

It can therefore be concluded that ECG-correlated scanning and image reconstruction remains

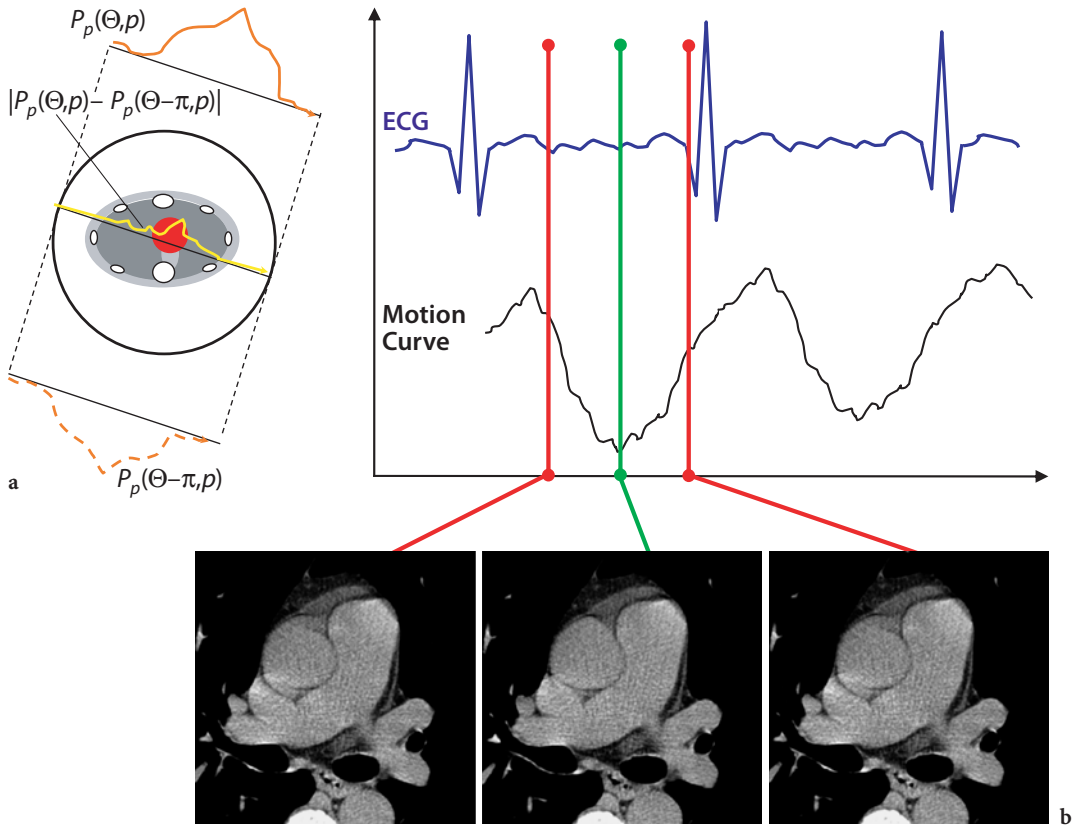

Fig. 4.39a, b. The principle of detection of cardiac motion from scan data. **a** The difference signal of opposite parallel projections is calculated and used as a measure for the motion and displacement of the cardiac anatomy in between measurement of the two projections. A difference signal is determined for every projection as the sum of the absolute values of the individual signal differences of all complementary rays in the considered opposite projections. **b** The difference signal correlated to the ECG that has been recorded during the scan is shown. Images that are reconstructed during the detected phase of low motion demonstrate fewer motion artifacts

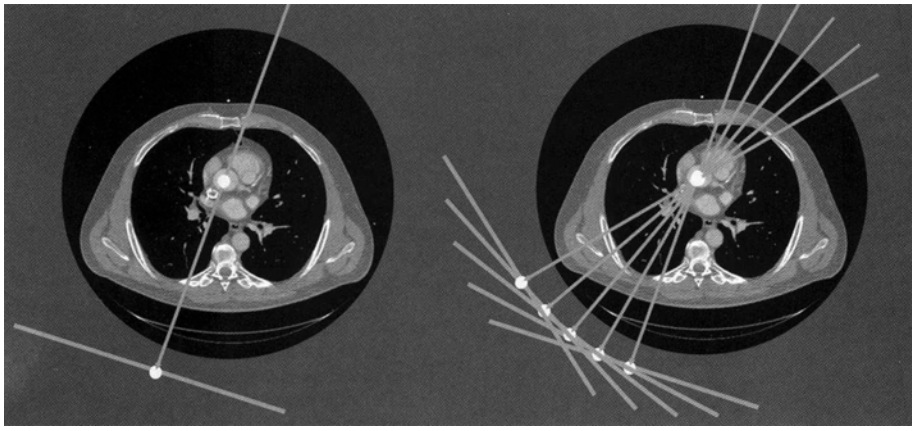

Fig. 4.40. Center of mass detection a within a projection and b for the object from two projections as the basis of Kymogram-gated reconstruction

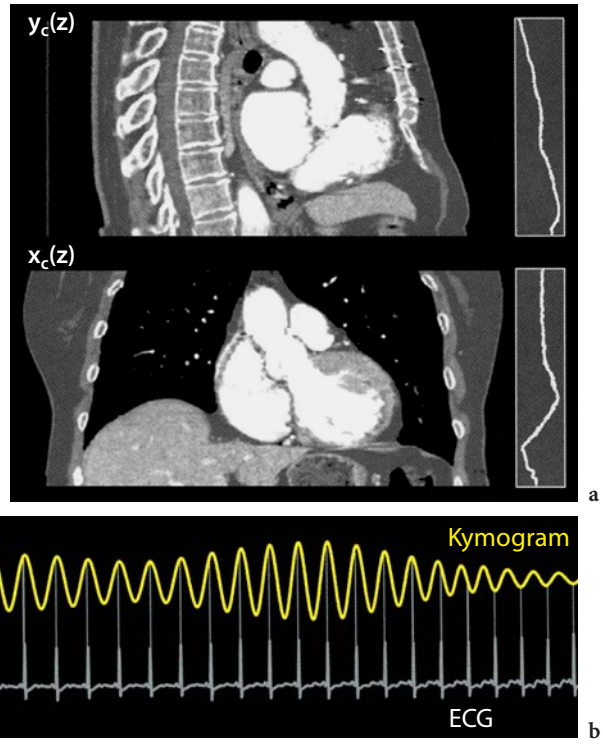

Fig. 4.41a, b. Principle of the separation of the Kymogram motion function and anatomical bias from the center of mass function. **a** The anatomical bias $x_c(z)$, $y_c(z)$ of the center of mass within the image plane has to be subtracted from the function of center of mass that depends on z-position and time. **b** The Kymogram results after subtraction of the anatomical bias from the center of mass function and correlates to the position of the R-waves

the method of choice to synchronize CT scanning with cardiac motion. If accurate automated P- and T-wave detection algorithms become available, ECG gating related to P- and T-waves will offer a promising alternative to R-wave-related ECG-gating. Other approaches to detect cardiac motion automatically from the projection data of the CT scan have demonstrated the feasibility of the principle, but they have yet to provide sufficient robustness in clinical routine. To date, the use of such algorithms is restricted to a back-up role for the ECG signal, e.g., in case of poor signal detection, R-wave misregistration, or failure of the ECG.

4.6 Radiation Exposure Considerations

Radiation exposure of patients during computed tomography and the resulting potential radiation hazards have recently gained increasing attention, both in the public and in the scientific literature (Brenner 2001, Nickoloff 2001). In particular, the radiation dose for ECG-synchronized cardiac scanning has been a topic of considerable controversy. This section will introduce the basic principles of radiation-dose measurement in CT, exposure estimations for ECG-gated cardiac examinations with 16-slice and 64-slice CT systems, and the most recent approaches to reduce radiation exposure during cardiac CT examinations.

4.6.1 Principles of Radiation Dose Measurement in CT

In CT, the average dose in the scan plane is best described by the weighted computerized tomographic dose index ($CTDI_w$) (Morin 2003, McCollough 2003), which is determined from $CTDI_{100}$ measurements both in the center and at the periphery of a 16-cm Lucite phantom for the head and a 32-cm Lucite phantom for the body. For the $CTDI_{100}$ measurements, a 100-mm-long ionization chamber

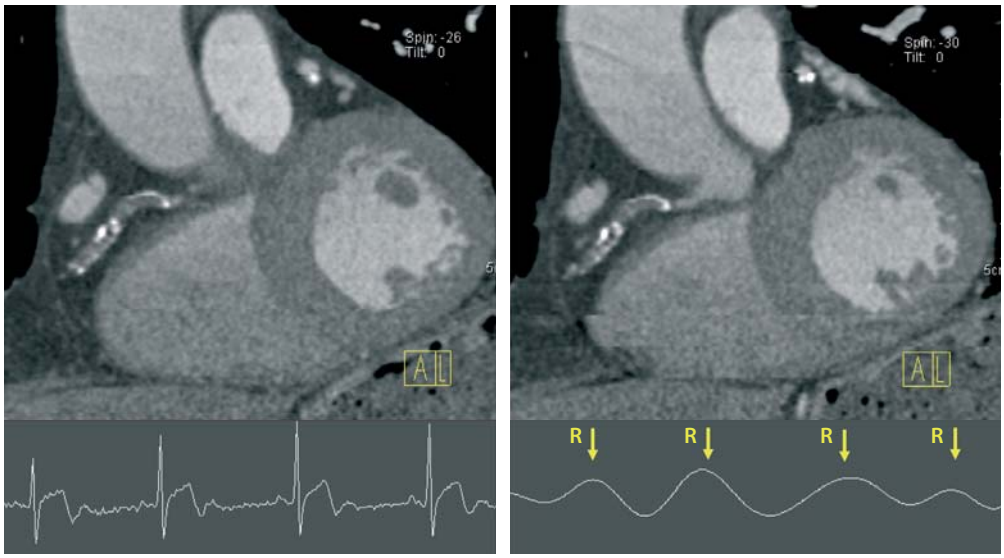

a b

Fig. 4.42a, b. Comparison of cardiac image quality of a 16-slice CT scanner with 0.42-s rotation time in a patient with regular sinus rhythm. Reconstruction with a ECG-gating (at 50% of the RR-interval) and **b** Kymogram-gating (at 50% of the interval between the peaks). The peaks of the Kymogram correlate well with the detected R-Waves. The Kymogram-gated reconstruction demonstrates image quality comparable to the ECG-gated reconstruction except for moderate registration artifacts at the beginning and end of the scan. (Case courtesy of Münster University, Germany)

is used. Figure 4.43 shows the typical equipment for dose measurements. $CTDI_w$, is a good estimate for the average patient dose as long as the patient's size is similar to that of the respective phantoms. $CTDI_w$, is defined according to (Eq. 4.11) (Morin 2003).

$$CTDI_w = 1/3\ CTDI_{100}\,(\text{center}) + 2/3\ CTDI_{100}\,(\text{periphery}) \qquad (4.11)$$

$CTDI_w$, given in mGy, is always measured in an axial scan mode. It depends on scanner geometry, slice collimation, beam pre-filtration, X-ray tube voltage (in kV), tube current (in mA), and gantry rotation time T_{rot}. The product of mA and T_{rot} is the mAs value of the scan. To obtain a parameter characteristic for the scanner used, it is helpful to eliminate mAs dependence and to introduce a normalized $(CTDI_w)_n$, given in mGy/mAs:

$$CTDI_w = mA \cdot T_{rot} \cdot (CTDI_w)_n = mAs \cdot (CTDI_w)_n \qquad (4.12)$$

$CTDI_w$ is a measure of the dose in a single axial scan and depends on X-ray tube voltage and slice collimation. The latter parameters are needed to specify $CTDI_w$. For multi-slice CT systems, $CTDI_w$ tends to increase with decreasing collimated slice width, as a consequence of the increasing relative contribution of the penumbra zones of the dose profiles. As a representative example, Figure 4.44 shows $CTDI_w$ at 120 kV for the 32-cm body phantom as a function of the total collimated width of the detector for a 4-slice CT system and a 16-slice CT system with similar system geometry. Scan protocols for different CT scanners should always be compared on the basis of $CTDI_w$ and never on the basis of mAs, since different system geometries can result in significant differences in the radiation dose applied at identical mAs.

$(CTDI_w)_n$ can be used to calculate the radiation dose for axial scans, both for standard applications and for ECG-triggered sequential scanning. For most CT scanners, the mAs value for axial scans, which is

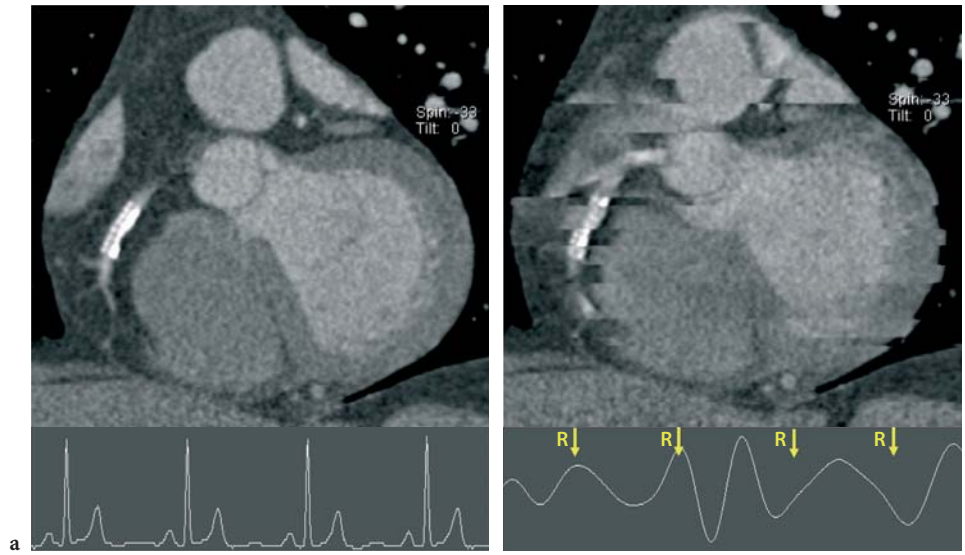

Fig. 4.43a, b. Comparison of cardiac image quality of a 16-slice CT scanner with 0.42-s rotation time in a patient with regular sinus rhythm. Reconstruction with a ECG-gating (at 50% of the RR-interval) and **b** Kymogram-gating(at 50% of the interval between the peaks). The peaks of the Kymogram correlate well with some R-waves during the scan but do not correlate well with the detected R-waves throughout the scan. The Kymogram-gated reconstruction demonstrates severe misregistration artifacts while the ECG-gated reconstruction yields artifact-free results. (Case courtesy of Münster University, Germany)

the product of tube current mA and slice exposure time T_{exp}, is indicated on the user interface. Usually, T_{exp} equals the gantry rotation time T_{rot}. For cardiac applications, however, partial scans are generally used for ECG-triggered sequential scanning. In this case, the slice exposure time is about two-thirds of the gantry rotation time. The principle of radiation exposure calculation for ECG-triggered scan protocols can be demonstrated with a practical example for ECG-triggered scanning of coronary calcium quantification. The slice exposure time of a 16-slice CT scanner for a partial scan at 0.42-s gantry rotation time is about 0.3 s. The scan protocol recommended by the manufacturer for ECG-triggered sequential scanning for coronary calcium quantification uses a tube current of 100 mA at a voltage of 120 kV. With these parameters, 100 × 0.3 mAs = 30 mAs are applied. This value is shown on the user interface. $(CTDI_w)_n$ = 0.072 mGy/mAs can be found in the data sheet of this scanner for the given protocol at 120 kV and for 12 × 1.5-mm collimation that provides 6 × 3-mm slices per scan. A $CTDI_w$ = 0.072 mGy/mAs × 30 mAs = 2.16 mGy can therefore be determined for this protocol (Flohr 2003).

For ECG-gated multi-slice spiral scans of the heart, the situation is more complicated. To represent the dose in a multi-slice spiral scan, it is essential to account for gaps or overlaps between the radiation-dose profiles from consecutive rotations of the X-ray source (Morin 2003). For this purpose, $CTDI_{vol}$, the volume $CTDI_w$, has been introduced

$$\begin{aligned} CTDI_{vol} &= 1/pitch \cdot CTDI_w = mAs \cdot 1/pitch \cdot (CTDI_w)_n \\ &= mA \cdot T_{rot} \cdot 1/pitch \cdot (CTDI_w)_n \end{aligned} \quad (4.13)$$

The factor 1/pitch accounts for the increasing dose accumulation with decreasing spiral pitch due to the increasing spiral overlap. In principle, Eq. 4.13 is valid for both single-slice and multi-slice spiral CT. For ECG-gated cardiac scanning, low pitch values (typically pitch = 0.2–0.35, depending on the number of detector rows, the gantry rotation time,

Fig. 4.44. Dose measurements in CT. The equipment consists of a 100-mm-long ionization chamber and a 32-cm Lucite phantom. With this set-up, the $CTDI_w$ value for the body is determined

and the number of segments used for image reconstruction) have to be used to ensure gap-less coverage of the heart volume in all phases of the cardiac cycle. The highly overlapping data acquisition has to be taken into account when calculating the dose for an ECG-gated spiral scan. Again, the principle of radiation exposure calculation for ECG-gated spiral scan protocols can be demonstrated with a practical example of an ECG-gated 16-slice spiral CT scan protocol used for coronary calcium quantification. The example protocol uses a 0.42-s rotation time, 16×1.5-mm collimation, pitch 0.28, 120 kV, and 100-mA tube current. The mAs value for this scan is 100 mA × 0.42 s = 42 mAs, which, in terms of the applied radiation dose, cannot directly be compared to mAs values for ECG-triggered sequential scanning, since in the latter the pitch dependency would be neglected. In fact, using $CTDI_w = 0.070$ mGy/mAs, the radiation dose in this case is 0.070 mGy/mAs × 42 mAs × 1/0.28 = 10.5 mGy. For spiral scanning, some manufacturers, such as Siemens and Philips, have introduced the concept of an "effective" mAs, which includes the factor 1/pitch into the mAs definition:

$$(\mathrm{mAs})_{\mathrm{eff}} = \mathrm{mA} \cdot T_{rot} \cdot 1/pitch = \mathrm{mAs} \cdot 1/pitch \quad (4.14)$$

For spiral scans, $(\mathrm{mAs})_{\mathrm{eff}}$ is indicated on the user interface. Inserting Eq. 4.14 into Eq. 4.13, the dose of a multi-slice spiral CT scan is given by

$$CTDI_{vol} = (\mathrm{mAs})_{\mathrm{eff}} \ \mathrm{x} \ (CTDI_w)_n \quad (4.15)$$

Other manufacturers (i.e., Toshiba and GE) have retained the conventional mAs definition, so that the user has to perform the 1/pitch correction. When comparing the scan parameters for CT systems of different manufacturers, the underlying mAs definition has to be taken into account. In the above example of an ECG-gated multi-slice spiral scan for coronary calcium quantification, the user applies 42 mAs, but 42 mAs × 1/0.28 = 150 effective mAs.

$CTDI_w$ is a measure of physical dose; it does not provide full information on the radiation risk associated with a CT examination. For this purpose, the concept of "effective dose" has been introduced by the ICRP (International Commission on Radiation Protection). The effective dose is given in milli-Sieverts (mSv). It is a weighted sum of the dose applied to all organs in a CT examination and includes both direct and scattered radiation. The weighting factors depend on the biological radiation sensitivities of the respective organs. Effective dose can be measured using whole-body phantoms, such as the Alderson phantom, or it is obtained by computer simulations using Monte Carlo techniques to determine scattered radiation. The effective patient dose depends on the scanned range. For a comparison of effective dose values for different protocols, scan ranges should be similar. A suitable program for calculation of effective dose values is, e. g., WinDose (Kalender 1999). This is a PC-based program that calculates organ dose and effective dose values for arbitrary scan parameters and anatomical ranges. Values for primary radiation have to be measured in terms of $CTDI_w$ and are used as input; values for scattered radiation are derived from Monte Carlo calculations.

The user has to keep in mind that both $CTDI_w$ and effective patient dose, which is derived from $CTDI_w$, give a correct estimation of the radiation dose for the patient only when the cross-section of the patient's anatomy is comparable in size to the cross-section of the phantom used for the evaluation of $CTDI_w$ (32-cm Lucite for the body). For smaller patients, the dose may be considerably higher (Fig. 4.45).

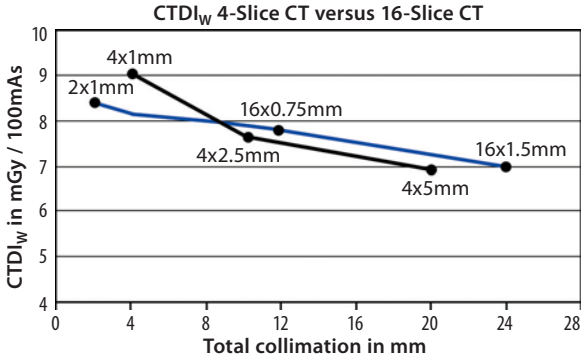

Fig. 4.45. $CTDI_w$ at 120 kV for the 32-cm body phantom as a function of the total collimated width of the detector for 4-slice (*black line*) and 16-slice (*blue line*) CT systems with similar geometries

4.6.2 Radiation Exposure for Selected Cardiac Examination Protocols

Typical values for the effective patient dose of selected multi-slice CT protocols are 1–2 mSv for a head examination, 5–7 mSv for a chest CT, and 8–11 mSv for CT of the abdomen and pelvis (McCollough 2003, Morin 2003). This radiation exposure must be appreciated in the context of the average annual background radiation, which is 2–5 mSv (about 3.6 mSv in the US).

This section provides estimates of the effective patient dose for selected cardiac CT protocols with 16-slice and 64-slice CT systems, using the Siemens SOMATOM Sensation 16 and Sensation 64 scanners as representative examples. The effective patient dose for the standard protocols recommended by the manufacturer was calculated with WinDose (Kalender 1999). The scan protocols included are ECG-triggered coronary calcium quantification, ECG-gated coronary calcium quantification, and ECG-gated coronary CT angiography. The scan range used is 12 cm for coronary calcium quantification and 10 cm for coronary CT angiography. The scan parameters recommended by the manufacturer are listed in Table 4.2. For sequential scans, the mAs values are based on the slice exposure times for an axial scan that is the partial-scan time. For spiral

Table 4.2. Scan protocols used for calculation of the effective patient dose

	ECG-triggered calcium scoring				ECG-gated calcium scoring				ECG-gated cardiac/coronary CT angiography			
	Sensation 16		Sensation 64		Sensation 16		Sensation 64		Sensation 16		Sensation 64	
Collimation (mm)	12 × 1.5		30 × 0.6		16 × 1.5		24 × 1.2		16 × 0.75		32 × 0.6* (*64 × 0.6 by z-FFS)	
Reconstructed slice (mm)	3.0		3.0		3.0		3.0		0.75/1.0		0.6/0.75	
Rotation time (s)	0.42	0.375	0.375	0.33	0.42	0.375	0.375	0.33	0.42	0.375	0.375	0.33
kV	120	120	120	120	120	120	120	120	120	120	120	120
mA	100	111	111	126	100	113	109	115	370	413	435	467
mAs	30	30	30	30	42	42	41	38	155	155	163	154
Pitch	n.a.		n.a.		0.28	0.25	0.24	0.20	0.28	0.25	0.24	0.20
Table feed	18 mm per axial scan		18 mm per axial scan		16 mm/s	16 mm/s	13.2 mm/s	16 mm/s	8 mm/s	8 mm/s	12.3 mm/s	11.7 mm/s
Effective mAs	n.a.	n.a.	n.a.	n.a.	150	170	170	190	555	620	680	770
$(CTDI_w)_n$ (mGy/mAs)	0.072	0.072	0.072	0.072	0.070	0.070	0.067	0.067	0.078	0.078	0.077	0.077
$CTDI_w$ (mGy)	2.2	2.2	2.2	2.2	10.5	11.9	11.4	12.7	43.3	48.4	52.4	59.3

scans, effective mAs values are used; these have been already corrected for spiral pitch, i. e., they take into account the dose accumulation with decreasing spiral pitch (see above). Table 4.3 summarizes the CTDIw values for the 32-cm body-phantom and values of the effective patient dose for the recommended standard protocols, for the 16- and the 64-slice CT systems. In Table 4.3, the scan parameters listed in Table 4.2 were used.

For ECG-triggered coronary calcium quantification with sequential scanning, patient dose is about 0.5 mSv for males and 0.68 mSv for females. Coronary calcium quantification with ECG-gated spiral scanning that results in reduced interscan variability (Ohnesorge 2002) increases the patient dose to 2.3–2.8 mSv for males and 3.3–3.9 mSv for females. ECG-gated high-resolution coronary CT angiography using thin-slice spiral data acquisition and yielding both adequate visualization of the small and complex cardiac and coronary anatomy and detection and classification of coronary plaques requires a dose of 7.9–10.8 mSv for males and 11.1–15.2 mSv for females. Improved longitudinal resolution by thinner collimation directly translates into increased patient dose if the signal-to-noise ratio of the images is maintained.

A comparison of radiation doses for different CT scanner types requires that imaging parameters, such as slice width, tube voltage, tube current, and scanned volume, be taken into account. If the high spatial resolution of modern multi-slice CT systems achieved with sub-millimeter slice collimation is not required, decreased longitudinal spatial resolution with slice-widths between 1.5 and 3.0 mm can always be traded off with a correspondingly reduced patient dose.

The pitch values in the ECG-gated multi-slice spiral CT protocols shown in Table 4.2 are selected such that the vast majority of patients can be scanned without significant protocol adjustments, including patients with low heart rates. Radiation exposure, however, can be reduced by increasing the pitch in patients with sufficiently high heart rates when respecting the constraint considerations given in Section 4.4.3 and in Figure 4.16. The radiation exposure is then reversed proportional to the pitch increase, as compared to the values presented in Tables 4.2 and 4.3.

Table 4.3. Values for the effective patient dose based on the scan protocols listed in Table 4.2

	ECG-triggered calcium scoring				ECG-gated calcium scoring				ECG-gated cardiac/coronary CT angiography			
	Sensation16		Sensation64		Sensation16		Sensation64		Sensation16		Sensation64	
Collimation (mm)	12 × 1.5		30 × 0.6		16 × 1.5		24 × 1.2		16 × 0.75		32 × 0.6 * (*64 × 0.6 by z-FFS)	
Rotation time (s)	0.42	0.375	0.375	0.33	0.42	0.375	0.375	0.33	0.42	0.375	0.375	0.33
$CTDI_w$ (mGy)	2.2	2.2	2.2	2.2	10.5	11.9	11.4	12.7	43.3	48.4	52.4	59.3
Scan range (mm)	120		120		120		120		100		100	
Effective patient dose (mSv), males without ECG-pulsing	0.5	0.5	0.5	0.5	2.3	2.6	2.5	2.8	7.9	8.9	9.6	10.8
Effective patient dose (mSv), females without ECG-pulsing	0.68	0.68	0.68	0.68	3.2	3.7	3.5	3.9	11.1	12.4	13.5	15.2
Effective patient dose (mSv), males with ECG-pulsing	n.a.	n.a.	n.a.	n.a.	1.2–1.6	1.3–1.8	1.3–1.8	1.4–2.0	4.0–5.5	4.5–6.2	4.8–6.7	5.4–7.6
Effective patient dose (mSv), female with ECG-pulsing	n.a.	n.a.	n.a.	n.a.	1.6–2.2	1.9–2.6	1.8–2.5	2.0–2.7	5.6–7.8	6.2–8.7	6.8–9.4	7.6–10.6

4.6.3 Exposure Reduction with ECG-Gated Tube-Current Modulation

The relatively high radiation exposure for ECG-gated multi-slice spiral imaging of the heart is caused by continuous X-ray exposure and data acquisition at low and highly overlapping spiral pitch (pitch << number of slices). The low spiral pitch is a consequence of the phase-consistent coverage of the heart volume in specific phases of the cardiac cycle. However, if the spiral pitch is limited such that one phase can be covered consistently, all other phases of the cardiac cycle can be covered as well. If reconstruction in different cardiac phases is not needed and instead only a very limited interval (i.e., diastolic phase) in the cardiac cycle is targeted during reconstruction, a significant portion of the acquired data and radiation exposure is redundant.

Prospective ECG triggering combined with "step-and-shoot" acquisition of axial slices has the benefit of smaller patient dose compared to ECG-gated spiral scanning, since scan data are acquired in the previously selected heart phases only. It does, however, not provide continuous volume coverage with overlapping slices and misregistration of anatomical details cannot be avoided. Furthermore, reconstruction of images in different phases of the cardiac cycle for functional evaluation is not possible. Since ECG-triggered axial scanning depends on a reliable prediction of the patient's next RR-interval based on the mean of the preceding RR-intervals, the method encounters its limitations for patients with severe arrhythmia. To maintain the benefits of ECG-gated spiral CT but reduce patient dose ECG-controlled dose modulation has been developed. On-line reduction of the tube output in each cardiac cycle during phases that are of less importance for ECG-gated reconstruction has a high potential for exposure reduction. The nominal tube output is only required during those phases of the cardiac cycle that will be reconstructed. During ECG-gated tube-current modulation, the tube output is modulated on-line with prospective ECG control (Ohnesorge 2000b, Jacobs 2002, Poll 2002), and commonly used ECG-gated reconstruction algorithms can be further used unchanged. Within every cardiac cycle, tube output is raised to the nominal level during a limited interval in a pre-selected phase (usually the diastolic phase) in which the data are most likely to be reconstructed with thin slices and a high signal-to-noise ratio needs to be maintained. During the remaining part of the cardiac cycle, the tube output can be reduced by about 80% by a corresponding decrease of the tube current $mA_{min} = 0.2\ mA_{max}$ (Fig. 4.46). Thus, continuous volume reconstruction is still possible in all phases of the cardiac cycle. In particular, functional imaging is still feasible, as it does not require thin slice reconstruction. For imaging during phases of reduced tube output, an appropriate signal-to-noise ratio can be maintained by primary or secondary reconstruction of thicker slices. The position of the windows of nominal tube output within the heart cycles needs to be defined prior to the scan in relation to the phase targeted for reconstruction.

The width of the time interval ΔT_N with nominal tube output during diastole has to be selected such that patient-individual shifting of the ECG gating interval is still possible to obtain the best possible image quality. Additionally, a well-defined overlap of ΔT_N with the window of temporal resolution (i.e., 165–250 ms) can compensate for inconsistent prospectively ECG-controlled timing of nominal tube output due to changes in heart rate during the scan. In addition, an extended length of the temporal window with nominal tube output allows for high-resolution reconstruction within an extended duration during the cardiac cycle; this may be useful for optimization of image quality. An appropriate trade-off of exposure reduction and ECG gating flexibility can be achieved with the selection of $\Delta T_N = 400$ ms. Shorter $\Delta T_N = 300$ ms for further exposure reduction may be possible for scanners with very fast rotation times (≥0.37 s). However, the possibility to reconstruct high-resolution images within an extended range of the cardiac cycle is then limited. The relative exposure reduction with ECG-controlled tube-current modulation as a function of heart rate is shown in Figure 4.47. For normal heart rates between 50 and 90 bpm, the exposure is reduced by 35–50% for $\Delta T_N =$ 400 ms and by 45–60% for $\Delta T_N = 300$ ms. Radiation exposure savings are maximized for low heart rates, as the total time with low tube output during the scan is high. For increasing heart rates, the relative reduction decreases, as the time intervals of low tube output

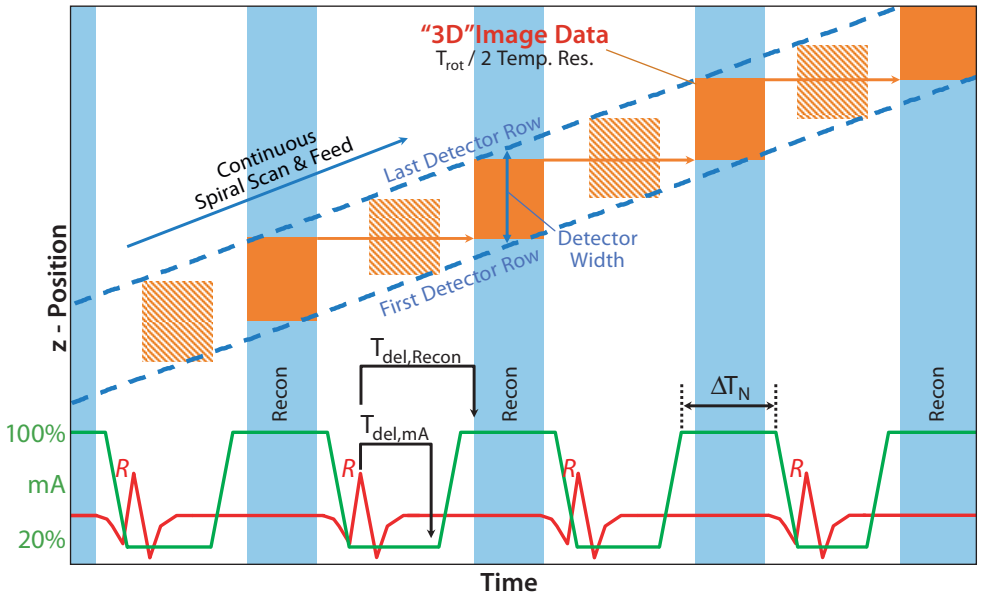

Fig. 4.46. Retrospectively ECG-gated 4-slice spiral scanning with prospectively ECG-controlled tube-current modulation for reduced radiation exposure. Tube current is at a nominal value (time interval ΔT_N) during diastole and is reduced by 80% during phases of high cardiac motion

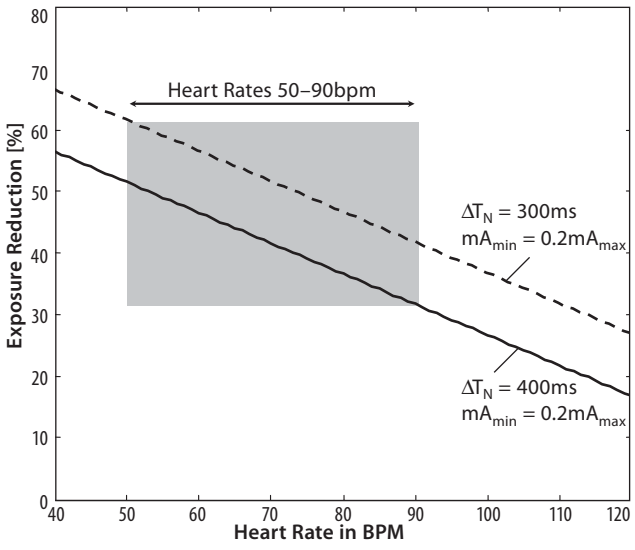

Fig. 4.47. Exposure reduction with ECG-controlled tube-current modulation dependent on heart rate for different time intervals ΔT_N of nominal tube output. A 35–55% reduction of exposure can be achieved for regular heart rates between 50 and 90 bpm using ΔT_N = 400 ms

are shorter. However, for very high heart rates, the selection of a higher spiral pitch can decrease exposure via shorter scan time as compared to low heart rates. Figure 4.48 directly compares two consecutive scans for quantification of coronary calcification in the same patient. The scans were performed without and with ECG-controlled tube output modulation, and equivalent reconstructions were carried out in the diastolic phase. For the patient with a stable heart rate between 58 and 61 bpm, an exposure reduction of 51% could be achieved with the same image and diagnostic qualities of the clinical result. An example for a CT angiography scan of the heart and coronary arteries using ECG-controlled tube-current modulation is shown in Figure 4.49. High signal-to-noise ratio is available for reconstruction during diastole with thin sections and high resolution. Reconstruction during systole for functional information shows lower signal-to-noise ratio; however, diagnostically sufficient image quality can be achieved with secondary multi-planar reformation (MPR) reconstruction. For the patient with a stable heart rate

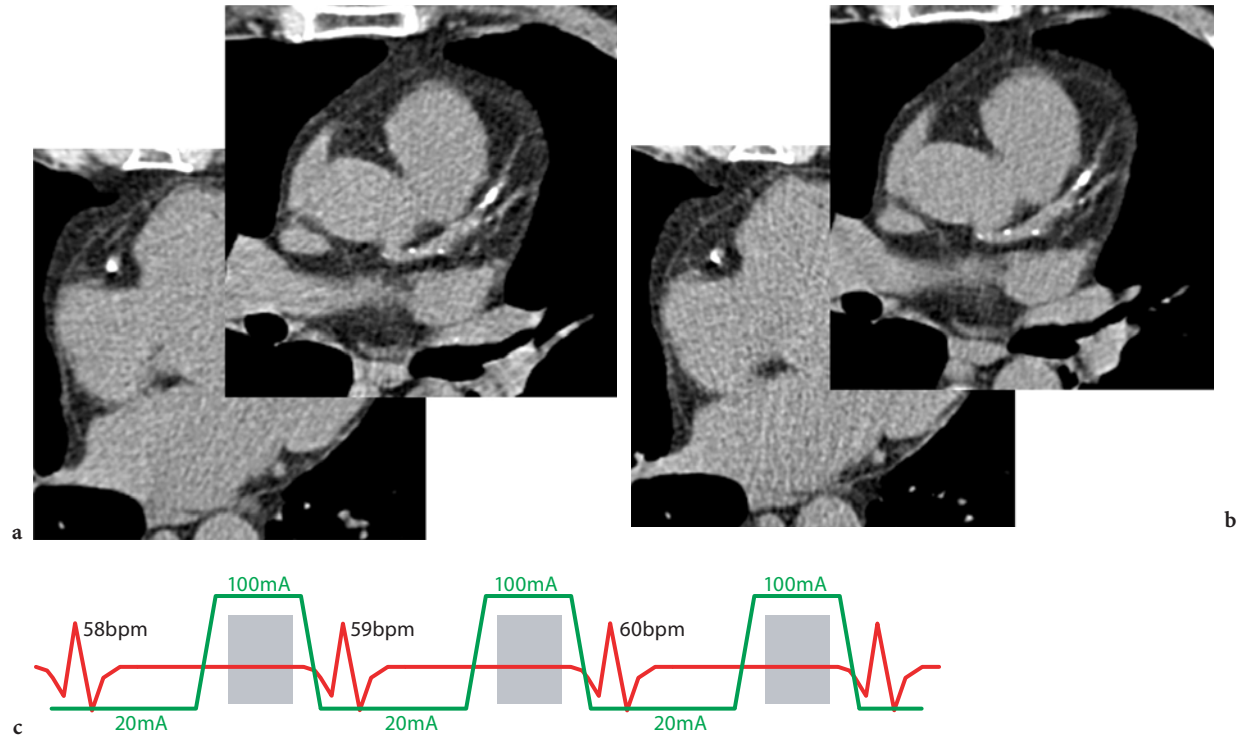

Fig. 4.48a–c. Case example of two repeated ECG-gated spiral scans of the same patient using a 4-slice CT scanner at 0.5-s rotation time and 4 × 2.5-mm collimation for imaging calcified plaques in the coronary arteries by applying ECG-controlled tube-current modulation. The patient showed stable sinus rhythm at heart rate 59 bpm during both scans. Calcifications in the left anterior descending and right coronary arteries that were identified with the first scan (**a**) can be accurately reproduced with the second scan (**b**). By ECG-controlled modulation of the tube current between 100 mA during diastole and 20 mA during systole (**c**), the amount of radiation can be reduced by 51% without compromising the signal-to-noise ratio for 59 bpm average heart rate. (Images courtesy of Klinikum Grosshadern, Munich, Germany)

between 74 and 77 bpm, the exposure reduction with ECG-gated tube-current modulation was about 37%. Clinical studies based on patients separated in two groups with similar patient parameters (i.e., patient size, heart rate variations, median heart rates) have demonstrated dose reductions of 40–50% in male and female patients without remarkable influence on image noise and image quality by using ECG-controlled tube-current modulation (Jakobs 2002).

Where available, this technique should be used for all patients with reasonably steady heart rates (Trabold 2003). However, if substantial arrhythmia is expected during the scan, prospective control of the tube-current modulation and retrospective positioning of the reconstruction intervals may not match and ECG-controlled tube-current modulation may not be adequately applied. To allow for more reliable use of ECG-controlled tube-current modulation in patients with irregular heart rates, new developments are under way that employ intelligent ECG analysis algorithms that detect extrasystolic beats in real time and disenable or adjust the temporal window for tube-current reduction in the affected heart beats (Fig. 4.50).

4.6.4 Optimization for Different Patient Sizes

In both ECG-triggered sequential scanning and ECG-gated spiral scanning, adaptation of the dose to patient size and weight is an important potential for

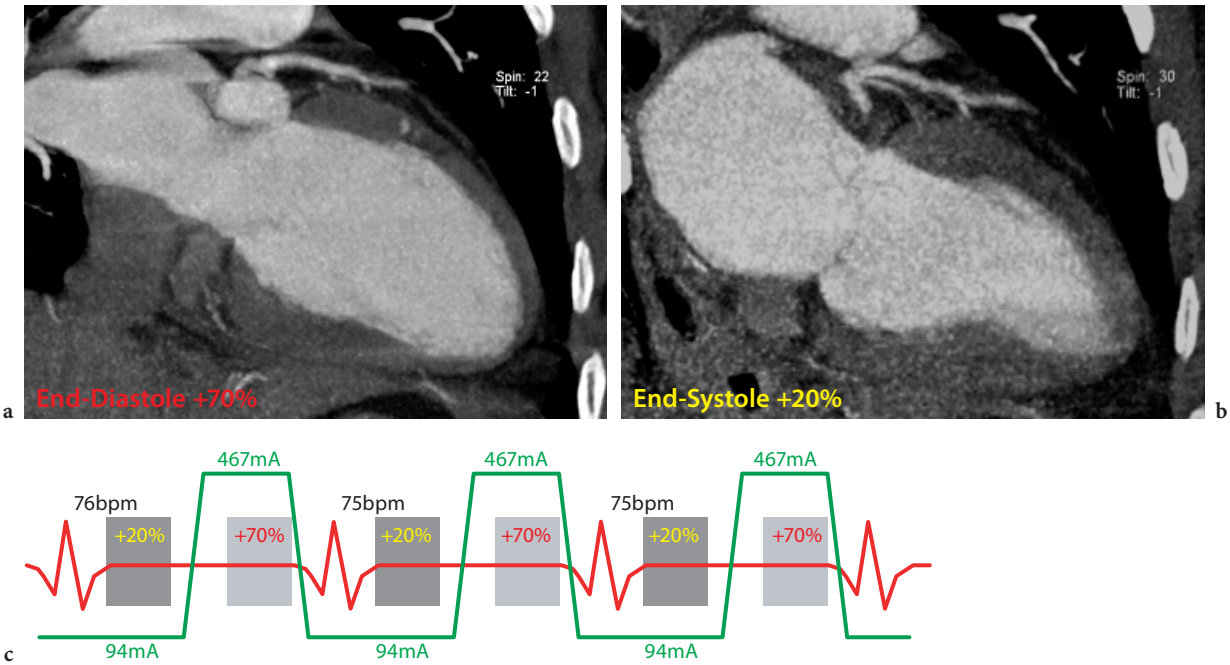

Fig. 4.49a–c. Example of a coronary CT angiography examination using a 64-slice CT scanner with 64 × 0.6-mm slices, 0.33-s rotation time, and ECG-controlled dose modulation. **a** End-diastolic image with full dose, reconstructed at 70% of the cardiac cycle; **b** end-systolic image with reduced dose, reconstructed at 20% of the cardiac cycle; **c** The ECG signal of the patient shows a stable heart rate between 74 and 77 bpm. Although the signal-to-noise ratio of the end-systolic image is reduced, it is considered adequate for functional evaluation. (Images courtesy of University of Erlangen, Germany)

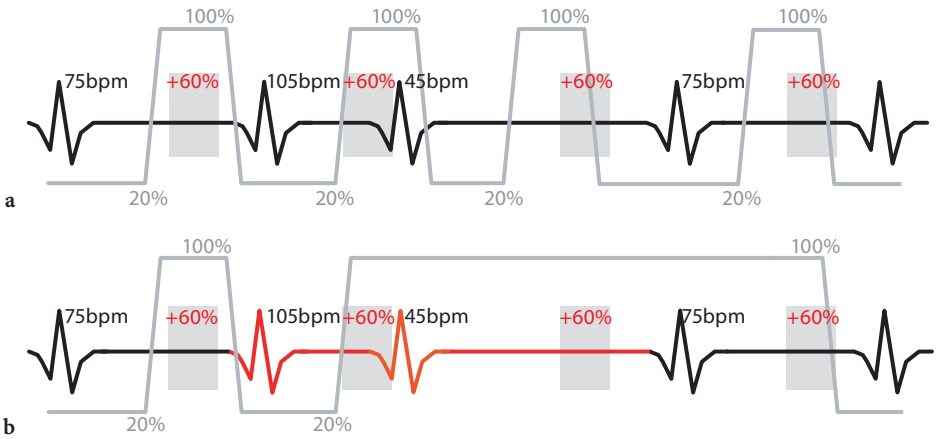

Fig. 4.50a, b. Automatic detection of extra-systolic heart beats during ECG-controlled tube-current modulation in a patient with a regular heart rate of 75 bpm. **a** An extra-systolic heart beat may lead to a mismatch in several consecutive heart beats of the temporal window with maximum tube output and desired cardiac phase for high-resolution image reconstruction. **b** If an extra-systolic heart beat is detected, the reduction of tube current can be disenabled during the affected heart beats and image quality can be maintained throughout the entire scan

dose reduction. For quantification of coronary calcifications, a reduction of the mean effective patient dose by 11.8% for males and 24.8% for females in a group of 50 patients was demonstrated by individual body-weight-adapted tube-current settings (Mahnken 2003). For cardiac and coronary CT angiography, a similar potential for radiation dose reduction has been reported (Jung 2003). The International Consortium of Standardization in Cardiac CT, a group of scientists, physicians, and CT manufacturers, has published recommendations to generate more accurate and calibrated results for coronary artery calcification independent of the scanner and of patient size. The researchers used an anthropomorphic calibration phantom with fixed amounts of calcium to derive dose recommendations for small, medium-sized, and large patients. The anthropomorphic calibration phantom consisted of tissue-, water- and bone-equivalent materials (QRM, Quality Assurance in Radiology and Medicine GmbH, Möhrendorf, Germany) and is shown in Figure 4.51 (Ulzheimer 2003). To account for different patient sizes, the original phantom can be used with up to two additional attenuation rings. The three categories for patient size are defined as small: < 32.0-cm lateral thickness, medium: 32.0- to 38.0-cm lateral thickness, and large: > 38.0-cm lateral thickness. An A/P localizer image (topogram, scout view) is used to determine the lateral thickness, which is measured from skin-to-skin, at the level of the proximal ascending aorta. Target noise levels of 20 HU for small and medium-sized patients and 23 HU for large patients in the corresponding calibration phantom are proposed. For ECG-gated spiral scanning of coronary artery calcification using a 16-slice CT scanner with 16 × 1.5-mm collimation, 0.42-s rotation time, and 120 kV, the following effective mAs values are feasible: small = 80–85 effective mAs, medium = 200–240 effective mAs, and large = 450–500 effective mAs. Similar relations can be found for high-resolution and cardiac coronary CT angiography protocols in which target noise levels of 15–20 HU with thin-slice reconstruction of 1 mm and below need to be achieved. The above example demonstrates the high potential for dose reduction, especially in medium-size and small patients, for coronary calcium quantification as well as cardiac and coronary CTA imaging protocols. In some modern CT scanners, the mAs value applied during an ECG-gated spiral scan can be automatically adapted to the average size of the patient (e.g., CARE Dose4D, Siemens, Forchheim, Germany).

4.6.5 Optimization of Contrast-to-Noise Ratio

Another means to reduce the radiation dose is to adapt the X-ray tube voltage to the intended application. Typically, 120 kV are used for quantification of coronary calcifications and for coronary CT angiography. In these two applications, however, the contrast-to-noise ratio for fixed patient dose can be increased by decreasing the X-ray tube voltage. As a consequence, to obtain a desired contrast-to-noise ratio, the patient dose can potentially be reduced by choosing lower kV settings of 80 or 100 kV. The potential for dose saving is more pronounced for small and medium-sized patients. Phantom measurements using small tubes filled with diluted contrast agent embedded in Lucite phantoms with different diameters (Schaller 2001) were used to demonstrate the potential to increase contrast and reduce dose in general vascular and cardiac CT angiography examinations in small and medium-sized patients when using 100 kV. Initial clinical experiences have confirmed this finding in patients weighing up to 90 kg (Fig. 4.52). Other studies (Jacobs 2003) compared ECG-gated spiral scan protocols using 120 and 80 kV for the quantification of coronary calcium. An 80-kV scan protocol was used in combination with ECG-controlled tube-current modulation, resulting in a significantly lower patient radiation exposure (0.72 mSv for 80 kV compared to 2.04 mSv for 120 kV). CTDI phantom measurements revealed a 65% reduction of radiation dose with the 80-kV protocol. In this study, the 80-kV protocol led to a significant reduction in radiation exposure during multi-slice CT coronary artery calcium screening, but did not affect the detection and quantification of coronary artery calcification. However, it should be noted that the maximum X-ray tube current available at 80 kV is generally not sufficient to scan larger patients and an increase in the tube voltage is required. In such patients, use of the 100-kV tube voltage may be a good compromise.

Fig. 4.51. Anthropomorphic calibration phantom (QRM Quality Assurance in Radiology and Medicine GmbH, Möhrendorf, Germany) recommended by the International Consortium for Standardization in Cardiac CT. The original phantom can be used with up to two additional attenuation rings to simulate small, medium-sized, and large patients

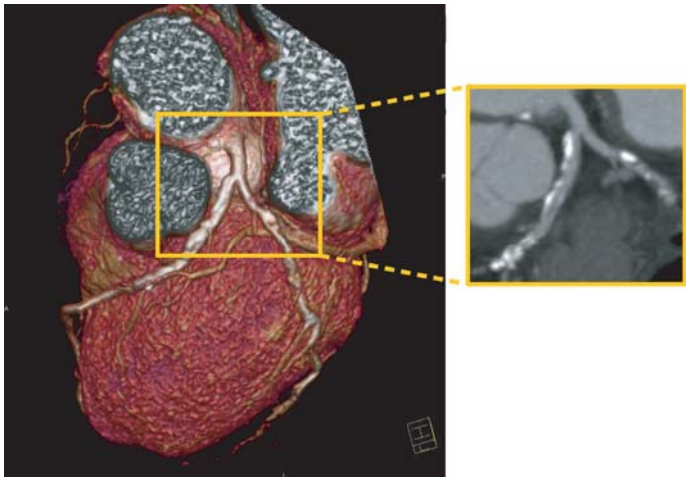

Fig. 4.52. Case example of a CT angiographic examination of the coronary arteries in a patient weighing 82 kg . The image was obtained on a 64-slice CT scanner with 64 × 0.6-mm slice acquisition and a 0.33-s rotation time. To reduce radiation exposure, 100-kV tube voltage and ECG-controlled tube-current modulation were used. The use of 100 kV instead of 120 kV reduces radiation exposure by about 33%, from 6.8 to 5.0 mSv. The high contrast-to-noise ratio allows visualization of the entire 3D cardiac and coronary anatomy and of atherosclerotic plaques in the left anterior descending and circumflex coronary arteries using an overlay of VRT and MIP displays. (Images courtesy of Medical University of South Carolina, Charleston, USA)

References

Achenbach S, Ropers D, Holle J, Muschiol G, Daniel WG, Moshage W (2000a). In-plane coronary arterial motion velocity: measurement with electron-beam CT. Radiology 216:457–463.

Bahner ML, Böse J, Lutz A, Wallschläger H, Regn J, van Kaick G. (1999). Retrospectively ECG-gated spiral CT of the heart and lung. Eur Radiol 9:106–109

Becker CR, Knez A, Jakobs TF, Becker A, Schöpf UJ, Brüning R, Haberl R, Reiser MF (1999). Detection and quantification of coronary artery calcification with electron-beam and conventional CT. Eur Radiol 9:620–624

Brenner D, Elliston C, Hall E, Berdon W (2001). Estimated risks of radiation-induced fatal cancer from pediatric CT. AJR 176:289 –296

Bruder H, Stierstorfer K, Ohnesorge B, Schaller S, Flohr T (2001). Segmented cardiac volume reconstruction – a novel reconstruction scheme for multi-slice cardiac CT. The Sixth International Meeting on Fully Three-Dimensional Image Reconstruction in Radiology and Nuclear Medicine, Pacific Grove, 2001, 161–164

Bruder H, Stierstorfer K, Ohnesorge B, Schaller S, Flohr T (2002). A novel reconstruction scheme for cardiac volume imaging with MSCT providing cone correction. SPIE Transactions on Medical Imaging

Flohr T, Schaller S, Ohnesorge B, Kopp AF, Klingenbeck-Regn K (1999). Evaluation of image artifacts in multi-slice spiral CT (abstract). Radiology 213(P):317

Flohr T, Ohnesorge B (2001). Heart-rate adaptive optimiza-

tion of spatial and temporal resolution for ECG-gated multi-slice spiral CT of the heart. J Comp Assist T 25(6): 907–923

Flohr T, Prokop M, Schöpf, Kopp A, Becker C, Schaller S, White R, Ohnesorge B (2002). A new ECG-gated multi-slice spiral CT scan and reconstruction technique with extended volume coverage for cardio-thoracic applications. Eur Radiol 12:1527–1532

Flohr T, Ohnesorge B, Bruder H, et al (2003). Image reconstruction and performance evaluation for ECG-gated spiral scanning with a 16-slice CT system. Med Phys 30(10):2650–2662

Flohr TG, Schöpf UJ, Küttner A, Halliburton SS, Bruder H, Süß C, Schmidt B, Hofmann L, Yucel EK, Schaller S, Ohnesorge BM (2003). Advances in cardiac multi-slice CT-imaging with 16-slice CT-systems. Acad Radiol 10: 1050–1058

Fischbach R (2004). Clinical evaluation of Kymogram-gated cardiac image reconstruction with 16-slice CT (abstract). Radiology 231(P)

Hong C, Becker,CR, Huber A, Schöpf UJ, Ohnesorge B, Knez A, Brüning R, Reiser MF (2001a). ECG-gated reconstructed multi-detector row CT coronary angiography: effect of varying trigger delay on image quality. Radiology 220:712–717

Hu H (1999). Multi-slice helical CT: scan and reconstruction. Med Phys 26 (1) 5–18

Hu H, Pan T, Shen Y (2000). Multi-slice helical CT: image temporal resolution. IEEE Transactions on Medical Imaging vol 19(5):384–390

Jakobs T F, Becker C R, Ohnesorge B, Flohr T, Suess C, Schoepf U J, Reiser MF (2002). Multi-slice helical CT of the heart with retrospective ECG-gating: reduction of radiation exposure by ECG-controlled tube current modulation. Eur Radiol 12: 1081–1086

Jakobs T F, Wintersperger B J, Herzog P, Flohr T, Suess C, Knez A, Reiser MF, Becker C R (2003). Ultra-low-dose coronary artery calcium screening using multi-slice CT with retrospective ECG-gating. Eur Radiol 13: 1923–1930

Jung B, Mahnken A H, Stargardt A, Simon J, Flohr T G, Schaller S, Koos A, Guenther R W, Wildberger J E (2003). Individually weight-adapted examination protocol in retrospectively ECG-gated MSCT of the heart. Eur Radiol 13: 2560–2566

Kachelrieß M, Kalender WA (1998). Electrocardiogram-correlated image reconstruction from subsecond spiral computed tomography scans of the heart. Med Phys 25: 2417–2431

Kachelrieß M, Ulzheimer S, Kalender WA (2000). ECG-correlated image reconstruction from subsecond multi-row spiral CT scans of the heart. Med Phys 27:1881–1902

Kachelrieß M, Sennst DA, Maxlmoser W, Kalender WA (2002). Kymogram detection and kymogram-correlated image reconstruction from subsecond spiral computed tomography scans of the heart. Med Phys 29(7):1489–1503

Kak AC, Slaney M (1998). Principles of computerized tomographic imaging. IEEE Press New York, p. 77–86

Kalender W (1995). Thin-section three-dimensional spiral CT: is isotropic imaging possible? Radiology 197:578–580

Kalender W A, Schmidt B, Zankl M, Schmidt M (1999). A PC Program for estimating organ dose and effective dose values in computed tomography. Eur Radiol 9:555–562

Klingenbeck K, Schaller S, Flohr T, Ohnesorge B, Kopp AF, Baum U (1999). Subsecond multi-slice computed tomography: basics and applications. Eur J Radiol 31(2):110–124

Kopp AF, Küttner A, Heuschmid M; Schröder S, Ohnesorge B, Claussen CD (2002). Multidetector-row CT cardiac imaging with 4 and 16 slices for coronary CTA and imaging of atherosclerotic plaques. Eur Radiol 12(Suppl.2):S17-S24

Loubeyre P, Angelie E, Grozel F, Abidi H, Minh VA (1997). Spiral CT artifact that simulates aortic dissection: image reconstruction with use of 180 degrees and 360 degrees linear-interpolation algorithms. Radiology 205:153–157

Mahnken A, Jung B, Wildberger J, et al (2003). Patient-size adapted scan protocols in coronary calcium scoring with multi-slice CT. Eu Radiol 13

McCollough C (2003). Patient dose in cardiac computed tomography. Herz 28:1–6

Mochizuki T, Murage K, Higashino H et al (2000). Two and three dimensional CT ventriculography: a new application of helical CT. AJR 174: 203–208

Morin R, Gerber T, McCollough C (2003). Radiation dose in computed tomography of the heart. Circulation 107:917–922

Nickoloff E, Alderson P (2001). Radiation exposure to patients from CT: reality, public perception, and policy. AJR 177:285–287

Ohnesorge B, Flohr T, Rienmüller R (1999). Procedure to determine the reconstruction window in CT examinations of the heart. European Patent Office

Ohnesorge B, Flohr T, Becker C R, Kopp A F, Knez A Baum U, Klingenbeck-Regn K Reiser MF (2000a). Cardiac imaging by means of electrocardiographically gated multisection spiral CT: initial experience. Radiology 217:564–571

Ohnesorge B, Flohr T, Becker CR, Kopp AF, Knez A, Reiser MF (2000b). Dose evaluation and dose reduction strategies for ECG-gated multi-slice spiral CT of the heart (Abstract). Radiology 217(P):487

Ohnesorge B, Flohr T, Becker CR, Knez A, Schöpf U, Klingenbeck K, Brüning R, Reiser MF (2001). Technical Aspects and Applications of Fast Multislice Cardiac CT. Medical Radiology, Diagnostic Imaging and Radiation Oncology, Multislice CT. Springer Verlag Berlin, Heidelberg. Chapter 15:121–130

Parker DL (1982). Optimal short scan convolution reconstruction for fanbeam CT. Med Phys 9(2):254–257

Poll L, Cohnen M, Brachten S, Ewen K, Modder U (2002). Dose reduction in multidetector row CT of the heart by use of ECG-controlled tube current modulation ("ECG-Pulsing"): phantom measurements. Rofo Fortschr Geb Rontgenstr Neuen Bildgeb Verfahr 174:1500–5

Sato Y, Kanmatsuse K, Inoue F, et al (2003). Noninvasive coronary artery imaging by multi-slice spiral computed tomography – a novel approach for a retrospectively ECG-gated reconstruction technique. Circ J 67: 107–111

Schaller S, Flohr T, Klingenbeck K, Krause J, Fuchs T, Kalender WA (2000). Spiral interpolation algorithm for multi-slice spiral CT. Part I: Theory. IEEE Transactions on Medical Imaging, 19(9):822–834

Schaller S, Niethammer M U, Chen X, Klotz E, Wildberger J E, Flohr T (2001). Comparison of signal-to-noise and dose values at different tube voltages for protocol optimization in pediatric CT (Abstract). Radiology 223(P), 366

Schöpf UJ, Helmberger T, Holzknecht N, Kang DS, Brüning RD, Aydemir S, Becker CR, Mühling O, Knez A, Haberl R, Reiser MF (2000). Segmental and subsegmental pulmonary arteries: evaluation with electron beam CT versus spiral CT. Radiology 214:433–439

Stanford W, Rumberger J (1992) Ultrafast computed tomography in cardiac imaging: principles and practise. Futura Publishing Company New York

Stehling MK, Turner R, Mansfield P (1991). Echo-planar imaging: magnetic resonance imaging in a fraction of a second. Science 254: 43–50

Taguchi K, Aradate H (1998). Algorithm for image reconstruction in multi-slice helical CT. Med Phys 25 (4):550–561

Trabold T, Buchgeister M, Küttner A, Heuschmid M, Kopp AF, Schröder S, Claussen CD (2003). Estimation of radiation exposure in 16-detector row computed tomography of the heart with retrospective ECG-gating. RöFo 175:1051–1055

Ulzheimer S, Kalender W A (2003). Assessment of calcium scoring performance in cardiac computed tomography. Eur Radiol 13(3): 484–97

Clinical Examination Protocols with 4- to 64-Slice CT

5

Bernd Ohnesorge

Contents

5.1 **Quantification of Coronary Artery Calcification** *127*
5.2 **CT Angiography of the Cardiac Anatomy and Coronary Arteries** *133*
5.3 **Cardiac Function Imaging** *141*
5.4 **Cardiothoracic Examination Protocols** *144*
References *148*

This chapter gives an overview of the scan protocols for the main cardiac imaging applications and for the various multi-slice CT technology levels that are in regular clinical use today. More protocols that are used in specific patient populations or under research conditions can be also found in Chap. 7.

The first multi-slice cardiac CT imaging protocols were already developed in 1999 (Ohnesorge 2000) for a broad range of clinical applications based on the first available 4-slice CT scanners. These represent the minimum technology level that is required for basic cardiac applications, such as coronary calcium scoring and display of the larger cardiac anatomy. More advanced applications, such as coronary artery diagnosis and assessment of cardiac function, have become feasible with the more recent introduction of 16- to 64-slice CT scanners with increased spatial and temporal resolution and shorter breath-hold times (Lawler 2004, Schoepf 2004, Schoenhagen 2004, Ohnesorge 2005, Flohr 2005, Gaspar 2005, Schoepf 2006, Lardo 2006). The protocols presented in this chapter are designed to provide a suitable balance of best possible clinical outcome, on the one hand, and minimum possible radiation exposure, on the other. The given parameters apply for a wide range of CT scanners from all major manufacturers and also indicate the minimum technology level needed for a certain clinical application. Where feasible, different protocol options using prospective ECG triggering or retrospective ECG gating are introduced, and the advantages and disadvantages discussed. For contrast-enhanced applications, we provide suggestions for contrast-agent protocols with optimized timing of vascular and anatomical enhancement. The discussion of clinical indications and evaluation techniques is not the subject of this chapter but of other chapters in this book.

5.1 Quantification of Coronary Artery Calcification

The quantification of coronary artery calcification by multi-slice CT is a growing clinical application, as it has been included as a useful test in the guidelines of several leading societies (Mieres 2005, de Backer 2005, Silber 2005, Clouse 2006). The reliable and reproducible quantification of coronary artery calcification requires a multi-slice CT scanner with simultaneous acquisition of at least four slices. Reference data bases for coronary calcification measured by multi-slice CT have been established based on 4-slice CT scanners (Schmermund 2002). Several validation studies have shown the comparability of results obtained with EBCT scanners and those generated by a 4-slice CT scanner with 0.5-s rotation time (Becker 2001, Kopp 2002, Nasir 2003). Despite shortcomings in temporal resolution, superior results compared to EBCT could be demonstrated in a considerable number of patients (Fig. 5.1). Protocols with

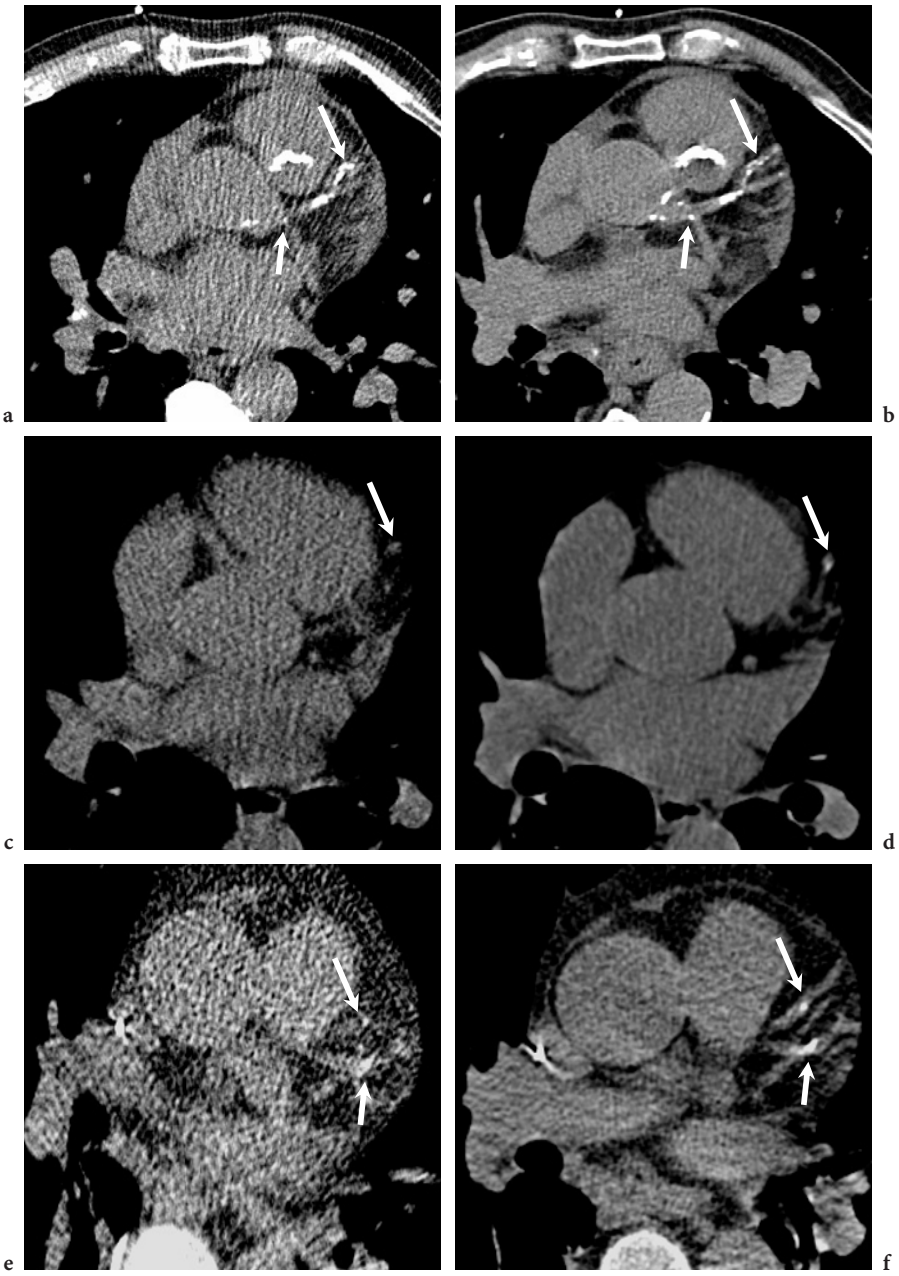

Fig. 5.1a–f. Axial images for quantification of coronary calcification. The images were obtained in the same patients with EBCT and 4-slice CT. EBCT scans were acquired using 3-mm slices and 100-ms temporal resolution, and 4-slice CT scans using 2.5-mm collimation, 0.5-s rotation time, and 250-ms temporal resolution. For both scanners, images were obtained using prospectively ECG-triggered acquisition. Calcified lesions can be detected without motion artifacts with 4-slice CT despite reduced temporal resolution. EBCT acquisitions (**a**, **c**, **e**) show lower signal-to-noise ratio and less spatial resolution than the corresponding 4-slice CT acquisitions (**b**, **d**, **f**) made with comparable radiation exposure. Small lesions are detected with higher sensitivity with 4-slice CT (**b** and **d**, *arrows*) than with EBCT (**a** and **c**, *arrows*). For obese patients, exposure can be increased with 4-slice CT to maintain diagnostic image quality in the detection of small lesions (**f**, *arrow*) whereas small lesions may be missed with EBCT due to noise levels that are too high (**e**, *arrow*). (Case studies courtesy of Klinikum Grosshadern, University of Munich, Germany)

comparable image-quality parameters were used to show that radiation exposure for coronary calcium measurement was equivalent with multi-slice CT and EBCT (Ulzheimer 2003). Reports stating that radiation exposure is substantially higher with multi-slice CT than with EBCT (Nasir 2003, Mieres 2005) were based on non-standardized and non-optimized multi-slice CT protocols.

In order to achieve the highest temporal resolution, the fastest available rotation time should always be used. Initial clinical experience demonstrated that scanners with 4- to 6 slices and a fastest rotation time of 0.5 to 0.6 s can provide adequate quality of results and can be routinely used. However, it was also demonstrated that 4-slice scanners with a fastest rotation time of 0.8 s do not meet the required standards in terms of detection accuracy and reproducibility due to the frequent presence of extensive motion artifacts (Goldin 2001). All multi-slice CT scanner generations with 4- or more slices can acquire data for coronary calcium quantification within comfortable breath-hold times. With the newest scanners, scan acquisition can be even accomplished in less than 10 s. Although the performance advantages of newer 16- to 64-slice CT scanners over 4- to 8-slice CT scanners may be limited when it comes to quantification of coronary artery calcification, the higher temporal resolution and the shorter breath-hold times still suggest an increased reproducibility of calcium measurements and increased detection accuracy of small calcifications. Modern 32- to 64-slice CT scanners provide up to 40-mm scan coverage per prospectively ECG-triggered acquisition; however, the full coverage is often not used for prospectively ECG-triggered scan protocols to avoid the presence of cone-beam artifacts. Retrospectively ECG-gated scan protocols, instead, can utilize the full available detector coverage, as cone-beam artifacts can be eliminated with special spiral reconstruction techniques.

Both prospectively ECG-triggered sequential scan protocols and retrospectively ECG-gated spiral scan and reconstruction protocols are in use for the quantification of coronary artery calcification (Tables 5.1, 5.2). The key advantage of prospectively ECG-triggered scan protocols is the lowest possible level of radiation exposure of less than 1 mSv due to the fact that the amount of scanned data is reduced to a minimum. However, retrospectively ECG-gated acquisition enables higher temporal resolution with

Table 5.1. Scan protocols for coronary calcium quantification with prospective ECG triggering

	4- to 6-slice CT	8- to 10-slice CT	16-Slice CT	32- to 40-slice CT	64-slice CT
Collimation (mm)	2.5–3.0	1.0–1.5	1.0–1.5	0.6[a], 1.0–1.25	0.6[a], 1.0–1.25
Slice width (mm)	2.5–3.0	2.5–3.0	2.5–3.0	2.4–3.0	2.4–3.0
Rotation time (s)	0.5–0.6	0.42–0.5	0.37–0.5	0.37–0.4	0.33–0.4
Temporal resolution (ms)	250–300	210–250	185–250	185–200	165–200
kV	120	120	120	120	120
mA	83–160	100–190	100–216	125–216	125–242
mAs (mA × T_{rot} × 2/3)	33–53	33–53	33–53	33–53	33–53
Table speed (mm/scan)	10–18	10–15	20–24	12[a], 28.8–40	18[a], 28.8–40
ECG trigger (% RR)	50	50	50	60	60
Reconstruction filter	Medium-sharp (B35f)[b]	Medium-sharp (B35f)[b]	Medium-sharp (B35f)[b]	Medium-sharp (B35f)[b]	Medium-sharp (B35f)[b]
Exposure (mSv)	0.7–1.1[c]	0.7–1.1[c]	0.5–0.8[c]	0.5–0.8[c]	0.5–0.8[c]
Scan direction	Craniocaudal	Craniocaudal	Craniocaudal	Craniocaudal	Craniocaudal
Scan time (s)	11–20[d]	16–20[d]	8–10[d]	17[a, d], 5–7[d]	11[a, d], 5–7[d]

[a] Special high-resolution protocol for SOMATOM Sensation 40 and 64, Siemens, Germany.
[b] Special nomenclature for reconstruction filters on Siemens SOMATOM CT scanners.
[c] Estimation for male patients and 12-cm scan range; for female patients, multiply by a factor of 1.4.
[d] Scan-time calculation for 12-cm scan range, assuming a heart rate of 70 bpm and scans in every other beat.

Table 5.2. Scan protocols for coronary calcium quantification with retrospective ECG gating

	4- to 6-slice CT	8- to 10-slice CT	16-slice CT	32- to 40-slice CT	64-slice CT
Collimation (mm)	2.0–2.5	1.0–1.5	1.0–1.5	1.0–1.25	1.0–1.25
Slice width (mm)	3.0	3.0	3.0	3.0	3.0
Slice increment (mm)	1.5	1.5	1.0	1.5	1.5
Rotation time (s)	0.5–0.6	0.42–0.5	0.37–0.5	0.37–0.4	0.33–0.4
Temporal resolution (ms)	250–300[a]	210–250[a]	185–250[a]	185–200[a]	165–200[a]
kV	120	120	120	120	120
mA	83–160	100–190	100–216	125–216	125–242
mAs (mA × T_{rot})	50–80	50–80	50–80	50–80	50–80
Effective mAs	125–267	143–285	143–320	200–400	200–400
Pitch	0.30–0.40	0.28–0.35	0.25–0.35	0.20–0.25	0.20–0.25
Table speed (mm/s)	6–8	6–10	10–16	16–22	16–22
ECG gating (% RR)	50	50	50	60	60
ECG dose modulation	Yes[b]	Yes[b]	Yes[b]	Yes[b]	Yes[b]
Reconstruction filter	Medium-sharp (B35f)[c]	Medium-sharp (B35f)[c]	Medium-sharp (B35f)[c]	Medium-sharp (B35f)[c]	Medium-sharp (B35f)[c]
Exposure (mSv)	1.6–2.2[d]	1.6–2.2[d]	1.4–1.9[d]	1.5–2.1[d]	1.5–2.1[d]
Scan direction	Craniocaudal	Craniocaudal	Craniocaudal	Craniocaudal	Craniocaudal
Scan time (s)	15–20[e]	12–20[e]	8–12[e]	6–8[e]	6–8[e]

[a] Temporal resolution based on single-segment algorithm can be increased with two or more segments.
[b] Recommended use of ECG dose modulation – if available for the multi-slice CT scanner being used.
[c] Special nomenclature for reconstruction filters on Siemens SOMATOM CT scanners.
[d] Estimation for a male patient with a heart rate of 70 bpm, 12-cm scan range; for a female patient, multiply by a factor of 1.4. It is assumed that ECG dose modulation is used (absence increases exposure by a factor of 1.5–2.0).
[e] Scan time calculation for 12-cm scan range

segmented reconstruction techniques, retrospective optimization of reconstruction phases, and the generation of overlapping slices (Figs. 5.2, 5.3). The higher-quality image data in combination with modern volumetric and mass-based quantification systems result in higher reproducibility of coronary calcium measurements (Ohnesorge 2002, Hong 2003, Moser 2004). With the use of ECG-controlled dose modulation, radiation exposure can be reduced to reasonably low levels, around 2 mSv (Jakobs 2002); nonetheless, this is still about two-fold higher than the level produced with prospectively ECG-triggered protocols. Scan times are quite comparable with both techniques in patients with normal heart rate; but if heart rates are below 60 bpm, scan times can increase substantially with prospective ECG triggering. The advantages and disadvantages of the two techniques suggest that prospectively ECG-triggered scan protocols are useful in asymptomatic patients at risk who present for initial assessment of coronary artery calcification. In asymptomatic patients at risk of developing coronary artery disease, asymptomatic patients with known presence of coronary artery calcification, and symptomatic patients with suspicion of coronary artery disease, retrospectively ECG-gated acquisition is the preferred choice.

Based on previous EBCT studies, a slice-width of 3.0 mm has been established as a standard for quantification of coronary calcification by CT (Agatston 1990, Callister 1998, O'Rouke 2000). Experimental studies have been conducted using thinner slices for better detection of smaller calcifications, but such protocols cannot yet be recom-

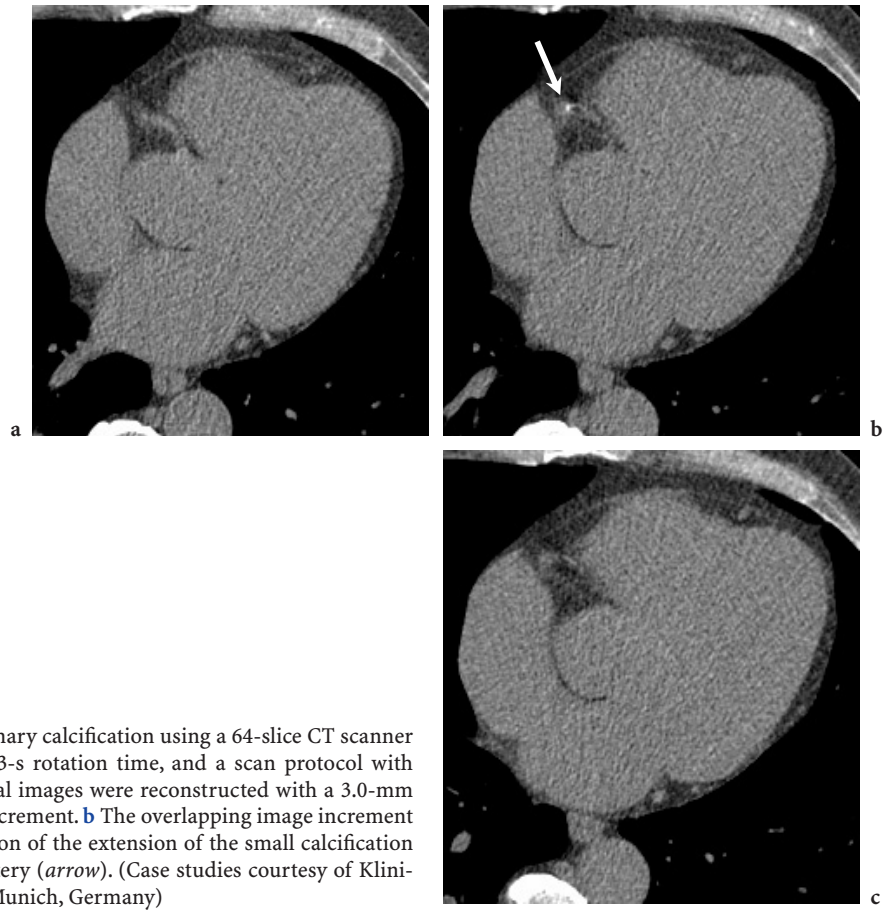

Fig. 5.2a–c. Quantification of coronary calcification using a 64-slice CT scanner with 1.2-mm collimation and 0.33-s rotation time, and a scan protocol with retrospective ECG gating. **a–c** Axial images were reconstructed with a 3.0-mm slice width and a 1.5-mm image increment. **b** The overlapping image increment allows for more accurate delineation of the extension of the small calcification in the proximal right coronary artery (*arrow*). (Case studies courtesy of Klinikum Grosshadern, University of Munich, Germany)

mended for clinical use due to the lack of standardization and the lack of comparability with clinical reference data bases (Hong 2003, Mühlenbruch 2005a). Therefore, all multi-slice CT scan protocols for coronary artery calcium measurement aim for an optimized selection of slice-collimation settings and image-reconstruction techniques to produce a reconstructed slice width that comes as close as possible to the standard of 3.0 mm. With prospectively ECG-triggered acquisition, the resulting slice width represents a multiple of the underlying collimated slice width as multiple collimated slices are combined during image reconstruction to thicker slices. In 4- to 6-slice CT scanners, the resulting slice width is usually equal to the collimated slice width. In CT scanners with 8-slices or more, the collimated slice width is usually less than 3.0 mm so that slices have to be combined during image reconstruction. Depending on the detector geometry, slice widths between 2.4 and 3.0 mm are generated from collimated slices of 1.0, 1.2, 1.25, and 1.5 mm, which are used in the currently available 8- to 64-slice CT scanners. In some special cases, the resulting slices are generated from a sub-millimeter collimation setting, which allows the reconstruction of well-defined 3.0-mm slices. If the slice width of the images that are used for calcium quantification differs from 3.0 mm, a correction factor (= 3.0 mm/slice width) has to be applied to semi-quantitative scores, such as the traditional Agatston score, that presume a slice width of 3.0 mm (Becker 2001, Kopp 2002). Spiral weighting algorithms that are applied during retrospectively ECG-gated image reconstruction enable the reconstruction of 3.0-mm slices indepen-

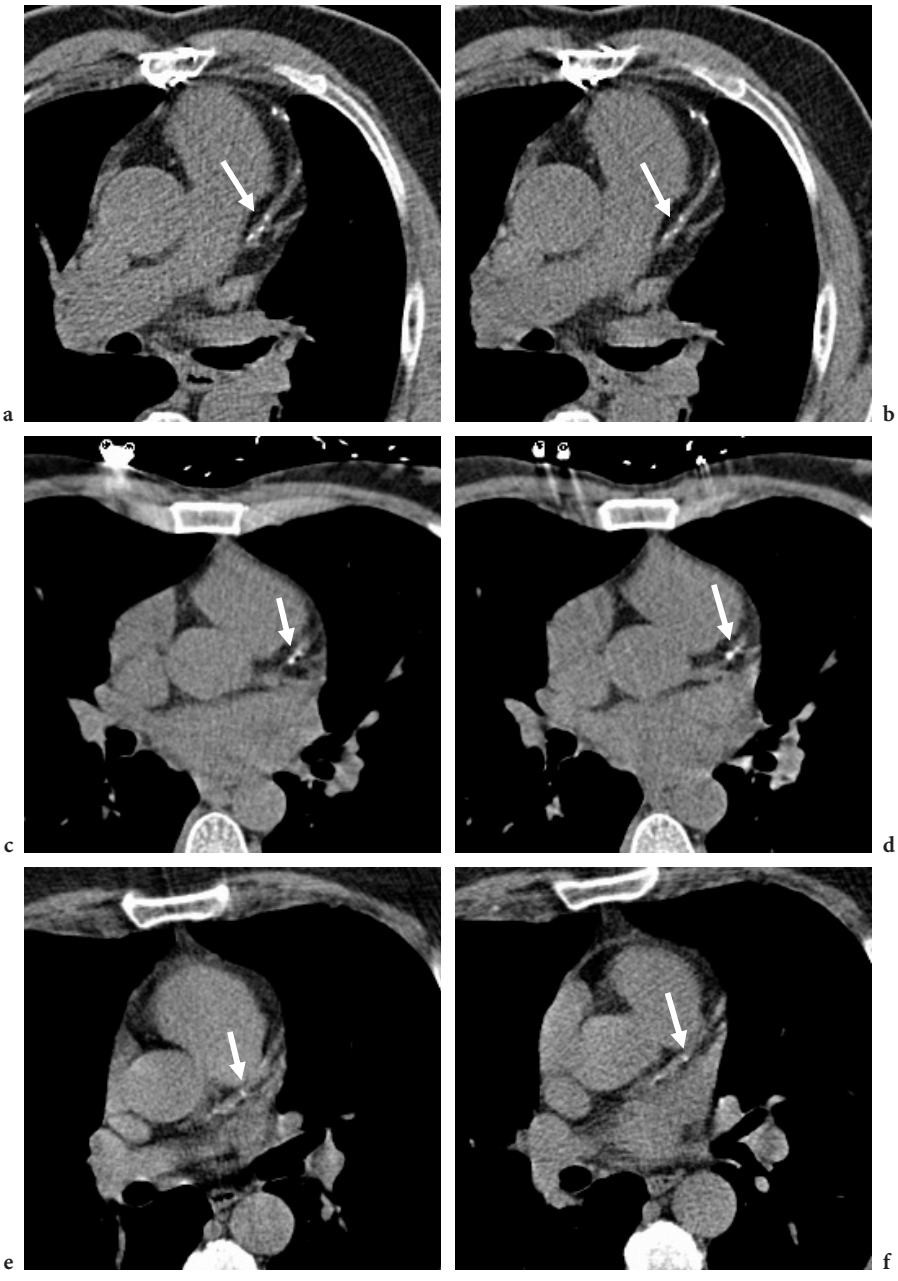

Fig. 5.3a–f. Representative case examples of repeat scan examinations for quantification of coronary calcification using 4-slice CT with 2.5-mm collimation, 0.5-s rotation time, and retrospectively ECG-gated spiral acquisition. Images were reconstructed with a 3.0-mm slice width and a 1.5-mm image increment. The score, location, and morphology of small calcified lesions can be accurately reproduced for a moderate heart rate of 63 bpm (**a** Agatston score 97, volume 83 mm^3, mass 20 mg; **b** Agatston score 110, volume 87 mm^3, mass 22 mg) and a higher heart rate of 96 bpm (**c** Agatston score 26, volume 34 mm^3, mass 5.5 mg; **d** Agatston score 29, volume 32 mm^3, mass 5.1 mg). For both examples, the interscan variability was less than 5%. Higher variability can be present for patients with very low total scores, high heart rates, and arrhythmic changes during the scan (**e** Agatston score 8, volume 12 mm^3, mass 2.0 mg; **f** Agatston score 13, volume 20 mm^3, mass 3.8 mg. However, calcifications can still be identified and reproduced in both scans. (Case studies courtesy of Klinikum Grosshadern, University of Munich, Germany)

dent of the collimated slice width. Normally, images are reconstructed at a distance of 1.5 mm (i.e., half of the reconstructed slice width) in order to maximize the volumetric information and optimize reproducibility of the coronary calcium measurements (Ohnesorge 2002).

As the quantification of coronary calcification is often applied in asymptomatic patients at risk or in patients with a low or intermediate likelihood of coronary artery disease, radiation exposure has to be kept at a minimum level. A kV setting of 120 kV has been established as a standard as it provides optimal contrast while avoiding blooming artifacts at low X-ray energy. In some scanners, 130 kV has to be used as alternative since 120 kV is not supported.

The mAs value is calculated from the applied mA value and the exposure time per slice and determines the signal-to-noise ratio in the axial image slice. In prospectively ECG-triggered acquisition, the exposure time per slice corresponds to two-thirds of the rotation time ($mAs = mA \times T_{rot} \times 2/3$), which equals the time of partial-scan acquisition during ECG-triggered acquisition. In retrospectively ECG-gated acquisition, most scanners use the rotation time T_{rot} as the exposure time per slice ($mAs = mA \times T_{rot}$). In addition, some scanners display an effective mAs value for retrospectively ECG-gated scan protocols that takes the relationship to pitch into consideration (effective $mAs = mA \times T_{rot}/pitch$). In normal patients weighing up to 90 kg, 33 mAs is used for prospective ECG triggering and 50 mAs for retrospective ECG gating. In large or obese patients weighing above 90 kg, up to 53 mAs can be used in prospective ECG triggering and up to 80 mAs in retrospective ECG gating in order to improve the detection accuracy of small calcium deposits (McCollough 2003). The mA levels have to be selected according to the present rotation time in order to achieve the required mAs. Subsequently, the radiation-exposure estimations given in (Tables 5.1 and 5.2) show a value range that accounts for the increased mAs in obese patients.

Prospectively ECG-triggered image acquisition or retrospectively ECG-gated image reconstruction should be targeted to mid-diastole, when the least amount of motion artifacts is expected. For 4- to 16-slice CT scanners, image reconstruction at 50% of the RR-interval is recommended. As rotation times become shorter and temporal resolution increases with modern 32- to 64-slice CT scanners, the reconstruction phase can be shifted to 60% of the RR-interval.

The reconstruction filter kernel greatly influences the in-plane spatial resolution and signal-to-noise ratio and thus the quantitative measurements. For coronary calcium measurements, a medium-sharp reconstruction filter kernel without edge enhancement (e.g., B35f for SOMATOM CT scanners, Siemens, Germany) is recommended that provides moderate image noise in low-dose acquisition protocols and about 10 lp/cm in-plane resolution. The 50% and 2% values of the modulation transfer function ρ are suggested by $\rho(50\%) \approx 4.0\ cm^{-1}$ and $\rho(2\%) \approx 9.0\ cm^{-1}$. Edge enhancement of the reconstruction filter kernel, as frequently used in chest examinations, should be avoided as it may lead to overestimation of scores and to misleading artifacts at the pericardium close to the coronary arteries.

5.2 CT Angiography of the Cardiac Anatomy and Coronary Arteries

The development of basic multi-slice cardiac CT scan reconstruction techniques and the first clinical evaluation of multi-slice CT angiography of the heart and coronary arteries involved the use of 4-slice CT scanners with a fastest rotation time of 0.5 s (Ohnesorge 2000, Achenbach 2000, Nieman 2001). Several studies demonstrated the feasibility of 4-slice CT scanners to non-invasively image the cardiac morphology and the coronary arteries but the performance of 4-slice CT scanners in terms of spatial resolution, temporal resolution, and breath-hold times was shown to be too limited for regular clinical use.

The availability of 8- to 10-slices per rotation with sub-millimeter collimation and a fastest rotation time of less than 0.5 s represent the minimum CT performance requirements for contrast-enhanced imaging of the heart and the coronary arteries. However, several studies demonstrated a substantial improvement of clinical robustness for cardiac and coronary artery diagnosis when using 16-slice

CT technology with sub-millimeter collimation and rotation time of less than 0.4 s (Küttner 2005, Mollet 2005a, Dorgelo 2005), which is therefore our recommended minimum performance level. The clinical robustness and diagnostic accuracy of CT angiography of the heart and coronary arteries benefits significantly from the further enhanced spatial resolution, temporal resolution, and reduced breath-hold times in 32- to 64-slice CT scanners (Gaspar 2004, Leschka 2005, Nikolaou 2005). Furthermore, a 32- to 64-slice CT scanner is usually a prerequisite for imaging of coronary stents and analysis of coronary plaque (Fig. 5.4, Figs. 5.7–5.9).

Retrospectively ECG-gated spiral acquisition has become the standard technique for high-resolution CT angiography of the heart and the coronary arteries (Table 5.3). The ability to reconstruct overlapping slices for increased z-axis resolution, the considerably shorter scan times, the ability to retrospectively optimize image reconstruction phases, and the option to increase temporal resolution with segmented reconstruction are key advantages that result in superior diagnostic image quality compared to prospectively ECG-triggered scanning. Only in very special applications, such as pediatric studies, are prospectively ECG-triggered protocols

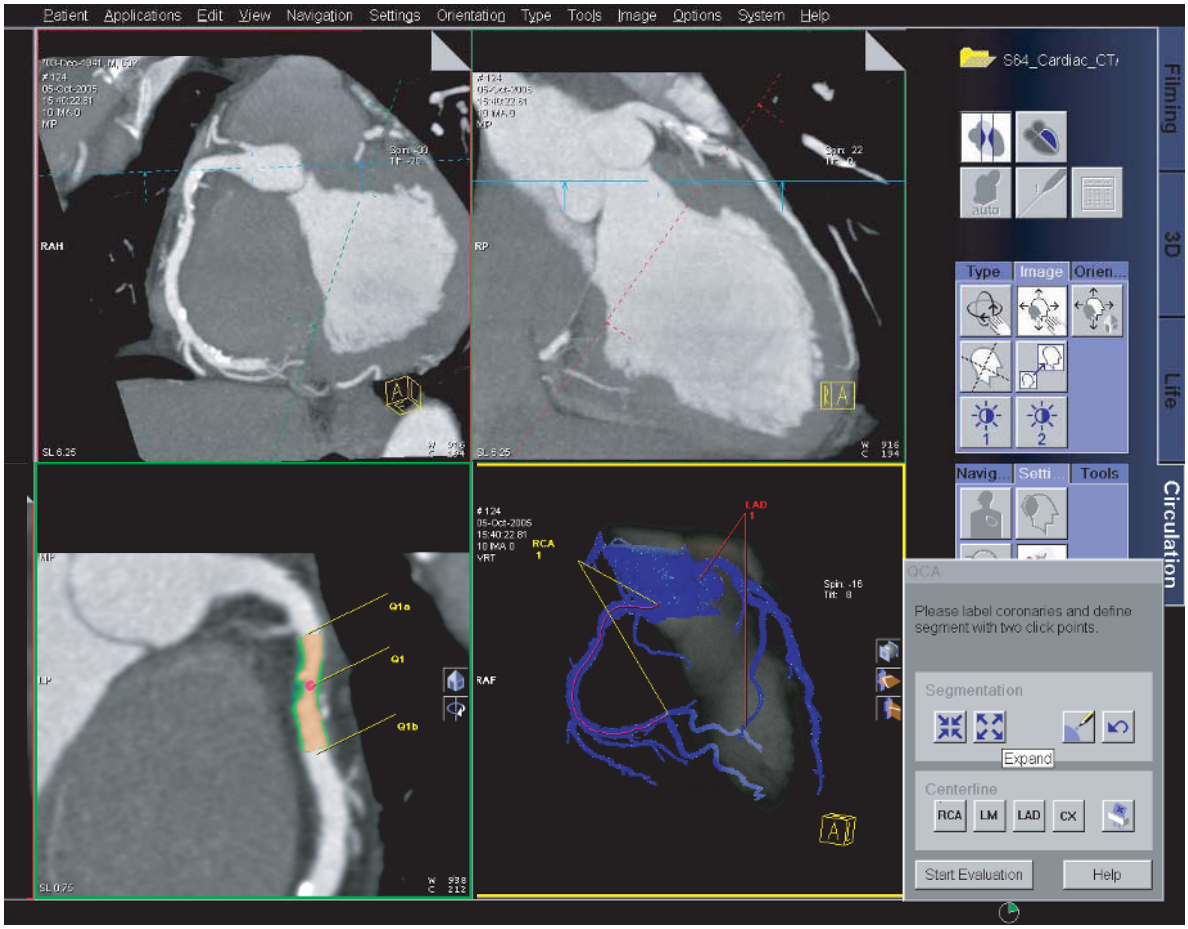

Fig. 5.4. Coronary CT angiography examination obtained with a 64-slice CT scanner with 0.6-mm collimation and 0.33-s rotation time. Automated segmentation of the coronary arteries and display with MIP reveals several lesions in the proximal left and right coronary arteries. With the resolution provided by 64-slice CT, plaque analysis becomes feasible using advanced segmentation tools. (Case study courtesy of University of Erlangen, Germany)

still in use for contrast-enhanced imaging of the heart morphology when minimization of radiation exposure is a major priority.

Sub-millimeter collimation and image reconstruction producing sub-millimeter slice width are important pre-requisites for high-resolution imaging of the cardiac and coronary anatomy. For imaging the heart and the coronary arteries with good contrast resolution, usually a slice-width between 0.75 and 1.0 mm is used. For special high-resolution reconstructions of stented or heavily calcified coronary segments, slice-width down to 0.6 mm can be achieved with the latest 64-slice CT scanners. In most multi-slice CT scanners, the thinnest possible reconstructed slice width is about 30–50% wider than the collimated slice width due to slice-broadening during spiral reconstruction. Multi-slice CT scanners that apply a flying focal spot in the z-direction ("double z-sampling") can generate a reconstructed slice width that is equivalent to the collimated slice width. The reconstruction increment depends on the reconstructed slice width. The z-axis resolution can be maximized with a reconstruction increment between one-half and two-thirds of the reconstructed slice width. Most 16- to 64-slice CT scanners that are available today can achieve a z-axis resolution of 0.5–0.7 mm, based on a 0.75–1.0 mm slice width. Recent 40- and 64-slice CT scanners that use the double z-sampling technique can provide a z-axis resolution as high as 0.4 mm, based on a reconstructed slice width of 0.6 mm. As described in a previous chapter, multi-slice CT scanners with double z-sampling technique double the number of scanned slices per rotation by using a flying focal spot in the z-direction. The detector coverage of those scanners, however, is usually smaller and scan times are correspondingly longer than those of multi-slice CT scanners with conventional design and the same number of slices. This currently available spectrum of different designs from different manufacturers explains the wide range of scan times for 32- to 64-slice CT scanners (Table 5.3).

In general, the shortest rotation time available should be used for CT angiography of the heart and coronary arteries in order to maximize temporal resolution. The shorter the rotation time the larger is the range of heart rates for which diagnostic image quality of small cardiac and coronary anatomy can be achieved. A rotation time of less than 0.4 s is a prerequisite to achieve robust image quality in patients with heart rates above 70 bpm (Küttner 2005, Mollet 2005a, Leschka 2005). However, heart rate control with β-blockers is still widely applied, even with a rotation time down to 0.33 s, which is available with the latest 64-slice CT scanners (Raff 2005, Mollet 2005b, Leber 2005, Alkadhi 2006). Segmented reconstruction techniques may be useful to increase temporal resolution and reduce motion artifacts in certain cases (Begemann 2005). However, multi-segment algorithms have shown to be clinically useful only up to a maximum of two segments for imaging of cardiac and coronary anatomy (de Gruiter 2006). Applying a slower rotation time in order to achieve higher temporal resolution for certain heart rates in combination with segmented reconstruction approaches cannot be recommended due to the lack of evidence in clinical routine. Using a slightly slower rotation time may only be practical in examinations of very obese patients, in order to achieve a higher contrast-to-noise ratio.

Similar to cardiac CT studies without contrast enhancement (see Sect. 5.1), a kV-setting of 120 kV has also been established as the standard in contrast-enhanced cardiac CT studies, as it can provide optimal iodine and tissue contrast while avoiding blooming artifacts. As mentioned above, in some scanners, 130 kV has to be used as an alternative if 120 kV is not supported. Lower kV settings, such as 100 kV, have the potential to provide a higher contrast-to-noise ratio; however, the evaluation of these protocols is still on-going. The mAs value is calculated from the applied mA value and the exposure time per slice and determines the signal-to-noise ratio in the axial image slice. Most scanners use the rotation time as the exposure time per slice for retrospectively ECG-gated acquisition (mAs = mA $\times$ T_{rot}). The mAs value translates into an effective mAs value that takes the spiral pitch into consideration (effective mAs = mA $\times$ T_{rot}/pitch). In normal patients weighing up to 90 kg, a setting of mAs = 150 is used for regular clinical use. In large or obese patients weighing above 90 kg, up to 200 mAs can be used in order to improve the visualization of small details. The mA levels have to be selected according to the present rotation time in order to achieve the required mAs value. The radiation exposure esti-

Table 5.3. Scan protocols for CT angiography of the heart with retrospective ECG gating

	8- to 10-slice CT	16-slice CT	32- to 40-slice CT	64-slice CT
Collimation (mm)	0.75–1.25	0.5–0.75	0.5–0.625	0.5–0.625
Slice width (mm)	1.0–1.5	0.8–1.0	0.6–0.9	0.6–0.9
Slice increment (mm)	0.5–0.8	0.5–0.7	0.4–0.6	0.4–0.6
Rotation time (s)	0.42–0.5	0.37–0.5	0.37–0.4	0.33–0.4
Temporal resolution (ms)	210–250[a]	185–250[a]	185–200[a]	165–200[a]
kV	120	120	120	120
mA	300–475	300–540	375–540	375–600
mAs (mA × T_{rot})	150–200	150–200	150–200	150–200
Effective mAs	430–710	430–800	600–800	600–990
Pitch	0.28–0.35	0.25–0.35	0.20–0.25	0.20–0.25
Table speed (mm/s)	5–7	6–8	8–15	12–22
ECG gating morphology (% RR)	50–60	50–60	40–70	40–70
ECG gating, end-systole (% RR)	10	10	10–20	10–20
ECG gating, end-diastole (% RR)	80	80	80–90	80–90
ECG dose modulation	Yes[b]	Yes[b]	Yes[b]	Yes[b]
Reconstruction filter	Medium-smooth (B25f)[c]	Medium-smooth (B25f)[c]	Medium-smooth (B25f)[c]	Medium-smooth (B25f)[c]
Exposure (mSv)	5.6–8.5[d]	5.0–8.2[d]	5.9–9.5[d]	5.9–9.5[d]
Scan direction	Craniocaudal	Craniocaudal	Craniocaudal	Craniocaudal
Scan time (s)	17–24[e]	15–20[e]	8–15[e]	6–10[e]
Contrast type (mg I/ml)	300–320	300–320	350–400	350–400
Contrast volume (ml)	120–150	100–120	80–100	60–80
Contrast flow (ml/s)	2.5–3.0	3.0–4.0	3.5–5.0	3.5–5.0
Contrast delay (s)	18–22	18–22	22–25	22–25

[a] Temporal resolution based on single-segment algorithm can be increased with two or more segments.
[b] Recommended use of ECG dose modulation – if available for the multi-slice CT scanner being used.
[c] Special nomenclature for reconstruction filters on Siemens SOMATOM CT scanners.
[d] Estimation for a male patient with a heart rate of 70 bpm, 12-cm scan range; for a female patient, multiply by a factor of 1.4. It is assumed that ECG dose modulation is used (absence increases exposure by a factor of 1.5–2.0).
[e] Scan time calculation for 12-cm scan range.

mations in Table 5.3 show a range to account for the increased mAs value in obese patients.

Optimal management of radiation exposure is particularly important for CT angiography examinations of the heart and the coronary arteries. The radiation exposure is largely dependent on the mAs per slice, the selected scan range, and the spiral pitch. Careful selection of the spiral pitch with minimal spiral overlap (pitch value as high as feasible), careful selection of the mAs per slice dependent on the patient's weight, limiting the scan range to the anatomy of interest, and a mandatory use of ECG-controlled dose modulation (Jakobs 2002) are important pre-requisites to minimize radiation exposure during retrospectively ECG-gated CT angiography examinations of the heart and the coronary arteries (Trabold 2003).

Usually, the entire cardiac and coronary anatomy can be covered in a 120-mm scan range within a reasonably short breath-hold time of less than 20 s with 16-slice CT and less than 10 s with 64-slice CT. In some applications, such as the evaluation of coronary bypass grafts, longer scan ranges up to 200 mm are necessary, thus resulting in longer breath-hold

times and higher radiation exposure. Due to the longer breath-hold time, ECG-gated sub-millimeter scanning of ranges larger than 200 mm can only be done with 32 - to 64-slice CT scanners.

The selection of the right image-reconstruction phase during the cardiac cycle is a key element to achieve diagnostic image quality for the entire cardiac anatomy, including all relevant segments of the coronary artery tree. Retrospective optimization of the reconstruction phase and reconstruction at different time points help to achieve good image quality in the majority of patients. For 16-slice CT scanners with rotation times around 0.4 s, the best image quality can usually be obtained between 50 and 60% of the RR-cycle. Due to the limited temporal resolution, motion artifacts have to be expected outside this interval. As rotation times become shorter and temporal resolution increases with modern 32- to 64-slice CT scanners, the interval can be extended to between 40 and 70% of the RR-cycle (Fig. 5.5), thus revealing stable image quality also at higher heart rates (Alkadhi 2006). With rotation time below 0.4 s, certain aspects of the cardiac anatomy, i.e., the right coronary artery, can often be visualized with

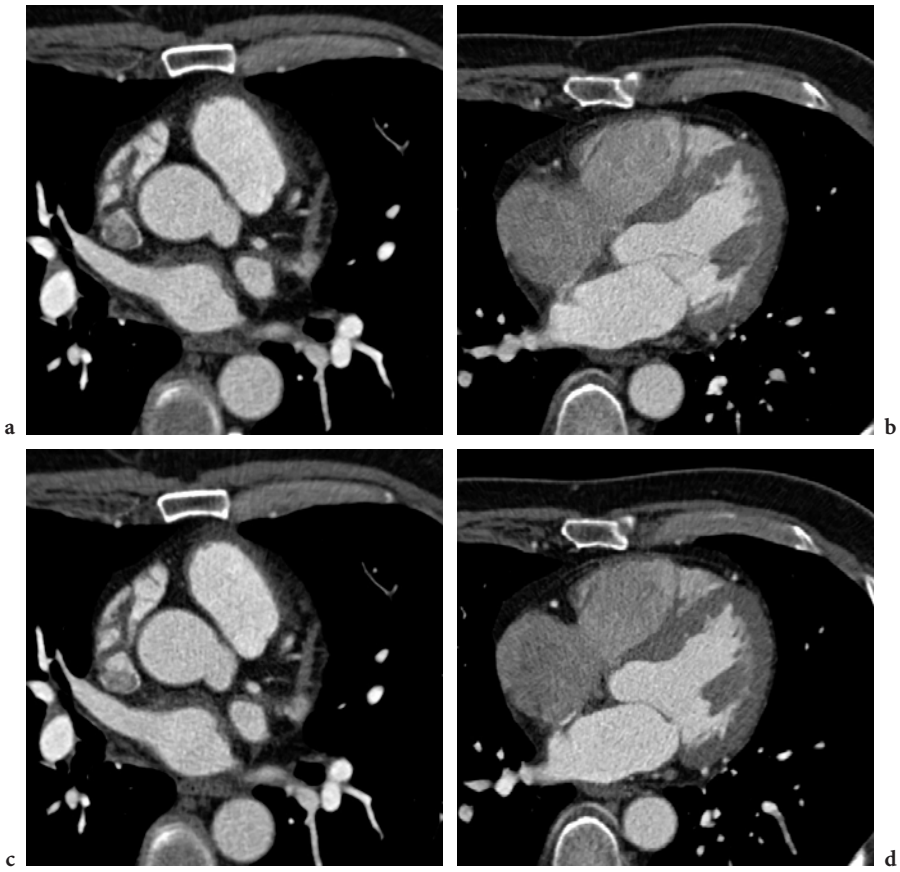

Fig. 5.5a–d. Coronary CT angiography examination in a patient with 82 bpm using a 64-slice CT scanner with 0.6-mm collimation and 0.33-s rotation time. Retrospectively ECG-gated image reconstruction was done at 70% (**a**, **b**) and 40% (**c**, **d**) of the RR-interval. While the left anterior descending coronary artery can be visualized free of motion at 70% (**a**), the right coronary artery is of diagnostic quality but shows some residual motion artifacts (**b**). Image reconstruction at 40% reveals both the left anterior descending (**c**) and right (**d**) coronary arteries with very good diagnostic quality. However, the best diagnostic quality was obtained using 70% reconstruction for diagnosis of the left anterior descending coronary artery (**a**) and 40% reconstruction for diagnosis of the right coronary artery (**d**). (Case study courtesy of Klinikum Grosshadern, University of Munich, Germany)

better quality in end-systole than in diastole when higher heart rates (above 75 bpm) are present (Wintersperger 2006).

Alternative ECG-gating parameters with absolute delay times in milliseconds in relation to the R-waves have also been used in several studies for analysis of the coronary arteries, but at this point there is no clear consensus whether one method is superior to the other. In case absolute ECG-gating parameters are preferred, the relative ECG-gating percentage parameters given above can easily be converted into absolute ECG-gating parameters in milliseconds when the patient's heart rate and average RR-interval times are taken into consideration:

$$\text{Absolute delay} = \text{relative delay} \times \text{RR-interval-time} \quad (5.1)$$

$$\text{Absolute reverse} = (100\% - \text{relative delay}) \times \text{RR-interval time} \quad (5.2)$$

For example, for a patient with 75 bpm heart rate during the scan (RR-interval-time = 800 ms) a relative delay of 60% would correspond to an absolute delay of 480 ms and to an absolute reverse of 320 ms. It should be noted that ECG editing tools have been shown to be useful to correct the position of a detected R-wave or to eliminate irregular heart beats from image reconstruction (Cademartiri 2006) (Fig. 5.6). Once an irregular beat is removed from the ECG trace, absolute ECG-gating phase parameters have to be used to correctly position the reconstruction intervals in relation to the valid R-waves. As a consequence, absolute ECG-gating parameters in combination with systolic image reconstruction (100–200 ms absolute-delay after R-wave) are generally preferred in patients with known absolute arrhythmia.

Also, in contrast-enhanced cardiac CT studies, the reconstruction filter kernel greatly influences in-plane spatial resolution and signal-to-noise ratio, and thus image quality and iodine and tissue con-

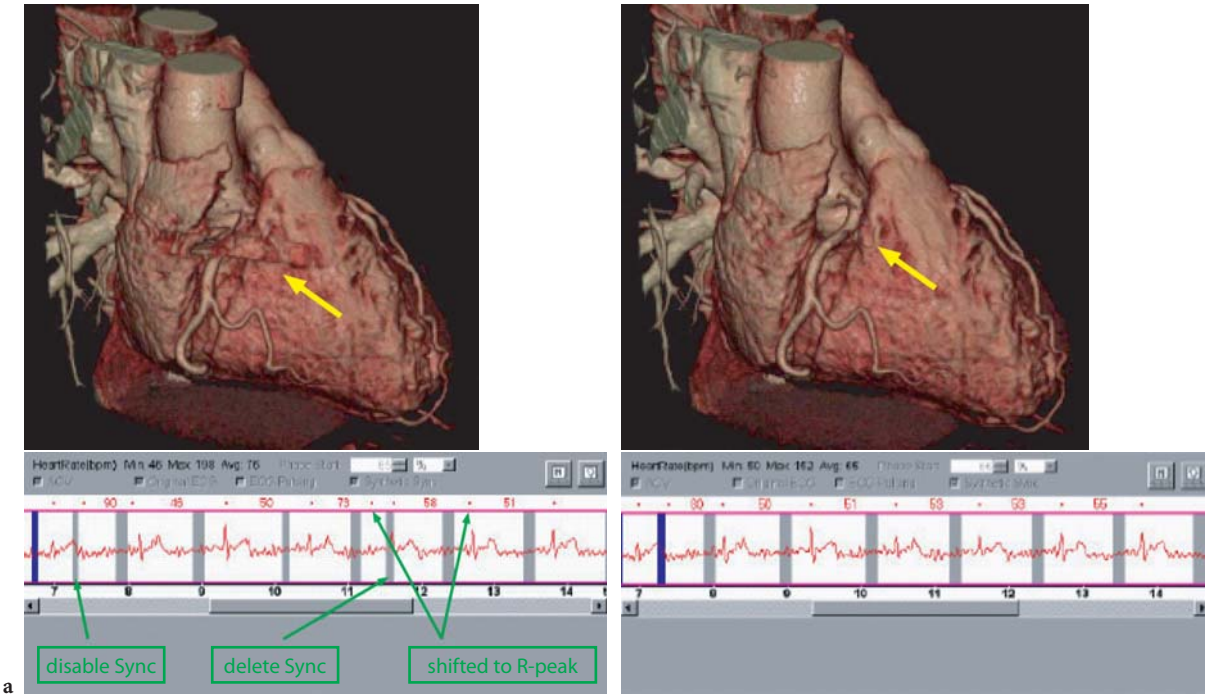

Fig. 5.6a, b. Coronary CT angiography examination using a 64-slice CT scanner with 0.6-mm collimation and 0.33-s rotation time in a patient with an average heart rate below 60 bpm but R-wave misregistration during the scan. **a** Image reconstruction using the recorded R-waves leads to non-diagnostic image quality due to major stair-step artifacts (*arrow*). **b** The use of an ECG editing tool to correct R-wave positions and elimination of extra beats restores the examination with perfectly diagnostic quality. (Case courtesy of Stanford School of Medicine, USA)

trast. As the basis for 3D visualization of the cardiac anatomy and the coronary artery lumen, a medium-smooth reconstruction filter kernel (e.g., B25f for SOMATOM CT scanners, Siemens, Germany) is recommended that provides low image noise, but maintains about 10 lp/cm in-plane resolution. The 50% and 2% values of the modulation transfer function ρ are suggested with $\rho(50\%) \approx 4.0\ cm^{-1}$ and $\rho(2\%) \approx 8.5\ cm^{-1}$. Special sharp reconstruction filter kernels that provide an in-plane resolution up to 12 lp/cm can be used to improve visualization of the coronary artery lumen in the presence of dense coronary artery calcifications or stents (e.g., B46f for SOMATOM CT scanners, Siemens, Germany) (Maintz 2003, Hong 2004, Maintz 2006, Seyfarth 2006) (Fig. 5.7–5.9). The in-stent lumen in coronary arteries can be reconstructed with less artifactual narrowing when using these types of special filter kernels (Hong 2004). The 50% and 2% values of the modulation transfer function ρ of these special sharp reconstruction filter kernels are suggested with $\rho(50\%) \approx 5.0\ cm^{-1}$ and $\rho(2\%) \approx 10.5\ cm^{-1}$. However, these kernels should not be used for the general assessment of cardiac and coronary anatomy,

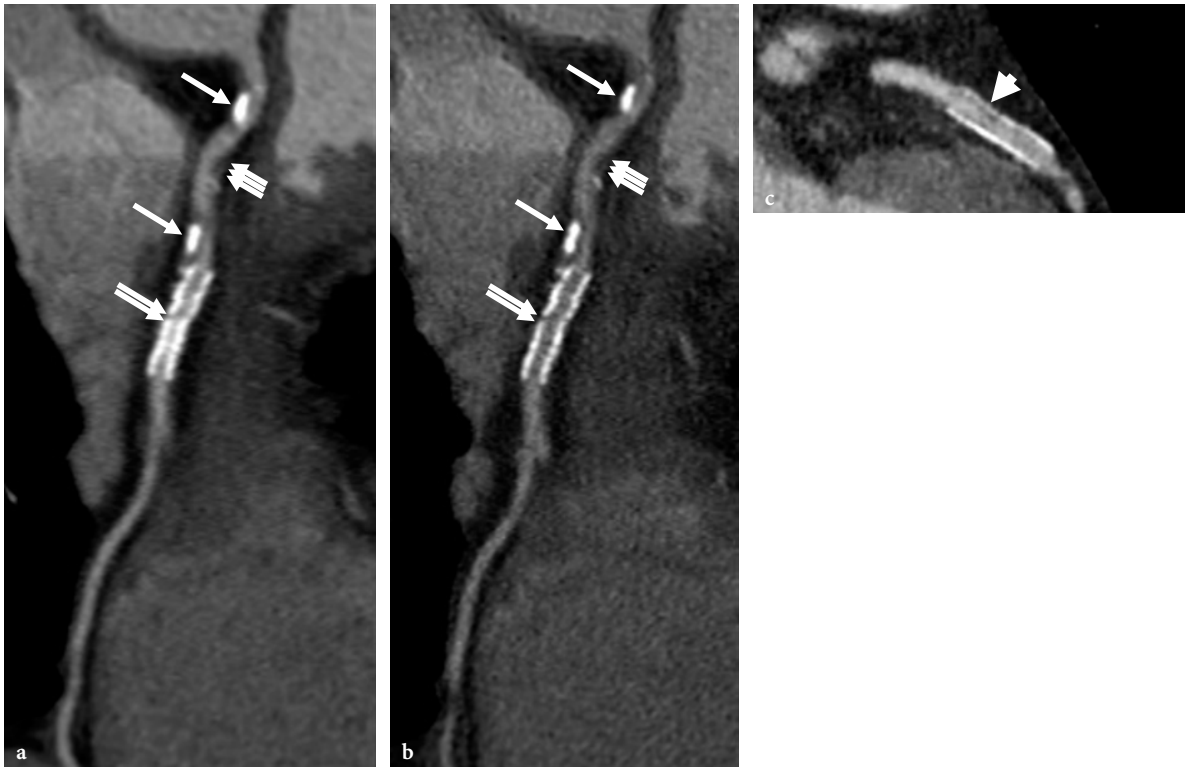

Fig. 5.7a–c. Coronary CT angiography examination using a 64-slice CT scanner with 0.6-mm collimation and 0.33-s rotation time in a patient with coronary artery disease and a stent in the right coronary artery. **a** The right coronary artery is displayed using curved MPR. Image reconstruction with 0.75-mm slice width and a medium-smooth filter kernel reveals good visualization of the soft-tissue lesion (*triple arrow*) but compromised visualization of the calcified lesions (*arrows*) and of the in-stent lumen (*double arrow*). **b**, **c** Image reconstruction with 0.6-mm slice width and an optimized sharper filter kernel improves visualization of the patent in-stent lumen and differentiation of the calcified lesions compared to the contrast-enhanced lumen. MPR display of a second stent in the left coronary artery reveals suspected wall irregularities in the stent (**c**, *arrowhead*). Image data reconstructed with sub-millimeter slice width and a medium-smooth filter kernel should be used for initial diagnosis of the cardiac anatomy and the coronary artery lumen, as they provide optimized soft-tissue delineation. Image data reconstructed with the thinnest possible slice width and a sharp filter kernel should then be used for further differential diagnosis of stented and heavily calcified coronary artery segments. (Case courtesy of the University of Erlangen, Germany)

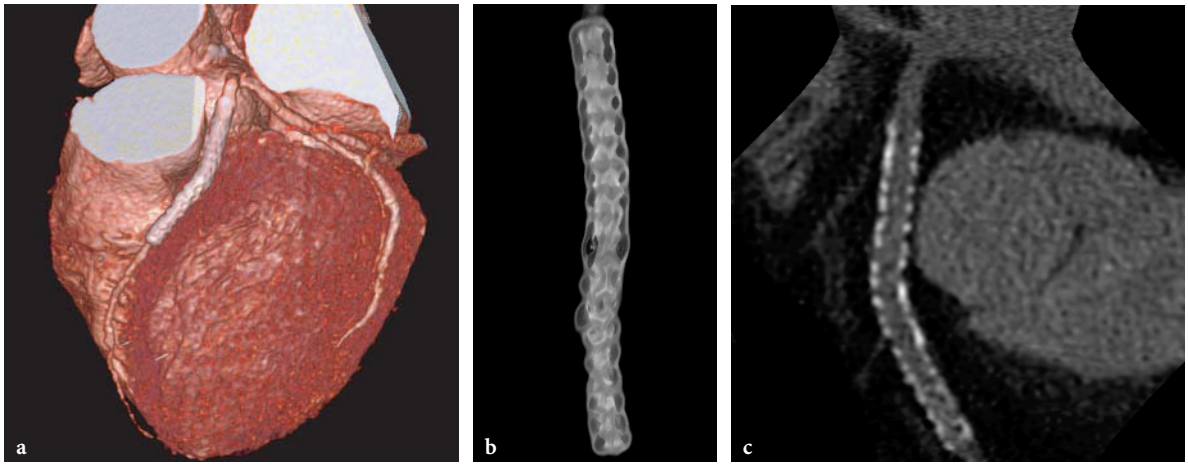

Fig. 5.8a–c. Coronary CT angiography examination using a 64-slice CT scanner with 0.6-mm collimation and 0.33-s rotation time in a patient with a long stent in the left anterior descending coronary artery. The location, extension, and properties of the stent are readily visualized with volume-rendering technique (VRT) display (**a**, **b**) Image reconstruction using a sharp filter kernel and curved MPR display (**c**) allows for optimal diagnostic visualization of the patent in-stent lumen over the entire course of the stent. (Case courtesy of Toyohashi Heart Center, Japan)

as in-plane resolution is increased at the expense of higher image noise.

Multi-slice CT scanners with an increasing number of slices can image the heart in shorter scan times. Subsequently, contrast timing can be optimized to higher peak enhancement with shorter duration of maximum enhancement (Cademartiri 2005). Therefore, the total amount of contrast agent can be reduced while flow rates and iodine concentration are increased with faster scanners. Although the total amount of contrast can be reduced, the use of a saline chaser bolus with a total volume of 40–60 ml and with the same flow rate is always recommended (Cademartiri 2004a). To optimize the shape of the bolus, longer delay times are used for faster scanners with more slices to produce a better "wash out" of the right heart with less contrast-related artifacts and to produce better contrast enhancement of the left heart and the coronary artery system. The delay times suggested in Table 5.3 provide optimized enhancement of the arterial cardiac system and of the left heart. Longer delay times are required to improve visualization of the venous cardiac system, such as the coronary sinus and coronary veins, which are of interest in electrophysiology (Mühlenbruch 2005b). Patient-individual contrast timing can be optimized using test-bolus injection or automated bolus triggering. Automated bolus triggering with reference to the peak enhancement in the ascending aorta has been shown to be feasible for optimized imaging of the coronary arteries (Cademartiri 2004b).

5.3 Cardiac Function Imaging

Any contrast-enhanced, retrospectively ECG-gated, multi-slice CT data set that has been acquired to visualize the cardiac anatomy and the coronary arteries according to Table 5.3 can be re-used for the assessment of cardiac function (Kopp 2005). Measurement of global cardiac function parameters by multi-slice CT is possible through image reconstruction of the heart in multiple phases of the cardiac cycle. Reconstruction of the cardiac anatomy and the left ventricle in the end-diastolic and end-systolic phases of the cardiac cycle enables the calculation of end-diastolic volume, end-systolic volume, ejection fraction, and left ventricular stroke volume.

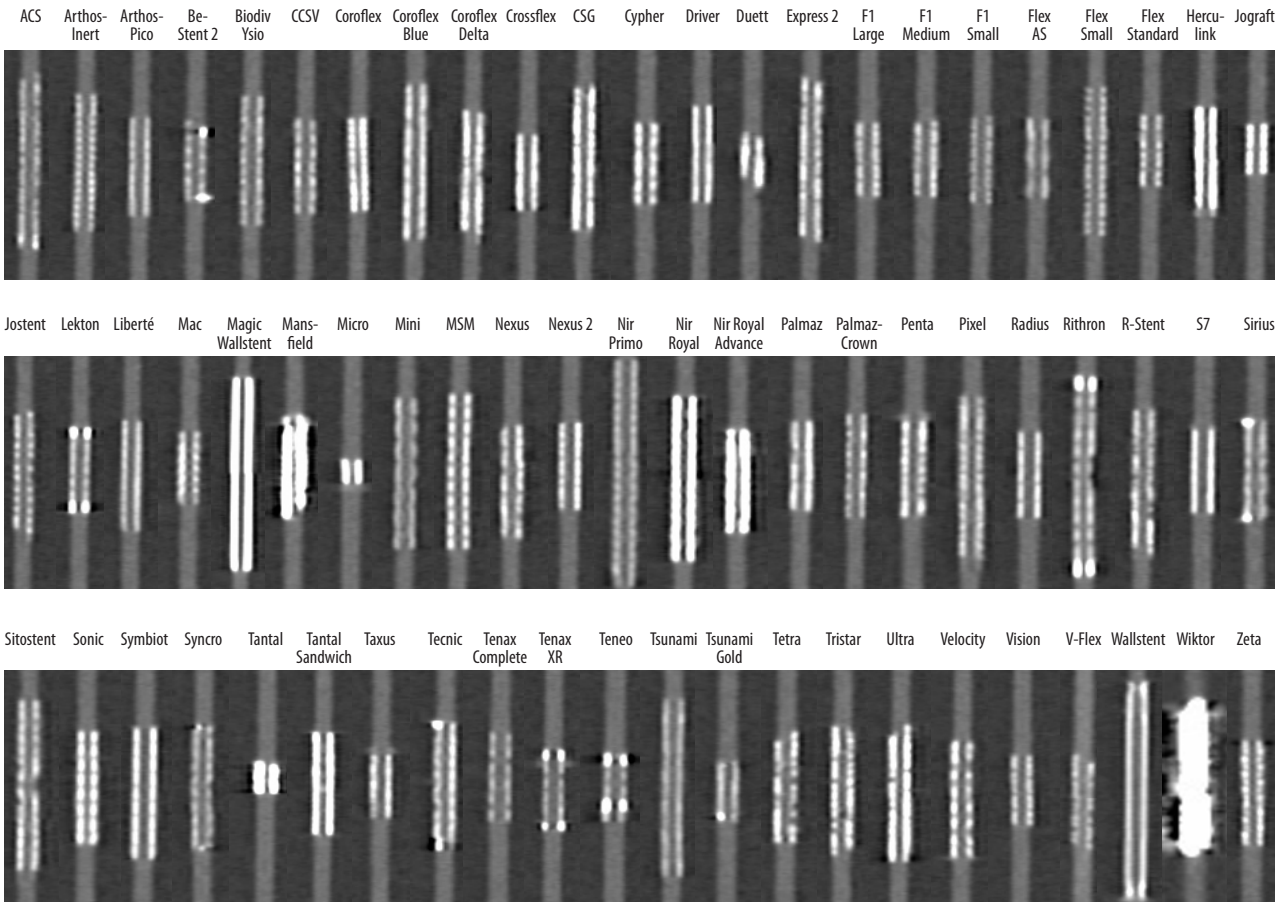

Fig. 5.9. Series of 68 coronary artery stents scanned using a 64-slice CT scanner with 0.6-mm collimation and 0.33-s rotation time. The stents were inserted into a coronary artery phantom with a lumen diameter of 3 mm. Images were reconstructed with the suggested clinical protocol using 0.6-mm slice width, 0.4-mm image increment, and a sharp reconstruction filter kernel (B46f for SOMATOM Sensation 64, Siemens, Germany), and displayed with MPR along the vessel axis. Despite the use of identical and optimized protocols, visualization of the in-stent lumen still strongly depends on the properties of the stent (Maintz 2006). (Data courtesy of Muenster University, Germany)

Image reconstruction at multiple equidistant time points throughout the cardiac cycle can reveal additional information on wall motion, which, however, is yet limited due to limited temporal resolution. The functional diagnosis of the myocardium is complemented by the first-pass perfusion information included in the initial contrast-enhanced study of cardiac morphology. Also, cardiac-function defects that are related to non-myocardial disease but caused by other reasons, such as constrictive pericarditis, can be assessed (Erffa 2006). It was also demonstrated that late enhancement of infarcted myocardium can be detected by multi-slice CT (Kopp 2005). However, late enhancement is not revealed from the initial scan of the cardiac morphology but requires an additional, retrospectively ECG-gated low-dose acquisition with about 3–5 min delay after the initial administration of contrast.

Early studies with 4- and first-generation 16-slice CT scanners demonstrated strong correlation of global cardiac function parameters measured by multi-slice cardiac CT with the gold standards catheter-ventriculography and MRI (Juergens 2002, Heuschmid 2003, Juergens 2004, Burgstahler

2005, Heuschmid 2005). In addition to the assessment of left ventricular function, the measurement of right ventricular function has been found feasible (Koch 2005, Raman 2005, Kim 2005, Rius 2006, Remy-Jardin 2006, Delhaye 2006). However, an overestimation of ventricular volumes and global cardiac function parameters as a result of limited temporal resolution was reported in several studies (Mahnken 2003, Kopp 2005). We therefore recommend multi-slice CT scanners with at least 16 slices and a rotation time of 0.4 s or less for the assessment of global cardiac function parameters as complementary information to the cardiac and coronary anatomy (Mahnken 2005a, Mahnken 2005b). The most recent 64-slice CT scanners with rotation times down to 0.33 s hold promise to provide sufficient temporal resolution for a more accurate assessment of global cardiac function parameters in relation to the gold standards and to enable the detection of regional wall motion abnormalities (Kopp 2005, Mahnken 2006). Modern evaluation tools can automatically segment the ventricle volumes from the thin-slice data set and support the accurate analysis of global cardiac function parameters (Fig. 5.10).

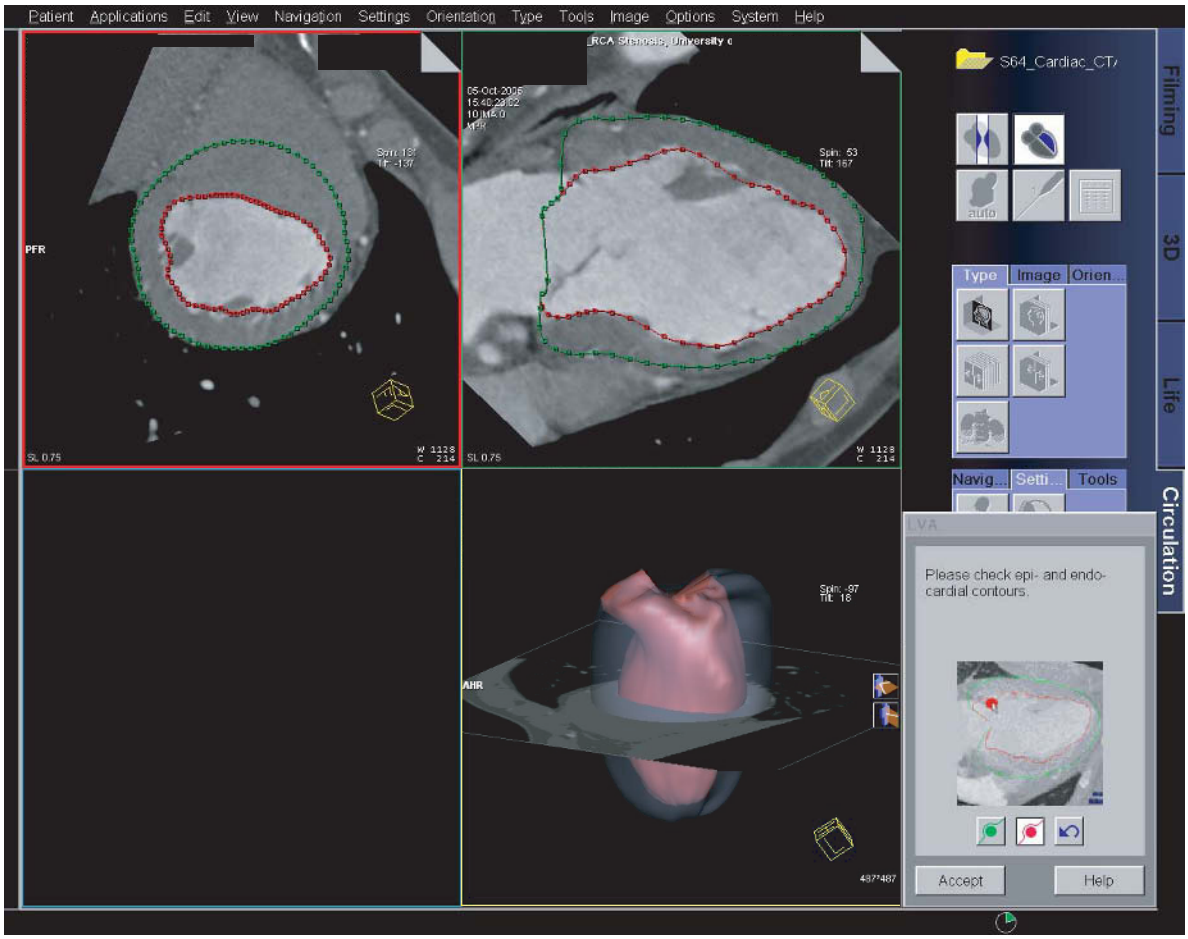

Fig. 5.10. Cardiac CT angiography examination obtained using a 64-slice CT scanner with 0.6-mm collimation and 0.33-s rotation time. Image data were reconstructed during end-diastole at 80% of the RR-interval. Automated volumetric segmentation and modeling of the left ventricular volume provide accurate input for the assessment of global cardiac function. (Case study courtesy of the University of Erlangen, Germany)

For end-systolic image reconstruction, a relative-delay ECG-gating parameter of about 10–20% of the RR-interval has to be selected; for end-diastolic reconstruction between 80% and 90% of the RR-interval is feasible (Table 5.3). The optimal phase parameters for end-systole and end-diastole are dependent on the patient's heart rate and vary from patient to patient, so that a patient-individual selection of the parameters is recommended using appropriate software tools. Absolute-delay ECG-gating parameters can be used alternatively for end-systolic reconstruction and absolute-reverse ECG-gating parameters for end-diastolic reconstruction. The parameters can again be derived from the recommended relative-delay percentage parameters as explained above. A true 4-dimensional reconstruction of the entire cardiac cycle for display of cardiac motion is feasible by selecting equidistant reconstruction time points throughout the entire cardiac cycle (Fig. 5.11). With the maximum temporal resolution given by today's available multi-slice CT scanners, 10–12 time points per cardiac cycle at a distance between 8 and 10% of the RR-interval are feasible to cover cardiac motion over the entire cardiac cycle (Fig. 5.11). Time points at a shorter distance will not improve the information but increase the amount of reconstructed image data.

Left- and right ventricular function parameters can be derived from the original axial slices or from multi-planar reconstructions (MPRs) orthogonal to the ventricular axes. A spatial resolution of 1–2 mm is sufficient for adequate delineation of the myocardium from the epicardium and from contrast-enhanced chambers. In order to minimize the total amount of reconstructed slices in a study, it is sufficient to use a slice width of about 2 mm with a slice increment between 1 and 2 mm for reconstruction of axial slices or MPRs that are used as input for cardiac function analysis.

Radiation exposure during cardiac CT angiography examinations can be minimized using retrospectively ECG-gated image acquisition with ECG-controlled dose modulation, which reduces the applied dose during the systolic phase of the cardiac cycle. Despite the subsequent presence of higher image noise during systole, delineation of the larger cardiac anatomy and evaluation of cardiac function parameters are still feasible.

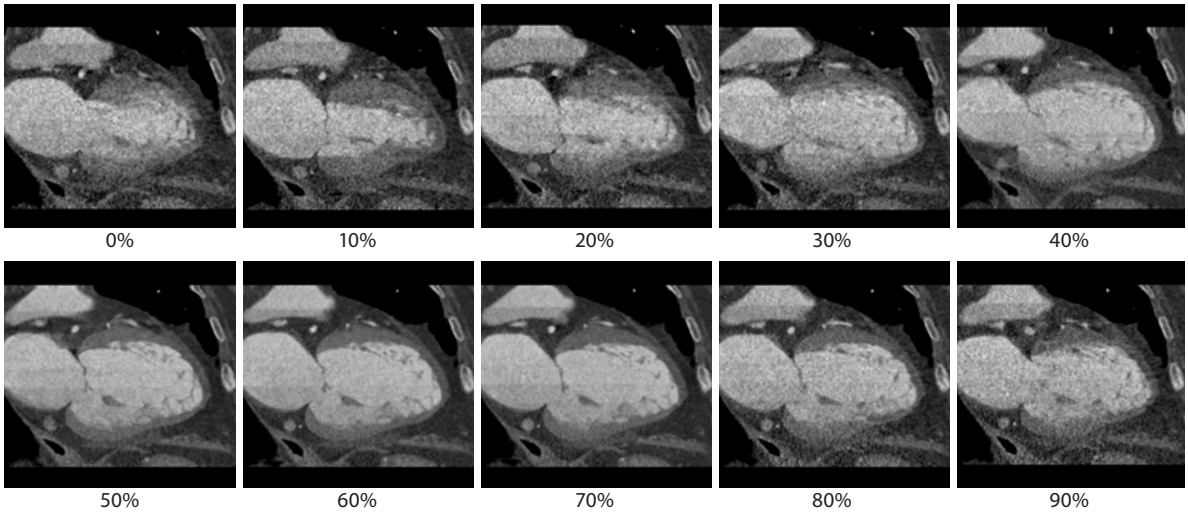

Fig. 5.11. Retrospectively ECG-gated image reconstruction of a patient with a normal ejection fraction of 65%, examined with 64-slice CT, 0.33-s rotation time, and ECG-controlled dose modulation. Images were reconstructed between 0 and 90% of the RR-interval at 10% distance. The motion of the left atrium, mitral valve, and left ventricle are displayed over the entire course of the cardiac cycle using MPR in the long heart axis. The high temporal resolution allows for visualization of end-diastole (at 90%) and end-systole (at 10%) virtually free of motion artifacts. ECG-controlled dose modulation does not compromise evaluation of global cardiac function, as noisier axial slices or MPRs with thicker slices are acceptable as input for segmentation of the chambers and ventricular analysis. (Case courtesy of the University of Erlangen, Germany)

The use of multi-segment reconstruction can increase temporal resolution and improve image quality in patients with higher heart rates and in phases of the cardiac cycle with rapid cardiac motion. Multi-segment reconstruction was shown to improve delineation of the ventricle resulting in better assessment of cardiac function parameters (Juergens 2005, Mahnken 2006). The accuracy of ventricular function measurement can be considerably improved using two segments instead of single-segment reconstruction. Protocols that enable image reconstruction with more than two segments for further improved temporal resolution cannot be recommended as they do not provide significant improvements in image quality but require scanning with reduced pitch values, which results in higher radiation exposure.

5.4 Cardiothoracic Examination Protocols

The use of ECG-correlated protocols for CT angiography of the cardiothoracic vasculature has become feasible with the advent of modern multi-slice CT scanners, since artifacts related to cardiac pulsation can be eliminated and diagnostic confidence can be increased (Hofmann 2004, Schoepf 2005). ECG-correlated imaging of the heart and cardiothoracic vessels with one CT scan can be particularly useful for comprehensive diagnosis in patients with chest pain, in patients after cardiothoracic intervention or surgery, and in adult or pediatric patients with suspected or known cardiothoracic abnormalities (Ohnesorge 2005, Gaspar 2005, White 2005, Ghersin 2006, Salem 2006). However, retrospectively ECG-gated multi-slice spiral scanning with high resolution and long scan ranges can require considerable amounts of radiation exposure, which is of particular concern in pediatric patients or in patients with low likelihood of disease. Therefore, scan techniques and protocols for ECG-correlated CT angiography of the chest have to be selected carefully according to the clinical indication and the considered patient population.

The availability of 16-slices per rotation and a fastest rotation time of less than 0.5 s represent the minimum CT performance requirements for contrast-enhanced imaging of the cardiothoracic vessels. Only scanners with this performance level can provide adequate breath-hold times for ECG-correlated coverage of the required scan range of about 300 mm at adequate z-axis resolution. Sub-millimeter collimation and rotation times less than 0.4 s are required for comprehensive assessment of the entire chest, including diagnosis of the coronary artery lumen. However, the performance and volume coverage of 16-slice CT scanners are too limited for accurate analysis of the coronary arteries in chest-pain protocols (White 2005). Special scan and reconstruction techniques that were developed to increase scan coverage with ECG-gating in 4- to 8-slice CT scanners demonstrated promising initial results but were found to be of limited use in routine clinical scanning (Flohr 2002).

In adult patients, retrospectively ECG-gated spiral acquisition is the recommended technique for high-resolution CT angiography of the cardiothoracic anatomy, as it provides the highest possible z-axis resolution within feasible breath-hold times and the ability to diagnose the cardiac and coronary anatomy together with that of the greater thoracic vessels. The corresponding scan protocols are derived from scan protocols used for imaging the heart (Table 5.3), but they have been optimized for an increased scan coverage of 300 mm (Table 5.4).

When using 16-slice CT scanners, a reasonable breath-hold time of less than 30 s cannot be achieved with protocols that apply sub-millimeter collimation. Therefore, slice-collimation between 1.0 and 1.5 mm has to be used, which means that the slice width is increased to 1.5–2.0 mm. Thus, visualization of the cardiac anatomy is still feasible but diagnosis of the coronary artery lumen in the smaller coronary artery segments will be compromised. Comprehensive diagnosis of the cardiothoracic vessels, including the coronary arteries, requires ECG-gated coverage of the entire chest with sub-millimeter collimation within a reasonable breath-hold time. Today's 32- to 40-slice CT scanners fulfill this requirement with scan times of 20–30 s. However, many patients who are referred for this type of examination suffer chest pain and may not be able to hold their breath much longer than 20 s; thus, the use of 64-slice CT scanners is generally recommended in such cases.

Some recent 64-slice CT scanners are equipped with special protocols for ECG-gated examinations of the chest, especially in patients with acute chest pain. These scanners use higher pitch values (up to 0.3) for increased scan speed and reduced radiation exposure (Johnson 2006).

Optimization of scan protocols to limit radiation exposure is extremely important for retrospectively ECG-gated CT angiography examinations of the chest. The mA, mAs, and kV settings used correspond to the recommendations for CT angiography of the heart and the coronary arteries. Again, increasing the mAs ($mAs = mA \times T_{rot}$) from 150 mAs to 200 mAs in obese patients above 90 kg is useful to improve diagnostic quality. In retrospectively ECG-gated acquisition, the mAs value translates into an effective mAs value (effective $mAs = mA \times T_{rot}/pitch$). In order to reduce radiation exposure, it is important to use pitch values as high as possible for the given scanner type and rotation time (e.g., pitch up to 0.3 for 64-slice CT scanner with 0.33 s rotation), even if image reconstruction is then limited to single-segment algorithms (Fig. 5.12). This approach, in combination with the mandatory use of ECG-controlled dose modulation, allows radiation exposure to be limited to about 12–15 mSv for a scan range of 300 mm. Without optimization of the protocols, radiation dose values up to 24 mSv have to be expected and even 40–50 mSv if ECG-controlled dose modulation is not used.

Dedicated contrast-agent protocols are required to provide continuously high enhancement over the entire scan range for vessels that show very different enhancement timing. As scan times do not differ significantly from scanner type to scanner type, also the contrast-injection protocols are similar for 16- to 64-slice CT scanners. In general, compared to protocols for the heart, more contrast volume is required as the bolus enhancement time has to be stretched over a longer scan time. While 120–150 ml of contrast agent is required for 16- to 40-slice CT scanners, the contrast volume can still be limited to 100–120 ml with 64-slice CT scanners, as the scan times are shorter. Flow rates between 3 and 4 ml/s are feasible for 16-slice CT scanners, whereas flow rates up to 5 ml/s provide better results for 32- to 64-slice CT scanners. The use of a saline chaser bolus with a total volume of 40–60 ml and with the same flow rate is always recommended (Cademartiri 2004a). Shorter delay times of 18–20 s are normally used to balance the enhancement of the thoracic aorta, heart chambers, pulmonary arteries, and coronary arteries.

Prospectively ECG-triggered protocols can be used for CT angiography of the chest in a limited spectrum of applications in which the cardiac anatomy is not of interest and only the greater thoracic vessels, such as the thoracic aorta, have to be examined. Such prospectively ECG-triggered protocols with limited spatial resolution can be derived from the protocols for coronary calcium quantification given for 16- to 64-slice CT scanners in Table 5.1 by using the settings for mA and mAs per slice and the contrast bolus parameters from Table 5.4.

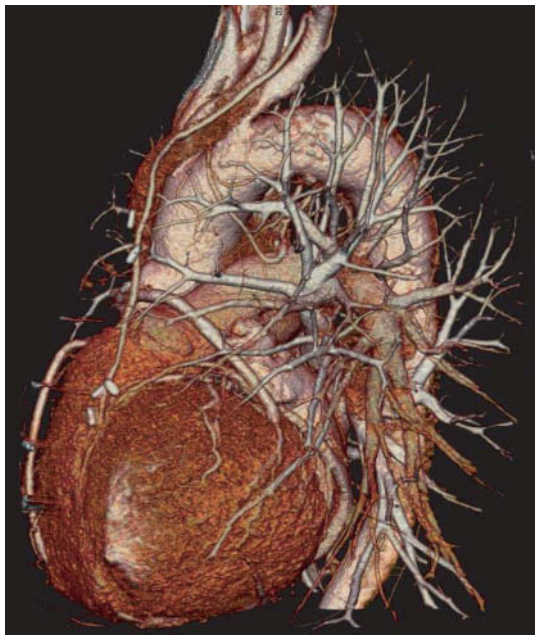

Fig. 5.12. Examination of a patient with coronary artery bypass grafts using 64-slice CT with 0.6-mm collimation and 0.33-s rotation time. The optimized scan protocol consisted of retrospective ECG gating and pitch 0.3; 64 slices were generated from 32 collimated detector rows using a flying focal spot in the z direction. Based on a table speed of 17.5 mm/s, the scan range of 25 cm could be covered in a 14-s breath-hold time. The enlarged heart, thoracic aorta, pulmonary arterial system, and the two arterial bypass grafts over their entire course can be visualized. (Case courtesy of Mayo Clinic Rochester, USA)

Table 5.4. Scan protocols for CT angiography of the chest in adults with retrospective ECG gating

	16-slice CT	32- to 40-slice CT	64-slice CT
Collimation (mm)	1.0–1.5	0.5–0.625	0.5–0.625
Slice width (mm)	1.5–2.0	0.6–0.9	0.6–0.9
Slice increment (mm)	1.0–1.3	0.4–0.6	0.4–0.6
Rotation time (s)	0.37–0.5	0.37–0.4	0.33–0.4
Temporal resolution (ms)	185–250[a]	185–200[a]	165–200[a]
kV	120	120	120
mA	300–540	375–540	375–600
mAs (mA × T_{rot})	150–200	150–200	150–200
Effective mAs	430–800	600–800	600–990
Pitch	0.25–0.35	0.20–0.30	0.20–0.30
Table speed (mm/s)	12–16	10–15	15–22
ECG gating morphology (% RR)	50–60	40–70	40–70
ECG gating, end-systole (% RR)	10	10–20	10–20
ECG gating, end-diastole (% RR)	80	80–90	80–90
ECG dose modulation	Yes[b]	Yes[b]	Yes[b]
Reconstruction filter	Medium-smooth (B25f)[c]	Medium-smooth (B25f)[c]	Medium-smooth (B25f)[c]
Exposure (mSv)	12–20[d]	12–24[d]	12–24[d]
Scan direction	Craniocaudal	Craniocaudal	Craniocaudal
Scan time (s)	19–25[e]	20–30[e]	14–20[e]
Contrast type (mg I/ml)	350–400	350–400	350–400
Contrast volume (ml)	120–150	120–150	100–120
Contrast flow (ml/s)	3.0–4.0	3.5–5.0	3.5–5.0
Contrast delay (s)	18–20	18–20	18–20

[a] Temporal resolution based on single-segment algorithm can be increased with two or more segments.
[b] Recommended use of ECGdose modulation – if available for the multi-slice CT scanner being used.
[c] Special nomenclature for reconstruction filters on Siemens SOMATOM CT scanners.
[d] Estimation for a male patient with a heart rate 70 bpm, 30-cm scan range; for a female patient, multiply by a factor of 1.4. It is assumed that ECG dose modulation is used (absence increases exposure by a factor of 1.5–2.0,
[e] Scan time calculation for 30-cm scan range

CT angiographic imaging of the heart and cardiothoracic vessels is frequently used to visualize congenital vascular disease in pediatric patients. In older children that can hold their breath, the above-given protocols for adults using retrospective ECG gating can be applied with much shorter scan ranges and significantly lower settings for mA and mAs per slice. A lower kV-setting of 100 or even 80 kV can be used to improve differentiation of soft tissue, to increase iodine contrast, and to further reduce radiation exposure. In children up to 2 years of age, 80 kV can be readily used, whereas 100 kV is recommended for children up to 10 years of age. In children between 10 and 18 years of age, the mA and mAs values given in Table 5.4 can be reduced by about a factor of two and even further in smaller children (Fig. 5.13). Retrospectively ECG-gated acquisition is often not feasible in young children and neonates, who usually cannot hold their breath during scanning. For those patients, prospectively ECG-triggered scan protocols with sub-millimeter collimation and ECG-trigger on the R-wave (relative delay 0%) or even normal spiral acquisition without ECG gating but with sub-millimeter collimation and maximum pitch (up to 1.75) are preferable (Fig. 5.14).

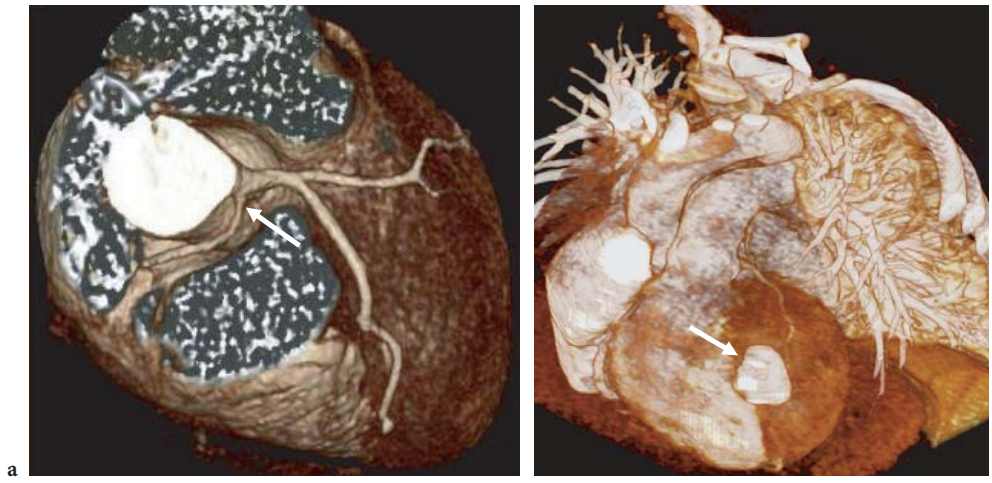

Fig. 5.13a, b. Retrospectively ECG-gated chest CT angiography examinations of two pediatric patients using a 16-slice CT scanner with 0.75-mm collimation, 0.37-s rotation time, and optimized protocols allowing reduced radiation exposure. **a** An anomalous origin of the right coronary artery (*arrow*) was accurately be diagnosed in a 13-year old boyusing a protocol with 40 mAs per slice, 120 kV, and 100-mm scan range. b For the examination of a 17-month old boy (**b**), 25 mAs per slice, 100 kV and a scan range of 80 mm was sufficient to correctly diagnose the presence of an aneurysmal pouch (*arrow*). (Cases courtesy of (**a**) Cleveland Clinic Foundation, USAand (**b**) Stanford School of Medicine, USA)

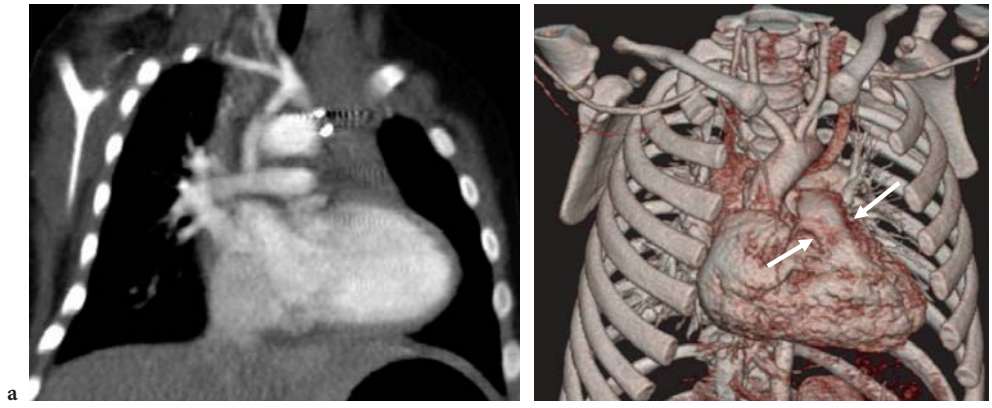

Fig. 5.14a, b. Chest CT angiography examinations of two pediatric patients. The images were obtained using a 16-slice CT scanner with 0.75-mm collimation and 0.37-s rotation time. **a** Prospective ECG-triggering, 80 kV and 25 mAs per slice were used in a 4-month old infant to display the cardiothoracic anatomy at minimum possible radiation exposure. **b** Alternatively, the larger cardiothoracic anatomy can also be visualized with low radiation exposure by using conventional multi-slice spiral protocols without ECG-correlation, as in a 14-month-old infant with absent pulmonary valve (*arrows*). (Cases courtesy of (**a**) MGH Boston, USA and (**b**) ASAN Medical Center, Seoul, Korea)

References

Achenbach S, Giesler T, Ropers D, et al (2001). Detection of coronary artery stenoses by contrast-enhanced, retrospectively electrocardiographically-gated, multislice spiral computed tomography. Circulation 103:2535–8

Agatston AS, Janowitz WR, Hildner FJ, Zusmer NR, Viamonte M, Detrano R (1990). Quantification of coronary artery calcium using ultrafast computed tomography. J Am Coll Cardiol 15:827–832

Alkadhi H, Leschka S, Marincek B, Wildermuth S et al (2006). Non-Invasive Coronary Angiography with 64-slice CT: effect of the average and the variability of the heart rate on image quality. Radiology, in press

Becker CR, Kleffel T, Crispin A, Knez A, Young Y, Schöpf UJ, Haberl R, Reiser MF (2001). Coronary artery calcium measurement: agreement of multirow detector and electron beam CT. Am J Roentgenol 176: 1295–1298

Begemann PG, van Stevendaal U, Manzke R et al (2005). Evaluation of spatial and temporal resolution for ECG-gated 16-row multidetector CT using a dynamic cardiac phantom. Eur Radiol 15(5):1015–1026

Burgstahler C, Heuschmid M, Beck T, et al (2005). Evaluation of global left ventricular myocardial function using retrospective ECG-gated 16-slice spiral computed tomography: comparison with MR and Echo. JACC 45:284A

Cademartiri F, Mollet N, van der Lugt A, et al (2004a). Non-invasive 16-row multislice CT coronary angiography: usefulness of a saline chaser. Eur Radiol 14:178–183

Cademartiri F, Nieman K, van der Lugt A, Raaijmakers RH, Mollet N, Pattynama PM, de Feyter PJ, Krestin GP (2004b). Intravenous contrast material administration at 16-detector row helical CT coronary angiography: test bolus versus bolus-tracking technique. Radiology 233:817–823

Cademartiri F, Mollet NR, van der Lugt A, McFadden EP, Stijnen T, de Feyter PJ, Krestin GP (2005). Intravenous contrast material administration at helical 16-detector row CT coronary angiography: effect of iodine concentration on vascular attenuation. Radiology 236:661–665

Cademartiri F, Mollet NR, Runza G, Baks T, Midiri M, McFadden EP, Flohr TG, Ohnesorge B, de Feyter PJ, Krestin GP (2006). Improving diagnostic accuracy of MDCT coronary angiography in patients with mild heart rhythm irregularities using ECG editing. AJR 186:1–5

Callister TQ, Cooil B, Raya SP, Lippolis NJ, Russo DJ, Raggi P (1998). Coronary artery disease: improved reproducibility of calcium scoring with an electron-beam CT volumetric method. Radiology 208:807–814

Clouse ME (2006). Noninvasive screening for coronary artery disease with computed tomography is useful. Circulation 113:125–135

De Backer G, Ambrosioni E, Borch-Johnsen K, et al (2003). European guidelines on cardiovascular disease prevention in clinical practice. Third Joint Task Force of European and Other Societies (Executive Summary). Eur Heart J 24:1601–1610

De Gruiter M, Flohr T, Oudkerk M (2006). A model for temporal resolution of multi-detector computed tomography of coronary arteries in relation to rotation time, heart rate and reconstruction algorithm. Eur Radiol, in press

Delhaye D, Remy-Jardin M, Teisseire A, Hossein-Foucher C, Leroy S, Duhamel A, Remy J (2006). Estimation of the right ventricular ejection fraction by multidetector-row CT: comparison with equilibrium radionuclide ventriculography. AJR (in press)

Dorgelo J, Willems TP, Geluk CA, van Ooijen PMA, Zijlstra F, Oudkerk M (2005). Multidetector computed tomography-guided treatment strategy in patients with non-ST elevation acute coronary syndromes: a pilot study. Eur Radiol 15:708–713

Erffa J, Daniel WG, Achenbach S (2006). Three-dimensional visualization of severe pericardial calcification in constrictive pericarditis using multidetector-row computed tomography. European Heart Journal 27:275

Flohr T, Prokop M, Schöpf, Kopp A, Becker C, Schaller S, White R, Ohnesorge B (2002). A new ECG-gated multi-slice spiral CT scan and reconstruction technique with extended volume coverage for cardio-thoracic applications. Eur Radiol 12:1527–1532

Flohr T, Schaller S, Stierstorfer K, Bruder H, Ohnesorge BM, Schoepf UJ (2005). Multi-detector row CT systems and image-reconstruction techniques. Radiology 235:756–773

Gaspar T, Halon DA, Schliamser J, et al (2004). Detection of coronary arterial narrowing with a new generation 40-slice multi-detector CT scanner in an unselected patient population. Int J Cardiovasc Imag 20:418 ff

Gaspar T, Halon D, Rubinshtein R, Peled N (2005). Clinical applications and future trends in cardiac CTA. Eur Radiol 15[Suppl 4]:D10-D14

Ghersin E, Litmanovich D, Dragu R, Rispler S, Lessick J, Amos O, Brook OR, Grubergc L, Beyar R, Engel A (2006). 16-MDCT Coronary angiography versus invasive coronary angiography in acute chest pain syndrome: a blinded prospective study (2006). Am J Roentgenol 186:177–184

Goldin JG, Yoon HC, Greaser LE, Heinze SB, McNitt-Gray MM, Brown MS, Sayre JW, Emerick AM, Aberle DR (2001). Spiral versus electron-beam CT for coronary artery calcium scoring. Radiology 221:213–221

Heuschmid M, Küttner A, Schröder S, et al (2003). Left ventricular functional parameters using ECG-gated multidetector spiral CT in comparison with invasive ventriculography. Fortschr Röntgenstr 175:1349–1354

Heuschmid M, Rothfuss J, Schröder S, et al (2005). Left ventricular functional parameters: comparison of 16-slice spiral CT with MRI. Fortschr Röntgenstr 177:60–66

Hong C, Bae KT, Pilgram TK (2003). Coronary artery calcium: accuracy and reproducibilityof measurements with multi-detector row CT – assessment of effects of different thresholds and quantification methods. Radiology 227: 795–801

Hong C, Chrysant GS, Woodard PK, Bae KT (2004). Coronary artery stent patency assessed with in-stent contrast

enhancement measured at multi-detector row CT angiography: initial experience. Radiology 233:286–291

Hofmann LK, Zou KH, Costello P, Schoepf UJ (2004). Electrocardiographically gated 16- section CT of the thorax: cardiac motion suppression. Radiology 233:927–933

Jakobs TF, Becker CR, Ohnesorge B, et al (2002). Multislice helical CT of the heart with retrospective ECG gating: reduction of radiation exposure by ECG-controlled tube current modulation. Eur Radiol 12(5):1081–1086

Johnson TR, Nikolaou K, Wintersperger BJ, Knez A, Boekstegers P, Reiser MF, Becker CR (2006). ECG gated 64 slice CT angiography for the differential diagnosis of acute chest pain. AJR (in press)

Juergens KU, Grude M, Fallenberg EM, et al (2002). Using ECG-gated multidetector CT to evaluate global left ventricular myocardial function in patients with coronary artery disease. Am J Roentgenol 179:1545–1550

Juergens KU, Grude M, Maintz D, et al (2004). Semiautomated analysis of left ventricular function using 16-slice multidetector-row computed tomography (MDCT) of the heart in comparison to steady-state-free-precession (SSFP) cardiac magnetic resonance imaging. Eur Radiol 14:S2–272

Juergens KU, Maintz D, Grude M, Boese JM, Heimes B, Fallenberg EM, Heindel W, Fischbach R (2005). Multi-detector row computed tomography of the heart: does a multi-segment reconstruction algorithm improve left ventricular volume measurements? Eur Radiol 15:111–117

Kim TH, Ryu YH, Hur J, et al (2005). Evaluation of right ventricular volume and mass using retrospective ECG-gated cardiac multidetector computed tomography: comparison with first pass radionuclide angiography. Eur Radiol 15:1987–1993

Koch K, Oellig F, Oberholzer K, et al (2005). Assessment of right ventricular function by 16 detector row CT: comparison with magnetic resonance imaging. Eur Radiol 15:312–318

Kopp AF, Ohnesorge B, Becker C, Schroder S, Heuschmid M, Kuttner A, Kuzo R, Claussen CD (2002). Reproducibility and accuracy of coronary calcium measurements with multi-detector row versus electron-beam CT. Radiology 225:113–119

Kopp AF, Heuschmid M, Reinmann A, et al (2005). Evaluation of cardiac function and myocardial viability with 16- and 64-slice multidetector computed tomography. Eur Radiol 15[Suppl 4]:D15-D20

Kuettner A, Beck T, Drosch T, et al (2005). Diagnostic accuracy of noninvasive coronary imaging using 16-detector slice spiral computed tomography with 188 ms temporal resolution. J Am Coll Cardiol 45:123–5

Lardo AC, Cordeiro MAS, Silva C, et al (2006). Contrast-enhanced multidetector computed tomography viability imaging after myocardial infarction – characterization of myocyte death, microvascular obstruction, and chronic scar. Circulation 113:394–404

Lawler LP, Pannu HK, Fishman EK (2005) MDCT evaluation of the coronary arteries, 2004: how we do it – data acquisition, postprocessing, display and interpretation. AJR 185:1402–1412

Leber AW, Knez A, Ziegler F, Becker A, Nikolaou K, Paul S, Wintersperger B, Reiser MF, Becker CR, Steinbeck G, Boekstegers P (2005). Quantification of obstructive and nonobstructive coronary lesions by 64-slice computed tomography – a comparative study with quantitative coronary angiography and intravascular ultrasound. JACC 46(1):147–154

Leschka S, Alkadhi H, Plass A, Desbiolles L, Gruenenfelder J, Marincek B, Wildermuth S (2005). Accuracy of MSCT coronary angiography with 64-slice technology: first experience. Eur Heart J 26: 1482–1487

Mahnken AH, Spuentrup E, Niethammer M, et al (2003). Quantitative and qualitative assessment of left ventricular volume with ECG-gated multislice spiral CT: value of different image reconstruction algorithms in comparison to MRI. Acta Radiol 604–611

Mahnken AH, Koos R, Katoh M, et al (2005a). Sixteen-slice spiral CT versus MR imaging for the assessment of left-ventricular function in acute myocardial infarction. Eur Radiol 15:714–720

Mahnken AH, Katoh M, Bruners P, et al (2005b). Acute myocardial infarction: assessment of left ventricular function with 16-detector row spiral CT versus MRI – imaging study in pigs. Radiology 236:112–117

Mahnken AH, Hohl C, Suess C, Bruder H, Mühlenbruch G, Das M, Günther RW, Wildberger JE (2006). Influence of heart rate and temporal resolution on left-ventricular volumes in cardiac multi-slice spiral CT: a phantom study. Invest Radiol (in press)

Maintz D, Seifarth H, Flohr T, Kraemer S, Wichter T, Heindel W, Fischbach R (2003). Improved coronary artery stent visualization and in-stent stenosis detection using 16-slice computed-tomography and dedicated image reconstruction technique. Invest Radiol 38: 790–795

Maintz D, Seifarth H, Raupach R, Flohr T, Rink M, Sommer T, Ozgun M, Heindel W, Fischbach R (2006). 64-slice multidetector coronary CT angiography: in vitro evaluation of 68 different stents. Eur Radiol (in press)

McCollough CH, Ulzheimer S, Halliburton SS, White RD, Kalender WA (2003). A multi-scanner, multi-manufacturer, international standard for the quantification of coronary artery calcium using cardiac CT (Abstract). Abstracts of the RSNA 2003. Radiology 229(P):630

Mieres JH, Shaw LJ, Arai A, et al (2005). Role of noninvasive testing in the clinical evaluation of women with suspected coronary artery disease. Consensus statement of the American Heart Association. Circulation 111:682–696

Mollet NR, Cademartiri F, Krestin GP, et al (2005a). Improved diagnostic accuracy with 16-row multi-slice computed tomography coronary angiography. J Am Coll Cardiol 45:128 –32

Mollet NR, Cademartiri F, van Mieghem CAG, Runza G, McFadden EP, Baks T, Serruys PW, Krestin GP, de Feyter PJ (2005b). High-Resolution spiral computed tomography coronary angiography in patients referred for diagnostic conventional coronary angiography. Circulation 112:2318–2323

Moser KW, Bateman TM, O'Keefe JH, Jr., McGhie AI (2004).

Interscan variability of coronary artery calcium quantification using an electrocardiographically pulsed spiral computed tomographic protocol. Am J Cardiol 93:1153–1155

Mühlenbruch G, Thomas C, Wildberger JE, Koos R, Das M, Hohl C, Katoh M, Günther RW, Mahnken AH (2005a). Effect of varying slice thickness on coronary calcium scoring with multislice computed tomography in vitro and in vivo. Invest Radiol 40:695–699

Mühlenbruch G, Koos R, Wildberger JE, Günther RW, Mahnken AH (2005b). Imaging of the cardiac venous system: comparison of MDCT and conventional angiography. AJR 185:1252–1257

Nasir K, Budoff MJ, Post WS, Fishman EK, Mahesh M, Lima JA, Blumenthal RS (2003). Electron beam CT versus helical CT scans for assessing coronary calcification: current utility and future directions. Am Heart J 146:969–977

Nieman K, Oudkerk M, Rensing B, et al (2001). Coronary angiography with multi-slice computed tomography. Lancet 357:599–603

Nikolaou K, Knez A, Rist C, Wintersperger B, Leber AW, von Ziegler F, Johnson T, Boekstegers P, Reiser MF, Becker CR (2005). 64-Slice Computed Tomography in the Diagnosis of Ischemic Heart Disease: Patient-based vs. Segment-based Analysis. AJR 185

Ohnesorge B, Flohr T, Becker C R, Kopp A F, Knez A Baum U, Klingenbeck-Regn K, Reiser MF (2000). Cardiac imaging by means of electrocardiographically gated multisection spiral CT: Initial Experience. Radiology 217:564–571

Ohnesorge B, Flohr T, Fischbach R, Kopp AF, Knez A, Schroder S, Schopf UJ, Crispin A, Klotz E, Reiser MF, Becker CR (2002). Reproducibility of coronary calcium quantification in repeat examinations with retrospectively ECG-gated multisection spiral CT. Eur Radiol 12:1532–1540

Ohnesorge BM, Hofmann LK, Flohr TG, Schöpf UJ (2005). CT for imaging coronary artery disease: defining the paradigm for its application. Int J Cardiovas Imaging 21: 85–104

O'Rouke RA, Brundage BH, Frölicher VF, et al (2000). ACC/AHA Expert Consensus Document on EBCT for the Diagnosis and Prognosis of Coronary Artery Disease. Circulation 102:126–140

Raff GL, Gallagher MJ, O'Neill WW, Goldstein JA (2005a). Diagnostic accuracy of noninvasive coronary angiography using 64-slice spiral computed tomography. JACC 46 (3): 552–557

Raman SF, Cook SC, McCarthy, et al (2005). Usefulness of multi-detector row computed tomography to quantify right-ventricular size and function in adults with either tetralogy of Fallot or transposition of the great arteries. Am J Cardiol 95:683–686

Remy-Jardin M, Delhaye D, Teissire A, Hossein-Foucher C, Delannoy-Deken V, Duhamel A, Remy J (2006). Multidetector-row CT of the right ventricular function: Impact of the methodological approach in the estimation of the right ventricular ejection fraction. AJR (in press)

Rius T,Sanz J, Kuschnir P, Salguero R, Fischbach R, Ohnesorge B, Fuster V, Poon M (2006). Assessment of left and right ventricular function with multi-detector row computed tomography (MDCT). Comparison with cardiac magnetic resonance (CMR). JACC (in press)

Salem R, Remy-Jardin M, Delhaye D, Khalil C, Teisseire A, Delannoy-Deken V, Duhamel A, Remy J (2006). Integrated cardio-thoracic imaging with ECG-gated 64-slice multidetector-row CT: initial findings in 133 patients. Eur Radiol (in press)

Schmermund A, Erbel R, Silber S (2002). Age and gender distribution of coronary artery calcium measured by four-slice computed tomography in 2030 persons with no symptoms of coronary artery disease. The MUNICH registry. Am J Cardiol 90:168–173

Schoenhagen P, Halliburton SS, Stillman AE, Kuzmiak SA, Nissen SE, Tuzcu EM, White RD (2004). Noninvasive imaging of coronary arteries: current and future role of multidetector row CT. Radiology 232:7–17

Schoepf UJ, Becker CR, Ohnesorge BM, Yucel EK (2004). CT of coronary artery disease. Radiology 232:18–37

Schoepf UJ, Savino G, Lake DR, Ravenel JG, Costello P (2005). The age of CT pulmonary angiography. J Thorac Imaging 20:273–279

Schoepf UJ, Zwerner PL, Savino G, Herzog C, Kerl M, Costello P (2006). How we do it: coronary CTA. Radiology (in press)

Seifarth H, Ozgun M, Raupach R, Flohr T, Heindel W, Fischbach R, Maintz D (2006). 64- versus 16-slice CT angiography for coronary artery stent assessment: in vitro experience. Invest Radiol 41:22–27

Silber S, Richartz BM (2005). Impact of cardiac CT and cardiac MR on the assessment of coronary risk (German). Z Kardiol 94 Suppl. 4:1–11

Trabold T, Buchgeister M, Küttner A, Heuschmid M, Kopp AF, Schröder S, Claussen CD (2003). Estimation of radiation exposure in 16-detector row computed tomography of the heart with retrospective ECG-gating. RöFo 175:1051–1055

Ulzheimer S, Kalender WA (2003). Assessment of contrary calcium scoring performance in cardiac computed tomography. Eur Radiol 13:484–497

White CS, Kuo D, Kelemen M, Jain V, Musk A, Zaidi E, Read K, Sliker C, Prasad R (2005). Chest Pain evaluation in the emergency department: Can MDCT provide a comprehensive evaluation? AJR 185:533–540

Wintersperger B, Rist C, Nikolaou K, Becker CR, et al (2006). Image quality, motion artifacts and reconstruction timing of 64-slice coronary CT angiography with 0.33 s rotation speed. Invest Radiology (in press)

6 Image Visualization and Post-processing Techniques

Thomas Flohr and Bernd Ohnesorge

Contents

6.1 Trans-axial Image Slices *151*
6.2 Multi-planar Reformation *153*
6.3 Maximum-Intensity Projection *154*
6.4 Volume-Rendering Technique *157*
6.5 Vessel Segmentation and Vessel Analysis *162*
6.6 Four-Dimensional Visualization and Functional Parameter Assessment *165*
6.7 Myocardial Perfusion Evaluation *169*
6.8 Quantification of Coronary Calcification *171*
References *176*

The application of imaging techniques to original axial images of a CT scan in order to derive additional information or hide unwanted information that distracts from the clinical findings is called image post-processing. Image post-processing requires modification of a 3D image volume, which in most cases consists of a stack of individual axial images. The fundamental 3D unit in this volume is called a «voxel». Ideally, volume image data are of high spatial resolution and isotropic in nature, i.e., each voxel is of equal dimensions in all three spatial axes, and forms the basis for image display in arbitrarily oriented imaging planes and advanced image post-processing techniques. With the advent of multi-slice CT and its on-going refinement, isotropic sub-millimeter voxels can be obtained for the majority of clinical examinations. This has improved the diagnostic quality of image post-processing such that it has become a vital component of medical imaging today, in particular for CT angiography (Prokop 1997, Rankin 1999, Addis 2001). The axial source images contain the basic information of a CT scan. They can be supplemented by basic 3D post-processing tools and advanced methods for the analysis of complex anatomy, automated quantification, and functional evaluation (Vogl 2002, van Ooijen 2003, de Feyter 2005).

6.1 Trans-axial Image Slices

Trans-axial image slices are the basic outcome of a multi-slice CT scan and include all of the acquired information. In cardiac CT examinations, axial images should be reviewed in all cases, e. g., by scrolling through them up and down in the craniocaudal direction, which gives a quick overview of the relevant cardiac structures, including the coronary arteries. The matrix size for axial images in CT is generally 512 × 512 picture elements (pixels). Considered as a part of a 3D image volume, an axial image is a layer of 512 × 512 voxels within that volume. The size of the voxel in the image plane (x-y direction) is determined by the in-plane pixel size and therefore by the reconstructed field-of-view (FOV). The size of the voxel in the longitudinal direction (z-direction) is given by the slice width and the image increment. The FOV of an axial image is the diameter of the area that is depicted in the image. The in-plane voxel size can be calculated as FOV divided by matrix size. Typically, a FOV of 150–180 mm is chosen for image reconstruction in cardiac CT imaging, resulting in 0.29- to 0.35-mm in-plane voxel size. The in-plane voxel size is frequently misinterpreted as the in-plane resolution of a CT image. Instead, image resolution is mainly determined by the CT system geometry, detector aperture, and convolution kernel

(filter) chosen for image reconstruction. Only in rare cases does the in-plane resolution correspond to the in-plane voxel size. Typical CT scanner geometries and convolution kernels used for cardiac CT examinations provide a resolution of 8–12 lp/cm, which corresponds to an object size of 0.4–0.6 mm that can be differentiated. The resolution in the image is determined by the geometry of the scanner and not by the voxel size. Given the 512 × 512 pixels in the image, a 150- to 180-mm FOV produces an in-plane voxel size of 0.29- to 0.35-mm. However, the image resolution remains to be 0.4–0.6 mm, depending on the scanner and filter kernel parameters. Further reducing the FOV for image reconstruction will therefore reduce the in-plane voxel size, but will not increase image resolution. Only in special cases, such as high-resolution thorax imaging with a large FOV of 350–400 mm, will the in-plane voxel size be the limiting factor for in-plane resolution. As an example of visualization of the cardiac anatomy in axial slices, Fig. 6.1 shows axial images, acquired using a 64-slice CT scanner, at different anatomical

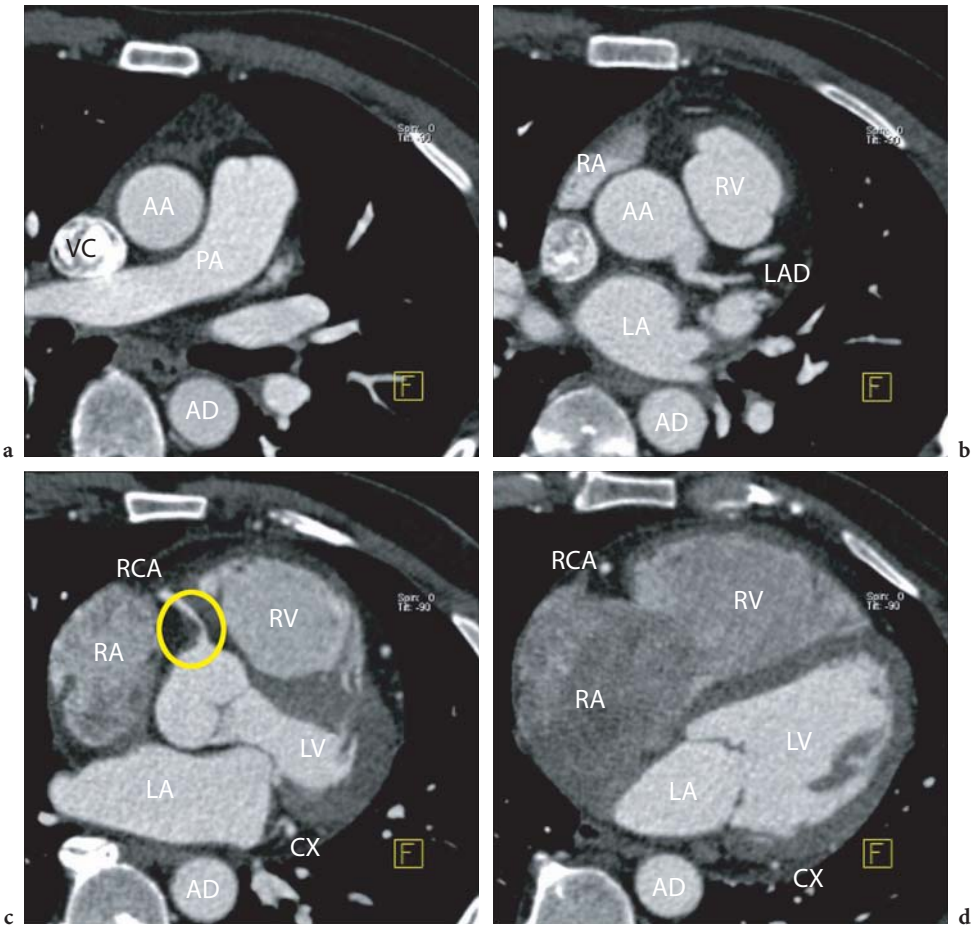

Fig. 6.1. Axial images at different anatomical levels (**a–d**, in craniocaudal direction) of a coronary CT angiography examination in a patient with a stenosis in the right coronary artery (*yellow circle*). The images were acquired using a 64-slice CT scanner with 64 × 0.6-mm slices per rotation and 0.75-mm slice width. Axial images include all of the information acquired in a CT scan and should be reviewed in any case, e.g., by scrolling through them. For better orientation, important anatomical landmarks have been labeled. *AA* Ascending aorta, *PA* pulmonary artery, *AD* descending aorta, *VC* vena cava, *RA* right atrium, *RV* right ventricle, *LA* left atrium, *LV* left ventricle, *LAD* left anterior descending coronary artery, *RCA* right coronary artery, *CX* circumflex artery. (Case courtesy of Erlangen University, Germany)

levels from a coronary CTA examination in a patient with a stenosis in the right coronary artery.

6.2 Multi-planar Reformation

In multi-planar reformations (MPRs), a plane is defined in a 3D image volume, and all voxels on that plane are visualized in a planar image. Simple examples of MPR orientations are sagittal and coronal views, which are widely used in general radiology but are of limited use in cardiac imaging due the complex course of the cardiac anatomy and the coronary arteries. Instead, oblique MPRs, which can be scrolled through similar to axial images, are the most helpful for cardiac CT. In this respect, two stacks of oblique planes are of particular interest: the planes parallel to a line along the left anterior descending artery (LAD), and the planes parallel to a line connecting the right coronary artery (RCA) and circumflex artery (CX) (Fig. 6.2). Scrolling through the first set of planes allows the tortuous course of the LAD to be followed, while scrolling through the second set of planes will display the anatomy of the RCA and CX.

MPR resolution depends on both the in-plane resolution of the original axial images and the through-plane resolution, which is a function of reconstruction slice width and image increment. For multi-slice spiral CT, through-plane resolution can be improved by reconstructing overlapping images with an increment that equals 50–70% of the reconstructed slice width. In this way, objects that are smaller than the reconstructed slicewidth can be resolved in the longitudinal (z-) direction. Depending on the orientation of the MPR, the relative influence of in-plane and longitudinal resolution varies, and so does the resulting MPR resolution for non-isotropic image data. Considering the typical in-plane resolution of about 0.5 mm for high-resolution cardiac CT angiography protocols, it is obvious that the reconstructed slice width of the axial source images should be as narrow as possible, at best sub-millimeter, to optimize MPR image quality. In general, the smallest available reconstruction slice width should be used as long as the signal-to-noise ratio of the images remains acceptable. For larger patients, the reconstruction of wider axial slices as an input for MPRs can be considered in order to find the best trade-off between image noise and longitudinal resolution. The latest generation of 64-slice CT systems can provide 0.4-mm longitudinal resolution using overlapping images with a reconstruction slice-width of 0.6 mm (Flohr 2004). As these scanners provide true isotropic image data with sub-millimeter resolution, the resolution of MPRs is then homogeneous and independent of the orientation of the MPR image planes.

To trade-off between image resolution and image noise, the MPR slice thickness can be modified. In that case, all voxels within a given distance orthogonal to the MPR plane are averaged, and a so-called slab-MPR is created. Slab-MPRs, e. g., with a slab thickness of 2–5 mm, are useful to reduce image noise and to visualize larger parts of tortuous cardiac anatomy.

Correct positioning of the MPR planes is critical for a correct diagnosis, as partial-volume effects may influence the assessment of anatomical details (Fig. 6.3). For this reason, multiple MPR stacks with different orientations and with overlapping reconstruction increments are widely used. On some CT scanners, pre-determined stacks of double-oblique MPRs along preferred planes can be directly reconstructed from the raw data to facilitate the clinical workflow (Fig. 6.4).

Alternatively, curved MPRs can be used that are defined on curved planes instead of straight planes and that capture the course of tortuous vessels and coronary arteries along their entire lengths in a single image (Fig. 6.5). To generate a curved MPR, the user interactively places multiple markers in the vessel of interest along its course while scrolling through the axial slices. The processing software then connects the markers with a fitted line and generates a MPR along this line. Newer evaluation software tools also provide an automated calculation of the centerline of the target vessel, which defines the curved visualization plane (see Sect. 6.5).

Curved MPR is particularly useful for displaying the in-stent lumen, as with this approach interference with the desired lumen information by the very dense stent material can be minimized (Fig. 6.6).

MPR techniques are readily and easily available and represent a standard feature on any basic 3D application package. MPRs do not require extensive

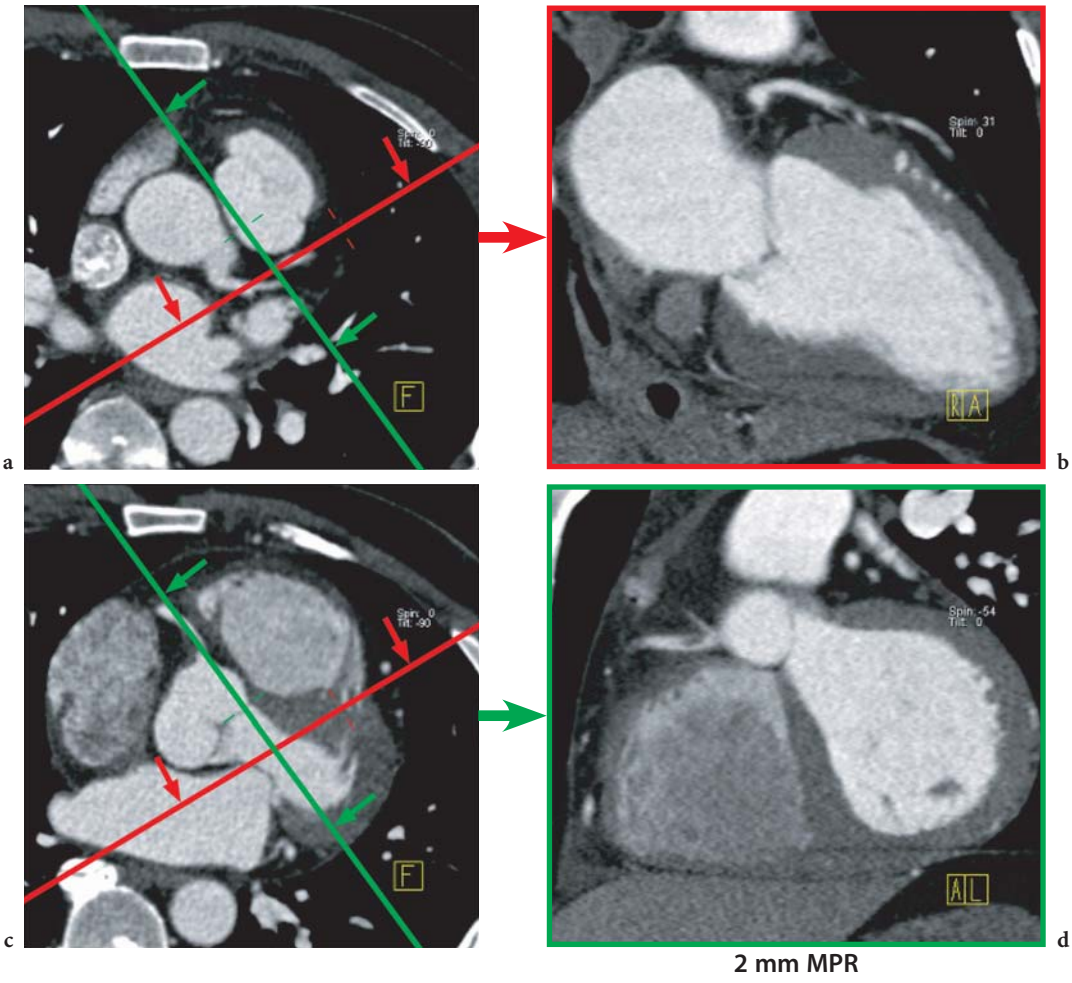

Fig. 6.2. Multiplanar reconstructions (MPRs) for a coronary CT angiography examination displaying the proximal *LAD* (**a**, **b**) and proximal *RCA* (**c**, **d**). The axial images were acquired using a 64-slice CT scanner with 64 × 0.6-mm slices per rotation and 0.75-mm slice width. MPR thickness was chosen to be 2 mm. The green and red lines in the axial images indicate the image planes of the MPRs. Stacks of MPRs in pre-defined directions are the basis for a standardized, routine evaluation of workflow. (Case courtesy of Erlangen University, Germany)

user interaction, such as the time-consuming manual segmentation of potentially overlapping structures that is needed in other post-processing approaches. Thus, MPRs are frequently used in routine clinical evaluation algorithms. They maintain the full information of the axial CT images, in particular the CT density values (HU values). However, since MPRs are operator-dependent, improper positioning of the MPR planes may introduce false-negative and false-positive stenoses, or incorrectly estimate the degree of stenoses. Interactive viewing of stacks of MPRs from multiple viewing angles combined with the use of curved MPRs is therefore recommended.

6.3 Maximum-Intensity Projection

Maximum intensity projections (MIPs) are arbitrarily oriented planar images similar to MPRs.

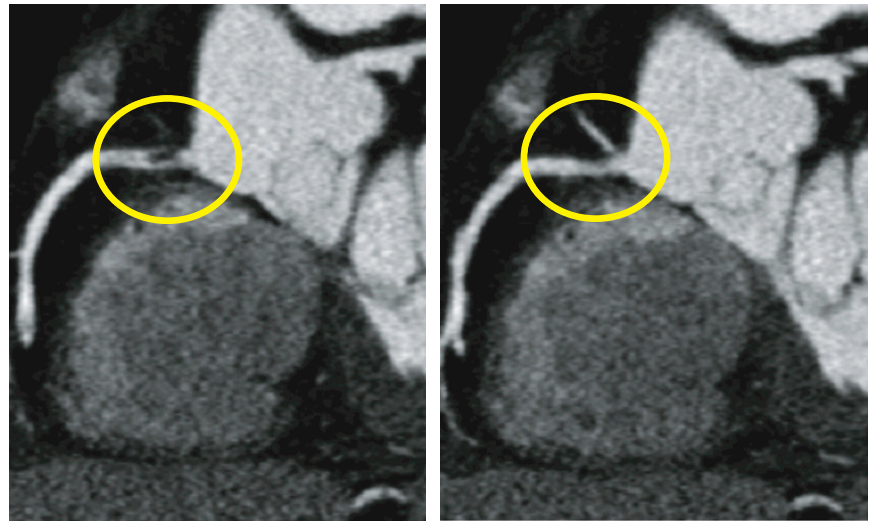

a b

Fig. 6.3a, b. Two MPRs on slightly shifted image planes along the RCA. While one MPR reveals a high-grade stenosis (**a**) the other has slightly shifted plane and reveals only a moderate stenosis (**b**) in the RCA (*yellow circles*). Positioning of the MPR planes is operator-dependent and improper positioning may introduce false-negative and false-positive stenoses or varyingly estimate the degree of stenoses. The use of MPRs from different viewing angles is therefore recommended. (Case courtesy of Erlangen University, Germany)

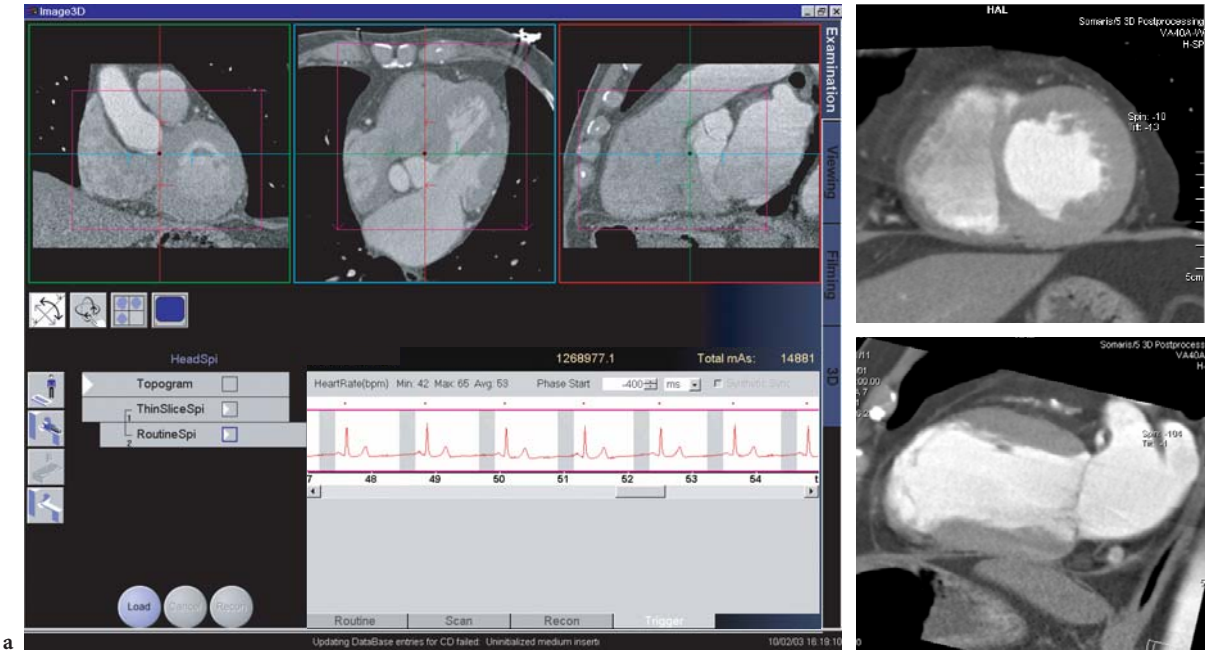

a b c

Fig. 6.4a–c. Direct MPR reconstruction for a cardiac CT examination obtained on a 16-slice CT scanner. True 3D-based planning of the MPR views (**a**) enables direct reconstruction of MPR stacks from the scan data with pre-defined MPR thickness and increment. The usual step of generating axial slices can be skipped. In the example given, MPR stacks in short (**b**) and long heart (**c**) axes are generated in diastolic phase. (Case courtesy of Tübingen University, Germany)

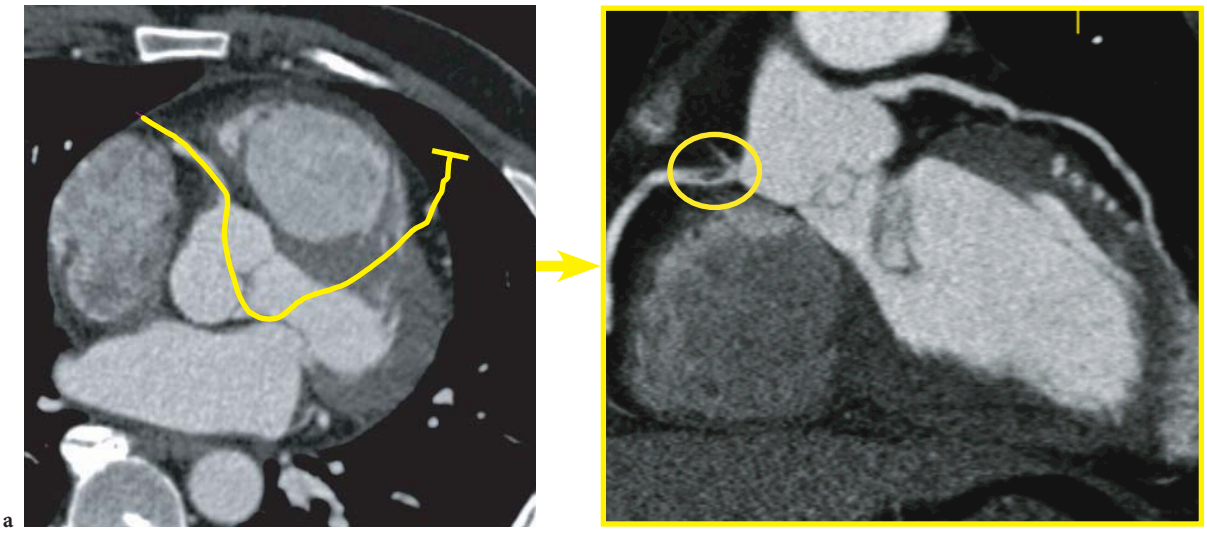

Fig. 6.5. Curved MPR for a coronary artery examination obtained on a 64-slice CT scanner. **a** The yellow line in the axial image indicates the curved image plane of the MPR, which has been generated manually by the user, with interactive placement markers in the vessel based on the axial slices. **b** The curved MPRs can be used to follow the course of a tortuous coronary artery along its entire length and reveals a high-grade stenosis in the proximal RCA (*yellow circle*). (Case courtesy of Erlangen University, Germany)

Each pixel of the 2D MIP image is generated from parallel rays that are cast through the 3D image volume. As result of the projection, the pixels in the MIP image represent the maximum CT number encountered in each ray. MIPs preserve the gray scale of the original axial images, and they reduce the visually perceived image noise without compromising the visually perceived image sharpness. The differentiation between contrast-enhanced vascular structures and background is good, and calcifications can be clearly depicted. However, MIPs do not provide any depth information, which is a drawback for the visualization of complex anatomy, such as the thoracic vessels, but does not play a major role for coronary artery imaging. MIPs are projection images, and thus high-density structures such as the contrast-filled cavities of the heart may overlap the coronary arteries in the projection direction and obscure structures of interest. For the same reason, hypo-attenuating intraluminal lesions may not be identified, unless they are adjacent to the vessel wall and the proper viewing direction has been chosen.

To avoid these shortcomings, thin-slab MIPs (Rubin 1993) have been introduced. These are obtained by first generating thin-slab MPRs from which the MIP images are reconstructed. In a thin-slab MIP, the maximum CT number within a given distance orthogonal to the MIP plane is displayed for every ray. For an evaluation of coronary arteries, the thickness of the slab has to be adjusted to the size and the course of the artery. Typical slab thicknesses range from 3 to 10 mm. In a standardized approach, the reconstruction of overlapping thin-slab MIP images with an increment smaller than the slab thickness (e.g., 1-mm increment for a 3-mm slab thickness) is recommended.

For visualization of cardiac and coronary anatomy, the same planes as discussed for slab MPRs should be considered (see Sect. 6.2). In particular, for diagnosis of the coronary arteries, planes in parallel to a line connecting RCA and CX, and planes in parallel to a line along the LAD should be used. MIPs with 5-mm thickness along the RCA and LAD are shown in Fig. 6.7, and can be directly compared to the corresponding MPR reconstructions that have been generated in identical planes (Fig. 6.2).

In a more interactive evaluation approach, thin-slab MIPs can be scrolled through the volume (sliding thin-slab MIPs). By carefully adjusting both the thickness and the orientation of the MIP plane, each

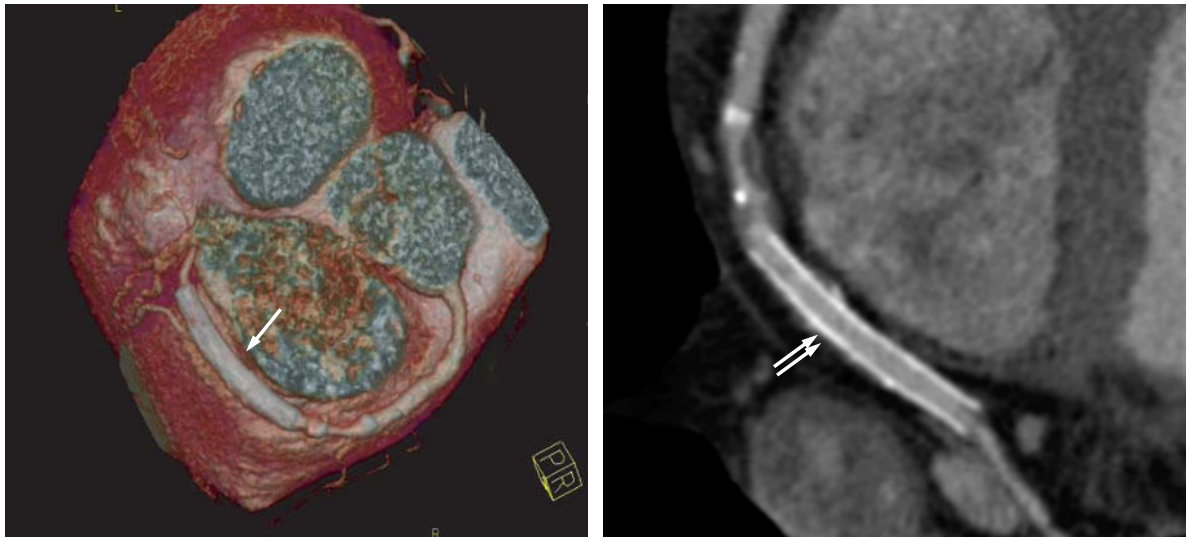

a b

Fig. 6.6a, b. Curved MPR for a coronary artery examination obtained on a 16-slice CT scanner with 16 × 0.75-mm collimation. The patent in-stent lumen of the stent in the distal RCA coronary artery can be demonstrated in VRT display (**a**, *arrow*) and is readily visualized with curved MPR reconstruction (**b**, *double arrow*). (Case courtesy of HSC Medical Center, Kuala Lumpur, Malaysia)

coronary artery can be displayed in its entire length in many cases. Similar to the automated generation of pre-defined MPR stacks, some CT scanners allow for reconstruction of pre-determined stacks of double-oblique MIPs along preferred planes directly from the raw data, thus facilitating the clinical workflow (Fig. 6.8).

More recent software platforms allow for the reconstruction of curved MIPs in analogy to curved MPRs (Raman 2003). In analogy to curved MPRs, curved MIPs are generated by the interactive placement of multiple markers in the vessel of interest along its course while scrolling through the axial slices. The processing software then connects the markers with a fitted line and generates a MIP along this line. Newer evaluation-software tools also provide an automated calculation of the centerline of the target vessel that defines the curved visualization plane (see Sect. 6.5). Some illustrative examples of in which curved MIPs are directly compared with curved MPRs in identical planes are shown in Fig. 6.9.

Similar to MPRs, MIPs are fast and readily available, and they are included in any basic 3D evaluation-software platform. In many institutions, MIPs are the basis for a standardized routine evaluation workflow. When the slab thickness is properly selected, visualization of non-calcified and mixed plaques is excellent (Fig. 6.10). However, MIPs use only a part of the available data, thus discarding information that is included in the original axial images. Relevant anatomical details may be obscured by overlapping structures, and stenoses may be under- or overestimated (van Ooijen 2003). MIPs are not recommended for the visualization of stents or heavily calcified coronary vessels, since the vessel lumen will be obscured due to the principle of the MIP projection (Fig. 6.10).

6.4 Volume-Rendering Technique

Direct volume-rendering techniques (VRTs) are advanced 3D post-processing methods that have meanwhile entered clinical routine due to continuous improvement in computer hardware and software. VRTs use all available data in the volume image. A

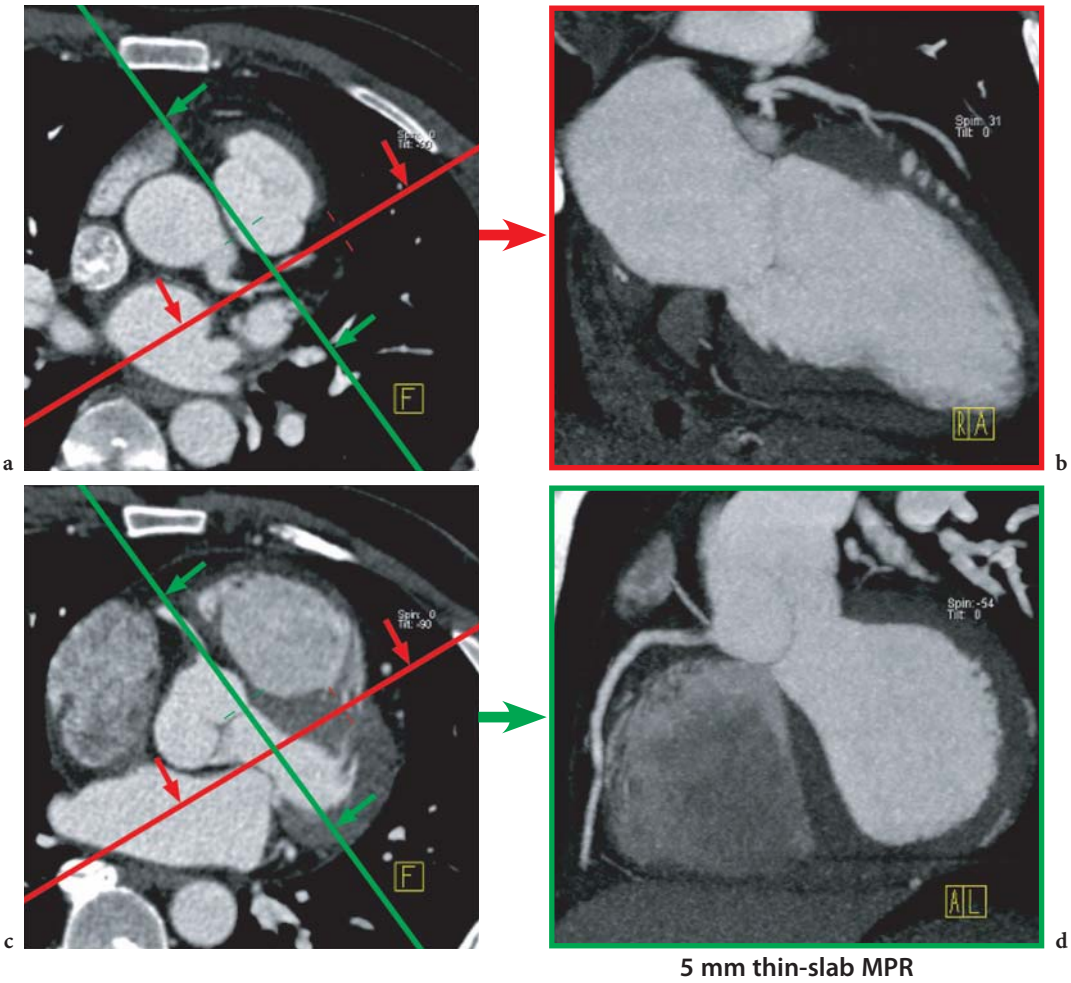

Fig. 6.7. Maximum-intensity projection (MIP) for a coronary CT angiography examination displaying the proximal LAD (**a**, **b**) and proximal RCA (**c**, **d**). The axial images were acquired using a 64-slice CT scanner with 64 × 0.6-mm slices per rotation and 0.75-mm slice width. MIP slab thickness was chosen to be 5 mm. The green and red lines in the axial images indicate the image planes of the MIPs. (Case courtesy of Erlangen University, Germany)

voxel-intensity histogram is generated, and several parameters, such as color, brightness and opacity, are assigned to each voxel according to its HU value. Similar to MIP projections, rays are cast through the 3D image volume. Unlike MIPs, however, all voxels along a ray contribute to the resulting pixel in the VRT image proportional to their opacities.

The opacities of all voxels are summed up using weighting factors. Assume walking along a ray through the object from voxel 1 to voxel (n – 1) and finally voxel n. The CT density Sum_n of the resulting pixel in the VRT image can be calculated according to the recursive equation (Eq. 6.1).

$$Sum_n = Op_n \cdot CT_n + (1 - Op_n) \cdot Sum_{n-1} \qquad (6.1)$$

Opn is the opacity of voxel n and CT_n is its HU value. An opacity of 0 ($Op_n = 0$) means that the corresponding voxel is completely transparent; it does not contribute to the resulting VRT image. An opacity of 1 ($Op_n = 1$) means that the corresponding voxel is completely opaque. Values between 0 and 1 charac-

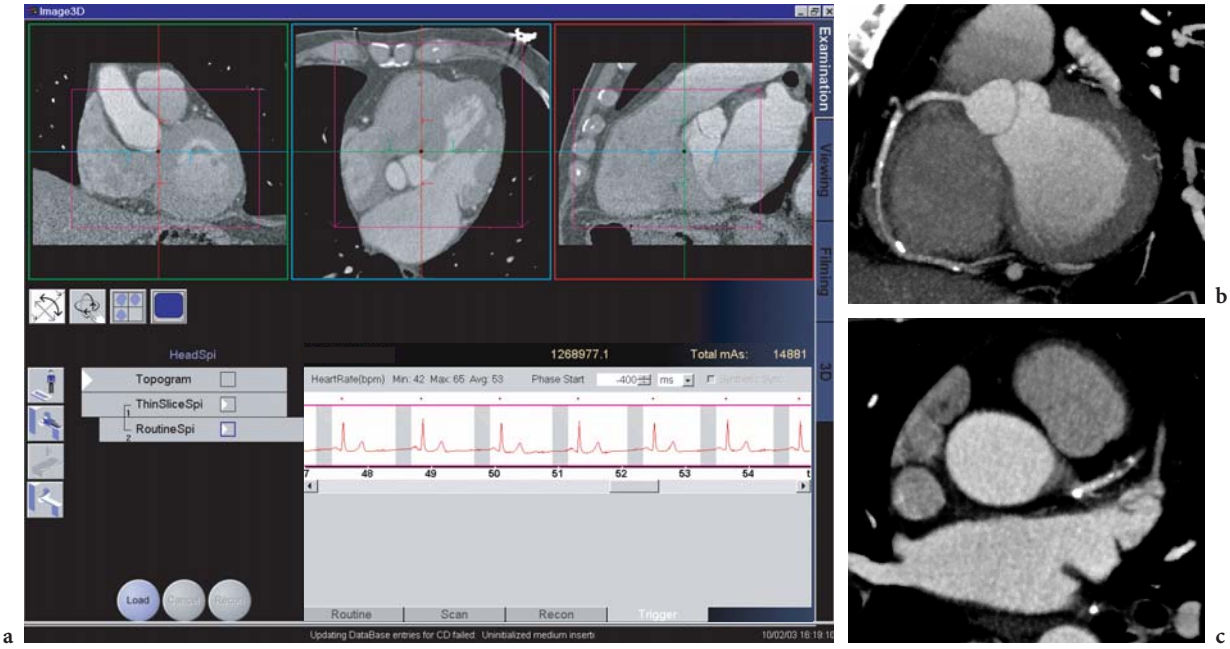

Fig. 6.8a–c. Direct MIP reconstruction for a cardiac CT examination obtained on a 16-slice CT scanner. True 3D-based planning of the MIP views (**a**) enables direct reconstruction of MIP stacks from the scan data with pre-defined MIP slab thickness and increment. The usual step of generating axial slices can be skipped. In the example, the MIP stacks are generated in diastolic phase using RAO (**b**) and LAO (**c**) projections. (Case courtesy of Tübingen University, Germany)

terize different degrees of transparency. It is obvious from Eq. 6.1 that when a pixel n with opacity $Op_n = 1$ is traversed, the contribution of all preceding voxels will be set to 0, since the term $(1 - Op_n)$ then equals 0. In other words, as soon as a completely opaque voxel has been traversed, only this voxel will be shown in the resulting image and all previously traversed voxels will be hidden. Assigning different opacities to different ranges of CT values enables the user to control the contribution of voxels within these CT density ranges to the resulting VRT image. The user can make these voxels more or less transparent, thus hiding or showing the corresponding anatomical details and adjusting the 3D depth, contrast, and transparency of the VRT image. The relevant anatomical structures in cardiac images are fat, with a CT density of approximately – 100 HU; soft tissue, with a CT density of approximately 50 HU; contrast-filled vessels, with a CT density of approximately 200–300 HU, and calcifications and bony structures with a CT density > 100–150 HU. Usually, linear, triangular, or trapezoidal functions are used to assign opacity to a certain CT density range. Figure 6.11 shows a gray-scale VRT reconstruction of a heart. At the bottom, the histogram of the CT values is shown together with the opacity curve. The opacity for all voxels with a CT density less than – 80 HU is set to zero and these voxels are not displayed in the resulting VRT. The opacity increases linearly in the range – 80 HU to 250 HU; constant maximum opacity is assigned to all voxels with a CT density > 250 HU. With these settings, soft tissue is relatively transparent and contrast filled vessels – the structures of interest – are relatively opaque. The visibility of the contrast filled coronary arteries is therefore enhanced. Figure 6.11 also demonstrates the effect of increasing maximum opacity levels.

Instead of gray values, colors can be attributed to the voxels according to their CT numbers (Fig. 6.12). Although the choice of colors is arbitrary, brownish red is most commonly used for soft tissue in the heart. To improve the visibility of boundaries between different tissue types and the delineation of anatomical structures, gradient transfer functions are used in more elaborate VRT approaches. For

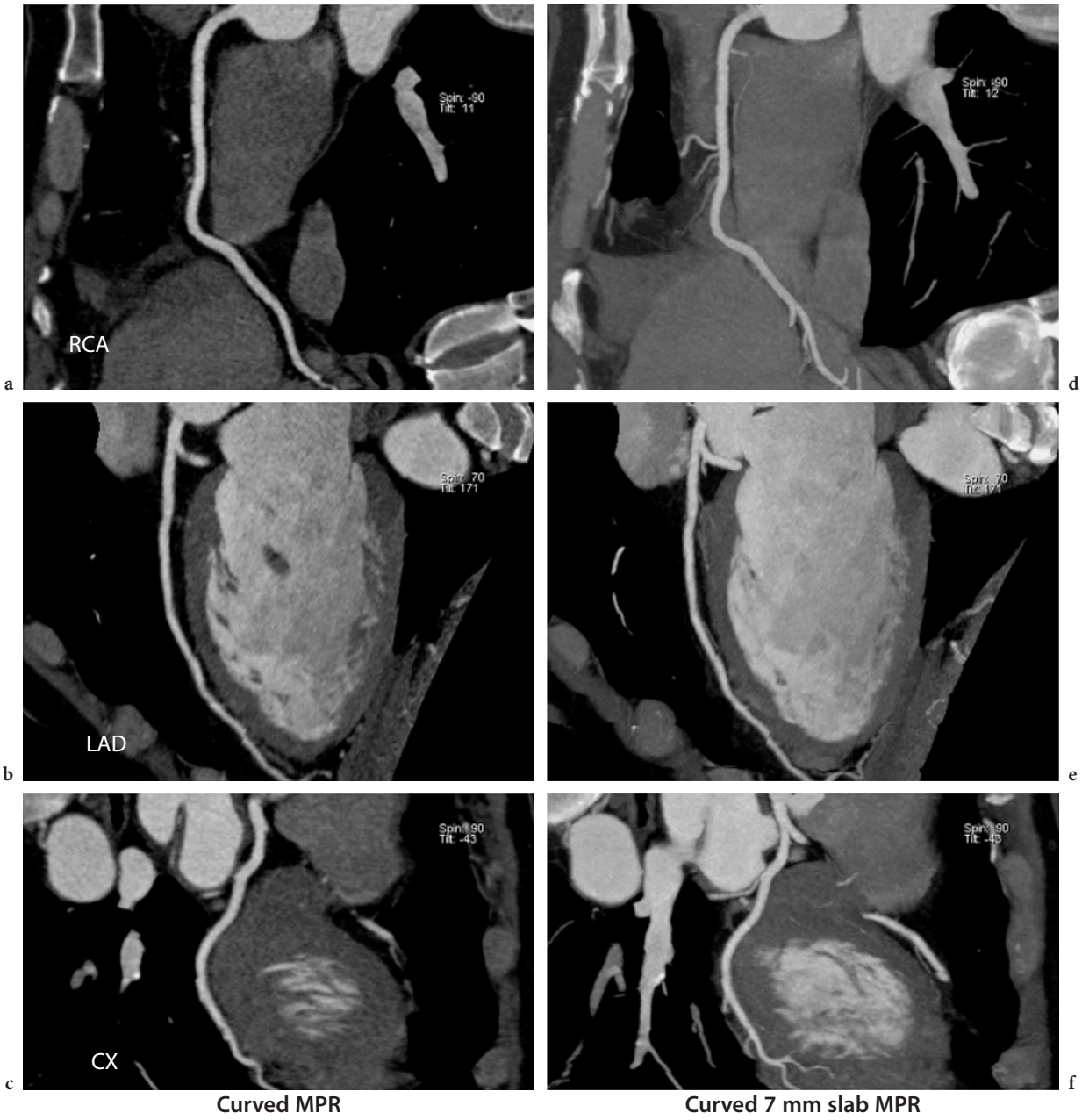

Fig. 6.9. Curved MPRs (**a–c**) and curved thin-slab MIPs (**d–f**) along the LAD, RCA and CX in a patient with normal coronary anatomy. The curved MPR was generated with 2-mm MPR thickness; for the curved MIP, the MIP slab thickness was 7 mm. The images were generated based on an automatically detected centerline of the vessels, which defines the curved visualization plane. The direct comparison shows that curved MIP provides a more detailed view of the coronary anatomy than curved MPR. (Case courtesy of Erlangen University, Germany)

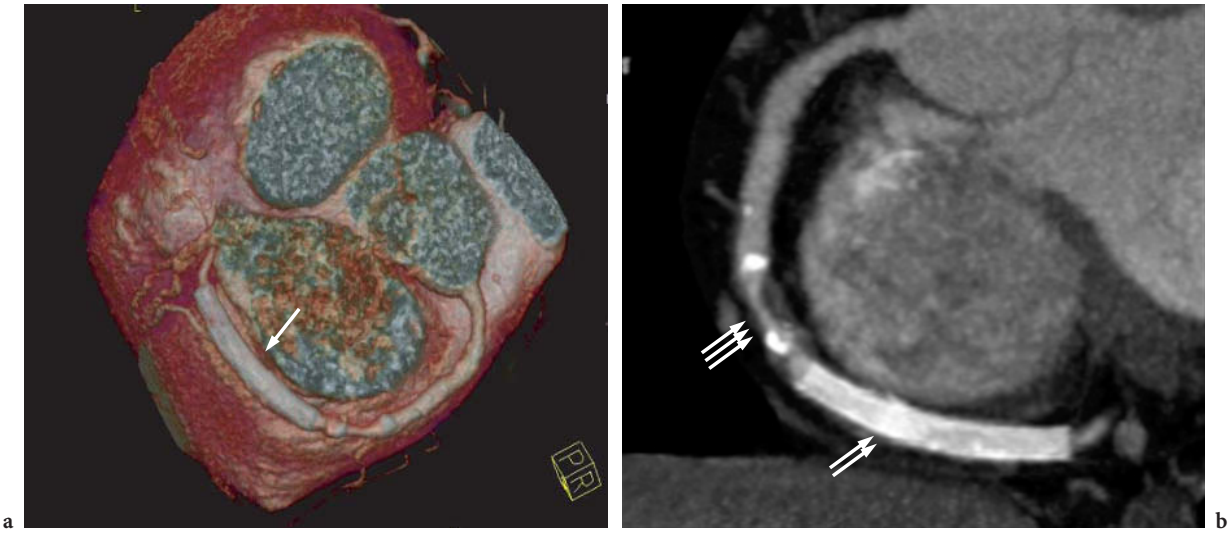

Fig. 6.10a, b. Manually defined curved MIP with 5-mm slab thickness for a coronary artery examination obtained on a 16-slice CT scanner with 16 × 0.75-mm collimation. The in-stent lumen of the stent in the distal RCA can be demonstrated in VRT display (**a**, *arrow*) and cannot be adequately visualized with curved MIP reconstruction (**b**, *double arrow*). Therefore, MPR is to be preferred over MIP for the visualization of in-stent lumen. However, visualization of the stenotic lesion and the corresponding mixed plaque (**b**, *triple arrow*) is excellent. (Case courtesy of HSC Medical Center, Kuala Lumpur, Malaysia)

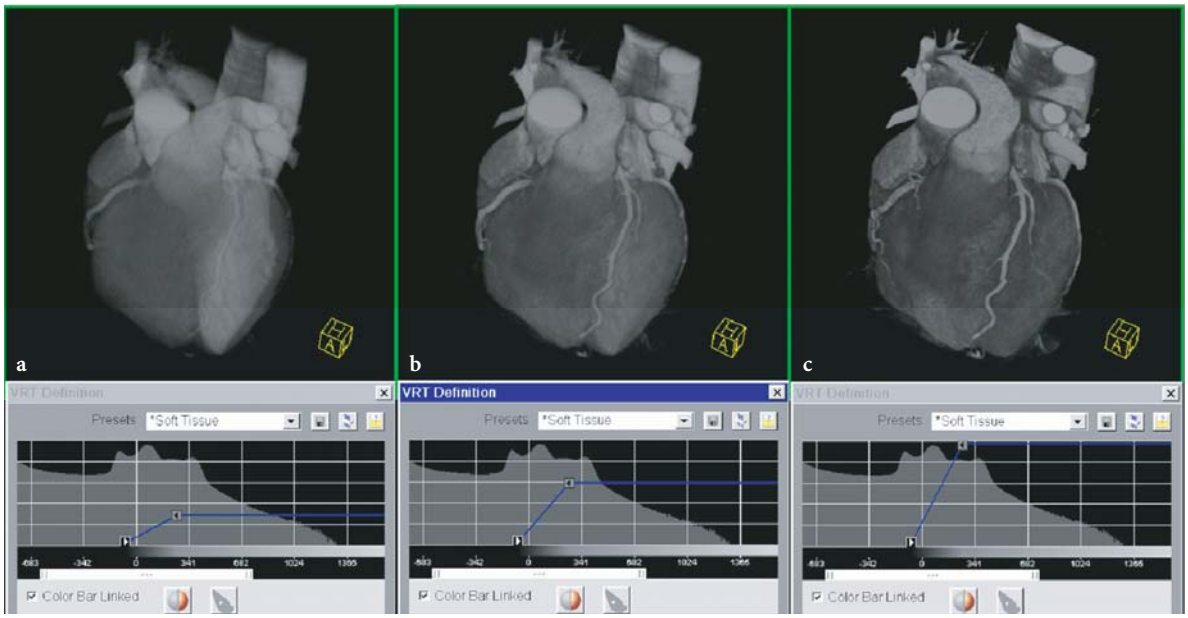

Fig. 6.11a–c. Volume-rendering images (VRTs) demonstrating the influence of opacity. An opacity value is assigned to each voxel according to its CT number, in order to make the voxel more or less transparent. The diagrams on the bottom indicate the histogram of the CT values and the respective opacity functions (*blue lines*). **a** When using low overall opacity the image looks transparent and has a large 3D depth but it lacks contrast. LAD and CX are hardly visible. **b** For medium overall opacity, the 3D depth decreases and contrast increases. **c** With high overall opacity, only the surface of the heart is visible, but the coronary arteries are much better and sharper delineated

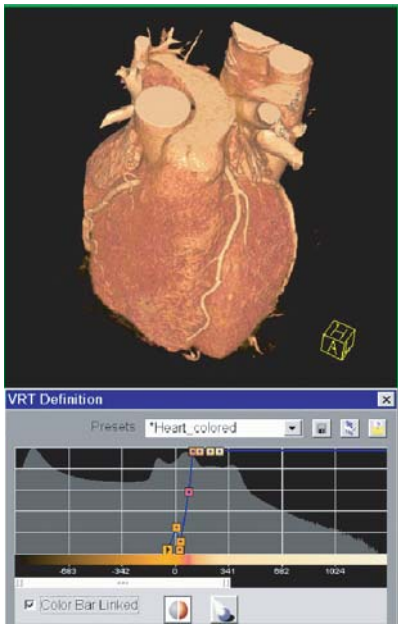

Fig. 6.12. In a VRT, colors instead of gray values can be attributed to the voxels according to their CT numbers. In this example, soft tissue is assigned a brownish red, whereas a lighter brown is used for the contrast-filled coronary arteries with higher CT numbers

this purpose, the opacity is modulated according to the local CT density gradients. In homogenous areas with small density changes (small gradients), the opacity is reduced; these areas will therefore be visualized more transparently. In areas with abrupt density changes, the opacity is increased. Furthermore, shading can be used to improve the 3D impression of the images.

VRTs require extensive user interaction for adequate imaging results. In many cases, the segmentation of overlapping structures is required, e.g., to remove the rib cage and the pulmonary vessels for a VRT visualization of the heart. Common approaches are the use of clip planes and volume of interest "punching". Alternativley, slab VRTs can be used for an interactive evaluation of anatomical details that are defined similar to slab-MPRs and slab-MIPs. With more recent and advanced cardiac evaluation packages, the heart can be automatically isolated and VRT display of the cardiac and coronary anatomy becomes feasible without further segmentation.

VRTs depend on a multitude of user-definable parameters. They are helpful for visualization of diagnostic results, in particular to referring physicians, but they are of limited use for primary diagnosis in cardiac CT examinations. The variety of parameters and settings and the lack of standardization impair the ability of VRTs to correctly assess coronary diameters and coronary artery stenoses (Mahnken 2003). However, VRTs provide good insight into the 3D relationship of anatomical structures and thus are helpful in the evaluation of aberrant coronary anatomy, such as anomalous coronary arteries, and bypass grafts (Fig. 6.13).

There are other 3D post-processing techniques related to VRT that can be used for cardiac CT, such as virtual endoscopy, which is known from CT colonography. Virtual endoscopy can provide spectacular visualization of the inner surface of contrast-filled coronary arteries (Fig. 6.14), but its clinical use in cardiac imaging remains to be shown.

6.5 Vessel Segmentation and Vessel Analysis

Recently, advanced vessel segmentation and vessel analysis tools have been introduced that provide the user with an optimized clinical workflow for assessing the lumen of coronary arteries, identifying and quantitating stenoses, evaluating the coronary wall, and investigating coronary stents. These advanced application packages make use of all available 3D post-processing techniques, such as MPRs, MIPs and VRTs, and combine and modify them with the goal of simplifying and streamlining the clinical workflow. In addition to these tools, detailed reporting functionality, e.g., based on DICOM-structured reporting, is an essential requirement for advanced cardiac and coronary analysis packages in order to integrate them into routine clinical workflow.

Advanced analysis packages typically show MPRs and a VRT of the cardiac image data set for a preliminary orientation, with the rib cage automatically removed so that only the relevant structures of the heart and the great vessels are displayed in the VRT image. Vessels can then be automatically segmented

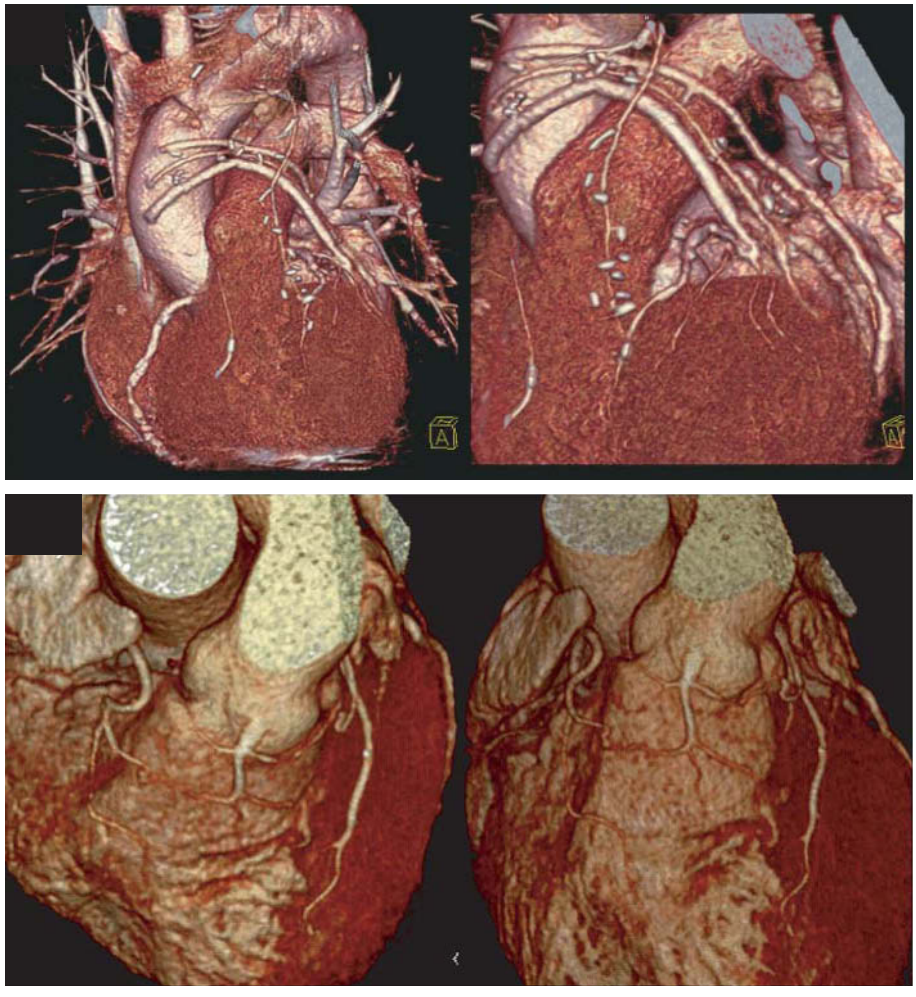

a

b

Fig. 6.13a, b. VRTs are mainly useful for a demonstration of the diagnosis. They provide good insight into the 3D relationship of anatomical structures, e.g., in the case of anomalous coronary arteries or bypass grafts. The two cases given as examples were obtained on a 64-slice CT scanner with 64 × 0.6-mm slices per rotation. **a** In one patient, four bypass grafts canbe accurately be localized using VRT. **b** In another patient, the VRT display reveals an anomalous coronary artery originating from the pulmonary trunk. (Cases courtesy of Medical University of South Carolina, USA)

to calculate curved MPRs or curved MIPs along the respective center lines. Two different types of vessel segmentation are currently used. In the "vessel probe" approach, a marker is placed with a mouse click in the vessel of interest, either in the MPRs or in the VRT representation. A centerline extending on both sides of the marker is calculated, and the corresponding vessel segment is displayed as a curved MPR. Vessel probe approaches are fast and intuitive. As a drawback, the length of the displayed vessel segment cannot always be controlled, as it often depends on the quality of the image data set, and side branches of the vessel cannot be traced in the same evaluation. In the "vessel segmentation" approach, the entire coronary artery tree is segmented as a first step. If certain arteries or branches are not initially recognized by the segmentation algorithm, they can usually be appended to the coronary tree by

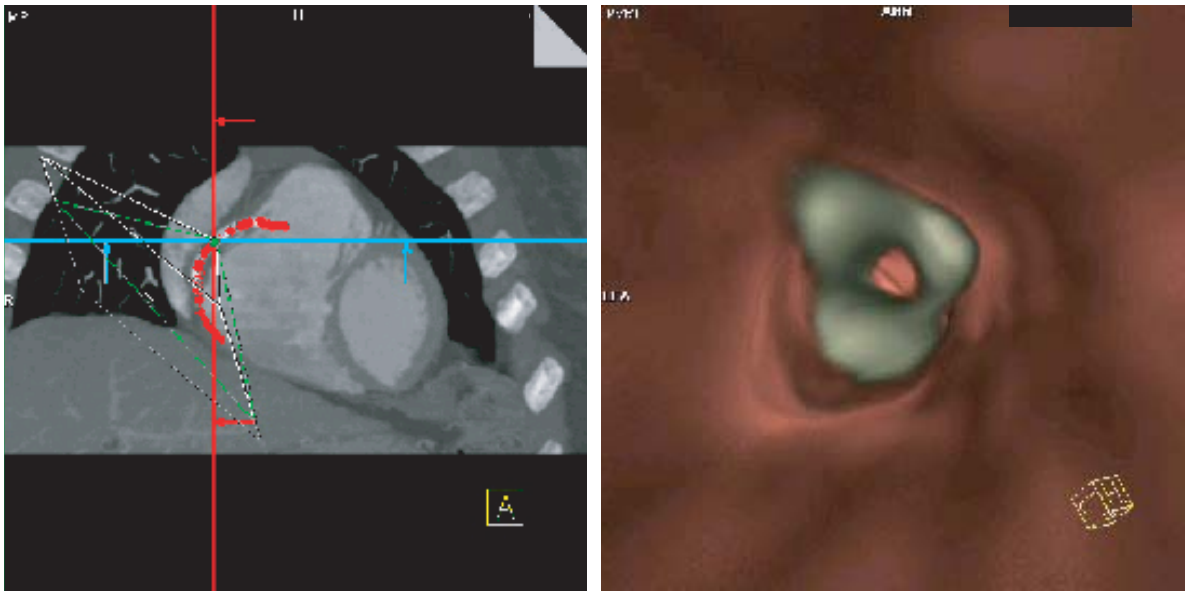

a b

Fig. 6.14a, b. Virtual endoscopic view with VRT visualization of a RCA based on an examination obtained on a 16-slice CT scanner with 16 × 0.75-mm collimation. **a** A path is being planned through the RCA that includes a stent. **b** The coronary artery lumen and stent struts can be visualized with virtual endoscopy. (Case courtesy of Mt. Sinai School of Medicine, New York, USA)

marking them with an additional mouse click. The isolated coronary tree is then displayed as a VRT image (Fig. 6.15), and the user can define centerlines between two arbitrary points on that tree as a basis for displaying the respective arteries or segments as curved MPRs or curved MIPs. Ideally, these curved MPRs (or curved MIPs) can be freely rotated to allow the inspection of plaques or stenoses from different viewing angles. MPRs on straight planes perpendicular to the centerline of the vessel are shown in addition to the curved MPR to facilitate the comprehensive evaluation of coronary stenoses, including calcified, fibrous, and lipid rich plaques. In some of these advanced application packages, the degree of a stenosis has to be manually measured (e.g., by a length measurement using an electronic ruler). In others, the degree of stenosis can be automatically determined by calculating area ratios of the vessel's cross-sections. As a representative example, Fig. 6.16 shows a screenshot of a comprehensive cardiac evaluation tool (syngo Circulation, Siemens, Forchheim, Germany) that provides automated segmentation of the coronary artery tree and subsequent measurement of stenosis.

As discussed in Sects. 6.2 and 6.3, curved MPRs and curved MIPs can be generated based on automatic calculation of the centerline of a segmented coronary artery that defines the curved visualization plane. Figures 6.17 and 6.18 demonstrate the feasibility of curved MPRs and curved MIPS with automated centerline detection in two patients with severe coronary artery disease. The cross-sectional images at the positions indicated by the markers are perpendicular to the vessel and allow for a detailed evaluation of plaques and wall changes, including density measurements.

In addition to vessel segmentation approaches, there is on-going development of advanced evaluation tools that help visualize and quantify plaques in the coronary arteries. Clinical studies have demonstrated the potential of multi-slice cardiac CT to not only detect but to some degree also characterize non-calcified and calcified plaques in the coronary arteries based on their CT attenuation (Schroeder 2001a, Schroeder 2001b, Leber 2004, Leber 2005). Figure 6.19 shows an example of a work-in-progress plaque evaluation tool with color-coding of voxels belonging to three different ranges of CT numbers

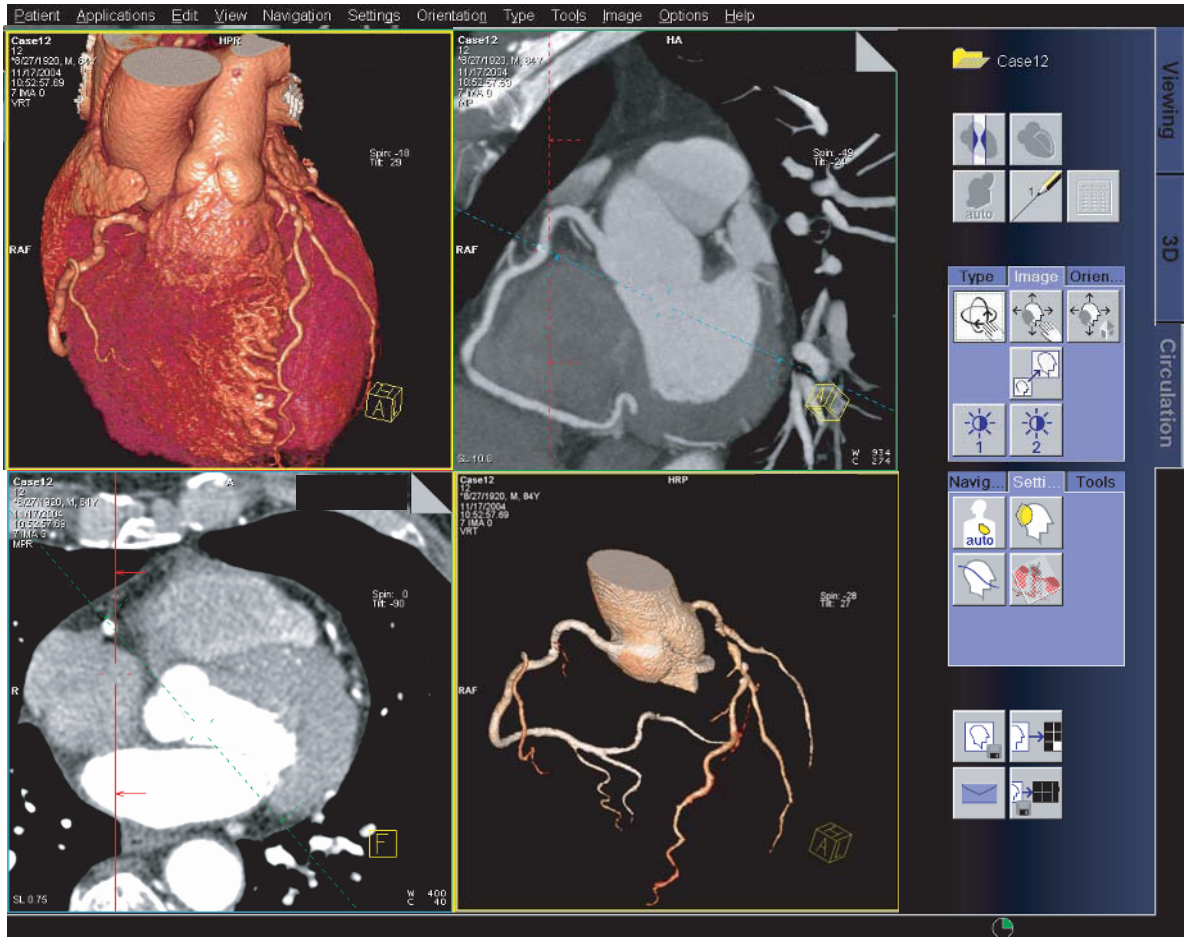

Fig. 6.15. An automated segmentation of the entire coronary artery tree, based on an examination obtained on a 64-slice CT scanner with acquisition of 64 × 0.6-mm slices per rotation. Based on the isolated heart with the rib cage removed (*upper left quadrant*), the software detects all coronary segments from a single marker (*lower right quadrant*) that was placed in the aorta just above the origin of the left main coronary arteries. (Case courtesy of Toyohashi Heart Center, Japan)

that may represent different types of plaques. The volume of the three compartments can be calculated, and an individual "plaque burden" can be derived for the patient. Clinical studies are needed to evaluate the potential and the clinical relevance of these plaque quantification tools. Ideally, they could, for example, be used to monitor the therapy response of patients undergoing medical treatment aimed at reducing their total plaque burden.

6.6 Four-Dimensional Visualization and Functional Parameter Assessment

Four-dimensional image data for the evaluation of functional parameters are readily available as an add-on for every retrospectively ECG-gated cardiac CT angiography examination. Compared to MR,

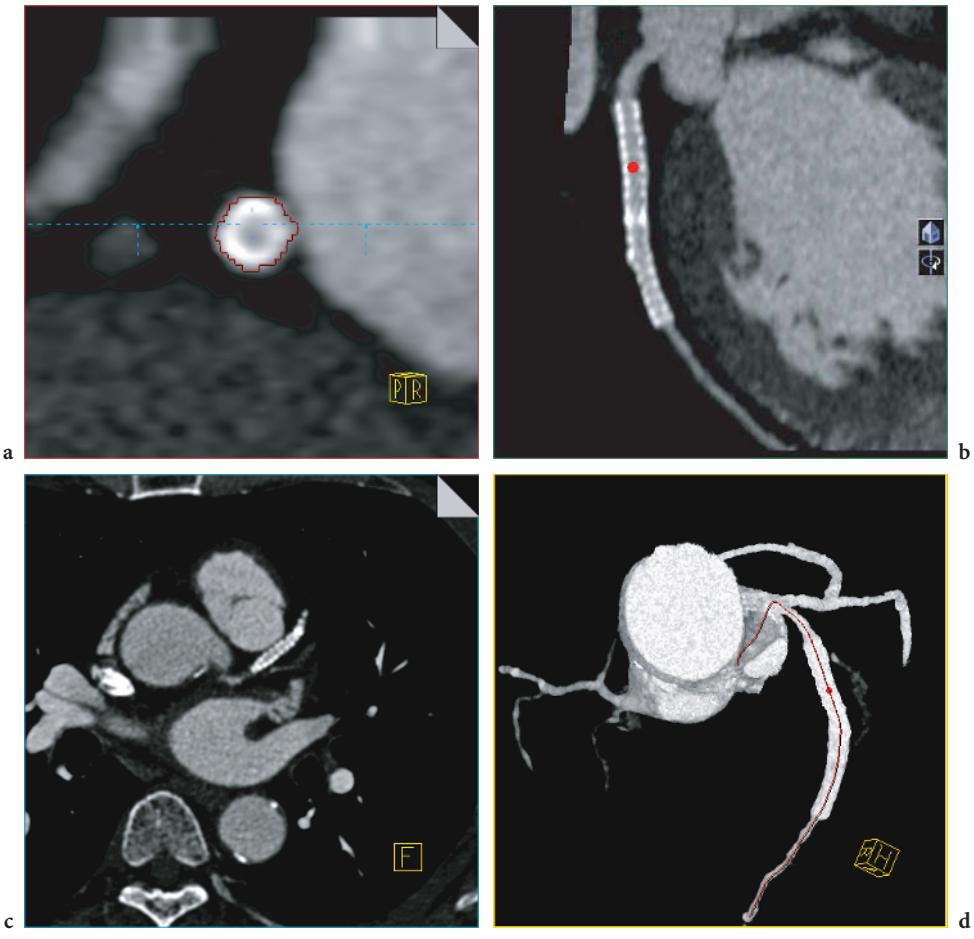

Fig. 6.16a–d. Example of a modern software-evaluation platform for automated segmentation and analysis of the coronary arteries based on an examination obtained on a 64-slice CT scanner with acquisition of 64 × 0.6-mm slices per rotation. **d** VRT visualization of the segmented coronary artery tree including the centerline (*indicated in red*) along the LAD is used for an overview. **b** An additional double-oblique MIP in the LAO helps to localize the exact position of the stent. **c** A curved MPR along the centerline allows for excellent visualization of the stent lumen due to isotropic sub-millimeter resolution. a A cross-section perpendicular to the centerline at the position indicated by the red marker allows for accurate measurement of the lumen. (Case courtesy of Erasmus University, Rotterdam, Netherlands)

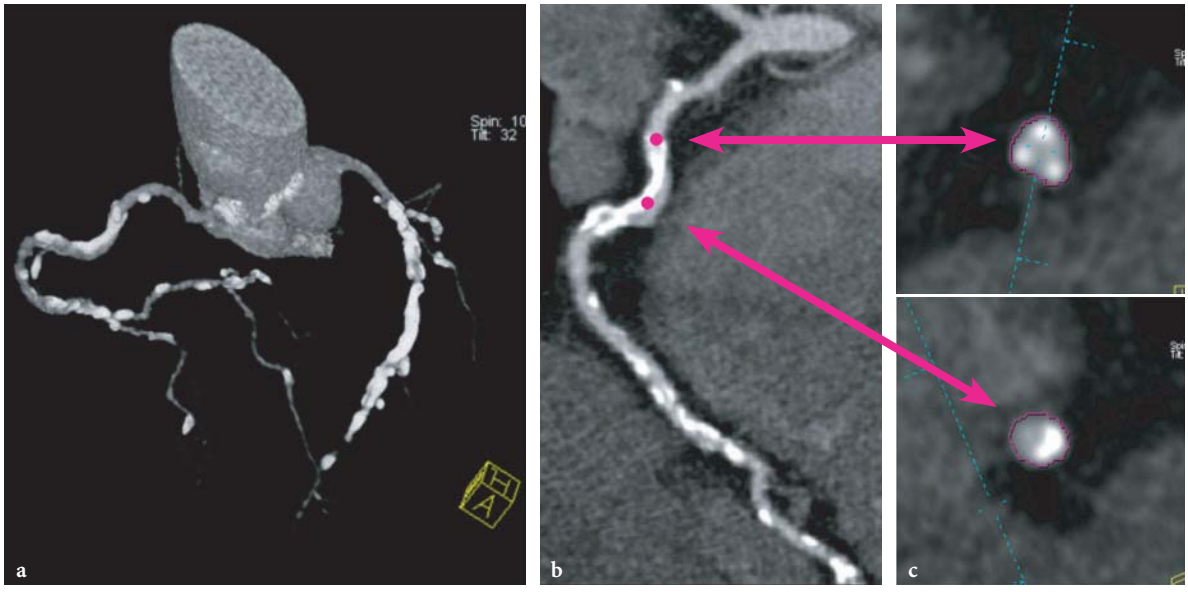

Fig. 6.17a–c. Automated coronary analysis for a patient examination obtained on a 64-slice CT scanner with acquisition of 64 × 0.6-mm slices per rotation. The software generates a the segmented coronary artery tree, **b** a curved MPR along the RCA, and c two cross-sections perpendicular to the centerline of the RCA for this patient with severe 3-vessel disease. The *pink dots* mark the positions of the cross-sectional images. (Case courtesy of New York University, USA)

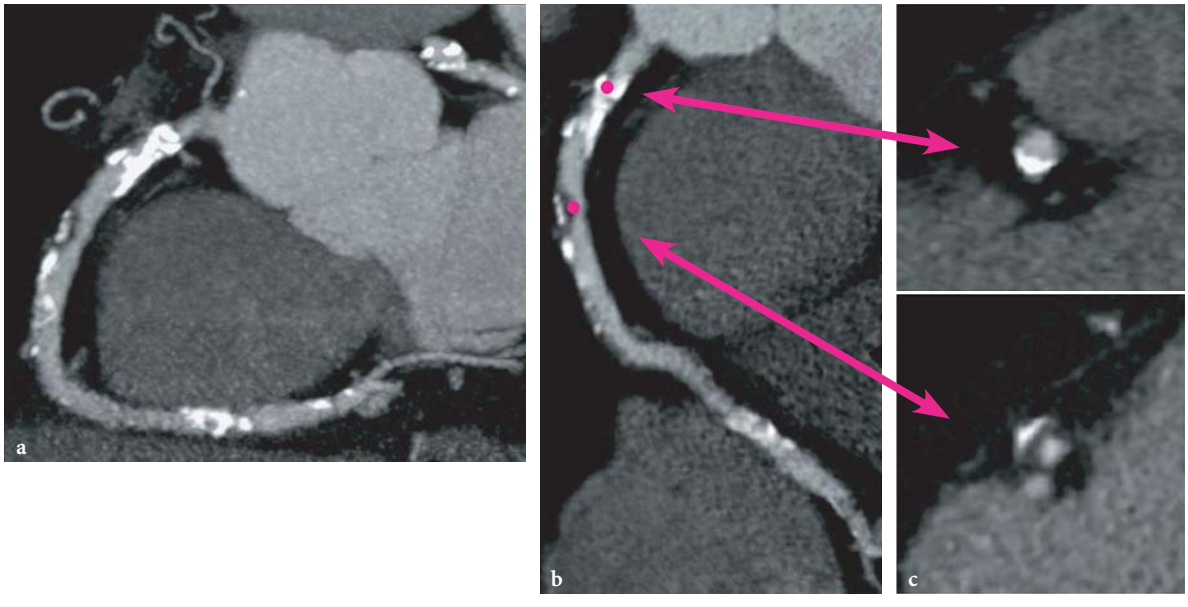

Fig. 6.18a–c. Automated coronary analysis for a patient examination obtained on a 64-slice CT scanner with acquisition of 64 × 0.6-mm slices per rotation. The software generates **a** a thin-slab curved MIP along the RCA and **b** a curved MPR along the RCA based on the detected center line and c two cross-sections perpendicular to the centerline of the RCA in this patient with severe 3-vessel disease. The *pink dots* mark the positions of the cross-sectional images. (Case courtesy of Mayo Clinic Rochester, Minnesota, USA)

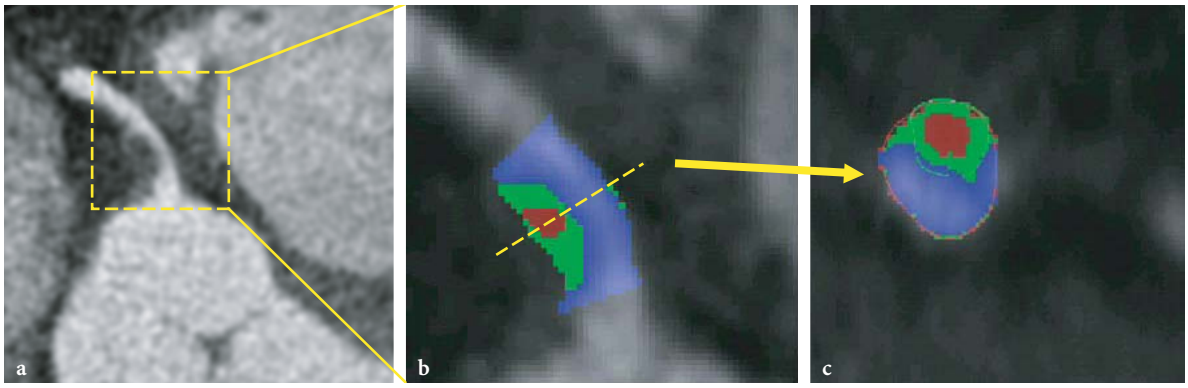

Fig. 6.19a–c. A work-in-progress plaque evaluation tool. Different colors are assigned to voxels within different ranges of CT numbers. **a** A MPR view reveals a significant stenotic lesion in the proximal RCA in this patient, who was scanned with a 64-slice CT scanner using 64 × 0.6-mm slices per rotation. **b** Color-coding can be applied to this MPR and **c** to **a** cross-sectional image perpendicular to the centerline cutting through the lesion. Red is used for voxels with CT numbers between –25 and 40 HU (potential "lipid" plaques), green for voxels with CT numbers between 40 and 110 HU (potential "fibrous" plaques), and blue for voxels with CT numbers between 110 and 445 HU (contrast-filled lumen). An additional threshold and color code can be defined for calcified plaques. (Case courtesy of Erlangen University, Germany)

multi-slice CT allows for a reliable assessment of left and right ventricular volumes, including left ventricular ejection fraction, and of regional wall motion at rest. Other parameters, such as peak filling rate, peak ejection rate, and regional wall motion under stress, cannot reliably be determined due to the still-limited temporal resolution of current multi-slice CT systems (Mahnken 2005a). Dedicated 4D visualization and evaluation tools are being developed to allow assessment of basic functional parameters from ECG-gated CT image data, such as end-systolic and end-diastolic volumes, stroke volume, ejection fraction, and myocardial mass. Advanced 4D visualization and quantification software also provides cine views of the beating heart and are generated from 3D data sets that were reconstructed at equidistant time points during the cardiac cycle. These tools can provide both visual and quantitative information regarding motion of the cardiac and coronary anatomy, ventricular wall motion, and ventricular wall thickening.

Series of complete 3D image data sets reconstructed in different phases of the cardiac cycle, at least in the end-systolic and end-diastolic phases (usually reconstructed with, respectively, 20 and 80% relative delay to the onset of the R-wave), are needed for functional evaluation. Some evaluation tools require input data in the form of double-oblique MPRs generated from the original axial slices along the short and long heart axess (Fig. 6.20). These MPRs can be reduced in their spatial resolution in order to limit the amount of data that has to be handled, e.g., by using 5- to 8-mm MPR thickness or a reduced 256 × 256 image matrix. The ability of some CT scanners to directly generate double-oblique MPRs along the short and long axes of the heart based on the raw scan data in different phases of the cardiac cycle (see Sect. 6.2) can simplify the clinical workflow. To derive functional parameters, such as ejection fraction and myocardial mass, endocardial and epicardial contours may have to be drawn manually for one slice position of the short axis view, followed by an automatic propagation to other slice positions between the base and the apex of the heart. Wall thickening is most commonly displayed in the form of a polar map based on short axis reformations, known as a "bulls-eye plot", following the AHA 17-segment classification.

More recent evaluation-software platforms require series of thin and overlapping axial slices in different phases of the cardiac cycle as an input for functional evaluation, similar to the input needed for cardiac anatomy and coronary artery analysis. A manual or automatic definition of the basal plane through the mitral valve, which separates the left ventricle from the left atrium, in both end-systole and end-diastole is generated, after which the blood pool in the left

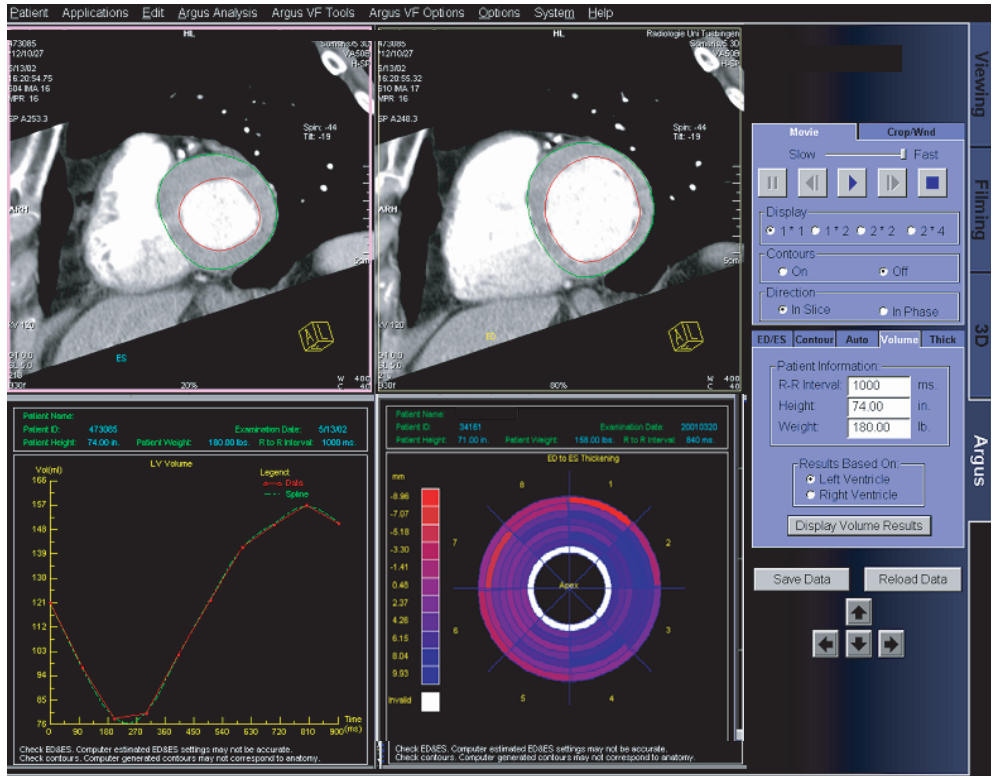

Fig. 6.20. CT examination of a patient with an occlusion of the left descending coronary artery using a 16-slice CT scanner with 16 × 0.75-mm collimation. Images for functional evaluation were reconstructed in 10 phases during the cardiac cycle, ranging from 0 to 90% of the RR-interval. The cardiac function evaluation software used in this example requires short-axis multi-planar reformations with 5- to 8-mm MPR thickness. It provides left ventricular volumes for all loaded phases, including end-systolic (*upper left*) and end-diastolic (*upper right*) volumes for determining ejection fraction (*lower left*). A "bulls-eye plot" for display of regional wall motion can also be generated (*lower right*). (Case courtesy of Tübingen University, Germany)

ventricle is automatically segmented to allow calculation of end-systolic and end-diastolic volumes, stroke volume, and ejection fraction (Fig. 6.21). With these software tools, segmentation of the ventricular blood pool can be conveniently adjusted for standardization purposes. This is particularly helpful for assessment of the papillary muscles during calculation of left ventricular volumes. The papillary muscles are included in some functional evaluation approaches, while they are excluded in others. With the help of refined cardiac models, endocardial and epicardial contours may be automatically detected – requiring only minor user interactions for a correction – as a basis for calculating myocardial mass and for analyzing wall thickening.

6.7 Myocardial Perfusion Evaluation

Myocardial perfusion can be assessed via dynamic measurement of the enhancement of the myocardium after injection of contrast, with the goal of differentiating viable from infarcted myocardium. An enhancement curve is determined by measuring HU values in defined small regions of interest (ROIs) in thick axial slices or oblique MPRs that are acquired during ECG-triggered scans in consecutive cardiac cycles. Standard ROI-based dynamic measurement tools are currently in use for generation of such enhancement curves. As evaluation of myocar-

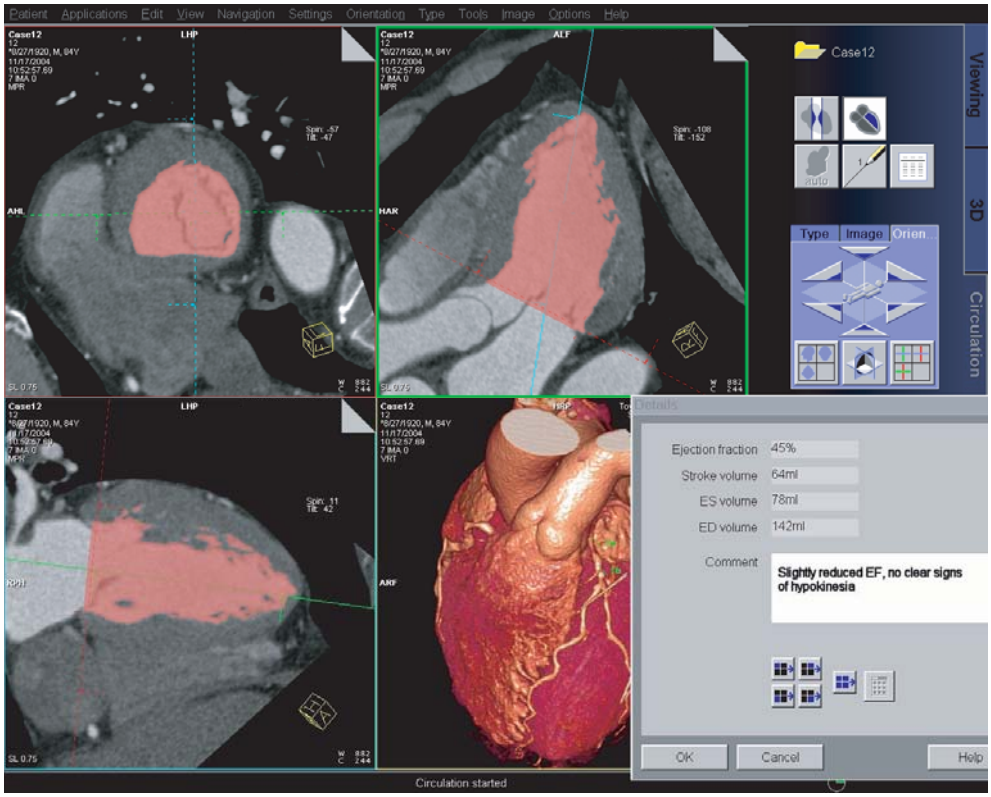

Fig. 6.21. Functional evaluation in a patient with a significant LAD stenosis, examined with a 64-slice CT scanner with 64 × 0.6-mm slices per rotation. The evaluation was done using comprehensive slice-based cardiac evaluation software. Thin-slice axial images in different phases of the cardiac cycle are needed as an input. Following manual definition of the basal plane in end-systole and end-diastole, the blood pool in the left ventricle is automatically segmented to allow calculation of end-systolic and end-diastolic volumes, stroke volume, and ejection fraction. The papillary muscles are excluded in this approach. (Case courtesy of Toyohashi Heart Center, Japan)

dial perfusion does not yet play a significant role in today's clinical practice and has not yet left the research state, this application is not yet supported by dedicated post-processing tools. The limited z-axis coverage of current multi-slice CT scanners, inherent HU value inconsistency during dynamic, ECG-triggered partial-scan acquisition, and the lack of clinical validation have hampered the establishment of myocardial perfusion measurement with multi-slice CT in clinical practice. However, initial promising clinical results have been obtained with the recently introduced fast 64-slice CT scanners, which feature faster rotation speeds and larger z-axis coverage.

Nonetheless, measurement of myocardial enhancement based on first-pass contrast enhancement is gaining attention as a potential tool to predict patient outcome after myocardial infarction (Paul 2003, Mahnken 2005b). Information on first-pass myocardial enhancement is readily available as a by-product of cardiac and coronary CT angiography examinations, similar to functional information. Figure 6.22 shows the use of a work-in-progress evaluation tool for a patient with myocardial infarction. The blood pool of the left ventricle has been segmented and removed to allow better differentiation of the subtle density changes in the myocardium. Density color-coding was applied to direct the attention of the user to areas with abnormal enhancement.

For the examination of patients with suspected myocardial infarction, the additional evaluation of

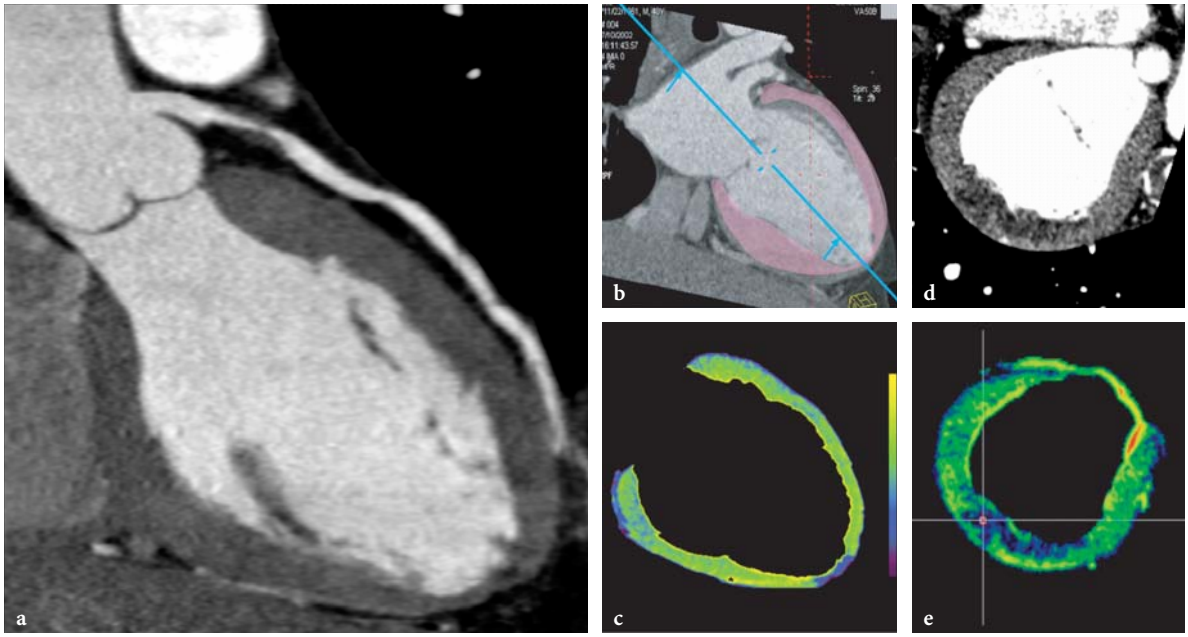

Fig. 6.22a–e. Evaluation of myocardial enhancement in a patient with suspected myocardial infarction, based on scan data acquired on a 64-slice CT scanner with 64 × 0.6-mm slices per rotation. **a** MIP reconstruction reveals a high-grade stenosis in the proximal LAD. **b**, **c** Automated segmentation of the myocardium allows the generation of a color-coded map using a work-in-progress software. Short-axis reformation allows for the evaluation of first-pass myocardial perfusion defects. **d** While the corresponding hypo-attenuated area in the myocardium can also be appreciated in the original MPR, **e** segmentation of the blood pool and color-coding facilitates (*blue color* for low perfusion) the diagnosis. (Case courtesy of Hôpital Marie Lannelongue, Paris, France)

late enhancement might be of clinical value. Visualization of late myocardial enhancement resulting from contrast leakage in infarcted myocardium requires an additional ECG-gated low-dose scan a few minutes after the first-pass cardiac or coronary CT angiography examination. While areas of hypo- or hyper-enhancement in the myocardium can also be detected in the source images, the subtle changes in HU values that have to be appreciated call for support of the user by means of advanced post-processing techniques.

6.8 Quantification of Coronary Calcification

The 3D visualization and post-processing techniques presented so far are predominantly intended for the visualization and quantitative evaluation of contrast-enhanced images from cardiac and coronary CTA examinations. The quantification of coronary calcification on the other hand is based on non-enhanced CT-images, yet it requires dedicated post-processing tools and quantification algorithms.

The earliest and still frequently used algorithm for the quantification of coronary artery calcium is the so-called Agatston score (Agatston 1990), which was developed primarily for electron beam CT (EBCT) but has been adapted for multi-slice CT protocols. The Agatston score is semi-quantitative and is based on slice-by-slice analysis of non-overlapping axial CT images. A CT-value threshold of 130 HU is commonly used for the identification of calcifications in every axial image (Fig. 6.23). All voxels in a slice that exceed this value are color-coded for an initial orientation. Among these suspicious voxels, which can represent false positives arising from image noise, the user has to manually pick the relevant coronary calcifications. Region-growing algorithms are used to identify all voxels belonging

to a lesion (Fig. 6.24). A score Ag(n) is calculated for each individual lesion n by multiplication of the area (in mm^2) with a co-factor (between 1 and 4) that depends on the HU-peak value in the considered lesion (Eq. 6.2).

$$Ag = \sum_n Ag(n) = \sum_n Area(n) \cdot CoFactor(n) \tag{6.2a}$$

$$CoFactor = \begin{cases} 1; & 130 \le Peak < 200 \\ 2; & 200 \le Peak < 300 \\ 3; & 300 \le Peak < 400 \\ 4; & Peak \ge 400 \end{cases} \tag{6.2b}$$

To reduce the influence of image noise, a minimum area $Area_{min}$ can be used to discard very small scores that probably represent noise pixels. The scores of the individual lesions are separately accumulated for the main coronary artery segments: left main (LM), LAD, CX, and RCA (Fig. 6.24). The sum of these separate scores yields a total score for the total calcified plaque burden.

The Agatston-scoring algorithm was developed for sequential image data and needs modification if overlapping slice data are processed. A straightforward approach is to calculate normalized scores AgN that are multiplied with the ratio of image reconstruction increment Inc and slice width SW (Ohnesorge 2000, Ohnesorge 2002):

$$AgN = \frac{Inc}{SW} \sum_n Area(n) \cdot CoFactor(n) \tag{6.3}$$

Due to the non-linear weighting operation with the integer variable CoFactor, the Agatston score is very prone to variations. Different studies have shown that the inter-scan variability of the scores can be more than 20% (Devries 1995, Becker 2000), particularly for small amounts of calcification; therefore, the reproducibility needs to be improved.

Alternative volumetric quantification algorithms have been developed that can process sequential and overlapping image data of different slice width as well as provide volume-equivalents (in mm^3) and mass-equivalents (in mg) of calcified plaques (Eqs. 6.4, 6.5). Non-linear operations that may increase inter-scan variability are eliminated. Isotropic interpolation procedures in between adjacent

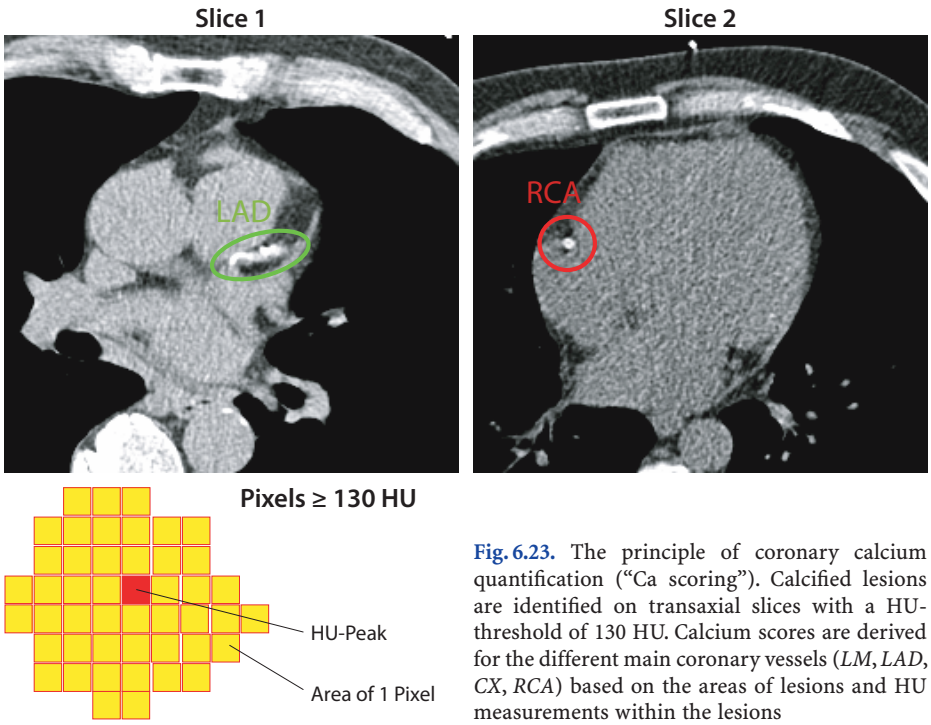

Fig. 6.23. The principle of coronary calcium quantification ("Ca scoring"). Calcified lesions are identified on transaxial slices with a HU-threshold of 130 HU. Calcium scores are derived for the different main coronary vessels (*LM*, *LAD*, *CX*, *RCA*) based on the areas of lesions and HU measurements within the lesions

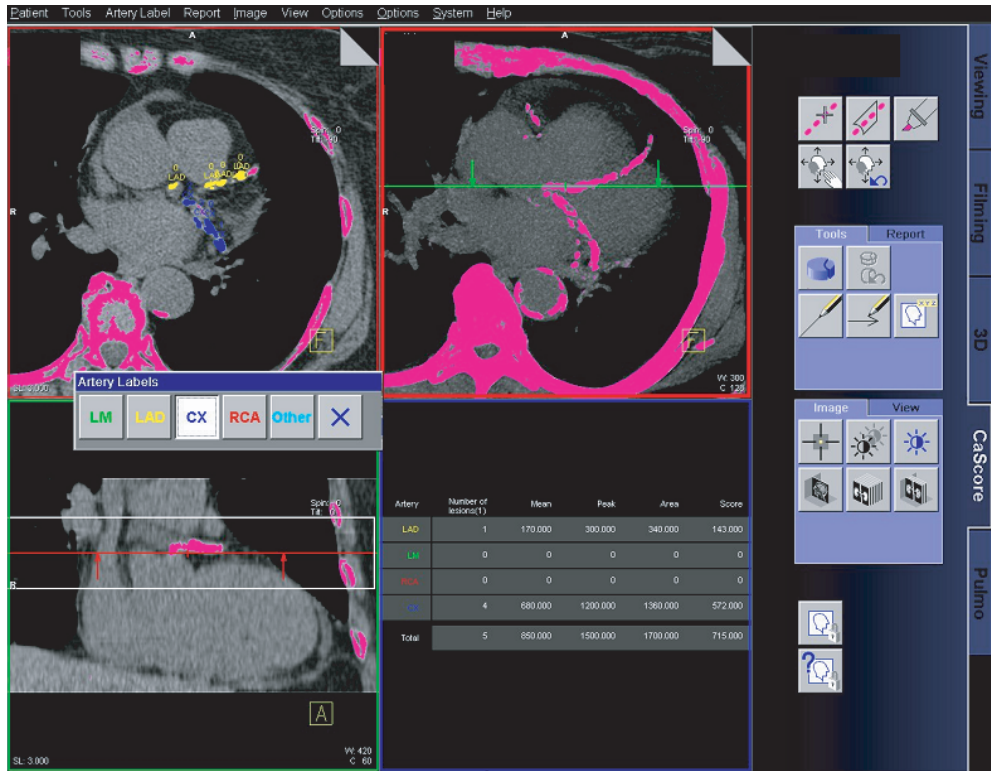

Fig. 6.24. Software platform used for the quantification of coronary calcification. Lesions exceeding the calcium threshold of 130 HU are identified with color-coding and segmented with 3D-based picking and region-growing tools. After segmentation, the lesions are assigned to the various coronary arteries (LM, LAD, CX, RCA). Coronary calcifications are quantified by means of Agatston score, calcium volume, and calcium mass calculation. Calibration factors that are pre-determined using phantom measurements and depend on the scan protocol form the basis for calculating calcium mass. The quantitative measurements are displayed and reported in table format

image slices can be used to reduce the influence of partial-volume errors for improved reproducibility (Callister 1998, Ohnesorge 2002).

$$Vol = \sum_n Vol(n) = \sum_n Area(n) \cdot Inc \tag{6.4a}$$

$$Mass = \sum_n Mass(n) \cdot = \sum_n Area(n) \cdot Inc \cdot \rho(MeanHU(n)) \tag{6.4b}$$

$$Vol_I = \sum_n Vol_I(n) = \sum_n Area(n) \cdot Inc \cdot W_I(n) \tag{6.5a}$$

$$Mass_I = \sum_n Mass_I(n) = \sum_n Area(n) \cdot Inc \cdot W_I(n) \cdot \rho(MeanHU(n)) \tag{6.5b}$$

The isotropic interpolation factor $W_I(n)$ takes information from the adjacent slices into account and modifies the contribution of a single image voxel to the score of an individual lesion. $W_I(n)$ may be greater or smaller than 1 depending on the propagation of a lesion (Fig. 6.25). Also, voxels that were not identified as part of a lesion due to a HU value < 130HU may contribute to the score of the lesion if corresponding voxels at the same image position in the adjacent

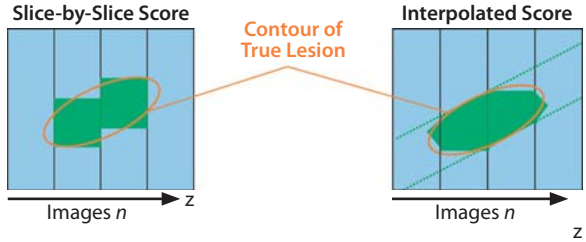

Fig. 6.25. Interpolation algorithms during volumetric quantification of coronary calcification. 3D-shaped calcified lesions may be detected in consecutive slices. Interpolation between the slices can be useful for better reproduction of the true plaque size

slice have a high contribution. A mass equivalent is calculated by multiplying the volume with a density factor ρ of the lesion. The latter is derived from the mean HU value in the plaque, which linearly depends on the mean density (in mg/mm^3). The density factor ρ and its HU value must be determined from appropriate calibration procedures (Ulzheimer 2003) for the scanner and according to the scan protocol used, and have to be included in the quantification software. A special phantom has been developed that allows for identification of calcium thresholds and calcium-mass calibration factors for different scan protocols (Fig. 6.26). The density factor ρ for an individual lesion n depends on the difference of the mean HU value in the lesion and the HU value of water as well as on a scanner- and scan-protocol-specific constant C_ρ as given in Eq. 6.6:

$$\rho(MeanHU(n)) = C_\rho \cdot (MeanHU(n) - HU_{Water}) \quad (6.6)$$

For example, for a frequently used scan protocol for a certain evaluated scanner (e.g., SOMATOM Sensation 16, Siemens, Germany with 16 × 1.5-mm collimation, 3-mm slice width, 120-kV tube voltage, 100-mA tube current), the constant C_ρ was determined by the phantom study as:

$$C_\rho = 0.84 \frac{mg}{cm^3 \cdot HU} \quad (6.7)$$

It could even be shown that, with such calibration efforts, coronary calcium mass can be accurately quantified from contrast-enhanced scans of the coronary arteries with thin-slice reconstruction, which shows increased sensitivity for smaller calcified lesions (Fig. 6.27). Based on an appropriate adaptation of the calibration factors, a high degree of correlation with the results of pre-contrast calcium scoring scan was shown (Hong 2002) (Fig. 6.28).

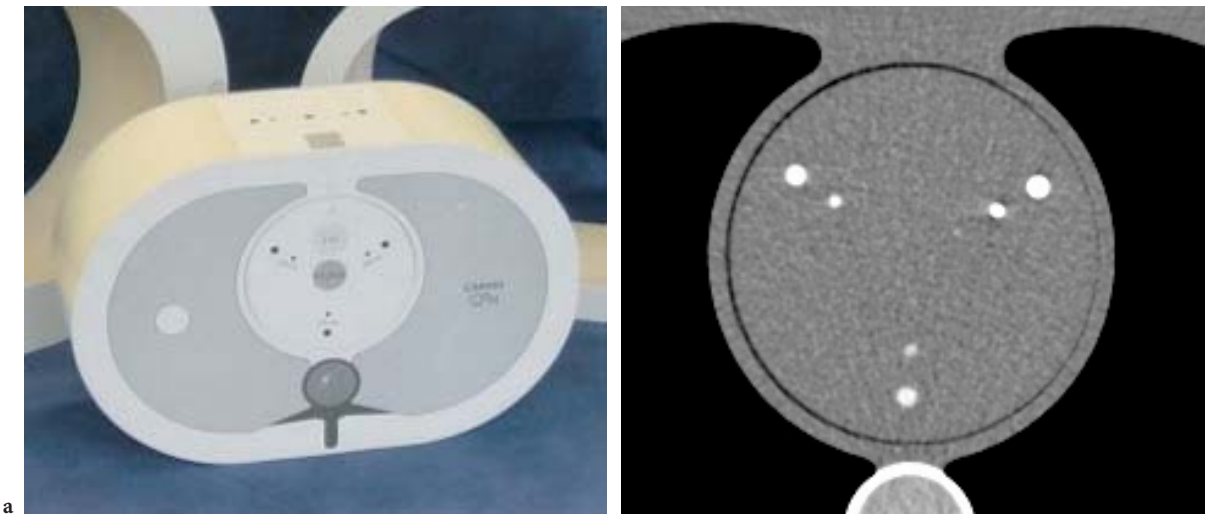

a b

Fig. 6.26. a The anthropromorphic chest phantom (Institute of Medical Physics, Erlangen, Germany and QRM, Möhrendorf, Germany) for determining the calibration factors for coronary calcium mass quantification. **b** The phantom contains a centered Lucite cylinder that simulates the heart and includes calibration inserts and calcium hydroxyapatite inserts of different dimensions and density that can be displayed in axial slices

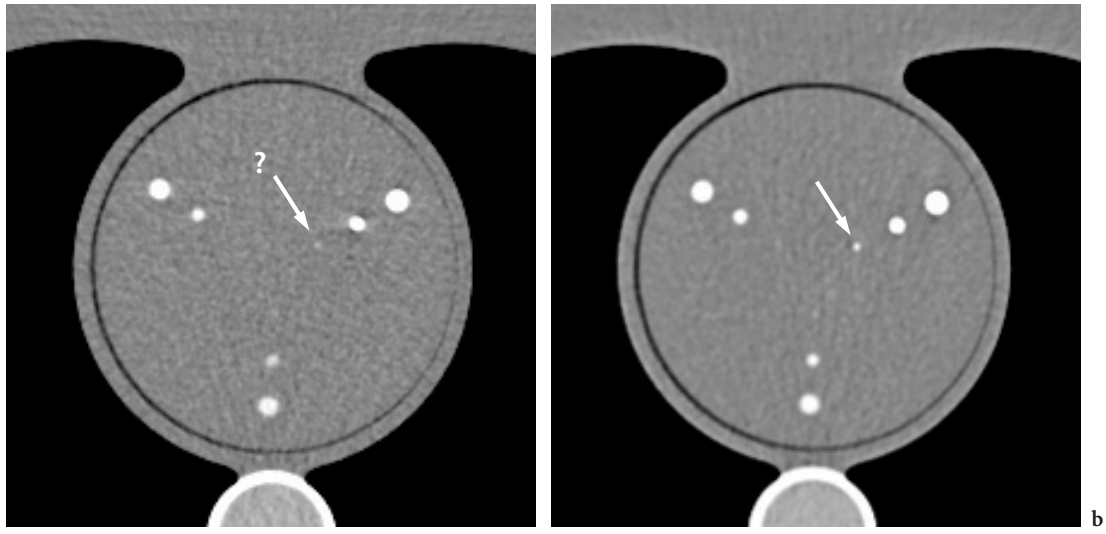

Fig. 6.27. Calibration phantom scanned with ECG-gated spiral acquisition on a 16-slice CT scanner using a 16 × 1.5-mm collimation, 3.0-mm slice width and b 16 × 0.75-mm collimation, 1.0-mm slice width. Smaller lesions can be identified with 1.0-mm slice width (smallest detectable lesion: 0.6 mg calcium hydroxyapatite; *arrows*). The best agreement between calcium mass detected with 1.0-mm slice width and that detected with 3.0-mm slice width and 130 HU threshold was achieved using a calibration coefficient C_ρ = 0.84 mg/(cm^3·HU) for the 3-mm slice-width and C_ρ = 0.88 mg/(cm^3·HU) at a modified calcium threshold of 350 HU for a 1.0-mm slice width

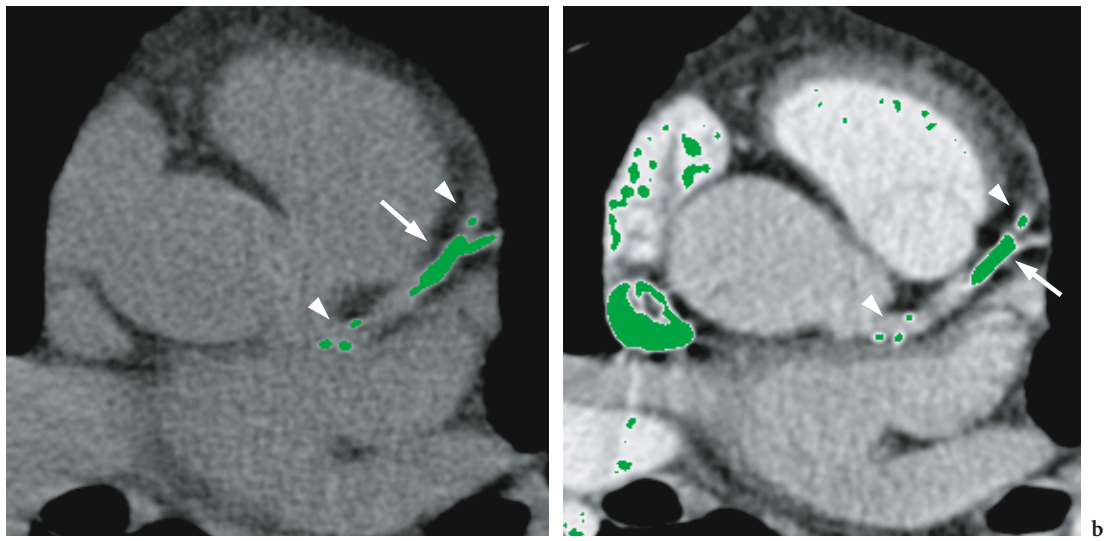

Fig. 6.28a, b. Examination of a 57-year-old male with calcified coronary artery plaques. **a** Spotty calcifications in the left main stem (*arrowheads*) and long calcifications in the mid-segment of the LAD (*arrow*) can be detected in the non-enhanced coronary calcium scan with 3.0-mm slice width and a 130-HU calcium threshold. **b** The same spotty calcifications (*arrowheads*) and long calcification (*arrow*) can be detected in the contrast-enhanced high-resolution scan with 1.25-mm slice width and 350-HU calcium threshold

The Agatston algorithm for quantification of coronary calcification is still frequently used. However, the Agatston score and the closely related acquisition parameters may not be an appropriate basis for coronary calcium quantification with a wide spectrum of different acquisition systems. With the advent from different manufacturers of multislice CT scanners with different scan parameters, cross-technology quality control and calibration methods gain importance. The most promising approach to establish a cross-industry standard is to use absolute mass quantification, which can include different scanner properties and protocol variations via phantom calibration (Hong 2002, Ulzheimer 2003). Moreover, recent studies indicate that the use of quantitative mass measurement provides better results for inter-scan and inter- and intra-observer variability than obtained with the traditional Agatston scoring method (Ohnesorge 2002). Therefore, assessing coronary artery calcification by evaluating absolute calcium mass shows great potential for increasing the accuracy, consistency, and reproducibility of coronary calcium measurements (Ulzheimer 2003) and will replace the traditional Agatston scoring system in the near future.

References

Addis KA, Hopper KD, Iyriboz TA, Liu Y, Wise SW, Kasales CJ, Blebea JS, Mauger DT (2001). CT angiography: in vitro comparison of five reconstruction methods. AJR 177: 1171–1176

Agatston AS, Janowitz WR, Hildner FJ, Zusmer NR, Viamonte M, Detrano R (1990). Quantification of coronary artery calcium using ultrafast computed tomography. JACC 15, 827–832

Becker CR, Jakobs TF, Aydemir S, Becker A, Knez A, Schöpf UJ, Brüning R, Haberl R, Reiser MF (2000). Helical and single-slice conventional CT versus electron beam CT for the quantification of coronary artery calcification. AJR 174:543–547

Callister TQ, Cooil B, Raya SP, Lippolis NJ, Russo DJ, Raggi P (1998). Coronary artery disease: improved reproducibility of calcium scoring with an electron-beam CT volumetric method. Radiology 208:807–814

Devries S, Wolfkiel CJ, Shah V, Chomka E, Rich S (1995). Reproducibility of the measurement of coronary calcium with ultrafast ct. Am J Cardiol 75:973–975

Feyter de PJ, Krestin GP (2005). Computed tomography of the coronary arteries. Chapter 2: Image post-processing. Taylor & Francis, Oxfordshire, UK

Flohr T, Stierstorfer K, Raupach R, Ulzheimer S, Bruder H (2004). Performance evaluation of a 64-slice CT-system with z-flying focal spot. Röfo Fortschr Geb Rontgenstr Neuen Bildgeb Verfahr. 176:1803–1810

Hong C, Becker,CR, Schöpf UJ, Ohnesorge B, Brüning R, Reiser MF (2002). Coronary artery calcium: absolute quantification in non-enhanced and contrast-enhanced multidetector-row CT studies. Radiology 223:474–480

Leber AW, Knez A, Becker A, Becker C, Ziegler F, Nikolaou K, Rist C, Reiser MF, White C, Steinbeck G, Boekstegers P (2004). Accuracy of multidetector spiral computed tomography in identifying and differentiating the composition of coronary atherosclerotic plaque. JACC 43(7): 1241–1247

Leber AW, Knez A, Ziegler F, Becker A, Nikolaou K, Paul S, Wintersperger B, Reiser MF, Becker C, Steinbeck G, Boekstegers P (2005). Quantification of obstructive and non-obstructive coronary lesions by 64-slice computed tomography. JACC 46(1)

Mahnken AH, Wildberger JE, Sinha AM, Dedden K, Stanzel S, Hoffmann R, Schmitz-Rode T, Günther RW (2003). Value of 3D-volume rendering in the assessment of coronary arteries with retrospectively ecg-gated multislice spiral CT. Acta Radiologica 44(3): 302 ff.

Mahnken AH, Katoh M, Bruners P, Spuentrup E, Wildberger JE, Günther RW, Buecker A (2005a). Acute myocardial infarction: assessment of left ventricular function with 16-detector row spiral CT versus MR imaging – study in pigs. Radiology 236:112–117

Mahnken AH, Koos R, Katoh M, Wildberger JE, Spuentrup E, Buecker A, Günther RW, Kühl HP (2005b). Assessment of myocardial viability in reperfused myocardial infarction using 16-slice computed tomography in comparison to magnetic resonance imaging. JACC 45 (12): 2042–2047

Ohnesorge B, Knez A, Becker CR, Schröder S, Kopp AF, Fischbach R, Haberl R, Reiser MF (2000). Reproducibility of coronary calcium scoring with EBCT and ECG-gated multislice spiral CT (Abstract). Circulation 102(18):II-398–399

Ohnesorge B, Flohr T, Fischbach R, Kopp AF, Knez A, Schröder S, Schöpf UJ, Crispin A, Klotz E, Reiser MF, Becker CR (2002). Reproducibility of coronary calcium quantification in repeat examinations with retrospectively ECG-gated multisection CT. Eur Radiol 12:1532–1540

Ooijen van PMA, Ho KY, Dorgelo J, Oudkerk M (2003). Coronary artery imaging with multidetector-row CT: visualization issues. Radiographics 23: e16

Paul JF, Dambrin G, Caussin C, Lancelin B, Angel C (2003). 16-slice computed tomography after acute myocardial infarction – from perfusion defect to culprit lesion. Circulation 108:373–374

Prokop M, Shin HO, Schanz A, Schaefer-Prokop CM (1997). Use of maximum intensity projections in CT angiography: a basic review. Radiographics 17(2):433–51

Raman R, Napel S, Rubin D (2003). Curved slab maximum

intensity projection. method and evaluation. Radiology 229:255–260

Rankin CS (1999). CT angiography (Review). Eur Radiol 9: 297–310

Rubin GD, Napel S, Jeffrey RB Jr (1993). STS-MIP: a new reconstruction technique for CT of the chest. J Comput Assist Tomogr 17(5):832–838

Schroeder S, Kopp A, Baumbach A, Meisner C, Kuettner A, Georg C, Ohnesorge B, Herdeg C, Claussen C, Karsch K (2001a). Noninvasive detection and evaluation of atherosclerotic coronary plaques with multi-slice computed tomography. JACC 37(5): 1430–1435

Schroeder S, Flohr T, Kopp AF, Meisner C, Kuettner A, Herdeg C, Baumbach A, Ohnesorge B (2001b). Accuracy of density measurements within plaques located in artificial coronary arteries by X-ray multislice CT: results of a phantom study. J Comput Assist Tomogr 25(6): 900–906

Vogl TJ, Nasreddin DA, Diebold T, Engelmann K, Ay M, Dogan S, Wimmer-Greinecker G, Moritz A, Herzog C (2002). Techniques for the detection of coronary atherosclerosis: multi-detector row CT coronary angiography. Radiology 223:212–220

Ulzheimer S, Kalender WA (2003). Assessment of calcium scoring performance in cardiac computed tomography. Eur Radiol 13 :484–497

Clinical Indications

7

Contents

7.1 Current and Future Clinical Potential *179*
7.2 Risk Assessment with Coronary Artery Calcium Screening *192*
7.3 Detection and Exclusion of Coronary Artery Stenosis *205*
7.4 Assessment and Interpretation of Atherosclerotic Coronary Plaques *214*
7.5 Coronary CT Angiography in Patients with Chest Pain *224*
7.6 Evaluation of Coronary Artery Bypass Grafts *232*
7.7 Patency Control of Coronary Stents *239*
7.8 Evaluation of the Coronary Anomaly, Fistula, Aneurysm, and Dissection *245*
7.9 Diagnosis of Congenital Heart Disease in Adults and Children *258*
7.10 Evaluation of Ventricular Function Parameters *266*
7.11 Imaging and Diagnosis of Cardiac Valves *281*
7.12 Visualization of Cardiac Tumors and Masses *288*
7.13 Imaging of the Pulmonary Veins in Patients with Atrial Fibrillation *296*
7.14 Potential of Myocardial Perfusion and Viability Studies *307*
7.15 Cardiothoracic Multi-Slice CT in the Emergency Department *317*

This chapter is intended to provide the reader with a comprehensive overview of the most recent clinical experience with multi-slice CT and recommendations for its clinical indications. Clinicians from Europe and the United States who are recognized world-wide as experts in their fields share their experience with respect to the currently most relevant clinical applications and indications of multi-slice cardiac CT. Institutions from all around the world have shared their latest case studies to further enhance the value of this chapter. The chapter starts with a review of the clinical usefulness of cardiac and coronary CT imaging, from the viewpoints of radiologists and cardiologists, and discusses the advances from 4- to 64-slice CT technology from a clinical perspective. This review is followed by sections that discuss in-depth the individual clinical findings based on 16-slice CT data and initial clinical experience with the latest 64-slice CT scanners.

7.1 Current and Future Clinical Potential

C. Becker, A. Knez

Contents

7.1.1 Cardiac Multi-slice CT Technique *179*
7.1.2 Coronary Calcium Screening *180*
7.1.3 Coronary CT Angiography *182*
7.1.4 Non-coronary Applications *189*
References *190*

7.1.1 Cardiac Multi-slice CT Technique

In recent years, improvements in multi-slice CT in terms of spatial and temporal resolution as well as acquisition speed has enabled reliable investigation of the heart and coronary arteries in a similar fashion as achieved with cardiac catheterization (Table 7.1). The accepted scan mode for cardiac multi-slice CT is retrospective ECG gating (Flohr 2001). In addition, various clinical indications have established the value of coronary calcium screen-

Table 7.1. Parameters for CT angiography and cardiac catheterization

	4-slice CT	16-slice CT	64-slice CT	Cardiac catheterization
Spatial resolution	1 mm	0.8 mm	0,4 mm	0,2 mm
Temporal resolution	250 ms	185–210 ms	165 ms	20 ms
Contrast volume	160 ml	120 ml	80 ml	~60 ml
Radiation exposure	~4–8 mSv	~5–10 mSv	~6–12 mSv	~3–4 mSv

ing and plaque imaging, coronary CT angiography (CTA), coronary bypass graft CTA, and assessment of myocardial morphology and function.

Coronary calcium screening enables investigation of the entire heart with 3-mm slices within one breath-hold and without the administration of contrast agent to the patient. Overlapping slice reconstruction has improved the reproducibility of coronary calcium quantification (Ohnesorge 2002). Protocols have been optimized so that the radiation exposure associated with this technique is reduced to a minimum (~2 mSv). ECG pulsing allows for a further 50% reduction in patient exposure by minimizing the redundant exposure that occurs during systole (Jakobs 2002). The reproducibility of the results obtained with coronary calcium scanning, as determined by multi-slice CT, is similar if not superior to measurements made with electron-beam CT.

Coronary CTA for plaque imaging and detection of coronary artery stenoses requires the highest level of temporal and spatial resolution. Depending on the technical possibilities, the scan and contrast protocols depend on the specific multi-slice CT scanner used. Temporal and spatial resolution improves with every new generation of multi-slice CT scanner (Figs. 7.1, 7.2). Further technical improvements are expected in the coming years and will mainly focus on shorter exposure times in order to image the heart at any heart rate and, in particular, the coronary arteries in the diastolic phase, when their diameters are widest.

The newest 64-slice CT technology has already emerged as a modality that allows image acquisition for the entire heart in about 10 s (or even less) with as little as 80 ml of contrast medium. The amount of contrast medium is therefore already comparable to that used in a cardiac catheter examination. In addition, the volume of contrast medium can be adapted for selective contrast enhancement of the left ventricle (Fig. 7.3).

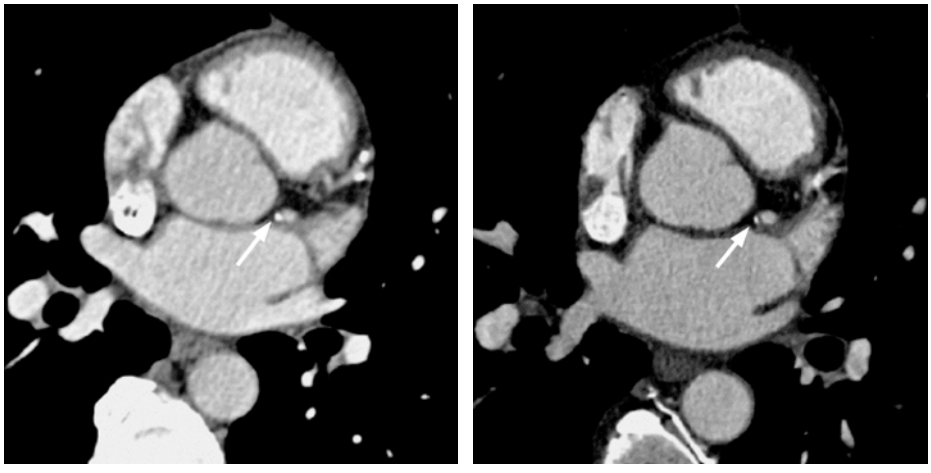

a b

Fig. 7.1a,b. Comparison between investigations with **a** 4-slice CT and **b** 64-slice CT. In addition to the fact the scan was acquired within 10 instead of 40 s with the 64-slice CT, the images reveal a higher spatial resolution and less blooming of calcium (*arrow*) in the coronary arteries

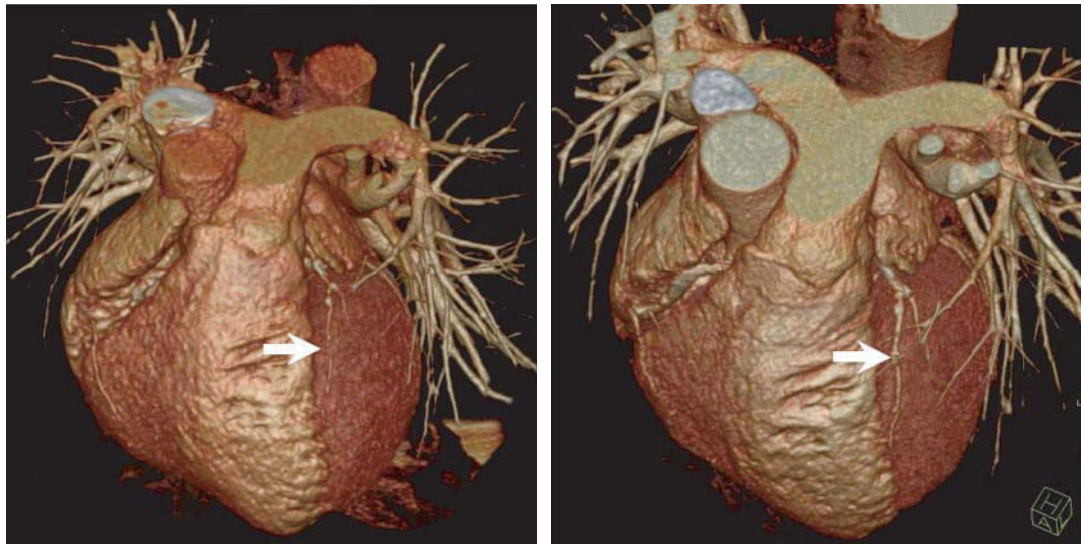

a b

Fig. 7.2a,b. In the volume rendering image, it becomes obvious that both the higher resolution and the dedicated contrast protocol lead to better visualization of the coronary arteries with 64-slice CT (**b**) than with 4-slice CT (**a**)

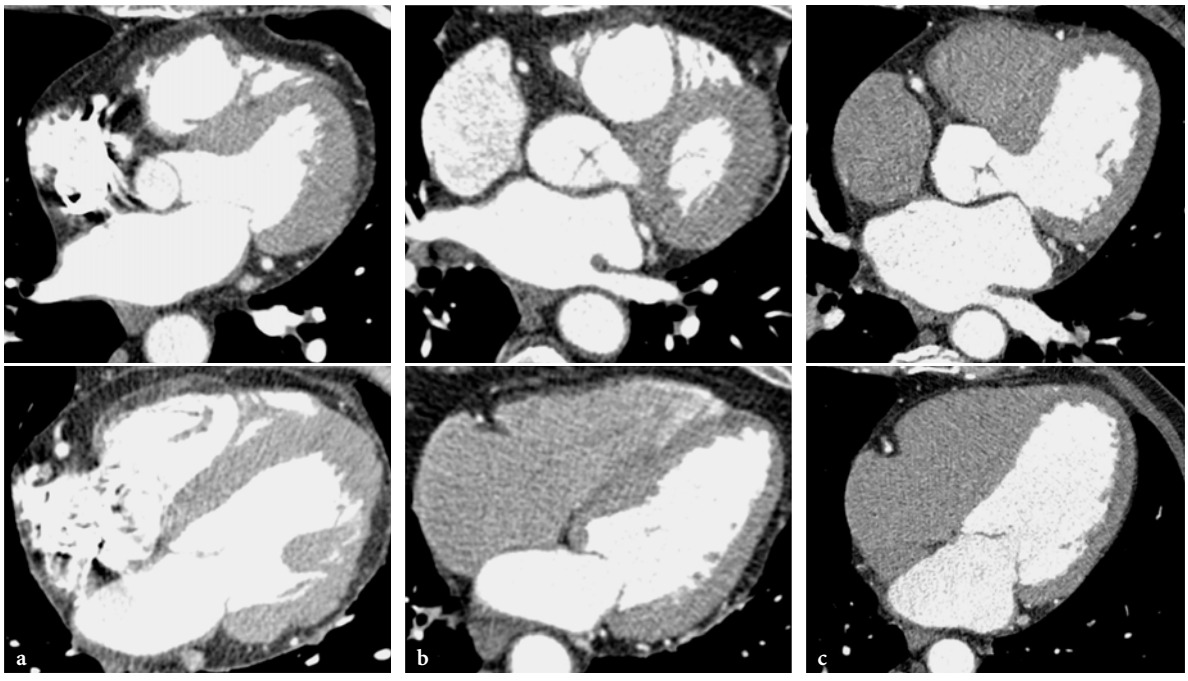

Fig. 7.3a–c. The scan time and therefore the amount of contrast media necessary can be reduced from 4-slice CT (**a**), to 16-slice CT (**b**), to 64-slice CT (**c**). With dedicated timing, selective enhancement of the left ventricle is possible with just 80 ml of contrast media

Thus, cardiac multi-slice CT has already emerged as a non-invasive clinical tool to demonstrate cardiac and coronary pathologies that are difficult or even impossible to detect by any other modality, even cardiac catheterization.

7.1.2 Coronary Calcium Screening

Coronary atherosclerosis begins as early as the first decade of life with endothelial dysfunction, proliferation of smooth muscle cells, and accumulation of fat (fatty streaks) in the coronary artery wall (Stary 1994). During later stages of the disease, these lesions may lead to the accumulation of cholesterol within the intimal and medial layer of the coronary artery wall and the formation of a fibrous cap separating the lipid pool from the arterial lumen (Stary 1995). Inflammatory processes, such as the invasion of macrophages and activation of matrix metalloproteases, weaken the fibrous cap (Pasterkamp 2000), which leaves the plaque vulnerable to rupture when exposed to shear stress. If this occurs, thrombogenic lipid material comes into contact with the blood. In the most unfortunate sequela, thrombus progression may turn the vulnerable plaque into a culprit lesion that occludes the coronary vessel, leading to myocardial ischemia, ventricular fibrillation, and death (Virmani 2000).

In many patients, unheralded myocardial infarction, associated with a mortality of approximately 20%, is the first sign of coronary artery disease (CAD). The likelihood of such an event strongly depends on risk factors, including hypertension, hypercholesteremia, smoking habit, family history, age, and gender. Based on these risk factors, the Framingham (Wilson 1998) and PROCAM (Assmann 2002) algorithms provide an estimation of the midterm (10-year) risk for an individual to experience a cardiac event. According to international guidelines, persons with a midterm risk of less than 10% are considered to be at low risk and usually do not require any specific therapy. Individual with a midterm risk of more than 20% are considered to be at high risk and thus equivalent to patients with CAD. Similar to patients with established CAD, these asymptomatic subjects may require intensive therapy ranging from life-style changes to lifetime medial treatment.

Approximately 40% of the population is considered to have a moderate midterm risk of 10–20%. Nonetheless, any of the stratification schemes suffers from a lack of accuracy in correctly determining risk, and uncertainty exists regarding how to treat subjects at intermediate risk. Thus, other tools that are able to provide information concerning the necessity to either reassure or to treat these subjects are needed. Currently, assessment of the atherosclerotic plaque burden is considered to provide valid information for this cohort (Greenland 2000).

It has recently been reported that the combined use of the Framingham risk assessment and the calcium measurement is superior to the selected use of the Framingham risk assessment alone (Greenland 2004). Grundy et al. proposed an alternative scheme in which the age score in the Framingham model is replaced by a scheme in which the coronary calcium percentiles are taken into account. If the amount of coronary calcium is between the 25th and 75th percentile, the Framingham risk score remains unchanged. If the amount of calcium is below the 25th or above the 75th percentile, the score is the same as for subjects approximately 10 years younger or older, respectively (Grundy 2001).

An international consortium comprising all CT vendors (Siemens, Toshiba, Philips, General Electric) and several leading research and clinical institutions has recently agreed upon a standardized measurement for coronary calcium. The consortium provides guidelines for standardized CT scan protocols for any company, as well as guidelines for calibration, quantification, and quality assurance. In addition, it has agreed upon absolute mass quantification as the algorithm with the highest inter-scanner reproducibility (Fig. 7.4). Once finalized, the consortium will also provide a web-based database entry allowing the event risk to be estimated according to Framingham, PROCAM, and other algorithms, also taking into account age- and gender-specific percentile rankings of the calcium mass (McCollough 2003).

7.1.3 Coronary CT Angiography

Contrast-enhanced CTA of the coronary arteries is a new application of multi-slice CT. Preliminary

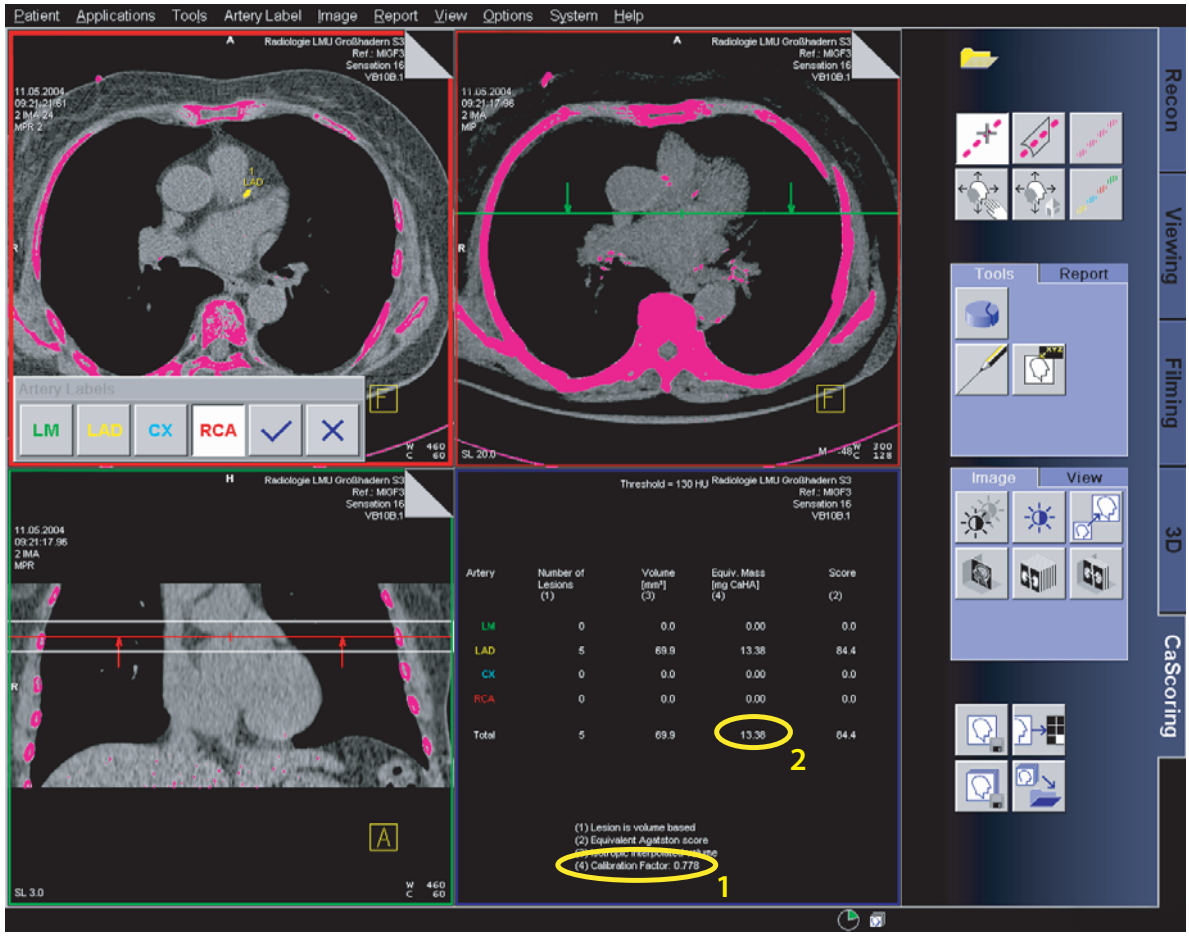

Fig. 7.4. Due to the low radiation and the fact that contrast medium is not required, coronary calcium screening remains a simple and effective tool to exclude or detect coronary atherosclerosis. An international consortium has agreed upon the calibrated (*circle 1*) absolute mass (*circle 2*) as the method of choice to quantify coronary calcium. The calcium mass is then assigned to age- and sex-dependent percentiles in order to incorporate it into conventional risk assessment

attempts in which coronary CTA and conventional catheter-based coronary angiography were compared with respect to the detection of coronary artery stenoses were encouraging (Achenbach 2001, Nieman 2001, Knez 2001). In particular, sensitivity and specificity values between 86 and 95% were reported for 16-slice CT (Nieman 2002, Ropers 2003). However, such high values can only be achieved if non-evaluable coronary segments are excluded from the analysis. In fact, most of the excluded coronary segments were excluded because of motion artifacts. With 16-slice CT technology and the related rotation speeds, fully motion-free images can only be achieved in patients with low and regular heart rates. Otherwise, patients undergoing CTA examination by 16-slice CT should be administered a β-blocker prior to the investigation in order to reduce the heart rate and thus improve image quality.

Other limitations of coronary multi-slice CTA include the difficulty in detecting stenoses and plaques if calcium or other dense materials, such as metallic stents, are present. The appearance of these components is exaggerated by CT, which prevents assessment of the coronary artery wall and lumen. With the newest 64-slice CT and its higher spatial

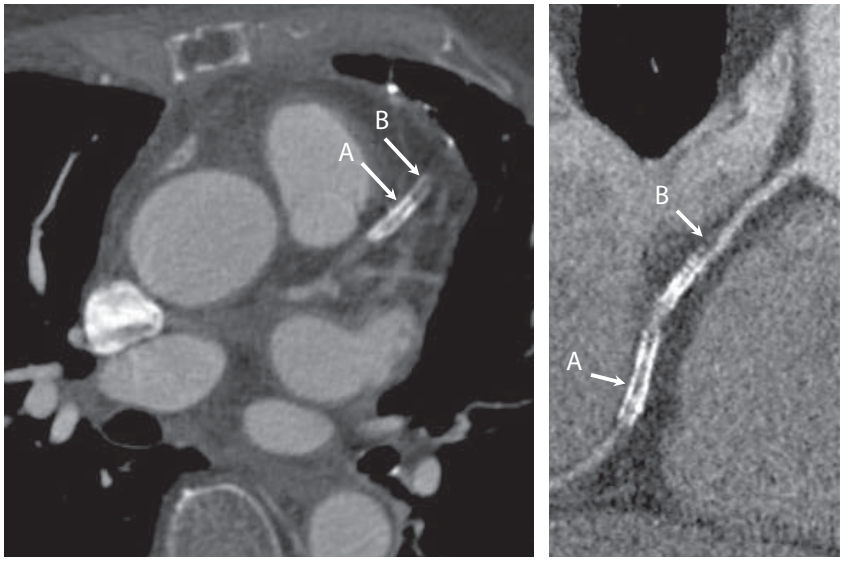

a b

Fig. 7.5. a Patient investigated with 64-slice CT. A thrombus clot is seen in the left anterior descending coronary artery within (*arrow* A) and distal (*arrow* B) to the stent. **b** Another patient with in-stent (*arrow* A) and pre-stent (*arrow* B) stenoses in the right coronary artery

resolution, the "blooming" artifact is substantially reduced and the lumens of larger stents (>3 mm in diameter) and thinner struts (>140 μm) are now assessable (Fig. 7.5).

In addition to displaying the contrast-filled lumen, as is the case in cardiac catheterization, CTA is a cross-sectional modality in that the coronary artery wall is also displayed. Coronary atherosclerotic changes may appear as calcified, non-calcified, or mixed plaques. In a recent study, Leber et al. reported that non-calcified lesions were predominantly found in patients with acute myocardial infarction whereas calcified lesions were found more often in patients with chronic stable angina (Leber 2003). In patients with an acute coronary syndrome, a non-calcified lesion in the coronary artery may correspond to an intra-coronary thrombus (Becker 2000).

The current gold standard to detect coronary atherosclerosis in vivo is intravascular ultrasound (IVUS). Studies comparing IVUS with multi-slice CT have shown good correlation between the echogeneity and CT density of coronary atherosclerotic lesions (Schröder 2001). The sensitivity and specificity of CT in the detection of calcified and non-calcified coronary atherosclerosis ranges from 78 to 94%, respectively.

CT density measurements in carotid arteries (Estes 1998) and heart specimen (Becker 2003) showed that CT densities of 50 and 90 HU within plaques are specific for lipid and fibrous tissue, respectively. In recent work by Langheinrich et al. using micro-CT and ultrahigh spatial resolution, the ability of CT to distinguish between different plaque components, such as lipid, fibrin, and calcium, was demonstrated. Interestingly, smooth muscle cell proliferation increases the CT density of the plaque (Langheinrich 2004).

Coronary CTA is also well-suited to visualize coronary anatomical anomalies and to identify patients in whom the aberrant coronary artery has its course in between the ascending aorta and the pulmonary outflow tract. In this particular location, the coronary artery is at risk for being squeezed in between the two major vessels, which may result in myocardial ischemia (Figs. 7.6, 7.7). Coronary CTA can also provide valid and useful information in patients with vasculitis, aneurysms (Fallenberg 2002), fistulas (Fig. 7.8), or dissection.

The current strength of coronary CTA is its high negative predictive value compared to cardiac catheterization. In patients with unspecific complaints or ambiguous stress tests, coronary CTA may serve as a reliable non-invasive alternative to rule out CAD (Fig. 7.9). Also, patients referred from the emergency department with atypical chest pain may benefit from a CTA investigation that allows all-at-

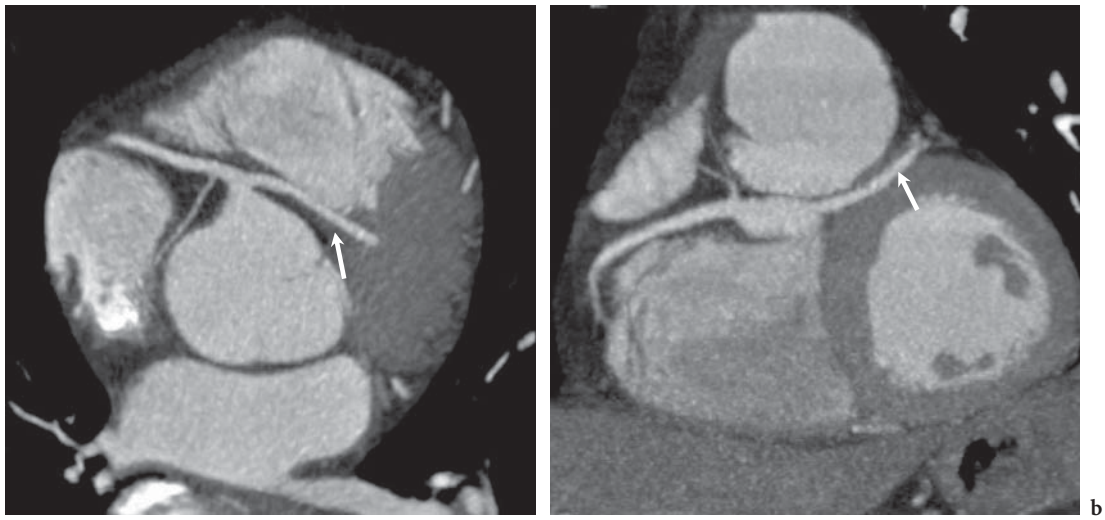

Fig. 7.6a,b. Common origin of the right and left coronary arteries displayed with axial maximum-intensity projection (MIP) (**a**) and double-oblique MIP (**b**). Scan data were acquired using 64-slice CT. The intramural course of the left coronary artery (*arrow*) between the aorta and the pulmonary outflow tract caused angina in this patient

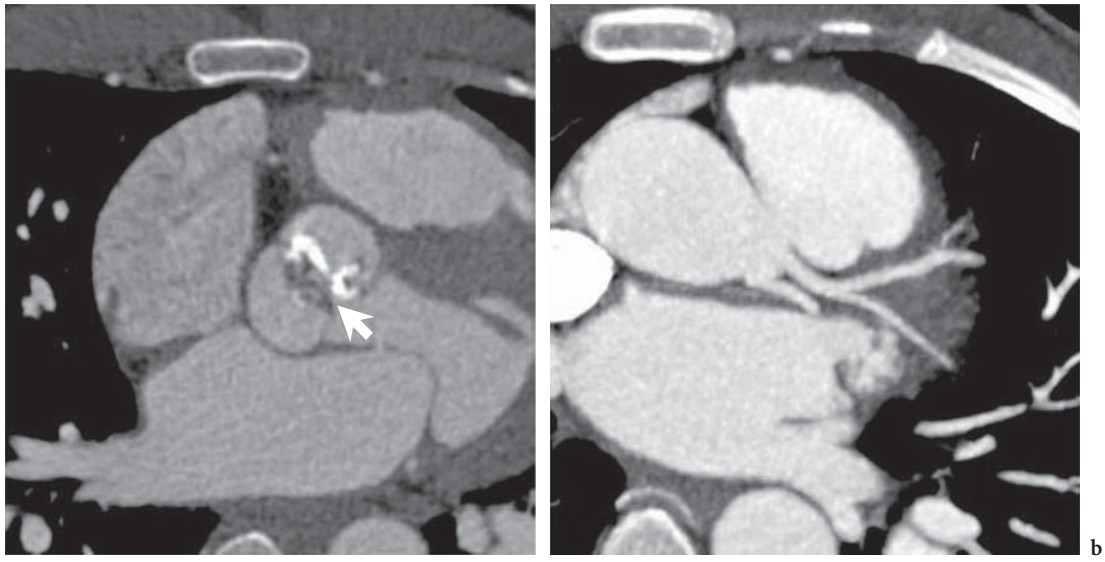

Fig. 7.7a,b. Patient investigated with 64-slice CT. Severe calcification and vegetation of a bicuspid aortic valve (**a**, *arrow*). This patient had a split left coronary artery with separate origins of the left anterior descending and the circumflex coronary artery (**b**)

once ruling in or out of pulmonary emboli, aortic dissection, or coronary thrombus (Fig. 7.10). Coronary CTA is also a valuable technique for assessing patients with acute coronary syndrome and unstable angina, since certain types of non-calcified lesions may indicate an increased risk of myocardial infarction in this particular cohort (Fig. 7.11). If the results of coronary CTA confirm the identification of patients at risk, further therapeutic strategies can subsequently be considered, such as intensive medi-

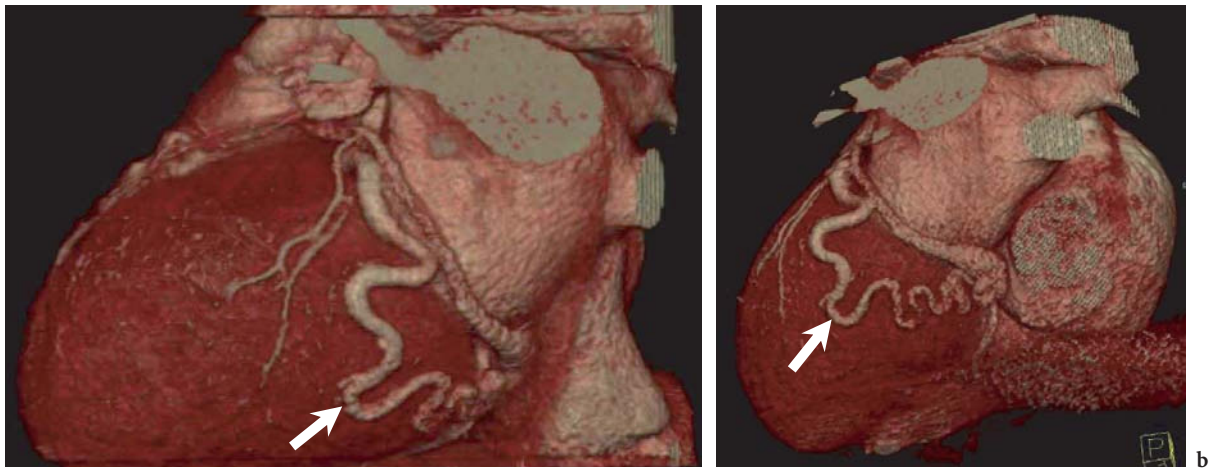

a b

Fig. 7.8a,b. Patient with a heart murmur examined with 16-slice CT. The coronary CT angiography (CTA) investigation and volume-rendering technique (VRT) demonstrate a fistula of the circumflex coronary artery (**a**, *arrow*) with kinking draining into the right atrium (**b**)

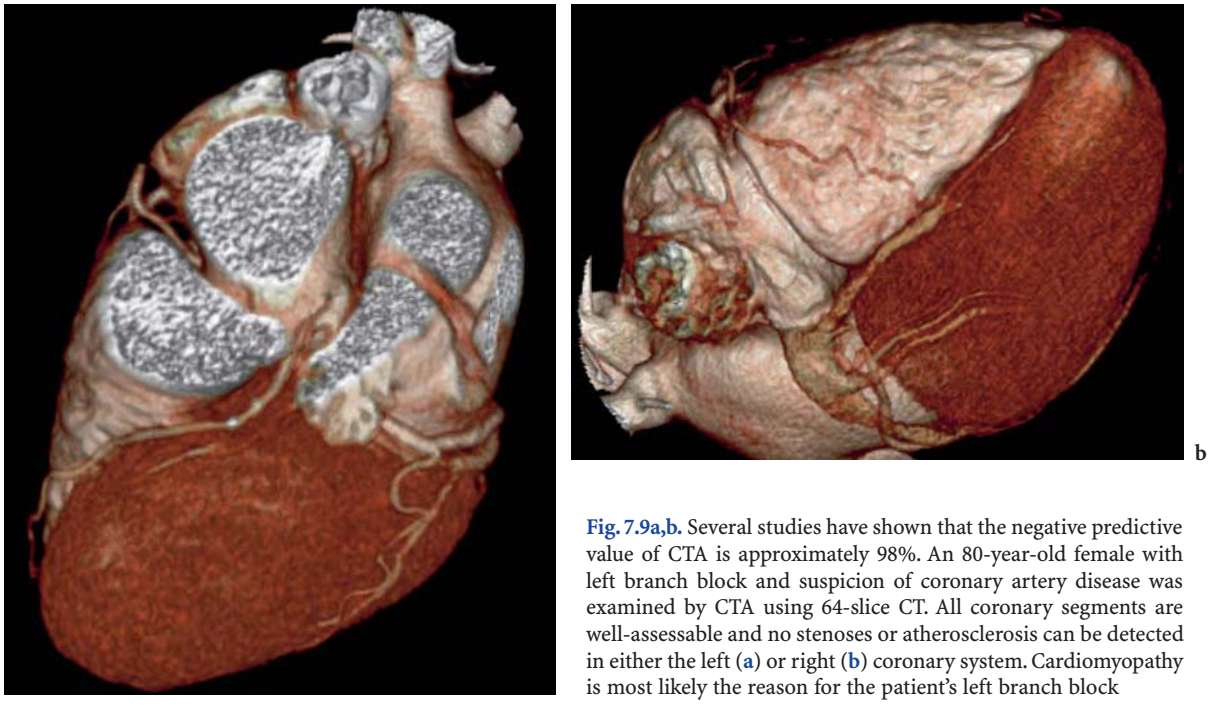

a b

Fig. 7.9a,b. Several studies have shown that the negative predictive value of CTA is approximately 98%. An 80-year-old female with left branch block and suspicion of coronary artery disease was examined by CTA using 64-slice CT. All coronary segments are well-assessable and no stenoses or atherosclerosis can be detected in either the left (**a**) or right (**b**) coronary system. Cardiomyopathy is most likely the reason for the patient's left branch block

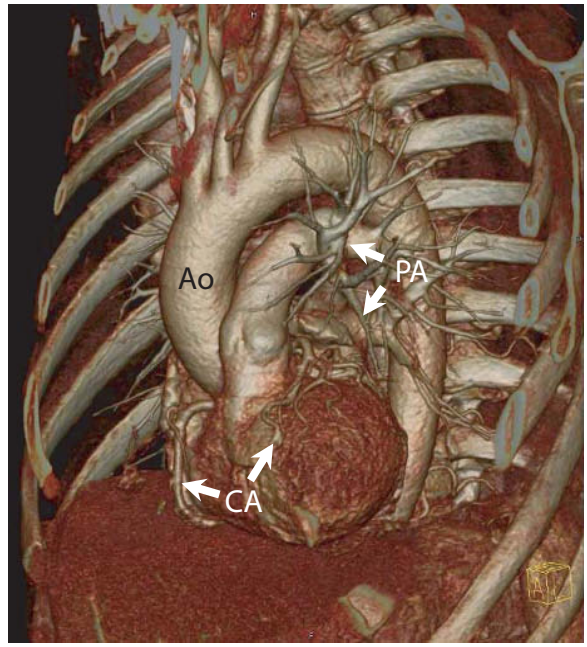

Fig. 7.10. A patient who presented with chest pain was investigated with 64-slice CT. Patients referred from the chest pain unit may benefit from a 64-slice CT scan of the entire chest with ECG gating, as this allows for complete assessment of the pulmonary (*arrow, PA*) and coronary (*arrow, CA*) arteries as well as the aorta (*Ao*)

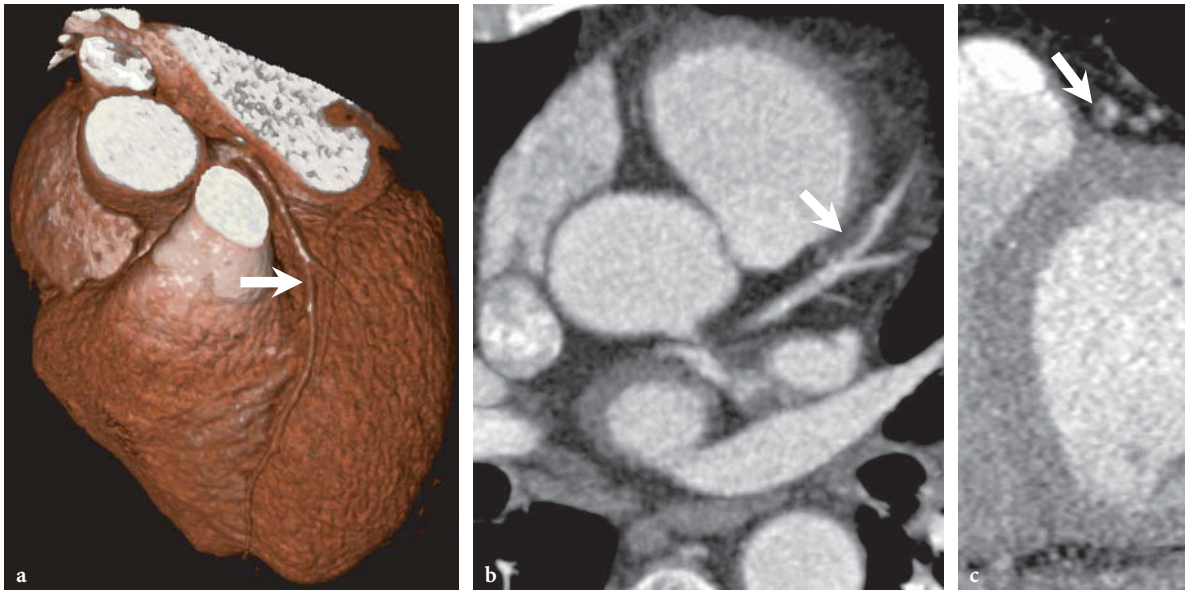

Fig. 7.11a–c. The 64-slice coronary CTA investigation of a patient with unstable angina without signs of myocardial ischemia. **a** Volume rendering of the dataset shows a regular vessel lumen. **b** The axial slice, however, demonstrates a well-defined plaque in the middle segment of the left anterior descending coronary artery (*arrow*). **c** Perpendicular reformatting demonstrates a vulnerable plaque with a low-density (fatty) center surrounded by higher-density (fibrous) tissue. Three weeks later, this plaque ruptured, resulting in an anterior wall infarction in this patient

cal treatment or invasive approaches, e.g., plaque sealing.

In patients with acute myocardial infarction, coronary CTA may be able to display the location as well as the culprit lesion in the coronary artery (Fig. 7.12) (Paul 2003). However, the key application of coronary CTA will be non-invasive triage of patients with stable angina for conservative therapy, interventional treatment, or bypass surgery, thus limiting the need for cardiac catheterization of patients in whom coronary interventions are likely to be unnecessary. Follow-up investigation after stent placement of bypass graft surgery (Fig. 7.13) is the second most important demand for this approach.

There remains a shortfall of large-scale clinical studies providing sufficient evidence for the widespread clinical use of coronary CTA. A first multicenter study (Garcia 2006) could demonstrate the clinical feasibility of coronary CTA in a larger patient cohort, however, the accuracy of the results was limited due to the use of older generation 16-slice CT technology. Nonetheless, with every new generation of multi-slice CT, the spatial and temporal resolution comes closer to that of cardiac catheterization. The present-day generation of 16- and 64-slice CT is already making some catheter investigations redundant, and the replacement of

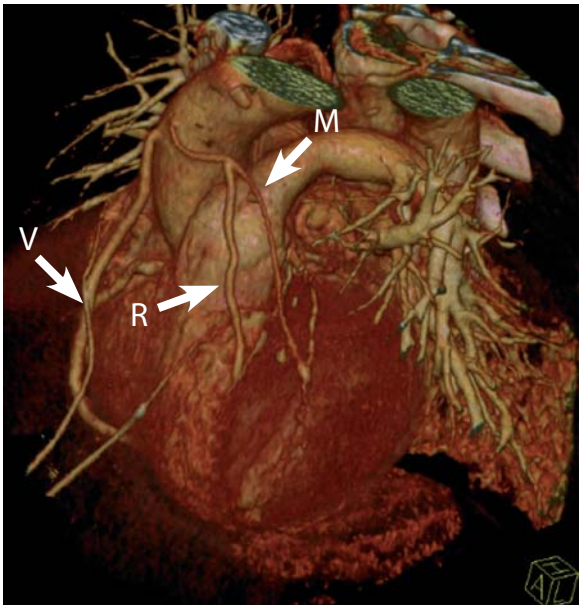

Fig. 7.13. Patient examined with 64-slice CT. An arterial T-graft of the internal mammary (*arrow, M*) and radial (*R*) arteries to the left anterior descending coronary artery, and to the diagonal branch and venous graft (*arrow, R*) to the right coronary artery. An additional and venous graft (*arrow, V*) supplies the right coronary artery. The 64-slice CT examination reveals that all three bypass grafts are open

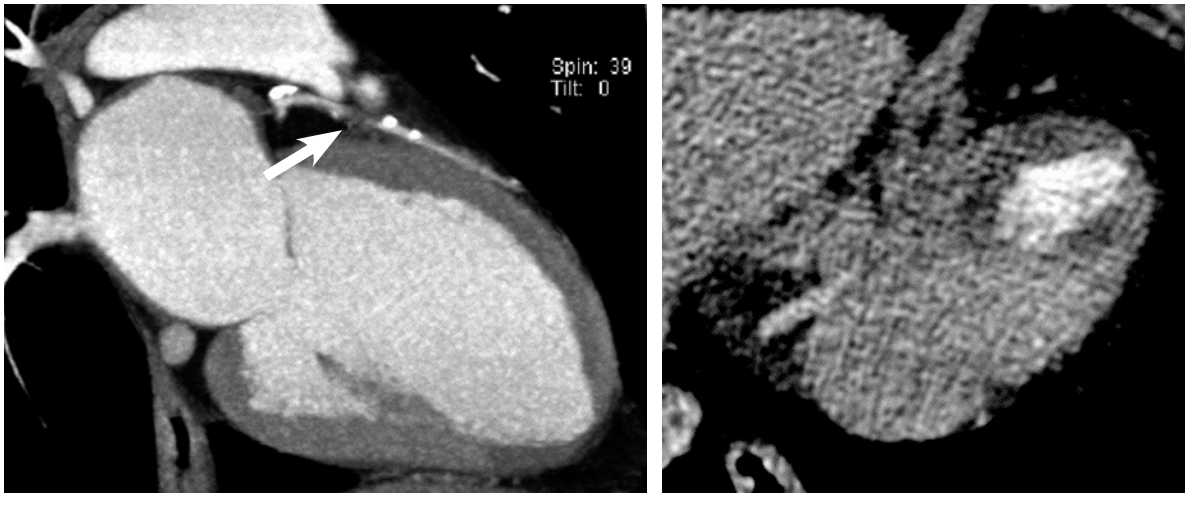

a b

Fig. 7.12a,b. Images of a patient with acute myocardial infarction. **a** A culprit lesion (*arrow*) is seen in the proximal left anterior descending coronary artery. **b** The consecutive myocardial infarction and the related perfusion defect (*arrow*) can also be delineated as a hypo-dense area in the anterior wall of the left ventricle

a significant number of diagnostic cardiac catheterizations by coronary CTA is foreseeable in the near- to mid-term future.

7.1.4 Non-coronary Applications

Contrast-enhanced multi-slice CT acquisition with ECG triggering or ECG-gated spiral scanning also accurately displays the cardiac morphology and allows the diagnosis of general cardiac diseases. The cardiac anatomy can be examined based on either a dedicated scan protocol with a specific clinical indication or as a by-product of a CTA of the coronary arteries. Clinical indications of multi-slice cardiac CT include visualization of cardiac masses, the cardiac valves, myocardial perfusion defects, pericardial disease, the thoracic aorta, and the pulmonary arteries and veins. Application of multi-slice CT as a primary tool in the diagnosis of cardiac morphology can be particularly useful in acute-care settings and in patients who have to be excluded from other imaging modalities, such as those with pacemakers and those with artificial or transplanted hearts. Retrospectively ECG-gated multi-slice CT examinations also enable basic cardiac function parameters to be visualized and quantified as an add-on to the anatomical information (Fig. 7.14). In addition, multi-slice CT examination of the cardiac venous system has proven to be very useful for planning electrophysiological (EP) ablation procedures (Fig. 7.15). Imaging of the general cardiac anatomy and cardiothoracic vasculature usually requires larger scan ranges with high resolution, which has limited the distribution of 4-slice CT scanners for this purpose. Recent 16- and 64-slice CT scanners, however, have overcome this limitation and provide scan ranges up to 20 cm within a short single breath-hold. Therefore, with the recent technology advances, ECG-gated multi-slice CT has developed into a robust routine tool for the non-invasive diagnosis of general cardiac diseases and non-invasive planning of EP procedures.

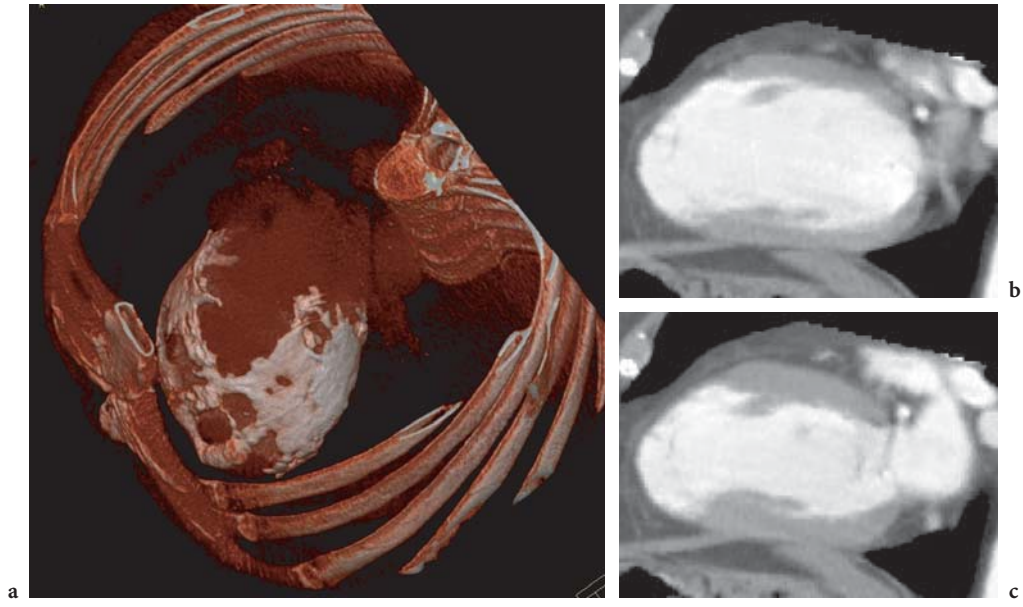

Fig. 7.14a–c. Patient with severe 3-vessel disease, pericarditis, and a functional defect was examined with 16-slice CT. **a** VRT reveals calcium deposits in the pericardium resulting from the pericarditis. Long-axis reconstruction in end-diastole (**b**) and end-systole (**c**) reveals the related reduced left ventricular function. (Case courtesy of Erlangen University, Germany)

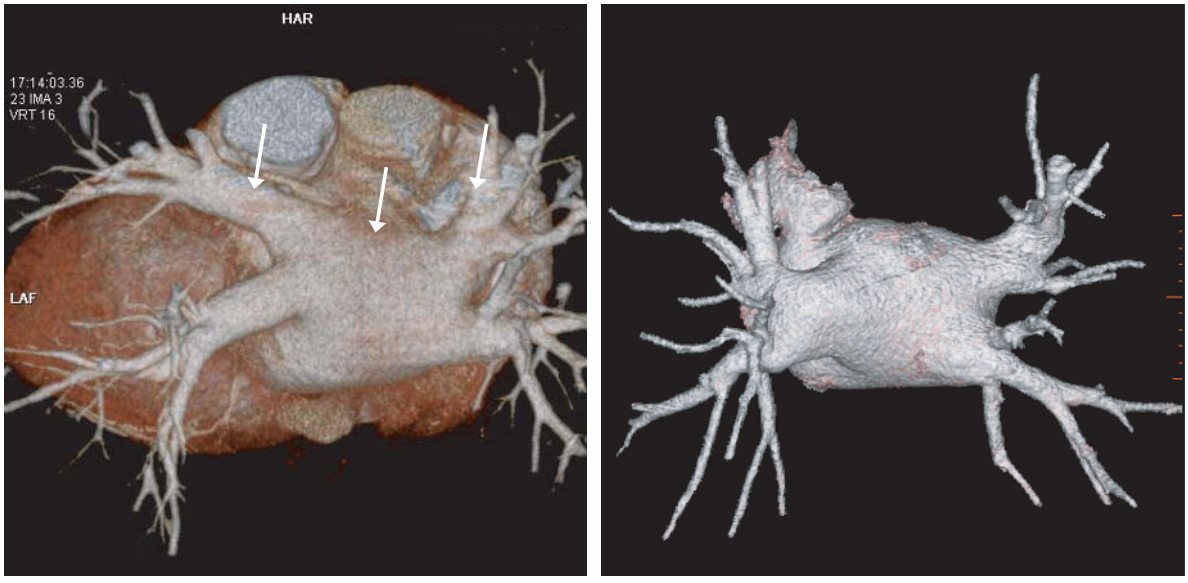

a b

Fig. 7.15a,b. Patient examined with 16-slice CT to visualize the pulmonary vein for planning of an ablation procedure. Special contrast agent protocols are required for imaging the cardiac venous system. High-quality image data of the pulmonary vein, including side branches (**a**, *arrows*) can be provided as input for special segmentation software (**b**). (Case courtesy of Massachusetts General Hospital, Boston, USA)

References

Achenbach S, Giesler T, Ropers D, et al (2001). Detection of coronary artery stenoses by contrast-enhanced, retrospectively electrocardiographically-gated, multislice spiral computed tomography. Circulation 103:2535–2538

Assmann G, Cullen P, Schulte H (2002). Simple scoring scheme for calculating the risk of acute coronary events based on the 10-year follow-up of the Prospective Cardiovascular Munster (PROCAM) Study. Circulation 105(3):310–315

Becker CR, Knez A, Ohnesorge B, Schoepf UJ, Reiser MF (2000). Imaging of noncalcified coronary plaques using helical CT with retrospective ECG gating. AJR Am J Roentgenol 175(2):423–424

Becker CR, Nikolaou K, Muders M, et al (2003). Ex vivo coronary atherosclerotic plaque characterization with multidetector-row CT. Eur Radiol 13(9):2094–2098

Estes J, Quist W, Lo Gerfo F, Costello P (1998). Noninvasive characterization of plaque morphology using helical computed tomography. J Cardiovasc Surg 39:527–534

Fallenberg M, Juergens KU, Wichter T, Scheld HH, Fischbach R (2002). Coronary artery aneurysm and type-a aortic dissection demonstrated by retrospectively ECG-gated multislice spiral CT. Eur Radiol 12(1):201–204

Flohr T, Ohnesorge B (2001). Heart rate adaptive optimization of spatial and temporal resolution for electrocardiogram-gated multislice spiral CT of the heart. J Comput Assist Tomogr 25(6):907–923

Garcia MJ, Lessick J, Hoffmann MHK (2006). Accuracy of 16-Row Multidetector Computed Tomography for the Assessment of Coronary Artery Stenosis. JAMA 296:403–411

Greenland P, Abrams J, Aurigemma GP, et al (2002). Prevention Conference V: Beyond secondary prevention: identifying the high-risk patient for primary prevention: noninvasive tests of atherosclerotic burden: Writing Group III. Circulation 101(1):E16–22

Greenland P, LaBree L, Azen SP, Doherty TM, Detrano RC (2004). Coronary artery calcium score combined with framingham score for risk prediction in asymptomatic individuals. JAMA 291(2):210–215

Grundy SM (2001). Coronary plaque as a replacement for age as a risk factor in global risk assessment. Am J Cardiol 88(2-A):8E-11E

Jakobs TF, Becker CR, Ohnesorge B, et al (2002). Multislice helical CT of the heart with retrospective ECG gating: reduction of radiation exposure by ECG-controlled tube current modulation. Eur Radiol 12(5):1081–1086

Knez A, Becker CR, Leber A, et al (2001). Usefulness of multislice spiral computed tomography angiography for determination of coronary artery stenoses. Am J Cardiol 88(10):1191–1194

Langheinrich AC, Bohle RM, Greschus S, et al (2004). Atherosclerotic lesions at micro ct: feasibility for analysis of

coronary artery wall in autopsy specimens. Radiology 231:675–681

Leber AW, Knez A, White CW, et al (2003). Composition of coronary atherosclerotic plaques in patients with acute myocardial infarction and stable angina pectoris determined by contrast-enhanced multislice computed tomography. Am J Cardiol 91(6):714–718

McCollough CH, Ulzheimer S, Halliburton SS, White RD, Kalender WA (2003). A multi-scanner, multi-manufacturer, international standard for the quantification of coronary artery calcium using cardiac CT (Abstract). Radiology 229(P):630

Nieman K, Oudkerk M, Rensing B, et al (2001). Coronary angiography with multi-slice computed tomography. Lancet 357:599–603

Nieman K, Cademartiri F, Lemos PA, Raaijmakers R, Pattynama PM, de Feyter PJ (2002). Reliable noninvasive coronary angiography with fast submillimeter multislice spiral computed tomography. Circulation 106(16):2051–2054

Ohnesorge B, Flohr T, Fischbach R, et al (2002). Reproducibility of coronary calcium quantification in repeat examinations with retrospectively ECG-gated multisection spiral CT. Eur Radiol 12(6):1532–1540

Pasterkamp G, Falk E, Woutman H, Borst C (2000). Techniques characterizing the coronary atherosclerotic plaque: influence on clinical decision making? J Am Coll Cardiol 36:13–21

Paul JF, Dambrin G, Caussin C, Lancelin B, Angel C (2003). Sixteen-slice computed tomography after acute myocardial infarction: from perfusion defect to the culprit lesion. circulation 108(3):373–374

Ropers D, Baum U, Pohle K, et al (2003). Detection of Coronary artery stenoses with thin-slice multi-detector row spiral computed tomography and multiplanar reconstruction. Circulation 107(5):664–666

Schroeder S, Kopp AF, Baumbach A, et al (2001). Noninvasive detection of coronary lesions by multislice computed tomography: results of the New Age Pilot Trial. Catheter Cardiovasc Interv 53(3):352–358

Stary HC, Chandler AB, Glagov S, et al (1994). A definition of initial, fatty streak, and intermediate lesions of atherosclerosis. A Report from the Committee on Vascular Lesions of the Council on Arteriosclerosis, American Heart Association. Circulation 89(5):2462–2478

Stary HC, Chandler AB, Dinsmore RE, et al (1995). A definition of advanced types of atherosclerotic lesions and a histological classification of atherosclerosis. A Report from the Committee on Vascular Lesions of the Council on Arteriosclerosis, American Heart Association. Circulation 92(5):1355–1374

Virmani R, Kolodgie FD, Burke AP, Frab A, Schwartz SM (2000). Lessons from sudden coronary death. A comprehensive morphological classification scheme for atherosclerotic lesions. Arterioscler Thromb Vasc Biol 20:1262–1275

Wilson PW, D'Agostino RB, Levy D, Belanger AM, Silbershatz H, Kannel WB (1998). Prediction of coronary heart disease using risk factor categories. Circulation 97(18):1837–1847

7.2 Risk Assessment with Coronary Artery Calcium Screening

R. Fischbach

Contents

7.2.2 Methods of Coronary Artery Calcification Quantification *192*
7.2.3 Multi-slice CT Examination Technique *195*
7.2.4 Clinical Applications of Coronary Calcium Measurement *197*
7.2.5 Further Clinical Applications of Calcium Scanning *200*
7.2.6 Conclusion *202*
References *203*

7.2.1 Introduction

Direct relationships between coronary artery calcification (CAC) and the presence, and to a modest degree, the extent and severity of coronary atherosclerotic disease (CAD) have been demonstrated in comparisons based on histology (Rumberger 1995), ultrasound (Baumgart 1997), and angiography (Kajinami 1997). This correlation of CAC with the amount of coronary artery plaque has raised significant interest in the noninvasive detection and quantification of coronary calcium for diagnosing coronary atherosclerosis and estimating the prognosis of patients with coronary heart disease. Electron-beam CT (EBCT) was the first accurate and sensitive noninvasive technique with which to quantify coronary calcium and it has been used in most clinical studies. Therefore, the relevant clinical data to date come from studies that were carried out using this specific CT technology and based on a standardized method for imaging, identifying, and quantifying calcified coronary artery plaque. Despite the different scanner technologies, major disagreements between calcium quantification results obtained in the same patients by EBCT vs. multi-slice CT have not been reported (Becker 2001, Stanford 2004).

Recent studies indicate that CAC quantification plays an important role in the assessment of cardiovascular disease risk in asymptomatic individuals with subclinical atherosclerosis. In this context, the primary goal in calcium scanning is to detect and quantify calcified coronary artery plaque and not to identify significant coronary artery obstruction, as is done in coronary CTA. The introduction of multi-slice CT has brought a rapidly increasing variety of multi-purpose CT systems that allow cardiac scanning using prospective ECG triggering or retrospective ECG gating. While this has allowed CAC quantification to become available to larger populations, it has made standardization of image acquisition protocols and quantification methods an increasingly important clinical issue.

7.2.2 Methods of Coronary Artery Calcification Quantification

The calcified coronary artery plaque is traditionally quantitated with a score developed by Agatston et al., in which the area of a calcified plaque with an attenuation of more than 130 HU is multiplied by a weighting factor that is based on the peak density of the calcified lesion, as depicted in Figure 7.16 (Agatston 1990). When applying the Agatston method to coronary calcium quantification using multi-slice CT technology, it has to be kept in mind that the Agatston score was initially designed for a specific modality (EBCT) and scan protocol. Any changes in image acquisition parameters, such as scan volume, section thickness, image increment, image reconstruction kernel, or X-ray spectrum, may influence the quantification result (Ulzheimer 2003). Due to the use of a non-linear weighting factor, the Agatston score is rather susceptible to partial-volume effects and has shown only limited reproducibility in repeat examinations. Another reason for the limited reproducibility of calcium quantification results is artifacts due to either cardiac motion or patient motion during the breath-hold.

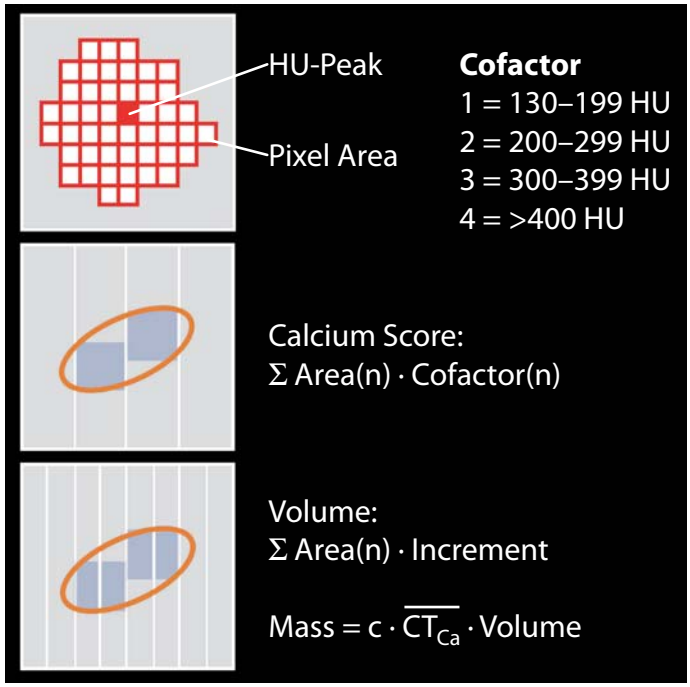

Fig. 7.16. Quantification methods to measure coronary artery calcification. The Agatston score or traditional calcium score is calculated by multiplying the calcified plaque area with a density-dependent weighting factor. The sum of all scores is the total calcium score. The volume score is the sum of the calcified area multiplied with the image increment. Calcium mass is proportional to the volume of the lesion times the average CT density of the lesion. n denotes a specific calcified lesion. c represents a calibration factor, $\overline{CT_{Ca}}$ the average CT HU-value of the lesion

In order to improve the inter-scan reproducibility, a volume-based quantification method has been introduced (Callister 1998, Ohnesorge 2002). Plain volume measurement is less susceptible to partial-volume effects and allows quantification independent from section thickness or image overlap. This becomes especially important when a spiral technique with overlapping image reconstruction is used. However, the different volume scoring methods that are currently available are influenced by an empirically chosen density threshold (130 HU), which has been shown to suffer from system and patient factors (McCollough 1995). An adapted density threshold for segmentation of a specific amount of coronary artery calcium, as opposed to a fixed density threshold, has been shown to improve the accuracy and comparability of calcium quantification on different scanners and using different scan protocols (Ulzheimer 2003). Since the measured volume of a calcified plaque is related to the registered attenuation of a lesion, changes in the X-ray radiation energy spectrum (determined by tube voltage) as well as hardware-associated factors that influence the X-ray absorption of a calcified coronary plaque will affect the measured volume score (Fig. 7.17). Therefore, a quantification method that is standardized, reproducible, and independent of scanner hardware and image acquisition parameters is required to produce accurate results. This is especially the case in view of the rapidly emerging diversity of the multi-slice CT systems available and the expected clinical role of multi-slice CT calcium quantification in coronary risk stratification.

Quantification of absolute coronary artery calcium mass, which can be reliably obtained regardless of differences in CT systems and scanning protocols if appropriate calibration is used, has been suggested to improve the reliability of calcium measurement (Ohnesorge, 2002, Hong 2002, Ulzheimer 2003). The CT scanner can be calibrated to an external standard or a calibration phantom can be included within the scan field, as in bone density measurement. Calcium mass is proportional to the mean CT number of a calcified plaque multiplied by the lesion volume. Since objects smaller than the section thickness are displayed with decreased mean CT numbers, calcium

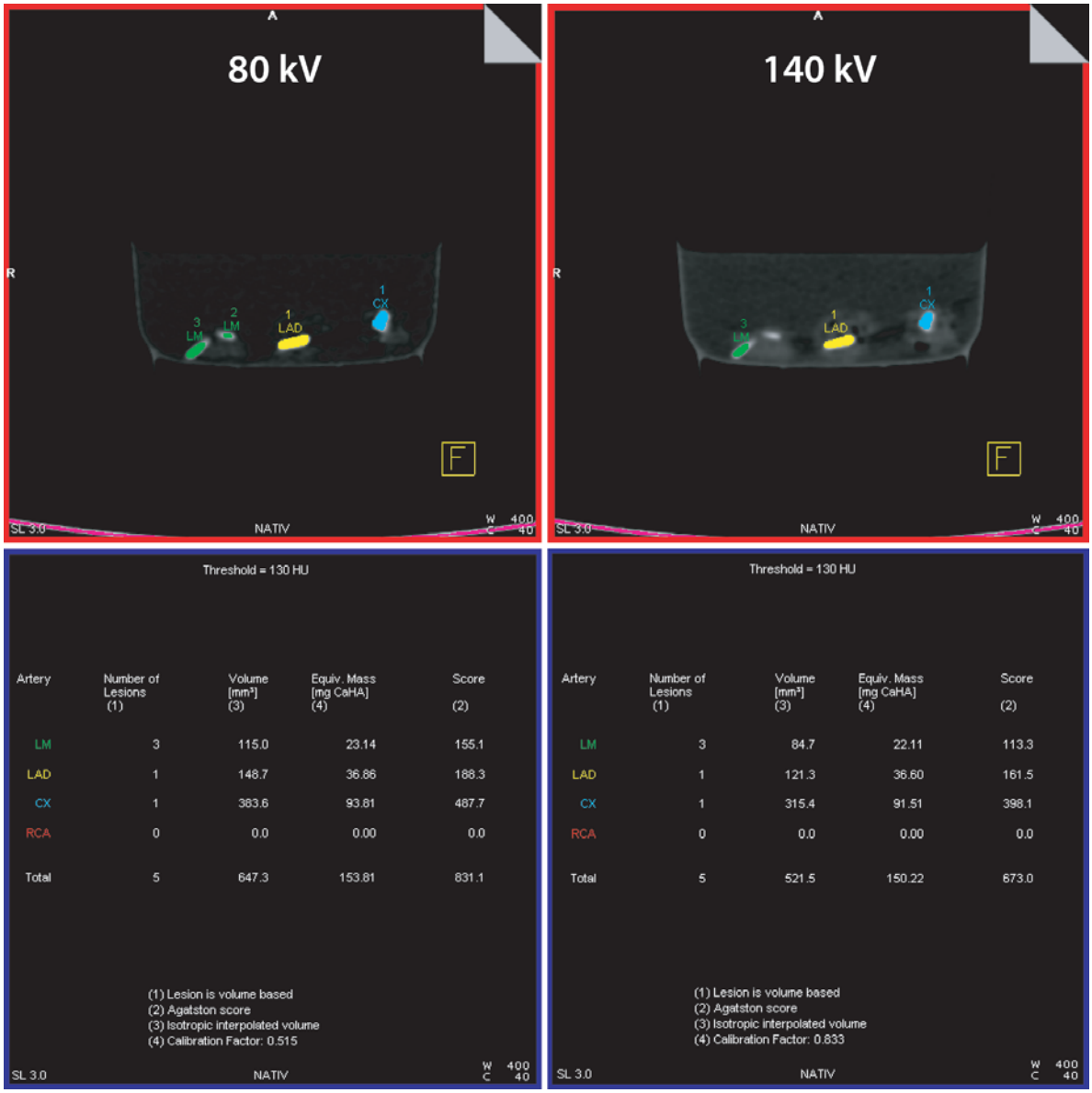

Fig. 7.17. Coronary calcium score and volume score are affected by the tube voltage. At 80 kV, the score of the simulated calcified plaque is 831, whereas it is 673 for the same lesions measured at 140 kV. The calibrated calcium mass remains constant. Note the different calibration factors used for the different scans (0.515 vs. 0.833)

mass automatically corrects for linear partial-volume effects. Calibrated calcium mass furthermore represents a real physical measure (mg calcium) and can be used across different CT systems and scanning techniques. For current and future applications of coronary artery calcium scoring, calibrated mass-based quantification seems superior to traditional quantification methods (Ohnesorge 2002, Ferencik 2003, Hong 2003) but validation in clinical practice is still pending. A major drawback regarding volume and mass scores is the lack of reference data for large populations, in contrast to data available for the Agatston score. Although calcium scoring results obtained with the Agatston method using multi-slice CT correlate well with results obtained by EBCT (Becker 2001), new reference databases for multi-slice CT coronary calcium quantification involving calibrated measurements for volume and mass quantification remain to be developed (Haliburton 2003).

7.2.3 Multi-slice CT Examination Technique

The coronary arteries are easily recognized in their epimyocardial course even in non-enhanced scans, as they are surrounded by low-attenuation perivascular fat. The scan extends form the mid-level of the left pulmonary artery down to the diaphragm (Fig. 7.18). All multi-slice CT scanners are able to cover this distance in a single breath hold. Imaging of coronary calcifications is typically done using a low-dose technique without contrast enhancement. The coronary arteries are well-depicted due to the surrounding epimyocardial fat (Fig. 7.19),

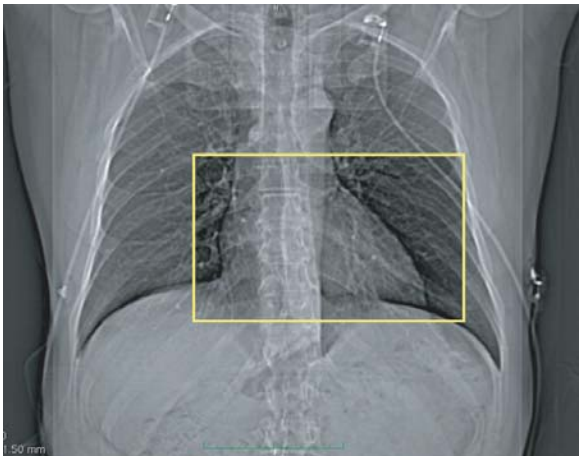

Fig. 7.18. Topogram showing the typical scan range and field of view for a calcium scoring exam from the mid-level of the left pulmonary artery down to the diaphragm

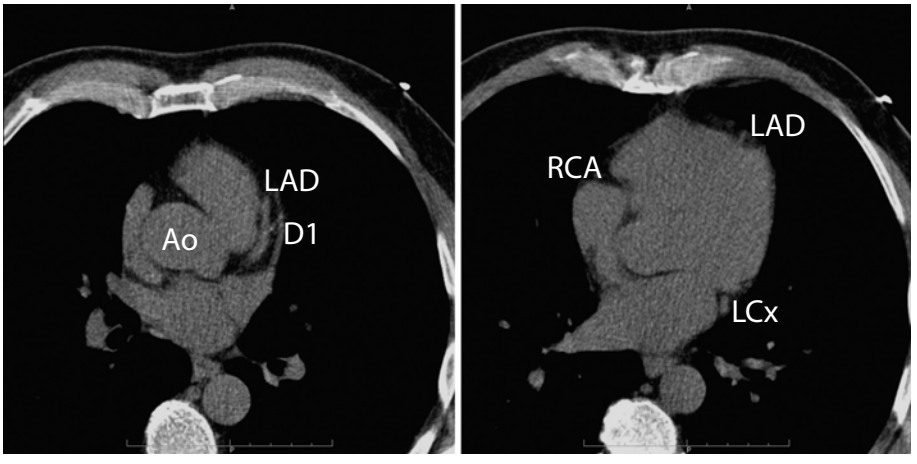

Fig. 7.19. Unenhanced coronary scan with 4-slice CT in an individual without detectable calcification. The coronary arteries are well seen in the epimyocardial course. Ao Aorta, LAD left anterior descending artery, D1 first diagonal branch, LCx left circumflex coronary artery, RCA right coronary artery

and even small calcium deposits are detected with high sensitivity (Fig. 7.20). Synchronization of the image acquisition (prospective ECG triggering) or image reconstruction (retrospective ECG gating) with cardiac motion is mandatory to scan the heart at reproducible positions in order to avoid gaps or overlaps, which would result in image mis-registration, as detailed in previous chapters.

7.2.3.1 Sequential Scanning with Prospective ECG Triggering

Calcium scanning has been carried out using prospective ECG triggering and scanning in a sequential mode in most clinical and research approaches. As long as the heart rate and rhythm remain constant, a prospective estimation of the duration of the next RR-interval will reliably position the scan in mid- to late diastole. In patients with varying heart rate or with arrhythmia, motion artifacts can impose a major problem for reliable calcium quantification (Mao 1996). While common scan windows for calcium scoring with EBCT are at 80% or 40% of the RR-interval, 50–60% of the RR-interval seems to be more appropriate with the current-generation multi-slice CT scanners in order to avoid motion artifacts. With prospectively ECG-triggered scanning, the section thickness depends on the detector design. Most 4-slice systems will acquire 2.5-mm sections instead of the established 3-mm section thickness. Other potential disadvantages of sequential scanning with multi-slice CT are discussed below.

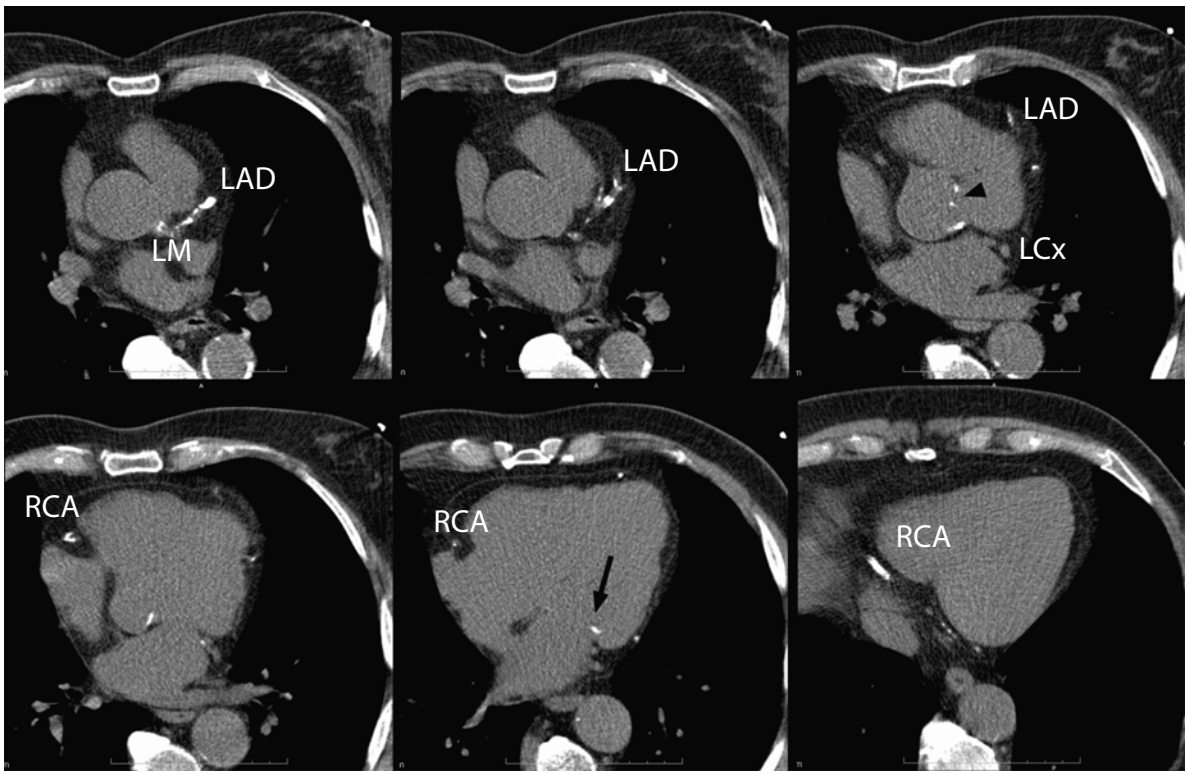

Fig. 7.20. 4-slice CT showing massive calcifications of all major coronary arteries in an asymptomatic person with increased cardiovascular disease risk. Note the aortic valve (*top, arrowhead*) and mitral valve (*bottom, arrow*) calcification. *LM* Left main coronary artery

7.2.3.2 Spiral Scanning with Retrospective ECG Gating

Spiral image acquisition has several advantages over sequential scanning. First, the continuous data acquisition speeds up the scanning process, which allows for the use of thinner section thickness to improve spatial resolution. Although it can be shown that a section thickness less than the traditionally used 3 mm can improve measurement accuracy, it is unclear whether clinical decision-making will be influenced by the improved spatial resolution. Moreover, the ability to reconstruct overlapping images without increasing scan time or radiation exposure to the patient seems more important than increased spatial resolution. Overlapping image reconstruction will improve the sensitivity for detecting small calcifications due to decreased partial-volume averaging and it has been shown to improve measurement reproducibility in repeat examinations, especially in patients with low plaque burden (Ohnesorge 2002, Moser 2004). Second, image reconstruction in ECG-gated spiral scanning can make use of multi-segment image reconstruction algorithms, as described in earlier chapters. Multi-segment reconstruction improves temporal resolution, a well-recognized factor in image quality. Retrospective ECG gating furthermore assures optimal agreement with the desired phase of the cardiac cycle and allows for retrospective optimization of the image reconstruction window should motion artifacts occur. Individual selection of the specific reconstruction window with the least amount of motion effects has resulted in the most reproducible scoring results (Fallenberg 2003). Overall, spiral multi-slice CT is more stable in terms of image quality and measurement reproducibility than competing sequential scanning techniques (Kopp 2002).

7.2.3.3 Radiation Exposure

With prospective triggering, the effective dose is approximately 1 mSv, which is similar to that of EBCT (McCollough 2003). Multi-slice CT with constant tube output during spiral scanning will more than double the radiation exposure, since radiation is emitted even in phases of the cardiac cycle that are not used for image reconstruction. ECG controlled tube output modulation can achieve a mean dose reduction of 48% for males and 45% for females (see previous chapters). Considering the advantages of spiral scanning regarding sensitivity, speed, and reproducibility of calcium measurements, a slightly higher effective dose for spiral data acquisition should be acceptable.

7.2.4 Clinical Applications of Coronary Calcium Measurement

7.2.4.1 Coronary Heart Disease and Risk Assessment

Coronary heart disease (CHD) remains the major cause of mortality and morbidity in the industrialized nations and accounts for 54% of all cardiovascular deaths and 22% of all deaths in the United States (American Heart Association 2002). Although the mortality rate from CHD declined by 25% from 1990 to 2000, the absolute number of deaths decreased only 7.6%. Sudden coronary death or nonfatal myocardial infarction is the first manifestation of disease in up to 50% of CHD victims and approximately 50% of patients with acute myocardial infarction die within the first month of the event. CHD typically manifests in middle-aged and older, predominantly male individuals. In the Framingham Heart Study, the lifetime risk of CHD for individuals at age 40 who were initially free of CHD was 49% in men and 32% in women (Lloyd-Jones 1999). Accordingly, it becomes clear that prevention of ischemic heart disease is the most efficient approach to reducing morbidity and mortality associated with cardiovascular disease. There is growing evidence that cholesterol-lowering drugs and anti-platelet drugs will reduce the risk for new-onset CHD in otherwise asymptomatic persons. Thus, the rationale for early detection of persons who are at high risk of developing a future coronary event is that detection during the subclinical stages of disease might permit the reliable identification of individuals at increased risk of an acute myocardial event and that those at high risk could potentially benefit from early preventive efforts.

Current guidelines stress clinical risk assessment as the key to the selection of persons for medical primary prevention. The presence and expression of a single cardiovascular risk factor is not a good predictor of a future coronary event, since risk factors interact in a complex way, making a simple risk assessment in the individual patient complicated. Well-recognized risk factors are tobacco smoking, high LDL cholesterol levels, low HDL cholesterol, diabetes mellitus, arterial hypertension, and a family history of premature myocardial infarction. Algorithms or scoring systems derived from large prospective epidemiological studies, such as the Framingham Study in the United States and the Prospective Cardiovascular Münster Study (PROCAM) in Europe, can be used to calculate a person's CHD risk (Assmann 2002, Wilson 1998). Risk calculation tables for the Framingham risk index and the PROCAM score are listed in Tables 7.2 and 7.3.

Risk-factor assessment is the established initial approach to identify populations at risk, as it is a way to evaluate the statistical probability that coronary atherosclerosis has developed. Despite the demonstrated efficacy of risk assessment in predicting future coronary events in a population, identification of the individual at risk remains unsatisfactory, mainly due to the wide variability of atherosclerosis manifestations in populations with identical risk-factor exposure. Coronary calcium scanning, in contrast, allows for direct visualization of calcified coronary plaque.

Although CAC is found more frequently in advanced atherosclerotic lesions, it is frequently present long before clinical manifestation of CAD and has been detected as early as the second decade of life. The process of calcium accumulation in atherosclerotic lesions seems to be actively regulated and involves mechanisms similar to those of bone formation and resorption (Wexler 1996). It is a matter of debate whether calcification of a plaque is a sign of stability or instability. Histomorphologic studies reveal that plaques with healed ruptures and fibroatheromas frequently are calcified whereas acute plaque ruptures show lesser amounts of calcium and plaque erosions usually do not show calcifications (Burke 2000, Burke 2001). Since the extent of CAC reflects the total plaque burden (Rumberger 1995, Schmermund 1999), the amount of calcified plaque may indicate the likelihood of the presence of potentially vulnerable lesions.

CAC is a surrogate marker for coronary atherosclerotic plaque, so that the coronary calcium score (CCS) reflects the life-long exposure of the arterial wall to a variety of risk factors and an individual's response to such risk-factor exposure. In short, calcium scanning can identify the individual in whom risk-factor exposure has led to the development of CAD. Assessment of coronary plaque burden may therefore provide a more accurate estimate of an individual's CHD risk.

7.2.4.2 Patient Selection for Risk Assessment

Most patients with established CHD have a 10-year risk for major coronary events (myocardial infarction and coronary death) greater than 20%. International expert guidelines recommend initiating treatment of hypertension and hypercholesterolemia in asymptomatic patients whose global 10-year risk for a coronary event exceeds 20%. As a consequence, it is questionable whether imaging studies to further stratify these high-risk individuals is of clinical value. Since one-third of all coronary events occur in persons at intermediate risk (10-year risk of 10–20%), there is considerable need to improve the sensitivity and specificity of risk prediction in this group (Schmermund 2001, Taylor 2000). For these reasons, the identification of persons at "intermediate risk" has become a clinically important challenge.

This implies that CAC quantification should be used primarily in patients who have already undergone clinical risk assessment. In individuals at intermediate risk for a coronary event, elevated calcium scores may indicate a higher risk category; conversely, a low or absent calcium score may establish a lower risk (Elkeles 2002, Greenland 2004). Clear definitions regarding which asymptomatic individuals will benefit from calcium scanning have not been provided. Therefore, the indication for calcium scoring should be based on referral from a qualified physician.

Table 7.2. Framingham point system for men (from: Adult Treatment Panel III at www.nhlbi.nih.gov/)

Risk factor	Points				
Age range	20–39	40–49	50–59	60–69	70–79
Smoking					
Nonsmoker	0	0	0	0	0
Smoker	8	5	3	1	1
Total cholesterol (mg/dl)					
< 160	0	0	0	0	0
160–199	4	3	2	1	0
200–239	7	5	3	1	0
240–279	9	6	4	2	1
≥ 280	11	8	5	3	1

Risk factor	Points	
HDL (mg/dl)		
< 40	2	
40–49	1	
50–59	0	
≥ 60	-1	
Systolic blood pressure (mmHg)	Untreated	Treated
< 120	0	0
120–129	0	1
130–139	1	2
140–159	1	2
≥ 160	2	3

10-year risk of event (%) dependent on total risk points														
Total points	<0	0–4	5–6	7	8	9	10	11	12	13	14	15	16	≥17
10-year risk (%)	<1	1	2	3	4	5	6	8	10	12	16	20	25	≥30

Table 7.3. PROCAM point system for men (from Assmann 2002)

Risk factor	Points
Age	
35–39	0
40–44	6
45–49	11
50–54	16
55–54	21
60–65	26
LDL cholesterol (mg/dl)	
< 100	0
100–129	5
130–159	10
160–189	14
≥ 190	20

Risk factor	Points
HDL cholesterol (mg/dl)	
< 35	11
35–44	8
45–54	5
≥ 55	0
Triglycerides (mg/dl)	
< 100	0
100–149	2
150–199	3
≥ 200	4
Smoking	
Nonsmoker	0
Smoker	8

Risk factor	Points
Diabetes mellitus	
No	0
Yes	6
Myocardial infarction in family history	
No	0
Yes	4
Systolic blood pressure (mmHg)	
120	0
120–129	2
130–139	3
140–159	5
160	8

10-year risk of event (%) dependent on total risk points														
Total points	≤20	20	28	32	35	38	40	43	45	48	51	54	57	≥60
10-year risk (%)	≤1	1	1.9	2.9	4.0	5.1	61	8.0	10.2	12.8	16.8	21.7	25.1	≥30

7.2.4.3 Coronary Artery Calcification and CHD Risk

A number of prospective studies have addressed the prognostic value of coronary calcium scanning of asymptomatic individuals in order to better predict the likelihood of coronary events. All of these studies found substantial increases in relative risk of a cardiovascular event in the presence of increased coronary calcium scores. Arad et al. reported an odds ratio of 22 for the prediction of myocardial infarction or death in 1173 self-referred men and women, when comparing event rates in the group with calcium scores > 160 versus those among subjects with scores < 160 (Arad 2000). Raggi et al. reported an odds ratio of 21.5 for suffering an acute myocardial infarction or cardiovascular death in subjects with a calcium score above the 75th percentile for age and gender when compared to individuals with a calcium score in the first quartile (Raggi 2000). In a study of 926 subjects who were either referred because of risk factors or self-referred, the highest calcium score quartile was associated with a relative risk of cardiovascular events of 7.8 compared to subjects without coronary calcification (Wong 2000). The calcium score and serum C-reactive protein (CRP) level may contribute independently to risk stratification for cardiovascular events. In 1461 patients without manifest CHD, the relative risk for individuals with the highest CRP and calcium scores was 7.5-fold greater than for those with the lowest respective values (Park 2002).

In a study of over 10,000 asymptomatic individuals who underwent cardiac risk-factor analysis and CCS, the calcium score was a significant independent predictor of mortality and it supplemented the prognostic information provided by risk-factor analysis (Shaw 2003).

7.2.4.4 Interpretation of Calcium Scoring Results

Empirical guidelines in the clinical interpretation of calcium scans in asymptomatic but at risk individuals have been suggested (Rumberger 1999). Calcium scores are divided into several categories (0–10, 11–100, 101–400, >401) in order to provide treatment recommendations and estimate CHD risk (Table 7.4). Since a high calcium score indicates a significant plaque burden, absolute values will provide a certain orientation when assessing a calcium scan, e.g., calcium scores > 100 are highly consistent with CAD and should lead to modification of risk factors. Very high calcium scores are associated with an exceedingly high risk of coronary events (Wayhs 2002). It has to be kept in mind, however, that age and gender are important determinants of the presence and extent of CAC. In addition, the prevalence of CAC increases with age and shows significant differences between men and women. As reported in a study of over 35,000 asymptomatic males and females (Hoff 2001), the median calcium score for men was 1 in individuals 40–44 years of age and 309 for individuals 70–74 years of age, while the corresponding values for women were 0 and 53 (Tables 7.5–7.7). These data stress the difficulties encountered when using absolute scores in an individual to estimate CHD risk or to make treatment recommendations. For example, a calcium score of 80 is well within the expected norm for a 64-year-old male, but suggests advanced atherosclerosis in a 44-year-old male (Table 7.6). The absolute calcium score should therefore be put into perspective with the expected norm. If the calcium score is above the 75th percentile or the median for age and gender, increased cardiovascular risk has to be assumed.

7.2.5 Further Clinical Applications of Calcium Scanning

7.2.5.1 Coronary Artery Calcification and Differential Diagnosis of Chest Pain

A positive coronary calcium scan has a low predictive value for identifying stenoses but a concomitant high negative predictive value for ruling out obstructive CAD in the absence of detectable calcifications. A negative predictive value close to 100% has been reported for coronary chest pain or myocardial infarction in subjects with acute symptoms and nonspecific ECG (Georgiou 2001, McLaughlin 1999). Knowledge of the presence or absence

Table 7.4. Guidelines for coronary calcium score interpretation (from Rumberger 1999)

Agatston score	Atherosclerotic plaque burden	Probability of significant coronary artery disease	Implications for cardiovascular risk	Recommendations
0	No plaque	Very unlikely, < 5%	Very low	Reassure patient; discuss general guidelines for primary prevention of CV diseases
1–10	Minimal	Very unlikely, < 10%	Low	Discuss general guidelines for primary prevention of CV diseases
11–100	Mild	Mild or minimal coronary stenoses likely	Moderate	Counsel about risk factor modification, strict adherence with primary prevention goals; daily aspirin administration
101–400	Moderate	Non-obstructive CAD highly likely; obstructive disease possible	Moderately high	Institute risk factor modification and secondary prevention goals; consider exercise testing; daily aspirin administration
> 400	Extensive	High likelihood (> 90%) of at least one significant coronary stenosis	High	Institute very aggressive risk factor modification; consider exercise or pharmacologic nuclear stress testing; daily aspirin administration

of coronary calcification may thus be helpful in making decisions regarding diagnostic or therapeutic measures.

7.2.5.2 Coronary Artery Calcification and Disease Progression

Several studies have tracked changes in coronary calcium. Score progression seems to be accelerated in patients with obstructive CAD compared with patients who have no clinically manifest disease (27% vs. 18%) (Janowitz 1991). A mean annual rate of calcium score increase for untreated patients of 24–36% has been found. Recent studies have shown the ability of calcium quantification to monitor the progression of coronary calcification and to document the effect of risk-factor modification and medical treatment (Achenbach 2002, Budoff 2000, Maher 1999). In 66 patients with coronary calcifications, the observed increase in coronary calcium volume score was 25% without treatment; it decreased to 8.8% under treatment with statins (Achenbach 2002). Progression of coronary artery calcium scores has substantial variability in patients with similar risk factors under treatment. Recent data suggest that subjects with increased progression of coronary calcium are at higher risk of sustaining a coronary event than subjects with slower progression rates (Raggi 2004). Since different progression rates might reflect differences in treatment response, monitoring of calcium score progression by CT could influence treatment modification.

Table 7.5. Coronary artery calcium scores in 35,246 asymptomatic men and women (from Hoff 2001)

	Total calcium score			
	Men		Women	
Age	Mean	Median	Mean	Median
< 40	12 ± 70	0.5	2 ± 14	0
40–44	27 ± 27	1	8 ± 97	0
45–49	57 ± 175	3	18 ± 186	0
50–54	121 ± 305	16	29 ± 135	0.5
55–59	203 ± 411	49	54 ± 189	1
60–64	350 ± 972	113	78 ± 250	3
65–69	464 ± 731	180	147 ± 338	24
70–74	665 ± 921	309	225 ± 515	53
> 74	836 ± 1053	473	258 ± 507	75

Table 7.6. Coronary artery calcium score percentiles for asymptomatic men (from Hoff 2001)

	Total calcium score			
Age	25th	50th	75th	90th
< 40	0	1	3	14
40–44	0	1	9	59
45–49	0	3	36	154
50–54	1	15	103	332
55–59	4	48	215	554
60–64	13	113	410	994
65–69	32	180	566	1299
70–74	64	310	892	1774
> 74	166	473	1071	1982

Table 7.7. Coronary artery calcium score percentiles for asymptomatic women (from Hoff 2001)

	Total calcium score			
Age	25th	50th	75th	90th
< 40	0	0	1	3
40–44	0	0	1	4
45–49	0	0	2	22
50–54	0	0	5	55
55–59	0	1	23	121
60–64	0	3	57	193
65–69	1	24	145	410
70–74	3	52	210	631
> 74	9	75	241	709

7.2.6 Conclusion

Atherogenesis is a dynamic process that represents the result of a life-long exposure of an individual to a variety of predisposing factors. Coronary plaque burden is a good predictor of future coronary events and coronary artery calcium reflects total plaque burden. The CCS can thus be of value in risk stratification of asymptomatic persons with moderate to increased coronary risk. However, long-term epidemiological studies are still needed to determine which patient populations could benefit from a calcium score examination in terms of risk stratification and risk-factor management. Currently, the data indicate that asymptomatic individuals at intermediate coronary risk (10-year risk 10–20%) in whom clinical decision-making is most uncertain may become the most important target population.

From the technological point of view, multi-slice CT scanning, especially using spiral technique with overlapping slice reconstruction and calcium quan-

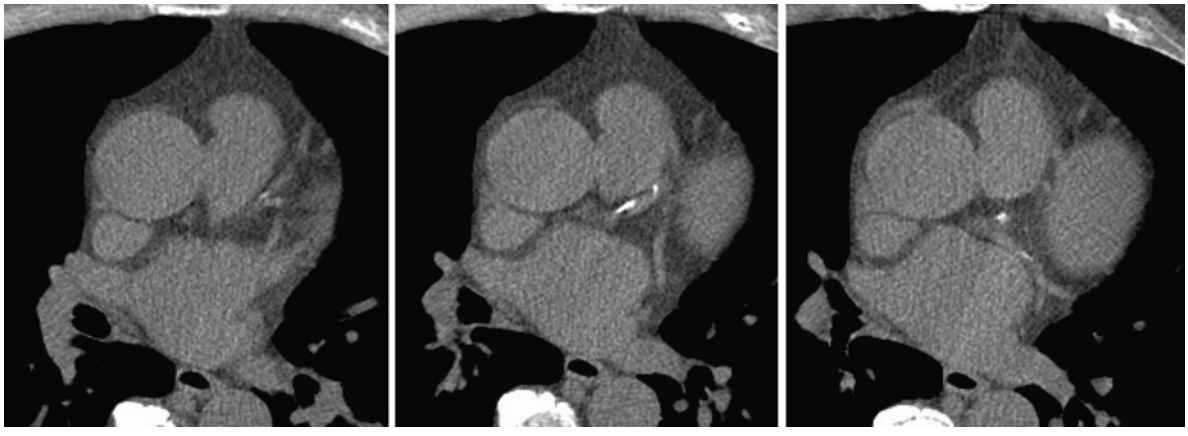

Fig. 7.21. Coronary calcium measurement in a patient with moderate calcifications who had a heart rate of 105 bpm during the scan. Data were acquired on a 64-slice CT scanner with 0.33-s rotation time. 3-mm slices were reconstructed with 1.5-mm image increment based on the acquisition of 64×0.6-mm slices per rotation and retrospective ECG gating. Despite the high heart rate, all calcifications are displayed accurately without motion artifact. (Case courtesy of Stanford University, USA)

tification based on calibrated calcium mass measurement, holds promise to become the reference approach of the future. Already, 4-slice CT scanners with 0.5-s rotation have demonstrated satisfactory accuracy of coronary artery calcium measurement in clinical practice. Due to higher spatial and temporal resolution, modern 16- and 64-slice CT scanners may further increase the sensitivity and reproducibility for detecting smaller amounts of calcium (Fig. 7.21).

References

Achenbach S, Ropers D, Pohle K, Leber A, Thilo C, Knez A, Menendez T, Maeffert R, Kusus M, Regenfus M, Bickel A, Haberl R, Steinbeck G, Moshage W, Daniel WG (2002). Influence of lipid-lowering therapy on the progression of coronary artery calcification: a prospective evaluation. Circulation 106:1077–1082

Agatston A, Janowitz W, Hildner F, Zusmer N, Viamonte M, Detrano R (1990). Quantification of coronary artery calcium using ultrafast computed tomography. J Am Coll Cardiol 15:827–832

American Heart Association (2002). Heart Disease and Stroke Statistics - 2003 Update. Dallas, Tex: American Heart Association

Arad Y, Spadaro LA, Goodman K, Newstein D, Guerci AD (2000). Prediction of coronary events with electron beam computed tomography. J Am Coll Cardiol 36:1253–1260

Assmann G, Cullen P, Schulte H (2002). Simple scoring scheme for calculating the risk of acute coronary events based on the 10-year follow-up of the prospective cardiovascular Munster (PROCAM) study. Circulation 105:310–315

Baumgart D, Schmermund A, Goerge G, Haude M, Ge J, Adamzik M, Sehnert C, Altmaier K, Groenemeyer D, Seibel R, Erbel R (1997). Comparison of electron beam computed tomography with intracoronary ultrasound and coronary angiography for detection of coronary atherosclerosis. J Am Coll Cardiol 30:57–64

Becker CR, Kleffel T, Crispin A, Knez A, Young J, Schoepf UJ, Haberl R, Reiser MF (2001). Coronary artery calcium measurement: agreement of multirow detector and electron beam CT. AJR Am J Roentgenol 176:1295–1298

Budoff M, Lane K, Bakhsheshi H, Mao S, Grassman B, Friedman B, Brundage B (2000). Rates of progression of coronary calcium by electron beam tomography. Am J Cardiol 86:8–11

Burke AP, Taylor A, Farb A, Malcom GT, Virmani R (2000). Coronary calcification: insights from sudden coronary death victims. Z Kardiol 89 Suppl 2:49–53

Burke AP, Weber DK, Kolodgie FD, Farb A, Taylor AJ, Virmani R (2001). Pathophysiology of calcium deposition in coronary arteries. Herz 26:239–244

Callister TQ, Cooil B, Raya SP, Lippolis NJ, Russo DJ, Raggi P (1998). Coronary artery disease: improved reproducibility of calcium scoring with an electron-beam CT volumetric method. Radiology 208:807–814

Elkeles RS, Dunlop A, Thompson GR, Neuwirth C, Gibson K, Rubens MB, Underwood SR (2002). Coronary calcification and predicted risk of coronary heart disease in asymptomatic men with hypercholesterolaemia. J Cardiovasc Risk 9:349–353

Fallenberg E, Juergens K, Maintz D, Grude M, Fischbach R, Heindel W (2003). Multidetector-row spiral CT for coronary artery calcium quantification: impact of reconstruction window on reproducibility and image quality (Abstract). Radiology 229(P), RSNA Abstract Book: 631

Ferencik M, Ferullo A, Achenbach S, Abbara S, Chan RC, Booth SL, Brady TJ, Hoffmann U (2003). Coronary calcium quantification using various calibration phantoms and scoring thresholds. Invest Radiol 38:559–566

Georgiou D, Budoff MJ, Kaufer E, Kennedy JM, Lu B, Brundage BH (2001). Screening patients with chest pain in the emergency department using electron beam tomography: a follow-up study. J Am Coll Cardiol 38:105–110

Greenland P, LaBree L, Azen SP, Doherty TM, Detrano RC (2004). Coronary artery calcium score combined with Framingham score for risk prediction in asymptomatic individuals. JAMA 291:210–215

Haliburton SS, Sell J, McCollough CH, Ulzheimer S, Kalender WA, White RD (2003). A Web-based multi-vendor, multi-institutional database of standardized coronary calcium measurements using cardiac CT (Abstract). Radiology 229(P), RSNA Abstract Book: 812

Hoff JA, Chomka EV, Krainik AJ, Daviglus M, Rich S, Kondos GT (2001). Age and gender distributions of coronary artery calcium detected by electron beam tomography in 35,246 adults. Am J Cardiol 87:1335–1339

Hong C, Becker CR, Schoepf UJ, Ohnesorge B, Bruening R, Reiser MF (2002). Coronary artery calcium: absolute quantification in nonenhanced and contrast-enhanced multi-detector row CT studies. Radiology 223:474–480

Hong C, Bae KT, Pilgram TK (2003). Coronary artery calcium: accuracy and reproducibility of measurements with multi-detector row CT–assessment of effects of different thresholds and quantification methods. Radiology 227:795–801

Janowitz WR, Agatston AS, Viamonte M, Jr (1991). Comparison of serial quantitative evaluation of calcified coronary artery plaque by ultrafast computed tomography in persons with and without obstructive coronary artery disease. Am J Cardiol 68:1–6

Kajinami K, Seki H, Takekoshi N, Mabuchi H (1997). Coronary calcification and coronary atherosclerosis: site by site comparative morphologic study of electron beam computed tomography and coronary angiography. J Am Coll Cardiol 29:1549–1556

Kopp AF, Ohnesorge B, Becker C, Schroder S, Heuschmid M, Kuttner A, Kuzo R, Claussen CD (2002). Reproducibility and accuracy of coronary calcium measurements with multi-detector row versus electron-beam CT. Radiology 225:113–119

Lloyd-Jones DM, Larson MG, Beiser A, Levy D (1999). Lifetime risk of developing coronary heart disease. Lancet 353:89–92

Maher JE, Bielak LF, Raz JA, Sheedy PF, 2nd, Schwartz RS, Peyser PA (1999). Progression of coronary artery calcification: a pilot study. Mayo Clin Proc 74:347–355

Mao SS, Oudiz RJ, Bakhsheshi H, Wang SJ, Brundage BH (1996). Variation of heart rate and electrocardiograph trigger interval during ultrafast computed tomography. Am J Card Imaging 10:239–243

McCollough C, Kaufmann R, Cameron B, Katz D, Sheedy P, Peyser P (1995). Electron beam CT: use of a calibration phantom to reduce variability in calcium quantification. Radiology 196:159–165

McCollough C (2003). Patient dose in cardiac computed tomography. Herz 28:1–6

McLaughlin VV, Balogh T, Rich S (1999). Utility of electron beam computed tomography to stratify patients presenting to the emergency room with chest pain. Am J Cardiol 84:327–328, A328

Moser KW, Bateman TM, O'Keefe JH, Jr., McGhie AI (2004). Interscan variability of coronary artery calcium quantification using an electrocardiographically pulsed spiral computed tomographic protocol. Am J Cardiol 93:1153–1155

Ohnesorge B, Flohr T, Fischbach R, Kopp AF, Knez A, Schroder S, Schopf UJ, Crispin A, Klotz E, Reiser MF, Becker CR (2002). Reproducibility of coronary calcium quantification in repeat examinations with retrospectively ECG-gated multisection spiral CT. Eur Radiol 12:1532–1540

Park R, Detrano R, Xiang M, Fu P, Ibrahim Y, LaBree L, Azen S (2002). Combined use of computed tomography coronary calcium scores and C-reactive protein levels in predicting cardiovascular events in nondiabetic individuals. Circulation 106:2073–2077

Raggi P, Callister TQ, Cooil B, He ZX, Lippolis NJ, Russo DJ, Zelinger A, Mahmarian JJ (2000). Identification of patients at increased risk of first unheralded acute myocardial infarction by electron-beam computed tomography. Circulation 101:850–855

Raggi P, Callister TQ, Shaw LJ (2004). Progression of coronary artery calcium and risk of first myocardial infarction in patients receiving cholesterol-lowering therapy. Arterioscler Thromb Vasc Biol 24:1272–1277

Rumberger JA, Simons DB, Fitzpatrick LA, Sheedy PF, Schwartz RS (1995). Coronary artery calcium area by electron-beam computed tomography and coronary atherosclerotic plaque area. A histopathologic correlative study. Circulation 92:2157–2162

Rumberger JA, Brundage BH, Rader DJ, Kondos G (1999). Electron beam computed tomographic coronary calcium scanning: a review and guidelines for use in asymptomatic persons. Mayo Clin Proc 74:243–252

Schmermund A, Denktas AE, Rumberger JA, Christian TF, Sheedy PF, 2nd, Bailey KR, Schwartz RS (1999). Independent and incremental value of coronary artery calcium for predicting the extent of angiographic coronary artery disease: comparison with cardiac risk factors and radionuclide perfusion imaging. J Am Coll Cardiol 34:777–786

Schmermund A, Erbel R (2001). New concepts of primary prevention require rethinking. Med Klin 96:261–269

Shaw LJ, Raggi P, Schisterman E, Berman DS, Callister TQ (2003). Prognostic value of cardiac risk factors and coronary artery calcium screening for all-cause mortality. Radiology 228:826–833

Stanford W, Thompson BH, Burns TL, Heery SD, Burr MC (2004). Coronary artery calcium quantification at multidetector row helical CT versus electron-beam CT. Radiology 230:397–402

Taylor AJ, Burke AP, O'Malley PG, Farb A, Malcom GT, Smialek J, Virmani R (2000). A comparison of the Framingham risk index, coronary artery calcification, and culprit plaque morphology in sudden cardiac death. Circulation 101:1243–1248

Ulzheimer S, Kalender WA (2003). Assessment of calcium scoring performance in cardiac computed tomography. Eur Radiol 13:484–497

Ulzheimer S, Shanneik K, McCollough CH, Halliburton SS, Kalender WA (2003). Advantages of using calcium mass in combination with a calcium density threshold for the quantification of coronary calcium (abstract). Radiology 229(P), RSNA Abstract Book: 428

Wayhs R, Zelinger A, Raggi P (2002). High coronary artery calcium scores pose an extremely elevated risk for hard events. J Am Coll Cardiol 39:225–230

Wexler L, Brundage B, Crouse J, Detrano R, Fuster V, Maddahi J, Rumberger J, Stanford W, White R, Taubert K (1996). Coronary artery calcification: pathophysiology, epidemiology, imaging methods, and clinical implications. A statement for health professionals from the American Heart Association. Circulation 94:1175–1192

Wilson PW, D'Agostino RB, Levy D, Belanger AM, Silbershatz H, Kannel WB (1998). Prediction of coronary heart disease using risk factor categories. Circulation 97:1837–1847

Wong ND, Hsu JC, Detrano RC, Diamond G, Eisenberg H, Gardin JM (2000). Coronary artery calcium evaluation by electron beam computed tomography and its relation to new cardiovascular events. Am J Cardiol 86:495–498

7.3 Detection and Exclusion of Coronary Artery Stenosis

K. Nieman, N. Mollet, F. Cademartiri, P. De Feyter

Contents

7.3.1 Introduction 205
7.3.2 Diagnostic Performance of 4-Slice CT 205
7.3.3 Diagnostic Performance of 16-Slice CT 206
7.3.4 Diagnostic Performance of 64-Slice CT 207
7.3.5 Image Processing and Analysis 208
7.3.6 Discussion 208
References 212

7.3.1 Introduction

Conventional coronary angiography is and will most likely remain the standard of reference for the detection of coronary stenosis, but with the expansion of therapeutic options there is also an increasing demand for less invasive coronary angiography. Multi-slice spiral CT is one, and arguably the most efficient, imaging modality for non-invasive assessment of the luminal integrity of the coronary arteries. While mechanical CT was long regarded as too slow to image moving organs, current state-of-the-art multi-slice spiral CT scanners offer a temporal resolution of less than 200 ms, a sub-millimeter isotropic resolution, and a total scan time of less than 20 s. Comparative studies suggest that the current diagnostic accuracy of spiral CT angiography warrants further clinical evaluation.

7.3.2 Diagnostic Performance of 4-Slice CT

Four-slice spiral CT scanners were the first generation of mechanical CT scanners to allow nearly motion-free imaging of the heart, with sufficient spatial resolution to visualize the small coronary arteries and enough detector rows to cover the entire heart within the time of a long breath-hold.

Between 2001 and 2002, a number of studies that compared 4-slice CT with conventional coronary angiography were published (Table 7.8). Despite the varying patient characteristics and methods of evaluation, these studies showed that detection of coronary stenoses by multi-slice CT was certainly feasible. As for adequate image quality, multi-slice CT detected significant coronary obstruction in the main branches and larger side branches with a sensitivity and specificity that varied between 75 and 95%, and 76 and 99%, respectively.

The number of vessels with an image quality that was considered adequate for assessment varied between 6 and 32%, which represented the main limitation of the technique at the time. Reported causes for non-assessability included motion artifacts, calcified plaque material, respiratory motion, advanced venous contrast enhancement, technical scanner failure, and arrhythmia. In a number of patients, the scan duration of up to 40 s was too long to maintain in a breath-holding position. A number of studies reported an overall sensitivity, which considers lesions in non-evaluable vessels as false-negative scores, that varied between 49 and 93% (Nieman 2001, Achenbach 2001, Knez 2001, Kopp 2002, Nieman 2002b,c, Giesler 2002).

While interpretability and diagnostic accuracy seem related to the diameter and proximity of the coronary segment, the right coronary artery appears to be more difficult to assess, which is related to the more extended motion radius and short interval of relative motionless of the vessel (Nieman 2002b, Wang 2001). In two studies, the diagnostic accuracy of multi-slice CT in relation to the patient's heart rate was evaluated. Giesler et al. divided 100 patients into four groups according to their heart rate during the scan. In patients with a heart rate of ≤60, 61–70, 71–80 min, and >80 bpm, motion artifacts were found in 8, 18, 41, and 22% of the coronary arteries, respectively (Giesler 2002). The overall sensitivity to detect a stenosis >70% of the arterial diameter was 67, 55, 35, and 22%, for each group, respectively. In a study by Nieman et al. 78 patients were equally divided into three groups according to their average heart rate (Nieman 2002b). In the low- (56±4 bpm),

Table 7.8. Diagnostic performance of 4- and 16-slice MSCT in the detection of coronary stenosis, with conventional angiography as the standard of reference

	β	N	Assess.	SD (%)	Excl (%)	Sens (%)	Spec (%)	PPV (%)	NPV (%)	Sens[a] (%)
4-slice										
Nieman 2001	–	31	Segment	50	27	81	97	81	97	68
Achenbach 2001	–	64	Branch	50	32	85	76	56	93	55
				70	32	91	84	59	98	58
Knez 2000	–	43	Segment	50	6	78	98	84	96	51
Vogl 2001	+	64	Segment	50	28	75	99	92	98	NR
Kopp 2002[a]	–	102	Segment	50	15	86	96	76	98	86
						93	97	81	99	93
Giesler 2002[b]	+	100	Branch	70	29	91	89	66	98	49
Nieman 2002b[a]	–	78	Segment	50	32	84	95	67	98	63
16-slice										
Nieman 2002c	+	58	Branch	50	0	95	86	80	97	95
Ropers 2003	+	77	Branch	50	12	92	93	79	97	73
64-slice										
Leschka 2005	–	67	Segment	50	0	94	97	87	99	94
Raff 2005	+	70	Segment	50	12	86	95	66	98	NR
			Branch	50		91	92	80	97	NR
			Patient	50		95	90	93	93	NR

Abbreviations: β β-Blocking pre-medication, *Assess.* branch- or coronary segment-based method of assessment, *SD* diameter reduction regarded as significant stenosis, *Excl* percentage of excluded segments/branches, *Sens* sensitivity, *Spec* specificity, *PPV,* NPV positive and negative predictive value after exclusion of non-assessable segments/branches, *Sens*[a] sensitivity including missed lesions in non-assessable segments/branches, *NR* not reported.
[a]Results by two observers, without consensus reading.
[b]Studies include patients from earlier publications.

intermediate- (67±3 bpm), and high-heart-rate group (82±9 bpm), 78, 73, and 54%, respectively of the segments were assessable, resulting in an overall sensitivity to detect luminal stenosis >50% of 82, 61, and 32%, respectively. The accuracy of multi-slice CT to classify patients as having no, single-, or multi-vessel disease, without exclusion of non-assessable segment, was 73, 54, and 42%, for each respective group.

7.3.3 Diagnostic Performance of 16-Slice CT

To compensate for the limitations encountered with 4-slice CT, the next generation of multi-slice CT scanners acquired up to 16 slices per rotation and were equipped with thinner detector rows to increase the spatial resolution and further shorten the total scan time. The faster gantry rotation reduced motion artifacts, although most investigators by then had incorporated β-receptor-blocking pre-medication in their scan protocol.

Two representative studies compared the performance of 16-slice CT with conventional coronary angiography (Table 7.8). Nieman et al. examined 58 patients with a (pre-medicated) heart rate of 57 bpm, and evaluated all coronary vessels with a minimal diameter of 2.0 mm (Nieman 2002c). Although 7% of the vessels contained poorly assessable sections, no vessels were excluded from the analysis, and 82/86 (95%) of the lesions were detected. The high sensi-

tivity, with all missed lesions in the left circumflex branch, came at the expense of a slightly lower specificity of 86%. In seven cases multi-slice CT revealed a significant stenosis but overestimated the degree of stenosis. As determined by quantitative coronary angiography, these overestimated coronary arteries contained mild stenoses, i.e., vessel diameter reduction between 40 and 49%. In 78% of the patients, a correct overall classification as having no, single- or multi-vessel disease could be given. Using 4-slice CT, the same investigators provided a correct classification in only 56% of the patients (Nieman 2002b). Ropers et al. evaluated 77 patients with a (pre-medicated) heart rate of 62 bpm, and evaluated all vessels with a diameter of more then 1.5 mm (Ropers 2003). After exclusion of 12% of the vessels, which were considered non-interpretable, significant stenoses were detected with a sensitivity and specificity of 92 and 93%. By regarding the missed lesions as false-negative interpretations, the overall sensitivity was 73%.

With the general availability of 16-slice CT scanners, more clinical studies have become available that provide important data concerning patient selection criteria. Hoffmann et al. demonstrated the limited value of 16-slice CT in the diagnosis of coronary stenosis in patients with a high likelihood of coronary artery disease (Hoffmann U 2004). The high prevalence of massive calcifications was one of the main reasons for the compromised sensitivity in the detection of high-grade stenosis. For better performance of 16-slice CT in patients with a high prevalence of coronary artery calcification, Kuettner et al. proposed obtaining a non-contrast pre-scan to determine the amount of calcification before administration of contrast agent (Kuettner 2004b). In that study, high sensitivity and specificity in the detection of high-grade coronary stenosis was demonstrated in patients with an Agatston score less than 1000 and calcium mass less than 250 mg. Mollet et al. suggested expanding the clinical spectrum of multi-slice coronary CTA to patients with stable angina and stable sinus rhythm (Mollet 2004). The compromised diagnostic accuracy in the presence of coronary calcification and motion artifacts remain the main limitations of 16-slice coronary CTA. Increasing temporal resolution with faster rotation time down to 370 ms reduced the presence of motion artifacts and increased diagnostic accuracy also in patients with higher heart rates (Kuettner 2005, Mollet 2005). Initial promising results were also achieved in the evaluation of coronary stenosis and the progression of coronary artery disease in patients after heart transplant, who usually present with high heart rates (Romeo 2005). Later studies carried out with 16-slice CT scanners from various manufacturers confirmed both the findings and the limitations that were demonstrated in the initial studies (Martuscelli 2004, Hoffmann M 2005).

7.3.4 Diagnostic Performance of 64-Slice CT

While 16-slice CT scanners can provide sufficiently short breath-hold times for multi-slice coronary CTA in most patients, further increased temporal and spatial resolution is still desirable to improve the diagnostic accuracy in the detection and grading of stenosis. The latest 64-slice CT scanners apply special sampling techniques to resolve details of less than 0.4 mm in size and can provide increased temporal resolution based on a reduced rotation time down to 0.33 s (Flohr 2004). Two preliminary studies compared the performance of these new 64-slice CT scanners with conventional coronary angiography in the detection of significant coronary stenosis (Table 7.8). Leschka et al. (2005) reported that the improved spatial and temporal resolution of 64-slice CT increased image quality and facilitated the assessment of CAD with increased diagnostic accuracy. The shortened scanning of 12 s allowed a decreased breath-hold time, better exploitation of the contrast medium with less enhancement of adjacent structures, and a lower dose of contrast medium. The high negative predictive value of 99% in that study suggests an important future role of multi-slice coronary CTA for reliably excluding CAD in patients with an equivocal clinical presentation. Although image degradation in patients with higher heart rates was still observed, no segments had to be excluded from the evaluation. Owing to the increased spatial resolution, Raff et al. (2005) demonstrated a high quantitative and qualitative diagnostic accuracy of 64-slice CT compared to

quantitative coronary angiography in a broad spectrum of patients. In their study, 12% of coronary segments had to be excluded from the evaluation. The applied 15-segment model included smaller coronary vessels with diameters that are regularly below 1.5 mm, and the majority of the excluded vessels comprised these smaller vessels. Nonetheless, 99% of all examined coronary branches could be evaluated, and patient-based analysis of the data revealed sensitivity, specificity, positive predictive value (PPV) and negative predictive value (NPV) all above 90%.

7.3.5 Image Processing and Analysis

For evaluation of the large amount of CT data, several post-processing techniques are available (Figs. 7.22–7.25). Maximum intensity projection (MIP) of a thin slab positioned parallel to a vessel of interest, selectively displaying the highest densities within this slab, is convenient for initial screening of the luminal integrity of the vessel. However, in the presence of extensive calcified plaque material or other high-density material, such as stents, this method is unsuitable. Particularly in these cases, multi-planar reformation (MPR), which uses maneuverable cross-sectional planes, is more effective. More advanced applications allow (semi-) automatic determination of the vessel's central lumen line, and reconstruction of curved cross-sections along the entire vessel, optionally under various rotational angles. Three-dimensional image reconstruction, such as shaded-surface display (SSD) and volume-rendering technique (VRT), provide a comprehensive overview of the cardiac anatomy, the location of lesions, and the myocardial tissue at risk. More so than 2D image presentation, 3D display of the coronary arteries is user-dependent and is therefore not well-suited for the initial coronary assessment, particularly in the presence of stents, extensive atherosclerosis, and, in particular, calcified plaque material (Figs. 7.25–7.27). Advanced post-processing techniques may mask image artifacts or otherwise result in incorrect interpretations of the data. Therefore, confirmation of any findings using the original axial source images is recommended.

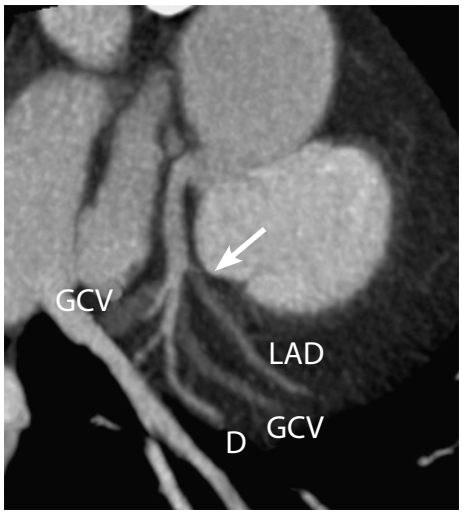

Fig. 7.22. *LAD* occlusion examined with 16-slice CT. Complete occlusion (*arrow*) of a small *LAD*, without any other visible plaque or calcium. The large diagonal branch (*D*) with the great cardiac vein (*GCV*) crosses underneath

7.3.6 Discussion

Multi-slice spiral CT is a relatively simple procedure that does not require arterial access or hospital admission. After optional pre-medication, i.e., a β-receptor blocker, the scan is performed in 20 s after intravenous injection of contrast medium. The entire procedure does not require more than 15 min. Images can be reconstructed during different cardiac phases, which allows retrospective selection of the phase with the least motion artifacts, but also assessment of ventricular performance. The imaging characteristics of multi-slice CT and conventional coronary angiography differ substantially, and none of the currently available non-invasive techniques should be expected to surpass the high image quality and diagnostic versatility of catheter-based techniques in the coming decade. There are, however, benefits to multi-slice CT compared to invasive coronary angiography, such as vessel-wall visualization and non-invasive quantification and

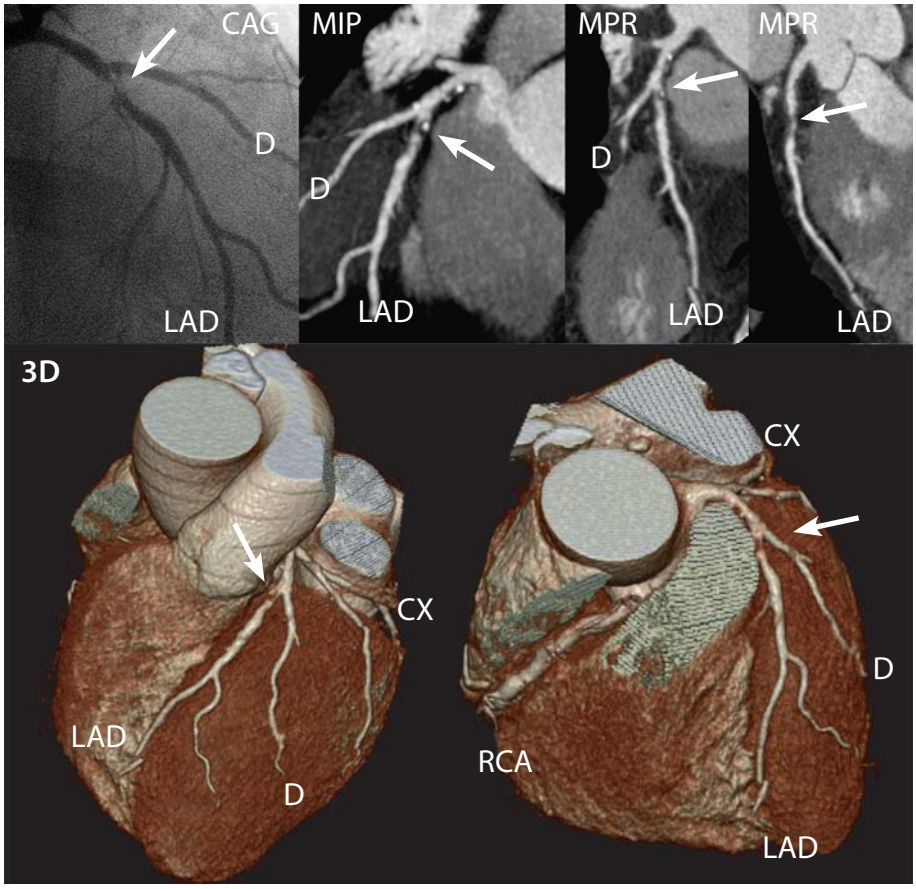

Fig. 7.23. A lesion in the *LAD* examined with 16-slice CT. Severe narrowing (*arrow*) of the *LAD* by a partially calcified plaque. Just distal from the first large diagonal branch, the lesion can be visualized using maximum-intensity projection (*MIP*), curved multi-planar reformation (*MPR*), and VRT (*bottom images*). It was confirmed by conventional coronary angiography (*CAG*)

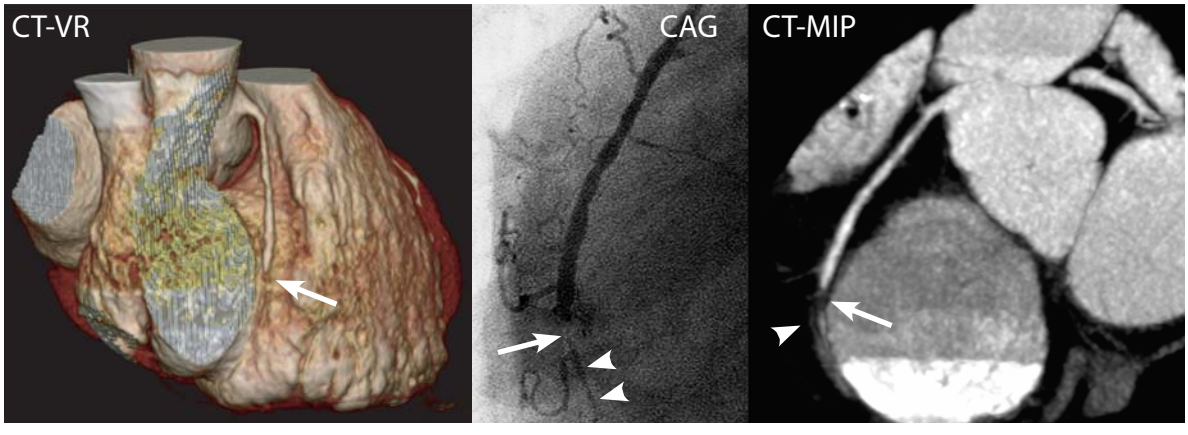

Fig. 7.24. An occlusion of the RCA examined with 16-slice CT. Complete occlusion (*arrow*) of the *RCA* with minimal retrograde filling of the distal part (*arrowhead*) can be appreciated using *MIP* or *3D VRT*, and is confirmed by *CAG*

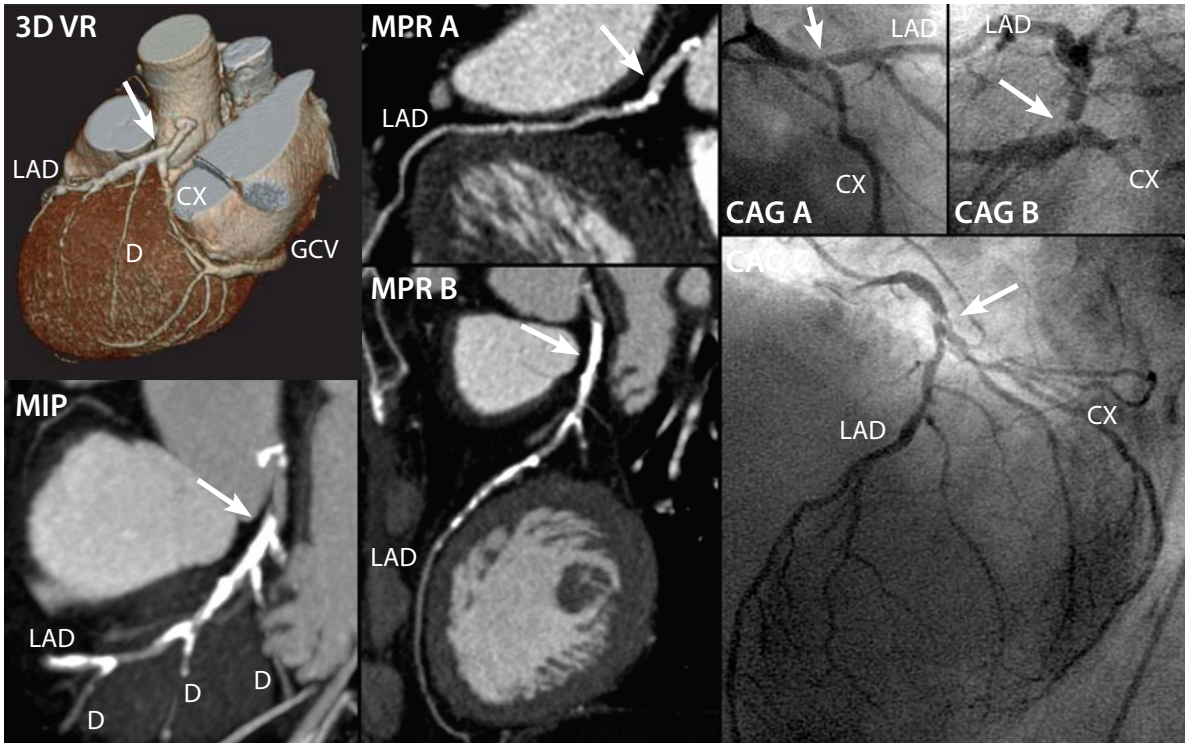

Fig. 7.25. A missed lesion due to coronary calcification, examined with 16-slice CT. The lesion (*arrow*) at the ostium of the *LAD*, according to *CAG*, was missed by multi-slice CT using different post-processing techniques: curved *MPR*, *MIP*, and *3D VRT*. The reason is extensive coronary wall calcification

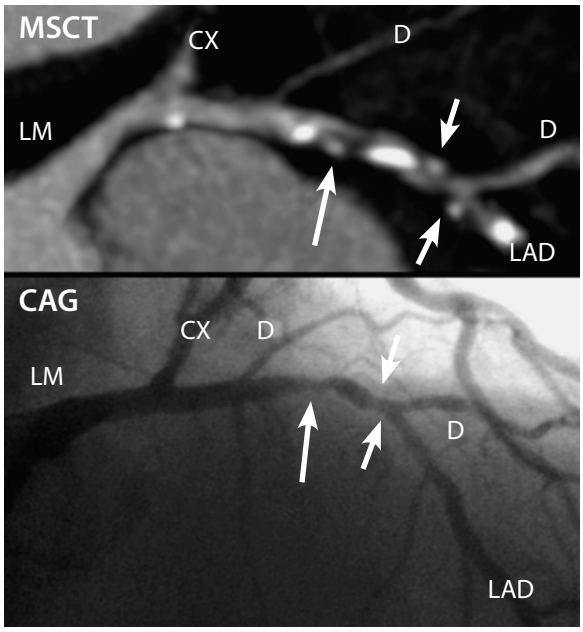

Fig. 7.26. Diffuse disease of the *LAD*, examined with 16-slice CT. The segment between the left circumflex (*CX*) and first diagonal branch (*D*) contains bright calcified and dark non-calcified plaque material. The conventional angiogram shows that, despite the corresponding locations of the plaques (*arrows*), the vessel is at no point narrowed by more than 50%. *LM* Left main coronary artery

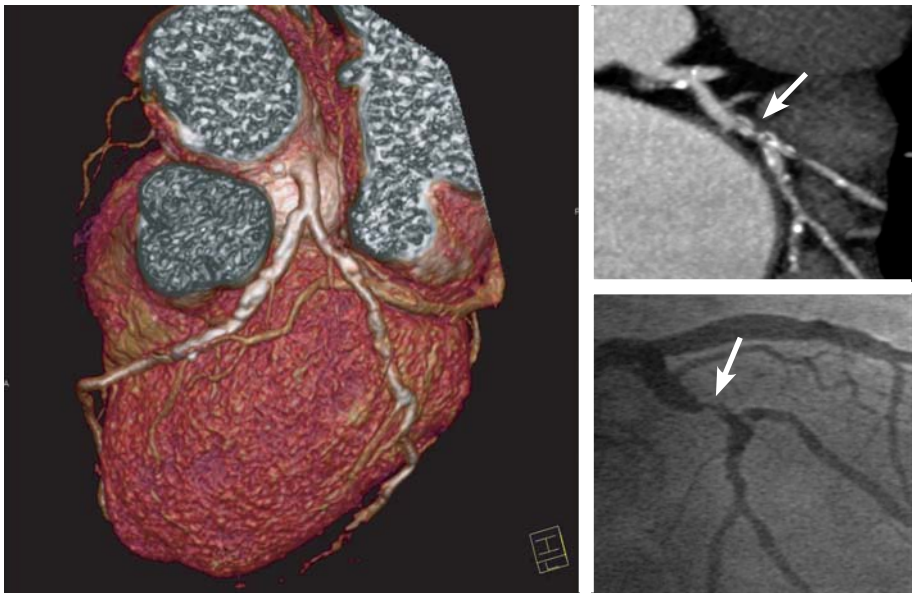

Fig. 7.27. Severe atherosclerotic lesions in the LAD and CX in a patient who had a heart rate between 89 and 93 bpm during the 64-slice CT examination. Owing to the increased temporal resolution of 64-slice CT, the coronary vessels can be evaluated free of motion artifacts. MIP reconstruction of the CX coronary artery revealed significant stenosis in conjunction with complex calcified and non-calcified plaque structures (*arrow*). The CX stenosis was confirmed by CAG

characterization of atherosclerotic plaque material (Fig. 7.26). The value and applicability of multi-slice CT plaque imaging is currently a topic of investigation and will be discussed in other chapters.

The advancements made in non-invasive coronary imaging with multi-slice CT are impressive, and the recent introduction of 64-slice CT has provided another significant improvement of diagnostic accuracy in the evaluation of coronary stenosis (Fig. 7.27). Nevertheless, some limitations remain that need to be addressed with future technology enhancements. The CT angiogram consists of data acquired during a number of heart beats and is reconstructed during a retrospectively selected time interval within the cardiac cycle. Strong alternation of the heart cycle duration, such as occurs in atrial fibrillation, results in reconstruction of slices during varying phases of cardiac contraction and longitudinal discontinuity of the CT angiogram. Highly attenuating material, such as calcium and stents, causes beam hardening artifacts and partial voluming, which can interfere with interpretation of the lumen diameter. Therefore, the lumen within stents and adjacent to severely calcified vessels is more difficult to evaluate. Despite continuing acceleration of the CT gantry rotation speed, motion artifacts remain a problem in patients with a fast heart rate.

While the overall image quality with 4- and 16-slice CT seems to be good in the majority of patients with a heart rate below 65–70 bpm, β-receptor blocking pre-medication in order to decelerate the heart rate during the scan is required in patients with a faster heart rate. Multi-segmental reconstruction algorithms that decrease the effective temporal resolution have not yet demonstrated diagnostically relevant improvements under clinical conditions. The recent development of 64-slice CT scanners with a rotation time down to 0.33 s holds promise that patients with a stable sinus rhythm can be successfully examined at heart rates up to 90 bpm, so that β-receptor blocking pre-medication can be

restricted to patients with heart rates over 90 bpm or to patients with possible arrhythmia during the scan (Leschka et al. 2005).

Considering the spatial resolution of the scanner in relation to the size of the coronary arteries, in addition to the small but never completely absent motion of the heart, one cannot expect multi-slice CT to quantify the severity of stenosis to an extent comparable to that achieved with conventional coronary angiography. Nevertheless, reproducible and user-independent quantification of stenosis severity is desired, particularly in the presence of extensive calcification. While the spatial resolution of 4- and 16-slice CT scanners is insufficient for quantitative coronary stenosis measurements, the latest 64-slice CT technology may allow such measurements with good correlation to conventional angiography in the main coronary segments (Raff et al. 2005). However, further enhancements of spatial and temporal resolution and standardized quantification tools are needed to improve the quantification accuracy of 64-slice CT over that of conventional angiography with quantitative coronary angiography (Leber et al. 2005).

Often, multi-slice coronary CTA is merely regarded as a non-invasive alternative to catheter-based coronary angiography. It is, however, unlikely that multi-slice CT will completely replace conventional angiography in the near future. Instead, multi-slice CT will need to find its own place as a diagnostic tool. For example, it could be used as a non-invasive coronary imaging device in patients with favorable characteristics and to rule-out of coronary disease in patients with low pre-test probability. Due to its less-invasive nature, the potential use of non-invasive CTA at an earlier stage in the work-up of patients with anginal symptoms, as an alternative to (functional) non-invasive tests, has been suggested. The additional value of atherosclerosis imaging of calcified and non-calcified plaque material needs further investigation. With the advent of 64-slice CT technology, multi-slice coronary CTA is increasingly being used in general clinical practice. The diagnostic and clinical success of multi-slice coronary CTA for specific indications will need to be evaluated in further clinical trials, in particular multi-center trials, to determine its role in cardiovascular medicine.

References

Achenbach S, Giesler T, Ropers D, et al (2001). Detection of coronary artery stenoses by contrast-enhanced, retrospectively electrocardiographically-gated, multislice spiral computed tomography. Circulation 103: 2535–2538

Flohr T, Stierstorfer K, Raupach R, Ulzheimer S, Bruder H (2004). Performance evaluation of a 64-slice CT system with z-flying focal spot. RöFo 176:1803–1810

Giesler T, Baum U, Ropers D, et al (2002). Noninvasive visualization of coronary arteries using contrast-enhanced multidetector CT: influence of heart rate on image quality and stenosis detection. Am J Roentgenol. 179: 911–916

Hoffmann U, Moselewski F, Cury RC, et al (2004). Predictive value of 16-slice multidetector spiral computed tomography to detect significant obstructive coronary artery disease in patients at high risk for coronary artery disease: patient- versus segment-based analysis. Circulation 110:2638–2643

Hoffmann M, Shi H, Schmitz BL, et al (2005). Noninvasive coronary angiography with multislice computed tomography. JAMA 293:2471–2478

Knez A, Becker CR, Leber A, et al (2001). Usefulness of multislice spiral computed tomography angiography for determination of coronary artery stenoses. Am J Cardiol. 88: 1191–1194

Kopp AF, Schröder S, Küttner A, et al (2002). Non-invasive coronary angiography with high-resolution multidetector-row computed tomography: results in 102 patients. Eur Heart J. 23: 1714–1725

Küttner A, Kopp A, Schroeder S, et al (2004a). Diagnostic accuracy of multidetector computed tomography coronary angiography in patients with angiographically proven coronary artery disease. JACC 43(5):831–839

Küttner A, Trabold T, Schroeder S, et al (2004b). Noninvasive detection of coronary lesions using 16-detector multislice spiral computed tomography technology – initial clinical results. JACC 44(6):1230–1237

Küttner A, Beck T, Drosch T, et al (2005). Diagnostic accuracy of noninvasive coronary imaging using 16-detector slice spiral computed tomography with 188 ms temporal resolution. J Am Coll Cardiol 45:123–125

Leber AW, Knez A, Ziegler F, Becker A, Nikolaou K, Paul S, Wintersperger B, Reiser MF, Becker CR, Steinbeck G, Boekstegers P (2005). Quantification of obstructive and nonobstructive coronary lesions by 64-slice computed tomography – a comparative study with quantitative coronary angiography and intravascular ultrasound. JACC 46(1): 147–154

Leschka S, Alkadhi H, Plass A, Desbiolles L, Gruenenfelder J, Marincek B, Wildermuth S (2005). Accuracy of MSCT coronary angiography with 64-slice technology: first experience. European Heart Journal 26: 1482–1487

Martuscelli E, Romagnoli A, D'Eliseo A, et al (2004). Accuracy of thin-slice computed tomography in the detection of coronary stenoses. Eur Heart J 25: 1043–1048

Mollet NR, Cademartiri F, Nieman K, et al (2004). Multislice

spiral CT coronary angiography in patient with stable angina pectoris. JACC 43(12): 2265–2270

Mollet NR, Cademartiri F, Krestin GP, et al (2005). Improved diagnostic accuracy with 16-row multi-slice computed tomography coronary angiography. J Am Coll Cardiol 45:128–132

Nieman K, Oudkerk M, Rensing BJ, et al (2001). Coronary angiography with multi-slice computed tomography. Lancet 357: 599–603

Nieman K, Rensing BJ, van Geuns RJ, et al (2002a). Non-invasive coronary angiography with multislice spiral computed tomography: impact of heart rate. Heart 88: 470–474

Nieman K, Rensing BJ, van Geuns RJM, et al (2002b). Usefulness of multislice computed tomography for detecting obstructive coronary artery disease. Am J Cardiol 89: 913–918

Nieman K, Cademartiri F, Lemos PA, et al (2002c). Reliable noninvasive coronary angiography with fast submillimeter multislice spiral computed tomography. Circulation 106: 2051–2054

Raff GL, Gallagher MJ, O'Neill WW, Goldstein JA (2005). Diagnostic accuracy of noninvasive coronary angiography using 64-slice spiral computed tomography. JACC 46 (3): 552–557

Romeo G, Houyel L, Angel CY, Brenot P, Riou JY, Paul JF (2005). Coronary Stenosis detection by 16-slice computed tomography in heart transplant patients: comparison with conventional angiography and impact on clinical management. J Am Coll Cardiol 45:1826–1831

Ropers D, Baum U, Pohle K, et al (2003). Detection of coronary artery stenoses with thin-slice multi-detector row spiral computed tomography and multiplanar reconstruction. Circulation 107: 664–666

Vogl TJ, Abolmaali ND, Diebold T, et al (2002). Techniques for the detection of coronary atherosclerosis: multi-detector row CT coronary angiography. Radiology 223: 212–220

Wang Y, Watts R, Mitchell I, et al (2001). Coronary MR angiography: selection of acquisition window of minimal cardiac motion with electrocardiography-triggered navigator cardiac motion prescanning–initial results. Radiology 218: 580–585

7.4 Assessment and Interpretation of Atherosclerotic Coronary Plaques

S. Achenbach

Contents

7.4.1 Clinical Background *214*
7.4.2 Clinical Concepts *215*
7.4.3 Visualization of Coronary Atherosclerotic Plaques *215*
7.4.4 Visualization of Non-calcified Plaques by Multi-slice CT *215*
7.4.5 Perspective *219*
References *221*

7.4.1 Clinical Background

Acute coronary events, such as unstable angina, myocardial infraction, or sudden cardiac death, are usually caused by erosion or rupture of a coronary atherosclerotic plaque. Exposure of thrombogenic material to the blood stream leads to platelet aggregation, and the resulting thrombus may partially or completely occlude the coronary artery lumen, leading to ischemia and possible myocardial necrosis. In the majority of cases, the "culprit lesion", i.e., the atherosclerotic plaque that ruptures or erodes to initiate the process outlined above, does not reduce the lumen of the coronary artery to a significant extent before the acute coronary event (Falk 1995, Little 1988, Little 1996). Most underlying lesions are non-stenotic; that is, they do not lead to significant obstruction of the blood flow prior to rupture. For this reason, many individuals are asymptomatic prior to their first coronary event and acute myocardial infarction or sudden death often occurs without previous symptoms to alert the patient to the fact that coronary atherosclerosis is present and acute ischemia is about to occur (Harper 1979).

Since targeted therapy, such as lipid-lowering medication, can substantially reduce the risk of coronary artery disease events (Sheperd 1995, Downs 1998), it is necessary to identify individuals who are at increased risk for acute coronary events in the asymptomatic stage. Traditionally, the classical cardiovascular risk factors have been used to identify individuals at risk – and most professional societies have endorsed their use to quantify an individual's risk for future coronary events. Specific algorithms have been developed that are based on atherosclerotic risk factors, such as the Framingham algorithm, which considers age, sex, total and HDL cholesterol levels, blood pressure, and smoking status [Adult Treatment Panel III 2001; in some versions also diabetes (Wilson 1998)], or the PROCAM algorithm, which incorporates age, LDL cholesterol, trigylcerides, blood pressure, diabetes, smoking, and family history of coronary disease, but is available only for men (Assmann 1993, Assmann 2002). These and other risk-prediction algorithms are established and useful in clinical practice but have limited predictive power, as the maximum relative risk that can be predicted is approximately a ten-fold increase compared to individuals without any risk factors. However, frequently, patients with acute coronary events have no "traditional" risk factors at all.

Since coronary disease events are caused by plaque rupture, it is an intriguing concept to use imaging methods that permit detection, quantification, and possibly also characterization of coronary atherosclerotic plaque to carry out individualized risk stratification. Assessment of coronary atherosclerotic plaque burden through quantification of coronary calcification has already been shown to be of high predictive value concerning the occurrence of future coronary events in asymptomatic individual and to permit better risk stratification than risk factor analysis (Raggi 2000, Shaw 2003, Vliegenhart 2002) (also see Sect. 7.2). Since, however, calcium constitutes only one component of plaque and non-calcified morphological structures, such as a large necrotic core and thin fibrous cap, are usually considered to indicate high propensity towards plaque rupture (Burke 2003), there is growing interest in the use of imaging to visualize and analyze non-calcified coronary atherosclerotic plaque components.

7.4.2 Clinical Concepts

Theoretically, plaque visualization and analysis through imaging may be useful in two related, but distinct clinical situations. First, in asymptomatic individuals with a certain constellation of risk factors, it can be difficult to make decisions about initiating, e.g., lipid-lowering therapy. Even modern guidelines leave room for individual decisions; for example, the NCEP-ATP III guidelines state that in individuals with 0 to 1 "traditional" risk factor and an LDL cholesterol level of 160–190 mg/dl, the use of lipid-lowering medication is "optional". It is currently assumed that imaging for further risk stratification is most useful in individuals who, based on analysis of traditional risk factors, seem to be at "intermediate risk" for coronary artery disease events (a risk between 5 and 20% over the next 10 years) (Taylor 2003, Greenland 2001).

Second, patients who have diffuse or localized atherosclerotic disease of the coronary arteries, as demonstrated by invasive angiography, but an absence of hemodynamically relevant coronary artery stenoses may profit from further work-up. There is justified hope that, in the future, imaging will guide certain interventions to specifically lower the risk of rupture of plaques deemed to be "vulnerable", i.e., those at high risk to cause ischemic events. However, even though fitting terms, such as "plaque sealing", have already been coined for such treatments (Meier 1997, Mercado 2003), it is a concept that still requires validation since no appropriate studies have been conducted thus far.

7.4.3 Visualization of Coronary Atherosclerotic Plaques

Invasive coronary angiography, the clinical "gold standard" for coronary artery visualization, is limited to providing a "luminogram" of the coronary arteries. The occurrence of coronary atherosclerotic plaque is usually accompanied by an outward growth of the vessel (compensatory enlargement), so that in spite of growing amounts of atherosclerotic plaque, the lumen remains unchanged. This process of usually referred to as "remodeling" (Glagov 1997). Therefore, invasive angiography is therefore unsuited to visualize coronary atherosclerotic plaque (Fig. 7.28), and, instead, intravascular ultrasound (IVUS) is considered the clinical method of choice (Mintz 2001). In IVUS, high-resolution cross-sectional images of the coronary artery wall are obtained. However, it is an extremely invasive and expensive modality and therefore unsuited for routine applications in risk stratification. Optical coherence tomography is also an invasive, cross-sectional imaging method that provides even better spatial resolution than IVUS (Brenzinski 1996, Jang 2002), but much like IVUS requires the catheter to be introduced into the coronary artery, is thus highly invasive and expensive, and not suited for routine applications.

Non-invasive imaging modalities that have been evaluated as to their ability to assess coronary atherosclerotic plaques include magnetic resonance imaging (MRI) and multi-slice CT (Fayad 2002). MRI offers the theoretical advantage of being free of potentially limiting side effects (such as radiation exposure and the need for contrast injection), but is fraught with limited spatial resolution and long examination times. Even though the ability to visualize coronary atherosclerotic plaques in-vivo has been shown (Fayad 2000, Botnar 2000, Kim 2002), these disadvantages have so far proven to severely limit clinical applications. Multi-slice CT, by contrast, is widely available, can be performed rapidly, and provides high-resolution images. The evaluation of multi-slice CT concerning its ability to visualize non-calcified coronary atherosclerotic plaques, first reported by Becker et al. (2000), has therefore been pursued by a number of research groups, With the increasingly sophisticated imaging technology, promising initial results have been obtained.

7.4.4 Visualization of Non-calcified Plaques by Multi-slice CT

While coronary calcifications, due to their high X-ray attenuation, can be assessed by CT in non-contrast-enhanced images, visualization of non-calcified plaque components requires intravenous contrast enhancement and the use of scan protocols

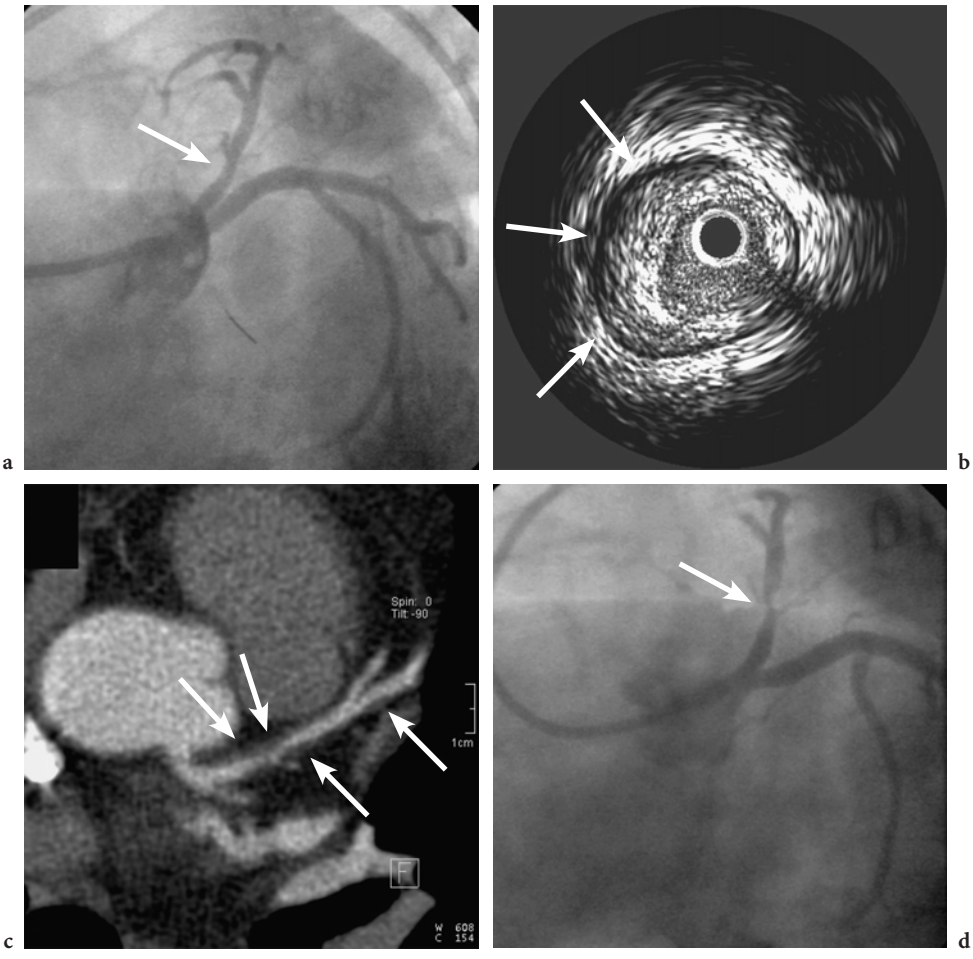

Fig. 7.28a–d. Case report: A 63-year-old female patient was admitted to the hospital because of chest pain at rest (unstable angina). Coronary angiography showed only non-significant stenosis of the proximal LAD (**a**). The patient was examined using intravascular ultrasound (IVUS) (**b**) and 16-slice CT (**c**). Both showed substantial amounts of non-calcified atherosclerotic plaque in the proximal LAD (*arrows*). The patient was discharged on aspirin and lipid-lowering medication. Two months after the first admission, she was admitted to the hospital again with an acute non-ST-elevation myocardial infarction. Immediate coronary angiography showed a tight stenosis in the proximal LAD (**d**, *arrow*). Plaque rupture had occurred at a site that had been free of significant stenosis but with substantial plaque burden, undetected by invasive angiography, at initial presentation.

with higher spatial resolution – and, consequently, substantially higher radiation exposure (Hunold 2003). Such scan protocols were initially used to visualize coronary artery stenoses (Nieman 2002, Ropers 2003); however, the observation that non-calcified coronary atherosclerotic plaque could frequently be visualized in these high-resolution CT scans of the coronary arteries (Becker 2000) sparked rapidly growing interest in using this imaging modality for the non-invasive detection, quantification, and characterization of coronary plaque in the context of risk assessment (Fayad 2002, Naghavi 2003). Several studies using 4-, 16-, and recently also 64-slice CT scanners have confirmed the ability of multi-slice cardiac CT to visualize non-calcified or partly calcified coronary atherosclerotic plaques (Fig. 7.29), but clinical applications will require thorough assessment and validation of the ability of CT to detect, quantify, and perhaps characterize the composition of coronary athero-

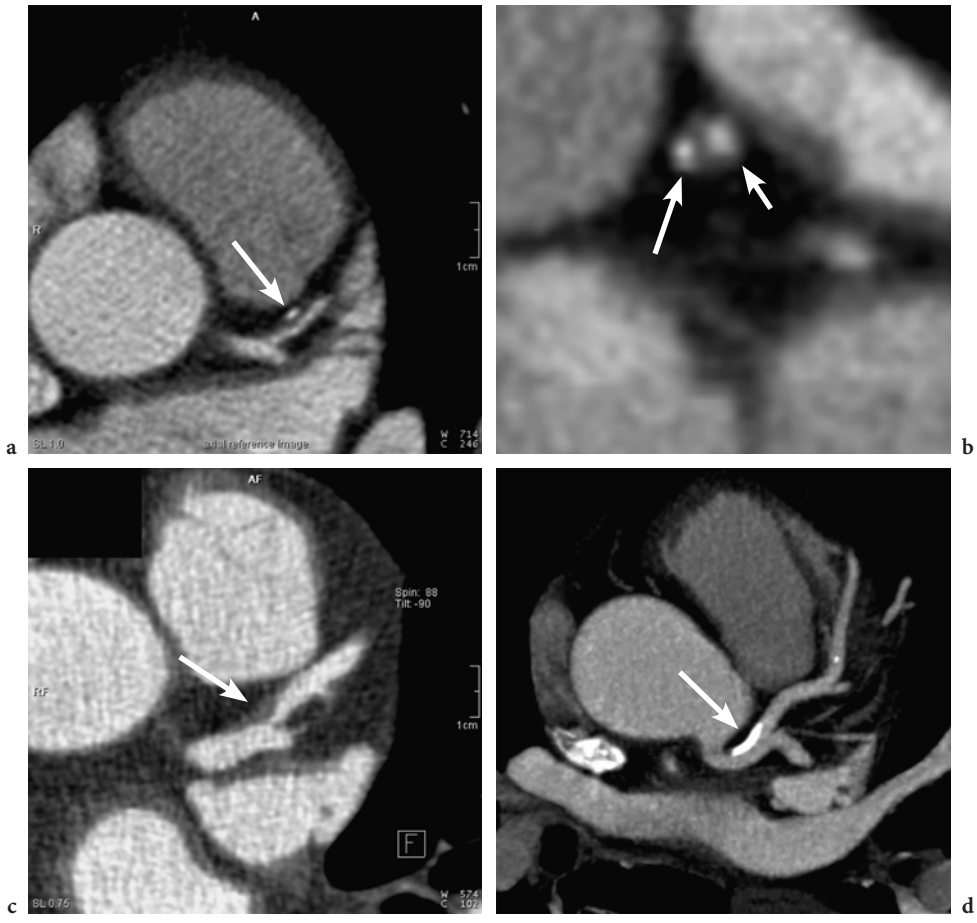

Fig. 7.29a–d. Coronary atherosclerotic plaque visualization with 16-slice CT. **a** A partly calcified plaque in the proximal LAD is depicted on an axial cross-sectional image with 1-mm slice thickness. **b** The cross-section of the LAD lesion shows the partly calcified plaque (*large arrow* calcified plaque, *small arrow* contrast-enhanced coronary artery lumen). **c** Non-calcified plaque (*arrow*) at the proximal LAD visualized with MPR. **d** Completely calcified plaque (*arrow*) in the LM in MIP

sclerotic plaques. Such evaluations are currently in an early stage and firm conclusions as to clinical applicability would be premature.

7.4.4.1 Detection of Non-calcified Plaques

Becker et al. (2003) reported a sensitivity of 66% for the ability of 4-slice CT to detect single coronary atherosclerotic plaques in ex-vivo heart specimens. In a recent in-vivo study done with 16-slice CT, Achenbach et al. (2004) analyzed 22 patients (83 coronary artery segments) by IVUS and multi-slice CT. A sensitivity of 78% and specificity of 87% for the detection of coronary artery segments with non-calcified plaque was reported. In a study of 37 patients, Leber et al. (2004) compared 16-slice CT to IVUS in 875 coronary artery segments, each 3 mm in length. Similar to the previous study, the authors also found a sensitivity of 78% for the detection of non-calcified plaque (specificity 92% for any plaque). Schoenhagen et al. (2003) provided area under the receiver operating characteristics curve values for plaque detection by 16-slice CT and IVUS in 46 coronary segments (14 patients). Values of 0.87–0.97 indicated the high accuracy of 16-slice CT for plaque detection com-

pared to IVUS (Schoenhagen 2003). Leber et al. (2005) compared the performance of new 64-slice CT technology, with enhanced spatial and temporal resolution, with those of IVUS in the detection of atherosclerotic plaques in 18 patients and 32 coronary branches that showed 55 lesions (Leber 2005). The authors found a sensitivity of 84% and a specificity of 91% in the detection of lesions compared to IVUS and a significantly increased accuracy compared to 16-slice CT. They concluded that contrast-enhanced 64-slice CT allows for the identification of proximal coronary lesions with excellent accuracy and that measurements of plaque and lumen areas correlated well with the results obtained with IVUS.

The drawback to all of these studies is that they were small. Thus, so far, information about the accuracy and reproducibility of multi-slice CT for plaque detection is limited, and both systematic validation of the methodology and further studies on a larger scale are advisable.

7.4.4.2 Quantification of Coronary Atherosclerotic Plaques

Currently, knowledge about the ability of CT techniques to quantify the amount of non-calcified coronary atherosclerotic plaque is extremely limited. In a phantom study, it was observed that under the prerequisite of using thin slice collimation, multi-slice CT may permit assessment of plaque volumes, but systematic overestimation of plaque volumes may occur (Schroeder 2001). Achenbach et al. described a close correlation (r = 0.8) but systematic underestimation of the mean plaque volume per coronary segment in multi-slice CT (24 ± 35 mm^3) compared to IVUS (43 ± 60 mm^3) (Achenbach 2004). The reason for this may have been the fact that limited image quality prevented plaque visualization by multi-slice CT in some segments, thus leading to a global underestimation of plaque volume.

7.4.4.3 Characterization of Coronary Atherosclerotic Plaques

Under the assumption that lipid-rich plaques have a higher risk of rupture with consequent thrombosis than fibrotic plaques, researchers have tried to use measurements of CT attenuation values to differentiate plaque types (Kopp 2001). Reports in which multi-slice CT and IVUS were compared demonstrated that CT could detect a variety of densities in coronary atherosclerotic plaques in vivo. In a study

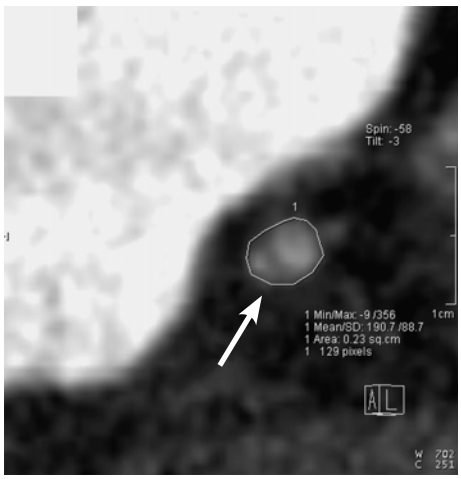

a

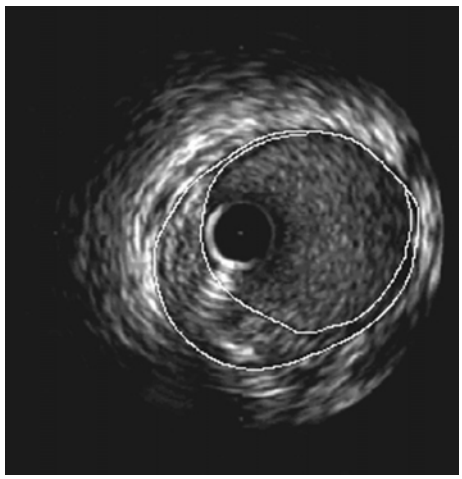

b

Fig. 7.30a,b. Quantification of atheroslcerotic plaque dimensions with 16-slice CT. **a** Cross-section of the proximal LAD, with an eccentric atherosclerotic plaque (arrow), reveals a vessel area of 0.23 cm^2. **b** The corresponding IVUS cross-section determines a vessel area of 0.21 cm^2

of 12 patients, Schroeder et al. (2001) found that plaques characterized as "hypo-echoic" or "soft" on IVUS – and thus usually assumed to be more likely to rupture – had a lower mean CT attenuation (14 ± 26 HU) than plaques characterized as "fibrotic" (91 ± 21 HU) or "calcified" (419 ± 194 HU). In the study mentioned above, Leber et al. (2004) found a mean density of 49 ± 22 HU for "soft", 91 ± 22 HU for "fibrous", and 391 ± 156 HU for calcified plaques. Similar observations were made ex vivo: In 21 specimens of carotid arteries, lipid-rich plaques could be distinguished from fibrous plaques by their mean CT attenuation (39 ± 12 HU vs. 90 ± 24 HU) (Estes 1997), and in ex-vivo heart specimens, densities of 47 ± 9 and 104±28 HU, respectively, were found for 33 lipid-rich and fibrous plaques (Becker 2003). Animal models have also confirmed the in-vivo and ex-vivo findings in human arteries. Viles-Gonzalez et al. (2004) reported lipid-rich plaques with a density of 51 ± 25 HU and fibrous-rich plaques with a density of 116 ± 27 HU based on 16-slice CT scans of rabbit aortas (Viles-Gonzalez 2004), (Table 7.9). It should be noted that a potential pitfall is that CT attenuation values of thrombus overlap with those measured by CT density for "soft" coronary atherosclerotic plaques. Here, the morphology of the lesion in relation to the vessel wall may give further distinguishing information.

Even though these findings are intriguing and certainly indicate an opportunity to detect and analyze coronary atherosclerotic plaques non-invasively by CT, it again needs to be pointed out that the current knowledge is preliminary and that the clinical implications of these initial findings are still unclear.

7.4.4.4 Clinical Results

Several smaller studies have investigated the visualization and detection of non-calcified coronary atherosclerotic plaques in defined patient subgroups without further validation. Fischbach et al. (2003) used 4-slice CT in a study of 100 subjects at high risk according to the PROCAM score. In more than 80% of cases, the coronary arteries of these patients showed calcified or non-calcified lesions (Fischbach 2003). The authors suggested classifying these high-risk individuals as pre-symptomatic patients with subclinical atherosclerosis. Leber et al. (2003) carried out contrast-enhanced 16-slice CT in 21 patients with acute myocardial infarction and 19 patients with stable angina. While 96% of plaques were calcified in patients with stable angina, only 76% of all plaques were calcified in patients after acute myocardial infarction. Ten percent of patients with acute myocardial infarction (2 out of 21) had no detectable calcium, but did have detectable non-calcified plaques (Leber et al. 2003). Similarly, Schroeder et al. (2003) reported that, out of 68 patients with risk factors for coronary artery disease, three out of 29 patients without calcified plaque had detectable non-calcified plaque (Schroeder 2003). Nikolaou et al. (2003) reported that seven of 48 (15%) patients investigated in another series had detectable non-calcified plaque in the absence of coronary calcification. All of these studies were limited by the lack of a validation method, such as IVUS, but the results seem to indicate that, in some cases, the presence of coronary atherosclerotic plaque may be possible without detectable calcium. Since no follow-up was performed in either study, the prognostic significance of this observation is unknown and it remains to be clarified whether the additional effort to detect non-calcified plaque (investigation time, contrast agent, and radiation) as compared to coronary calcium imaging alone is justified, especially since false-positive findings are well possible.

7.4.5 Perspective

Experience collected with coronary calcium detection by CT over many years provides clear evidence that the assessment of coronary atherosclerotic plaque burden by CT can be a useful prognostic marker. Initial data concerning imaging of non-calcified plaque by CT demonstrated that multi-slice CT may indeed be able to detect and quantify the presence and amount of non-calcified plaque with impressive accuracy and that limited conclusions concerning the characterization of plaque can be drawn from measurements of CT attenuation within

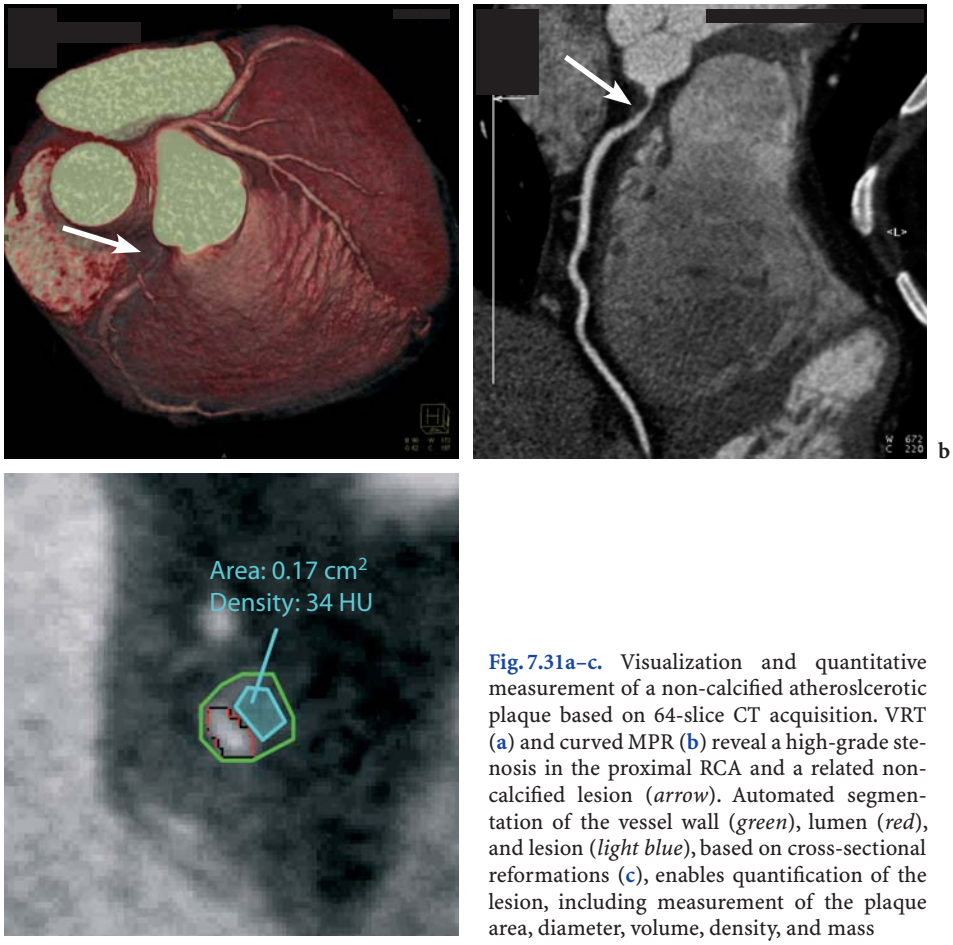

Fig. 7.31a–c. Visualization and quantitative measurement of a non-calcified atheroslcerotic plaque based on 64-slice CT acquisition. VRT (**a**) and curved MPR (**b**) reveal a high-grade stenosis in the proximal RCA and a related non-calcified lesion (*arrow*). Automated segmentation of the vessel wall (*green*), lumen (*red*), and lesion (*light blue*), based on cross-sectional reformations (**c**), enables quantification of the lesion, including measurement of the plaque area, diameter, volume, density, and mass

Table 7.9. CT attenuation measured in various types of atherosclerotic plaques by multi-slice CT

Author	Material, scanner	Lipid-rich plaque	Fibrous plaque	Calcific plaque
Estes 1998	Carotid endatherectomy (ex-vivo), 1-slice	39 ± 12 HU	90 ± 24 HU	–
Schroeder 2001	Coronary plaque (in vivo), 4-slice	14 ± 26 HU	91 ± 21 HU	419 ± 159 HU
Leber 2003	Coronary plaque (in vivo), 16-slice	49 ± 22 HU	91 ± 22 HU	391 ± 156 HU
Becker 2003	Coronary plaque (ex vivo), 4-slice	47 ± 9 HU	104 ± 28 HU	–
Viles-Gonzalez 2004	Aortic plaque in rabbit (in vivo), 16-slice	51 ± 25 HU	116 ± 27 HU	–

the atherosclerotic lesion. Future developments will be two-fold: First, steady improvements of scanner technology has occurred during the past several years and will continue to occur. It is thus reasonable to expect that the accuracy for plaque detection and the ability to provide some sort of plaque characterization will also continue to improve. Second, there is currently a paucity of clinical data concerning the prognostic significance of the observations that have been made so far. Appropriately conducted clinical trials will need to deliver evidence that multi-slice CT plaque imaging can provide useful data – either

in primary risk assessment of asymptomatic individuals or, more likely, in the assessment of the propensity of non-stenotic lesions discovered in invasive coronary angiography to rupture and cause acute coronary events at a later time. The recently introduced 64-slice CT scanners with high spatial and temporal resolution in conjunction with semi-automated measurement tools will serve as a robust basis for further clinical evaluation (Fig. 7.33).

These developments will have to be accompanied by the design and verification of appropriate treatment methods. The combination of non-invasive imaging for risk assessment and effective interventions to lower the risk of coronary events will only then offer a life-saving approach for thousands and thousands of patients.

References

Achenbach S, Moselewski F, Ropers D, Ferencik M, Hoffmann U, MacNeill B, Pohle K, Baum U, Anders K, Jang IK, Daniel WG, Brady TJ (2004). Detection of calcified and noncalcified coronary atherosclerotic plaque by contrast-enhanced, submillimeter multidetector spiral computed tomography: a segment-based comparison with intravascular ultrasound. Circulation 109:14–17

Adult Treatment Panel III (2001). Expert panel on detection, evaluation, and treatment of high blood cholesterol in adults. Executive Summary of the Third Report of the National Cholesterol Education Program (NCEP). Expert Panel on Detection, Evaluation, and Treatment of High Blood Cholesterol in Adults. JAMA 285:2486–2497

Assmann G (1993). Lipid metabolism disorders and coronary heart disease. MMV-Medizin-Verlag, München

Assmann G, Cullen P, Schulte H (2002). Simple scoring scheme for calculating the risk of acute coronary events based on the 10-year follow-up of the prospective cardiovascular Muenster (PROCAM) study. Circulation 105:310–315

Becker CR, Knez A, Ohnesorge B, Schoepf UJ, Reiser MF (2000). Imaging of noncalcified coronary plaques using helical CT with retrospective ECG gating. Am J Roentgenol 175:423–444

Becker CR, Nikolaou K, Muders M, Babaryka G, Crispin A, Schoepf UJ, Loehrs U, Reiser MF (2003). Ex vivo coronary atherosclerotic plaque characterization with multi-detector-row CT. Eur Radiol 13: 2094–2098

Botnar RM, Stuber M, Kissinger KV, Kim WY, Spuentrup E, Manning WJ (2000). Noninvasive coronary vessel wall and plaque imaging with magnetic resonance imaging. Circulation 102:2582–2587

Brezinski ME, Tearney GJ, Bouma BE, Izatt JA, Hee MR, Swanson EA, Southern JF, Fujimoto JG (1996). Optical coherence tomography for optical biopsy: properties and demonstration of vascular pathology. Circulation 99:1965–1971

Burke AP, Virmani R, Galis Z, Haudenschild CC, Muller JE (2003). 34th Bethesda Conference: Task force #2–What is the pathologic basis for new atherosclerosis imaging techniques? J Am Coll Cardiol 41:1874–1886

Downs JR, Clearfield M, Wis S, Whitney E, Shapiro DR, Beere PA, Langendorfer A, Stein EA, Kruger W, Gotto AJ (1998). Primary prevention of acute coronary events with lovastatin in men and women with average cholesterol levels: results of AFCAPS/TexCAPS. JAMA 279:1615–1622

Estes JM, Quist WC, Lo Gerfo FW, Costello P (1998). Noninvasive characterization of plaque morphology using helical computed tomography. J Cardiovasc Surg (Torino) 39:527–534

Falk E, Shah PK, Fuster V (1995). Coronary plaque disruption. Circulation 92:657–671

Fayad ZA, Fuster V, Nikolaou K, Becker C (2002). Computed tomography and magnetic resonance imaging for noninvasive coronary angiography and plaque imaging: current and potential future concepts. Circulation 106:2026–2034

Fayad ZA, Fuster V, Fallon JT, Jayasundera T, Worthley SG, Helft G, Aguinaldo JG, Badimon JJ, Sharma SK (2000). Noninvasive in vivo human coronary artery lumen and wall imaging using black blood magnetic resonance. Circulation 102:506–501

Fischbach R, Heindel W, Assmann G, et al. Multi-slice CT in asymptomatic high-risk persons (2003). symposium of the international task force for prevention of coronary heart disease: an evaluation of emerging techniques for identifying sub-clinical atherosclerosis. Scoul, Switzerland

Glagov S, Bassiouny HS, Sakaguchi Y, Goudet CA, Vito RP (1997). Mechanical determinants of plaque modeling, remodeling and disruption. Atherosclerosis 131:13–14

Greenland P, Smith Jr SC Jr, Grundy SM (2001). Improving coronary heart disease risk assessment in asymptomatic people: role of traditional risk factors and noninvasive cardiovascular tests. Circulation 104:1863–1867

Harper RW, Kennedy G, De Sanctis RW, Hutter AM (1979). The incidence and pattern of angina prior to acute myocardial infraction: A study of 577 cases. Am Heart J 97:178–183

Hunold P, Vogt FM, Schmermund A, Debatin JF, Kerkhoff G, Budde T, Erbel R, Ewen K, Barkhausen J (2003). Radiation exposure during cardiac CT: effective doses at multi-detector row CT and electron-beam CT. Radiology 226:145–152

Jang IK, Bouma BE, Kang DH, Park SJ, Park SW, Seung KB, Choi KB, Shishkov M, Schlendorf K, Pomerantsev E, Houser SL, Aretz HT, Tearney GJ (2002). Visualization of coronary atherosclerotic plaques in patients using optical coerence tomography: comparison with intravascular ultrasound. J Am Coll Cardiol 39:604–609

Kim WY, Stuber M, Bornert P, Kissinger KV, Manning WJ, Botnar RM (2002). Three-dimensional black-blood cardiac magnetic resonance coronary vessel wall imaging detects positive arterial remodeling in patients with nonsignificant coronary artery disease. Circulation 106:296–299

Kopp AF, Schroeder S, Baumbach A, Kuettner A, Georg C, Ohnesorge B, Heuschmid M, Kuzo R, Claussen CD (2001). Non-invasive characterisation of coronary lesion morphology and composition by multislice CT: first results in comparison with intracoronary ultrasound. Eur Radiol 11:1607–1611

Leber AW, Knez A, White CW, Becker A, von Ziegler F, Muehling O, Becker C, Reiser MF, Steinbeck G, Boekstegers P (2003). Composition of coronary atherosclerotic plaques in patients with acute myocardial infarction and stable angina pectoris determined by contrast-enhanced multislice computed tomography. Am J Cardiol 91:714–718

Leber AW, Knez A, Becker A, Becker C, von Ziegler F, Nikolaou K, Rist C, Reiser MF, White C, Steinbeck G, Boekstegers P (2004). Accuracy of multidetector spiral computed tomography in identifying and differentiating the composition of coronary atherosclerotic plaques: a comparative study with intracoronary ultrasound. J Am Coll Cardiol 43:1241–1247

Leber AW, Knez A, Ziegler F, Becker A, Nikolaou K, Paul S, Wintersperger B, Reiser MF, Becker CR, Steinbeck G, Boekstegers P (2005). Quantification of obstructive and nonobstructive coronary lesions by 64-slice computed tomography – a comparative study with quantitative coronary angiography and intravascular ultrasound. JACC 46(1):147–154

Little WC, Constantinescu M, Applegate RJ, Kutcher MA, Burrows MT, Kahl FR. Santamore WP (1988). Can coronary angiography predict the site of a subsequent myocardial infarction in patients with mild-to-moderate coronary artery disease? Circulation 78:1157–1166

Little WC, Applegate RJ (1996). Role of plaque size and degree of stenosis in acute myocardial infarction. Cardiol Clin 14:221–228

Mintz GS, Nissen SE, Anderson WD, Bailey SR, Erbel R, Fitzgerald PJ, Pinto FJ, Rosenfield K, Siegel RJ, Tuzcu EM, Yock PG (2001). American College of Cardiology clinical expert consensus document on standards for acquisition, measurements and reporting of intravascular ultrasound studies (IVUS). J Am Coll Cardiol 37:1478–1492

Meier B (1997). Plaque sealing or plumbing for coronary artery stenoses? Circulation 96:2094–2095

Mercado N, Maier W, Boersma E, Bucher C, de Valk V, O'Neill WW, Gersh BJ, Meier B, Serruys PW, Wijns W (2003). Clinical and angiographic outcome of patients with mild coronary lesions treated with balloon angioplasty or coronary stenting. Implications for mechanical plaque sealing. Eur Heart J 24:541–551

Naghavi M, Libby P, Falk E, Casscells SW, Litovsky S, Rumberger J, Badimon JJ, Stefanadis C, Moreno P, Pasterkamp G, Fayad Z, Stone PH, Waxman S, Raggi P, Madjid M, Zarrabi A, Burke A, Yuan C, Fitzgerald PJ, Siscovick DS, de Korte CL, Aikawa M, Airaksinen KE, Assmann G, Becker CR, Chesebro JH, Farb A, Galis ZS, Jackson C, Jang IK, Koenig W, Lodder RA, March K, Demirovic J, Navab M, Priori SG, Rekhter MD, Bahr R, Grundy SM, Mehran R, Colombo A, Boerwinkle E, Ballantyne C, Insull W Jr, Schwartz RS, Vogel R, Serruys PW, Hansson GK, Faxon DP, Kaul S, Drexler H, Greenland P, Muller JE, Virmani R, Ridker PM, Zipes DP, Shah PK, Willerson JT (2003). From vulnerable plaque to vulnerable patient: a call for new definitions and risk assessment strategies: Part II. Circulation 108:1772–1778

Nieman K, Cademartiri F, Lemos PA, Raaijmakers R, Pattynama PM, de Feyter PJ (2002). Reliable noninvasive coronary angiography with fast submillimeter multislice spiral computed tomography. Circulation 106:2051–2054

Nikolaou K, Sagmeister S, Knez A, Klotz E, Wintersperger BJ, Becker CR, Reiser MF (2003). Multidetector-row computed tomography of the coronary arteries: predictive value and quantitative assessment of non-calcified vessel-wall changes. Eur Radiol 13: 2505–2512

Raggi P, Callister TQ, Cooil B, He ZX, Lippolis NJ, Russo DJ, Zelinger A, Mahmarian JJ (2000). Identification of patients at increased risk of first unheralded acute myocardial infarction by electron-beam computed tomography. Circulation 101: 850–855

Ropers D, Baum U, Pohle K, Anders K, Ulzheimer S, Ohnesorge B, Schlundt C, Bautz W, Daniel WG, Achenbach S (2003). Detection of coronary artery stenoses with thin-slice multidetector row spiral computed tomography and multiplanar reconstruction. Circulation 107:664–666

Schoenhagen P, Tuzcu EM, Stillman AE, Moliterno DJ, Halliburton SS, Kuzmiak SA, Kasper JM, Magyar WA, Lieber ML, Nissen SE, White RD (2003). Non-invasive assessment of plaque morphology and remodeling in mildly stenotic coronary segments: comparison of 16-slice computed tomography and intravascular ultrasound. Coron Artery Dis 14:459–462

Schroeder S, Kopp AF, Baumbach A, Meisner C, Kuettner A, Georg C, Ohnesorge B, Herdeg C, Claussen CD, Karsch KR (2001). Noninvasive detection and evaluation of atherosclerotic coronary plaques with multislice computed tomography. J Am Coll Cardiol 37:1430–1435

Schroeder S, Kopp AF, Ohnesorge B, Flohr T, Baumbach A, Kuettner A, Herdeg C, Karsch KR, Claussen CD (2001). Accuracy and reliability of quantitative measurements in coronary arteries by multi-slice computed tomography: experimental and initial clinical results. Clin Radiol 56:466–474

Schroeder S, Kuettner A, Kopp AF, Heuschmidt M, Burgstahler C, Herdeg C, Claussen CD (2003). Noninvasive evaluation of the prevalence of noncalcified atherosclerotic plaques by multi-slice detector computed tomography: results of a pilot study. Int J Cardiol 92:151–155

Shaw LJ, Raggi P, Schisterman E, Berman DS, Callister TQ (2003). Prognostic value of cardiac risk factors and coronary artery calcium screening for all-cause mortality. Radiology 228:826–833

Sheperd J, Cobbe SM, Ford I, Isles CG, Lorimer AR, Macfarlane PW, McKillp JH, Packard CJ (1995). Prevention of coronary heart disease with pravastatin in men with hypercholesterolemia. N Engl J Med 333:1301–1307

Taylor AJ, Merz CN, Udelson JE (2003). 34th Bethesda Conference: Executive summary–can atherosclerosis imaging techniques improve the detection of patients at risk for ischemic heart disease? J Am Coll Cardiol 41(11):1860–1862

Viles-Gonzalez JF, Poon M, Sanz J, Rius T, Nikolaou K, Fayad ZA, Fuster V, Badimon JJ (2004). In vivo 16-slice, multidetector-row computed tomography for the assessment of experimental atherosclerosis – comparison with magnetic resonance imaging and histopathology. Circulation 110:1467–1472

Vliegenthart R, Oudkerk M, Song B, van der Kuip DA, Hofman A, Witteman JC (2002). Coronary calcification detected by electron-beam computed tomography and myocardial infarction. The Rotterdam Coronary Calcification Study. Eur Heart J 23:1596–1603

Wilson PWF, D`Agostino RB, Levy D, Belanger AM, Silbershatz H, Kannel WB (1998). Prediction of coronary heart disease using risk factor categories. Circulation 97:1837–1847

7.5 Coronary CT Angiography in Patients with Chest Pain

A. Küttner, S. Schröder

Contents

7.5.1 Clinical Background *224*
7.5.2 Methods and Protocols *225*
7.5.3 Results in a Representative Patient Population *226*
7.5.4 Discussion *228*
7.5.4.1 Current Indications and Limitations of Multi-slice CT Coronary Angiography *228*
7.5.4.2 Image Quality of Non-invasive Multi-slice CT Coronary Angiography *229*
7.5.4.3 Usefulness of Multi-slice CT as an Imaging Technique in Patients with Unclear Chest Pain *229*
7.5.4.4 Study Limitations *230*
7.5.5 Conclusions *230*
References *230*

7.5.1 Clinical Background

Coronary artery disease is the leading cause of morbidity and mortality in the Western world. While conventional invasive coronary angiography (ICA) is still the gold standard in the diagnosis of CAD, it is limited by its invasiveness and related possible complications. Mortality is quoted with 0.1% and the total risk of major complications with 1.7% (Scanlon 1999). The majority of all diagnostic ICAs are not followed by therapeutic interventions. For example, in 2001, 611,882 diagnostic ICAs were performed in Germany alone, but coronary interventions took place only in 195,280 cases (Mannebach 2002). Thus, there is growing interest in non-invasive technologies to diagnose and visualize CAD (Achenbach 2001). Different non-invasive imaging techniques have been evaluated in the past few years, and EBCT, MRI, and multi-slice spiral CT are currently under clinical investigation. Initial promising results with regard to the detection of coronary atherosclerosis have been reported for EBCT in that a large number of experimental and clinical studies demonstrated that this technique is useful to detect the presence of CAD by determining coronary calcifications (Erbel 2000, Rich 2002). In addition, EBCT was used to visualize the coronary arteries non-invasively. The results were encouraging, despite 25% non-assessable coronary segments (Achenbach 1998). Also, MRI coronary angiography was evaluated in a multi-center trial consisting of 109 patients. However, it is still in a state of clinical research, since analysis was restricted to proximal vessel segments only (84% with diagnostic image quality), and specificity in excluding coronary lesions was low (42%) (Kim 2001). Due to improvements in temporal and spatial resolution, multi-slice CT scanners can be used for the non-invasive visualization of human coronary arteries (Ohnesorge 2000, Kopp 2000). Promising results were reported for the first-generation with 4 detector slices (Nieman 2001, Achenbach 2001, Gerber 2002, Kopp 2002), and even better results for the second scanner generation with 16 detector slices. The non-assessability of a significant portion of coronary segments has been reported as the main limitation of 4-slice CT, whereas no coronary segments, not even distal segments or side branches, had to be excluded in a study comparing the results in 58 patients with conventional ICA (Nieman 2002b). In that study, a 95% sensitivity and an 86% specificity in the detection of coronary stenoses >50% were reported (Nieman 2002b). The very recent introduction of 64-slice CT has provided further enhancement of temporal and spatial resolution compared to 16-slice CT (Flohr 2004). This newest CT generation holds promise that very high accuracy in the detection of hemodynamically significant coronary lesions can be achieved also in patients with higher heart rates (Leschka 2005).

In the following, we present our experience with regard to the usefulness of multi-slice coronary CTA as a first- line imaging technique for further clinical decision-making in patients with known or suspected CAD and low to intermediate probability of a severe coronary lesion. The data are discussed with respect to a cohort of consecutive patients that were

examined with 4-slice and 16-slice CT technology between the years 2001 and 2003. Although newer CT technology has become available in the meantime, the conclusions that can be derived from these findings are still up to date and valid also for newer scanner generations. Remarks on potential improvements of clinical outcomes with the enhanced temporal and spatial resolution of newer 16- and 64-slice CT scanners are included in the respective sections.

7.5.2 Methods and Protocols

This section describes the results obtained for 136/142 (96%) consecutive patients who had been referred to the interdisciplinary Cardiac Imaging Outpatient Clinic of our institution to undergo non-invasive coronary angiography using multi-slice CT. Based on encouraging results of comparative studies with ICA (Kopp 2002), multi-slice CT examinations of the heart were already being performed at our institution in selected patients on a routine clinical basis, e.g., for the exclusion of CAD.

The initial contact with potential candidates was by telephone to evaluate the indication for coronary imaging. All patients were advised to consult an established cardiologist to perform further non-invasive examinations (e.g. exercise ECG, echocardiography, blood tests) and to evaluate the necessity of further diagnostics. All patients had to be referred by a cardiology and/or internal medicine specialist to get an appointment in our Cardiac Imaging Outpatient Clinic.

Multi-slice CT examinations were indicated in the presented study group of patients based on clinical suspicion of CAD or progression of CAD after PTCA or CABG-surgery because of chest pain and/or positive stress tests.

Cardiovascular risk factors had been evaluated by the referring doctors and were defined as follows: smoking, hyperlipidemia, hypertension, or diabetes mellitus. Positive stress tests were defined as examinations (exercise ECG, myocardial perfusion imaging) with pathological results as judged by the referring doctors.

7.5.2.1 Multi-slice CT Examination

Of the 136 multi-slice CT scans, 114 (84%) were performed using 4-slice CT and 22 (16%) with a 16-slice CT scanner. Routine protocols were used as mentioned elsewhere in this book. A native scan was performed to quantify coronary calcifications; a contrast-enhanced scan was done to assess the vessel wall and the coronary lumen (Fig. 7.32).

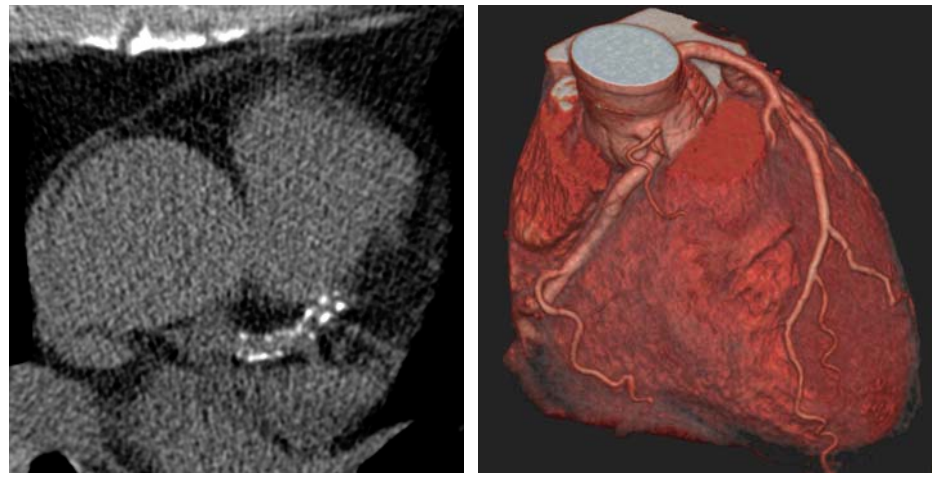

Fig. 7.32a,b. 16-slice CT examination of a patient with chest pain. **a** A non-contrast scan is performed prior to the contrast-enhanced study to evaluate the amount of calcification. **b** The contrast-enhanced study demonstrates no hemodynamically relevant stenosis, and no coronary catheterization was recommended

7.5.2.2 Interpretation of the Multi-slice CT Scans

Image quality was determined on contrast-media-enhanced axial slices for each coronary vessel segment. For segmentation of the coronary arterial tree, a modified AHA classification was used. A coronary segment was considered to have diagnostic image quality if it was visualized in its entire length, and if the vessel lumen was accurately distinguishable from the adjacent tissue.

Image quality of the multi-slice CT scans was graded as: 1, excellent; 2, good; 3, sufficient; 4, not diagnostic according to the number of assessable segments with diagnostic image quality (10–11 segments, excellent; 8–9 segments, good; 7–8 segments, diagnostic; <7 segments, not diagnostic).

7.5.2.3 Clinical Recommendations

Based on the clinical data and the multi-slice CT examination, the following recommendations were made:

Group I:
No coronary angiography recommended.

- Ia: No severe stenosis was detected on multi-slice CT scans, but the initiation of medical therapy (aspirin, lipid-lowering, β-blockade, ACE inhibitor, statin) was recommended.
- Ib: CAD was excluded by multi-slice CT (no calcified or non-calcified plaques detectable, Agatston score: 0).

Group II:
Coronary angiography recommended. Additionally, the initiation of medical therapy (aspirin, lipid-lowering, β-blockade, ACE inhibitor, statin) was recommended.

- IIa: Detection of a hemodynamically relevant lesion.
- IIb: Insufficient image quality or severe calcifications prohibiting accurate determination of lesion severity.

7.5.2.4 Clinical Follow-Up

Patients were interviewed by telephone to inquire about their further clinical course. The following topics were evaluated: (a) whether the referring doctors complied with the recommendation based on the multi-slice CT examinations; (b) the results of coronary angiographies, if performed; (c) the correspondence between coronary angiography and multi-slice CT results; (d) the patient's clinical symptoms (graded as: 1, better; 2, equal; 3 worse), quality of life (graded as: 1, better; 2 equal; 3 worse), and with the Cardiac Imaging Outpatient Clinic (graded as: 1,very satisfied; 2, satisfied; 3, not satisfied). Also, the medication was evaluated at follow-up.

7.5.3 Results in a Representative Patient Population

In the study group of 136 patients, the following cardiovascular risk factors and clinical characteristics were reported (Table 7.10).

7.5.3.1 Indication for Performing a Multi-Slice CT Scan of the Heart

Of the 136 patients, 95 (69.8%) patients had the clinical suspicion of CAD: due to the finding of angina in 83 (87.4%), and/or pathological exercise ECG in 29 (30.5%), and/or pathological myocardial perfusion imaging in two (2.1%), and/or pathologic intimal media thickness in 14 (14.7%).

Known CAD with suspicion of progression of disease was found in 24 (17.6%) of the 136 patients: due to the finding of angina in 16 (66.6%), and/or pathological exercise ECG in five (20.8%), and/or pathological myocardial perfusion imaging in one (4.2%).

Seventeen (12.5%) of the 136 patients had a CABG in their medical history. Of these, cardiac-CT was performed due to the finding of angina in 14 (82.4%), and/or pathological exercise ECG in four (23.5%), and/or pathological myocardial perfusion imaging in one (5.9%).

Table 7.10. Clinical characteristics in the study group. *SD* Standard deviation

	N (± SD)	%
Patient cohort	136 Patients (104 male, 32 female)	
Age (years)	60 ± 10	
Hypertension	103/136	75.6
Hyperlipidemia	98/136	72.1
Familiar predisposition	37/136	27.2
Smoking	24/136	17.6
Diabetes mellitus	19/136	13.9
β-blockade	47/136	34.6

7.5.3.2 Image Quality of Cardiac CT

Within the presented cohort of 136 patients, 40 scans were of excellent image quality, 27 were good, 60 had a diagnostic image quality, and nine were graded as not diagnostic. Of those nine scans, eight were 4-slice CT examinations but only one was a 16-slice CT examination. The main reasons for non-assessable coronary segments in the not diagnostic exams were the presence of severe calcification or motion artifacts.

7.5.3.3 Recommendations Based on Cardiac CT

Group I, for which ICA was not recommended, comprised 77 (56.6%) of the 136 patients:

- Ia: In 51 (37.5%) patients because no severe stenosis was detected.
- Ib: In 26 (19.1%) patients because of exclusion of CAD.

Group II, for which ICA was recommended, comprised 59 (43.4%) of the 136 patients:

- IIa: In 38 (27.9%) because of severe stenosis was detected.
- IIb: In 21 (15.4%) because of insufficient image quality (9/21) or severe calcifications prohibiting an accurate determination of lesion severity (12/21).

The severity of CAD in group I and group II was classified according to the multi-slice CT findings as follows:

- Ia: In 31 of the 51 patients, there were vessel wall alterations but no severe lesions: 1-vessel disease in seven patients, 2-vessel disease in two patients, and 3-vessel disease in 11 patients.
- Ib: CAD was excluded in all 26 patients.
- IIa: One-vessel disease was found in 18 of the 38 patients, five had 2-vessel disease, and 15 had 3-vessel disease.
- IIb: Not applicable.

The Agatston-scores in group I and group II were as follows:

- Ia: 151 ± 251
- Ib: 0
- IIa: 395 ± 945
- IIb: 1111 ± 1957

7.5.3.4 Follow-Up Results

Clinical follow-up was through a telephone interview in 136 of the 142 (96%) patients who had been examined in the Cardiac Imaging Outpatient Clinic. Of the remaining six (4%) patients who could not be contacted, two had died (1 patient because of esophageal carcinoma, 1 because of sudden death of unknown reason), one patient refused participation in the follow-up interview, and four patients could not be contacted because they had moved. Although ICA had been recommended based on the multi-slice CT results in 59 (43%) of the136 patients, it was actually performed in 27 (20%). The ICA findings corresponded to those obtained with multi-slice CT in 18 (67%) of these 27 patients. In two patients, false-negative multi-slice CT results became overt, and in seven patients false-positive results were revealed. The detailed follow-up results are summarized in Table 7.11.

7.5.3.5 Satisfaction, Symptoms, and Quality of Life at Follow-Up

Of the 136 patients, 58 (42%) reported improved clinical symptoms and 42 (31%) improved quality of life after multi-slice CT examination. Clinical

symptoms were unchanged in 86 (61%) patients and quality of life was unchanged in 91 (67%). Four (3%) patients reported aggravated clinical symptoms, and three (2.2%) reduced quality of life. The results are summarized in Table 7.12.

7.5.4 Discussion

The presented study demonstrates that multi-slice coronary CTA can be useful in selected patients with unclear chest pain to close the gap between non-invasive modalities and ICA in the diagnosis of CAD. The false-negative examinations obtained with 4-slice CT, while rare, still occur and thus limit wide clinical use of this technology. No false-negative examinations were reported in our study in the sub-group of patients examined with 16-slice CT, which indicates a higher clinical reliability of this technique. Further increased robustness can be expected with the introduction 64-slice CT with even better temporal and spatial resolution (Fig. 7.33).

7.5.4.1 Current Indications and Limitations of Multi-slice CT Coronary Angiography

Since multi-slice coronary CTA is, by nature, a purely diagnostic procedure, its application should be restricted to patients who have a low or inter-

Table 7.11. Clinical follow-up results according to telephone interviews focusing on the correspondence between the results of invasive coronary angiography (*ICA*) and multi-slice CT (*MSCT*)

Patient group	Group I (n = 77)		Group II (n = 59)	
Subgroup	Ia (n = 51)	Ib (n = 26)	IIa (n = 38)	IIb (n = 21)
ICA recommended	0	0	38	21
ICA performed	4	0	16	7
Corresponding results with MSCT	2	0	10	6
Non-corresponding results	2[a]	0	6[b]	1[b]

[a]False-negative results.
[b]False-positive results.

Table 7.12. Satisfaction, clinical symptoms and quality of life of the study group at follow-up

		Group I (n = 77)		Group II (n = 59)	
	Level	Ia (n = 51)	Ib (n = 26)	IIa (n = 38)	IIb (n = 21)
Symptoms[a]	1	18	13	12	5
	2	33	13	24	14
	3	0	0	2	2
Quality of life[b]	1	16	10	12	4
	2	35	16	25	15
	3	0	0	1	2
Satisfaction[c]	1	18	11	7	6
	2	32	14	28	14
	3	1	1	3	1

[a]Symptoms: *1* better, *2* equal, *3* worse.
[b]Quality of life: *1* better, *2* equal, *3* worse.
[c]Satisfaction: *1* very satisfied, *2* satisfied, *3* not satisfied.

mediate probability of hemodynamically relevant stenosis or to the clarification of coronary anomalies (Nieman 2002a). In addition, a further selection of patients suitable for multi-slice CT is advisable. With 4-slice and 16-slice CT scanners, patients with atrial fibrillation, stents, extreme obesity (body mass index >35 kg/m^2) or chronic obstructive pulmonary disease are not likely to profit from the examination, since a diagnostic image quality is uncertain (Gerber 2002). In patients with higher heart rates, 4-slice and 16-slice CT scanners cannot provide sufficient temporal resolution to assure diagnostic image quality. A reduction to <65 bpm by using β-blocker pre-medication has been recommended (Kopp 2001, Nieman 2002a, Schroeder 2002). The higher temporal and spatial resolution of the latest generation of 64-slice CT scanners in combination with increased X-ray power and reduced breath-hold times (Flohr 2004, Leschka 2005) may enable diagnostic image quality also in patients with a substantial degree of obesity, shortness of breath, higher heart rate, and stents.

Radiation exposure is still one of the methodological limitations of multi-slice CT, especially when compared with MRI. By using advanced tube-current modulation methods, exposure could be reduced by 50% to approximately 4–5 mSv (Jakobs 2002). With these techniques, the exposure is of the same order of magnitude as natural background radiation or as ICA for diagnostic purposes (Becker 1999).

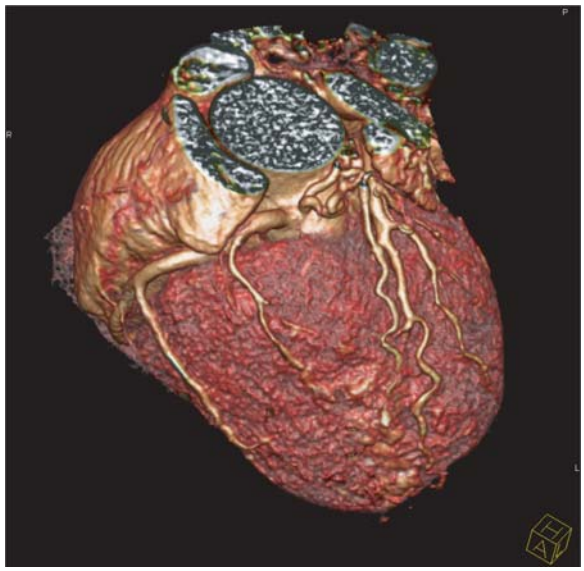

Fig. 7.33. 64-slice CT examination of a patient with chest pain. No β-blocker medication was used and the patient had a heart rate between 71 and 78 bpm during the scan. The entire coronary artery tree can be readily assessed despite the higher heart rate

7.5.4.2 Image Quality of Non-invasive Multi-slice CT Coronary Angiography

In this study, the majority of multi-slice CT scans were obtained using a 4-slice scanner. Image quality was sufficient to visualize a mean of 8.2 ± 2.7 out of 11 coronary segments (Table 7.11). Still, the number of false-negative (n = 2) and false positive (n = 7) multi-slice CT results compared with ICA was low. The two patients with false-negative results were examined with 4-slice CT and showed severe coronary calcifications (Agatston scores 470 and 1087, respectively) as determined on native scans. Severe coronary calcifications are known to limit the accurate determination of stenosis severity by 4-slice CT scanners (Kuettner 2002). It is evident that multi-slice coronary CTA is of limited use in patients with severe calcifications (Agatston score > 1000, calcium mass > 250 mg) when using 4-slice or 16-slice CT scanners. Based on its higher spatial resolution, the new 64-slice CT scanner generation has the potential to provide more accurate results also in patients with higher degrees of calcification (Nikolaou 2005).

7.5.4.3 Usefulness of Multi-slice CT as an Imaging Technique in Patients with Unclear Chest Pain

Multi-slice CT was found to be useful to evaluate the need for an ICA in the investigated cohort of patients. While 113of the 136 patients (83%) presented with chest pain, only 42 (31%) had positive stress tests, eight of which were in patients without clinical symptoms. However, all 136 patients desired further clarification by an imaging technique and were referred by established colleagues to our Car-

diac Imaging Outpatient Clinic. In the presented cohort, an ICA was performed in a minority of patients (27/136, 20%), and the recommendation of the Cardiac Imaging Outpatient Clinic was followed in a majority of patients (86/136, 71%), especially in group I patients, for whom ICA was not recommended. No coronary angiographies were performed in patients with exclusion of CAD (group Ib), and only in four patients without evidence of severe lesions (group Ia). In this latter group, ICA could thus be avoided in 73 of 77 (95%) of the patients.

The most important and reliable parameter indicating a successful revascularization procedures is clinical symptoms. In the presented cohort, almost a third of the patients reported improved clinical symptoms (58/136, 42%) and quality of life (42/136, 31%) at follow-up, despite no revascularization or significant change of medical therapy. In addition, 130/136 (96%) patients were satisfied with the Cardiac Imaging Outpatient Clinic and the opportunity of non-invasive coronary imaging. Furthermore, the use of multi-slice CT appears to reduce costs in this selected group of patients with unclear chest pain, as hospital stay can be shortened.

Multi-slice coronary CTA is a safe procedure. Complications occurred in only one patient, in whom there was extravasation of the contrast agent. The number of complications was low because patients with contraindications for iodated contrast agents were not examined.

7.5.4.4 Study Limitations

The majority of patients of our study group were investigated using 4-slice CT. Substantially improved reliability of results has been proven with 16-slice CT and, even better reliability with 64-slice CT technology (Flohr 2002, Heuschmid 2002, Nieman 2002b, Leschka 2005).Thus, further studies are needed to evaluate, whether also the excluded groups of patients with chest pain might profit from a multi-slice CT examination of the heart. The multi-slice CT scans in the presented cohort were performed using two scanner generations, both of which are useful to visualize the coronary arteries non-invasively (Nieman 2001, Kopp 2002, Nieman 2002b). The principal conclusions are valid for both scanner generations and can also be expanded to the newer 16-slice and 64-slice CT scanner technology. Our results underline that multi-slice CT warrants further attention in clinical cardiology.

7.5.5 Conclusions

Multi-slice CT is a new and evolving non-invasive technology to visualize the coronary arteries. It was found to be safe and reliable to detect or exclude the presence of quality-of-life-limiting CAD. Multi-slice CT appears to be useful as a first-line imaging technique in carefully selected patients to evaluate the need for ICA. While clinical reliability of 4-slice CT scanners is questionable in patients with higher heart rates, severe calcification, shortness of breath, and high body mass index, 16-slice CT and, even more so, 64-slice CT provide sufficient robustness to justify introducing multi-slice coronary CTA for patients with chest pain into clinical practice. Further studies with larger patient numbers and the use of later-generation scanner technology are required to underline the place of multi-slice CT in the diagnostic algorithm of CAD in patients with chest pain.

References

Achenbach S, Moshage W, Ropers D, Nossen J, Daniel WG (1998). Value of electron-beam computed tomography for the noninvasive detection of high-grade coronary-artery stenoses and occlusions [see comments]. N Engl J Med 339(27):1964–1971

Achenbach S, Daniel WG (2001). Noninvasive coronary angiography – an acceptable alternative? N.Engl.J Med 345(26):1909–1910

Achenbach S, Giesler T, Ropers D, Ulzheimer S, Derlien H, Schulte C et al (2001). Detection of coronary artery stenoses by contrast-enhanced, retrospectively electrocardiographically-gated, multislice spiral computed tomography. Circulation 103(21):2535–2538

Becker C, Schatzl M, Feist H, Bauml A, Schopf UJ, Michalski G et al (1999). Assessment of the effective dose for routine protocols in conventional CT, electron beam CT and coronary angiography. Fortschr Rontgenstr 170(1):99–104

Erbel R, Schmermund A, Mohlenkamp S, Sack S, Baumgart D (2000). Electron-beam computed tomography for detection of early signs of coronary arteriosclerosis. Eur Heart J 21(9):720–732

Flohr T, Bruder H, Stierstorfer K, Simon J, Schaller S, Ohnesorge B (2002). New technical developments in multislice CT, part 2: sub-millimeter 16-slice scanning and increased gantry rotation speed for cardiac imaging. Rofo Fortschr Geb Rontgenstr Neuen Bildgeb Verfahr. 174(8):1022–1027

Flohr T, Stierstorfer K, Raupach R, Ulzheimer S, Bruder H (2004). Performance evaluation of a 64-slice CT system with z-flying focal spot. RöFo 176:1803–1810

Gerber TC, Kuzo RS, Karstaedt N, Lane GE, Morin RL, Sheedy PF et al (2002). Current results and new developments of coronary angiography with use of contrast-enhanced computed tomography of the heart. Mayo Clin Proc 77(1):55–71

Heuschmid M, Kuttner A, Flohr T, Wildberger JE, Lell M, Kopp AF et al (2002). Visualization of coronary arteries in CT as assessed by a new 16 slice technology and reduced gantry rotation time: first experiences. Rofo Fortschr Geb Rontgenstr Neuen Bildgeb Verfahr 174(6):721–724

Jakobs TF, Becker CR, Ohnesorge B, Flohr T, Suess C, Schoepf UJ et al (2002). Multislice helical CT of the heart with retrospective ECG gating: reduction of radiation exposure by ECG-controlled tube current modulation. Eur Radiol. 12(5):1081–1086

Kim WY, Danias PG, Stuber M, Flamm SD, Plein S, Nagel E et al (2001). Coronary magnetic resonance angiography for the detection of coronary stenoses. N Engl J Med 345(26):1863–1869

Kopp AF, Ohnesorge B, Flohr T, Georg C, Schroder S, Kuttner A et al (2000). Cardiac multidetector-row CT: first clinical results of retrospectively ECG-gated spiral with optimized temporal and spatial resolution. Rofo Fortschr Geb Rontgenstr Neuen Bildgeb Verfahr. 172(5):429–435

Kopp AF, Schroeder S, Kuettner A, Heuschmid M, Georg C, Ohnesorge B et al (2001). Coronary arteries: retrospectively ECG-gated multi-detector row ct angiography with selective optimization of the image reconstruction window. Radiology 221(3):683–688

Kopp AF, Schroeder S, Kuettner A, Baumbach A, Georg C, Kuzo R, Ohnesorge B, et al (2002). Non-invasive coronary angiography with high resolution multidetector-row computed tomography. Results in 102 patients. Eur.Heart J. 23(21):1714–1725

Kuettner A, Rieger T, Brunn J, Burgstahler C, Heuschmid M, Trabold T et al (2002). Validität der Multidetektor-CT-Koronarangiographie unter Berücksichtigung des Agatston-Scores bei Patienten mit angiographisch nachgewiesener koronarer Herzerkrankung (KHK). Rofo Fortschr. Geb. Rontgenstr. Neuen Bildgeb.Verfahr. 174:S140 (V3.04)

Leschka S, Alkadhi H, Plass A, Desbiolles L, Gruenenfelder J, Marincek B, Wildermuth S (2005). Accuracy of MSCT coronary angiography with 64-slice technology: first experience. Eur Heart J 26

Mannebach H, Hamm C, Horstkotte D (2002). 18th report of performance statistics of heart catheterization laboratories in Germany. Results of a combined survey by the Committee of Clinical Cardiology and the Interventional Cardiology (for ESC) and Angiology Working Groups of the German Society of Cardiology-Cardiovascular Research for the year 2000. Z.Kardiol. 91(9):727–729

Nieman K, Oudkerk M, Rensing BJ, van Ooijen P, Munne A, van Geuns RJ et al (2001). Coronary angiography with multislice computed tomography. Lancet 357(9256):599–603

Nieman K, Rensing BJ, van Geuns RJ, Vos J, Pattynama PM, Krestin GP et al (2002a). Non-invasive coronary angiography with multislice spiral computed tomography: impact of heart rate. Heart 88(5):470–474

Nieman K, Cademartiri F, Lemos PA, Raaijmakers R, Pattynama PM, de Feyter PJ (2002b). Reliable noninvasive coronary angiography with fast submillimeter multislice spiral computed tomography. Circulation 106(16):2051–2054

Nikolaou K, Knez A, Rist C, Wintersperger B, Leber AW, von Ziegler F, Johnson T, Boekstegers P, Reiser MF, Becker CR (2005). 64-Slice computed tomography in the diagnosis of ischemic heart disease: patient-based vs. segment-based analysis. AJR 185

Ohnesorge B, Flohr T, Becker C, Kopp AF, Schoepf UJ, Baum U et al (2000). Cardiac imaging by means of electrocardiographically gated multisection spiral CT: initial experience. Radiology 217(2):564–571

Rich S, McLaughlin VV (2002). Detection of subclinical cardiovascular disease: the emerging role of electron beam computed tomography. Prev Med 34(1):1–10

Scanlon PJ, Faxon DP, Audet AM, Carabello B, Dehmer GJ, Eagle KA et al (1999). ACC/AHA guidelines for coronary angiography. A report of the American College of Cardiology/American Heart Association Task Force on Practice Guidelines (Committee on Coronary Angiography). Developed in collaboration with the Society for Cardiac Angiography and Interventions. J Am Coll.Cardiol 33(6):1756–824

Schroeder S, Kopp AF, Kuettner A, Burgstahler C, Herdeg C, Heuschmid M et al (2002). Influence of heart rate on vessel visibility in noninvasive coronary angiography using new multislice computed tomography. Experience in 94 patients. Clin Imaging 26(2):106–111

7.6 Evaluation of Coronary Artery Bypass Grafts

A. Küttner, A. Kopp

Contents

7.6.1 Clinical Background *232*
7.6.2 Protocol to Assess Graft Patency and Native Vessels with Multi-slice CT *233*
7.6.2.1 Regulation of Patient Heart Rate *233*
7.6.2.2 Assessment of Coronary Calcium Burden *233*
7.6.2.3 Measurement of Circulation Time and Diagnostic Scan *233*
7.6.2.4 Image Reconstruction *234*
7.6.2.5 Visualization Techniques *234*
7.6.3 Results in a Representative Patient Population *235*
7.6.4 Conclusion *237*
References *238*

7.6.1 Clinical Background

Coronary artery bypass grafting is one of the most common procedures for the treatment of symptomatic CAD. In excess of 570,000 procedures were carried out in 1999 in the US alone (Nieman 2003). Early follow-up studies on the treatment of CAD using CABG in Europe (European Coronary Surgery Study Group 1982) and in the USA (Cameron 1995) indicated that CABG resulted in significant short-term relief from the symptoms of CAD, as well as improved mortality rates in certain patient sub-groups. However, longer-term follow-up studies have demonstrated a significant recurrence of disease between 1 and 6 years following treatment. More than 20% of treated patients presented with chest pain within 1 year of CABG, a figure that rose to > 40% at 6 years post-treatment. Furthermore, up to 25% of grafts were found to be occluded within 5 years of CABG (Cameron 1995, Fitzgibbon 1996, Yusuf 1994). Relapse is thought to result either from reoccurrence and progression of disease in the native vessels or from de novo disease in the bypass graft, with venous grafts apparently proving to be more susceptible than arterial grafts to de novo synthesis (Loop 1986, Lytle 1985). Clearly then, one of the key issues for successful treatment management and securing improved mortality rates for symptomatic CAD patients is monitoring of graft patency and disease progression in both the distal run-off and the other native coronary arteries.

For the purposes of follow-up and monitoring, non-invasive techniques are preferable from both a patient care and cost perspective. MRI and CT are obvious candidates, and both have been used to successfully monitor graft patency (Kreitner 2004). However, limitations in these imaging technologies have previously hindered the follow-up of disease in the native coronary vessels distal to the grafts (Ropers 2001, Nieman 2003). The introduction, in 1998, of multi-slice CT scanners acquiring 4 slices per rotation revolutionized cardiac imaging, not only facilitating the assessment of graft patency (Ropers 2001, Froehner 2002) but also allowing visualization of the coronary arteries. Although early studies were hampered by relatively long acquisition times and associated prolonged breath-hold, motion artifacts at higher heart rates, and limited spatial resolution, cardiac CT imaging quickly became an important part of CAD diagnosis and follow-up. The next generation of 16-slice CT scanners, with faster gantry rotation times down to 0.37 s per rotation, became available in 2002. This scanner technology provided significant improvement of diagnostic cardiac imaging as it allowed visualization of smaller coronary vessels with improved resolution and volume coverage (Flohr 2002, Nieman 2002, Ropers 2003). A recent study by Schlosser et al. demonstrated that 16-slice CT allows for reliable differentiation between patent and occluded bypass grafts and an accurate detection of graft stenosis (Schlosser 2004). In a study of 51 patients, the authors found 96% sensitivity, 95% specificity, 81% positive predictive value, and 99% negative predictive value for the detection of significant stenosis in grafts compared to conventional coronary angiography. Spatial and temporal resolution has been further improved with the recent introduction of 64-slice CT scanners. Coronary bypass graft imaging can strongly benefit from this development,

as 64-slice CT scanners enable significantly faster volume coverage and reduced breath-hold times for the required larger scan ranges.

In this section, we discuss our approach to the assessment of bypass graft patency and diagnosis of the corresponding native cardiac vessels using the most recent 16-slice CT technology. Our conclusions and recommendations are based on the latest clinical studies and our own experience with a limited number of consecutively examined patients. Although 64-slice CT technology has since become available, the conclusions from our findings are also valid also for the newer scanner generations. Remarks on foreseeable improvements of clinical outcomes with the enhanced temporal resolution, spatial resolution, and volume coverage of 64-slice CT scanners and a report of preliminary clinical experience using the new technology for examinations of coronary bypass grafts are included in the respective sections.

7.6.2 Protocol to Assess Graft Patency and Native Vessels with Multi-slice CT

At our institution, a standardized work-flow is used for routine cardiac CT examinations. Prior to the CT exam, β-blockers are administered to regulate the patient's heart rate. A native scan is then performed to assess calcium burden, and the circulation rate is determined before administering IV contrast and starting the diagnostic scan. Images are then post-processed and the data reported. Here we describe the protocol developed at our institution to assess coronary bypass graft patency and native vessel disease using multi-slice CT. We present the results of a study in which a total of 43 bypass grafts in 13 patients were examined with 16-slice CT .All of the patients had previously undergone conventional angiography.

7.6.2.1 Regulation of Patient Heart Rate

In our experience, most patients with CABG present with a history of long-term β-blocker treatment for existing CAD. However, an additional β-blocker 45 min prior to the scan is recommended for all patients in order to stabilize heart rate during breath-hold. This also maximizes the benefits of the ECG-dependent dose modulation algorithm, which minimizes radiation exposure. Typically, 100 mg metroprolol p.o. 45 min prior to the scan is administered.

7.6.2.2 Assessment of Coronary Calcium Burden

A native scan (i.e., without contrast medium) was performed first in order to assess the calcium burden of the coronary vessels. All patients were scanned with a standardized protocol using retrospective ECG gating with 16 × 1.5-mm collimation, 3.0 mm slice-width, 133 mAs, 120 kV, and a table-feed of 3.8 mm/rotation in the craniocaudal direction.

7.6.2.3 Measurement of Circulation Time and Diagnostic Scan

To evaluate the circulation time, 20 ml of contrast media (at 4 ml/s, 400 mg iodine/ml) and a chaser bolus of 30 ml saline was administered into an antecubital vein. The correct scanning delay was established by measuring CT attenuation values in the ascending aorta, taking the last slice with maximum contrast as the circulation time. Alternatively, automated bolus detection can be used. The rationale for not applying an automated bolus detection system is based on subsequent difficulty of patient compliance with the breath-hold necessary for longer scan ranges and breath-hold times between 22 and 27 s. Using a dual-head power injector, 80 ml intravenous contrast agent plus a 20-ml chaser bolus was injected (50 ml at 4.0 ml/s followed by 30 ml at 2.5 ml/s). The CT scan was started at the diaphragm caudally and ended in the mid-ascending aorta cranial to all coronary ostia and the origin of all venous grafts. In our study, the contrast-enhanced scan was acquired with 16-slice CT using the following protocol: 16 × 0.75-mm collimation, 0.37-s rotation time, table-feed 3.8 mm/rotation, pitch 0.25, and 650 effective mAs at 120 kV tube voltage. The latest 64-slice CT scanners allow for faster volume coverage combined with faster rotation

times, down to 0.33 s, and higher spatial resolution with the acquisition of 0.6-mm slices. Owing to the larger detector coverage, the breath-hold time can be reduced to about 10–15 s depending on the scanner geometry used. ECG pulsing with reduced tube current during systole should be used whenever possible to minimize radiation exposure. It should not be used in patients with extra systoles and variable heart rate. In our study, ECG pulsing was used for all patients. Generally, we have found no need to adapt scanning protocols for cardiac imaging of patients with prior CABG procedure in comparison to those without bypass grafts. The key adaptation has been extension of the scan range to include the ascending aorta (Fig. 7.34). To date, there is no conclusive data as to whether the proximal part of internal mammary artery (IMA) grafts, including its origin from the subclavian artery, should be included in the scan range. Most centers prefer to limit the scan range to the proximal ascending aorta due to dose considerations.

7.6.2.4 Image Reconstruction

For image reconstruction, a standard reconstruction algorithm was used. Generally, the reconstruction window is set to start at 60% of the RR-interval for all native images and for contrast-enhanced scans. If coronary segments show motion artifacts, an additional test series, ranging from 20 to 75% relative to the RR-interval, in which single slices are reconstructed in 5% steps for a given z-position is recommended. The time point with the least motion artifacts is then chosen to reconstruct the entire stack of images of the multi-slice CT scan. With 16-slice CT, we typically use a slice thickness of 0.75–1.0 mm with an increment of 0.5–0.8 mm. With 64-slice CT, spatial resolution can be increased by the reconstruction of well-defined 0.6-mm slices with an increment of 0.4–0.5 mm. Independent of the number of slices, a medium-smooth reconstruction kernel should be used for optimized contrast-to-noise ratio in the axial slices (e.g., B25f on SOMATOM Sensation 16 or 64, Siemens Medical Solutions).

7.6.2.5 Visualization Techniques

Generally, advanced post-processing techniques, such as 3D VRT and curved MIPs are too time-consuming and often of limited use for diagnosis. However, bypass grafts, especially sequential grafts,

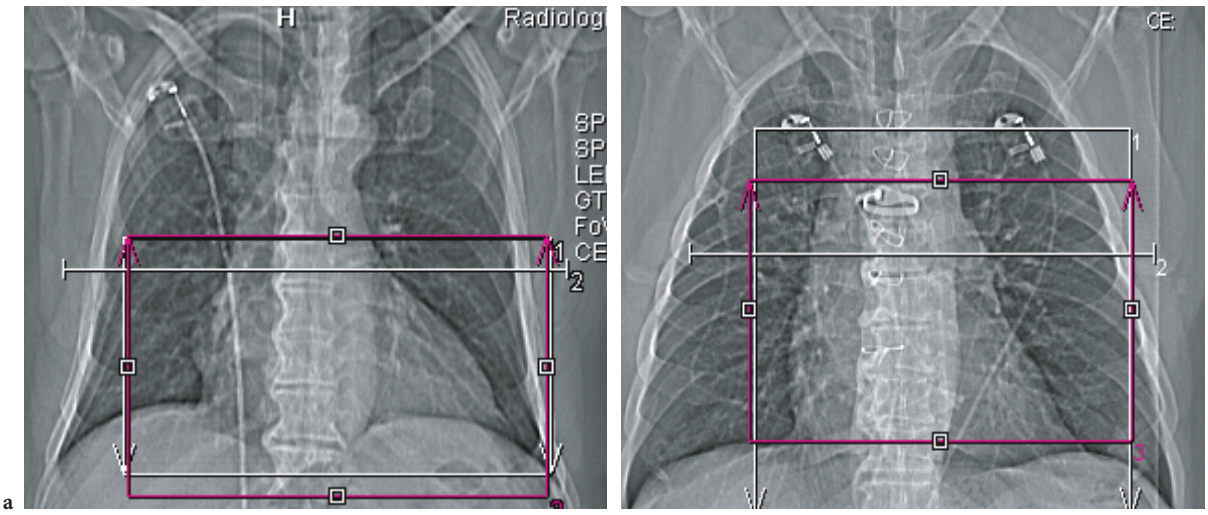

a b

Fig. 7.34a,b. Topograms displaying the scan ranges for examining a normal heart without bypasses (**a**) and a heart with bypass grafts (**b**). To examine bypass grafts, the scan range is extended to the middle of the aortic arch

are considerably tortuous and therefore difficult to visualize in a single plane. Thus, curved MIP has proven to be the most appropriate technique to assess the entire graft (Fig. 7.35–7.37). In general practice, information about the precise number of grafts and the exact location of distal anastomoses is often unavailable; thus, 3D volume rendering of the entire cardiac anatomy is helpful in many cases.

7.6.3 Results in a Representative Patient Population

In the considered patient cohort, 43 grafts from 13 patients who had also undergone conventional angiography were scanned using 16-slice CT and the above mentioned protocol. Of those 43 bypass grafts, 41 (95%) could be analyzed, including the

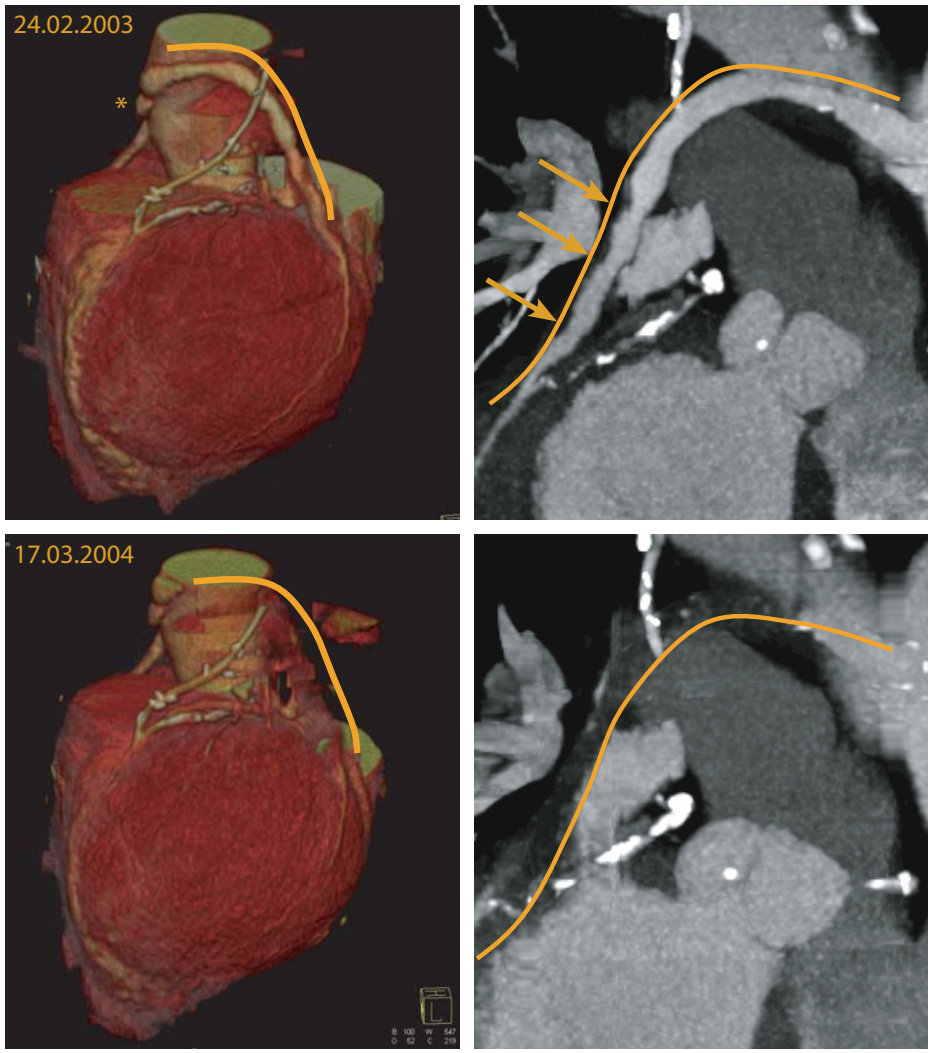

Fig. 7.35a–d. Patient examined with 16-slice CT with triple venous bypass grafts on the RCA, CX, and D1, and an additional internal mammary artery (*IMA*) graft on the LAD. Prior to the first scan in 2003 (**a** VRT, **b** curved MIP) a total occlusion of the venous graft on D1 was known (marked by *). All other grafts were fully patent. On the follow-up scan 1 year later, the large graft on the CX is also occluded (**c** VRT, d curved MIP). Orange lines indicate the original course of the occluded D1 venous graft (**a–d**). The first scan demonstrates non-calcified graft angiopathy (**b**, *arrows*)

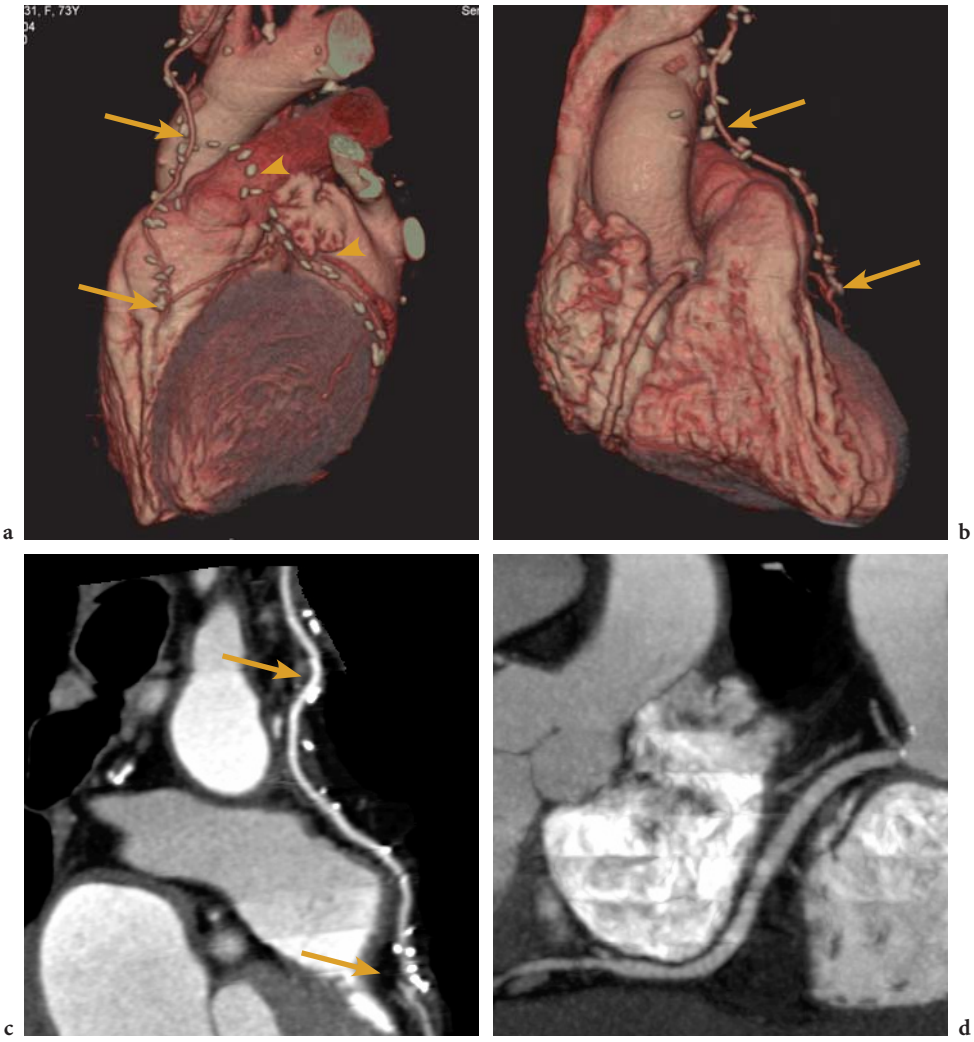

Fig. 7.36a–d. 16-slice CT examination of a 74-year-old female patient with CABG procedure with IMA graft onto the LAD and a radial artery graft onto the CX. No venous graft material was available due to venous stripping surgery for treatment of chronic venous insufficiency. The patient presented for a follow-up examination for the CABG procedure 6 months earlier. The IMA graft is patent with no signs of stenosis in its entire course (**a–c**, *arrows*), whereas the radial graft is totally occluded (**a**, *arrowheads*), a common complication for this particular graft type. The dominant RCA reveals no pathology (**b**, **d**)

native coronary vessel. Two IMA grafts could not be evaluated due to severe metal artifacts related to clips and/or the non-assessability of the distal anastomoses and the native coronary vessel. The remaining 11 IMA grafts and the 30 other grafts (28 venous grafts, 1 right IMA graft and 1 radial artery graft) could be correctly diagnosed regarding bypass patency, proximal and distal anastomosis, and distal run-off. According to conventional angiography results,16 of 43 (37%) grafts showed a significant stenosis (> 70%). All 16 of these grafts were also correctly diagnosed by multi-slice CT (sensitivity: 100%) (Figs. 7.35, 7.36). The two non-assessable grafts and the corresponding coronary vessels did not show significant stenosis in conventional angiography. One graft showed a 50% anastomosis stenosis in conventional angiography that was also detected by multi-slice CT. Of the 27 grafts without

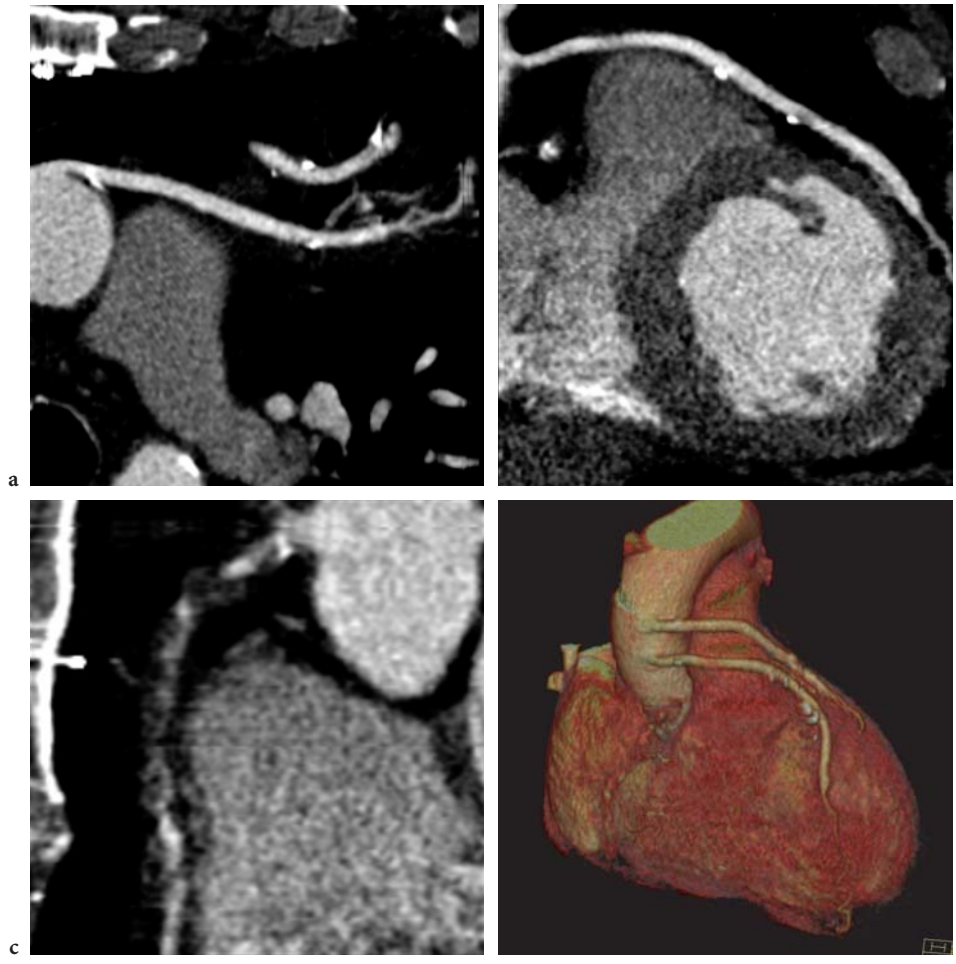

Fig. 7.37a–d. 16-slice CT examination of a 62-year-old patient with known 2-vessel-disease and prior CABG procedure, with two venous grafts on the LAD and first obtuse marginal branch (M1). The patient presented with angina under stress ECG. Both venous grafts are fully patent with an absence of stenosis in the proximal anastomoses, the bypass-graft itself, the distal anastomosis, and the distal run-offs. The use of curved MIP facilitates the diagnosis of LAD (**a**) and M1 (**b**) grafts. Reconstruction of the RCA in curved MIP (**c**) and VRT (**d**) reveals a total RCA occlusion, explaining the patient's symptoms

severe lesion, as assessed by conventional coronary angiography, 25 also showed no significant stenosis using multi-slice CT (specificity 93%, positive predictive value 89%, negative predictive value 100%) (Fig. 7.37). It can be expected that the number of non-assessable grafts will be further minimized and diagnostic accuracy increased using 64-slice CT scanners, which have higher temporal and spatial resolution and reduced breath-hold time compared to 16-slice CT (Fig. 7.38).

7.6.4 Conclusion

Our data demonstrate the excellent diagnostic quality of multi-slice CT technology when applied to the follow-up and evaluation of CABG treatment in symptomatic CAD patients. Multi-slice CT facilitates imaging of both graft and native vessels with unheralded detail, thereby allowing confident evaluation and diagnosis, which ultimately will lead

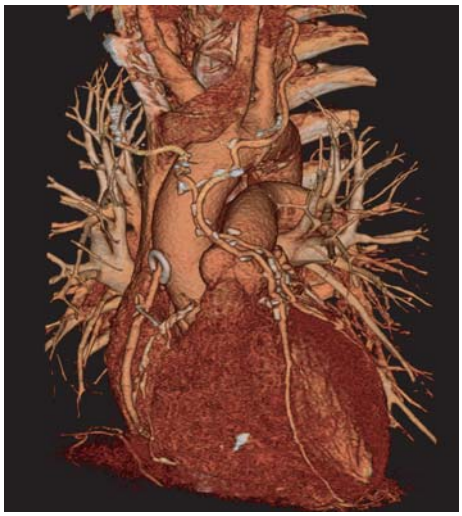

Fig. 7.38. 64-slice CT examination of a patient with 3-vessel-disease and prior CABG procedure with two IMA grafts onto the LAD and CX, and one venous graft onto the RCA. A scan range of 25 cm was selected so that the IMA grafts could be visualized over their entire course. Despite this long range. the scan could be completed in less than 20 s. Clip artifacts are minimal due to the higher spatial resolution with 64-slice CT. VRT demonstrates patency of all three grafts as well as the distal anastomoses and the run-off of the native vessels. (Case courtesy of Toyohashi Heart Center, Tokyo, Japan)

to more successful long-term disease management (Schlosser 2004). In addition, multi-slice CT may be useful in the planning process of new minimally invasive bypass graft surgery procedures (Herzog 2003, Begemann 2005). The new scanner generation, with up to 64 slices per rotation and faster gantry rotation time down to 0.33 s, further increases the clinical robustness of this technique.

References

Begemann PG, Arnold M, Detter C, et al (2005). Evaluation of retrospectively ecg-gated 4-row multi-detector CT in patients planned for minimal invasive coronary artery bypass grafting. Fortschr Röntgenstr RöFo 177:1084–1093

Cameron AA, Davis KB, Rogers WJ (1995). Recurrence of angina after coronary artery bypass surgery: predictors and prognosis (CASS Registry). Coronary Artery Surgery Study. J Am Coll Cardiol 26(4):895–899

European Coronary Surgery Study Group (1982). Long-term results of prospective randomised study of coronary artery bypass surgery in stable angina pectoris. Lancet 2(8309):1173–1180

Fitzgibbon GM, Kafka HP, Leach AJ, Keon WJ, Hooper GD, Burton JR (1996). Coronary bypass graft fate and patient outcome: angiographic follow-up of 5,065 grafts related to survival and reoperation in 1,388 patients during 25 years. J Am Coll Cardiol 28(3):616–626

Flohr T, Bruder H, Stierstorfer K, Simon J, Schaller S, Ohnesorge B (2002). New technical developments in multislice CT. Part 2: sub-millimeter 16-slice scanning and increased gantry rotation speed for cardiac imaging. Rofo Fortschr Geb Rontgenstr Neuen Bildgeb Verfahr 174(8):1022–1027

Froehner S, Wagner M, Schmitt R, et al (2002). Multislice CT of aortocoronary venous bypasses and mammary artery bypasses: evaluation of bypasses and their anastomoses. Roentgenpraxis 54:163–173

Herzog C, Dogan S, Diebold T, et al (2003). Multi-detector row CT versus coronary angiography: preoperative evaluation before totally endoscopic coronary artery bypass grafting. Radiology 229:200–208

Kreitner KF, Ehrhard K, Kunz RP, et al (2004). Non-invasive assessment of coronary artery bypass grafts – an update. Fortschr Röntgenstr RöFo 174:1079–1088

Loop FD, Lytle BW, Cosgrove DM, Stewart RW, Goormastic M, Williams GW, Golding LA, Gill CC, Taylor PC, Sheldon WC (1986). Influence of the internal-mammary-artery graft on 10-year survival and other cardiac events. N Engl J Med 314(1):1–6

Lytle BW, Loop FD, Cosgrove DM, Ratliff NB, Easley K, Taylor PC (1985). Long-term (5 to 12 years) serial studies of internal mammary artery and saphenous vein coronary bypass grafts. J Thorac Cardiovasc Surg 89(2):248–258

Nieman K, Cademartiri F, Lemos PA, Raaijmakers R, Pattynama PM, De Feyter PJ (2002). Reliable noninvasive coronary angiography with fast submillimeter multislice spiral computed tomography. Circulation 106(16):2051–2054

Nieman K, Pattynama PM, Rensing BJ, Van Geuns RJ, De Feyter PJ (2003). Evaluation of patients after coronary artery bypass surgery: CT angiographic assessment of grafts and coronary arteries. Radiology 229(3):749–756

Ropers D, Baum U, Pohle K, Anders K, Ulzheimer S, Ohnesorge B, Schlundt C, Bautz W, Daniel WG, Achenbach S (2003). Detection of coronary artery stenoses with thin-slice multi-detector row spiral computed tomography and multiplanar reconstruction. Circulation 107(5):664–666

Ropers D, Ulzheimer S, Wenkel E, Baum U, Giesler T, Derlien H, Moshage W, Bautz WA, Daniel WG, Kalender WA, Achenbach S (2001). Investigation of aortocoronary artery bypass grafts by multislice spiral computed tomography with electrocardiographic-gated image reconstruction. Am J Cardiol 88(7):792–795

Schlosser T, Konorza T, Hunold P, et al (2004). Noninvasive visualization of coronary artery bypass grafts using 16-detector row computed tomography. JACC 44(6): 1224–1229

Yusuf S, Zucker D, Peduzzi P, Fisher LD, Takaro T, Kennedy JW, Davis K, Killip T, Passamani E, Norris R (1994). Effect of coronary artery bypass graft surgery on survival: overview of 10-year results from randomised trials by the Coronary Artery Bypass Graft Surgery Trialists Collaboration. Lancet 344(8922):563–570

7.7 Patency Control of Coronary Stents

K. Nieman, N. Mollet, F. Cadamartiri, P. de Feyter

Contents

7.7.1 Introduction 239
7.7.2 CT Imaging Characteristics of Stents 239
7.7.3 Post-processing and Analysis 240
7.7.4 In Vivo Coronary Stent Imaging 241
7.7.5 Conclusion 242
References 244

7.7.1 Introduction

The use of percutaneous intervention (PCI) for the treatment of ischemic coronary artery disease has expanded dramatically over the last two decades. Initially, balloon angioplasty offered an alternative to bypass surgery in focal lesions, but it involved a considerable risk of acute dissection, thrombosis, or late coronary re-stenosis. Continuous technical innovation has expanded the indications for PCI and reduced both the procedural risk and the occurrence of post-procedural re-stenosis. Nowadays, most interventions involve intra-coronary expansion of stents. Still, until the introduction of coated stents, neointimal hyperplasia caused clinically significant re-stenosis in at least 20% of patients (Kiemeneij 2001). Although the occurrence of re-stenosis may be less in the future with increasing use of drug-eluting stents, the progression of atherosclerotic degeneration in the remaining coronary arteries is not affected (Morice 2002).

Multi-slice spiral CT allows minimally invasive angiographic imaging of the coronary arteries. The diagnostic accuracy to detect coronary stenoses is good (Nieman 2001, Achenbach 2001), particularly in the absence of extensive vascular calcification and in patients with low heart rates: The introduction of 16-slice and 64-slice CT scanners with sub-millimeter resolution have resulted in further improvements (Nieman 2002, Ropers 2003, Leschka 2005).

Patients who previously underwent PCI often developed recurrent symptoms due either to re-stenosis at the location of the previous obstruction or to progression of atherosclerosis at other sites. Post-PCI patients are more likely to require repeated angiographic coronary evaluation, so that a non-invasive technique would therefore be desired. Possible clinical indications for multi-slice coronary CTA could include suspected early occlusion of stents after the procedure, late in-stent restenosis, or progression of coronary artery disease in non-stented vessel segments.

7.7.2 CT Imaging Characteristics of Stents

Stents are small catheter-delivered expandable devices that maintain the lumen diameter after dilatation or restore endothelial integrity after vessel dissection. The devices are expected to sustain considerable inward radial force, while maintaining longitudinal flexibility. Most stents are laser-cut stainless steel meshes, of which recent designs include coating with a drug to prevent restenosis. Currently used stents have variable radiopacity, and consequently, variable visibility on conventional X-ray angiography.

Most stents are well-visible on CT images. The CT density of natural tissues in and around the coronary artery is much lower than the density of the metal stent material. Intravenous contrast enhancement used in multi-slice CT results in a lower concentration of contrast medium and in less X-ray attenuation of the intra-coronary lumen compared to conventional angiography with selective intra-coronary contrast injection. As a consequence, stents appear as bright structures on multi-slice CT images.

In vitro sub-millimeter multi-slice CT imaging of static coronary stents (Nieman 2003) has shown that the stent struts appear significantly larger than their actual size (Fig. 7.39). A combination of partial voluming caused by the limited spatial resolution in relation to the diameter of the stent struts, beam hardening artifacts, and a slightly widened slice-sensitivity profile related to spiral scanning are likely

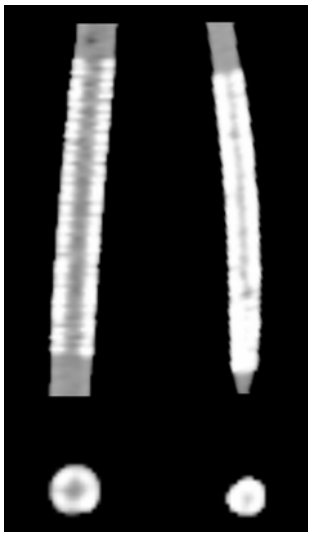

Fig. 7.39. In vitro imaging (4-slice CT, 0.5-mm detector collimation) of stents in contrast-enhanced silicon tubes: Synthesis Star 4.0 and 3.0 mm (CardioVascular Dynamics, Irvine, USA). While the magnitude of the blooming effect seems similar in both stents, only a very limited area of relatively artifact-free lumen remains in the 3.0-mm stent

responsible for this blooming effect, or increased CT density outside the actual location of the stent itself. As a result the coronary lumen within the stent has a higher density that extends from the vessel wall and decreases towards the center. Depending on the size of the vessel and the metal density of the stent, depiction of a variable central part of the vessel will remain unaffected by the stent-related artifacts (Fig. 7.39). Particularly small radiopaque stents (3.0-mm diameter) result in a density increment throughout the lumen (Nieman 2003). In general, stent-related artifacts and visualization of the in-stent lumen strongly varies with different stent types, depending on stent diameter, caliber of the stent struts, and stent material (Maintz 2003a). Use of the thinner slice-collimation available with the newer 16-slice and 64-slice CT scanners in combination with special edge-preserving reconstruction kernels for higher in-plane resolution improves visualization of the in-stent lumen (Maintz 2003a, Maintz 2003b).

7.7.3 Post-processing and Analysis

Various post-processing techniques exist for evaluation of CT coronary angiograms, including MPR, thin-slab MIP, curved reformations, various 3D reconstructions such as shaded-surface display (SSD), VRT, and virtual endoscopy. Cross-sectional images, either the axial source images or (curved) MPRs, are best-suited for evaluation of the coronary lumen within the stent. The anatomical location of stents can be nicely visualized with VRT (Fig. 7.40). When evaluating a stented coronary artery, the exaggerated stent appearance, and consequently the decreased lumen diameter, need to be taken into account and do not necessarily imply in-stent restenosis (Fig. 7.41). Complete or near-complete stent obstruction will become clear by an overall density that is lower than that of the other coronary segments (Fig. 7.42). Visualization of tissue within the stent without significant obstruction requires the highest possible resolution, beyond the capabilities of 4- and 16-slice CT scanners. The latest 64-slice CT scanners, however, with spatial resolution below

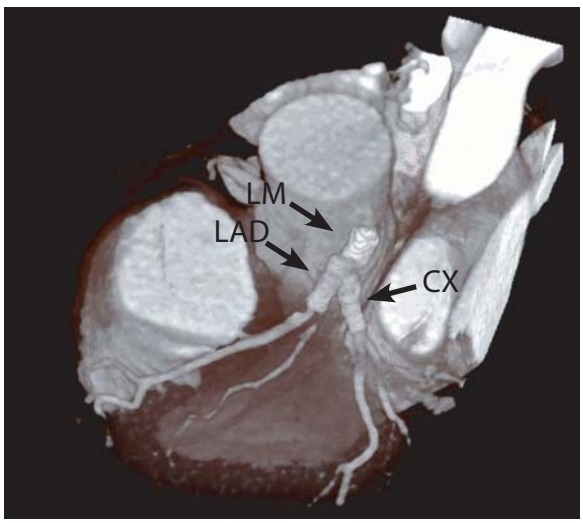

Fig. 7.40. Three-dimensionally reconstructed CT angiogram (4-slice CT with 1.0-mm detector collimation) of a patient with three stents in the *LM*, *LAD*, and *CX*

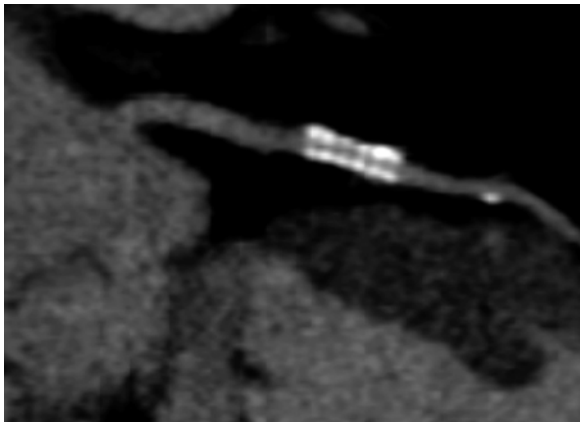

Fig. 7.41. A 3.0-mm diameter stent in the LAD, imaged with contrast-enhanced 16-slice CT. Visualization of the in-stent lumen is compromised due to blooming artifacts

0.4 mm, may provide sufficient resolution to also visualize mild and moderate in-stent stenosis.

More advanced post-processing techniques are less suitable for the evaluation of coronary stents. External 3D display does generally not show the intra-coronary lumen. Adjustment of the display settings to correct for the presence of the stent and particularly the stent-related artifacts is not readily done and does not substantially improve interpretation. MIP of thin slabs is a useful method for initial evaluation of the coronary arteries, but the high density value of the stent material leads to further over-projection and precludes assessment of the coronary lumen. Therefore, curved MPR and cross-sectional MPR perpendicular to the vessel lumen are the most useful techniques for visualizing the in-stent lumen.

7.7.4 In Vivo Coronary Stent Imaging

While the feasibility and diagnostic accuracy of detection of obstructive coronary disease by multislice CT imaging has been described extensively, the usefulness of this approach in patients who have undergone coronary intervention and subsequent stent placement has only been evaluated in preliminary and small studies. EBCT has been used in CTA after balloon angioplasty, but nowadays few patients undergo PCI without implantation of stents (Achenbach 1997).

In-vivo imaging of coronary stents requires scan protocols that are optimized for spatial resolution. As in imaging of the native coronary vessels, imaging of coronary stents is influenced by cardiac motion, depending on the heart rate and the location of the

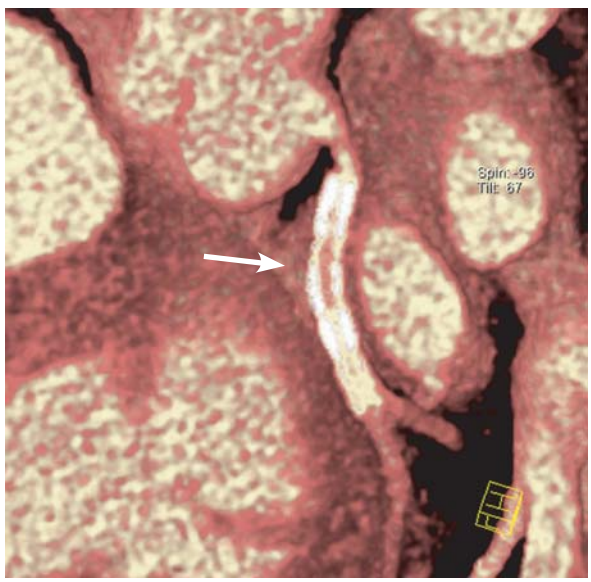

a

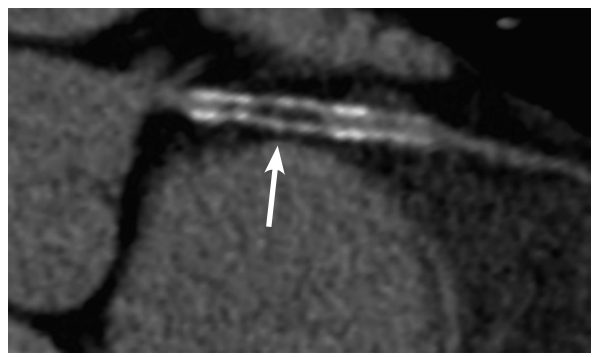

b

Fig. 7.42a,b. Occluded stent in the CX coronary artery examined with 16-slice CT using clipped 3D reconstruction (**a**) and curved MPR (**b**). The low-density material (arrow) represents the occlusion in the mid-section of the stent

stent, and by the presence of calcified plaque material in the vessel wall. Because a blooming artifact depends on the spatial resolution in relation to the vessel diameter, the effect on smaller stented vessels is greater.

While 4-slice CT cannot reliably visualize stented coronary vessels and in-stent lumen, 16-slice CT combined with a sufficiently slow heart rate can provide a reasonably good assessment of coronary artery segments with stents (Fig. 7.43). Although no large comparative studies have been published, there seems to be consensus about the ability of 16-slice CT to accurately assess stent patency and to recognize complete stent occlusion (Hong 2003). Hong et al. investigated 19 patients with 16-slice CT to follow-up and confirm stent patency 1–3 weeks after stent placement. A total of 26 stents were investigated with different reconstruction techniques and stented lumen diameters were measured. Five patients had heart rates of more than 70 bpm during the scan and the six stents could not be reliably assessed due to motion artifacts. In the remaining 20 stents, stent patency was accurately determined. The use of a special reconstruction kernel resulted in improved accuracy of the delineation of the in-stent lumen diameter and of the diameter of the vessel lumen proximal and distal to the stent. In contrast to the assessment of coronary arteries without stents, the detection of moderate stenosis in stented coronary vessels with 16-slice CT is regarded as less reliable, due to blooming artifacts that cover the tissue and the lumen near the stent struts. Blooming artifacts also limit qualitative interpretation of the plaque material within the stent. As a result, the role of 16-slice CTA after PCI is limited to the detection of disease progression in the coronary segments without stents, detection of stenosis near the edges of the stent, assessment of stent patency, and detection of in-stent occlusion and perhaps high-grade stenosis.

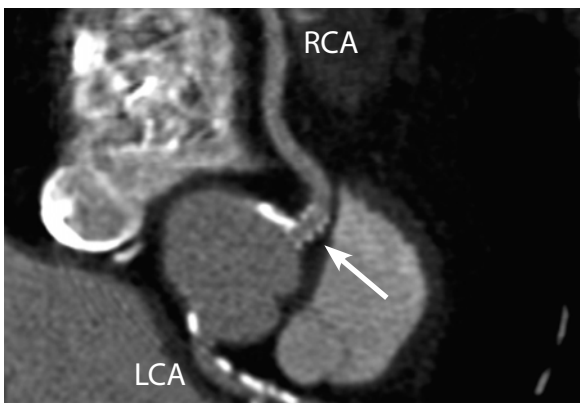

Fig. 7.43. Low-opaque stent (arrow) in the ostium of the *RCA*, visualized with curved MPR. There is practically unhindered interpretability of the vessel lumen, which was imaged with 16-slice CT. *LCA* Left coronary artery

Better stent visualization has become possible with further improvement of the spatial resolution with 64-slice CT by implementation of thinner detector slices combined with a flying focal spot sampling technique in the z-direction (Figs. 7.44, 7.45). Dedicated image reconstruction and post-processing techniques have been developed to further reduce stent-related image artifacts and more accurately depict the coronary lumen adjacent to the stent. In a very recent study, Rist et al. used 64-slice CT to examine 44 stented coronary arteries in 23 patients. The authors evaluated the detection accuracy of significant pre-stent, in-stent, and post-stent stenosis compared to conventional angiography (Rist 2005). Conventional angiography revealed four pre-stent, five in-stent, and three post-stent stenoses with >50% lumen narrowing in the 44 stented segments. With 64-slice coronary CTA, the sensitivity for pre-stent stenosis was 75%, the specificity 95%, NPV 97%, and PPV 60%; for in-stent stenosis, sensitivity was 80%, specificity 97%, NPV 95%, and PPV 75%; for post-stent stenosis, sensitivity was 67%, specificity 85%, NPV 97%, and PPV 25%. The high specificity and high NPV suggest that 64-slice CT with improved spatial resolution can rule-out significant coronary stenosis also in stented vessels.

Stent manufacturers have introduced stents with thinner struts and less radiopaque material. In particular, the latest-generation drug-eluting stents are usually less radiopaque than conventional stents. These newer stents improve multi-slice CT evaluations in that blooming artifacts are largely reduced (Fig. 7.46).

7.7.5 Conclusion

While the diagnostic accuracy of coronary CTA in non-stented vessels has reached the stage of clinical applicability, the use of multi-slice CT after coro-

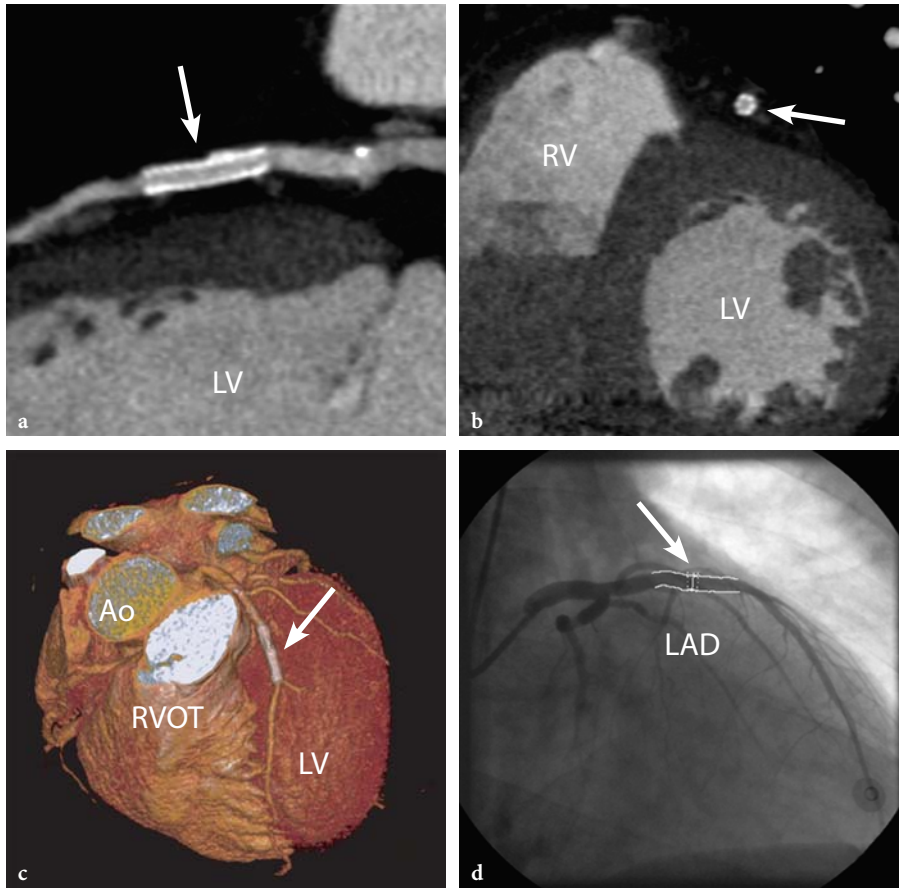

Fig. 7.44a–d. Patent stent in the LAD, examined with 64-slice CT. Curved MPR (**a**) and cross-sectional MPR (**b**) reveals a patent lumen without the presence of stenosis. VRT reconstruction demonstrates the run-off of the native vessel (**c**). Conventional angiography confirms the 64-slice CT findings (**d**). (Case courtesy of Grosshadern Clinic, University of Munich, Germany)

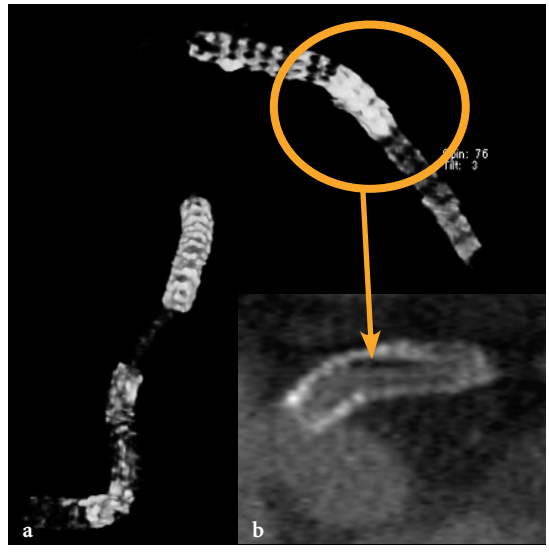

Fig. 7.45a,b. 64-slice CT examination of a patient with long extending stents of the LAD and RCA. VRT reconstruction with a special setting to mimic radiography demonstrates the stents and the strut structure (**a**). Curved MPR reveals a moderate in-stent restenosis in the LAD stent (**b**). (Case courtesy of Toyohashi Heart Center, Tokyo, Japan)

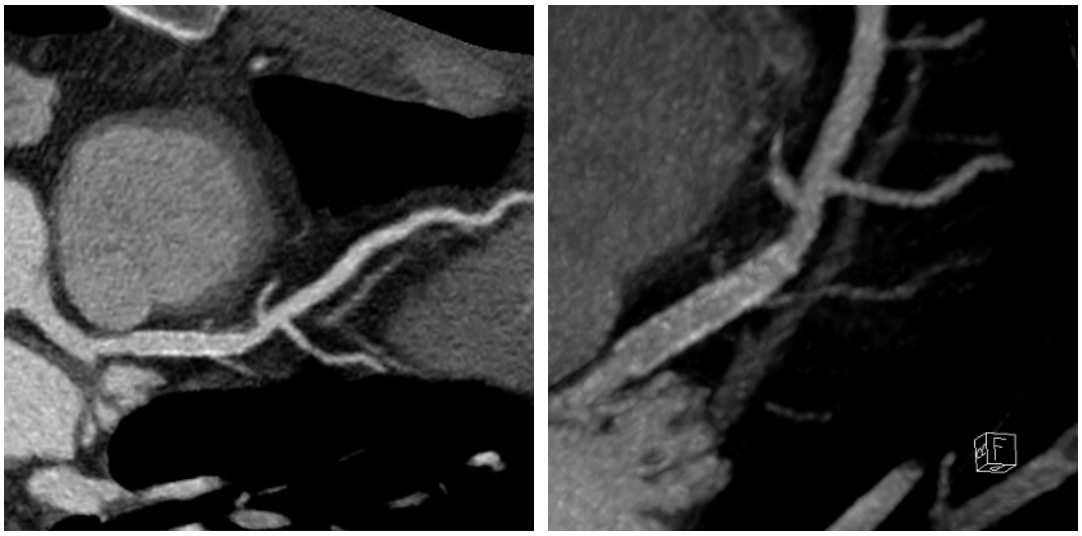

a b

Fig. 7.46a,b. 64-slice CT examination of a patient after placement of a drug-eluting stent in the proximal LAD. The low-opaque stent can be visualized with curved MPR (**a**) and curved MIP (**b**), with practically unhindered interpretability of the patent vessel lumen. (Case courtesy of Sarawak Heart Center, Kuching, Malaysia)

nary intervention with stent placement is still challenging. With 16-slice CT scanners, assessment is restricted to determining stent patency and total stent occlusion; however, the latest 64-slice CT scanners holds promise to enable significant stenosis of stented coronary segments to be reliably excluded.

References

Achenbach S, Moshage W, Bachmann K. Detection of high-grade restenosis after PTCA using contrast-enhanced electron beam CT (1997). Circulation 96: 2785–2788

Achenbach S, Giesler T, Ropers D, et al (2001). Detection of coronary artery stenoses by contrast-enhanced, retrospectively electrocardiographically-gated, multislice spiral computed tomography. Circulation 103: 2535–2538

Hong C, Chrysant GS, Woodard PK, Bae KT (2004). Coronary artery stent patency assessed with in-stent contrast enhancement measured at multi-detector row CT angiography: initial experience. Radiology 233:286–291

Kiemeneij F, Serruys PW, Macaya C, et al (2001). Continued benefit of coronary stenting versus balloon angioplasty: five-year clinical follow-up of Benestent-I trial. J Am Coll Cardiol 37: 1598–603

Leschka S, Alkadhi H, Plass A, Desbiolles L, Gruenenfelder J, Marincek B, Wildermuth S (2005). Accuracy of MSCT coronary angiography with 64-slice technology: first experience. European Heart Journal 26

Maintz D, Juergens KU, Wichter T, Grude M, Heindel W, Fischbach R (2003a). Imaging of coronary artery stents using multislice computed tomography: in vitro evaluation. Eur Radiol 13:830–835

Maintz D, Seifarth H, Flohr T, Kraemer S, Wichter T, Heindel W, Fischbach R (2003b). Improved coronary artery stent visualization and in-stent stenosis detection using 16-slice computed-tomography and dedicated image reconstruction technique. Invest Radiol 38: 790–795

Morice MC, Serruys PW, Sousa JE, et al (2002). A randomized comparison of a sirolimus-eluting stent with a standard stent for coronary revascularization. N Engl J Med. 346: 1773–1780

Nieman K, Oudkerk M, Rensing BJ, et al (2001). Coronary angiography with multi-slice computed tomography. Lancet 357: 599–603

Nieman K, Cademartiri F, Lemos PA, et al (2002). Reliable noninvasive coronary angiography with fast submillimeter multislice spiral computed tomography. Circulation 106: 2051–2054

Nieman K, Cademartiri F, Raaijmakers R, Pattynama P, de Feyter P (2003). Noninvasive angiographic evaluation of coronary stents with multi-slice spiral computed tomography. Herz 28: 136–142

Rist C, Ziegler F, Nikolaou K, Wintersperger BJ, Johnson T, Reeder SB, Busch S, Knez A, Boekstegers P, Reiser MF, Becker CR (2006). Assessment of coronary artery stent patency and restenosis using 64-slice computed tomography. Eu Radiol (in press)

Ropers D, Baum U, Pohle K, et al (2003). Detection of coronary artery stenoses with thin-slice multi-detector row spiral computed tomography and multiplanar reconstruction. Circulation 107: 664–666

7.8 Evaluation of the Coronary Anomaly, Fistula, Aneurysm, and Dissection

S. Fröhner

Contents

7.8.1 Introduction *245*
7.8.2 Anomalies of the Coronary Arteries *245*
7.8.3 Coronary Artery Fistulas *246*
7.8.4 Myocardial Bridges *251*
7.8.5 Coronary Aneurysms *254*
7.8.6 Coronary Dissection *254*
7.8.7 Coronary Vasculitis *256*
7.8.8 Conclusion *256*
References *256*

7.8.1 Introduction

Non-atherosclerotic lesions of the coronary arteries present as a manifold and heterogeneous spectrum with different clinical relevance and distinguishing congenital and acquired forms. The acquired non-atherosclerotic diseases of the coronary arteries have different causes. They can develop over a long time and remain clinically inconspicuous, or they can result in life-endangering acute clinical symptoms. Catheter angiography is not able to demonstrate all of these anomalies in detail, especially complex anomalous courses, because selective probing and subsequent interpretation of vessel anatomy is difficult and the angiographer is not aware of an atypical location of the vessel orifice.

Multi-slice CT, in particular the newly available 16- and 64-slice CT scanners with their ability to generate nearly isotropic voxels, represent a highly promising tool to visualize coronary arteries with respect to their origin and course. MPR, thin MIP, SSD, and VRT allow for accurate visualization of the coronary arteries, including the detection and characterization of anomalies of the coronary artery system.

7.8.2 Anomalies of the Coronary Arteries

Coronary artery anomalies constitute 1–3% of all congenital malformations of the heart. In approximately 0.46–1% of the normal population, anomalies of the coronary arteries are found incidentally during catheter angiography or autopsy.

The etiology of coronary artery anomalies is still uncertain. Maternal transmission of some types has been suggested, particularly when only a single coronary artery is involved. Familial clustering is also reported for one of the most common anomalies, in which the left circumflex coronary artery (CX) originates from the right sinus of Valsalva. Anomalies of the coronary arteries may also be associated with Klinefelter's syndrome and trisomy 18 (i.e., Edwards syndrome). Cardiac causes for early and sudden infant death include anomalies of the coronary arteries; the Bland-White-Garland-Syndrome may be one relevant cause. Anomalies of the coronary arteries found in children may be associated with other congenital anomalies of the heart like Fallot's syndrome, transposition of the great arteries, Taussig-Bing heart (double-outlet right ventricle), or common arterial trunk.

The normal anatomy (Fig. 7.47) of the coronary arteries is well-known. The left main coronary artery (LMA) arises from the left sinus of Valsalva (LSV) and bifurcates into the left anterior descending (LAD) and CX. The right coronary artery (RCA) originates from the right sinus of Valsalva (RSV).

Anomalies of the coronary arteries can concern their origin, course, and aberrant distal branches.

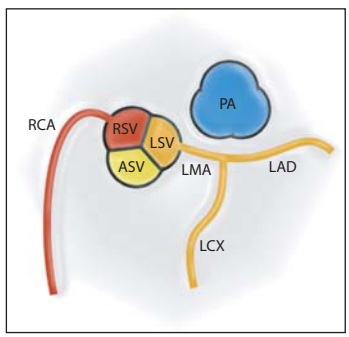

Fig. 7.47. The normal anatomy of the coronary arteries

Common variants are anomalies with origin from the contralateral side of the aortic bulb. These include an origin of the LMA or the LAD from the RSV or the proximal RCA and an origin of the RCA from the LSV or the LMA. There are four possible pathways for these aberrant vessels to cross over to their regular peripheral locations: (1) "anterior course" ventral to the pulmonary trunk or the right ventricular outflow tract, (2) "interarterial course" between the pulmonary artery and aorta, (3) "septal course" through the interventricular septum, and (4)"retro-aortic course". Clinically, course anomalies of the coronary arteries are subdivided into "malignant" and "non-malignant" forms. Malignant forms are associated with an increased risk of myocardial ischemia or sudden death and mostly show a course between the pulmonary artery and aorta (i.e., "interarterial"). The most common case is an origin of the RCA from the LSV that courses between the aortic bulb and the pulmonary artery. Anomalies of the LMA or the LAD arising from the RSV with a similar course are associated with higher cardiac risk, too. It is suggested that myocardial ischemia and sudden death result from transient occlusion of the aberrant coronary artery, due to an increase of blood flow through the aorta and pulmonary artery during exercise or stress. The reason is either a kink at the sharp leftward or rightward bend at the vessel's ostium or a pinch-cock mechanism between the aorta and pulmonary artery. Up to 30% of such patients are at risk for sudden death. Courses of anomalously long coronary arteries ventral to the pulmonary artery may be associated with a higher risk of myocardial ischemia. Dilatation of the pulmonary trunk in pulmonary hypertension can lead to a stretching mechanism of the aberrant vessel that causes lumen reduction and consecutive myocardial ischemia.

An origin of the left (or right) coronary artery from the pulmonary artery (Bland-White-Garland-Syndrome for the left coronary artery) has to be considered as malignant. The LMA arises from the left or posterior aspect of the pulmonary trunk immediately above a pulmonary sinus of Valsalva. If collaterals are well-developed, the RCA and its major branches are dilated and tortuous. This anomaly is frequently associated with myocardial ischemia and sudden death in early childhood. Clinically silent forms can also be found. The aberrant coronary artery is mostly fed by collaterals from the other coronary arteries. Early detection is mandatory for successful and surgical intervention, which is absolutely required. Other courses do not lead to clinical symptoms, but are incidental findings in catheter angiography, CT of the coronary arteries, or autopsy. In case of planned cardiac surgery, these anomalies nevertheless acquire increasing importance in order to avoid being endangered by accidental surgical injuries, for example, a retro-aortic course of the CX in mitral valve surgery. Therefore, every anomaly of origin and course of the coronary arteries should be described accurately prior to cardiac surgery. If catheter angiography does not provide detailed information, multi-slice CT should be performed to depict the exact courses of aberrant coronary vessels. Finally, aberrant coronary arteries have been discussed to carry a higher risk of arteriosclerosis, in particular a retro-aortic-coursing CX. Thus, careful attention must be paid to these vessels in patients with atypical chest pain or pathological ECG findings.

The following figures are a diagrammatic collection of the most important and frequent coronary anomalies for the LMA (Fig. 7.48), LAD (Fig. 7.49), CX (Fig. 7.50), RCA (Fig. 7.51), and other complex anomalies (Fig. 7.52). The exclamation mark in the figure indicates a malignant anomaly. Coronary anomalies can be reliably identified with 16-slice CT and 64-slice CT, as demonstrated by the case examples given in Figures 7.53–7.57.

7.8.3 Coronary Artery Fistulas

Coronary artery fistulas are a rare condition representing arteriovenous communications between one or several coronary arteries and the right heart chambers (right atrium, right ventricle, 65%) or central veins (superior or inferior vena cava, coronary sinus, or pulmonary artery, 17%). The hemodynamics resemble those of an extracardiac left-to-right shunt.

In many cases, the amount of blood flow through the coronary fistula is small. Other cases represent "high-flow" coronary fistulas with diminished per-

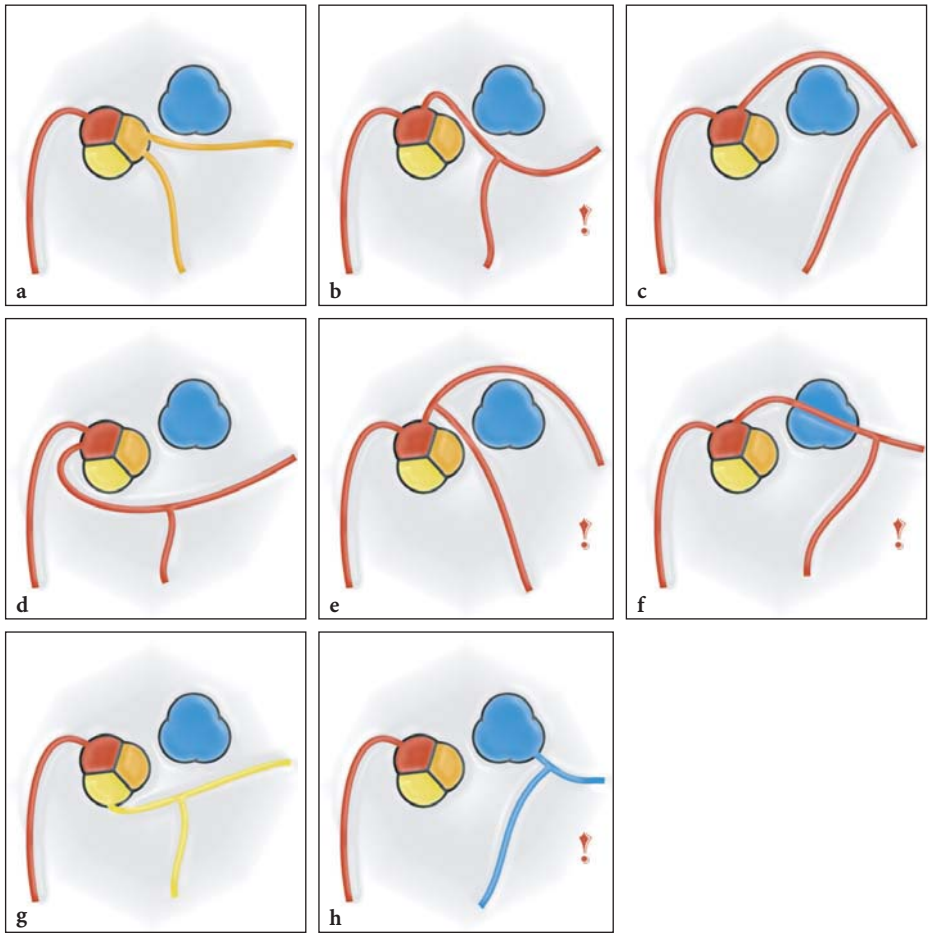

Fig. 7.48a–h. Possible anomalies of the left main coronary artery (LMA). **a** Separate ostia of the LAD and LCx from the left sinus of Valsalva; no clinical relevance. **b** Origin of the LMA from the right sinus of Valsalva, interarterial course; "malignant". **c** Origin of the LMA from the right sinus of Valsalva, anterior course; no clinical relevance. **d** Origin of the LMA from the right sinus of Valsalva, retro-aortic course; no clinical relevance. **e** Origin of the LMA from the right sinus of Valsalva, anterior course of the LAD, interarterial course of the CX; "malignant". **f** Origin of the LMA from the right sinus of Valsalva, septal course; "malignant". **g** Origin of the LMA from the coronary sinus of Valsalva, no clinical relevance. **h** "Bland-White-Garland-Syndrome", origin of the LMA from the pulmonary artery; "malignant"

fusion of the portion of the myocardium supplied by the arterial feeder of the fistula. A so-called hemodynamic steal phenomenon may occur. In high-flow fistulas, the feeding coronary artery is dilated and often tortuous. Focal saccular aneurysms may develop, which eventually can become calcified and/or thrombosed; aneurysm ruptures have also been reported. Up to 50% of such fistulas arise from the RCA.

The anatomy of coronary artery fistulas can range from abstruse courses up to a spider-like configuration and they can arise from more than one coronary artery. Numerous communications between the coronary artery and the terminating localization can rule out the need for surgical correction. Pediatric patients tend to be especially symptomatic and may present with atypical and typical chest pain and myocardial ischemia associated with ECG alter-

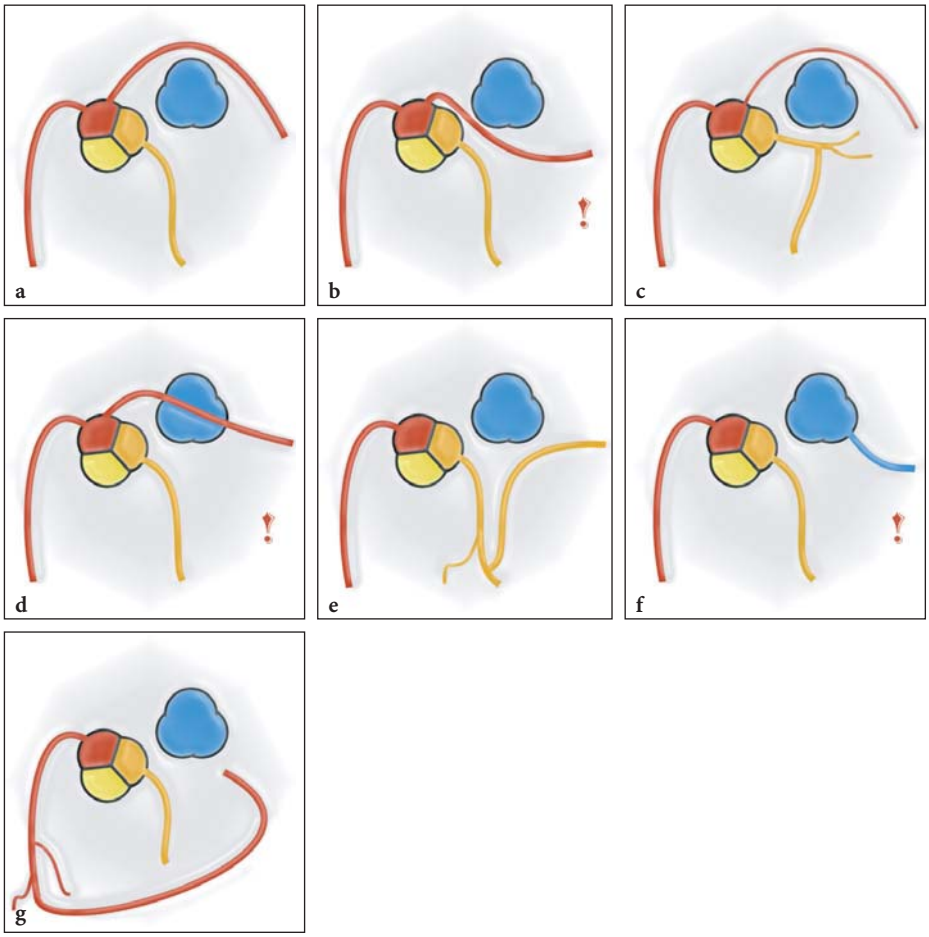

Fig. 7.49a–g. Possible anomalies of the LAD. **a** Origin of the LAD from the right sinus of Valsalva, anterior course; no clinical relevance. **b** Origin of the LAD from the right sinus of Valsalva, interarterial course; "malignant". **c** Origin of distal branches of the LAD from the right sinus of Valsalva, anterior course; no clinical relevance. **d** Origin of the LAD from the right sinus of Valsalva, septal course; "malignant". **e** Origin of the LAD from branches of the CX; no clinical relevance. **f** "Bland-White-Garland-Syndrome" of the LAD, origin from the pulmonary artery; "malignant". **g** Origin of the LAD from the distal RCA; no clinical relevance

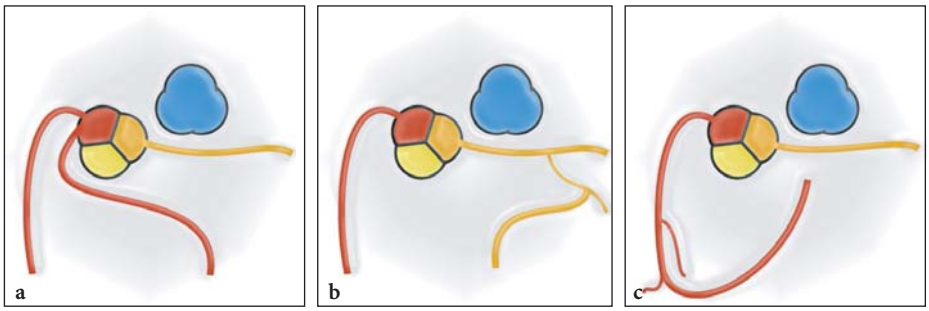

Fig. 7.50a–c. Possible anomalies of the CX. **a** Origin of the CX from the right sinus of Valsalva, retro-aortic course; no clinical relevance. **b** Origin of the CX from branches of the LAD; no clinical relevance. **c** Origin of the CX from distal branches of the RCA; no clinical relevance

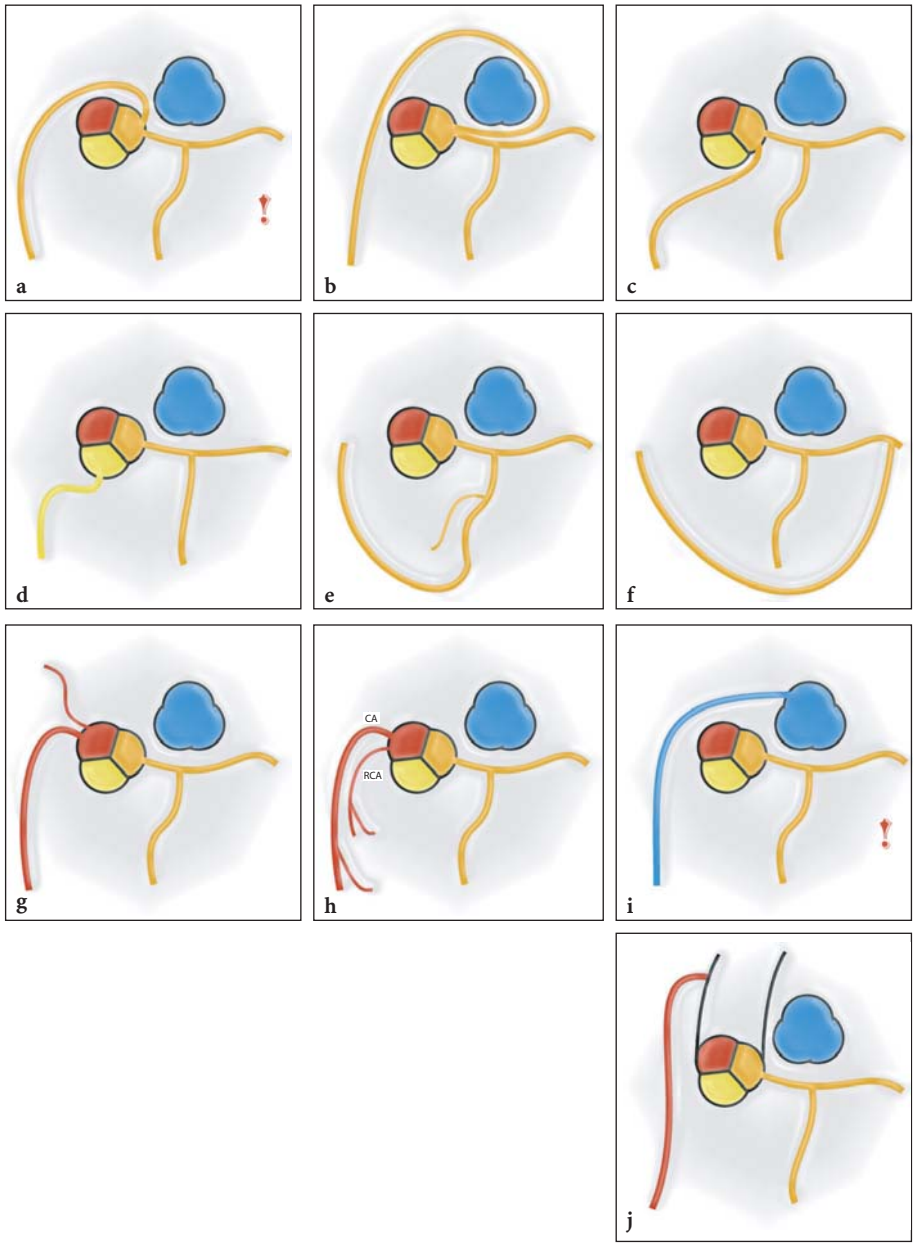

Fig. 7.51a–j. Possible anomalies of the RCA. **a** Origin of the RCA from the left sinus of Valsalva, interarterial course; "malignant". **b** Origin of the RCA from the left sinus of Valsalva, anterior course; no clinical relevance. **c** Origin of the RCA from the left sinus of Valsalva, retro-aortic course; no clinical relevance. **d** Origin of the RCA from the coronary sinus of Valsalva; no clinical relevance. **e** Origin of the RCA from branches of the CX; no clinical relevance. **f** Origin of the RCA from branches of the LAD, no clinical relevance. **g** Sinus node artery with its own ostium; no clinical relevance. This "anomaly" is found in up to 45% of patients undergoing catheter angiography; thus it could be considered a "normal variant". **h** Dominant conus artery (CA) with separate ostium; the CA supplies the main segment of the RCA, which is a small vessel, with an early division. The reverse situation is also possible: separate ostia of the CA and RCA, but the CA is the smaller vessel. **i** Origin of the RCA from the pulmonary artery, so called reversed Bland-White-Garland syndrome; "malignant". **j** Ectopic origin of the RCA from the aorta, the brachiocephalic trunk, or the right common carotid artery; no clinical relevance

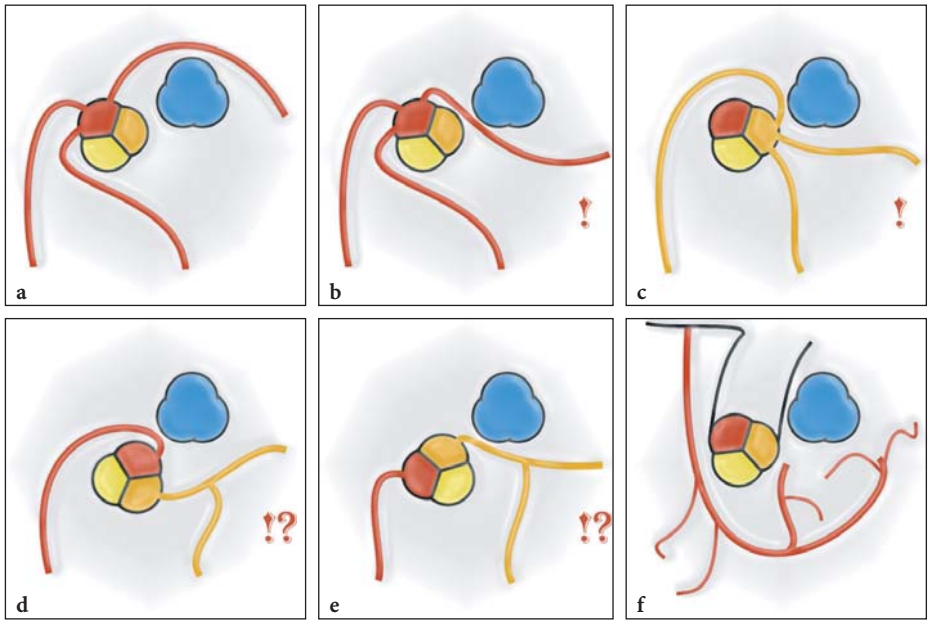

Fig. 7.52a–f. Other complex coronary anomalies. **a** Origin of RCA, CX, and LAD from the right sinus of Valsalva, anterior course of the LAD; no clinical relevance. **b** Origin of RCA, CX, and LAD from the right sinus of Valsalva, interarterial course of the LAD; "malignant". **c** Origin of RCA, CX, and LAD from of the left sinus of Valsalva, interarterial course of the RCA; "malignant". **d** Clockwise rotation of the aortic root with potential interarterial course of the RCA; depending on the extent of the malrotation, potentially "malignant". **e** Counter-clockwise rotation of the aortic root with a potential interarterial course of the LMA; depending on the extent of the malrotation, potentially "malignant". **f** "Single coronary artery", ectopic origin, for example, out of the brachiocephalic trunk

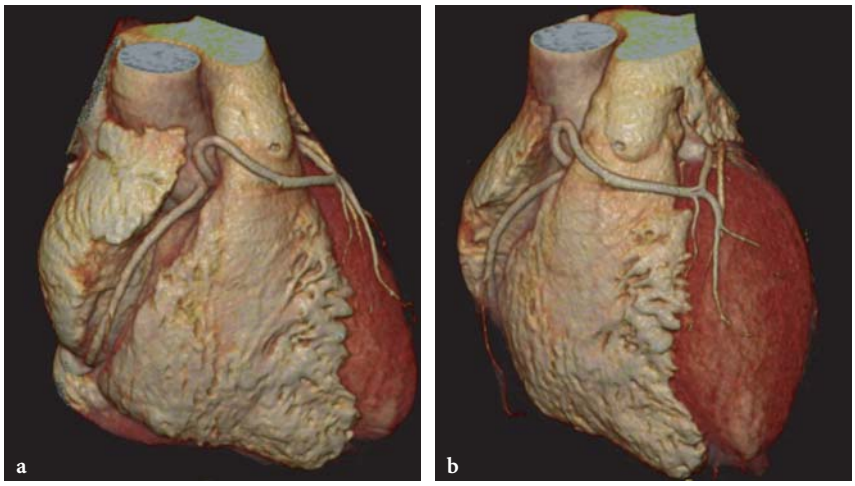

Fig. 7.53a,b. 16-slice CT examination demonstrating the origin of the LMA from a common ostium with the RCA at the right sinus of Valsalva. The artery courses ventral to the pulmonary artery to the left side. Volume-rendering reconstructions in ventral view (**a**) and along the course of the LMA ventral to the pulmonary trunk before the artery branches into the LAD and CX (**b**). Note the ectopic origin of the first diagonal branch out of the LMA

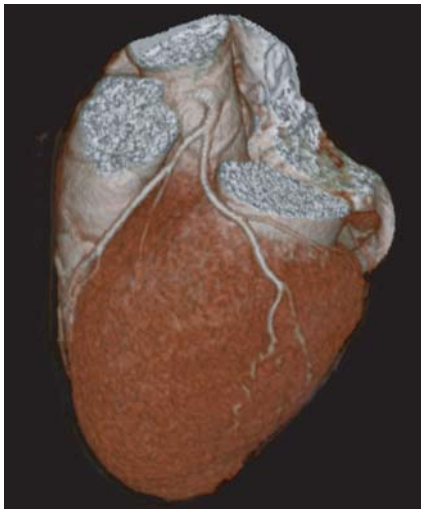

Fig. 7.54. 16-slice CT examination showing an ectopic origin of the LMA cranial to the left sinus of Valsalva; displayed with volume-rendering reconstruction

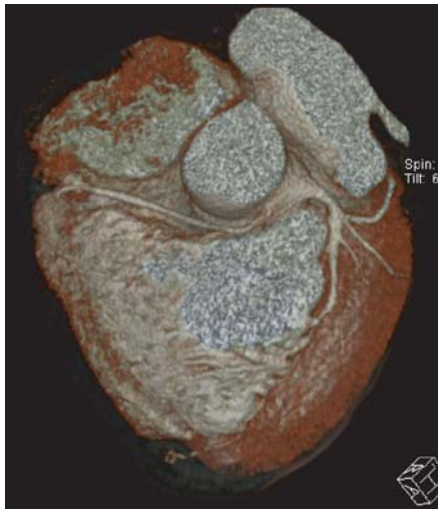

Fig. 7.56. 16-slice CT examination of an abnormal origin of the RCA from the left sinus of Valsalva, interarterial course. Note the narrowing of the proximal part of the RCA during its interarterial course. Volume-rendering reconstruction

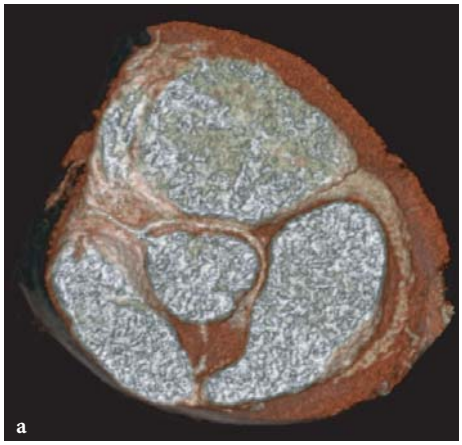

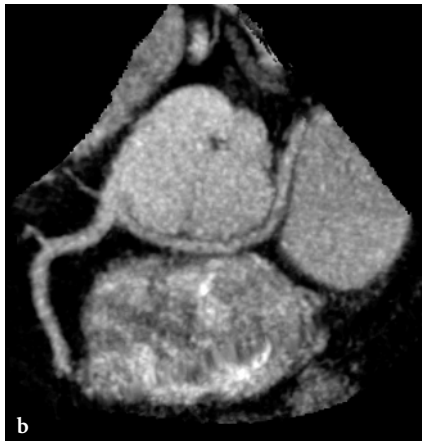

Fig. 7.55a,b. 16-slice CT examination of an abnormal origin of the CX from the right sinus of Valsalva, retro-aortic course. Displayed with volume rendering (**a**) and MIP reconstruction (**b**)

ations. Coronary artery fistulas should be treated surgically, with embolization or stenting of the communications. Even small fistulas with a hemodynamically low significant shunt should be closed to prevent further progression and complications. Spontaneous closure of a coronary artery fistula is extremely rare, but has been reported.

Some of the many types of possible fistulas are shown in Figure 7.58. As demonstrated in the case examples in Figures 7.59 and 7.60, 16-slice CT and 64-slice CT can reliably visualize a coronary fistula

7.8.4 Myocardial Bridges

Normally, the coronary arteries and their major branches course in the epicardial fat, but occasionally they course beneath the myocardium for various distances. Myocardial bridging is a congenital anomaly that is due to the failure of exteriorization of the primitive intratrabecular network of the affected coronary artery. Although this entity is almost always benign, cases of acute myocardial

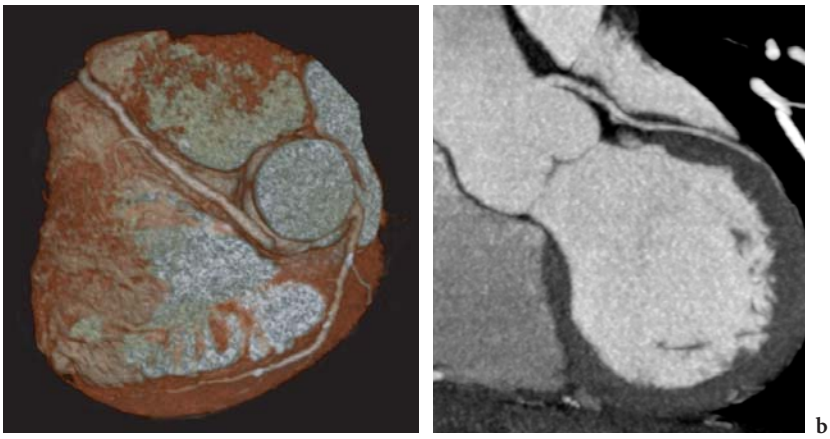

Fig. 7.57a,b. 16-slice CT examination of a clockwise malrotation of the aortic trunk, leading to an interarterial course of the RCA. Note the additional ectopic origin of the LMA above the left sinus of Valsalva. Visualization with volume-rendering reconstruction (**a**) and thin-MIP reconstruction (**b**) showing the aberrant origin of the LMA

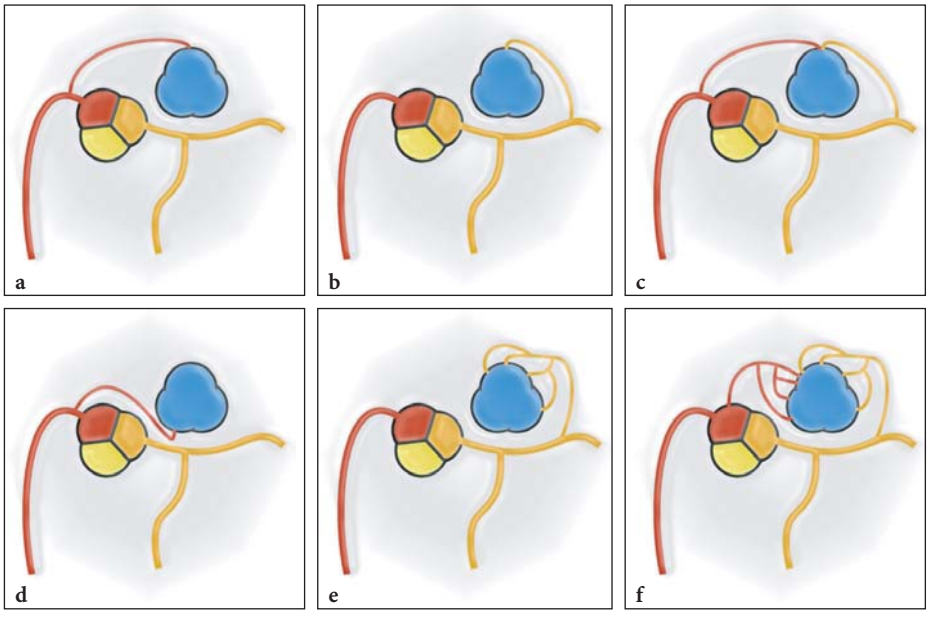

Fig. 7.58a–f. Possible coronary artery fistulas. **a** Fistula from the RCA to the pulmonary artery or other right-sided lumina. **b** Fistula from the LAD to the pulmonary artery or other right sided lumina. c Fistula from both the RCA and the LAD to the pulmonary artery or other right-sided lumina. **d** Fistula from the RCA to the pulmonary artery with an interarterial course. **e** Spider-like fistula from the LAD to the pulmonary artery or other right-sided lumina. **f** Spider-like fistula from both the LAD and the RCA to the pulmonary artery or other right-sided lumina

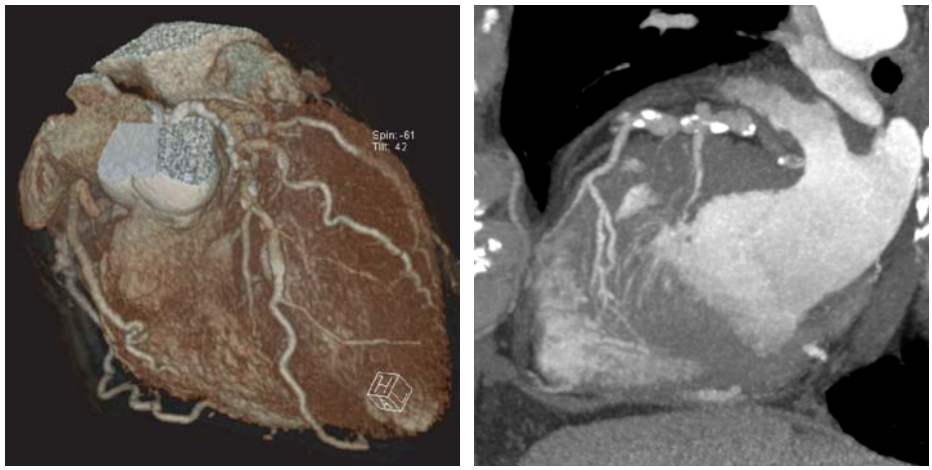

a b

Fig. 7.59a,b. 16-slice CT examination of a spider-like fistula from the LAD coursing through the interventricular septum and subepicardial to the right ventricle with multiple feeding vessels. Display with volume-rendering reconstruction viewed from the top (**a**) and with thin-MIP along a mid-ventricular short-axis section (**b**), showing the multiple fistulas through the interventricular septum to the right ventricle

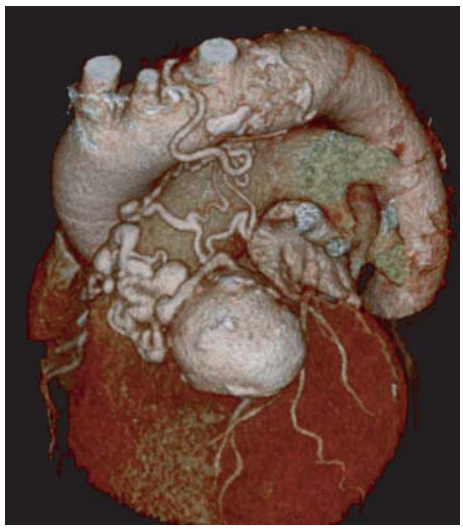

Fig. 7.60. Contrast-enhanced 16-slice CT coronary angiography with 16 × 0.75-mm collimation. Visualization of the left heart anatomy with 3D VRT reveals a complex and large fistula arising from the LAD and connecting to the ascending aorta. (Case courtesy of Hong Kong Sanatorium Hospital, China)

ischemia, cardiogenic shock, and even sudden death have been reported. Most patients do not have typical symptoms, such as angina, and their exercise stress tests are negative. Myocardial bridges are a common finding in autopsy. The incidence at postmortem examination is about 30–55%. In catheter angiography, they are detected in < 10% of patients. Any left coronary branch may be involved. The mid-segment of the LAD is by far the most common site. Males have a higher prevalence (70%). Myocardial bridges are also more common in patients with idiopathic left ventricular hypertrophy. Since the right ventricular systolic pressure is lower than the aortic pressure and the myocardial wall tension is smaller, myocardial bridges of the RCA system do not cause symptoms. The coronary artery is compressed during systole, and this can be demonstrated angiographically. Coronary blood flow occurs primarily during diastole. In myocardial bridges, blood flow may be hampered during increasing tachycardia. The presence of myocardial bridging distal to coronary lesions should be seriously considered to present a potential risk factor for intracoronary thrombus formation.

Unlike coronary angiography, multi-slice CT is capable of simultaneously depicting the course of the abnormal coronary vessel in direct relation to the myocardium. Reconstruction methods of choice

are thin perpendicular MPR or VRT. The systolic narrowing of the lumen can best be shown by reconstructing the data set at a systolic phase of the cardiac cycle and by comparing systolic and diastolic data sets. Multi-slice CT is thus a promising tool in detecting and depicting myocardial bridges, as demonstrated in Figure 7.61.

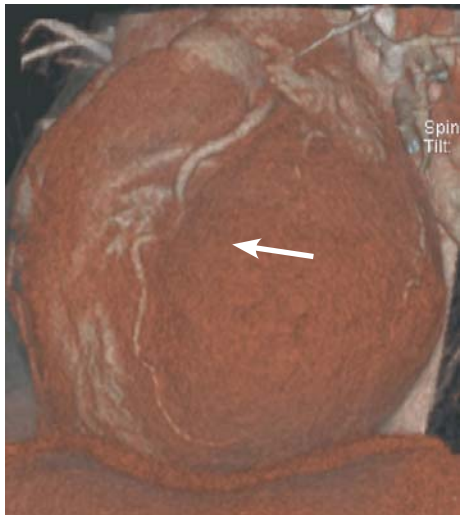

Fig. 7.61. 16-slice CT examination of a myocardial bridge (*arrow*) in the mid-segment of the LAD

7.8.5 Coronary Aneurysms

Coronary artery aneurysms are rarely characterized by abnormal dilatation of a focal portion or diffuse segments of the coronary artery. They are diagnosed incidentally at autopsy or at angiography in patients with symptoms of myocardial ischemia. The most frequent cause of aneurysms of the coronary arteries is atherosclerosis. In this regard, the dilatative form of atherosclerosis must be mentioned. An inflammatory pathogenesis that affects vessel wall modifications is Kawasaki syndrome, which is a clinically unspecific, acute, self-limited vasculitis of early childhood characterized by fever, bilateral nonexudative conjunctivitis, erythema of the lips and oral mucosa, changes in the extremities, rash, and cervical lymphadenopathy. Coronary artery aneurysms may develop in about 25% of untreated children. Aneurysms can also occur in Takayasu arteritis. Vascular lesions causing aneurysms may result from chronic Chlamydia pneumoniae infection. Matrix metalloproteinases (MMPs) may be involved in the pathogenesis of arterial aneurysms due to increased proteolysis of the extracellular matrix of the arterial wall. Coronary artery aneurysms may also rarely develop in patients with systemic lupus erythematosus, sustained herpes virus infection, repetitive activation of virus-related antigens, suppressed immune state, Marfan syndrome, or multiple peripheral aneurysms. A frequent complication of coronary aneurysms is rupture, which mostly has a lethal outcome.

Multi-slice CT is able to depict the aneurysmal lumen as well as thrombus formation within the aneurysm. While 16-slice CT is capable of visualizing the dilated course of the vessels (Fig. 7.62), 64-slice CT accurately reveals the complex atherosclerotic changes (Fig. 7.63).

7.8.6 Coronary Dissection

Dissection of coronary artery is a quite rare but very acute entity. The most frequent cause is iatrogenic, i.e., catheter-induced. It highly important whether the aortic root is involved in the dissection process or not. Involvement of the aortic root may ultimately necessitate a complete replacement of the aortic-arch, perhaps with single re-implantation of the supra-aortic branches. Spontaneous coronary artery dissection is an important cause of acute coronary syndromes. It has been described to be associated with bodily stress, such as during sporting activities and even sexual intercourse. Presentation depends on the extent of the dissection and the location of the vessels involved. It can also occur predominantly in women during or after pregnancy. The association of coronary dissection with positive testing for anti-cardiolipin antibody or anti-phospholipid antibody, as seen in rheumatoid diseases, has been noted. The dissection membrane is best depicted in source images or thin-slice MPR perpendicular to the vessel course.

Dissections of the coronary arteries are seldom diagnosed by multi-slice CT, except the clinically

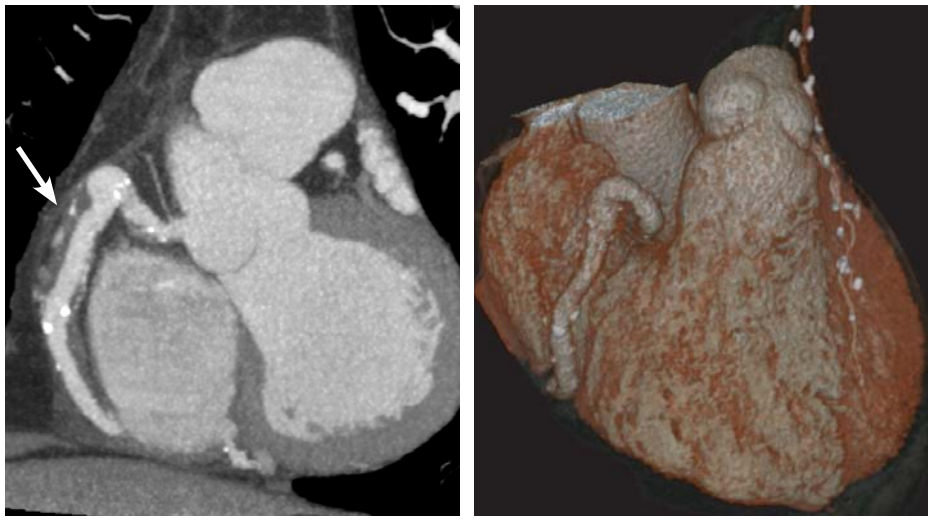

Fig. 7.62a,b. 16-slice CT examination of an aneurysm of the proximal RCA with extended thrombotic changes of the vessel wall. Displayed with thin-MIP projection (**a**) and volume-rendering reconstruction (**b**). The thrombus is visualized with thin-MIP (arrow in **a**). It is not shown in VRT display (**b**) but note a left IMA bypass to the distal LAD

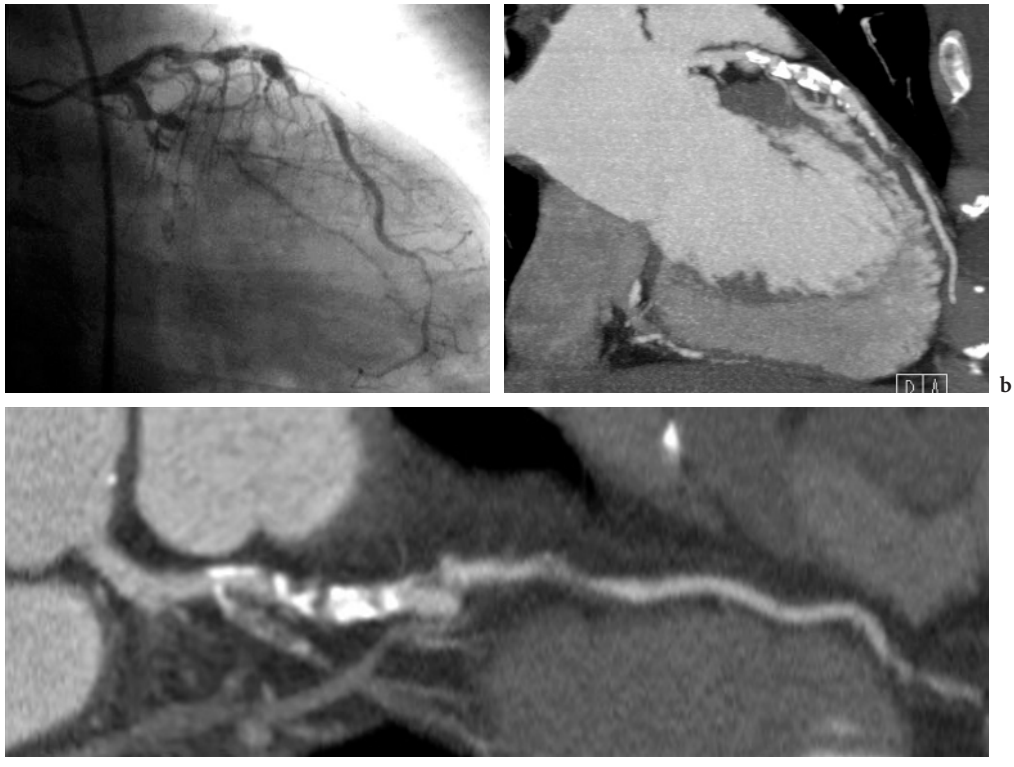

Fig. 7.63a–c. 64-slice CT examination of coronary aneurysms in the LAD. Conventional angiography demonstrates an abnormal course of the vessel (**a**) but does not allow visualization of the atherosclerotic changes. MPR along the long axis (**b**) and curved MPR (**c**) reveal the complex atherosclerotic lesions. (Case courtesy of Healthscan, Kuala Lumpur, Malaysia)

silent, chronic forms, which may be seen accidentally during CT scans for other medical conditions. The acute and clinically apparent forms are the domain of catheter angiography because of the option of immediate interventional therapy.

7.8.7 Coronary Vasculitis

Vasculitis-related lesions were mentioned previously. Only secondary alterations, such as aneurysms, stenoses, and acute and sub-acute closure of coronary arteries, can be depicted with multi-slice CT. As noted above, Kawasaki syndrome can cause coronary artery anomalies, including coronary fistulas and aneurysms in 20–25% of patients. In spite of early therapy, which consists of intravenous gamma-globulin and aspirin, coronary involvement may develop during the first years after diagnosis, even if there is early regress of the main underlying disease. In Kawasaki syndrome in particular, there may be peripheral occlusion of the coronary arteries and aneurysm. The specifically alteration of the arterial wall cannot be detected in multi-slice CT yet, due to the limited spatial resolution. There is no specific sign of coronary vasculitis in CT imaging. In other types of investigations, the value of multi-slice CT in detecting vasculitis has to be evaluated, e.g., in inflammatory thickening of the vessel wall.

7.8.8 Conclusion

In the last few years, multi-slice CT has become an alternative to catheter angiography. CTA is now the method of choice for detecting coronary arteries anomalies, fistulas, and aneurysms due to the 3D capability of this technique. Moreover, it is non-invasive, reproducible, and operator-independent. Especially in complex anomalies, if catheter angiography is not possible, multi-slice CT can accurately depict the anatomy of the heart and vessels. In contrast to catheter angiography, the thrombotic portion of aneurysms can be visualized with multi-slice CT. The new generation of CT scanners, with up to 64 slices, may improve image quality and resolution due to the smaller slice thickness and shorter breath-hold time. However, the ability of multi-slice CT to detect dissection and vasculitis of coronary arteries remains to be proven in future studies.

References

Chaitman BR, Lesperance J, Saltiel J, Bourassa MG (1976). Clinical, angiographic, and hemodynamic findings in patients with anomalous origin of the coronary arteries. Circulation 53: 122–131

Cheitlin MD, DeCastro CM, McAllister HA (1974). Sudden death as a complication of anomalous left coronary origin from the anterior sinus of Valsalva. Circulation 50: 780–787

Click RL, Holmes DR Jr, Vlietstra RE, Kosinski AS, Kronmal RA (1989). Anomalous coronary arteries: Location, degree of atherosclerosis and effect on survival – A report from the Coronary Artery Surgery Group. J Am Coll Cardiol 13: 531–537

Dirksen MS, Langerak SE, de Roos A, Vliegen HW, Jukema JW, Bax JJ, Wielopolski PA, van der Wall EE, Lamb HJ (2002). Malignant right coronary artery anomaly detected by magnetic resonance angiography. Circulation 106: 1881–1882

Ishikawa T, Brandt PW (1985). Anomalous origin of the left main coronary artery from the right anterior aortic sinus: Angiographic definition of anomalous course. Am J Cardiol 55: 770–776

Kragel AH, Roberts WC (1988). Anomalous origin of either the right or left main coronary artery from the aorta with subsequent coursing between aorta and pulmonary trunk: Analysis of 32 necropsy cases. Am J Cardiol 62: 771–777

McConnell MV, Stuber M, Manning WJ (2000). Clinical role of coronary magnetic resonance angiography in the diagnosis of anomalous coronary arteries. J Cardiovasc Magn Reson 2: 217–224

Post JC, van Rossum AC, Bronzwaer JG et al (1995). Magnetic resonance angiography of anomalous coronary arteries. A new gold standard for delineating the proximal course? Circulation 92: 3163–3171

Reddy GP, Chernoff DM, Adams JR, Higgins CB (1998). Coronary artery stenoses: assessment with contrast-enhanced electron-beam CT and axial reconstructions. Radiology 208: 167–172

Roberts WC (1986). Major anomalies of coronary arterial origin seen in adulthood. Am Heart J 111: 941–963

Roberts WC, Siegel RJ, Zipes DM (1982). Origin of the right coronary artery from the left sinus of Valsalva and its functional consequences: Analyses of 10 necropsy patients. Am J Cardiol 49: 863–868

Ropers D, Moshage W, Daniel WG, Jessl J, Gottwik M, Achenbach S (2001). Visualization of coronary artery anomalies and their anatomic course by contrast-enhanced electron

beam tomography and three-dimensional reconstruction. Am J Cardiol 87: 193–197

Samarendra P, Kumari S, Hafeez M, Vasavada BC, Sacchi TJ (2001). Anomalous circumflex coronary artery: benign or predisposed to selective atherosclerosis. Angiology 52:521–526

Serota H, Barth CW III, Seuc CA, Vandormael F, Kern MJ (1990). Rapid identification of the course of anomalous coronary arteries in adults: The "dot and eye" method. Am J Cardiol 65: 891–898

Smith GT (1962). The anatomy of the coronary circulation. Am J Cardiol 9: 327–342

Taylor AM, Thorne SA, Rubens MP, Jhooti P, Keegan J, Gatehouse PD, Wiesmann F, Grothues F, Somerville J, Pennell DJ (2000). Coronary artery imaging in grown up congenital heart disease: Complementary role of magnetic resonance and x-ray coronary angiography. Circulation 101: 1670–1678

Van Ooijen PMA, Dorgelo J, Tukker W, Zijlstra F, Oudkerk M (2004). Visualization of anomalous coronary anatomy using multi-detector computed tomography (Abstract). Eur Radiol 14 (Suppl 2): 326

Yamanaka O, Hobbs RE (1990). Coronary artery anomalies in 126,595 patients undergoing coronary arteriography. Cathet Cardiovasc Diagn 21: 28–40

Yoshimura N, Hamada S, Takamiya M, Kuribayashi S, Kimura K (1998). Coronary artery anomalies with a shunt: evaluation with electron-beam CT. J Comput Assist Tomogr 22: 682–686

7.9 Diagnosis of Congenital Heart Disease in Adults and Children

J.-F. Paul

Contents

7.9.1 Introduction 258
7.9.2 Technical Aspects and Imaging Protocols 258
7.9.2.1 Neonates and Young Infants 258
7.9.2.2 Infants Over 7 Years of Age and Adults 259
7.9.2.3 Dose Considerations 259
7.9.2.4 Contrast-Injection Protocol 260
7.9.2.5 Sedation of Infants 260
7.9.2.6 Post-processing 260
7.9.3 Clinical Indications 261
7.9.3.1 Pulmonary Arteries 261
7.9.3.2 Coronary Arteries 261
7.9.3.3 Aorta and Collaterals 261
7.9.3.4 Upper-Airways Compression of Vascular Origin 261
7.9.3.5 Anomalous Venous Return 262
7.9.3.6 Post-intervention Evaluation 263
7.9.4 Improvements with 64-Slice CT 263
7.9.5 Conclusion 263
References 265

7.9.1 Introduction

An accurate, 3D evaluation of the cardiac and related arterial anatomy is critical for the clinical management of adult and pediatric patients with complex congenital heart disease. 3D imaging has to be able to demonstrate the shapes of, and spatial relationships between, the great arteries, proximal branch pulmonary arteries, and anomalous pulmonary venous or systemic connections. Three-dimensional information about extra-cardiac morphological characteristics may determine subsequent surgical intervention.

Magnetic resonance imaging has been recommended by a task force report as the first-choice technique for many congenital heart diseases (Association of European Pediatric Cardiologists 1998). MRI appears, on initial consideration, to be an ideal technique because there is no radiation burden, which is a substantial advantage, especially in neonates and young children. However, it also suffers various limitations: the major one being the need for prolonged sedation and close monitoring, especially of infants with cyanotic heart disease, whose condition is often unstable. For such patients, intensive-care pediatricians must be present during the MRI examination. Also, the spatial resolution of MR images is lower than that of CT images, which can be a significant drawback for visualization of small anatomical structures.

More recently, helical CT has been proposed for 3D anatomical visualization in patients with congenital heart disease (Kawano 2000). Helical technology allows volume acquisition in a short period of time and provides good-quality 3D vascular images, even for neonates and infants. The multi-slice CT technology now available has much faster acquisition times , which substantially reduces respiratory artifacts. Furthermore, image synchronization with the cardiac rhythm is now possible, and this should reduce problems associated with heart motion. In our surgical center, which specializes in congenital heart disease, multi-slice CT with the evolution from 4- to 16- and, very recently, 64-slice technology has rapidly become an important complementary imaging technique for both pre- and post-operative management of patients (Lee 2004).

7.9.2 Technical Aspects and Imaging Protocols

The first issue is whether ECG-gated acquisition should be used for congenital heart disease patients, and the second concerns optimization of radiation exposure.

7.9.2.1 Neonates and Young Infants

It is not possible to make neonates and young infants hold their breath. Consequently, we do not use ECG-gated techniques for acquisition, because respira-

tory artifacts greatly degrade images, and such artifacts are substantial with ECG-gated acquisition (because acquisition is slow) (Paul 2002). Similarly, the cardiac rhythm of babies with cyanotic congenital heart disease is very high, generally between 140 and 180 bpm, making cardiac motion-free images impossible. The third reason for not using retrospectively ECG-gated cardiac acquisition is that it requires a higher radiation dose than non-ECG-gated thoracic CT, because only a part of the dose (i.e., the dose delivered during diastole) is used for creating images. Organ sensitivity to radiation is much higher in babies than in adults. Indeed, recent reports suggest that the risk of developing cancer in the future cannot be totally ruled out (Brenner 2001) after medical radiation exposure. This risk increases with radiation dose.

In our experience, the principle of "going as fast as possible" still allows good image quality in neonates with congenital heart disease; furthermore, the short acquisition times minimize respiratory artifacts. With 4-slice CT, the thorax of babies can be scanned in 3–4 s using 2.5-mm collimation, 0.5-s rotation time, and a table-feed of 20 mm per s (pitch 2). The images are of higher quality than those obtained using a slice thickness of 1 mm, which requires longer acquisition times associated with thinner collimation, and thus more respiratory artifacts. Very short acquisition times (≤ 5 s) allow apnea in intubated babies, and the images obtained are free of respiratory artifacts. With 16-slice CT, the thorax of a baby can be scanned in about 4 s using 0.75-mm slices or in 2 s using 1.5-mm collimation.

7.9.2.2 Infants Over 7 Years of Age and Adults

There are two options for older infants and young adults: either conventional breath-hold angio-CT acquisition or ECG-gated acquisition. The protocol should be chosen according to clinical considerations. If, for example, coronary visualization is required to detect a possible anatomical variant, ECG-gated protocols are recommended. ECG gating is often not required in other cases and should only be applied when appropriate due to the related increase in radiation dose.

7.9.2.3 Dose Considerations

Radiation exposure is a major public-health issue. CT contributes greatly to the population dose due to medical exposure, as it makes up 35% of the total dose delivered during diagnostic examinations although it represents only 4% of such examinations (Nagel 2002). The ALARA principle (as low as reasonably achievable) is a good rule of thumb: dose reduction is necessary but examination quality must be maintained without losing diagnostic information. While the thorax is a region of low-attenuation, substantial dose reduction during chest CT is feasible because of the high inherent contrast. In August 2001, the ALARA conference of the Society for Pediatric Radiology considered the issue of dose reduction by decreasing the kilovoltage (Slovis 2002). In our center, we decided to apply the ALARA principle as far as possible to neonates and babies with congenital heart disease, and then implement some systematic rules:

- No topogram (responsible for unnecessary additional radiation dose)
- Consistent use of 80 kV settings whenever feasible
- Adaptation of the mAs to the child's weight (starting from 17 mAs)
- Only one phase acquisition when possible
- Systematic protection of non-scanned organs

A setting of 80 kV for pediatric patients is the rule in our center. Reducing the kV from 120 to 80 kV decreases the radiation dose by 65% at constant tube-current setting, as radiation dose varies with the square of the kV. This setting is sufficient for good-quality images, as long as the mAs are adjusted according to the child's weight. The other advantage of using only 80 kV is that the amount of contrast medium injected can also be reduced – because low kV is more sensitive to contrast (iodine has a high atomic number) than higher settings.

The tube-current is adapted to body weight for neonates and infants. For example for thoracic imaging, we scan neonates using 17–30 mAs and 80 kV, babies using 30–45 mAs. The minimum exposure setting allowed with the 16-slice CT used in our institution is 80 kV and 17 mAs using

0.75-mm collimation and a table-feed of 18 mm/s. Previous studies suggested that CT delivers much lower radiation doses than conventional angiography (Westra 2002). Appropriate exploitation of anatomical data acquired from CT may therefore be used to limit the number of views acquired with angiography, and sometimes replace conventional angiography altogether. Thus, CT may allow total radiation exposure of congenital heart disease patients to be reduced.

7.9.2.4 Contrast-Injection Protocol

Neonates and babies. The injection dose must be adapted to the baby's weight. We currently use 2 cc per kg. At 80 kV, the rate of injection can be as low as 0.5 cc per s in neonates through a catheter placed in the vein of the hand. Higher rates may be used with a central catheter (femoral or jugular). We use a power injector to ensure a continuous and regular flow rate, and the rate of injection is 0.5 cc/kg to 1 cc/s depending on the site of injection. The start delay for neonates and infants is 15 s for peripheral injection, and 10 s for central venous injection. To ensure vascular contrast during the acquisition, we increase the amount of contrast medium in some cases according to the rule: Time of injection = start delay + time of acquisition. Accordingly, acquisition is never "too late" for good vascular enhancement, because acquisition ends with the end of injection, so the peripheral veins still contain contrast medium when acquisition ends.

Precautions for venous access. Peripheral venous access is always done in the pediatric unit. Injection in the right arm is preferable (but not obligatory) to avoid artifacts in the innominate left brachiocephalic vein. In some cases, venous connections are congenitally abnormal or surgically modified. Any available relevant information can be important before the scan procedure, as the scan injection protocol may have to be adapted accordingly. Venous visualization may be obtained at first pass, with a high concentration of contrast medium, or sometimes later, at the time of venous return. The optimal injection protocol depends on the particular venous anatomy. The catheter is tested for permeability before the injection. It is essential to avoid any air injection during the scan procedure. All bubbles should be removed when connecting the catheter to the power injector. Because many patients with congenital heart disease have right-to left-shunt, air injection through venous access could cause systemic air embolism, with possible fatal consequences.

7.9.2.5 Sedation of Infants

General anesthesia is never necessary in our experience. In addition, we do not administer any sedative drugs to neonates . For infants, we recommend oral or intra-rectal sedation (or both) before the CT procedure in order to prevent agitation during the acquisition, which may result in poorer image quality and, as a consequence, occasionally, re-examination. Sedation is not always necessary if the baby is quiet. Experienced technicians are required in the CT room for good management of the babies: experience and knowledge of baby management and a calm attitude are important. Our sedation protocol for infants includes intra-rectal administration of 0.3 mg/kg Midazomal 15 min before examination. Additional sedative drugs may be useful (1 mg/kg hydroxyzine, per os, 1 h before examination). With experienced technicians, the mean total examination time in the CT room is 20 min. Qualified medical monitoring may be sometimes necessary during the examination, depending on the clinical condition of the baby, and oxygen saturation should be closely monitored.

7.9.2.6 Post-processing

Even if all information is available on axial CT images, 3D imaging with VRT is our first-line approach for interpretation due to the complexity of spatial variations of anatomical structures. VRT allows initial comprehensive imaging of anomalies whereas MIP images are used subsequently for vessel-by-vessel interpretation.

7.9.3 Clinical Indications

7.9.3.1 Pulmonary Arteries

Pulmonary artery evaluation is frequently required for patients with pulmonary atresia with ventricular septal defect, tetralogy of Fallot, truncus arteriosus, or suspicion of pulmonary sling. With a 16-slice CT, we usually use 0.75-mm collimation and obtain 1-mm slice width with an increment of 0.5 mm. High resolution is beneficial for evaluating pulmonary artery stenosis.

7.9.3.2 Coronary Arteries

Anomalous coronary arteries are frequently associated with congenital heart disease. The most frequent anomalous finding is a left coronary artery originating from the right coronary sinus, but many variants are possible, even the coronary artery originating from pulmonary arteries. The "normal" position of coronary origins may be different from usual; for example, in cases of tetralogy of Fallot, because of the rotation of the aorta: the origin of the LMA is typically at 6 o'clock and that of the RCA at 1 o'clock. Detection of an anomalous origin of the coronaries is especially important before surgery when a ventriculotomy is planned, as accidental lesion during intervention of the coronary artery crossing the right ventricle can be fatal.

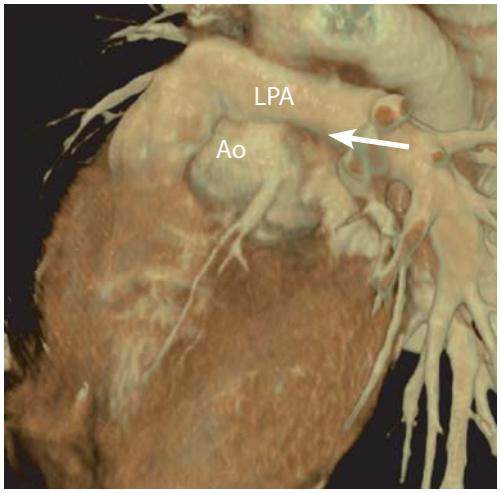

Fig. 7.64. 4-slice CT evaluation of re-implanted coronary arteries in a 9-year old girl, who underwent surgery just after birth for transposition of the great vessels (arterial switch). The 4-slice CT shows the normal anatomical position of the coronary arteries 9 years after surgery. Note the left pulmonary artery crossing in front of the aorta. *Ao* Aorta, *LPA* left pulmonary artery

In older patients with congenital heart disease, if the patient can hold his or her breath for a sufficiently long time, ECG-gated acquisition may be the technique of choice. Free-motion artifact visualization is then possible, allowing accurate evaluation of the coronary artery tree (Fig. 7.64). To avoid heart-motion artifacts, the heart rate must be regular and, if possible, < 70 bpm; excellent results are generally obtained at 55–60 bpm. We use an ECG pulsing technique except in patients with arrhythmia, so as to reduce the radiation dose by about 40%, all others factors being equal.

7.9.3.3 Aorta and Collaterals

Evaluation of the aortic anatomy is essential in cases of aortic coarctation (Fig. 7.65) or suspicion of aortic arch anomalies. In patients with pulmonary atresia with ventricular septal defect, major aorto-pulmonary collateral arteries (MAPCA) often originate from the origin of the descending aorta. It is essential to determine the size and spatial relationship of these arteries when planning surgical intervention. Thin collimation (1 mm with a 4-slice CT, 0.75 mm with a 16-slice CT), is of value as it provides high-resolution images. Such images are, in turn, useful for evaluating aortic stenosis, especially in patients with aortic coarctation, for better assessment of vessel narrowing.

7.9.3.4 Upper-Airways Compression of Vascular Origin

Central-airway compression of vascular origin can result from various situations. The most frequently observed are: aortic arch anomalies (Fig. 7.66), pulmonary artery sling, dilated pulmonary arteries, and posteriorly displaced aorta (switch intervention). Non-enhanced CT is sufficient to detect steno-

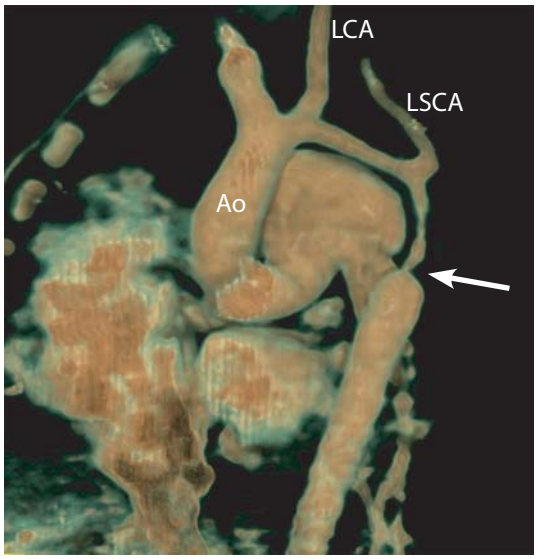

Fig. 7.65. Aortic coarctation in a 1-month-old baby examined with 16-slice CT. Total interruption of aortic arch was suspected from echocardiography. The 16-slice CT showed long stenosis of the aorta with post-ductal severe narrowing (*arrow*). *LCA* Left carotid artery, *LSCA* left subclavian artery

sis of the central airways, but contrast enhancement is required to identify the vascular origin. In babies, we currently use the same protocol as for visualization of the pulmonary arteries or aorta. In addition to MIP reconstructions, VRT is very effective for showing central-airway narrowing (Fig. 7.66b). However, airway compression can be more distal, which makes diagnosis of vascular compression difficult. Evidence of air trapping on parenchymal windowing is indicative of this type of compression.

7.9.3.5 Anomalous Venous Return

Multi-slice CT is very effective in the detection of pulmonary or systemic anomalous venous return. ECG-gated acquisitions are usually not necessary because venous structures are not very sensitive to cardiac motion (Fig. 7.67). The injection site and timing of acquisition must be chosen carefully, since the timing at which opacification is best depends on the venous drainage, and any anomalous venous drainage may affect optimal timing. Additional delayed acquisition may be necessary to opacify the entire venous system. To avoid artifacts associated

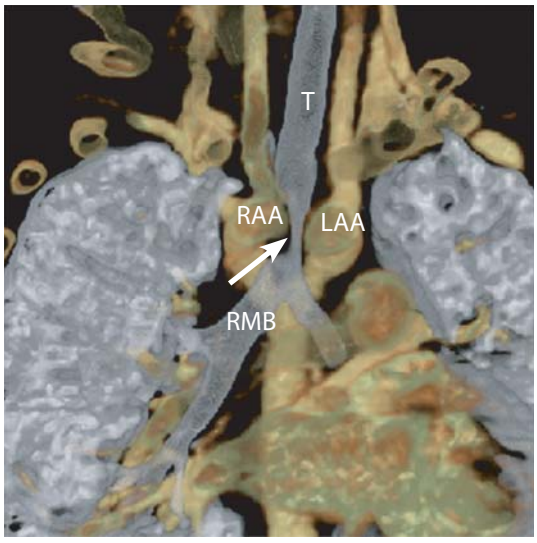

a

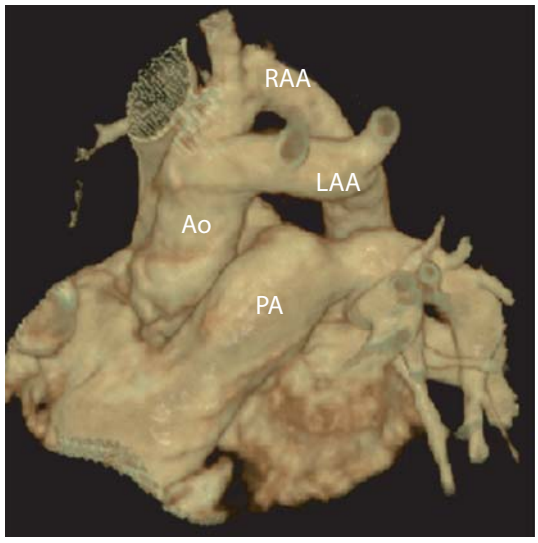

b

Fig. 7.66a,b. Severe respiratory distress in a newborn. **a** The 16-slice CT examination using VRT clearly shows a complete double aortic arch responsible for tracheal compression in a 5-month-old patient weighing 5 kg. **b** Using the same data set, VRT (displaying both airways and vascular structures) clearly reveals compression of the trachea (*T*) by the right aortic arch (*RAA*). *LAA* Left aortic arch, *Ao* ascending aorta, *PA* pulmonary artery

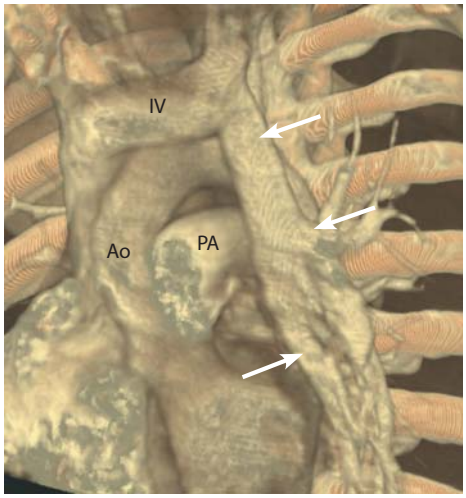

Fig. 7.67. 16-slice CT image of totally abnormal left venous return in a 25-year-old man with dyspnea. All left pulmonary veins (*arrows*) are connected to the innominate vein. *IV* Innominate vein

with concentration of the contrast medium in the veins, a low rate of injection is recommended.

7.9.3.6 Post-intervention Evaluation

Post-operative evaluations are required in various clinical situations, for example, for assessment of bypass patency (Fig. 7.68) or suspicion of mediastinitis. The CT protocol should be adapted to the clinical context. In many cases, radiation exposure can be less than that of the standard protocol because there is generally no need for detailed anatomic information. For example, to search for mediastinitis, a single, delayed (3–5 min) acquisition may be sufficient. In contrast, conduit patency can be tested by acquisition at the arterial phase alone. CT assessments of the altered vascular anatomy may also be useful for follow-up after complex surgical repair.

7.9.4 Improvements with 64-Slice CT

With the recently developed 64-slice CT scanners, the thorax of a baby can be scanned in 1–2 s with the thinnest collimation, usually 0.6 mm (Fig. 7.69). Therefore, no compromise in spatial resolution has to be made even at the minimum scan time. The faster rotation time of the new scanners, down to 0.33 s, improves image quality also at higher heart rates, and heart rate control is no longer mandatory in adult patients. The increased spatial resolution of 0.4 mm that is possible with 64-slice CT even allows for visualization of the coronary arteries in babies, thus enabling the detection of congenital coronary artery disease at a very early age (Fig. 7.70). In older children and adults, the increased volume-coverage speed provides very comfortable breath-hold times of 5–10 s, during which the thorax can be covered with ECG gating at the maximum possible resolution (Fig. 7.71).

7.9.5 Conclusion

Precise 3D visualization of anomalous extra-cardiac anatomy in congenital heart disease patients can be routinely obtained using multi-slice CT. In addition to providing a major, additional, non-invasive diagnostic tool for the evaluation of congenital heart disease, multi-slice CTA offers an alternative to angiography. While radiation-dose considerations, especially for neonates and infants, remain a draw-

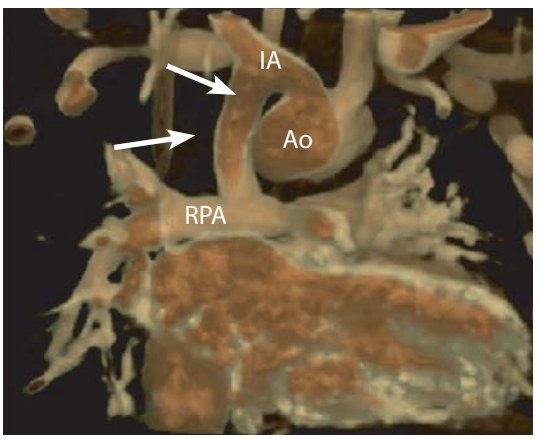

Fig. 7.68. Post-operative evaluation in a newborn with pulmonary atresia and ventricular defect, examined with 16-slice CT. A shunt between the innominate artery and the right pulmonary artery (Blalock anastomosis) is clearly apparent (*arrows*). *RPA* Right pulmonary artery, *IA* innominate artery

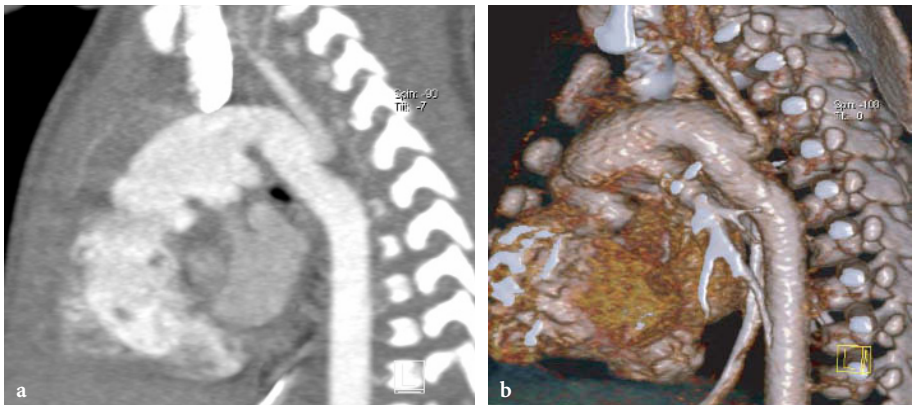

Fig. 7.69a,b. 64-slice CT examination of a neonate. The image is displayed in MIP (a) and VRT (b). With a 0.33-s rotation time, the thorax of the neonate is covered in less than 2 s

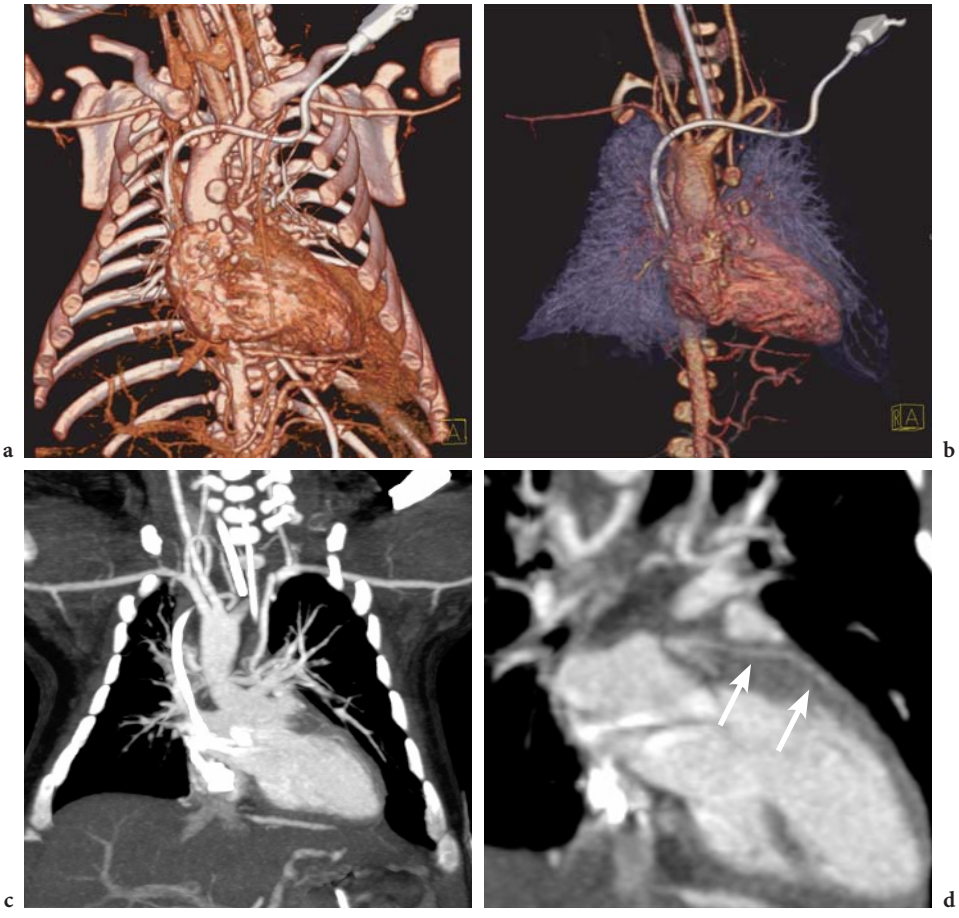

Fig. 7.70a–d. ECG-gated 64-slice CT examination of an 8-week-old baby. The cardiothoracic anatomy can be visualized with VRT (a, b) and MPR (c). Owing to the high spatial resolution, an abnormal course of the coronary artery could be ruled-out (*arrows* in d). (Case courtesy of Tübingen University, Germany)

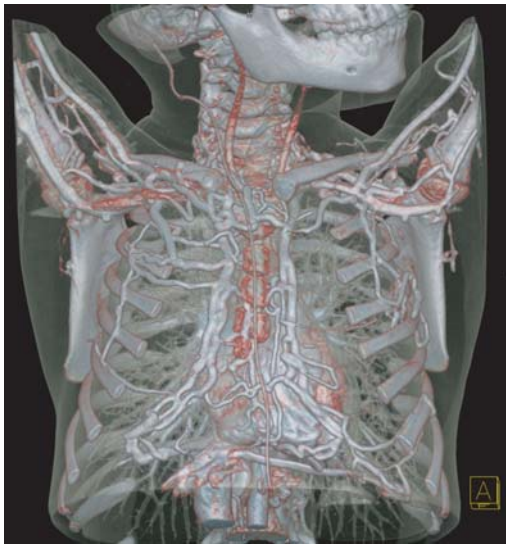

Fig. 7.71. 64-slice CT examination of an 8-year-old child with complex malformation of the thoracic vasculature. The scan was acquired in a 6-s breath-hold with 80 kV and without use of ECG-gating to minimize radiation exposure. (Case courtesy of MUSC, Charleston, USA)

back of this technique, excellent image quality is possible even at very low exposure.

References

Brenner D, Elliston C, Hall E, Berdon W (2001). Estimated risks of radiation-induced fatal cancer from pediatric CT. AJR Am J Roentgenol 176:289–96

Kawano T, Ishii M, Takagi J, Maeno Y, Eto G, Sugahara Y, Toshima T, Yasunaga H, Kawara T, Todo K, Kato H (2000). Three-dimensional helical computed tomographic angiography in neonates and infants with complex congenital heart disease. Am Heart J 139:654–660

Lee EY, Siegel MJ, Sierra LM, Foglia RP (2004). Evaluation of angioarchitecture of pulmonary sequestration in pediatric patients using 3D MDCT Angiography. AJR 183:183–188

Nagel HD et al (2002). In: Radiation exposure in computed tomography: Fundamentals, influencing parameters, dose assessment, optimization, scanner data, terminology. 2nd edn. Offizin Paul Hartung Druck, Hamburg, Germany pp. 1–3

Paul JF, Serraf A (2002). Truncus arteriosus and double aortic arch. Circulation 105:e170

Slovis TL (2002). ALARA conference proceedings. The ALARA concept in paediatric CT: intelligent dose reduction (Editorial). Pediatr Radiol 32:217–231

Task Force of the European Society of Cardiology, in collaboration with the Association of European Paediatric Cardiologists (1998). The clinical role of magnetic resonance in cardiovascular disease. Eur Heart J 19:19–39

Westra SJ, Hurteau J, Galindo A, McNitt-Gray MF, Boechat MI, Laks H (1999). Cardiac electron-beam CT in children undergoing surgical repair for pulmonary atresia. Radiology 213:502–512

7.10 Evaluation of Ventricular Function Parameters

K.-U. Jürgens, R. Fischbach

Contents

7.10.1 Introduction *266*
7.10.2 Determination of Cardiac Function Parameters with Multi-slice CT *267*
7.10.2.1 Calculation of Ventricular Volume *267*
7.10.2.2 Calculation of Ejection Fraction, Stroke Volume, and Cardiac Output *268*
7.10.2.3 Assessment of Regional Function *268*
7.10.3 Data Acquisition and Image Reconstruction *269*
7.10.4 Image Analysis *270*
7.10.5 Limitations *270*
7.10.6 Clinical Considerations *272*
7.10.6.1 Measurement of Left Ventricular Function *272*
7.10.6.2 Accuracy and Reproducibility of Left Ventricular Volume and Function Measurement *273*
7.10.6.3 Myocardial Viability *274*
7.10.6.4 Right Ventricular Disease *276*
7.10.7 Summary and Outlook *277*
References *279*

7.10.1 Introduction

The accurate and reproducible determination of left ventricular myocardial function is fundamental to the diagnosis, disease stratification, treatment planning, and estimation of prognosis of patients with ischemic and non-ischemic cardiomyopathy (Schocken 1992, White 1987). Analysis of left ventricular myocardial function includes the determination of global and regional function parameters. Global cardiac function is represented by the ejection fraction, stroke volume, and cardiac output, which are derived from diastolic and systolic left ventricular volume measurements. Regional function parameters include myocardial wall thickness and systolic wall thickening; these provide more detailed information on the functional state and viability of ischemic and non-ischemic myocardial segments. Analysis of ventricular volume and secondary function parameters are clinically useful to:

- Determine the magnitude of dysfunction and the level of compensation, e.g., in patients with clinically manifest coronary heart disease or dilative and hypertrophic cardiomyopathy
- Measure the response to a therapy, e.g., revascularization or medical treatment
- Assess a patient's risk for future cardiac events and prognosis for survival

The assessment of ventricular function may provide information for the initial diagnosis of coronary heart disease in symptomatic patients, although left ventricular function does not sensitively reflect the severity of coronary artery stenosis, since contraction remains normal until coronary blood flow is reduced below a critical threshold. The relationship between the severity of coronary artery stenosis and ventricular function in the ischemic region is therefore nonlinear and ventricular function decreases exponentially once blood flow falls below resting levels. Since regional or global ventricular dysfunction may also result from cardiomyopathy or valvular disease, left ventricular dysfunction is not specific to coronary heart disease or acute myocardial infarction, since unstable angina may also depress ventricular function.

Multi-slice CT of the heart is being increasingly used to assess coronary artery and cardiac morphology. Image reconstruction in multi-slice CTA has been optimized for coronary artery visualization, but with ECG-gated spiral acquisition, image data are available for any phase of the cardiac cycle (Ohnesorge 2000). Thus, retrospective image reconstruction in specific heart phases can be used to determine end-systolic and end-diastolic ventricular volumes as well as myocardial wall thickness. This section will discuss the potential of multi-slice CT in the assessment of ventricular function with regard to accuracy, limitations, and clinical applications.

7.10.2 Determination of Cardiac Function Parameters with Multi-slice CT

7.10.2.1 Calculation of Ventricular Volume

The ventricular volume changes throughout the cardiac cycle (Fig. 7.72). The mechanical cycle starts with an isovolumetric contraction at the end of ventricular filling. The increase in ventricular pressure results in the ejection of blood into the systemic and pulmonary circulation. This is followed by isovolumetric ventricular relaxation and then by the ventricular filling period. Ventricular volume changes are similar in the right and the left chambers of the heart. Left ventricular volume can be measured using the following approaches:

- The *area-length method* uses a vertical or horizontal long-axis view (Fig. 7.73a). It has been developed to allow for ventricular volume measurements with catheter coronary angiography based on a limited number of available projections. The ventricular area (A) and the length from apex to the mitral valve plane (*L*) are used to calculate the left ventricular volume (*V*) according to the formula:

$$V = \frac{8}{3} \times \frac{A^2}{\pi \cdot L}$$

- The *Simpson's method* employs contiguous *short-axis* image sections of the left ventricle (Fig. 7.73b). It was developed for MR ventricular volume measurements that produce short-axis images in a single image sequence. The cross-sectional images have a certain section thickness (*S*) and are adjacent one to another. The left ventricular volume (*V*) is calculated by adding all cross-sectional areas (*A*) multiplied with the section thickness (*S*) as:

$$V = \sum A_N \times S$$

- A threshold-based direct volume measurement is achieved using a segmentation technique in imaging modalities that depict density or signal-intensity differences between the myocardium and cardiac chambers. The signal difference can be produced by contrast-enhanced blood in the cardiac chambers. The sum of all contiguous voxels exceeding a predefined attenuation threshold represents the total chamber volume.

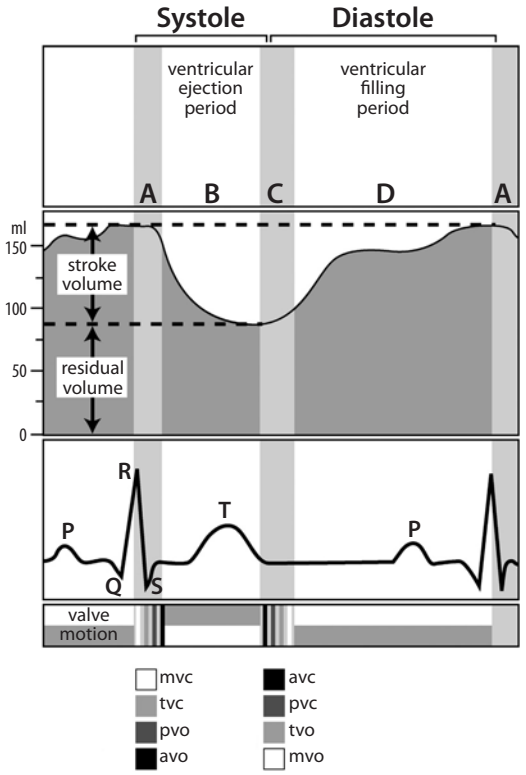

Fig. 7.72. The electrical and mechanical events during the cardiac cycle: left ventricular volume curve, electrocardiogram, and valvular events are depicted. *A* Isovolumetric contraction phase, *B* ventricular ejection period, *C* isovolumetric relaxation phase, *D* ventricular filling period. mV/mV Mitral valve closing/opening, Tec/to tricuspid valve closing/opening, pro/PVC pulmonary valve opening/closing, Ave/Ave aortic valve opening/closing

The Simpson's method and direct volumetry do not rely on geometric assumptions and thus are preferred over the area-length method for accurate ventricular volume determination with multi-slice CT. Short axis MPRs can be generated from a multi-slice CT axial image data set in different phases of the cardiac cycle and can then be used as input for the Simpson's method. However, as multi-slice CT produces thin-slice volumetric data, voxel-based methods for direct volumetry are well-suited for CT-based calculations of ventricular volume.

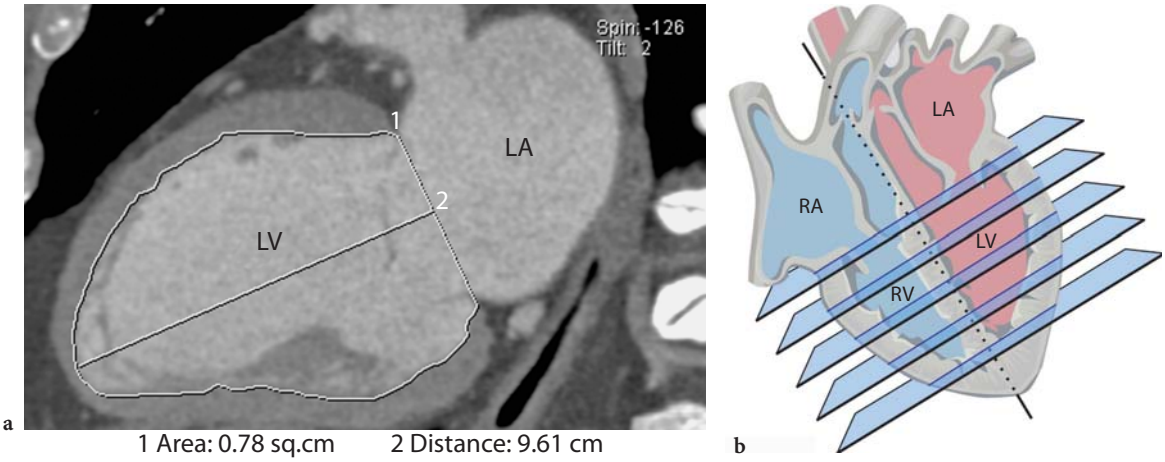

Fig. 7.73. a Area-length method for determination of left ventricular volume. Left ventricular dimension and area are measured on a vertical long-axis reformation. **b** Simpson's method for left ventricular volume measurement. A series of short-axis images is used for area measurement. Every cross-sectional area is multiplied with the section thickness to give the ventricular volume. *RA* Right atrium, *RV* right ventricle, *LA* left atrium, *LV* left ventricle

7.10.2.2 Calculation of Ejection Fraction, Stroke Volume, and Cardiac Output

The normal ventricle ejects about two-thirds of its end-diastolic volume during systolic contraction. The ventricular ejection fraction (EF) describes the relative change of ventricular volume from end-diastolic volume (EDV) to end-systolic volume (ESV) and reflects global ventricular function. EF is calculated according to:

$$EF = \frac{(EDV - ESV)}{EDV} \times 100\%$$

The stroke-volume (SV) is the absolute change in ventricular volume [SV (ml) = EDV–ESV]. Cardiac output (CO) is the SV multiplied by the heart rate, which means the pumped blood volume per minute [CO (ml/min) = SV × heart rate].

7.10.2.3 Assessment of Regional Function

Systolic contraction results in a significant reduction of ventricular volume and a thickening of the ventricular myocardial wall. The thickness of the left ventricular myocardial wall is between 6 and 8 mm in diastole and between 10 and 14 mm in systole. Normal wall thickening of the left ventricular myocardium during systole is approximately 5 mm. Systolic contraction requires functional muscle tissue and an adequate regional blood supply. Scar tissue does not contract and thus does not show systolic wall thickening. The reduction of regional coronary blood flow below a critical threshold also prevents normal contraction. Due to the coronary flow reserve, only high-grade lesions will reduce coronary blood flow below this critical level at rest. Coronary blood flow increases significantly under physical stress, such that flow-obstructing lesions become symptomatic, resulting in regional hypoperfusion and thus impaired ventricular contraction. Stress imaging techniques, using exercise or drugs that induce vasodilatation to cause regional hypoperfusion, make use of this fact to diagnose obstructive coronary artery disease based on the occurrence of impaired wall motion under stress.

Stress imaging requires serial measurements, which are easily achieved with cine magnetic resonance imaging (CMR) and ultrasound but represent a major limitation for CT due to the need for repeated contrast injections and radiation exposure. Despite these limitations, CT can still reveal basic information on regional wall function at rest. Systolic and diastolic image reconstructions depict changes in

wall thickness, and multi-phase reconstructions even allow analysis of ventricular wall motion over the cardiac cycle.

Wall motion abnormalities can be qualitatively assessed (Fig. 7.74). An area with impaired contraction or wall thickening is called hypokinetic; a paradoxical outward motion during systolic contraction is called dyskinesis. In accordance with other cross-sectional cardiac imaging modalities, the segment model of the American Heart Association should be used to describe the exact location of abnormal motion (Cerqueira 2002).

7.10.3 Data Acquisition and Image Reconstruction

Since information on virtually any cardiac phase is contained in an ECG-gated multi-slice CT spiral data set, images from end-systolic and end-diastolic phases can be retrospectively produced using ECG gating without the need for additional radiation exposure or administration of contrast material. From the reconstructed axial CT images, quantitative information on ventricular volume changes throughout the cardiac cycle can be derived.

Pure ventricular function analysis is not the focus of multi-slice CT, since other non-invasive imaging modalities, which do not require ionizing radiation or administration of potentially nephrotoxic contrast media, are available. In most cases, functional assessment will be carried out complementary to coronary CTA, and the imaging protocols are the same. While coronary CTA aims for selective enhancement of the coronary arteries and left ventricle, homogenous contrast enhancement in all cardiac chambers is crucial for the reliable detection of cardiac contours, especially if right ventricular parameters are to be assessed. A biphasic injection of contrast agent with a second phase at reduced flow or – if a double-head injector is available – at 50% contrast-agent concentration and constant flow volume will produce adequate right ventricular opacification without artifacts from excessive contrast density in the right atrium or ventricle. Some multi-slice CT scanners provide prospective tube-current modulation with coronary artery scan protocols. As tube current is reduced during the systolic phase, image noise increases significantly. Since cardiac function studies do not need high-resolution images and make use if thicker section thickness, tube-current modulation should not prevent the assessment of cardiac function. However, published reports have not included tube-current modulation with their imaging protocols.

For global functional assessment, only a systolic and a diastolic phase is needed. To identify the proper image reconstruction windows, a single axial image is reconstructed every 5% of the RR-interval at a representative mid-ventricular level. The appropriate reconstruction windows for the systolic and diastolic phases are visually identified as the images showing the minimum and maximum ventricular diameter and checked against the ECG. The systolic phase is usually found at 25% of the RR-interval and the end-diastolic phase at around 85% (Juergens 2004).

This approach to determine the systolic and diastolic phases is vulnerable to criticism, since the

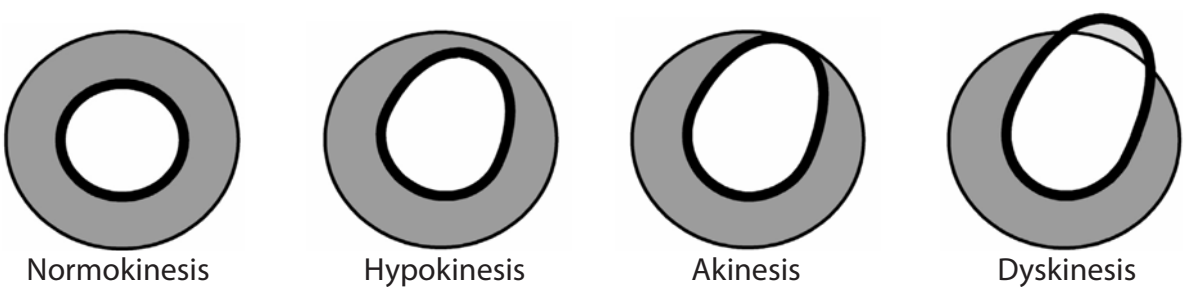

Fig. 7.74. Qualitative assessment of regional left ventricular (LV) wall motion. Regular LV wall motion is classified as normokinesis. Disturbances of LV wall motion are graded into hypokinesis (reduced regional systolic wall thickening), akinesis (absent regional systolic wall thickening), and dyskinesis (outward movement of the LV wall segment during systolic contraction)

transverse plane does not visualize the left ventricle in its appropriate anatomical axis. However, possible systematic errors should be minimal if the reference plane is chosen properly, i.e., at a level showing the anterior and posterior leaflets of the mitral valve and the anterior papillary muscle. The alternative would be to produce axial image sets every 5–10% of the cardiac cycle and visually determine the maximum and minimum ventricular volume from short-axis reformations. This method produces enormous amounts of unnecessary axial images and is very time-consuming due to the reconstruction time and extensive post-processing tasks involved. With the advanced raw-data reconstruction algorithms provided by some manufacturers, short-axis images can be directly produced from the acquired raw data (Fig. 7.75). This approach reduces the number of images created for the assessment of cardiac function and allows integrating global as well as regional function analyses seamlessly into a coronary CT study.

If direct reconstruction of short- and long-axis MPRs is not available, the same views can be generated manually with a few post-processing steps that are based on the axial images. A vertical long-axis view is produced along a line from the apex of the left ventricle to the middle of the mitral valve. Based on this long-axis view, a stack of secondary reformations in an orientation perpendicular to the vertical long axis and parallel to the mitral valve plane is created to encompass the entire left ventricle. The same approach is possible based on a horizontal long-axis reformation. The section thickness for the short-axis images is usually set to 8 mm, in analogy to CMR protocols.

7.10.4 Image Analysis

Diastolic and systolic left ventricular volumes can be calculated using standard software for distance and area measurements with the area-length method or Simpson's method. Software packages adapted from validated CMR analysis tools that semi-automatically measure ventricular volume and wall thickness are commercially available and help to speed up analysis and reporting. For the analysis of global function, only the endocardial borders of the left or right ventricle are needed. Endocardial contours are either automatically detected by the software or manually traced on systolic and diastolic short-axis images. The most basal slice lies just forward of the atrioventricular ring and should display the myocardium in at least 50% of its perimeter. The most apical slice is the last image showing a contrast-opacified lumen. By convention, the papillary muscles are included in the ventricular lumen. The analysis time is 10–15 min.

Endocardial and epicardial contours are required to assess wall thickness and systolic wall thickening, and to estimate cardiac mass. If regional wall motion is to be displayed, at least eight to ten heart phases are needed. Images from corresponding slice positions can be viewed in a cine loop to visually assess motion abnormalities. The analysis software will provide quantitative information on ventricular volume and wall thickness over time as well as volumes normalized to body surface area, which enables comparison to normal values (Table 7.13).

7.10.5 Limitations

Imaging of the moving heart requires a modality with a high temporal resolution in order to achieve artifact-free display of myocardial contraction over the cardiac function cycle and determination of peak systolic contraction. Usually, multi-slice cardiac CT reconstruction algorithms used for coronary artery visualization achieve a temporal resolution that is equivalent to the time for a 180° rotation and thus to half of the system rotation time. Two-segment reconstruction algorithms have also been introduced; these provide a temporal resolution that is one-fourth the rotation time at certain heart rates.

Thus, 250-ms temporal resolution using one segment and down to 125-ms temporal resolution using two segments were reached by the first 4-slice systems, with 500-ms rotation time. The newest 16-slice CT scanners provide rotation time down to 370 ms, and the latest 64-slice CT scanners even down to to 330 ms, thus improving temporal resolution even further. With rotation times of 400 ms or less and the use of up to two segments for image reconstruction, the assessment of global cardiac function with

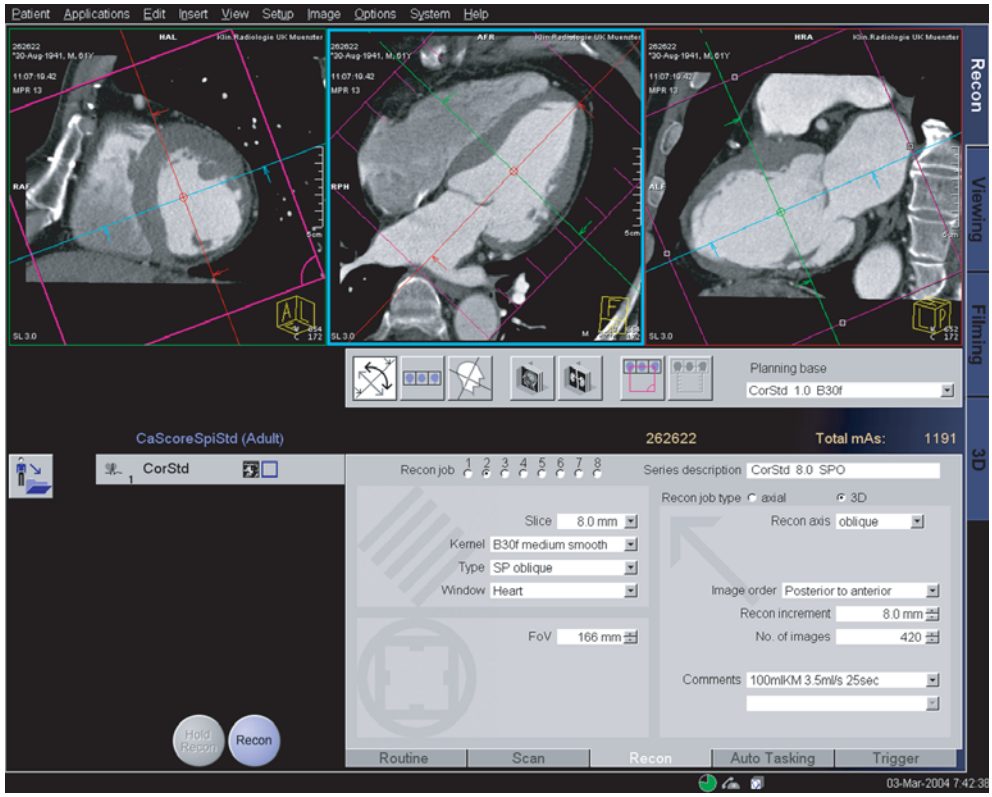

a

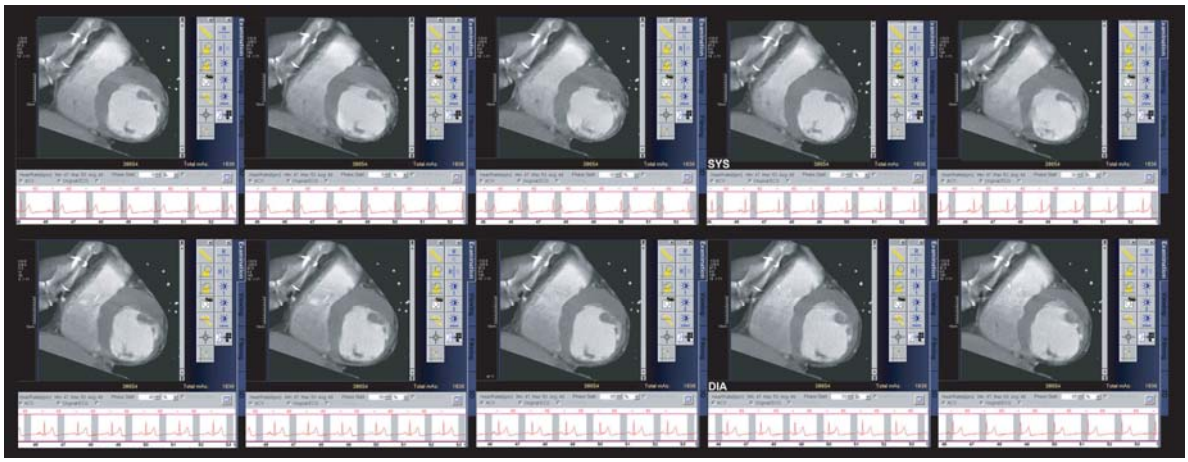

b

Fig. 7.75a,b. Direct generation of short-axis images from a multi-slice CT data set. **a** The appropriate orientation is interactively defined and a series of short-axis images is produced without the need to generate primary axial reformations. **b** Direct reconstruction of short-axis MPRs from mid-ventricular level images allows for easy identification of maximum contraction and maximum dilatation. Systolic and diastolic image series are then used for ventricular volume measurement

Table 7.13a. Global left ventricular (*LV*) and right ventricular (*RV*) function parameters adapted from cine magnetic resonance imaging data in healthy volunteers. *EDV* End-diastolic volume, *ESV* end-systolic volume, *EF* ejection fraction, *BSA* base area (from Sandstede 2000, Alfakih 2003)

	Males	Females
Left ventricle		
LV-EDV (ml)	102–235	96–174
LV-EDV/BSA (ml/m^2)	53–112	56–99
LV-ESV (ml)	29–93	27–71
LV-ESV/BSA (ml/m^2)	15–45	14–40
LV-EF (%)	55–73	54–74
LV mass (g)	85–181	37–67
LV mass/BSA (g/m^2)	46–83	–
Right ventricle		
RV-EDV (ml)	111–243	83–178
RV-EDV/BSA (ml/m^2)	111–243	48–103
RV-ESV (ml)	47–111	32–72
RV-ESV/BSA (ml/m^2)	25–53	18–42
RV-EF (%)	48–63	50–70

Table 7.13b. Regional LV function parameters adapted from CMR data in healthy volunteers (from Sandstede 2000, Alfakih 2003). *EDWT* End-diastolic wall thickness, *ESWT* end-systolic wall thickness, *SWT* systolic wall thickness, *SWTH* systolic wall thickening

	Males	Females
Left ventricle		
EDWT (mm)	7.6 ± 1.4	6.3 ± 1.0
ESWT (mm)	13.2 ± 1.8	12.2 ± 1.6
SWT (mm)	5.5 ± 0.8	5.8 ± 1.2
SWTH (%)	75 ± 16	96 ± 24

multi-slice CT is feasible. Multi-segment reconstruction algorithms using up to four segments have been developed to increase the temporal resolution for better assessment of regional function parameters. Using four segments and a rotation time of 370 ms, a temporal resolution of less than 50 ms can be realized. However, clinical experience with these image reconstruction algorithms is still limited.

Despite a pronounced improvement in temporal resolution, multi-segment algorithms suffer from several limitations. The spiral pitch has to be reduced to prevent degradation of the slice-sensitivity profile, which in turn adversely affects endocardial contour definition (Juergens 2005). A low pitch increases the scan time and, consequently, the radiation dose. Furthermore, optimal temporal resolution is only reached for a very specific heart rate, but heart rate only rarely remains constant for the duration of the entire scan.

7.10.6 Clinical Considerations

7.10.6.1 Measurement of Left Ventricular Function

Determination of global left ventricular function has a high clinical impact, since it is the strongest determinant of pump failure and death due to myocardial infarction (Shah 1986). Different non-invasive imaging modalities allow assessment of ventricular function and will eventually determine the potential role of multi-slice CT in this setting. Trans-thoracic echocardiography is a widely available, relatively inexpensive, and mobile modality for cardiac imaging. However, image acquisition is acoustically window and operator-dependent. The accuracy of quantitative left ventricular function measurement is hampered due to geometric assumptions of left ventricular shape, especially in remodeled hearts with complex and irregular shape changes.

Radionuclide ventriculography is commonly used to measure left ventricular EF, but it is hampered by its limited temporal and spatial resolution as well as the prolonged preparation and examination times (Lethimonnier 1999). Gated-perfusion single-photon emission computed tomography (SPECT) allows three-dimensional assessment of cardiac function and is especially useful when perfusion needs to be assessed. However, diagnostic accuracy is limited in small and large ventricles because of the technique's restricted spatial resolution. Furthermore, definition of ventricular borders in ventricular segments with circumscribed thinning after infarction can be difficult, due to very low

emission from these areas. The need for repeated radionuclide injections in sequential studies may also be problematic since radiation exposure cannot be neglected. The dose equivalent for myocardium and a blood-pool marker is about 8×10^{-1} mSv per 100 MBq with ^{99m}Tc-Tetrofosmin; 750–900 MBq ^{99m}Tc-Tetrofosmin are commonly used for first-pass radionuclide ventriculography.

EBCT has long been used successfully to measure cardiac function and mass; however, such systems are costly and the limited number of scanners available restricts access to this modality. Scanning is commonly done with prospective ECG synchronization in a sequential technique and thus suffers from the well-known limitations of this approach.

Currently, CMR is the gold standard for determining cardiac function. Its well-evaluated, documented advantages include the lack of radiation exposure, the avoidance of contrast-medium injection, and the excellent temporal resolution. Furthermore, short-axis images are easily produced and secondary reformations are not needed. There are few limitations and contraindications; for example, CMR is rather susceptible to irregular or changing heart rates and cannot be performed in patients with implanted pacemakers or defibrillators.

Due to the availability of the many competing imaging modalities, radiation exposure and the need for iodinated contrast material injection will prevent multi-slice CT from becoming a first-line modality for pure cardiac function evaluation. Still, the many advantages of multi-slice CT are apparent: (1) It does not rely on geometric assumptions when measuring cardiac chamber volumes and direct voxel-based volumetry can be applied; (2) it has an outstanding spatial resolution, data acquisition is quickly performed in a single breath-hold, and cardiac implants do not represent a contraindication; (3) cardiac function data are contained in any coronary artery CT study. Since multi-slice CT is becoming an accepted tool for coronary artery visualization, the combination of coronary artery imaging and global left ventricular function determination as a one-step procedure constitutes a promising approach to obtaining a conclusive cardiac assessment. At present, normal values for cardiac chamber volumes and global function, as determined from multi-slice CT, have not been published. Therefore, quantitative multi-slice CT data have to be referenced to normal values established by CMR or echocardiography. A synopsis of global and regional parameters of ventricular function determined by CMR is given in Table 7.13.

7.10.6.2 Accuracy and Reproducibility of Left Ventricular Volume and Function Measurement

Several studies have been published on the evaluation of left ventricular volume and function determination by multi-slice CT. End-diastolic and end-systolic volumes as well as left ventricular EF determined by multi-slice CT showed good agreement with respective measurements from cineventriculography, echocardiography, and CMR in patients with suspected or manifest coronary heart disease (Table 7.14). All authors reported a slight overestimation of left ventricular end-systolic volumes by multi-slice CT compared to CMR, resulting in a systematic underestimation of left ventricular EF of 1–7% (Juergens 2004a, Mahnken 2003, Grude 2003). The most likely explanation of this observation is the lower temporal resolution achieved by multi-slice CT systems compared to CMR. A temporal resolution of 30–50 ms per image is required to accurately capture the maximum systolic contraction, especially in patients with higher heart rates. The multi-slice CT scanners that have been used for referenced clinical studies had a fastest rotation time of 500 ms (4-slice CT) and 420 ms (16-slice CT) and image reconstruction was done using single-segment and 2-segment reconstruction. Thus, the temporal resolution provided was between 125 and 250 ms for 4-slice CT and between 105 and 210 ms for 16-slice CT. Due to the limited temporal resolution, end-systolic volumes were usually overestimated and thus EF was underestimated. Due to the faster rotation times of the newer 16-slice and recent 64-slice CT scanners, the improved temporal resolution will result in even better agreement between multi-slice CT and CMR measurements.

At present, the assessment of left ventricular function from multi-slice CT coronary angiography data sets has not entered clinical routine. Experience with multi-slice CT and cardiac function assessment has

Table 7.14. Comparison of LV-EDV and LV-ESV determined from multi-slice CT of the heart. Results are compared to cine-ventriculography (CVG), 2D-echocardiography (2D-Echo), and CMR using turbo-gradient echo (TGrE) and steady-state free precession (SSFP) cine sequences

Author	N	Modality compared to MSCT	LV-EDV	LV-ESV	LV-EF	LV-EF: MSCT vs. other modality (%)
Juergens 2002	22	CVG	–	–	0.80	–11.5 ± 5.7
Hundt 2002[a]	30	CVG	0.72	0.88	0.76	–13.7 ± 11
Heuschmid 2003[a]	25	CVG	0.59	0.82	0.88	–17 ± 9
Boehm 2004[a]	20	CVG	–	–	0.83	–4.7 ± 7.1
Dirksen 2002[a]	15	2D-echo	–	–	0.93	–1.3 ± 4.5
Grude 2003[a]	28	TGrE-CMR	0.92	0.90	0.90	–7.9 ± 5.6
Mahnken 2003[a]	16	SSFP-CMR	0.99	0.99	0.98	–0.9 ± 3.6
Juergens 2004a[b]	30	SSFP-CMR	0.93	0.94	0.89	–0.25 ± 4.9
Coche 2004[a]	14	SSFP-CMR	0.84	0.90	0.98	–
Juergens 2004b[b]	29	SSFP-CMR	0.95	0.96	0.95	–2.1 ± 4.8

[a]CT data were acquired using 4-slice CT technology.
[b]CT data were acquired using 16-slice CT technology.

been limited by the small patient numbers reported to date and by the rather homogenous patient populations (Juergens 2004a, Juergens 2002, Heuschmid 2003, Mahnken 2003, Grude 2004, Boehm 2004). Most reports describe patients with coronary heart disease and normal ranges of left ventricular size, configuration, and function. Since multi-slice CT is a true volumetric modality, enlarged or grossly deformed hearts should not influence the accuracy of the measurements. A recent study demonstrated that global cardiac function parameters were accurately determined by 16-slice CT in patients with left ventricular dysfunction or left ventricular dilatation (Juergens 2004b). Thinned left ventricular wall segments and reduced or absent systolic wall thickening after myocardial infarction was clearly delineated (Figs. 7.76, 7.77).

Only a few studies have used multi-slice CT to focus on the detection and quantification of regional myocardial dysfunction (Dirksen 2002, Mahnken 2003). Areas of impaired motion were identified with good reliability compared to echocardiography and CMR, but a definitive role for multi-slice CT needs to be further defined once improved post-processing tools and scanners with improved temporal resolution become widely available.

Reproducibility of global function parameters seems acceptable based on the available reports. The inter-observer variability was 2–11% for left ventricular end-diastolic volume and 6–9% for end-systolic volume. The corresponding values for CMR are 2–6%.

7.10.6.3 Myocardial Viability

The determination of left ventricular myocardial damage and its consecutive dysfunction is important with regard to the clinical management of patients with coronary heart disease, especially if viable myocardium can be detected and myocardial revascularization might lead to improvement in left ventricular function and patient survival. The "late enhancement" phenomenon, initially described for CT of the heart, has become the cornerstone for detection of myocardial scar tissue and assessment of myocardial viability with CMR. Recently the technique has been re-transferred to multi-slice CT to investigate myocardial viability (Koyama 2004).

Initial observations made in a study comparing the myocardial enhancement patterns seen with CT

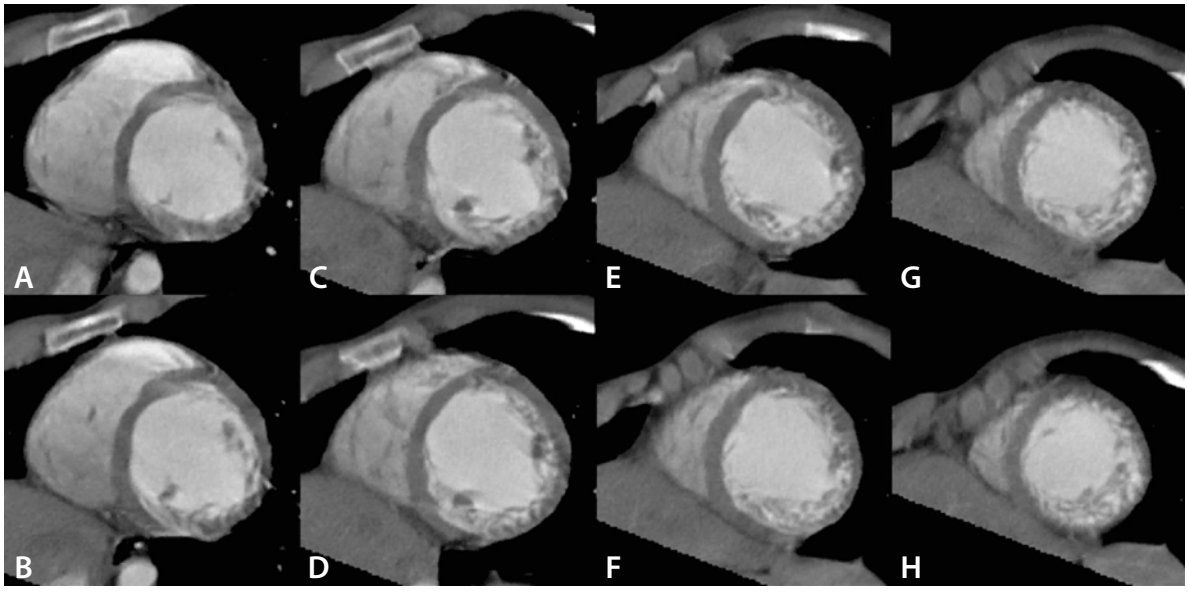

a

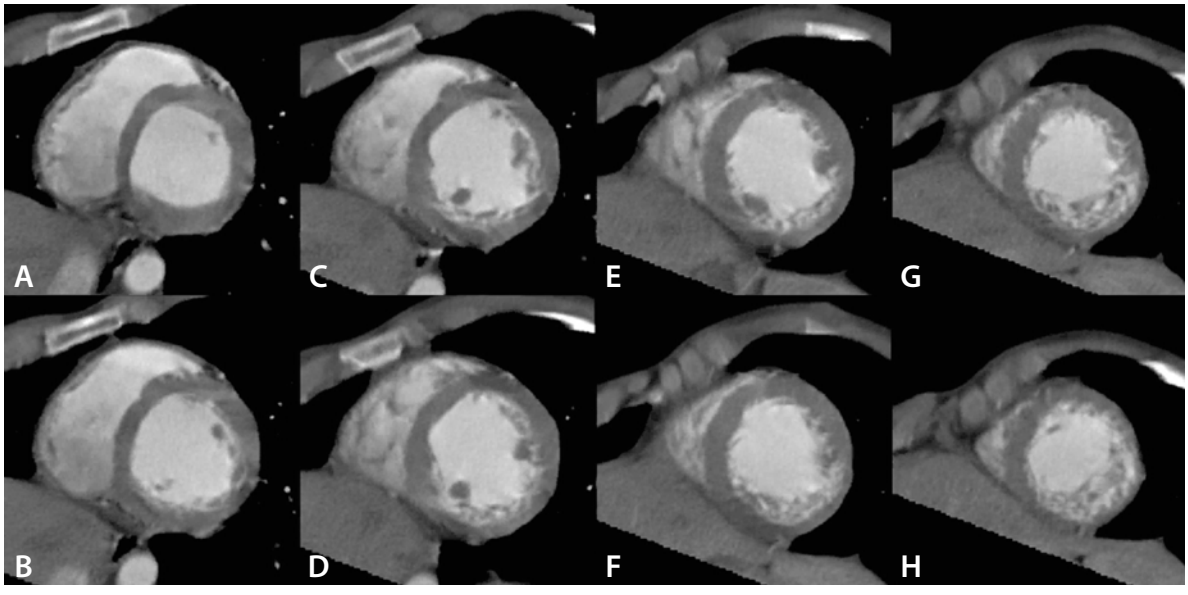

b

Fig. 7.76a,b. 16-slice CT study from a 29-year-old man suffering from dilatative cardiomyopathy. Short-axis diastolic (**a**) and systolic (**b**) image reconstructions each from eight contiguous levels (A–H) of the left ventricle illustrate its heavily dilated cavity (end-diastolic volume: 357.8 ml) and global hypokinesis (left ventricular ejection fraction: 22.1%)

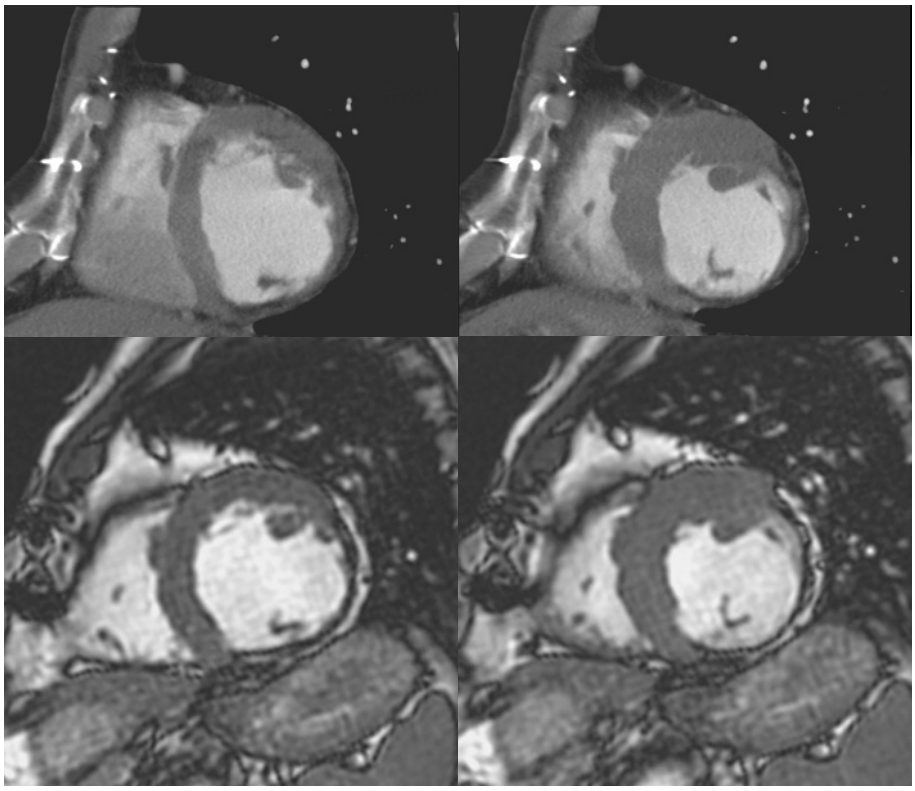

Fig. 7.77. 16-slice CT study from a 64-year-old male patient with 2-vessel coronary artery disease who underwent bypass surgery. Diastolic (left column) and systolic (right column) short-axis reformations from 16-slice CT (upper row) and cine magnetic resonance imaging (CMR, lower row) studies demonstrate reduced left ventricular diastolic myocardial wall thickness and absent systolic wall thickening in the lateral and inferior myocardium. calculation of the left ventricular ejection fraction (LVEF) with 16-slice CT and CMR correspond well (LV-EF by 16-slice CT = 60.6%, LV-EF by CMR = 61.7%)

those of dual isotope SPECT showed that the extent of an early myocardial enhancement deficit could predict subsequent myocardial wall thickness and wall motion recovery in patients after successful revascularization (Koyama 2002).

7.10.6.4 Right Ventricular Disease

Even though published reports on ventricular function determination have focused on the left ventricle, multi-slice CT seems to also be a promising modality for the diagnosis of right ventricular diseases. The excellent spatial resolution is advantageous for the depiction of the rather thin right ventricular myocardium, and CT does not suffer from acoustic window or signal intensity limitations. Right ventricular shape can be well-depicted if an appropriate contrast-injection protocol is used (see above).

Right ventricular enlargement has been reported to be a prognostic factor and a predictor of early death in patients with acute pulmonary embolism (Quiroz 2004, Schoepf 2004). Even though conventional multi-slice chest CTA protocols were used in these studies, the application of ECG-gated protocols may help to eliminate underestimation or overestimation of right ventricular enlargement in future clinical use.

Fatty replacement of the right ventricular myocardium is easily depicted with CT and is an important finding in arrhythmogenic right ventricular cardiomyopathy (ARVC). ARVC is a genetic cardiomyopathy characterized by right ventricular enlargement, hypertrophied trabeculations, abundant epicardial fat, and fibro-fatty replacement of right ventricular musculature, all of which lead to ventricular arrhythmia and right ventricular failure. Exclusion or confirmation of ARVC is especially important in young adults presenting with clinical symptoms that may vary from occasional palpitations to syncope or even to sudden cardiac death. At present, only preliminary data on the detection of morphologic and functional pathologies in ARVC with multi-slice CT have been published (Bomma 2003). While the ability to detect regional abnormalities of right ventricular wall motion needs to be further investigated, multi-slice CT offers a large potential to initially diagnose right ventricular abnormalities and to follow patients with ARVC after implantation of a defibrillator.

7.10.7 Summary and Outlook

Although the assessment of cardiac function with multi-slice CT has not entered clinical routine, several studies using 4-and 16-slice CT scanners have shown that the determination of cardiac chamber volumes and, consequently, global cardiac function parameters is feasible, and the results are in good agreement with established imaging modalities as cine ventriculography, echocardiography, and the gold-standard CMR. The limited temporal resolution of 4-slice CT scanners and first generation 16-slice CT scanners results in an overestimation of end-systolic volume and an underestimation of EF compared to CMR. However, the faster rotation speeds of the newer 16-slice and the latest 64-slice CT scanners, with rotation times down to 330 ms, combined with multi-segment reconstruction algorithms are expected to provide significantly better end-systolic image quality (Fig. 7.78) and even better agreement of global cardiac function parameters measured by CMR. Newly developed cardiac post-processing tools enable a true volumetric segmentation of the contrast-enhanced cardiac chambers based on the thin-slice data sets (Fig. 7.79). Reconstruction of short-axis MPRs as input for Simpson's calculation will no longer be required. These new semi-automated tools can provide a comprehensive analysis of global cardiac function parameters in 2–3 min. Consequently, the clinical applicability of global left ventricular functional assessment with multi-slice CT will substantially increase. Nonetheless, careful development of standardized quantification methods and successful evaluation in relation to the gold-standard modalities will be required.

Regional function analysis, such as regional wall motion and wall thickening, is possible with 16-slice CT for patients at rest. The further improvement in temporal resolution provided by 64-slice CT scanners in combination with multi-segment reconstruction is a prerequisite for obtaining agreement with the results of CMR analyses and for carrying out imaging studies of patients under physical stress.

Due to the radiation exposure and the need to inject iodinated contrast material, multi-slice CT may be the first-line modality for cardiac function evaluation only in a select group of patients, such as those with contra-indications for CMR. However, as cardiac function data are contained in any coronary artery CT study and since multi-slice CT is becoming an accepted tool for coronary artery visualization, the combination of coronary artery imaging and global left ventricular function determination as a one-step procedure constitutes a promising approach to a conclusive cardiac assessment.

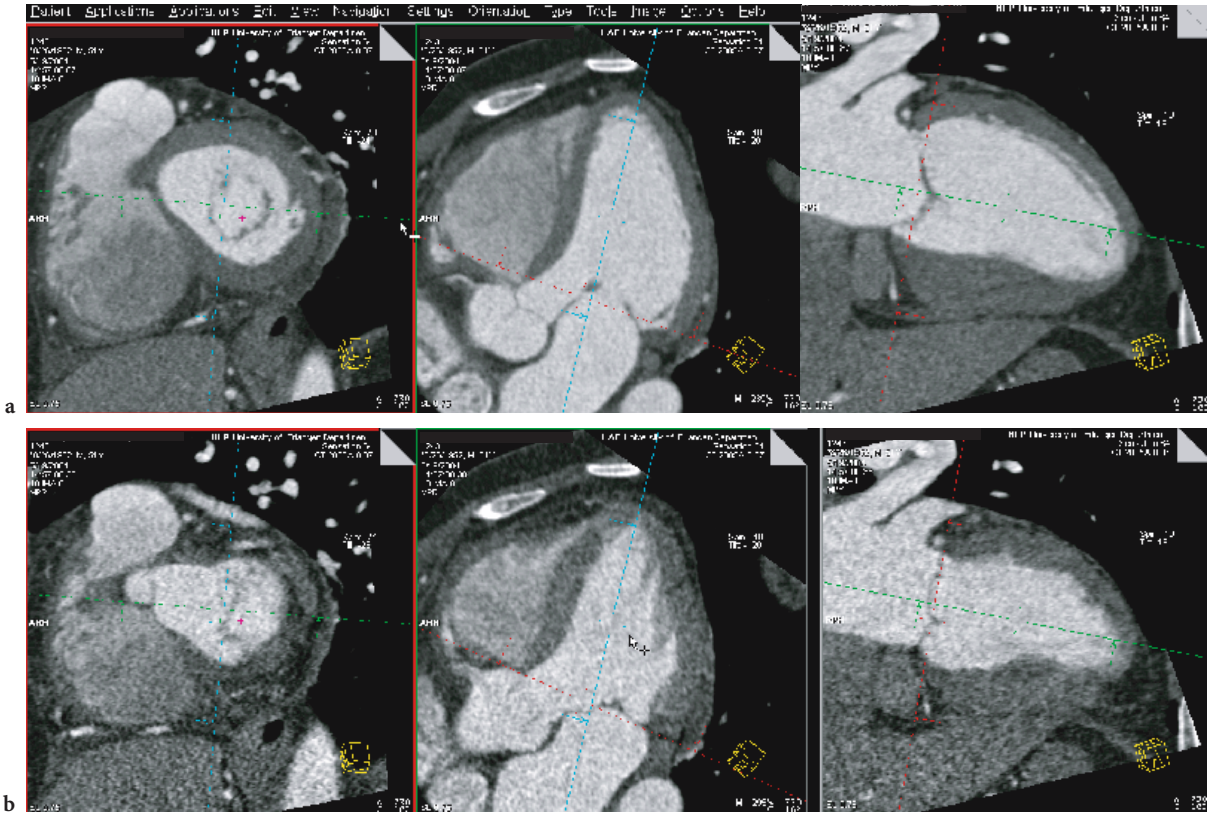

Fig. 7.78a,b. A patient with a normal EF of 59% was examined with 64-slice CT, 330-ms rotation time, and ECG-pulsed acquisition. Due to the high temporal resolution, the images in end-diastole (**a**) and in end-systole (**b**) are virtually free of motion artifacts. ECG pulsing causes the relatively high image noise in systolic reconstruction. However, the use of ECG pulsing does not compromise cardiac function evaluation since noisier axial slices or MPRs with thicker slices are acceptable as input for segmentation of the chambers and for ventricular analysis

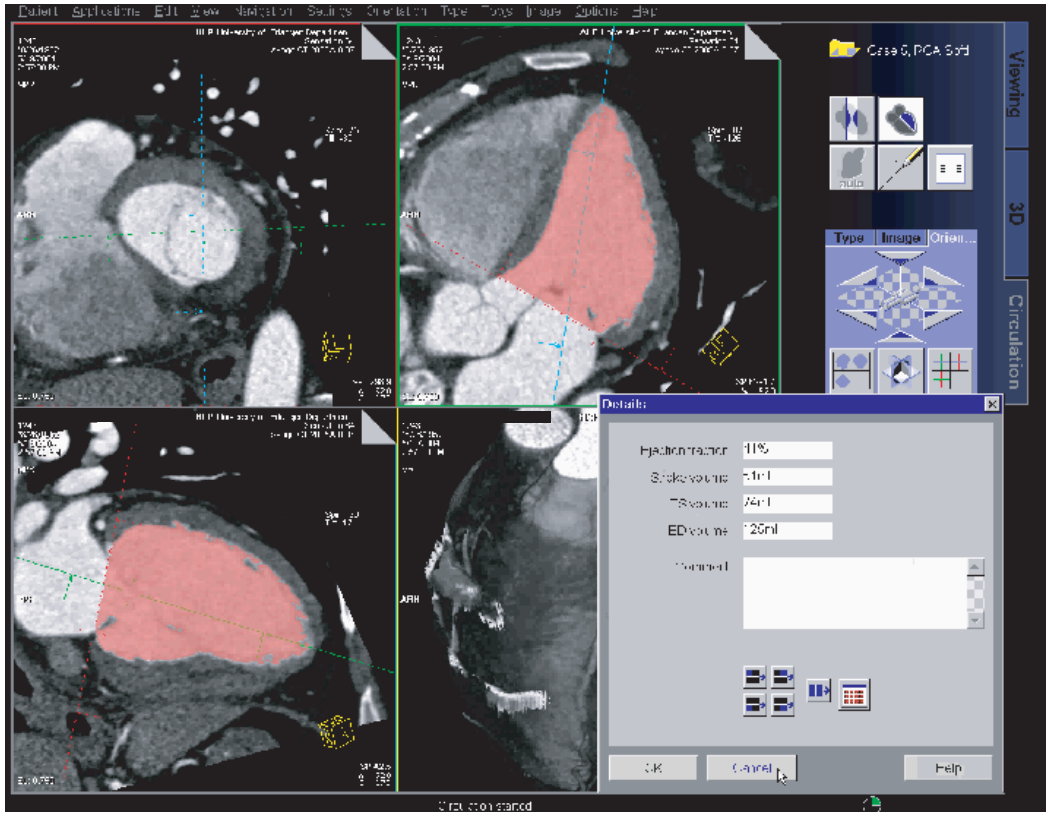

Fig. 7.79. New evaluation platform for semi-automated cardiac function assessment illustrated with a 64-slice cardiac CT data set. Ventricular volumes are calculated with a threshold- and voxel-based segmentation of the contrast-enhanced blood within the ventricle. Start-plane and end-plane of the segmentation are positioned in the plane of the mitral valve and at the apex of the heart. The thresholds were selected such that the papillary muscles are not included in the volume calculation

References

Alfakih K, Plein S, Thiele H, Jones T, Ridgway JP, Sivananthan MU (2003). Normal human left and right ventricular dimensions for MRI as assessed by turbo gradient echo and steady-state free precession imaging sequences. J Magn Reson Imaging 17:323–329

Boehm T, Alkadhi H, Roffi M, et al (2004). Time-effectiveness, observer-dependence, and accuracy of measurements of left ventricular ejection fraction using 4-channel MDCT. Fortschr Röntgenstr 176:529–537

Bomma C, Tandri, Nasir K, et al (2003). Role of helical CT in qualitative and quantitative evaluation of arrhythmogenic right ventricular dysplasia. Pacing Clin Electrophysiol 26 (Suppl 1):965

Cerqueira MD, Weissman NJ, Dilsizian V, et al (2002). Standardized myocardial segmentation and nomenclature for tomographic imaging of the heart. A statement for healthcare professionals from the Cardiac Imaging Committee of the Council on Clinical Cardiology of the American Heart Association. Circulation 105:539–542

Coche E, Belge B, Vlassenbroeck A, et al (2004). Accurate assessment of left ventricular volumes and ejection fraction using retrospectively gated multislice cardiac CT: comparison with cine MRI. Eur Radiol 14:S2–270

Dirksen MS, Bax JJ, de Roos A, et al (2002). Usefulness of dynamic multislice computed tomography of left ventricular function in unstable angina pectoris and comparison with echocardiography. Am J Cardiol 90:1157–1160

Grude M, Juergens KU, Wichter T, et al (2003). Evaluation of global left ventricular myocardial function with electrocardiogram-gated multidetector computed tomography. com-

parison with magnetic resonance imaging. Invest Radiol 38:653–661

Heuschmid M, Küttner A, Schröder S, et al (2003). Left ventricular functional parameters using ECG-gated multidetector spiral CT in comparison with invasive ventriculography. Fortschr Röntgenstr 175:1349–1354

Hundt W, Siebert K, Becker C, Knez A, Rubin GD, Reiser MF (2002). Assessment of global left ventricular function: comparison of multidetector computed tomography with left ventriculography. Radiology 225(P):388

Juergens KU, Grude M, Fallenberg EM, et al (2002). Using ECG-gated multidetector CT to evaluate global left ventricular myocardial function in patients with coronary artery disease. Am J Roentgenol 179:1545–1550

Juergens KU, Grude M, Maintz D, et al (2004a). Multi-detector row CT of left ventricular function with dedicated analysis software versus mr imaging: initial experience. Radiology 230:403–410

Juergens KU, Grude M, Maintz D, et al (2004b). Semiautomated analysis of left ventricular function using 16-slice multidetector-row computed tomography (MDCT) of the heart in comparison to steady-state-free-precession (SSFP) cardiac magnetic resonance imaging. Eur Radiol 14:S2–272

Juergens KU, Maintz D, Grude M, et al (2005). Multidetector-row computed tomography of the heart: Does a multi-segmented reconstruction algorithm improve left ventricular volume measurements? Eur Radiol 15:111–117

Koyama Y, Matsuoka H, Higashino H, Kawakami H, Ito T, Mochizuki T (2003). Myocardial perfusion pattern by two-phase contrast CT predicts clinical outcome in patients with acute myocardial infarction after successful reperfusion therapy. Radiology 225(Suppl P):153

Koyama Y, Mochizuki T, Higaki J (2004). Computed tomography assessment of myocardial perfusion, viability, and function. J Magn Reson Imaging 19:800–815

Lethimonnier F, Furber A, Balzer P, et al (1999). Global left ventricular cardiac function. Comparison between magnetic resonance imaging, radionuclide angiography, and contrast angiography. Invest Radiol 34:199–203

Mahnken AH, Spuentrup E, Niethammer M, et al (2003). Quantitative and qualitative assessment of left ventricular volume with ECG-gated multislice spiral CT: value of different image reconstruction algorithms in comparison to MRI. Acta Radiol 604–611

Mahnken AH, Spüntrup E, Wildberger JE, et al (2003). Quantification of cardiac function with Multislice Spiral CT using retrospective ECG-gating: comparison with MRI. Fortschr Röntgenstr 175:83–88

Ohnesorge B, Flohr T, Becker C R, Kopp A F, Knez A Baum U, Klingenbeck-Regn K, Reiser MF (2000). Cardiac imaging by means of electrocardiographically gated multisection spiral CT: Initial Experience. Radiology 217:564–571

Quiroz R, Kucher N, Schoepf UJ, et al (2004). Right ventricular enlargement on chest computed tomography; prognostic role in acute pulmonary embolism. Circulation 109:2401–2404

Sandstede J, Lipke C, Beer M, et al (2000). Age- and gender-specific differences in left and right ventricular cardiac function and mass determined by cine magnetic resonance imaging. Eur Radiol 10:438–442

Schocken DD, Arrieta MI, Leaverton PE, Ross EA (1992). Prevalence and mortality rate of congestive heart failure in the United States. J Am Coll Cardiol 20:301–305

Schoepf UJ, Kucher N, Kipfmueller F, et al (2004). Right ventricular enlargement on chest computed tomography; a predictor of early death in acute pulmonary embolism. Circulation 110:3276–3280

Shah PK, Maddahi J, Staniloff HM, et al (1986). Variable spectrum and prognostic implications of left and right ventricular ejection fraction in patients with and without clinical heart failure after acute myocardial infarction. Am J Cardiol 58:387–393

White HD, Norris RM, Brown MA, Brandt PWT, Whitlock RML, Wild CJ (1987). Left ventricular end-systolic volume as the major determination of survival after recovery from myocardial infarction. Circulation 76:44–51

7.11 Imaging and Diagnosis of Cardiac Valves

J. Willmann

Contents

7.11.1 Introduction *281*
7.11.2 Technical Considerations *281*
7.11.3 Valvular Morphology *282*
7.11.3.1 Aortic Valve *282*
7.11.3.2 Mitral Valve *283*
7.11.4 Valvular Disease *283*
7.11.4.1 Aortic Valve *283*
7.11.4.2 Mitral Valve *285*
7.11.5 Limitations *285*
7.11.6 Conclusion *286*
References *286*

7.11.1 Introduction

With the introduction of multi-slice CT technology in 1998 and the subsequent continuous development of the technique, an increasing number of patients with cardiac disease are being examined using multi-slice CT. The technology combines high temporal and spatial resolution, which allows a non-invasive assessment of the moving heart with high morphological details. Combined with retrospective ECG gating, the clinical indications of multi-slice CT are considered to be the detection and quantification of coronary artery stenosis and calcification, evaluation of CABG patency and stenosis, as well as the diagnosis of pericardial abscess formation, constrictive pericarditis, and cardiac tumors and thrombus (Hahn 2004, Willmann 2004). A comprehensive work-up of patients with cardiac symptoms also includes assessment of the cardiac valves. Important information about the cardiac valves can be obtained from the same single multi-slice CT data set acquired for imaging other cardiac structures and no additional multi-slice CT scanning is required for evaluation of the cardiac valves.

In this section, the capability of multi-slice CTA in imaging and diagnosis of the aortic and mitral valves is described.

7.11.2 Technical Considerations

To assess the anatomical details of the cardiac valves, the use of contrast medium is suggested. However, in the quantification of aortic or mitral valve calcification by multi-slice CT scanning, intravenous contrast medium is not required. The technical imaging protocols for the different generations of multi-slice CT scanners are summarized in Chapter 6 of this book.

For contrast-enhanced multi-slice CT scanning, optimal contrast can be obtained either by the test bolus or bolus-tracking method. In the test bolus method, the optimal delay time of a multi-slice CT scan is determined by visually evaluating the contrast material at the level of the aortic valve by obtaining ten consecutive transverse images after intravenous administration of 20 ml of contrast medium. The time of optimal contrast at the level of the aortic valve is chosen as the delay time for the subsequent multi-slice CT scan of the heart. In the bolus-tracking technique, repetitive measurements of contrast enhancement at the level of the aortic valve are obtained after intravenous administration of the total amount of contrast material. When a preset contrast enhancement level (between 100 and 150 HU) is reached, the multi-slice CT scan is initiated automatically.

Multi-slice CT scanning is done with a total of 80–120 ml non-ionic iodinated contrast material administered intravenously using a power injector at a flow rate of 3–5 ml/s and followed by a saline chaser of 30–50 ml at the same flow rate.

The digital ECG file of the patient obtained during multi-slice CT scanning is used to retrospectively reconstruct the multi-slice CT data set at different reconstruction intervals within the cardiac cycle. The aortic and mitral valves are best evaluated by MPRs, which are obtained parallel and perpendicular to the aortic and mitral valve annulus.

7.11.3 Valvular Morphology

7.11.3.1 Aortic Valve

The aortic valve consists of the aortic valve annulus and the three aortic valve cusps (right and left cusps as well as non-coronary, posterior cusp) with their free edges (Fig. 7.80). Bicuspid aortic valve (two cusps) is the most common congenital anomaly, with an estimated incidence between 0.9 and 2% in the general population. In bicuspid aortic valve, there is usually one larger (conjoined) cusp that contains a shallow ridge (raphe) representing the line of congenital fusion of the two cusps. Usually there are two complete commissures. The presence of a partially fused commissure (also called high raphe) predisposes towards eventual stenosis.

Optimal image quality of the anatomical details of the aortic valve can be obtained during diastole (closed aortic valve). This corresponds to a reconstruction interval between 50 and 70% of the cardiac cycle. To assess the aortic valve orifice, the multi-slice CT data set is reconstructed during systole (opened aortic valve) at an optimal reconstruction interval between 0 and 20% of the cardiac cycle.

The anatomical details of the aortic valve are best assessed using contrast medium. In a prospective study, 25 patients with aortic valve stenosis were examined using 4-slice CT. The annulus and cusps of the aortic valve, including the free edges of the cusps, were better visualized on contrast-enhanced than on non-enhanced multi-slice CT (Willmann 2002a). Multi-slice CT also allows reliable differentiation between the bicuspid and tricuspid aortic valves. There was 100% agreement between multi-slice CT and echocardiography with respect to aortic valve morphology using contrast-enhanced multi-slice CT, whereas there was a mismatch between multi-slice CT and echocardiography in two patients examined by non-enhanced multi-slice CT (Willmann 2002a). Further studies using the newer 16- and 64-slice CT technologies are needed to assess whether multi-slice CT reconstructed during diastole also differentiates between a tricuspid and a bicuspid aortic valve with a high raphe. Multi-slice CT also allows accurate measurement of the diameter of the aortic valve annulus (Fig. 7.81a). With this approach, the diameter correlates highly

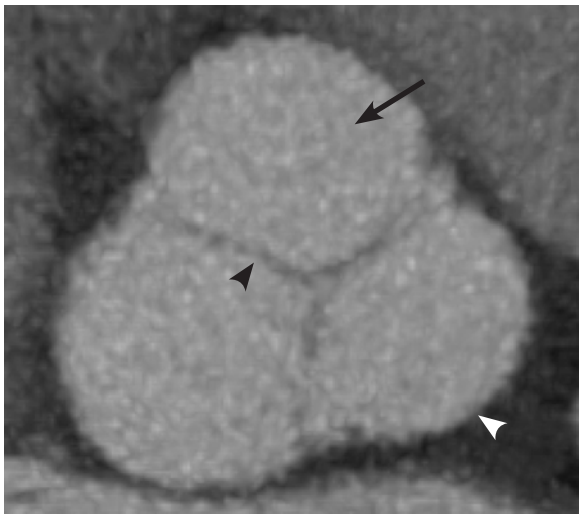

Fig. 7.80. Multi-planar reconstruction of a tricuspid aortic valve reconstructed parallel to the aortic valve annulus. Aortic valve annulus (*white arrowhead*), aortic valve cusp (*arrow*) with free edge of the aortic valve cusp (*black arrowhead*). Retrospective ECG-gated reconstruction of multi-slice CT data set were obtained at 60% of the cardiac cycle

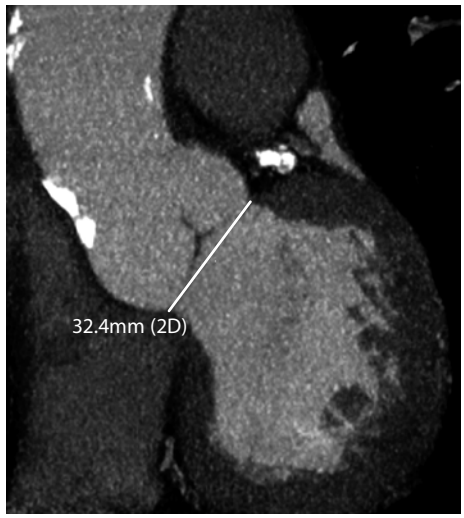

Fig. 7.81. Visualization of the aortic valve based on a 16-slice CT examination. MPR perpendicular to the aortic valve annulus allows accurate preoperative assessment of aortic valve annulus diameter

with intraoperative measurement, despite a mean overestimation of 0.7 mm on multi-slice CT data sets (Willmann 2002a). However, also in this application, improved accuracy can be expected with the sub-millimeter resolution of 16- and 64-slice CT scanners (Fig. 7.81b).

7.11.3.2 Mitral Valve

The anatomical details of the mitral valve and its apparatus include the anterior (aortic) and posterior (mural) mitral valve leaflets, the anterolateral and posteromedial commissures, the mitral valve annulus, tendinous cords, and papillary muscles (Fig. 7.82). The anterior leaflet is in fibrous continuity with the aortic valve and meets the posterior leaflet to form an arc-shaped closure line called the zone of apposition. Due to the fast and complex movement of the mitral valve within the cardiac cycle, imaging of the valve by multi-slice CT is challenging. The best image quality of the anatomical details of the mitral valve can be obtained during time intervals within the cardiac cycle, during which there is the least movement of the valve. This corresponds to either systole (closed valve; best image quality between 0 and 20% of the cardiac cycle) or diastole (open valve; best image quality between 50 and 70% of the cardiac cycle), whereas image quality is degraded during the transitional time.

The image quality of the mitral valve and its apparatus was assessed on multi-slice CT scans in a prospective study of 20 patients with mitral valve disease who underwent 4-slice CT and echocardiography preoperatively (Willmann 2002b). Good to excellent image quality of the mitral valve annulus and its leaflets were obtained in 15 of 20 patients (75%). In 19 of 20 patients (95%), visibility of the papillary muscles was good or excellent. The visibility of the tendinous cords was inferior. In 14 of 20 patients (70%), they were not or only moderately visible (Willmann 2002b). The small size of the tendinous cords, between 0.5 and 1 mm, and their high anatomical variability may have contributed to the non-diagnostic image quality in a large percentage of patients in this study. It can be expected that the improved spatial and temporal resolution of 16- and 64-slice CT scanners will allow reliable delineation of the entire mitral valve morphology in a higher proportion of patients (Fig. 7.83).

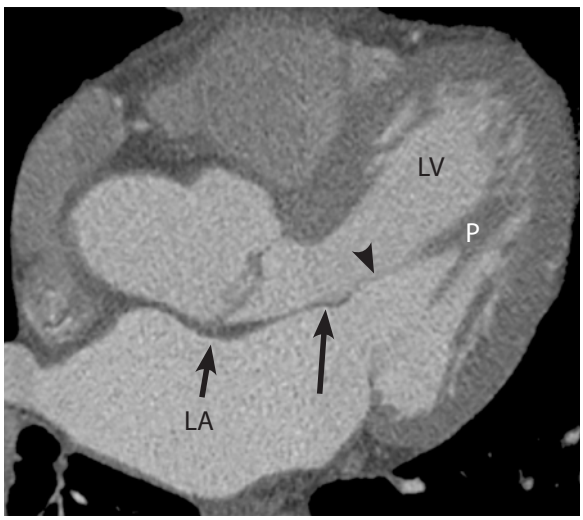

Fig. 7.82. Multi-planar reconstruction of a mitral valve obtained perpendicular to the mitral valve annulus demonstrates the mitral valve leaflet (*arrow*), mitral valve annulus (*small arrow*), and tendinous cord (*arrowhead*). P Papillary muscle

7.11.4 Valvular Disease

7.11.4.1 Aortic Valve

Multi-slice CT is highly accurate method for the detection and quantification of calcification. From the point of view of cardiology and cardiac surgery, accurate assessment of aortic valve calcification by multi-slice CT is of particular interest. The amount of aortic valve calcification has been identified as a strong predictor for both the progression and the outcome of patients with aortic valve stenosis (Otto 1999, Rosenhek 2000). The significant association between aortic valve calcification and hypercholesterolemia suggest an important role of lipids in the etiology of aortic valve calcification. Lipid-lowering pharmacological therapy with HMG CoA reductase inhibitors was shown to have a positive therapeutic effect on the natural history of calcific aortic val-

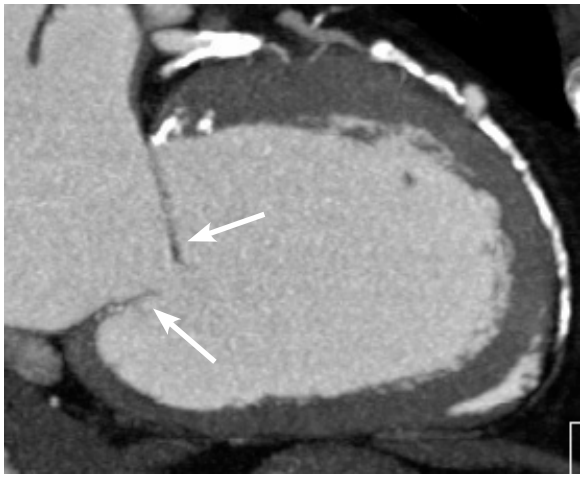

Fig. 7.83. Multi-planar reconstruction of a 16-slice cardiac CT examination along the long axis of the heart through the mitral valve plane. The increased spatial resolution of 16-slice CT enables improved visualization of the mitral valve flaps (*arrows*) compared to 4-slice CT

vular disease (Shavelle 2002). Therefore, an imaging modality for accurate quantification of aortic valve calcium in patients with aortic valve stenosis is desirable.

From a surgical point of view, preoperative knowledge of the extent and exact localization of the aortic valve and annulus calcification is of paramount interest, since extensive calcification may lead to technical difficulties during surgery. Reinsertion of the coronary arteries after aortic root replacement, as well as placement and fixation of the aortic valve prosthesis into the aortic valve annulus are complicated by calcification of the aortic valve root and aortic valve annulus (Mullany 2000). In addition, preoperative awareness of the presence of aortic valve calcification extending to the interventricular septum may be useful, as this finding predicts the need for permanent pacing postoperatively (Boughaleb 1994). Finally, the long-term performance of a biological aortic valve prosthesis has been demonstrated to be related to calcification of the aortic valve cusps, and accurate quantification of aortic valve calcification may predict the long-term performance of the biological aortic valve prosthesis (Melina 2001).

Only a few studies have as yet addressed the value of multi-slice CT for quantification of aortic valve calcification (Willmann 2002a, Morgan-Hughes 2003, Cowell 2003). Based on a semi-quantitative grading scale for aortic valve calcification, an agreement of 84% between multi-slice CT findings and visual evaluation of the calcification status of the aortic valves as assessed during surgery was demonstrated (Fig. 7.83) (Willmann 2002a). The volumetric quantification technique for calcium assessment described by Callister et al. (Callister 1998), was shown to be highly reliable in the quantification of aortic valve calcium. Mean inter-scan variability was only 7.9% for quantification of aortic valve calcification in 50 patients who underwent multi-slice CT (Morgan-Hughes 2003); however, in that study, the inter-scan variability was higher (10–20%) in patients with low to moderate aortic valve calcium (Morgan-Hughes 2003).

A moderate but significant correlation between semi-quantitative assessment of aortic valve calcification by multi-slice CT and the mean pressure gradient of the aortic valve, as obtained using transthoracic Doppler echocardiography, could be demonstrated in a study of 25 patients who underwent both multi-slice CT and surgery (Willmann 2002a). In another study with 50 patients, a highly significant relation between aortic valve calcification, as determined by multi-slice CT, and the instantaneous peak velocity gradient across the aortic valve as well as the aortic valve area was demonstrated (Willmann 2002a). Cowell et al. (Cowell 2003), in another study, concluded that heavy aortic valve calcification, as seen on multi-slice CT, suggests the presence of sever aortic valve stenosis requiring urgent cardiologic assessment, whereas patients with a lesser degree of aortic valve calcification may be screened for aortic stenosis and monitored for disease progression.

The accuracy of aortic valve calcification measurement was validated in a histomorphometric study of EBCT (Pohle 2004). The mean difference between the amount of calcium of the explanted aortic valves, as determined by EBCT and histomorphometric analysis, was as low as –0.5% ± 5.9% (Pohle 2004). While similar results can be assumed for multi-slice CT, this needs to be verified by prospective studies.

7.11.4.2 Mitral Valve

Multi-slice CT allows assessment of the morphological pathologies typically seen in patients with mitral valve disease, including thickening of the mitral valve leaflets, mitral valve annulus calcification (MAC), and calcifications of the leaflets. According to echocardiographic criteria (Davidoff 2001) mitral valve leaflets are considered abnormally thickened if their free edges are > 2 mm in diameter; thickening of the leaflets is > 5 mm is considered to be extensive thickening. The presence of MAC and calcifications of the mitral valve leaflets are diagnosed when isolated or confluent areas of calcifications are identified on the mitral valve annulus or leaflets. If the thickness of MAC is > 5 mm, this is referred to as heavy calcification (Adler 1998).

Exact evaluation and quantification of mitral valve leaflet thickness is possible with multi-slice CT, with an agreement compared to echocardiography and surgery of 95–100%, as shown in a study with 20 patients with mitral valve disease (Willmann 2002b).

A potential indication of multi-slice CT for functional assessment of the mitral valve in patients who may not undergo echocardiography or MRI is the diagnosis of residual systolic anterior movement of the mitral valve and tendinous cords. In a study of ten patients with hypertrophic obstructive cardiomyopathy who underwent percutaneous transluminal septal myocardial ablation, there was excellent agreement between 4-slice CT and echocardiography with regard to the diagnosis of residual systolic anterior movement of the mitral valve (de Vos 2004). Assessment of the mitral valve on video loops obtained from multi-slice CT images reconstructed at different reconstruction intervals of the cardiac cycle may be useful for this indication.

Multi-slice CT may also provide a non-invasive alternative for trans-thoracic or trans-esophageal echocardiography in the early identification of perivalvular abscesses complicating endocarditis, since timely surgery is needed before widespread destruction of the valve occurs (Willmann 2002b).

7.11.5 Limitations

A major limitation of multi-slice CT scanning of the cardiac valves is the fact that functional imaging of the valves, including calculation of a pressure gradient along the aortic and mitral valve, is not possible with multi-slice CT. A second limitation is related to the radiation exposure of the patient during scanning. Since the data are acquired with an overlapping helical pitch and continuous radiation exposure, there is a considerable amount of applied radiation (Hunold 2003). Improvements in the amount of exposure have been achieved with the recent generation multi-slice CT scanners. While the spatial resolution of 4- and 16-slice CT scanners are usually sufficient to visualize the valvular morphol-

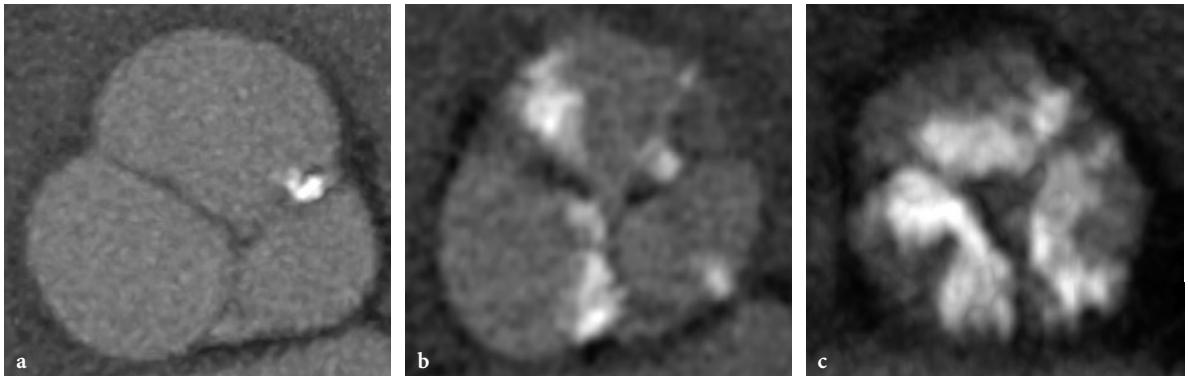

Fig. 7.84a–c. Semi-quantitative assessment of aortic valve calcification on MPR obtained parallel to the aortic valve annulus in three different patients. **a** Mild aortic valve calcification, **b** moderate aortic valve calcification, **c** heavy aortic valve calcification

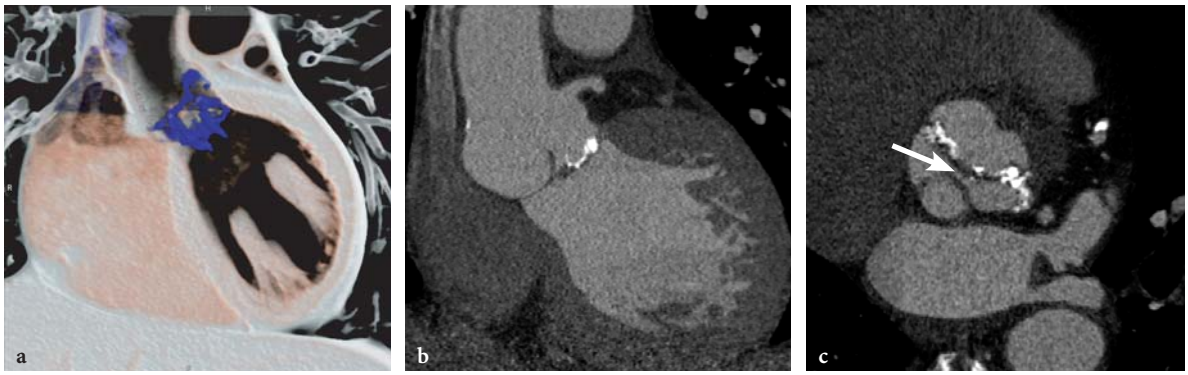

Fig. 7.85a–c. Cardiac 64-slice CT examination of a patient with aortic valve disease. Images were reconstructed during the diastolic phase at 60% of the RR-interval. VRT reconstruction (**a**) and MPR (**b**) reveal extensive calcification. MPR through the valve plane (**c**) demonstrates incomplete closing of the aortic valve (*arrow*)

ogy, the temporal resolution is often insufficient to allow for motion-free imaging of the systolic phase, and thus does not allow assessment of valvular function. The increased spatial and temporal resolution of the latest 64-slice CT scanners holds promise that also functional defects of the valves can be visualized (Fig. 7.85).

7.11.6 Conclusion

Multi-slice CT is a continuously evolving technology that is increasingly used for cardiovascular applications, in particular to assess the coronary arteries and CABGs. A comprehensive work-up of these patients, however, also includes assessment of the cardiac valves. Some of the important information about the valves can also be obtained from the same multi-slice CT scan obtained during imaging of the coronary arteries or CABGs, obviating the need of an additional scan.

Since the velocity of the blood and thus the pressure gradient along the aortic and mitral valve cannot be determined from multi-slice CT imaging, information provided by this approach about the cardiac valves is mostly restricted to morphological diagnosis. For example, multi-slice CT is particularly valuable for monitoring aortic valve calcium in patients on lipid-lowering therapy. Due to the radiation exposure inherent with the technique, however, the indications for repetitive multi-slice CT scans need to be restricted to patients who cannot be assessed thoroughly with echocardiography or MRI. Accurate quantification of aortic valve area, early detection of perivalvular abscess formation, and diagnosis of residual systolic anterior movement of the mitral valve and tendinous cords in patients with hypertrophic obstructive cardiomyopathy after percutaneous transluminal septal myocardial ablation may become other diagnostic niches of multi-slice CT in cardiac imaging.

References

Adler Y, Koren A, Fink N, et al (1998). Association between mitral annulus calcification and carotid atherosclerotic disease. Stroke 29: 1833–1837

Boughaleb D, Mansourati J, Genet L, Barra J, Mondine P, Blanc JJ (1994). Permanent cardiac stimulation after aortic valve replacement: incidence, predictive factors and long-term prognosis. Arch Mal Coeur Vaiss 87: 925–930

Callister TQ, Cooil B, Raya SP, Lippolis NJ, Russo DJ, Raggi P (1998). Coronary artery disease: improved reproducibility of calcium scoring with an electron-beam CT volumetric method. Radiology 208: 807–814

Cowell SJ, Newby DE, Burton J, et al (2003). Aortic valve calcification on computed tomography predicts the severity of aortic stenosis. Clin Radiol 58: 712–716

Davidoff R, McTiernan A, Constantine G, et al (2001). Echocardiographic examination of women previously treated with fenfluramine: long-term follow-up of a randomized, double-blind, placebo-controlled trial. Arch Intern Med 161: 1429–1436

de Vos S RA, Berg JT, Cramer M, Rensing B, Doevendans P, Pro-

kop M (2004). First evaluation of mitral valve movement with 40-slice CT (abstract). Eur Radiol 14: R 17

Hahn D (2004). Modern imaging of the heart, MRI or MSCT?. Rofo Fortschr Geb Rontgenstr Neuen Bildgeb Verfahr 176: 1215–1218

Hunold P, Vogt FM, Schmermund A, et al (2003). Radiation exposure during cardiac CT: effective doses at multi-detector row CT and electron-beam CT. Radiology 226: 145–152

Melina G, Rubens MB, Amrani M, Khaghani A, Yacoub MH (2001). Electron beam tomography for cusp calcification in homograft versus Freestyle xenografts. Ann Thorac Surg 71: 368–370

Morgan-Hughes GJ, Owens PE, Roobottom CA, Marshall AJ (20039. Three dimensional volume quantification of aortic valve calcification using multislice computed tomography. Heart 89: 1191–1194

Mullany CJ (2000). Aortic valve surgery in the elderly. Cardiol Rev 8: 333–339

Otto CM, Lind BK, Kitzman DW, Gersh BJ, Siscovick DS (1999). Association of aortic-valve sclerosis with cardiovascular mortality and morbidity in the elderly. N Engl J Med 341: 142–147

Pohle K, Dimmler A, Feyerer R, et al (2004). Quantification of aortic valve calcification with electron beam tomography: a histomorphometric validation study. Invest Radiol 39: 230–234

Rosenhek R, Binder T, Porenta G, et al (2000). Predictors of outcome in severe, asymptomatic aortic stenosis. N Engl J Med 343: 611–617

Shavelle DM, Takasu J, Budoff MJ, Mao S, Zhao XQ, O'Brien KD (2002). HMG CoA reductase inhibitor (statin) and aortic valve calcium. Lancet 359: 1125–1126

Willmann JK, Weishaupt D, Lachat M, et al (2002a). Electrocardiographically gated multi-detector row CT for assessment of valvular morphology and calcification in aortic stenosis. Radiology 225: 120–128

Willmann JK, Kobza R, Roos JE, et al (2002b). ECG-gated multi-detector row CT for assessment of mitral valve disease: initial experience. Eur Radiol 12: 2662–1669

Willmann JK, Weishaupt D, Kobza R, et al (2004). Coronary artery bypass grafts: ECG-gated multi-detector row CT angiography–influence of image reconstruction interval on graft visibility. Radiology 232: 568–577

7.12 Visualization of Cardiac Tumors and Masses

B. Wintersperger

Contents

7.12.1 Introduction *288*
7.12.2 Imaging Techniques *290*
7.12.3 Epidemiology of Cardiac Masses and Clinical Application of CT *290*
7.12.3.1 Benign Cardiac Tumors *290*
7.12.3.2 Cardiac Thrombi *291*
7.12.3.3 Malignant Cardiac Tumors *291*
7.12.4 Conclusion *293*
References *295*

7.12.1 Introduction

Compared to other referrals, multi-slice CT imaging of cardiac masses is rather uncommon. Two-dimensional echocardiography is still the modality of choice in screening for cardiac masses (Felner 1985, Salcedo 1992, Link 1995), as it represents an easy, non-invasive real-time approach with bedside capabilities. Assuming optimal examination circumstances, 2D echocardiography can detect cardiac masses and even small masses attached to the cardiac valves as well as their impact on valve and global cardiac function within the same examination (Olson 1996). However, image quality is mainly dependent on the patient's habitus and the examiner's skills. Restrictions arise in examining obese patients due to the resulting limited acoustic windows, and right ventricle assessment may be hampered in patients with pulmonary emphysema. Also, evaluation of the extra-cardiac extent of a mass might not be assessable.

Multi-slice CT imaging has been proven to generate artifact-free cross-sectional images that can be reconstructed in any desired plane. Cardiac motion can be frozen at any time point of the cardiac cycle and the high spatial resolution allows assessment of the cardiac anatomy and morphology (Wintersperger 2003). The large field-of-view (FoV) in a scan plane of usually 50 cm enables not only visualization of the heart itself but also of the surrounding mediastinal structures and the entire chest. This may be especially valuable in patients with advanced malignant cardiac masses.

Although the work-up of patients with cardiac masses is not the primary focus of multi-slice cardiac CT imaging, this technique still provides a valuable tool in such cases and as a complementary analysis in patients who undergo examination of the coronary arteries. Beside the evaluation of solid cardiac tumors, there is increasing evidence that multi-slice cardiac CT is a very sensitive technique in screening for ventricular and atrial thrombi.

7.12.2 Imaging Techniques

Multi-slice CT imaging of cardiac masses is basically no different than other contrast-enhanced cardiac scan applications, such as imaging the coronary arteries or cardiac morphology in congenital heart disease. Detailed background information about multi-slice cardiac CT imaging algorithms can be found in the technical chapters of this book. However, because of the dependency on the individual scanner and data acquisition settings, a few basics regarding the imaging of cardiac masses will be considered here.

To benefit from the 3D capability of cardiac multi-slice cardiac CT and its ability to show dynamic information based on multi-phasic reconstructions, the use of retrospective ECG-gated scan techniques and algorithms is strongly recommended. This allows assessment of cardiac morphology not only in the axial plane but also, based on MPR, along any desired plane, including the individual cardiac axes.

Multi-slice CT allows for very thin collimated slices of 1 mm with 4-slice CT scanners and sub-millimeter with 16- and 64-slice CT scanners. Such high resolution is advantageous for the assessment of coronary arteries but is usually unnecessary for the assessment of cardiac masses. For this application, a slice thickness in the range of 2–3 mm is suf-

ficient. This reduces the data acquisition time and enables scanning of the heart within a short breath-hold also with 4-slice CT. Nonetheless, the further increased volume coverage speed and higher temporal resolution of 16- and 64-slice CT scanners results in reduced motion artifacts, a smaller amount of contrast agent, and improved visualization of the cardiac chambers due to the absence of contrast artifacts in the right heart. Also, coronary or valvular disease often goes along with the presence of benign masses and it is therefore desirable to assess all pathologies in one examination. Moreover, as cardiac masses may cause arrhythmia and atrial fibrillation, high temporal resolution for adequate image quality becomes very important (Fig. 7.86).

With overlapping slice reconstruction, MPR can be used to demonstrate the exact location and extent of masses and tumors. In the follow-up of cardiac tumors, even non ECG-gated multi-slice CT scanning may be used to show gross tumor progression and pulmonary metastasis in malignant disease.

Multi-slice CT offers the potential to depict specific features, such as fatty tissue of mass calcification, even on non-contrast-enhanced scans. However, exact allocation of mass boundaries and mass depiction or exclusion requires the use of iodated contrast agent. Optimized protocols for contrast injection have been extensively published and have primarily focused on coronary artery assessment. On 16- and 64-slice CT, such protocols enable a high degree of opacification of the left ventricle and coronary artery while restricting the amount of contrast within the right atrium and ventricle in order to avoid high-contrast streak artifacts (Wintersperger 2003). However, for mass depiction and differential diagnosis, the opacification of all cardiac chambers

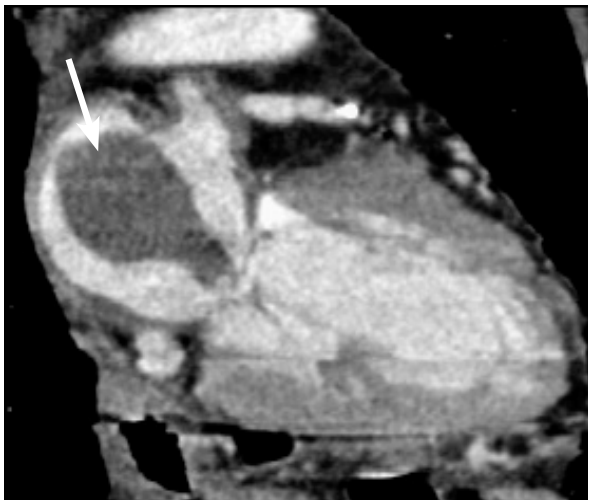

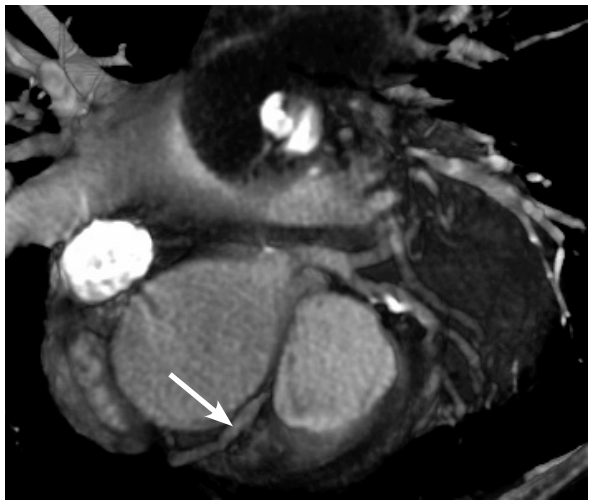

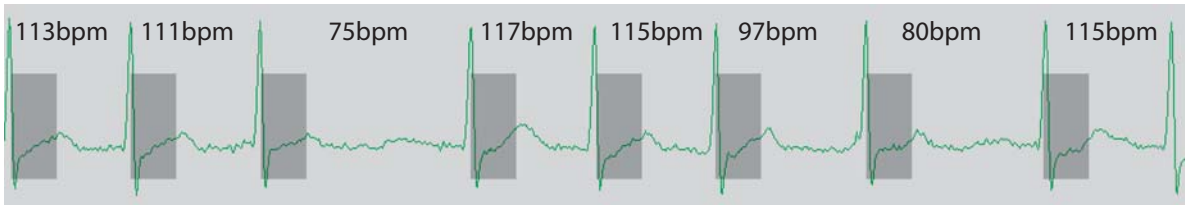

Fig. 7.86a–c. 4-slice CT examination of a patient with a primary osteosarcoma in the left atrium (variable heart rate 75–122 bpm). ECG-gated reconstruction in systole (0% of the RR-interval) allows visualization of the tumor and the proximal coronary arteries. Motion artifacts are present due to the limited temporal resolution of 4-slice CT (125–250 ms) but visualization of the lesion is still sufficient. **a** Tumor in the left atrium (*arrow*) in sagittal MPR. **b** Tumor in the left atrium and abnormal right coronary artery (*arrow*) in 3D VRT. c ECG signal showing rapidly changing heart rate

is mandatory. Appropriate visualization of the right atrium and the ventricles can be achieved with different scan and injection regimens:

- Scanning during the second pass of the contrast agent (lower overall opacification)
- Change of injection protocol using a different low-density chaser bolus (Table 7.15)

Nevertheless, the right atrium will still remain the focus of artifacts that may also be caused by the influx of non-opacified blood from the inferior vena cava.

7.12.3 Epidemiology of Cardiac Masses and Clinical Application of CT

Cardiac masses have to be differentiated from primary and secondary tumors. While primary cardiac tumors arise within the heart itself, secondary tumors are most commonly due to metastasis of malignancies primarily located outside the heart or to direct tumor spread and invasion of masses located adjacent to the heart (e.g., bronchogenic carcinoma). Secondary cardiac tumors are about 20 to 40 times more frequent than primary ones, which show a prevalence in the range of 0.0017–0.33% (Burke 1995). In addition to the evaluation of cardiac neoplasms, multi-slice CT imaging is also increasingly being used in the suspicion of cardiac thrombi.

7.12.3.1 Benign Cardiac Tumors

About two-thirds of all primary cardiac tumors are benign, and half of these are cardiac myxomas (Burke 1995). Other benign tumors are papillary fibroelastoma (~8%), fibroma (~5%), and lipoma (~4%) (Burke 1995). In children, rhabodomyoma accounts for the majority of such tumors.

Although cardiac myxomas can be found in any cardiac chamber; in about ~75% of patients they are located in the left atrium (Fig. 7.87). Another 20% of myxomas are located within the right atrium, only 5% arise within either the left or the right ventricle, and in very rare instances myxomas can be found at multiple locations or they may be associated with the Carney complex (autosomal dominant syndrome) (Carney 1985). Myxomas usually show a heterogeneous low attenuation sometimes in conjunction with calcification due to regressive changes (Tsuchiya 1984) (Fig. 7.87). Especially within the left atrium, they are usually attached to the oval fossa and often present with a stalk, allowing them to move during the cardiac cycle. With the use of multi-phase reconstructions and cine mode image display, the mobility of myxomas and possible mitral valve protrusion can be depicted in multi-slice CT (Feuchtner 2004).

Although recently published data of multi-slice CT reported the depiction of even small valvular pathologies (Willmann 2002a, Willmann 2002b), in the depiction of papillary fibroelastomas, which are usually attached to cardiac valves (usually < 1 cm in diameter), echocardiography is still superior to multi-slice CT. As this tumor entity may cause recurrent embolic events due to adherent thromboembolic material, multi-slice cardiac CT may be helpful to exclude thrombi within the cardiac cavities.

Lipomatous tumors are usually readily diagnosed by CT based on the specific imaging features of fatty tissue. However, with respect to the pathology findings, two different entities have to be differentiated:

Table 7.15. Injection regimens for 16-slice CT cardiac imaging (based on 300 mg iodine/ml). *CTA* contrast timing, *CTA* CT angiography

Purpose of study	CTA only	CTA/tumor/function
	Test bolus/bolus triggering ("CareBolus")	
Delay	+6 s	+10 s
Volume	100 ml	120 ml
Flow rate	±4 ml/s (1.2 g/s)	±5 ml/s (1.5 g/s)
Bolus chaser	50 ml NaCl	**50 ml NaCl**

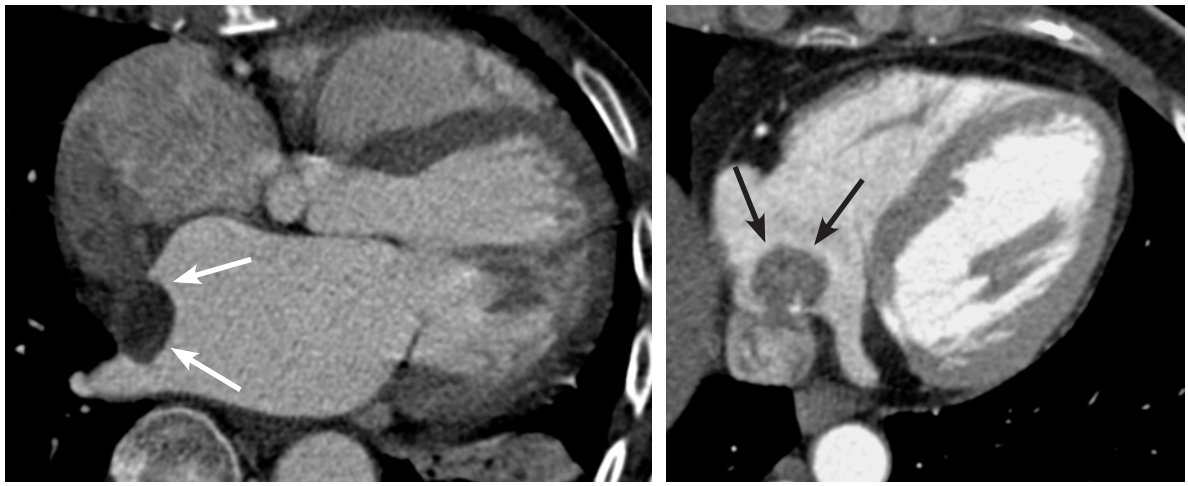

Fig. 7.87. Retrospectively cardiac gated 16-slice CT of cardiac myxomas within the left atrium (**a**) and right atrium (**b**). Both myxomas (*arrows*) show a typical, rather low attenuation; note the small calcifications (**b**)

- Lipomas
- Lipomatous hypertrophy of the interatrial septum

Lipomas are usually found on the epicardial surface but may also be intracavitary and may present at any site of the atria or ventricles. Lipomatous hypertrophy consists of accumulated fatty tissue of more than 2 cm within the interatrial septum and usually sparing the oval fossa. Based on the tissue features, these tumors can be seen in non-enhanced scans (Kamiya 1990, Hayashi 1996).

In addition to the above-mentioned solid tumors, pericardial cysts represent a benign lesion that needs to be differentiated from other tumors.

7.12.3.2 Cardiac Thrombi

Intracardiac thrombi may be caused by a variety of different pathologies and may occur in any cardiac chamber. They are responsible for about 15% of all ischemic strokes and their presence represents a major risk factor for stroke. Early identification with subsequent therapy is therefore of paramount importance.

Besides other causes of cardiac thrombi, especially in patients with artificial devices (e.g., prosthetic valves, pacemakers), atrial fibrillation or wall motion abnormalities are known risk factors. Thrombi primarily present as filling defects within opacified cardiac chambers and may have different appearances depending on their location (Fig. 7.88, 7.89). While thrombi due to wall motion abnormalities within the ventricles (most commonly, within the left ventricle) usually are crescent-shaped when located next to infarcted or abnormal myocardial wall segments (often within the apex) (Fig. 7.88), clots within the atria usually presents as round or oval-shaped, solid, low-density masses. In the atria, they may often be found within the atrial appendages (Fig. 7.89). Compared to echocardiography, the benefits of multi-slice CT are its large field of view and mostly patient-independent image quality. Cardiac thrombi may even be easily visualized in non-ECG-gated routine chest CT examinations (Fig. 7.89).

7.12.3.3 Malignant Cardiac Tumors

Compared to secondary cardiac tumors, primary cardiac malignancies are rather rare. Of the cardiac primary masses, only about 25% are malignant (Burke 1995). They are often asymptomatic until they become large, and even then they produce nonspecific symptoms (Araoz 1999). Early depiction of

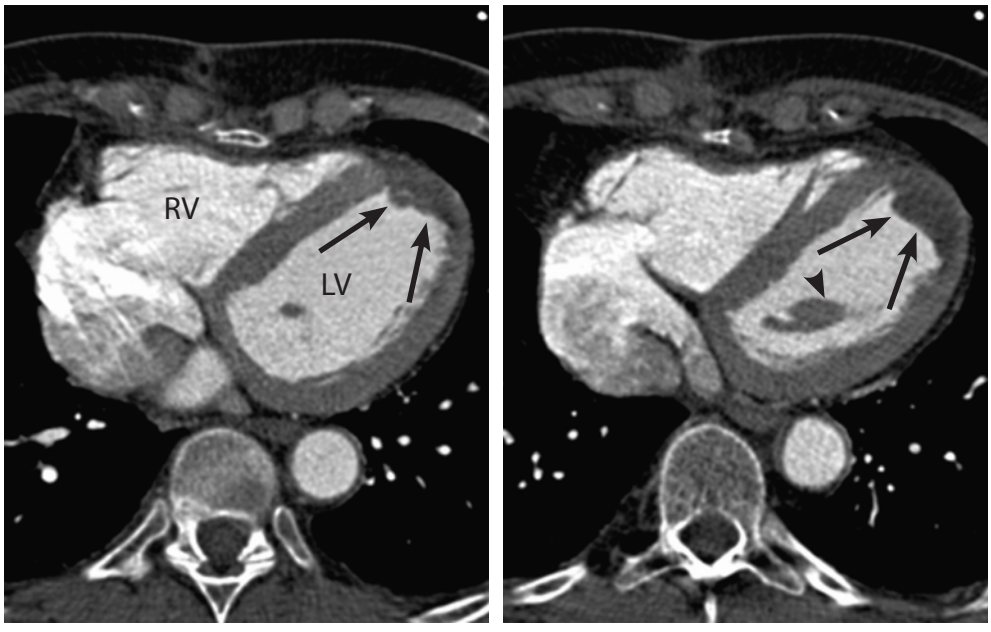

a b

Fig. 7.88a,b. Cardiac 16-slice CT examination of a patient after myocardial infarction. The ventricular anatomy is displayed in two axial levels (**a**, **b**). At the apex, a crescent-shaped low-density rim consistent with a ventricular thrombus (*arrows*) can be identified. The intracavitary structure (*arrowhead*) represents the posterior papillary muscle

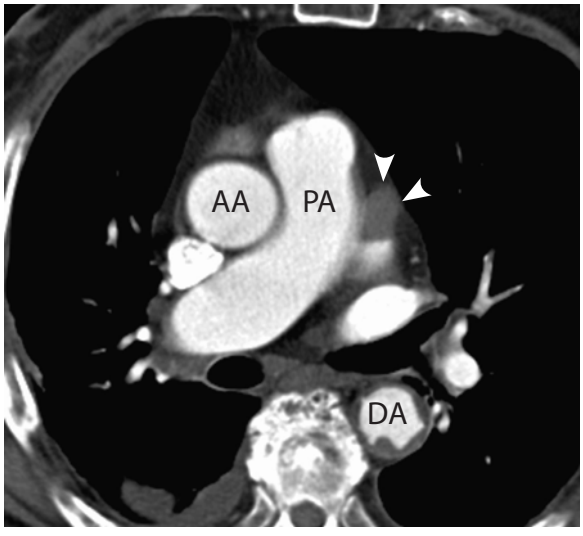

Fig. 7.89. Non ECG-gated 4-slice CT scan of the chest with a low-density structure within the left atrial appendage (*arrowheads*), which, based on chronic atrial fibrillation, represents an atrial thrombus. *AA* Ascending aorta, *DA* descending aorta

cardiac malignancies allows conservative treatment to be initiated sooner and the need for more radical surgical treatment, including heart transplantation, to be recognized earlier (Uberfuhr 2002). Multislice CT can be used to accurately image the heart and the surrounding mediastinum and therefore to evaluate the extent of disease. Angiosarcoma represents the most common cardiac sarcoma (~35–40%) and is usually located within the right atrium (~75% of patients) (Janigan 1986). Based on its composition, this tumor usually shows contrast enhancement, which may be combined with areas of necrosis. In addition, angiosarcoma tends to invade the pericardium, which might be demonstrated by pericardial effusion (Figs. 7.90, 7.91).

Rhabdomyosarcomas do not show a predominant location within the heart. They can usually be well-differentiated from the myocardium on enhanced scans. Furthermore, they may invade the cardiac valves and tend to recur after resection. There are a number of other malignant entities of primary cardiac tumors that also may show predominant loca-

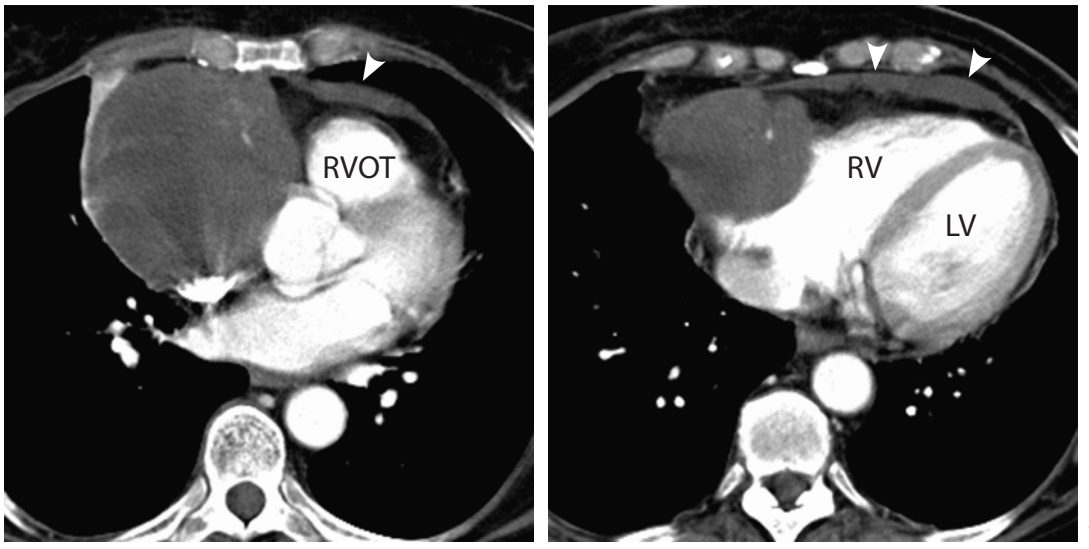

a b

Fig. 7.90a, b. Patient with a very large angiosarcoma arising from the right atrium, examined with 16-slice CT. The cardiac anatomy is displayed in two axial levels (**a**, **b**).The mass already invades the pericardial sac, as evidenced by pericardial effusion (*arrowheads*). *RVOT* Right ventricular outflow tract

tions (Table 7.16). Secondary cardiac malignancies, such as metastatic disease or direct tumor invasion from primary lesions adjacent to the heart, often have imaging features similar to those of the primary tumor.

In the setting of malignant cardiac disease, multi-slice CT is often used not only for primary diagnosis but also for follow-up after chemotherapy, resection, or even cardiac transplantation. To obtain detailed information on the primary lesion itself, ECG gating is recommended, whereas non ECG-gated techniques are adequate for staging examinations in the assessment of metastatic lesions from primary cardiac tumors.

7.12.4 Conclusion

Multi-slice cardiac CT is a promising clinical tool in the assessment of cardiac masses. The use of this modality in cardiac imaging is rapidly growing, and its application in imaging cardiac masses and thrombi certainly indicates a valuable niche. Since the requirements are less demanding than those of coronary CTA, adequate results can be achieved with less sophisticated multi-slice CT scanner generations. However, as a prerequisite for cardiac CT imaging, ECG-based data-acquisition strategies and algorithms are necessary. The higher temporal resolution and faster coverage of the newer 16- and 64-slice CT scanners can reduce the volume of contrast agent that is required and allows evaluation of patients with higher and irregular heart rates (Fig. 7.92). The acquisition of 3D data sets even allows for multi-planar imaging of cardiac tumors. While multi-slice CT might be inferior to MRI in the exact evaluation of the tumor entity, it is superior to in staging of the primary tumor and in identifying possible metastasis within the chest and abdomen.

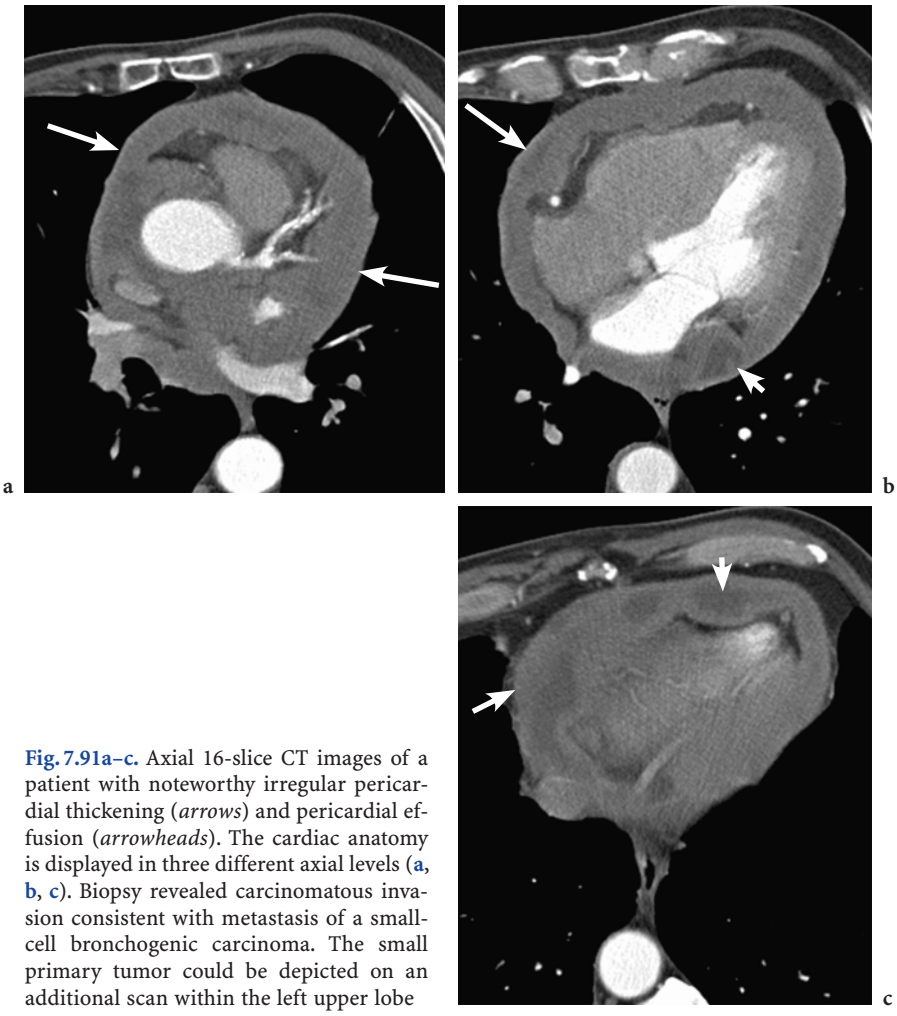

Fig. 7.91a–c. Axial 16-slice CT images of a patient with noteworthy irregular pericardial thickening (*arrows*) and pericardial effusion (*arrowheads*). The cardiac anatomy is displayed in three different axial levels (**a**, **b**, **c**). Biopsy revealed carcinomatous invasion consistent with metastasis of a small-cell bronchogenic carcinoma. The small primary tumor could be depicted on an additional scan within the left upper lobe

Table 7.16. Overview of the most frequent cardiac tumors: frequency and common location [adapted from Burke (1995) and Araoz (1999, 2000)]

Entity	Characteristic	Approximate frequency (%)	Most common location
Myxoma	Benign	~29	Left atrium
Angiosarcoma	Malignant	~9	Right atrium
Fibroelastoma	Benign	~8	Cardiac valves
Rhabdomyoma	Benign	~5	Ventricles
Fibroma	Malignant	~5	Ventricles
Lipoma	Benign	~4	No predominance
Osteosarcoma	Malignant	~3	Left atrium
Leimyosarcoma	Malignant	~3	Left atrium
Rhabdomyosarcoma	Malignant	~2	No predominance
Lymphoma	Malignant	~2	Right atrium

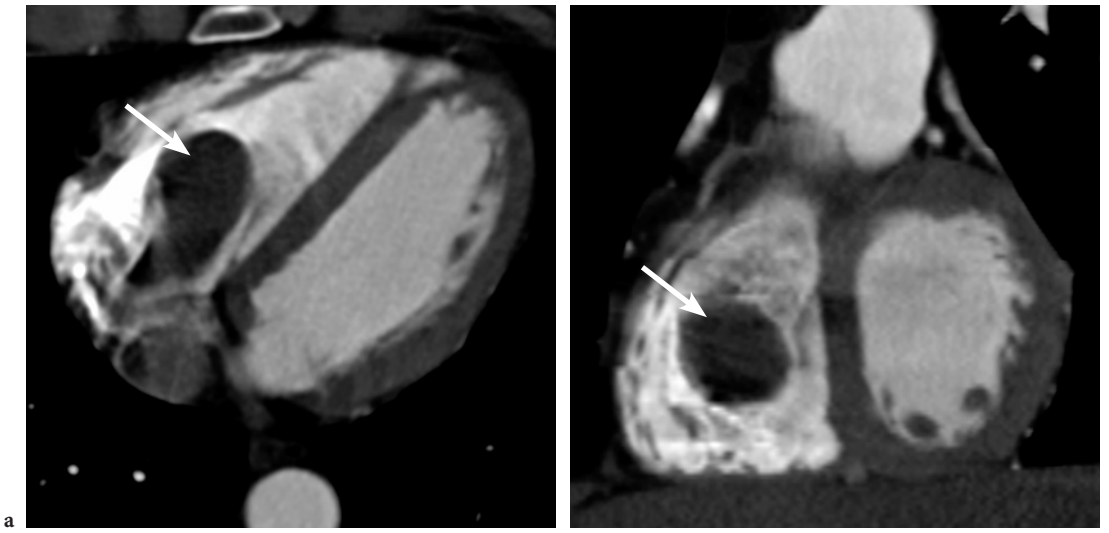

Fig. 7.92a,b. 64-slice CT examination of a patient with a heart rate of 89–97 bpm during the scan. A shorter contrast delay time was selected such that both left and right ventricles show enhancement. Axial slice (**a**) and MPR (**b**) reveal a thrombus in the right ventricle (*arrow*). The fast rotation speed of 0.33 s enables high temporal resolution and image reconstruction free of motion artifacts

References

Araoz PA, Eklund HE, Welch TJ, Breen JF (1999). CT and MR imaging of primary cardiac malignancies. Radiographics 19:1421–1434

Araoz PA, Mulvagh SL, Tazelaar HD, Julsrud PR, Breen JF (2000). CT and MR imaging of benign primary cardiac neoplasms with echocardiographic correlation. Radiographics 20:1303–1319

Burke A, Virmani R (1995). Tumors of the heart and great vessels. Washington D.C.: Armed Forces Institute of Pathology

Carney JA, Gordon H, Carpenter PC, Shenoy PV, Go VL (1985). The complex of myxomas, spotty pigmentation and endocrine overactivity. Medicine 64:270–283

Felner JM, Knopf WD (1985). Echocardiographic recognition of intracardiac and extracardiac masses. Echocardiography 2:3

Feuchtner G, Mueller S, Bonatti J, Friedrich G, zur Nedden D, Smekal A (2004). Images in cardiovascular medicine. Prolapsing atrial myxoma: dynamic visualization with multislice computed tomography. Circulation 109:e165–166

Hayashi H, Wakabayashi H, Kumazaki T (1996). Ultrafast computed tomography diagnosis of an epicardial lipoma in the pericardial sac: the split pericardium appearance. J Thorac Imaging 11:161–162

Janigan DT, Husain A, Robinson NA (1986). Cardiac angiosarcomas: a review and a case report. Cancer 57:852–859

Kamiya H, Ohno M, Iwata H, et al (1990). Cardiac lipoma in the interventricular septum: evaluation by computed tomography and magnetic resonance imaging. Am Heart J 119:1215–1217

Link KM, Lesko NM (1995). MR evaluation of cardiac/juxtacardiac masses. Top Magn Reson Imaging 7:232–245

Olson LJ, Tajik AJ (1996). Valvular heart disease. In: Skorton DJ, Schelbert HR, Wolf GL, Brundage BH (eds) Cardiac imaging. 2nd edn. W.B. Saunders, Philadelphia, pp. 365–394

Salcedo EE, Cohen GI, White RD, Davison MB (1992). Cardiac tumors: diagnosis and management. Curr Probl Cardiol 17:73–137

Tsuchiya F, Kohno A, Saitoh R, Shigeta A (1984). CT findings of atrial myxoma. Radiology 151:139–143

Uberfuhr P, Meiser B, Fuchs A, et al (2002). Heart transplantation: an approach to treating primary cardiac sarcoma? J Heart Lung Transplant 21:1135–1139

Willmann JK, Kobza R, Roos JE, et al (2002a). ECG-gated multi-detector row CT for assessment of mitral valve disease: initial experience. Eur Radiol 12:2662–2669

Willmann JK, Weishaupt D, Lachat M, et al (2002b). Electrocardiographically gated multi-detector row CT for assessment of valvular morphology and calcification in aortic stenosis. Radiology 225:120–128

Wintersperger BJ, Nikolaou K, Jakobs TF, Reiser MF, Becker CR (2003). Cardiac multidetector-row computed tomography: initial experience using 16 detector-row systems. Crit Rev Comput Tomogr 44:27–45

7.13 Imaging of the Pulmonary Veins in Patients with Atrial Fibrillation

M. Poon, C. Learra

Contents

7.13.1 Introduction *296*
7.13.1.1 Nomenclatures *296*
7.13.1.2 Clinical Presentation *297*
7.13.2 Pharmacological Treatment Options *297*
7.13.2.1 Thromboembolic Complications *297*
7.13.2.2 Treatment of Atrial Fibrillation: Rate vs. Rhythm Control *297*
7.13.2.3 Clinical Outcomes of Pharmacological Treatments *297*
7.13.3 Non-pharmacological Treatment of Atrial Fibrillation: Catheter Ablation *298*
7.13.3.1 Anatomy and Physiology of the Pulmonary Veins *298*
7.13.3.2 Anatomic Variants of the Pulmonary Veins *298*
7.13.3.3 Radiofrequency Ablation *299*
7.13.4 The Role of Imaging in the Era of Catheter Ablation of the Pulmonary Veins *299*
7.13.5 Multi-slice CT Imaging of the Pulmonary Veins and Left Atrium *299*
7.13.5.1 Scan Protocol *299*
7.13.5.2 Image Post-processing *300*
7.13.6 The Role of Multi-slice CT in Catheter Ablation of Afib *302*
7.13.6.1 Pre-ablation *302*
7.13.6.2 Ablation *302*
7.13.6.3 Post-ablation *302*
7.13.7 Conclusions *303*
References *305*

7.13.1 Introduction

Atrial fibrillation (Afib) is the most common cardiac dysrhythmia requiring treatment and it accounts for approximately one-third of hospitalizations for rhythm disturbances (Fuster 2001). Over 2.2 million Americans have paroxysmal or persistent Afib (Go 2001, Page 2004). Afib is much more common in the elderly, as evidenced by the fact that the prevalence of Afib in patients over the age of 80 is greater than 6% (Fuster 2001). As the population of developed countries ages in the next 50 years, it is expected that Afib will become a major health-related issue and a contributor to rising health-care costs (Wolf 1991, Flegel 1987). The increased rate of death due to Afib is mainly attributed to cardiac-related rather than due to thromboembolism (Dries 1998). In patients examined by nuclear myocardial perfusion studies, the presence of Afib is a poor prognosticator. Furthermore, Abidov et al. recently reported that, in these patients, the finding of Afib independently increases the risk of adverse cardiac events to an extent greater than perfusion and function variables (Abidoy 2004).

The treatment of Afib has evolved greatly in the last decade. Nonetheless, the pharmacological approach has not been optimal due to a myriad of drug-related side effects, and surgical treatment is effective but not practical. As catheter ablation of Afib continues to gain popularity and wider acceptance in the medical community, advanced tomographic imaging of the heart, particularly using multi-slice CT, begins to take on a more important role in the planning and follow-up of patients undergoing this procedure.

7.13.1.1 Nomenclatures

Afib can be classified as either acute or chronic. Systemic conditions, such as excessive alcohol intake, pulmonary disease, pulmonary embolism, or hyperthyroidism, are known contributing causes of acute or new-onset Afib. Chronic Afib can be permanent, persistent, or paroxysmal. In permanent Afib, the heart is unable to convert to sinus rhythm. Persistent Afib usually lasts longer than 30 days and will not revert back to sinus rhythm without interventions, such as with chemical agents or electrical cardioversion. Paroxysmal Afib is relatively common, occurs unpredictably, and is usually short-lived and self-terminating. In about 45% of patients, paroxysmal Afib occurs without associated underlying disease and as such it is known as "lone Afib" (Levy 1999). However, all types of Afib are associated with an increased risk of stroke.

7.13.1.2 Clinical Presentation

Symptoms of Afib usually relate to the rapid heart rate and the irregularity of the rhythm. Afib is not well-tolerated in elderly individuals with left ventricular hypertrophy and diastolic dysfunction or in patients with significant mitral valve disease or restrictive cardiomyopathy. The majority of patients with Afib complain of palpitation, dyspnea, fatigue, light-headedness, and syncope. Hemodynamic compromise in Afib patients is due to the loss of atrioventricular synchrony and atrial contribution to diastolic filling, stroke volume, and cardiac output. Chronic persistent tachycardia may result in a potentially reversible form of cardiomyopathy (Lemery 1987, Packer 1986). Up to 21% of cases of newly diagnosed Afib are asymptomatic (Kerr 1996). Unfortunately, the first presentation of asymptomatic Afib could be a devastating neurological event, such as stroke or transient ischemic attack.

7.13.2 Pharmacological Treatment Options

7.13.2.1 Thromboembolic Complications

All patients over the age of 60 and with chronic Afib should be placed on either antiplatelet therapy or oral anticoagulants. The latter is recommended in those patients with mitral stenosis or a history of thromboembolism, diabetes mellitus, coronary artery disease, hypertension, prosthetic heart valves, documented atrial thrombus on trans-esophageal echocardiogram, congestive heart failure, or thyrotoxicosis (Fuster 2001, Page 2004, Albers 2001).

7.13.2.2 Treatment of Atrial Fibrillation: Rate vs. Rhythm Control

The primary goal in the treatment of acute or chronic Afib is to achieve either rhythm or rate control. However, it is a well-recognized clinical fact that the current pharmacological treatment options for either form of Afib are neither effective nor safe. It is clinically easier to achieve rate control than rhythm control. Rate control agents include β-blockers, calcium-channel blockers, and digoxin. These can be used alone or in combination, depending on the clinical limitations of the underlying comorbid disorders of the patient and the initial response to the selected treatment. β-Blockers are usually more effective than calcium channel blockers for rate control, while digoxin is mainly used as adjunctive therapy and rarely as a first-line treatment option. The goal is to achieve a resting heart rate of 60–80 bpm or an exercise heart rate of 90–115 bpm (Fuster 2001). Rate control can be problematic in patients with tachy-brady syndrome or sick-sinus syndrome, in which a pacemaker is often needed to avoid profound bradycardia resulting from any one of the three rate control agents.

With the exception of β-blockers, most rhythm control agents are associated with significant adverse effects and usually are not recommended in patients with structural heart disease, either hypertrophic or dilated cardiomypathy. Most recently, the use of class IC anti-arrhythmic agents, such as propafenone and flecainide, was shown to be effective for out-patient treatment of recurrent Afib in patients with a normal heart or mild heart disease (Alboni 2004). Class III and IA agents are not recommended in patients with QT-interval prolongation. The most effective and the least pro-arrhythmic antifibrillatory agent, amiodarone, is associated with significant side effects, especially with long-term and high-dose usage (Hohnloser 1995).

7.13.2.3 Clinical Outcomes of Pharmacological Treatments

Mortality and morbidity were comparable using long-term rate or rhythm control treatment in patients with persistent Afib (van Gelder 2002, Wyse 2002, Carlsson 2003, Hohnloser 2000). Similar favorable results with rate control treatment in patients with lone Afib have been reported (Rienstra 2004). Thus, rate control is an accepted and safe treatment option for Afib in patients with minimal symptoms or in patients with great difficulty in maintaining sinus rhythm. Anticoagulation is needed regardless of which control method is used.

7.13.3 Non-pharmacological Treatment of Atrial Fibrillation: Catheter Ablation

The discovery that the pulmonary veins harbor the spontaneous wavelets that lead to the onset of paroxysmal Afib has ushered in a new non-pharmacological treatment option for paroxysmal Afib using radiofrequency catheter ablation (Haissaguerre 1998). The ablation technique has evolved over the past few years, from the use of focal vein ablation to circumferential ablation near the ostia of the pulmonary veins with or without additional left atrial linear lesions (Oral 2003, Hsu 2004). While catheter ablation was initially used to treat patients with mostly normal left ventricular function, more recently this approach has been found to also be useful in restoring and maintaining sinus rhythm in patients with Afib and congestive heart failure (Hsu 2004, Chen 2004).

The maze procedure consists of surgically isolating the Afib-initiating wavelets by creating long, superficial surgical incisions in the left atrium. The resulting scars block electrical conduction of the wavelets that lead to paroxysmal Afib. This surgical treatment is effective and is usually done at the time of open-heart surgery, particularly during repair or replacement of the mitral valve (Cox 1993).

7.13.3.1 Anatomy and Physiology of the Pulmonary Veins

The pulmonary veins are formed by the confluence of small venules originating from the lung periphery. These venules merge into larger veins, converge toward the lung root, and eventually enter the left atrium. Typically there are four pulmonary veins, designated as right superior (RS), right inferior (RI), left superior (LS), and left inferior (LI); however, four discrete pulmonary venous orifices in the left atrium are present in only 75–80% of individuals (Ho 2003). The principal function of the pulmonary veins is to return oxygenated blood from the lungs to the left atrium. The vascular structure of the pulmonary veins, which is similar to that of other veins in the body, consists of three layers: a thin endothelium, an irregular medial layer of smooth muscle and fibrous tissue, and a thick fibrous adventitia. The inner lining of the left atrium is continuous with the pulmonary veins in that the left atrial myocardium is embedded in the media of the proximal portion of all four pulmonary veins, forming sleeve-like extensions. The amount of myocardial penetration into the pulmonary veins varies from species to species and it also varies between the upper and lower veins. The presence of myocardial cells in the pulmonary veins is thought to play an important role in determining the electrophysiological properties of these veins. Unlike the smooth muscle of the pulmonary veins, striated muscle within the left atrium and the sleeve-like extensions are electrically active. It has been implicated that the veno-atrial junction and the myocardium in the veins help initiate and maintain Afib (Shah 2001). The RS vein drains the right upper and middle lobes of the lung. The LS vein drains the left upper and the lingular lobes. The inferior veins drain the lower lobes of their respective sides. The RS pulmonary vein is usually the largest, and the ostial size of the superior pulmonary veins is usually larger than that of the inferior veins. In their report of 42 patients with Afib, Scharf et al. reported the following average sizes of the pulmonary veins: RS: 19.8 mm, LS: 19.2 mm, RI: 16.0 mm, and LI: 17.3 mm (Scharf 2003).

7.13.3.2 Anatomic Variants of the Pulmonary Veins

The anatomy of the pulmonary veins is more variable than that of the pulmonary artery. Embryologically, the entire network of pulmonary veins originates from a single common pulmonary vein. Anatomical variations in the number, branching patterns, and length of the pulmonary trunk (defined as the distance from the ostium to the first ordered branch) occur as a result of the under- or over-incorporation of the common pulmonary vein into the left dorsal atrium (Bliss 1995). An extreme and rare form of under-incorporation involves the persistence of the common pulmonary vein such that it forms a narrowing in the left atrium (generally known as cor triatriatum). Other common anomalies include: joint pulmonary vein, either common left or common right pulmonary vein (in

2.4–25% of individuals); separate right middle lobe pulmonary vein (19–23%); and anomalous pulmonary venous return (<1%) (Scharf 2003, Cronin 2003, Lacomis 2003).

7.13.3.3 Radiofrequency Ablation

Access to the pulmonary veins and left atrium is obtained via a trans-septal approach through a patent foramen ovale or a trans-septal puncture under fluoroscopic guidance. Typically, one mapping (Lasso) catheter and one ablation catheter are needed to perform standard radiofrequency (RF) ablation, which employs a tissue temperature of up to 52°C with a maximum power output of 30–40 W (Hsu 2004, Ho 2001). Anticoagulation with intravenous heparin is administered following insertion of the catheters to maintain the prothrombin time at greater than twice the patient's control value. Ablation is performed at or within 5 mm of the pulmonary vein ostia to reduce the risk of pulmonary vein injury and subsequent development of pulmonary vein stenosis (Cronin 2004).

7.13.4 The Role of Imaging in the Era of Catheter Ablation of the Pulmonary Veins

Of the imaging modalities currently available for visualizing the pulmonary veins, MRI and CT are the most noninvasive, reproducible, and free of technical problems related to the operator or acoustic window. Today, multi-slice CT with advanced cardiac gating has distinct advantages over MRI in that multi-slice CT is significantly faster in image data acquisition and less problematic in scanning patients who are claustrophobic or have implanted devices. Multi-slice CT allows a 3D view of the heart and thus unlimited viewing angles. Furthermore, it is able to provide important additional image information on coronary artery anatomy and function without the need for additional contrast administration or radiation exposure (Achenbach 2001, Juergens 2002). Multi-slice CT with 16 or more detector slices offers a significant improvement in temporal and spatial resolution compared to earlier single- or 4-slice CT. As such, 16 or more detector slices allow a more precise determination of the ostial diameter and an accurate assessment of anatomical anomalies and pathology that might affect the success of the procedure or contribute to procedural complications.

A recent report by Wood et al. evaluated the accuracy of assessment of pulmonary vein anatomy in patients with Afib (Wood 2004). Four imaging modalities were compared: multi-slice CT, transesophageal echocardiogram, intracardiac echocardiography (ICE), and venography. Multi-slice CT identified the greatest number of pulmonary ostia followed by ICE. Compared with multi-slice CT or ICE, venography overestimated and TEE underestimated ostial diameters (Wood 2004). Yuan et al. recently reported the intra- and inter-observer variability of pulmonary vein measurements from multi-slice CTA (Yuan 2004). The study found that pulmonary vein ostial measurements have fewer variables when made by a single observer and mean diameter measurements are more precise than a single, maximum diameter measurement (Yuan 2004).

7.13.5 Multi-slice CT Imaging of the Pulmonary Veins and Left Atrium

7.13.5.1 Scan Protocol

In order to evaluate the pulmonary veins and left atrium, we use a similar protocol to the one that we routinely use for coronary CTA. This protocol is optimized for non-invasive coronary angiography. All ECG-gated images shown in this section were obtained with a 16-slice CT scanner. For contrast-enhanced multi-slice CT of the heart, the following parameters were employed: 16 × 0.75-mm collimation, 0.42-s rotation time, temporal resolution of 105–210 ms, 120 kV, and 500 mAs, resulting in a total scan time of about 28 s to cover the entire thorax, from the apices to the lung bases. The entire scan was acquired during a breath-hold following deep inspiration, using retrospective electrocardiographic gating. One hundred ml of iodinated con-

trast agent were infused at 4 ml/s using a dual injector. This was followed by a chaser bolus of 50 ml of saline at the same flow rate. Arrival of the contrast agent in the ascending aorta was monitored using an automatic bolus-tracking system. Data acquisition was started 4–6 s after the attenuation coefficient in the ascending aorta reached a pre-set threshold of 100 HU. Alternatively, we found that the use of a timing bolus instead of the automatic bolus-tracking system was equally efficacious but the timing protocol required an additional small amount of contrast infusion. For the timing bolus, 20 ml of iodinated contrast agent were infused at 4 ml/s followed by a similar bolus of 50 ml of saline at the same flow rate. For coverage of the entire thorax, a time delay duration was used that was equal to the time it took for the bolus contrast plus saline chaser to reach the peak of the timing bolus curve. The data sets were reconstructed at mid- to end-diastole for optimal image quality, with a 1.0-mm slice thickness, in 0.6-mm increments. Spatial resolution of the reconstructed images was 0.6 × 0.6 × 1.0 mm.

ECG gating significantly improves overall image quality. The entire data set can be used to assess the anatomy and pathology of the coronary arteries and veins. This additional information may be useful when assessing the presence of coronary artery anomalies, arterial patency, and coronary venous anatomy prior to the placement of a bi-ventricular pacemaker.

7.13.5.2 Image Post-processing

Image post-processing is routinely done on a dedicated work-station that generates 3D models of the left atrium and pulmonary veins. The 3D model of the left atrium and its associated pulmonary veins and appendage is reconstructed to eliminate surrounding structures, such as the aorta, vertebral column, ribs, lung parenchyma, and peripheral pulmonary arteries (Fig. 7.93). The optimal view of the pulmonary veins and left atrium without overlap from adjacent structures, such as the proximal segments of the pulmonary arteries, is a dorsal-cranial view with right or left posterior oblique angulations (Fig. 7.94). To measure the diameter and area of a pulmonary vein, the central axis of each pulmonary vein is first identified in 3D images (Fig. 7.95). A slice oblique to the central axis of the chosen image is obtained by rotating the image perpendicular to the center line. The oblique plane is then adjusted until the plane is just distal to the junction of the pulmonary vein and the left atrium. The area of the pulmonary vein ostium is measured by manually tracing out the lumen in the oblique MPR view and the minimum and maximum ostial diameters are measured with digital calipers along perpendicular lines drawn by the operator through the center line of the ostium. The same procedure is repeated for all the ostia of the pulmonary veins.

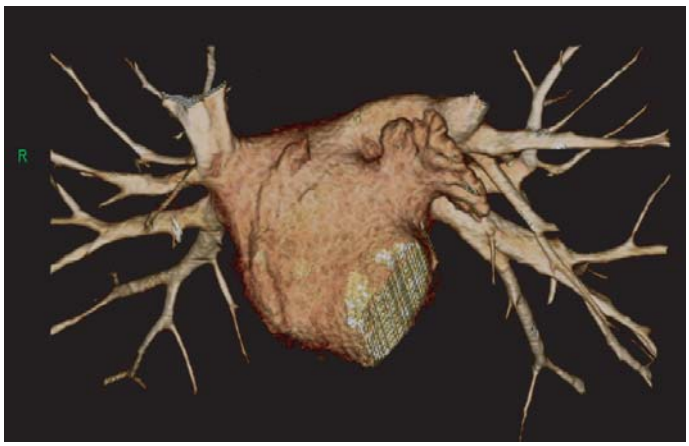

Fig. 7.93. 3D image of the left atrium and its associated pulmonary veins and appendage obtained using 16-slice CT and 16 × 0.75-mm collimation

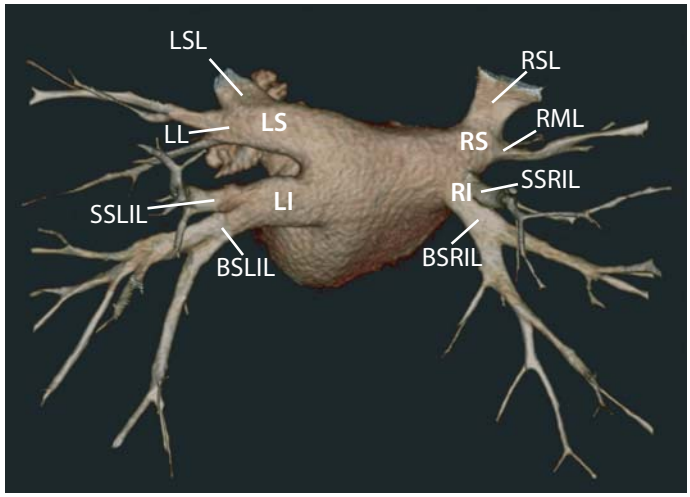

Fig. 7.94. Dorsal cranial view of the left atrium and pulmonary veins reconstructed from a data set obtained with 16-slice CT using 16 × 0.75-mm collimation. *L/RS* Left/right superior, *L/RI* left/right inferior, *LL* left lingula, *RML* right middle lobe, *L/RSL* left/right superior lobe, *SSLIL/SSRIL* superior segment of left/right inferior lobe, *BSL/BSRIL* basilar segment of left/right inferior lobe

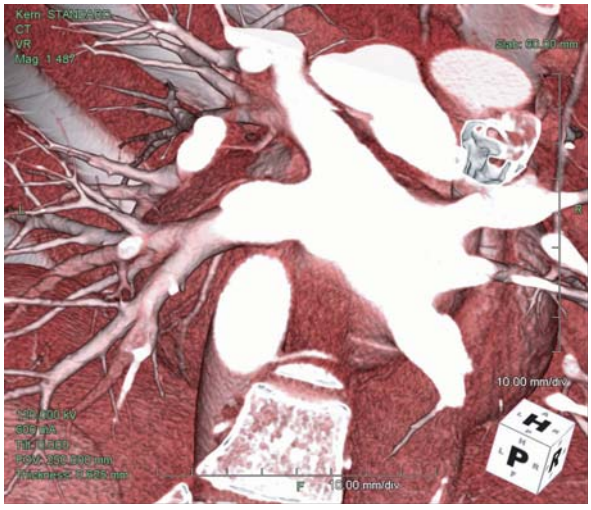

a

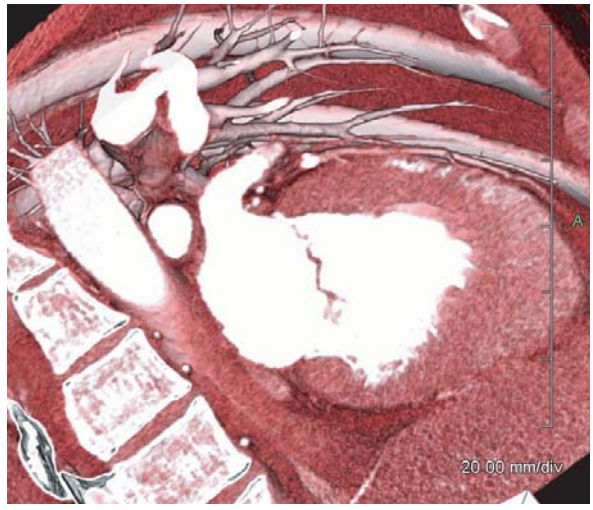

b

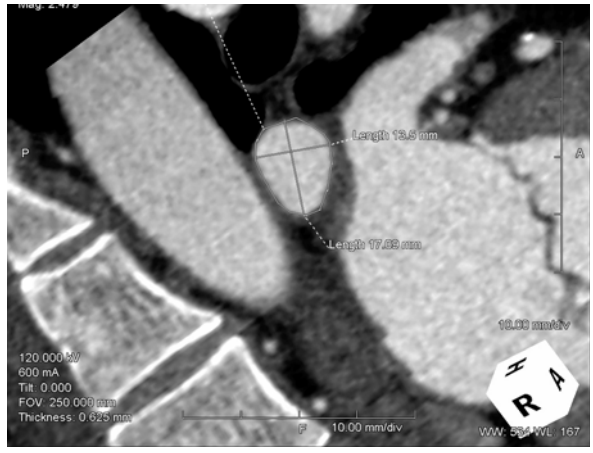

c

Fig. 7.95. a 3D view of the LA and pulmonary veins. **b** Oblique clip-plane perpendicular to the center line of the left inferior pulmonary vein. **c** Measurements of pulmonary vein maximum and minimum diameters in oblique MPR view. Data were obtained with 16-slice CT using 16 × 0.75-mm collimation and 0.37-s rotation speed

7.13.6 The Role of Multi-slice CT in Catheter Ablation of Afib

Today, multi-slice CT has become a versatile tool in the field of cardiac imaging. It provides important 3D anatomical information of the entire thorax, has an unlimited field-of-view, and is completely non-invasive. In addition, multi-slice CT greatly decreases the potential complications often associated with this highly technical and laborious procedure. It provides valuable 3D information of the atria and their associated venous connections from both epicardial and endocardial perspectives. The role of multi-slice CT in the clinical assessment of patients for catheter ablation of Afib can be divided into three phases:

7.13.6.1 Pre-ablation

Multi-slice CT can be a valuable imaging tool for the pre-ablation assessment of the anatomy and anatomical variants, e.g., an anomalous pulmonary vein. It allows accurate sizing of the pulmonary vein ostia in order to avoid catheter-vein mismatch. Moreover, it aids in the evaluation of potentially disastrous procedure-related thromboembolic complications from atrial septal aneurysm with thrombus, right atrial thrombus (Fig. 7.96), left atrial tumor (Fig. 7.97), or left atrial appendage thrombus (Fig. 7.98).

7.13.6.2 Ablation

A high-resolution 3D image of the left atrium facilitates mapping of the pulmonary vein ostia and placement of the electrophysiology and ablation catheters. Software is currently being developed to incorporate 3D images generated from multi-slice CT into the work-station used for carrying out RF catheter ablation of the pulmonary veins (Fig. 7.99)

7.13.6.3 Post-ablation

The potential for post-procedural complications related to RF ablation cannot be understated. Routine follow-up CT is not only indicated, but a good clinical practice after RF ablation. The reported complications include pulmonary vein stenosis or

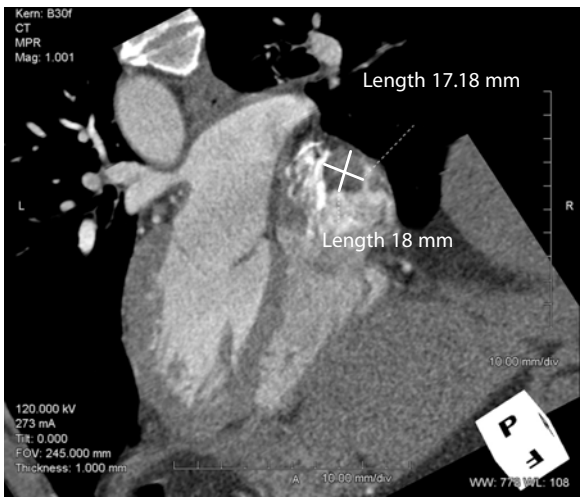

Fig. 7.96. MPR image and dimensions of a right atrial thrombus. Data were obtained using 16-slice CT with 16 × 0.75-mm collimation and 0.42-s rotation time

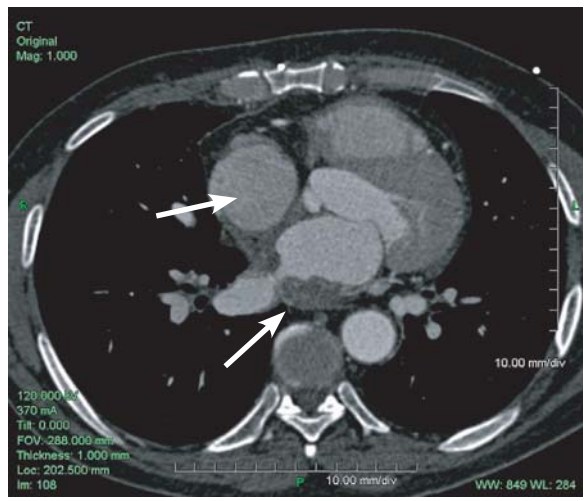

Fig. 7.97. Left atrial osteosarcoma (*white arrows*) invading the right inferior pulmonary vein Data were obtained using 16-slice CT with 16 × 0.75-mm collimation and 0.42-s rotation time

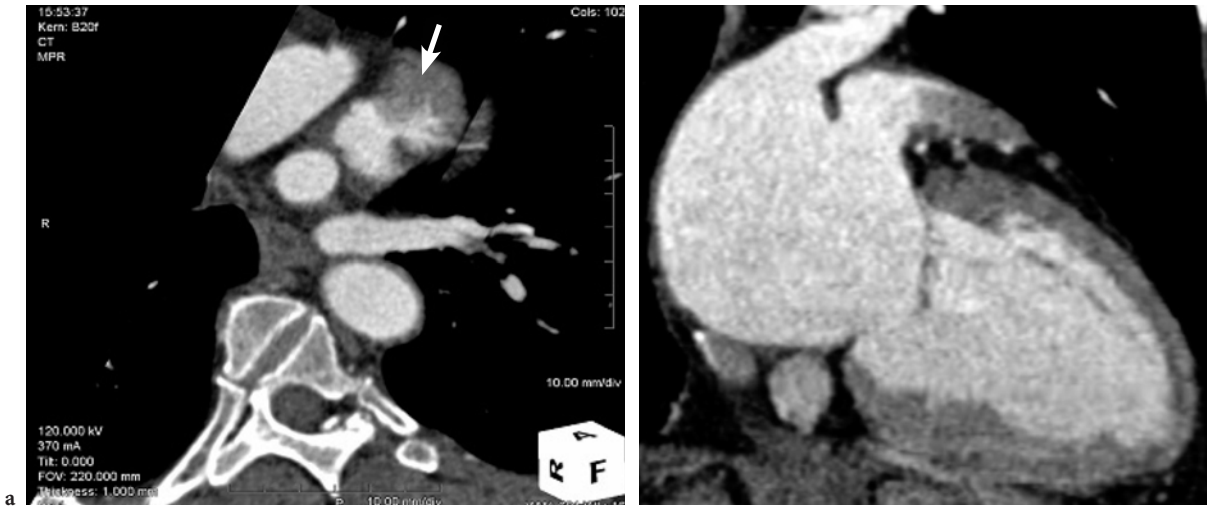

a b

Fig. 7.98a,b. Left atrial appendage thrombus (*white arrow*) and a large left atrium in a patient with chronic atrial fibrillation on oral anticoagulant. **a** Axial view, **b** two-chamber view. Data were obtained using 16-slice CT with 16 × 0.75-mm collimation and 0.42-s rotation time

infarction (Ravenel 2002, Yang 2001, Robbins 1998), pulmonary vein or left atrial perforation and hematoma (Wu 2001), and pericardial effusion/tamponade, pulmonary fibrosis, pulmonary hypertension (Ravenel 2002). Focal stenosis of the pulmonary vein is observed frequently after RF catheter ablation applied within the vein, but usually is without clinical significance. However, ablation within multiple pulmonary veins may cause pulmonary hypertension. Atrio-esophageal fistula is a known complication of RF ablation for Afib. Treatment of pulmonary vein stenosis using trans-catheter angioplasty alone yielded favorable results in up to one year of follow-up (Qureshi 2003). Purerfellner et al. also reported favorable clinical outcome during up to 9 months of follow-up in a group of highly symptomatic patients with ablation-related pulmonary vein stenosis who were treated with dilatation alone or dilatation plus stenting (Purerfellner 2004).

7.13.7 Conclusions

Afib is a common medical problem with potentially catastrophic consequences. Anticoagulation is indicated in patients over the age of 60, and in patients with significant structural heart disease. Pharmacological options for the two common treatment methods, rate and rhythm control, are less than ideal due to the numerous and potentially harmful effects of the drugs. The discovery that the pulmonary veins are the potential source of the wavelets that initiate the paroxysm of Afib has opened up a new treatment option for this common ailment. RF catheter ablation has been demonstrated to be efficacious in the treatment of paroxysmal Afib and selected cases of persistent Afib. RF ablation is equally effective in patients with normal or compromised cardiac function. Pre-ablation planning and post-procedural follow up evaluation are best done non-invasively with tomographic imaging. Multi-slice CT has emerged as the non-invasive image modality of choice in the pre- and post-ablation assessment of patients undergoing Afib ablation. For this application, 16-slice CT scanners have been shown to provide appropriate anatomical information. The newer 64-slice CT scanners, with improved temporal and spatial resolution, will further improve visualization of the pulmonary system in patients with irregular heart rate during the scan. The increased volume coverage of 64-slice CT allows evaluation of the entire arterial and pulmonary system within one examination and with one injection of contrast agent (Fig. 7.100).

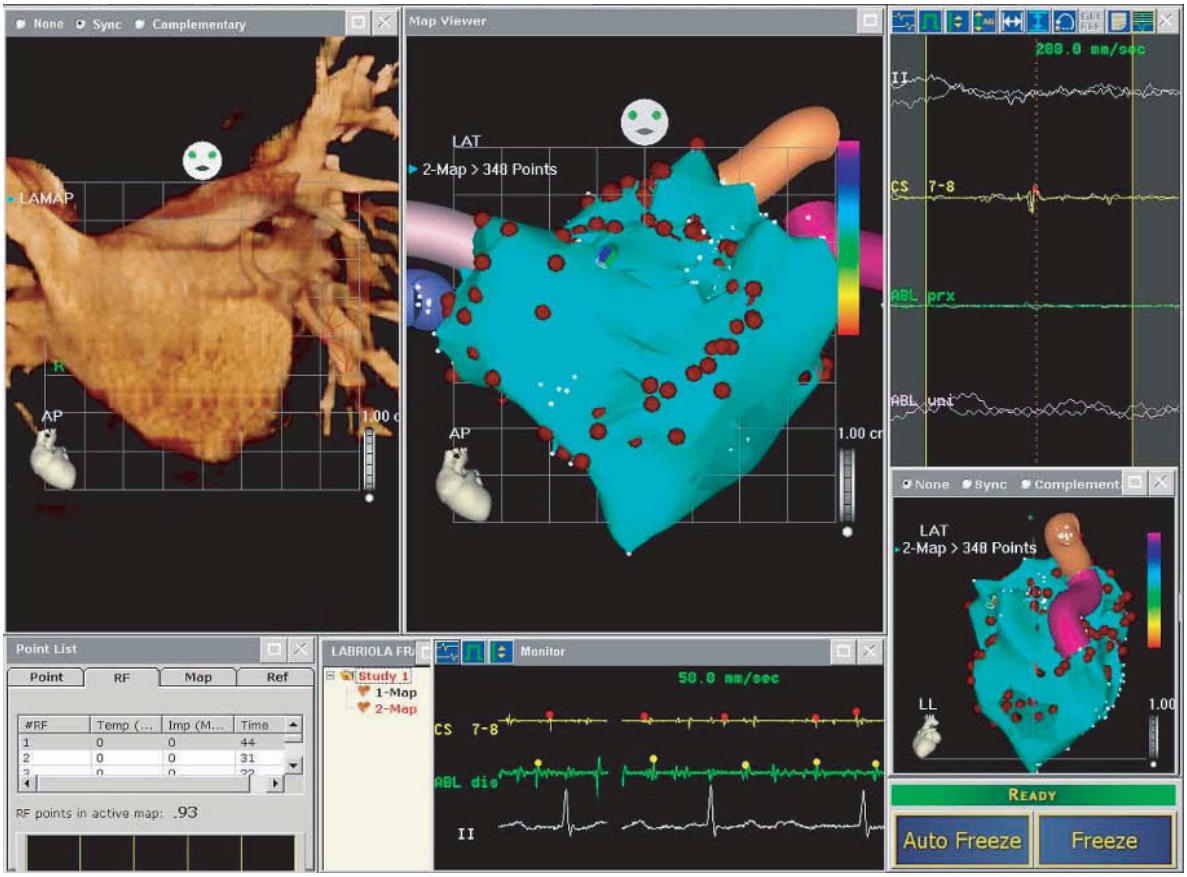

Fig. 7.99. Screen shot of a planning work-station for performing RF ablation of the pulmonary veins. An AP view of the volume-rendered image (upper left) of the pulmonary veins and the left atrium generated from a 16-slice CT examination with 16 × 0.75-mm collimation and 0.37-s rotation time. The same view can be generated on the mapping system, with red circles showing the ablation sites, as a basis for electrophysiological mapping of the ablation procedure

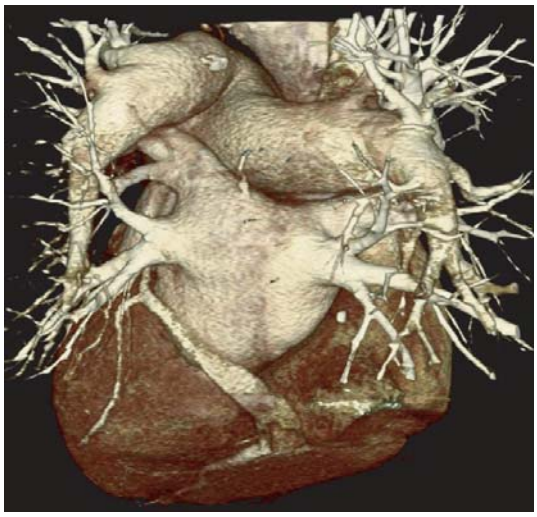

Fig. 7.100. ECG-gated 64-slice CT examination of the arterial and pulmonary system. A large scan range of 28 cm can be examined with temporal and high spatial resolution in a breath-hold time of less than 20 s, thus covering the entire thoracic vasculature, including the pulmonary vein. (Case courtesy of Mayo Clinic Rochester)

References

Achenbach S, et al (2001) Detection of coronary artery stenoses by contrast-enhanced, retrospectively electrocardiographically-gated, multislice spiral computed tomography. Circulation 103(21): 2535–2538

Abidov A, et al (2004). Prognostic implications of atrial fibrillation in patients undergoing myocardial perfusion single-photon emission computed tomography. J Am Coll Cardiol 44(5): 1062–1070

Albers GW, et al (2001). Antithrombotic therapy in atrial fibrillation. Chest 119(1 Suppl): 194S-206S

Alboni P, et al (2004). Outpatient treatment of recent-onset atrial fibrillation with the "pill-in-the-pocket" approach. N Engl J Med 351(23): 2384–2391

Bliss DF, Hutchins GM (1995). The dorsal mesocardium and development of the pulmonary veins in human embryos. Am J Cardiovasc Pathol 5(1): 55–67

Carlsson J, et al (2003). Randomized trial of rate-control versus rhythm-control in persistent atrial fibrillation: the Strategies of Treatment of Atrial Fibrillation (STAF) study. J Am Coll Cardiol 41(10): 1690–1696

Chen MS, et al (2004). Pulmonary vein isolation for the treatment of atrial fibrillation in patients with impaired systolic function. J Am Coll Cardiol 43(6): 1004–1009

Cox JL, et al (1993). Five-year experience with the maze procedure for atrial fibrillation. Ann Thorac Surg 56(4): 814–824

Cronin P, et al (2004). MDCT of the left atrium and pulmonary veins in planning radiofrequency ablation for atrial fibrillation: a how-to guide. AJR Am J Roentgenol 183(3): 767–778

Dries DL, et al. (1998). Atrial fibrillation is associated with an increased risk for mortality and heart failure progression in patients with asymptomatic and symptomatic left ventricular systolic dysfunction: a retrospective analysis of the SOLVD trials. Studies of left ventricular dysfunction. J Am Coll Cardiol 32(3): 695–703

Flegel KM, Shipley MJ, Rose G (1987). Risk of stroke in non-rheumatic atrial fibrillation. Lancet 1(8532): 526–529

Fuster V, et al (2001). ACC/AHA/ESC guidelines for the management of patients with atrial fibrillation: executive summary. A Report of the American College of Cardiology/American Heart Association Task Force on Practice Guidelines and the European Society of Cardiology Committee for Practice Guidelines and Policy Conferences (Committee to Develop Guidelines for the Management of Patients With Atrial Fibrillation): developed in Collaboration With the North American Society of Pacing and Electrophysiology. J Am Coll Cardiol 38(4): p. 1231–1266

Go AS, et al. (2001). Prevalence of diagnosed atrial fibrillation in adults: national implications for rhythm management and stroke prevention: the AnTicoagulation and Risk Factors in Atrial Fibrillation (ATRIA) Study. Jama, 285(18): p. 2370–2375

Haissaguerre M., et al (1998). Spontaneous initiation of atrial fibrillation by ectopic beats originating in the pulmonary veins. N Engl J Med 339(10): 659–666

Ho SY, et al (2001). Architecture of the pulmonary veins: relevance to radiofrequency ablation. Heart 86(3): 265–270

Ho SY (2003). Pulmonary vein ablation in atrial fibrillation: does anatomy matter? J Cardiovasc Electrophysiol 14(2): 156–157

Hohnloser SH, Singh BN (1995). Proarrhythmia with class III antiarrhythmic drugs: definition, electrophysiologic mechanisms, incidence, predisposing factors, and clinical implications. J Cardiovasc Electrophysiol 6(10 Pt 2): 920–936

Hohnloser SH, Kuck KH, Lilienthal J (2000). Rhythm or rate control in atrial fibrillation-Pharmacological Intervention in Atrial Fibrillation (PIAF): a randomised trial. Lancet 356(9244): 1789–1794

Hsu LF, et al (2004). Catheter ablation for atrial fibrillation in congestive heart failure. N Engl J Med 351(23): 2373–2383

Juergens KU, et al (2002) Using ECG-gated multidetector CT to evaluate global left ventricular myocardial function in patients with coronary artery disease. AJR Am J Roentgenol 179(6): 1545–1550

Kerr C, et al (1996). Follow-up of atrial fibrillation: The initial experience of the Canadian Registry of Atrial Fibrillation. Eur Heart J 17 Suppl C: 48–51

Oral H, et al (2003). Catheter ablation for paroxysmal atrial fibrillation: segmental pulmonary vein ostial ablation versus left atrial ablation. Circulation 108(19): 2355–2360

Lacomis, JM, et al (2003). Multi-detector row CT of the left atrium and pulmonary veins before radio-frequency catheter ablation for atrial fibrillation. Radiographics 23: S35–50

Lemery R, et al (1987). Reversibility of tachycardia-induced left ventricular dysfunction after closed-chest catheter ablation of the atrioventricular junction for intractable atrial fibrillation. Am J Cardiol 60(16): 1406–1408

Levy S, et al (1999). Characterization of different subsets of atrial fibrillation in general practice in France: the ALFA study. The College of French Cardiologists. Circulation 99(23): 3028–3035

Packer DL, et al (1986). Tachycardia-induced cardiomyopathy: a reversible form of left ventricular dysfunction. Am J Cardiol 57(8): 563–570

Page RL (2004), Clinical practice. Newly diagnosed atrial fibrillation. N Engl J Med 351(23): 2408–2416

Purerfellner H, et al (2004). Incidence, management, and outcome in significant pulmonary vein stenosis complicating ablation for atrial fibrillation. Am J Cardiol 93(11):1428–1431, A10

Qureshi AM, et al (2003). Transcatheter angioplasty for acquired pulmonary vein stenosis after radiofrequency ablation. Circulation 108(11): 1336–1342

Ravenel JG, McAdams HP (2002). Pulmonary venous infarction after radiofrequency ablation for atrial fibrillation. AJR Am J Roentgenol 178(3): 664–666

Rienstra M, et al (2004). Clinical characteristics of persistent

lone atrial fibrillation in the RACE study. Am J Cardiol 94(12): 1486–1490

Robbins IM, et al (1998). Pulmonary vein stenosis after catheter ablation of atrial fibrillation. Circulation 98(17): 1769–1775

Scharf C, et al (2003). Anatomy of the pulmonary veins in patients with atrial fibrillation and effects of segmental ostial ablation analyzed by computed tomography. J Cardiovasc Electrophysiol 14(2): 150–155

Shah DC, Haissaguerre M, Jais P (2001). Toward a mechanism-based understanding of atrial fibrillation. J Cardiovasc Electrophysiol 12(5): 600–601

Van Gelder IC, et al (2002). A comparison of rate control and rhythm control in patients with recurrent persistent atrial fibrillation. N Engl J Med 347(23): 1834–1840

Wolf PA, Abbott RD, Kannel WB (1991). Atrial fibrillation as an independent risk factor for stroke: the Framingham Study. Stroke 22(8): 983–988

Wood MA, et al (2004). A comparison of pulmonary vein ostial anatomy by computerized tomography, echocardiography, and venography in patients with atrial fibrillation having radiofrequency catheter ablation. Am J Cardiol 93(1): 49–53

Wu CC, et al (2001). Pulmonary vein dissection during mapping of atrial fibrillation. J Cardiovasc Electrophysiol 12(4): 505

Wyse DG, et al (2002). A comparison of rate control and rhythm control in patients with atrial fibrillation. N Engl J Med 347(23): 1825–1833

Yang M, et al (2001). Identification of pulmonary vein stenosis after radiofrequency ablation for atrial fibrillation using MRI. J Comput Assist Tomogr 25(1): 34–35

Yuan XP, et al (2004). Assessment of intra- and interobserver variability of pulmonary vein measurements from CT angiography. Acad Radiol 11(11): 1211–1218

7.14 Potential of Myocardial Perfusion and Viability Studies

K. Nikoalou, B. Wintersperger

Contents

7.14.1 Introduction *307*
7.14.2 Principles of Myocardial Perfusion Assessment *307*
7.14.3 Technical Considerations of Multi-slice CT *308*
7.14.4 Study Data on Myocardial Perfusion Imaging Using Multi-slice CT *308*
7.14.5 Assessment of Myocardial Viability with Multi-Slice CT *310*
7.14.5.1 Pathological Mechanisms in Myocardial Infarction and Appearance on CT *310*
7.14.5.2 Imaging Myocardial Infarctions – Competing Modalities and Actual Data *312*
7.14.5.3 Additional Findings: Infarct Sequelae *313*
7.14.6 Conclusion *313*
References *315*

7.14.1 Introduction

Coronary artery disease (CAD) is among the leading causes of death within developed countries. Multi-slice CT has already been evaluated within the last 5 years regarding its ability to assess the coronary artery tree and coronary artery stenosis. In these evaluations, coronary artery CTA was used to show cardiac and coronary morphology as well as pathologic changes. The topic of coronary artery CTA is highlighted and explored in other chapters.

The coronary artery wall undergoes pathologic changes in which plaques develop, subsequently causing luminal narrowing and thus impaired blood supply of the downstream myocardium. Imaging of these changes in myocardial blood flow and therefore myocardial perfusion is the focus of perfusion imaging techniques by different approaches. For example, nuclear medicine techniques, such as SPECT and positron emission tomography (PET), are clinically used for the assessment of myocardial perfusion in the diagnosis of CAD. Within the last decade, also MRI techniques have been applied to assess myocardial perfusion using first-pass techniques. The pharmacological and physiological principles of perfusion imaging in MRI and CT are basically the same. EBCT has already shown that perfusion studies can also be carried out using a multi-slice CT scanning technique.

7.14.2 Principles of Myocardial Perfusion Assessment

In recent years, a number of studies have used multi-slice CT to demonstrate myocardial perfusion deficits. Most of the studies used either single-volume data acquisition during the angiographic phase or double-exposure with the acquisition of an additional delayed-phase data set. However, this approach is based on static rather than dynamic imaging. The resulting data sets therefore represent a kind of blood volume distribution (early phase) and a delayed contrast distribution, i.e., an approach similar to delayed imaging in MRI (Naito 1992, Koyama 2004). This delayed data set focuses on the visualization of "myocardial viability", a technique that is commonly used in MRI and was already described in the early days of CT imaging (Higgins 1979, Higgins 1980). The evaluation of myocardial viability and the demonstration of infarcted areas with different CT techniques will be discussed later in this section.

Myocardial perfusion imaging with CT is based on the dynamic visualization of a contrast agent during its first pass through the cardiac chambers, coronary arteries, and myocardium. Within the last decade, first-pass perfusion imaging using MRI has been extensively analyzed. A combination of rest and stress studies was shown to even allow the myocardial perfusion reserve to be calculated and hemodynamically significant vessel changes to be reliably assessed (Wilke 1993, Schwitter 2001, Nagel 2003). While in MRI the linearity of the contrast agent concentration and the signal intensity is limited over a certain concentration range and variable with sequence parameter changes, this is not

the case for CT, which provides a constant linearity of contrast concentration and density. The underlying basic principle of first-pass perfusion imaging is based on the indicator dilution theory and the Stewart-Hamilton equation (Meier 1954):

Blood Volume (BV) = Blood Flow (F) × Mean Transit Time (MTT)

Quantitative myocardial perfusion (ml min^{-1} g^{-1}) is defined as myocardial blood flow (ml min^{-1}) per myocardial mass (g). However, to apply the indicator dilution theory in clinical perfusion imaging using CT or MRI, a few assumptions have to be made concerning contrast agent properties and bolus profiles. CT perfusion imaging techniques based on the above-mentioned methods have already been tested using EBCT scanners. In animal studies, EBCT perfusion measurements correlated well with either microsphere measurements or results of intracoronary Doppler ultrasound (Wolfkiel 1987, Mohlenkamp 2000).

7.14.3 Technical Considerations of Multi-slice CT

The basic principle of myocardial perfusion imaging in CT has already been proven within EBCT studies. Consistent with those results, multi-slice CT scanners should also be able to acquire comparable data to generate adequate signal-time-curves. CT brain perfusion imaging in patients who suffered acute stroke was evaluated using multi-slice CT scanners (Koenig 1998, Koenig 2001). However, cardiac perfusion imaging is complicated by rapid cardiac motion, respiratory artifacts, and the complex anatomy of the heart and its position within the chest. While EBCT is capable of tilted slice data acquisition (by table angulations), multi-slice CT scanners are only able to acquire data in the transaxial plane. Furthermore, CT perfusion imaging requires the acquisition of contrast bolus dynamics for an adequate signal–time curve. Therefore, repeated measurements at identical slice positions with a temporal resolution of 1–2 s are mandatory. Multi-slice CT scanners are thus restricted to work without table movement during data acquisition instead of acquiring an entire cardiac volume data set. Despite the recent development of 64-slice scanners, the current detector width is still restricted to a maximum of 4 cm, which represents the maximum volume that can be covered without moving the patient table. Complete coverage of the left ventricle myocardium and all coronary artery territories is therefore impossible at present. In addition, data acquisition itself has to be ECG-related to avoid major motion artifacts. Basically, two different acquisition modes are possible:

- Prospective ECG triggering with radiation being triggered by the R-peak.
- Retrospective ECG gating a co-registration of the acquired data and the ECG trace.

For both modes, the table feed has to be set to zero in order to scan at identical positions. Although retrospective ECG gating is of major benefit in coronary calcium scoring and coronary CTA based on its volume data set capability, in CT myocardial perfusion imaging it only exposes the patient to a redundant dose of radiation. Therefore, prospectively ECG-triggered modes are preferred, although the time point of scanning during the cardiac cycle has to be pre-defined. Coverage of the entire first pass of contrast agent has to be ensured owing to a scan time of approximately 30–40 s (Fig. 7.101). High temporal resolution is mandatory and therefore the interval between scans at identical positions should not exceed 1–2 heartbeats. As full myocardial coverage is not possible, the scan level should be adjusted to the lower boundary of the mitral valve annulus in order to at least cover parts of each coronary artery territory (Fig. 7.102). Overall, a perfusion sequence with multi-slice CT scanners is comparable to an ECG-triggered test bolus technique. To obtain a reasonable signal–time curve with a modest amount of contrast, high-speed injections with a saline flush (~40–50 ml at 5–8ml/s) are preferable.

7.14.4 Study Data on Myocardial Perfusion Imaging Using Multi-slice CT

At present, few data are available on the use of multi-slice CT in myocardial perfusion imaging. Animal

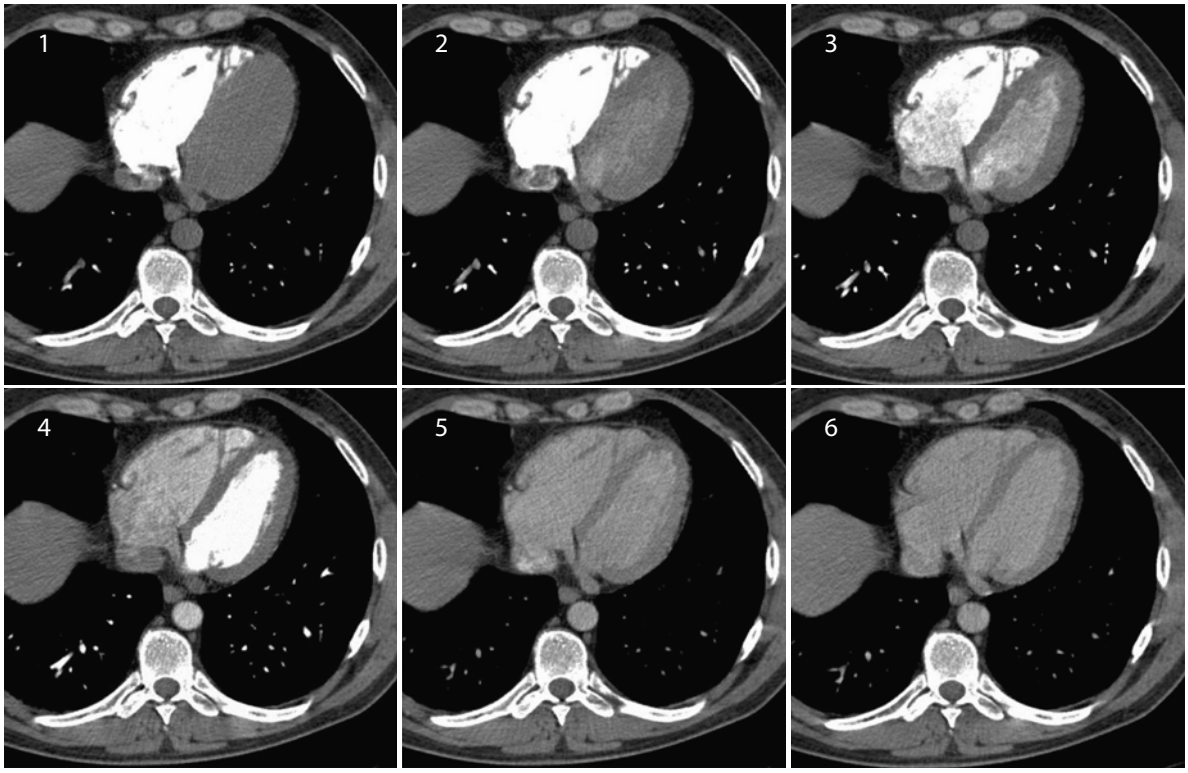

Fig. 7.101. Consecutive images of a dynamic 16-slice CT perfusion scan at identical positions (1–6). After the arrival of concentrated contrast media in the right atrium and ventricle (1, 2), the bolus passes the pulmonary vasculature and arrives within the left ventricle (2–4). The contrast then passes through the myocardium (4–6)

studies involving a combination of rest and stress perfusion scanning showed that differences in myocardial perfusion can be assessed using multi-slice CT imaging (So 2002, Stantz 2002). In addition, it was shown that the coronary perfusion reserve can be derived from multi-slice CT data (Hadway 2003). Wintersperger et al. presented preliminary data from a small patient series. Reasonable results in the quantification of absolute blood flow were obtained using Fermi function modeling (Wintersperger 2002). However, this study was only carried out in patients at rest and using an ECG triggered test bolus technique in conjunction with a rapid bolus injection of contrast media (40 ml at 8 ml/s + NaCl chaser). The results of absolute blood quantification in the patients were close to those from normal myocardium (0.73±0.20 ml/g/min) (Fig. 7.103) (Wintersperger 2002). Although these data show promise, limita-

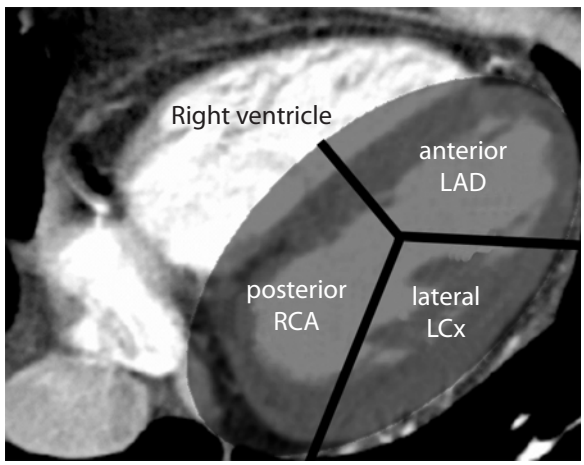

Fig. 7.102. Approximate distribution of coronary artery supply territories at the level of the lower mitral valve annulus. This distribution is subject to variations based on the coronary supply type

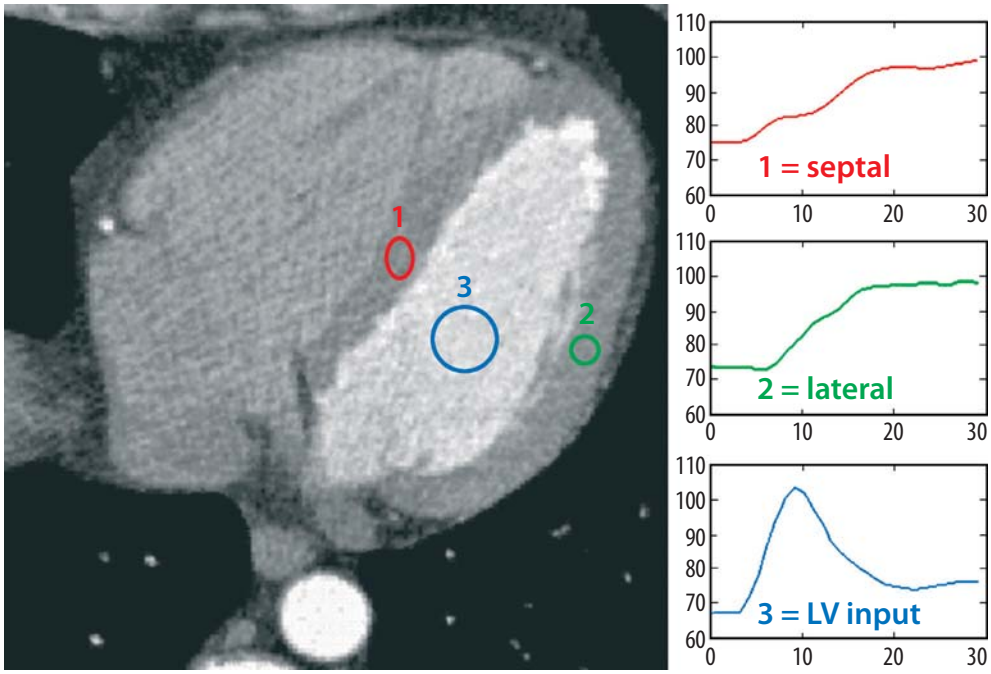

Fig. 7.103. Signal-time–density curves of a perfusion data set demonstrating the up-slope of the curve within the septal (1) and lateral (2) myocardium compared to the LV input function (3)

tions to the technique also have to be considered. Stantz et al. stated that one of the major limitations, beside the restricted coverage of the ventricle, is the high image noise compared to only a modest signal increase after contrast injection (Stantz 2002). In addition, the influx of highly concentrated contrast media to the left atrium and ventricle leads to beam hardening artifacts within the interventricular septum (Fig. 7.104). Along with such image artifacts, also the doubled radiation exposure of a combined rest and stress study needs to be considered.

7.14.5 Assessment of Myocardial Viability with Multi-Slice CT

7.14.5.1 Pathological Mechanisms in Myocardial Infarction and Appearance on CT

Ischemic changes in the myocardium after coronary arterial occlusion consist of disruption of cell membrane function and integrity and increased permeability of small vessel walls. In contrast-enhanced CT, the initial area of low attenuation primarily reflects myocardial edema, i.e., the pronounced water content of the myocardium, followed by infiltration of inflammatory cells. Subsequently, necrotic myocardium is replaced by fibrous and/or fatty tissue, which is also characterized by a reduction of attenuation in CT as compared to normal myocardium. In the early phase after contrast infusion, the infarct area is detectable as a perfusion defect (Fig. 7.105). This, however, is not specific for infarctions, since similar findings can occur in severe local ischemia (but no infarction) or other cardiac diseases causing perfusion inhomogeneities, such as hypertrophic cardiomyopathy. Also, myocardial contrast enhancement depends on a number of independent variables, e.g., the contrast injection protocol or the cardiac output. That is why a significant variance of measured CT attenuation (measured in Hounsfield Units, HU) can be observed in normal and infarcted myocardium; that is, no absolute HU values can be defined, but the relative measurement of normal and infarcted

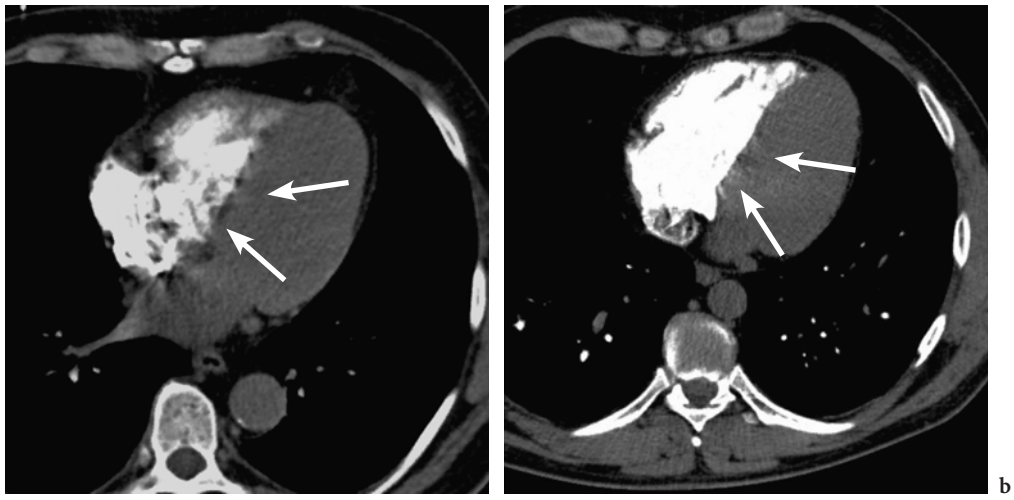

Fig. 7.104a,b. Early images of perfusion data sets during right atrial (**a**) and right ventricular (**b**) contrast influx showing marked artifacts within the area of the interventricular septum (*arrows*). These artifacts hampers signal post-processing

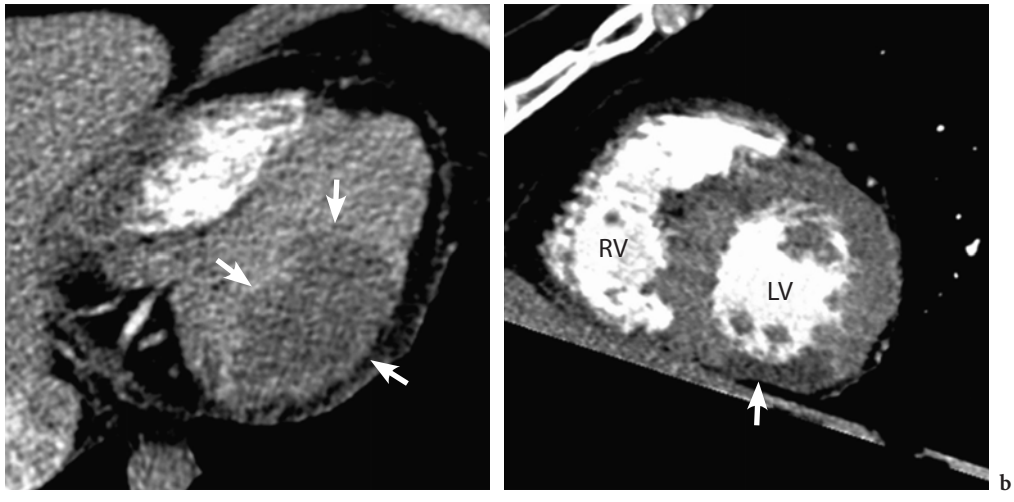

Fig. 7.105a,b. 16-slice CT examination of a 52 year-old male patient. The original axial image of the inferior left ventricular wall reveals a recent infarction (<30 days), depicted as a moderately circumscribed area with CT densities of 60-80 HU (**a**, *arrows*). In the same patient, the multi-planar reformation (*MPR*) in a short axis view clearly depicts the extent of the inferior myocardial infarction and shows mild wall thinning in (**b**, *arrow*)

tissue is the decisive factor (Nikolaou 2004). Wall thinning in the left ventricle is one of the indirect findings associated with the healing process after myocardial infarction (Fig. 7.106). In a longitudinal CT study of patients with myocardial infarction, the wall thickness at the site of infarction decreased significantly over time (Masuda 1984).

7.14.5.2 Imaging Myocardial Infarctions – Competing Modalities and Actual Data

Various imaging modalities have been tested for the detection and exact assessment of myocardial infarctions. MRI and nuclear medicine procedures seem to be favorable, as these modalities combine the assessment of myocardial perfusion and function and are able to assess myocardial viability (Kim 1999, Kitagawa 2003). A number of reports on the application of CT in patients with myocardial infarction have been promising, including animal studies (Huber 1981, Slutsky 1983) and experience with EBCT (Schmermund 1998, Georgiou 1992, Georgiou 1994). However, the clinical application of CT in the diagnosis of myocardial infarctions has not become popular thus far.

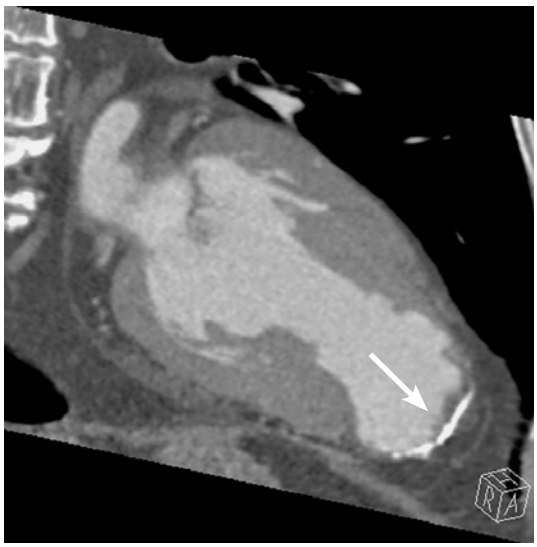

Fig. 7.106. 16-slice CT examination demonstrating a circumscribed apical aneurysm in a 60-year-old male patient after myocardial infarction (*arrow*)

Early experiments in animal models and subsequently in human subjects suggested that in vivo imaging for detection, sizing, and dating of myocardial infarctions was possible using single-slice, non-spiral CT systems (Masuda 1984, Huber 1981, Adams 1976, Kramer 1984). The principal limitations of these early techniques were the low temporal and spatial resolution as well as inadequate imaging of the inferior wall because of the inability to obtain short-axis views of the left ventricle (Georgiou 1992). The clinical introduction of EBCT brought about a significant improvement in image quality and the diagnostic possibilities of cardiac CT imaging, and it has been shown to yield insight into morphological (Georgiou 1992) and functional changes after myocardial infarction, including analysis of cardiac function (Schmermund 1998) and myocardial perfusion (Berman 2001). Recently, multi-slice CT has been validated as a very useful non-invasive diagnostic method in patients with various cardiac diseases (Ohnesorge 2000). Due to the combination of fast rotation time and multi-slice acquisition with a high spatial resolution, multi-slice CT is able to simultaneously provide detailed information on cardiac morphology (Becker 2000) and the coronary arteries (Achenbach 2001, Becker 2002, Knez 2001, Nieman 2001a). The first promising case reports showed the capability of the technique to detect myocardial infarctions (Nieman 2001b, Hilfiker 2003).

In a recent study, Nikolaou et al. attempted to retrospectively validate the use of routine, contrast-enhanced multi-slice CT of the coronary arteries to detect myocardial infarctions using 16-slice CT technology (Nikolaou 2004). The standard multi-slice CTA protocol was not changed in that study, i.e., no additional scans to detect late enhancement effects were performed, and no additional radiation dose was administered to the patients. In 27 of 106 patients investigated, myocardial infarctions were present. Multi-slice CT detected 23 of 27 infarctions correctly, resulting in an overall sensitivity of 85%. Seven false-positive results were recorded, resulting in an overall specificity of 91%. In 95 of 106 patients, multi-slice CT made a correct diagnosis (infarction present: yes/no), resulting in an overall diagnostic accuracy of 90%. Infarctions were detected on first-pass, contrast-enhanced datasets

evaluating CT attenuation (HU) and wall thickness. Abnormal focal decrease of myocardial CT attenuation and abnormally reduced regional myocardial wall thickness were taken as signs of myocardial infarction. It could be shown that recent infarctions were more difficult to detect using multi-slice CT, as the decrease in HU in the early arterial phase or the presence of wall thinning was not as pronounced as in chronic infarctions. Possible reasons for false-positive findings using multi-slice CT for infarct detection might be a variety of causes other than infarctions that lead to perfusion defects or perfusion irregularities, as described above. False-positive results are typically more often detected in the posterior or inferior ventricular wall. Several studies reported that CT underestimates the true extent of a myocardial infarction (Schmermund 1998). This might be related to patchy and subendocardial infarctions, as collateral perfusion in the area of infarcted myocardium can obscure foci of necrosis surrounded by normal myocardium. In conclusion, one should interpret infarct size as assessed by contrast-enhanced, arterial-phase multi-slice CT as an approximation of the true infarct size rather than as an absolute measurement.

In several CT studies, delayed contrast enhancement was observed in the area of infarction (approx. 10 min to several hours after contrast administration), primarily in recent infarctions, but also detectable in chronic infarctions (Masuda 1984). However, detection of such delayed enhancement requires additional scans with an increased dose of radiation to the patient and prolonged examination times; therefore, it has hardly been used in clinical routine. The main focus of future studies should therefore be assessment of the diagnostic power of contrast-enhanced CT to detect myocardial infarctions using the standard protocol for CTA of the coronary arteries. Any additional diagnostic information that can be derived from these standard CTA examinations would be of considerable interest.

7.14.5.3 Additional Findings: Infarct Sequelae

Multi-slice CT provides information on cardiac morphology in great detail, including findings or complications related to myocardial infarctions, such as left ventricular aneurysms, intramural calcifications, intracavitary thrombi, or infarct involvement of the papillary muscles. Contrast ventriculography still represents a clinically relevant method for detecting left ventricular aneurysms and mural thrombi (Friedman 1995). Both CT and conventional angiography deliver important information on myocardial aneurysms, although relying on different imaging findings. Diagnostic criteria for the detection of aneurysms on CT scans are based on anatomic definition, i.e., wall thinning and wall protrusion, which differs from the angiographic criteria (Flaherty 2001). CT does not include wall movement disturbance, while contrast ventriculography includes both anatomic protrusion of the left ventricle and functional disturbance of the wall movement, but does not consider localized wall thinning of the aneurysm. Left ventricular thrombosis is one of the most significant complications of myocardial infarction. Two-dimensional echocardiography and MRI have been validated as reliable methods for the detection of thrombi (Barkhausen 2002, Chen 1993). Opacification of the left ventricular cavity during contrast ventriculography precisely reveals the surface area of thrombi, but the border between thrombi and the endocardium cannot always be identified sufficiently (Ezekowitz 1990). Multi-slice CT allows for identification of subtle differences in the attenuation of cardiac structures and can clearly distinguish mural from free-floating thrombi. Additionally, other possibly significant complications after myocardial infarction, such as calcification of the myocardium and pericardial effusion, are easily detected on CT images.

7.14.6 Conclusion

Myocardial perfusion imaging using multi-slice CT techniques basically provides an approach that is comparable to EBCT. However, coverage of the entire myocardium is currently not possible and therefore restricts this technique to very specialized clinical applications and research protocols. Further developments of multi-slice CT scanners may lead to even wider detector systems (area detectors) and might

therefore eventually allow coverage of the entire ventricular myocardium. As known from MRI and SPECT studies, perfusion imaging needs to be done not only at rest but also after stress induction. Reliable stress imaging with multi-slice CT will require substantial improvement of temporal resolution. Since obtaining scans at rest and at stress would lead to a further increase of radiation exposure, in addition to new detector techniques for myocardial coverage a noteworthy reduction of necessary dose is essential.

Standard arterial-phase CTA of the coronary arteries can provide important additional information on the myocardium, including the possibility of detecting myocardial infarctions, with information on infarct size and age. The simultaneous depiction of the coronary arteries in considerable detail, especially with the latest 64-slice CT technology, provides the opportunity to allocate the infarct area to the specific vascular supply territory (Fig. 7.107). Future developments in post-processing software will enable the assessment of global and regional myocardial function from multi-slice CT datasets. These findings underscore the clinical value of contrast-enhanced cardiac multi-slice CT with respect to its ability to deliver both non-invasive angiographic images of the coronary arteries and considerable information on the myocardium (Chiou 2005).

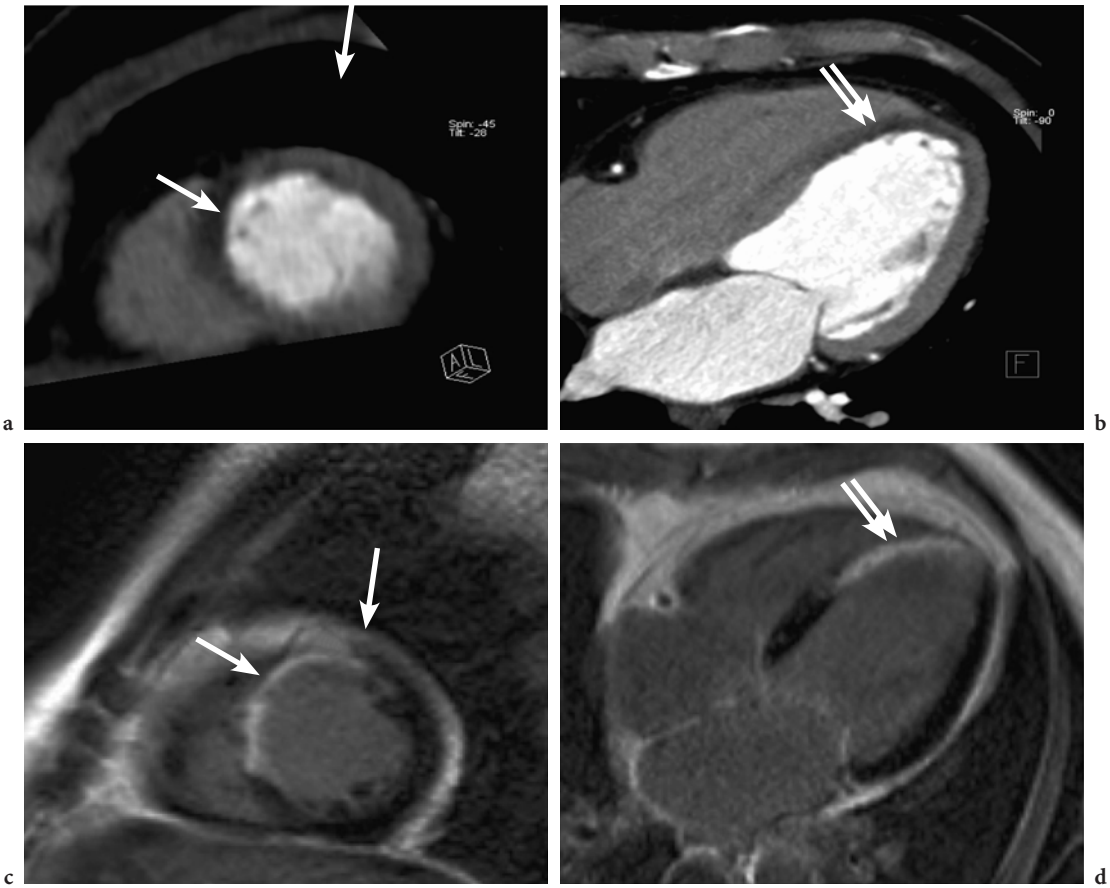

Fig. 7.107a–d. 64-slice CT examination of a patient with suspected myocardial infarction, correlated with a late enhancement MRI study. **a**, **b** CT examination reveals perfusion defects (*arrows*, *double arrow*). **c**, **d** In the MRI study, the same territories show late enhancement indicating infarcted myocardium. Optimized administration of contrast agent delivers total wash-out of the right heart, thus eliminating contrast artifacts. (Case courtesy of Sarawak General Hospital, Kuching, Malaysia)

References

Adams DF, Hessel SJ, Judy PF, Stein JA, Abrams HL (1976). Computed tomography of the normal and infarcted myocardium. Am J Roentgenol 126(4):786–791

Achenbach S, Giesler T, Ropers D, Ulzheimer S, Derlien H, Schulte C et al (2001). Detection of coronary artery stenoses by contrast-enhanced, retrospectively electrocardiographically-gated, multislice spiral computed tomography. Circulation 103(21):2535–2538

Barkhausen J, Hunold P, Eggebrecht H, Schuler WO, Sabin GV, Erbel R et al (2002). Detection and characterization of intracardiac thrombi on MR imaging. Am J Roentgenol 179(6):1539–1544

Becker CR, Knez A, Leber A, Treede H, Ohnesorge B, Schoepf UJ et al (2002). Detection of coronary artery stenoses with multislice helical CT angiography. J Comput Assist Tomogr 26(5):750–755

Becker CR, Ohnesorge BM, Schoepf UJ, Reiser MF (2000). Current development of cardiac imaging with multidetector-row CT. Eur J Radiol 36(2):97–103

Berman DS, Schisterman EF, Miranda R, Friedman JD, Hayes SW, Lewin HC et al (2001). Nuclear cardiology and electron-beam computed tomography: competitive or complementary? Am J Cardiol 19;88(2A):51E-55E

Chen C, Koschyk D, Hamm C, Sievers B, Kupper W, Bleifeld W (1993). Usefulness of transesophageal echocardiography in identifying small left ventricular apical thrombus. J Am Coll Cardiol 21(1):208–215

Chiou KR, Wu MT, Hsiao SH, Mar GY (2005). Safety and accuracy of multidetector row computed tomography for early assessment of residual stenosis of the infarct-related artery and the number of diseased vessels after acute myocardial infarction. Am Heart J 149:701–708

Ezekowitz MD (1990). Identifying left ventricular thrombi. Clin Cardiol 13(4 Suppl 6):VI31-VI33

Flaherty GT, O'Neill MN, Daly KM, Folan-Curran J (2001). True aneurysm of the left ventricle: a case report and literature review. Clin Anat 14(5):363–368

Friedman BM, Dunn MI (1995). Postinfarction ventricular aneurysms. Clin Cardiol 18(9):505–511

Georgiou D, Bleiweis M, Brundage BH (1992). Conventional and ultrafast computed tomography in the detection of viable versus infarcted myocardium. Am J Card Imaging 6(3):228–236

Georgiou D, Wolfkiel C, Brundage BH (1994). Ultrafast computed tomography for the physiological evaluation of myocardial perfusion. Am J Card Imaging 8(2):151–158

Hadway J, Sykes J, Kong H, Lee TY (2003). Coronary perfusion reserve as measured by ct perfusion. Radiology 229:305

Higgins CB, Siemers PT, Newell JD, Schmidt W (1980). Role of iodinated contrast material in the evaluation of myocardial infarction by computerized transmission tomography. Evaluation of myocardial ischemic damage of various ages by computerized transmission tomography. Time-dependent effects of contrast material. Invest Radiol 15(6 Suppl):176–182

Higgins CB, Siemers PT, Schmidt W, Newell JD (1979). Evaluation of myocardial ischemic damage of various ages by computerized transmission tomography. Time-dependent effects of contrast material. Circulation 60(2):284–291

Hilfiker PR, Weishaupt D, Marincek B (2001). Multislice spiral computed tomography of subacute myocardial infarction. Circulation 104(9):1083

Huber DJ, Lapray JF, Hessel SJ (1981). In vivo evaluation of experimental myocardial infarcts by ungated computed tomography. AJR Am J Roentgenol 136(3):469–473

Kim RJ, Fieno DS, Parrish TB, Harris K, Chen EL, Simonetti O et al (1999). Relationship of MRI delayed contrast enhancement to irreversible injury, infarct age, and contractile function. Circulation 100(19):1992–2002

Kitagawa K, Sakuma H, Hirano T, Okamoto S, Makino K, Takeda K (2003). Acute myocardial infarction: myocardial viability assessment in patients early thereafter comparison of contrast-enhanced MR imaging with resting (201)Tl SPECT. Single photon emission computed tomography. Radiology 226(1):138–144

Knez A, Becker CR, Leber A, Ohnesorge B, Becker A, White C et al (2001). Usefulness of multislice spiral computed tomography angiography for determination of coronary artery stenoses. Am J Cardiol 88(10):1191–1194

Koenig M, Klotz E, Luka B, Venderink DJ, Spittler JF, Heuser L (1998). Perfusion CT of the brain: diagnostic approach for early detection of ischemic stroke. Radiology 209(1):85–93

Koenig M, Kraus M, Theek C, Klotz E, Gehlen W, Heuser L (2001). Quantitative assessment of the ischemic brain by means of perfusion-related parameters derived from perfusion CT. Stroke 32(2):431–437

Koyama Y, Mochizuki T, Higaki J (2004). Computed tomography assessment of myocardial perfusion, viability, and function. J Magn Reson Imaging 19(6):800–815

Kramer PH, Goldstein JA, Herkens RJ, Lipton MJ, Brundage BH (1984). Imaging of acute myocardial infarction in man with contrast-enhanced computed transmission tomography. Am Heart J 108(6):1514–1523

Masuda Y, Yoshida H, Morooka N, Watanabe S, Inagaki Y (1984). The usefulness of x-ray computed tomography for the diagnosis of myocardial infarction. Circulation 70(2):217–225

Meier P, Zierler KL (1954). On the theory of the indicator-dilution method for measurement of blood flow and volume. J Appl Physiol 6(12):731–44

Mohlenkamp S, Lerman LO, Lerman A, Behrenbeck TR, Katusic ZS, Sheedy PF2 et al (2000). Minimally invasive evaluation of coronary microvascular function by electron beam computed tomography. Circulation 102(19):2411–2416

Nagel E, Klein C, Paetsch I, Hettwer S, Schnackenburg B, Wegscheider K et al (2003). Magnetic resonance perfusion measurements for the noninvasive detection of coronary artery disease. Circulation 108(4):432–437

Naito H, Saito H, Takamiya M, Hamada S, Yamada N, Imak-

ita S et al (1992). Quantitative assessment of myocardial enhancement with iodinated contrast medium in patients with ischemic heart disease by using ultrafast x-ray computed tomography. Invest Radiol 27(6):436–442

Nieman K, Oudkerk M, Rensing BJ, van Ooijen P, Munne A, van Geuns RJ et al (2001a). Coronary angiography with multislice computed tomography. Lancet 357(9256):599–603

Nieman K, van Ooijen P, Rensing B, Oudkerk M, de Feyter PJ (2001b). Four-dimensional cardiac imaging with multislice computed tomography. Circulation 103(12):E62

Nikolaou K, Knez A, Sagmeister S, Wintersperger BJ, Reiser MF, Becker CR (2004). Assessment of myocardial infarctions using multirow-detector computed tomography. J Comput Assist Tomogr 28(2):286–292

Ohnesorge B, Flohr T, Becker C, Kopp AF, Schoepf UJ, Baum U et al (2000). Cardiac imaging by means of electrocardiographically gated multisection spiral CT: initial experience. Radiology 217(2):564–571

Schmermund A, Gerber T, Behrenbeck T, Reed JE, Sheedy PF, Christian TF et al (1998). Measurement of myocardial infarct size by electron beam computed tomography: a comparison with 99mTc sestamibi. Invest Radiol 33(6):313–321

Schwitter J, Nanz D, Kneifel S, Bertschinger K, Buchi M, Knusel PR et al (2001). Assessment of myocardial perfusion in coronary artery disease by magnetic resonance: a comparison with positron emission tomography and coronary angiography. Circulation 103(18):2230–2235

Slutsky RA, Mattrey RF, Long SA, Higgins CB (1983). In vivo estimation of myocardial infarct size and left ventricular function by prospectively gated computerized transmission tomography. Circulation 67(4):759–765

So A, Hadway J, Acharya KC, Pan T, Lee TY (2002). Quantitative myocardial perfusion measurment with CT scanning. Radiology 225:P308

Stantz KM, Liang Y, Meyer CA, Teague SD, March K (2002). In vivo myocardial perfusion measurements by ECG-gated multi-slice computed tomography. Radiology 225:308P

Wilke N, Simm C, Zhang J, Ellermann J, Ya X, Merkle H et al (1993). Contrast-enhanced first pass myocardial perfusion imaging: correlation between myocardial blood flow in dogs at rest and during hyperemia. Magn Reson Med 29(4):485–497

Wintersperger BJ, Ruff J, Becker CR, Knez A, Huber A, Nikolaou K et al (2002). Assessment of regional myocardial perfusion using multirow-detector computed tomography (MDCT). Eur Radiol 12 (Suppl1):S294

Wolfkiel CJ, Ferguson JL, Chomka EV, Law WR, Labin IN, Tenzer ML et al (1987). Measurement of myocardial blood flow by ultrafast computed tomography. Circulation 76(6):1262–1273

7.15 Cardiothoracic Multi-Slice CT in the Emergency Department

U.-J. Schöpf

Contents

7.15.1 ECG-Gated Multi-Slice CT Scanning of the Chest *317*
7.15.2 Patients with Equivocal Chest Pain in the Emergency Department *320*
7.15.3 64-Slice CT as a Triage Tool in the Emergency Department *320*
References *324*

7.15.1 ECG-Gated Multi-Slice CT Scanning of the Chest

Cardiac motion artifacts degrade the diagnostic quality of thoracic CT. Some of these artifacts are recognized as an important source of potential diagnostic error (Loubeyre 1997). Synchronization of the CT scan acquisition with the patient's ECG reduces cardiac motion artifacts and enables non-invasive visualization of the coronary arteries (Ohnesorge 2000, Schöpf 2004a) and other cardiac anatomy.

ECG synchronization has also been shown to improve image quality at CT imaging of non-cardiac thoracic structures (Schöpf 1999, Hofmann 2004). ECG-synchronized acquisition during high-resolution CT of the lung eliminates artifacts attributable to cardiac motion (Fig. 7.108) and thus improves the diagnosis of diffuse lung disease. In many institutions, retrospective ECG gating has become an integral component in the imaging protocol of suspected disease of the ascending aorta. The use of ECG gating avoids pulsation and doubling artifacts of the aortic root and the ascending aorta (Flohr 2002) (Fig. 7.109), which often are misinterpreted by less-experienced observers as aortic dissection and may result in unnecessary emergency surgery. In select cases, in which critical therapeutic decisions (i.e., anticoagulation in high-risk patients) hinge on the diagnosis or exclusion of pulmonary embolism, ECG gating may be used to improve diagnostic quality at pulmonary CTA to differentiate between artifactual filling defects in the pulmonary arteries, caused by cardiac pulsation, and real thromboembolic clots (Fig. 7.110). ECG gating may also refine the derivation of functional parameters from contrast-enhanced CTA, which provides an important tool for risk stratification in patients with acute pulmonary embolism (Schöpf 2004b).

However, the through-plane spatial resolution that can be achieved with retrospectively ECG-gated technique using 4- or 8-slice multi-slice CT scanners is limited by the relatively long scan duration inherent to data oversampling. Thus, high-resolution acquisition can only be achieved for relatively small volumes, i.e., the coronary arterial tree, but not for extended coverage of the entire chest. The advent of 16-slice CT scanners enabled a substantial volume of the body to be scanned with retrospective ECG gating and high through-plane resolution in a single breath-hold (Flohr 2003). This capability allows non-invasive assessment of systemic manifestations of atherosclerotic disease throughout the body with sufficient vascular detail to evaluate the coronary arteries based on a single, contrast-enhanced scan (Fig. 7.111).

Although 16-, 32-, and 40-slice CT scanners enable comprehensive assessment of the entire arterial system for atherosclerosis and other vascular disease, they are still limited by several obstacles. For example, the current state-of-the-art for coronary CTA for non-invasive assessment of coronary artery disease comprises acquisition of sub-millimeter sections (Flohr 2003), but this is difficult to achieve for large anatomic volumes. In addition, the robustness of previous multi-slice CT generations with respect to faster and more irregular heart rates still requires the use of β-blockers for rate control in a substantial percentage of patients. Breath-hold times are still relatively long, which poses a particular difficulty if this technique is to be used to evaluate critically ill patients, whose ability to cooperate during scan acquisition is limited. Similarly, long scan times prohibit simultaneous assessment of the pulmonary arterial and systemic arterial circulation

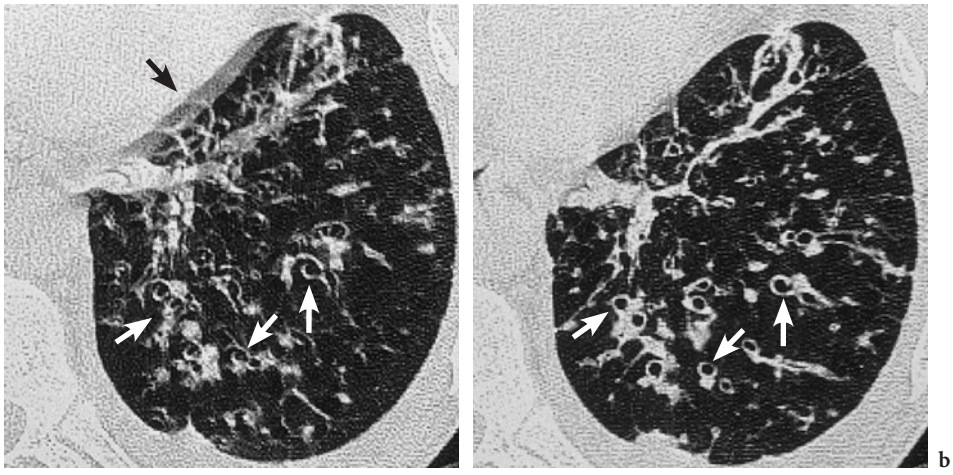

Fig. 7.108a,b. Non-ECG triggered (**a**) and ECG-triggered (**b**) high-resolution CT scans obtained with 4-slice CT at the same level of the paracardiac parenchyma in a 24-year-old man who underwent lung transplantation. Mild dilatation and bronchial wall thickening in the left lower lobe (*white arrows*) are better seen in the ECG-triggered study than in the conventional scan. Also, note blurring of the cardiac border (*black arrow*) in the non-ECG triggered scan

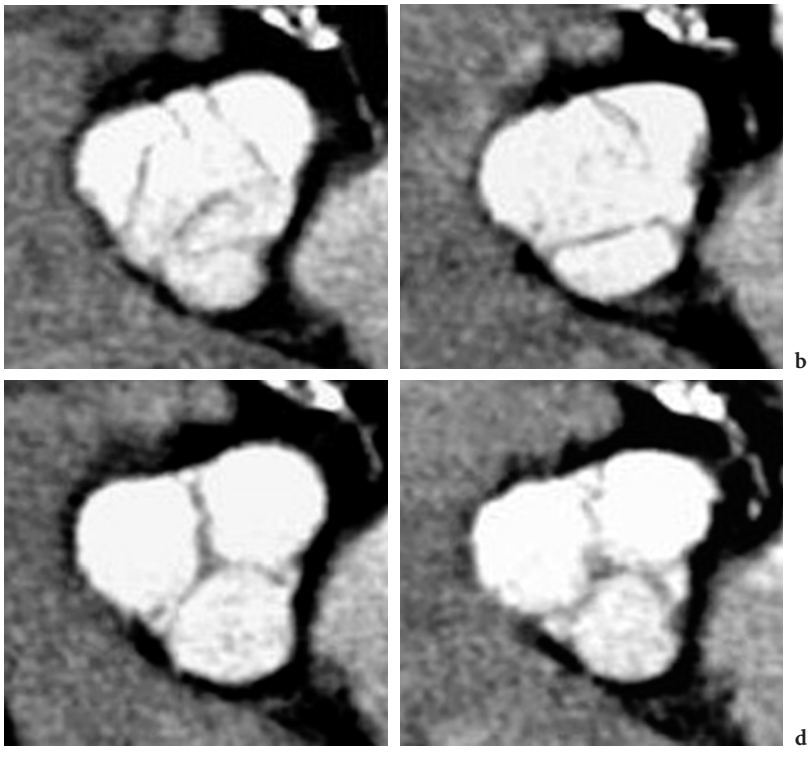

Fig. 7.109a–d. A 54-year-old man with a mean heart rate of 62 bpm, examined with 4-slice CT. Double-oblique multi-planar reformats of the aortic root at the level of the aortic valve as seen from a cranial perspective. Image reconstruction was referenced to four different time points during the cardiac cycle. Motion artifacts during systolic opening of the valve at 0% RR (**a**) and 20% RR (**b**) preclude clear demarcation of the valvular cusps. Delineation of the cusps is best at mid-diastolic closure at 60% RR (**c**) and slightly deteriorates again during late diastole at 80% RR (**d**)

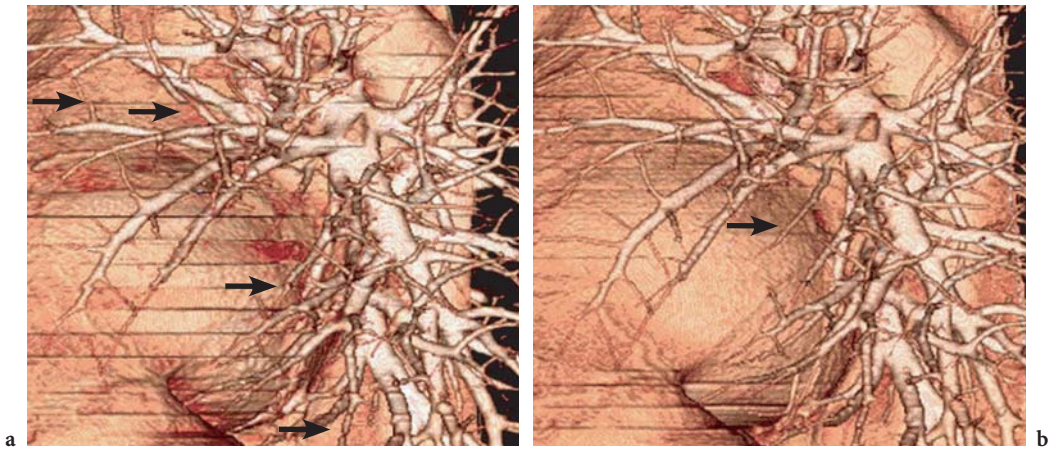

Fig. 7.110a,b. Contrast-enhanced multi-slice CT angiography using 4-slice CT in a 60-year-old woman with a mean heart rate of 73 bpm during scan acquisition. Focused, colored volume-rendered display of the paracardiac pulmonary circulation seen from a left lateral perspective. Image reconstruction with use of 0% RR (**a**) and 80% RR (**b**) as respective starting points. Image reconstruction during late diastole (b) results in a reduction of stair-stepping artifacts (*arrows*), which cause artifactual discontinuity of vessels during systole (**a**). A small subsegmental branch (*arrow*) of a pulmonary artery that supplies the lingula of the left upper lobe of the lung is only visualized at image reconstruction during late diastole (**b**)

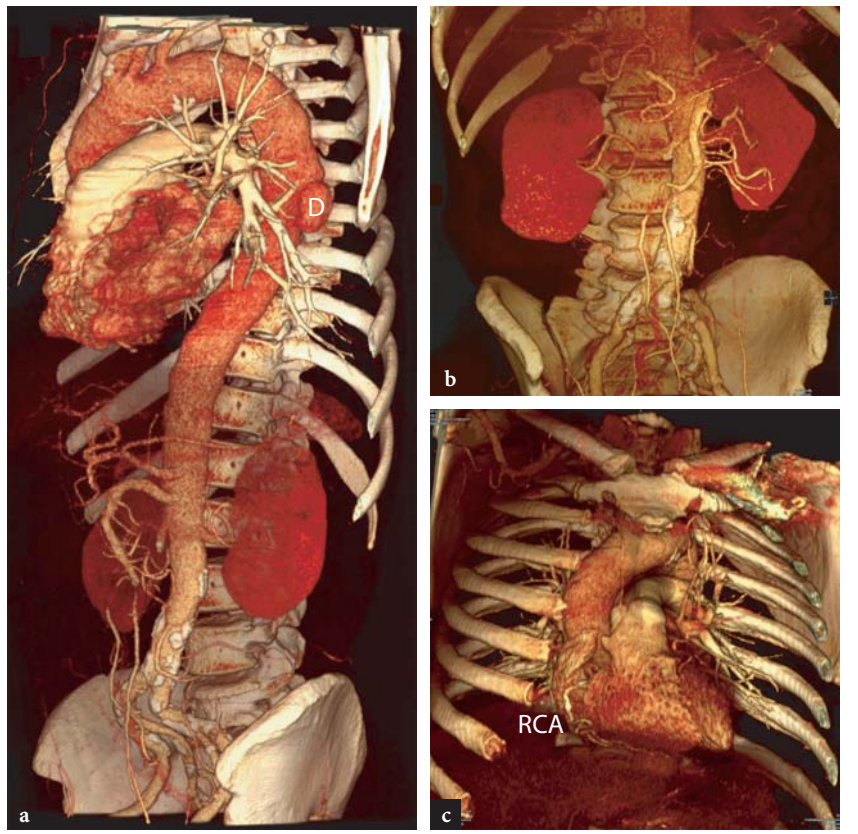

Fig. 7.111a–c. Comprehensive systemic assessment of cardiovascular disease. A 55-year-old male with epigastric pain was examined using 16-slice CT angiography with a gantry rotation time of 420 ms and retrospective ECG gating. The CT scan demonstrates a circumscribed type B dissection of the descending thoracic aorta originating distal to the origin of the left subclavian artery (**a**, **b**). In addition, extensive atherosclerotic changes with heavy calcifications are noted in the wall of the abdominal aorta (**b**). High-resolution image acquisition and the absence of cardiac pulsation artifacts owing to retrospective ECG synchronization enables assessment of the coronary artery tree from the same scan (**c**) and shows extensive atherosclerotic changes of the RCA

in a single, high-resolution ECG-gated scan, as these scans would require unreasonably high amounts of contrast material to maintain enhancement of both vascular systems throughout the scan. These limitations prevented application of the previous generation of multi-slice CT scanners to achieve another coveted goal: comprehensive assessment of patients with acute chest pain, typically in an emergency department setting.

7.15.2 Patients with Equivocal Chest Pain in the Emergency Department

Every year, over 1.5 million Americans are admitted to the hospital after presenting to the emergency department with acute chest pain. Only a small percentage of those admitted have coronary syndromes, whereas the vast majority of patients have non-cardiac diagnoses. In many patients, the findings on initial evaluation are equivocal or indeterminate. Rapid diagnostic assessment of the causes of the acute chest pain would provide a suitable hospital-based test that could substantially reduce mortality and treatment costs (Lee 1987, Yusuf 1988, Oler 1996).

Several strategies have emerged to manage these patients. Patients with typical features of unstable angina or acute myocardial infarction, such as ECG changes typical of ischemia, or those with known CHD and prolonged cardiac-type pain are at substantial risk of adverse events and hospital admission is mandatory (Pozen 1984, Panju 1998). On the opposite end of the spectrum, patients with no risk factors for CHD, no clinical features of cardiac chest pain, and a normal ECG are usually discharged home. A diagnostic dilemma, however, exists for the substantial number of patients who present with acute chest pain with an intermediate probability of having CHD and a normal or non-diagnostic ECG.

Recently, new cardiac enzyme tests have improved early sensitivity and specificity for detecting acute myocardial infarction. However, these tests do not achieve acceptable levels of sensitivity until at least 6 h after the onset of pain. As patients typically present earlier than this, a period of observation is inevitably combined with use of such tests, which prolongs hospital stay. In order to improve the sensitivity for diagnosis of unstable angina, provocative cardiac testing (typically exercise treadmill) has been used in combination with monitoring, enzyme testing, and provocative testing. This strategy has become widespread in the USA, usually in a designated chest pain observation unit (Zalenski 1998). Although this approach is more sensitive than enzyme testing alone, it exerts a significant cost burden on the health-care system. Current strategies therefore range from low-cost, low-benefit (discharge home) to high-cost, high-benefit (hospital admission). Data relating to these strategies are emerging but remain largely anecdotal. Yet, the potential burden in terms of morbidity, mortality, and socioeconomic resources demands a coherent and rational approach.

The common way of ruling out coronary artery disease as the underlying cause is coronary catheterization, which consequently is done in many patients who have chest pain but no typical clinical presentation for coronary artery stenosis or blockage. Although the presence of coronary artery disease is unlikely, these patients usually undergo this invasive procedure just to rule out the remote possibility that significant coronary artery disease is causing their symptoms. With invasive coronary angiography, contrast material is directly injected into the coronary arteries, thus allowing their visualization as a cast-like fluoroscopic X-ray image. Unfortunately, coronary catheterization is expensive and invasive and the risk to the patient is not negligible. Also, coronary angiography is not capable of identifying other causes of chest pain, such as aortic dissection or pulmonary embolism. Thus, additional imaging is frequently necessary, increasing the length of stay, costs, and radiation exposure to the patient. The ability to differentiate cardiac and non-cardiac causes of acute chest pain without the need for such an invasive procedure would greatly benefit affected individuals and decrease the costs for a comprehensive diagnostic work-up.

7.15.3 64-Slice CT as a Triage Tool in the Emergency Department

With the advent of 64-slice CT, a tool is now available to effectively eliminate previous limitations of CT

and enable the rapid triage of patients with equivocal chest pain. Since 64-slice CT provides isotropic spatial resolution of less than 0.4 mm, visualization of small vascular detail is greatly enhanced. Gantry rotation times of 330 ms significantly improve the temporal resolution of cardiac CT scan acquisitions to a constant 165 ms at all heart rates. This improved temporal resolution directly translates into substantially enhanced robustness of cardiac scan acquisition at higher and more irregular heart rates. In turn, this reduces the need for rate control and significantly increases the percentage of patients in whom a fully diagnostic scan can be obtained. The need for using artifact-prone multisegment reconstruction algorithms for improving temporal resolution is reduced. Breath-hold times are significantly decreased. With accurate timing of the contrast bolus, the rapid scan acquisition enables ECG-gated interrogation of both the pulmonary arterial and systemic arterial circulation of the chest with a single injection of a standard bolus of contrast material (Fig. 7.112). The combination of these achievements should fulfill the technical prerequisites for integrating 64-slice CT into the diagnostic algorithm of patients with equivocal chest pain.

The technical obstacles for the clinical application of this test are being overcome; thus, the appropriate indication of this test within the work-up of chest pain patients still needs to be carefully defined. Certainly, patients who have a very low pre-test likelihood of coronary artery disease and whose benignity of symptoms would warrant speedy discharge from the emergency department are unlikely to benefit from this test. However, patients with a very high pre-test likelihood of coronary artery disease as a source of their chest pain (e.g., known CHD, ST elevation, positive cardiac markers) will undergo conventional work-up including catheterization anyhow. For such patients, the use of 64-slice CT as an additional diagnostic test will likely not be beneficial but rather detrimental, as the onset of specific therapy (e.g., thrombolysis, stent placement) may be delayed and complicated by an additional load of iodine, which may impede lengthy catheter interventions. Instead, 64-slice CT seems exceedingly well-suited for quickly and non-invasively triaging patients with equivocal presentation, non-diagnostic ECG, and initially negative serum markers for acute myocardial injury (Fig. 7.113). As described above, such patients ordinarily undergo a period of observation with serial assessment of ECG and cardiac markers and eventually further work-up, such as stress testing (Braunwald 2002). In these patients, the inclusion of 64-slice CT into the diagnostic algorithm would enable rapid diagnosis of common non-cardiac causes of acute chest pain, such as acute pulmonary embolism (Schöpf 2004c), aortic dissection, or aortic and pulmonary aneurism, each of which is difficult to diagnose with the tools and tests comprising the conventional work-up of patients with chest pain (Fig. 7.114). Similarly, important additional diagnoses that impact on patient management in the presence or absence of a specific reason for chest pain are very amenable to CT visualization (Fig. 7.115). There is agreement that negative coronary CTA is associated with a very high negative predictive value for the exclusion of significant coronary artery stenosis (Schoepf 2004a). Thus, significant coronary artery disease as a source of symptoms in patients with acute chest pain should be safely ruled out by a negative CT coronary angiogram (Fig. 7.116) of sufficient diagnostic quality. If significant coronary artery disease can be specifically diagnosed by the contrast enhanced 64-slice CT scan (Fig. 7.117), treatment can be initiated. There will still be patients in whom the CT scan will not be fully diagnostic or explanatory for their symptoms. Those patients will still have to

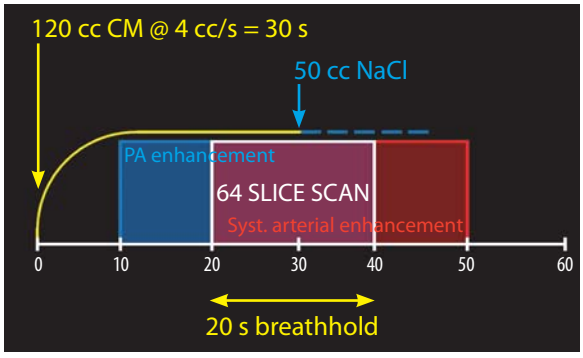

Fig. 7.112. Sample contrast-media injection protocol for 64-slice CT of the chest. A bolus of 120 ml of contrast material, injected at 4 ml/s enables high-resolution (i.e., sub-millimeter) ECG-gated image acquisition during a 20-s overlap phase, with contrast enhancement of the systemic and PA side of the thoracic vasculature

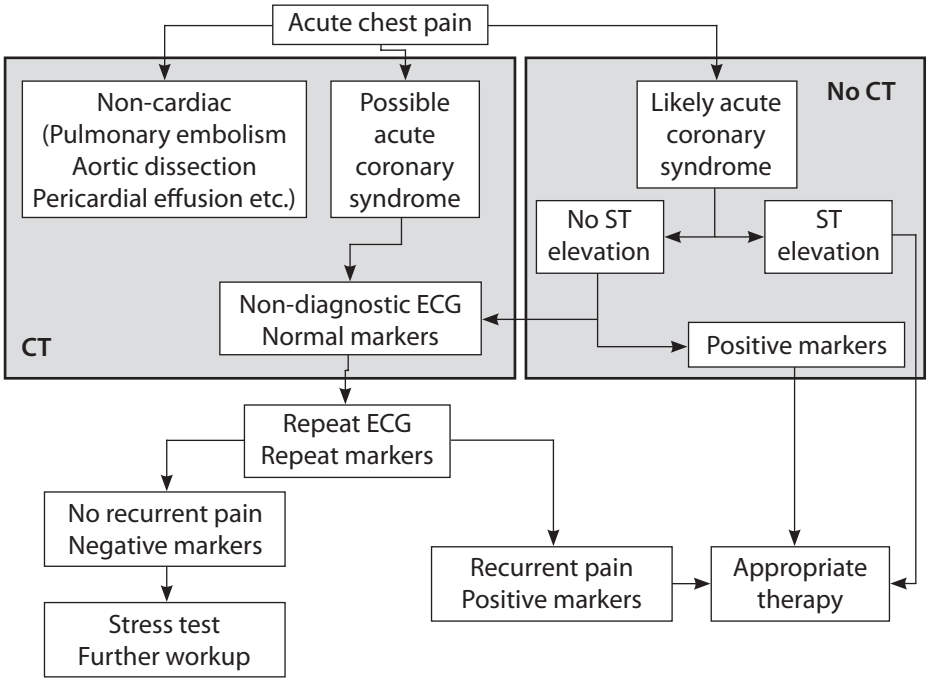

Fig. 7.113. Coronary CT angiography in the clinical work-up of patients with acute chest pain in the emergency department. CT investigation of patients with a high likelihood (ST-elevation and/or positive cardiac markers) of having an acute coronary syndrome will not benefit

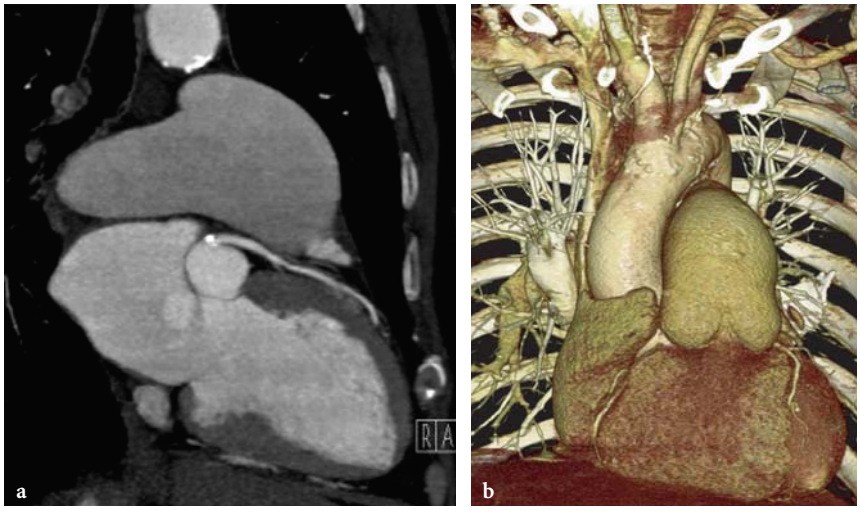

Fig. 7.114a,b. ECG-gated 64-slice CT examination of a patient with chest pain. A scan range of 25 cm was covered in an 18 s breath-hold time. A pulmonary aneurysm is evident in sagittal MPR (**a**) and VRT reconstruction (**b**). MPR reconstruction also reveals a calcified lesion in the left main coronary artery but no related coronary stenosis. (Case courtesy of Mayo Clinic Rochester)

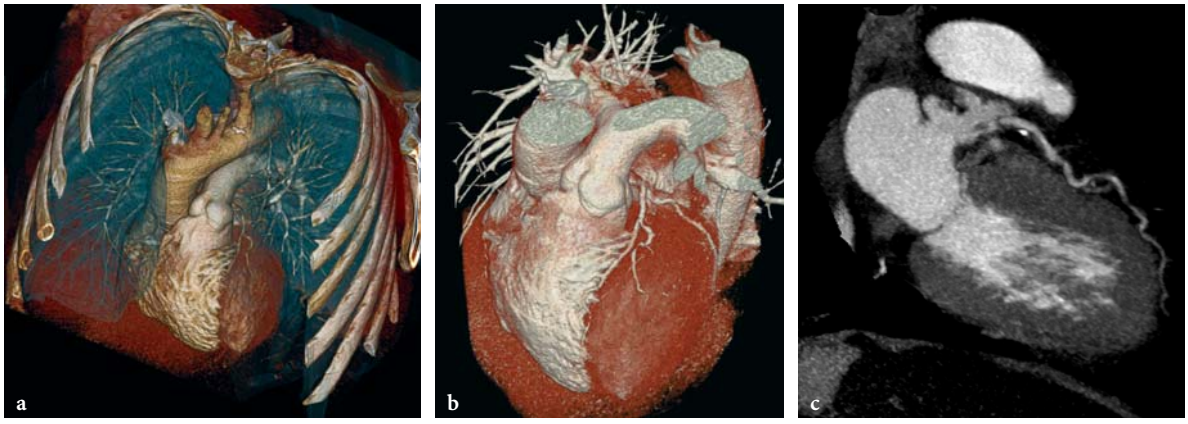

Fig. 7.115a–d. A 52-year-old man with a smoking history of 25 pack years presented to the emergency department with acute chest pain. **a** Contrast-enhanced 64-slice CT angiography of the entire thorax with a gantry rotation time of 330 ms and retrospective ECG gating ruled out acute pulmonary embolism as the reason for his chest pain. **b** Focused reconstruction of the coronary arteries showed diffuse atherosclerotic disease. **c** MIP in a right anterior oblique perspective of the LAD showed atherosclerotic plaque in the inferior, anteromedial wall of the LAD. The plaque is mildly obstructive and consists of non-calcified tissue adjacent to a calcified nodule. **d** Analysis of lung-window reconstructions of the entire chest revealed incidental squamous-cell carcinoma of the left upper lobe of the lung

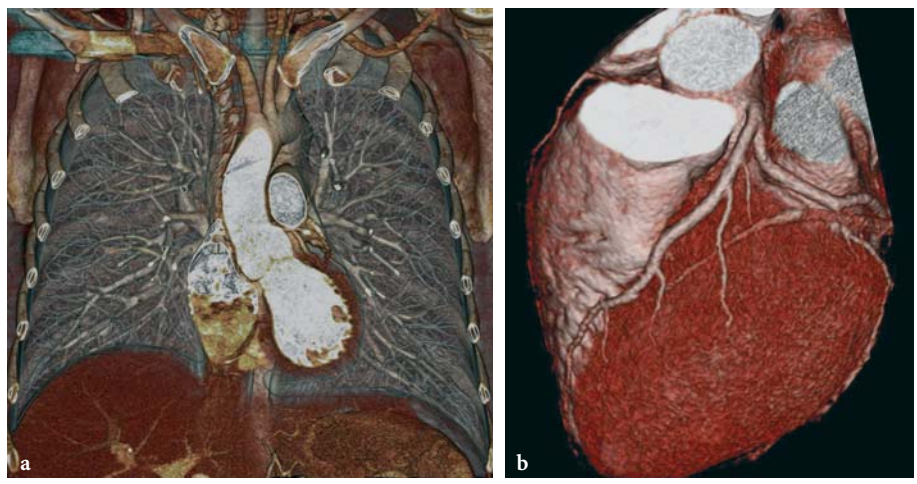

Fig. 7.116a,b. A 59-year-old woman presenting to the emergency department with acute chest pain. Contrast-enhanced, retrospectively ECG-gated 64-slice CT study of the entire chest with 0.6-mm collimation was acquired within a total scan time of 19 s. Volume-rendered display of the entire thorax (**a**) and focused display of the coronary artery tree (**b**) show normal vascular anatomy, thus ruling out pulmonary embolism, aortic dissection, and coronary artery disease as the underlying cause of chest pain in this patient

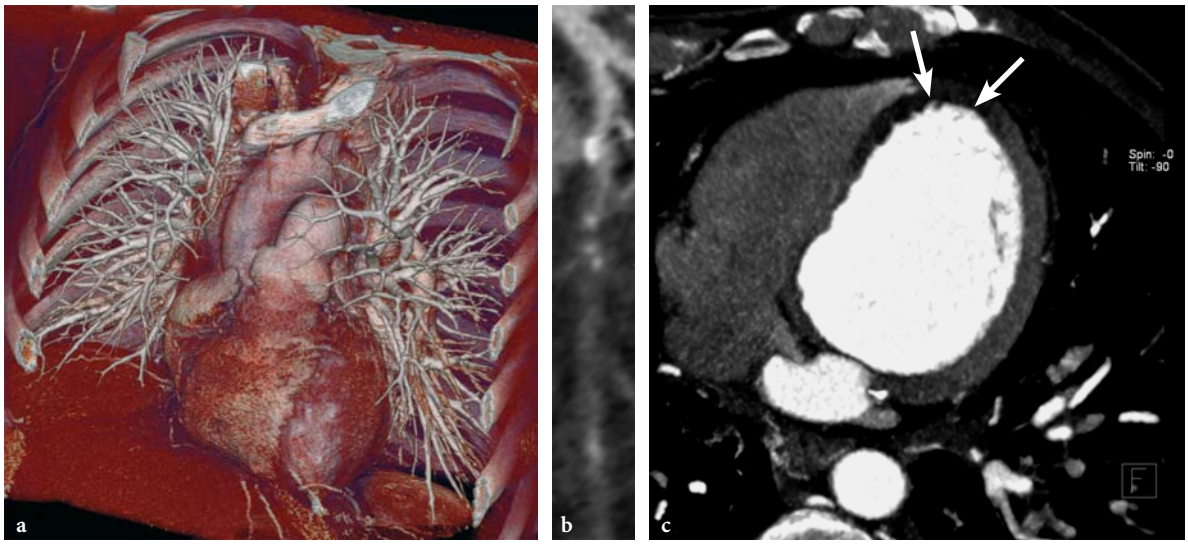

Fig. 7.117a–c. A 57-year-old man presenting to the emergency department with acute chest pain. Non-diagnostic ECG, initial cardiac blood markers negative for acute myocardial ischemia. **a** Contrast-enhanced, retrospectively ECG-gated 64-slice CT study of the entire chest with 0.6-mm collimation was acquired within a total scan time of 21 s. The results ruled out acute pulmonary embolism as a reason for chest pain. **b** Curved multi-planar reformat shows subtotal thrombosis of the LAD. **c** Axial MIPs show areas of myocardial hypoattenuation (*arrows*) in the LAD territory, corresponding to acute myocardial infarction

undergo the conventional work-up for acute chest pain, but their number should be greatly reduced. Precious room time in conventional cardiac catheter suites, which is currently wasted for performing merely diagnostic angiograms, can be more cost-effectively dedicated to those patients who absolutely require actual intervention. Thus, an overall positive effect on the length of stay and cost to the health-care environment is anticipated.

References

Braunwald E, Antman EM, Beasley JW, et al (2002). ACC/AHA 2002 guideline update for the management of patients with unstable angina and non-ST-segment elevation myocardial infarction–summary article: a report of the American College of Cardiology/American Heart Association Task Force on Practice Guidelines (Committee on the Management of Patients With Unstable Angina). J Am Coll Cardiol 40:1366–1374

Flohr T, Prokop M, Becker C, et al (2002). A retrospectively ECG-gated multislice spiral CT scan and reconstruction technique with suppression of heart pulsation artifacts for cardio-thoracic imaging with extended volume coverage. Eur Radiol 12:1497–1503

Flohr T, Schoepf U, Kuettner A, et al (2003). Advances in cardiac imaging with 16-section CT systems. Acad Radiol 10:386–401

Hofmann LK, Zou KH, Costello P, Schoepf UJ (2004). Electrocardiographically gated 16-section CT of the thorax: cardiac motion suppression. Radiology 233:927–933

Lee TH, Rouan GW, Weisberg MC, et al (1987). Sensitivity of routine clinical criteria for diagnosing myocardial infarction within 24 hours of hospitalization. Ann Intern Med 106:181–186

Loubeyre P, Angelie E, Grozel F, Abidi H, Minh VA (1997). Spiral CT artifact that simulates aortic dissection: image reconstruction with use of 180 degrees and 360 degrees linear-interpolation algorithms. Radiology 205:153–157

Ohnesorge B, Flohr T, Becker C, Schoepf UJ, et al (2000). Cardiac imaging by means of electrocardiographically gated multisection spiral CT: initial experience. Radiology 217:564–571

Oler A, Whooley MA, Oler J, Grady D (1996). Adding heparin to aspirin reduces the incidence of myocardial infarction and death in patients with unstable angina. A meta-analysis. Jama 276:811–815

Panju AA, Hemmelgarn BR, Guyatt GH, Simel DL (1998). The rational clinical examination. Is this patient having a myocardial infarction? JAMA 280:1256–1263

Pozen MW, D'Agostino RB, Selker HP, Sytkowski PA, Hood WB (1984). A predictive instrument to improve coronary-care-unit admission practices in acute ischemic heart disease. A prospective multicenter clinical trial. N Engl J Med 310:1273–1278

Schoepf UJ, Becker CR, Bruening RD, et al (1999). Electrocardiographically gated thin-section CT of the lung. Radiology 212:649–654

Schoepf UJ, Becker CR, Ohnesorge BM, Yucel EK (2004a). CT of coronary artery disease. Radiology 232:18–37

Schoepf UJ, Kucher N, Kipfmueller F, Quiroz R, Costello P, Goldhaber SZ (2004b). Right ventricular enlargement on chest computed tomography: a predictor of early death in acute pulmonary embolism. Circulation 110:3276–3280

Schoepf UJ, Goldhaber SZ, Costello P (2004c). Spiral computed tomography for acute pulmonary embolism. Circulation 109:2160–2167

Yusuf S, Wittes J, Friedman L (1988). Overview of results of randomized clinical trials in heart disease. II. Unstable angina, heart failure, primary prevention with aspirin, and risk factor modification. JAMA 260:2259–2263

Zalenski RJ, Rydman RJ, Ting S, Kampe L, Selker HP (1998). A national survey of emergency department chest pain centers in the United States. Am J Cardiol 81: 1305–1309

Future Technical Developments in Cardiac CT

8

Bernd Ohnesorge

Contents

8.1 **Limitations and Pitfalls with Today's Multi-slice CT** *327*
8.1.1 Temporal Resolution *327*
8.1.2 Volume Coverage *328*
8.1.3 Spatial Resolution and Signal-to-Noise Ratio *329*
8.1.4 Radiation Exposure *331*
8.2 **A Future for Electron-Beam CT?** *332*
8.3 **Future Possibilities with Area Detector CT** *334*
8.4 **New Frontiers with Dual-Source CT** *335*
8.4.1 Dual-Source CT: System Concept and Design *338*
8.4.2 Dual-Source CT: Cardiac Scanning Principles and Techniques *339*
8.4.3 Dual-Source CT: System Performance Evaluation *342*
8.4.4 Dual-Source CT: Clinical Scan Protocols and Preliminary Clinical Results *347*
References *357*

Multi-slice cardiac CT has undergone very rapid technical development since the introduction of 4-slice CT scanners in 1999. However, even with the 64-slice CT scanners of the latest generation, technical challenges remain that lead to limitations in the clinical spectrum and to the exclusion of certain patient cohorts. In this chapter, we will summarize the shortcomings and most frequent pitfalls of today's multi-slice CT scanners and discuss avenues of potential future development aimed at overcoming those obstacles. After the discussion of potential future developments of electron-beam CT and multi-slice CT with more slices and larger detector coverage, we will introduce a new – so-called dual-source CT – scanner concept and discuss the initial clinical experience with these machines. This new scanner technology uses two X-ray sources and two detectors simultaneously and has become available for general use in 2006.

8.1 Limitations and Pitfalls with Today's Multi-slice CT

8.1.1 Temporal Resolution

Motion artifacts in patients with higher or irregular heart rates remain the most important challenge for multi-slice cardiac CT imaging. In order to consistently achieve diagnostic image quality in clinical routine, most authors recommend the administration of beta-blockers to slow down the heart rate and to introduce a stable sinus rhythm in patients with irregular heart beat (Fig. 8.1). However, a singnificant portion of non-assessable coronary segments can still occur when using older 16-slice CT scanners with slower grantry rotation speeds (Garcia 2006). The most recent generation of 64-slice CT systems provides gantry rotation times down to 0.33 s, resulting in a stable temporal resolution of 165 ms. While image quality at higher heart rates and robustness of the method in clinical routine seem to be significantly improved with these systems, several authors still propose the administration of β-blockers for patients that present with a heart rate over 65–70 bpm (Leber 2005, Raff 2005, Ropers 2006, Ehara 2006, Ong 2006). Leschka et al. and Ehara et al. reported that in addition to absolute heart rate, increasing heart rate variabil-

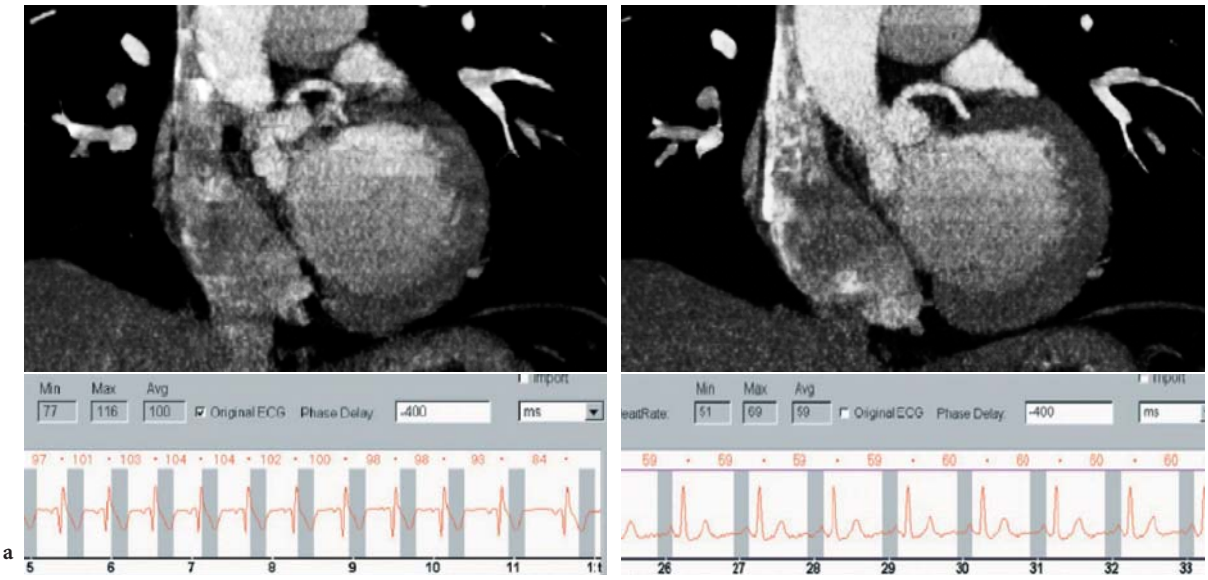

Fig. 8.1a,b. Coronary CT angiography examinations of a patient with a high and irregular heart rate. A 64-slice CT scanner with 0.6-mm collimation and 0.33-s rotation time was used. **a** Motion and stair-step artifacts are present in the first examination, during which the patient's heart rate varied between 84 and 104 bpm. **b** After the administration of β-blockers, the patient showed stable sinus rhythm between 56 and 60 bpm during the scan and diagnostic image quality could be achieved. (Case study courtesy of Klinikum Grosshadern, University of Munich, Germany)

ity reduces image quality (Leschka 2006, Ehara 2006). Wintersperger et al. (2005) demonstrated the ability of 64-slice CT with a gantry rotation time of 0.33 s to produce diagnostic image quality with a low number of non-diagnostic segments in patients with heart rates up to 92 bpm. The authors observed good image quality in diastole for patients with heart rates < 65 bpm and good image quality in end systole for patients with heart rates > 75 bpm, while image quality in the intermediate heart rate range of 65–75 bpm was compromised and neither diastolic nor systolic reconstruction reliably yielded optimal results.

Due to the limited temporal resolution compared to MRI, cardiac function parameters determined by multi-slice CT still show systematic errors because of a consistent overestimation of systolic volumes. The evaluation of myocardial wall motion is still limited by motion artifacts that are present during those phases of the cardiac cycle with rapid cardiac motion.

Further improved temporal resolution, at best < 100 ms at all heart rates, is desirable in the future to completely eliminate the need for to control the heart rate. Increased gantry rotation speed rather than multi-segment reconstruction approaches is preferable for robust clinical performance (Haliburton 2003). Obviously, significant development efforts are needed to account for the substantial increase in mechanical forces (~ 17 G for 0.42-s rotation time, ~ 28G for 0.33-s rotation time) and increased data transmission rates. Rotation times of < 0.2 s (mechanical forces > 75G), which are required to provide a temporal resolution of less than 100 ms, independent of the heart rate, appear to be beyond today's mechanical limits.

8.1.2 Volume Coverage

The detector z-coverage used for high-resolution imaging of the heart has significantly increased, from about 4 mm (4 × 1-mm collimation) with the first 4-slice CT scanners up to values between 19.2 and 40 mm with today's 64-slice CT scanners. This

increased coverage with 64-slice CT results in very short breath-hold times of 6–10 s for imaging the heart and 14–20 s for an ECG-gated scan of the chest. Therefore, detector-coverage no longer represents a limitation of multi-slice CT with regard to breath-hold time in cardiac imaging, as clinically reasonable scan ranges can be covered in comfortably short scan times. Nevertheless, even with today's available detector coverage of up to 40 mm, a retrospectively ECG-gated image data set still consists of several image slabs originating from multiple consecutive heart beats. The width of one image slab originating from one heart beat is determined by the detector z-coverage and thus the number of heart beats contributing to the entire data set decreases with increasing detector z-coverage. However, the downside of increasing the width of the image slabs per heart beat is that larger portions of the data set may be distorted in case of an ectopic beat during the scan (Fig. 8.2). The availability of an ECG-editing tool to correct for ectopic beats is of special importance in such cases. While the number of heart beats contributing to a scan is clinically not relevant as long as breath-hold times are short enough, it still may be useful to develop CT scanners in the future with a detector z-coverage of ≥ 12 cm in order to cover the entire heart in one single heart beat, thus avoiding any step artifacts. However, increased volume coverage should not be preferred over enhanced temporal resolution from a cinical point of view.

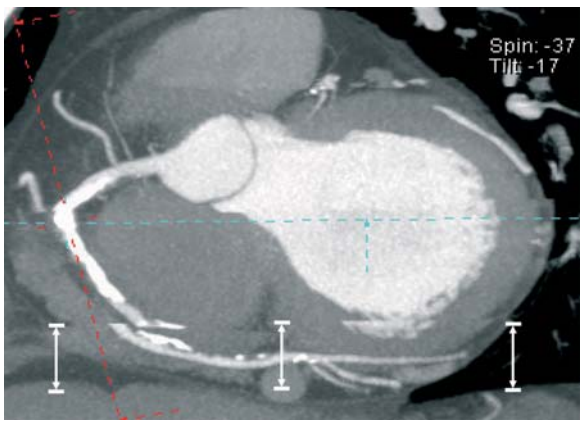

Fig. 8.2. Coronary CT angiography examination using a 64-slice CT scanner. An ectopic beat during the scan results in a parallel shift of a large image slab (range described by *arrows*). The width of the displaced image slab is determined by the coverage of the detector. (Case courtesy of Xuan Wu Hospital, China)

Another potential advantage of CT scanners with increased detector volume coverage is the coverage of larger portions of the heart for evaluation of myocardial perfusion. Currently, to study dynamic contrast enhancement indicating potential perfusion defects caused by coronary artery narrowing, only limited ranges of the myocardium can be covered with ECG-correlated scan protocols in the absence of table motion (Fig. 8.3). However, there is very limited clinical experience with regard to the clinical potential of myocardial perfusion measurements with multi-slice CT. Extensive basic research with today's CT scanners to evaluate the feasibility of cardiac perfusion CT is still needed before this application can serve as a motivation for the development of a new CT scanner generation with larger detector coverage.

8.1.3 Spatial Resolution and Signal-to-Noise Ratio

High spatial resolution is particularly important for accurate diagnosis of the coronary arteries and other small cardiac anatomy. Evaluation of heavily calcified coronary segments, coronary stents, and smaller coronary segments as well as quantification of coronary artery stenosis in particular require a spatial resolution significantly below 1 mm. The spatial resolution of retrospectively ECG-gated scans of the heart has significantly improved with the advent of multi-slice CT scanners with sub-millimeter collimation. The latest generation of 64-slice CT scanners can provide an isotropic spatial resolution down to 0.4 mm. Using flying focal spot techniques in the z-direction provides a spatial resolution of about 0.4 mm along the z-axis. At the same time, dedicated reconstruction filter kernels have been developed that improve in-plane resolution to about 0.4 mm (~ 12 lp/cm). Nevertheless, the diagnosis of heavily calcified or stented coronary artery segments with high positive predictive value is still challenging and limited to the larger coronary segments (Figs. 8.4, 8.5).

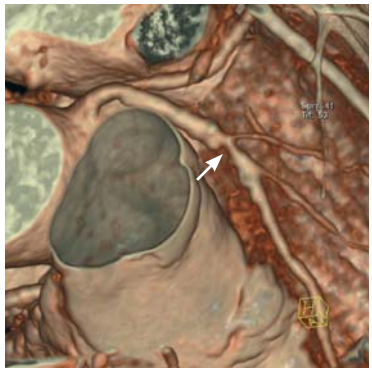

a

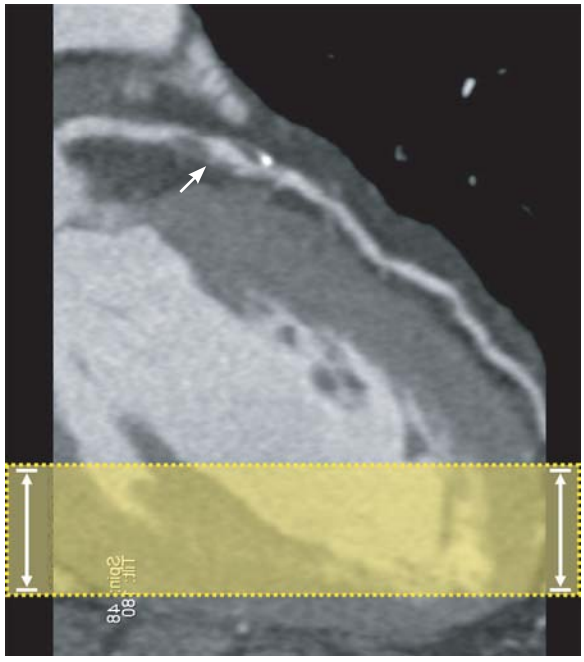

b

Fig. 8.3a,b. Coronary CT angiography examination of a patient with chest pain. The examination was carried out using a 64-slice CT scanner with 0.6-mm collimation and 0.33-s rotation time. **a** Visualization of the left anterior descending coronary artery reveals high-grade stenosis in the proximal segment (*arrow* in **a** and **b**). For further evaluation of myocardial perfusion in the affected area using a dynamic scan protocol without table movement, only limited coverage is available (28.8 mm in this scanner, range described by the yellow shaded band). (Case courtesy of MUSC, Charleston, USA)

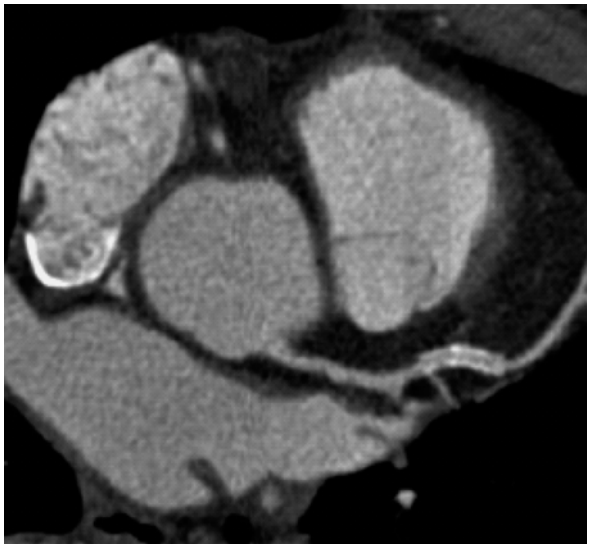

a

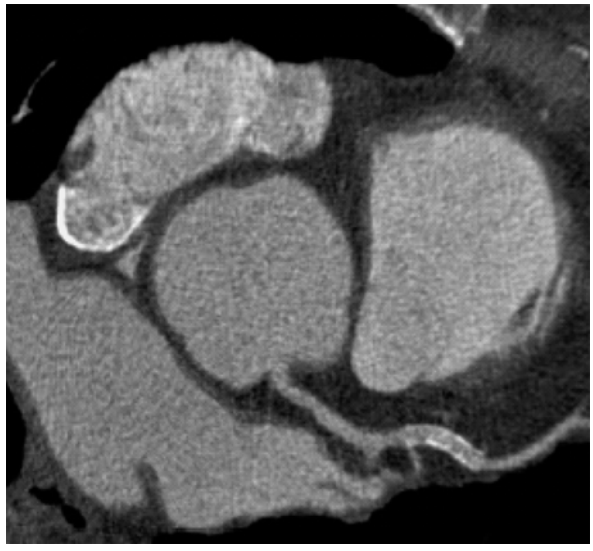

b

Fig. 8.4a,b. Coronary CT angiography examination of a patient with a stent (3-mm diameter) in the left anterior descending coronary artery. The examination was carried out using a 64-slice CT scanner with 0.6-mm collimation and 0.33-s rotation time. **a** Visualization of the in-stent lumen is compromised with 0.75-mm slice width and a medium-smooth reconstruction filter kernel. **b** Patency of the 3-mm stent can only be demonstrated using a special reconstruction technique consisting of a slice width of 0.6-mm and a special sharp reconstruction filter kernel. The in-stent lumen of stents with diameter < 3 mm often cannot be evaluated with currently available 64-slice CT scanners. (Case courtesy of Erlangen University, Germany)

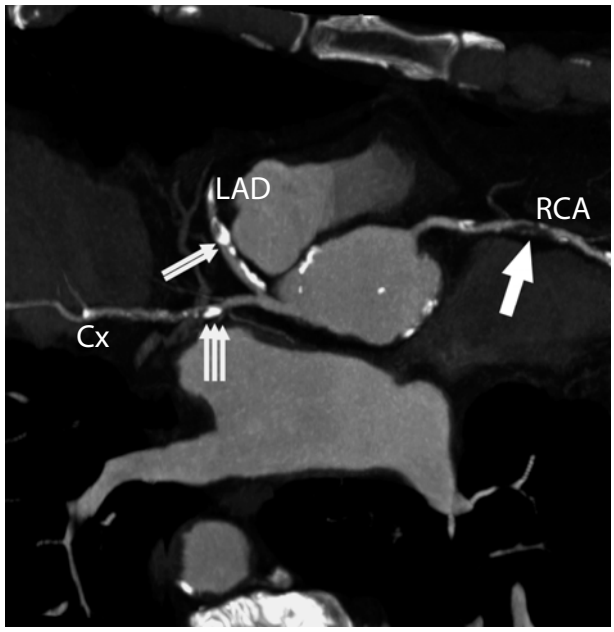

Fig. 8.5. Coronary CT angiography examination of a patient with chest pain. The examination was carried out using a 64-slice CT scanner with 0.6-mm collimation and 0.33-s rotation time. Visualization of all main coronary artery segments in maximum intensity projection (*MIP*) display reveals multiple lesions. The non-calcified stenosis in the right coronary artery (*RCA*) can be readily assessed (*arrow*). While the calcified stenosis in the left anterior descending coronary artery (LAD) can be accurately diagnosed (*double arrow*), evaluation of the lesion in the narrower circumflex coronary artery (*CX*) is more difficult due to the blooming of the calcified plaque (*triple arrow*). (Case courtesy of MUSC, Charleston, USA)

A higher spatial resolution of about 0.25 mm would be desirable for quantitative grading of coronary stenosis in 10% steps, as this would provide reliable detection of stenosis in small calcified and stented coronary arteries and improve the differentiation of coronary plaques. However, spatial resolution in the range of 0.25 mm requires substantially smaller detector elements, with a detector width of about 0.3 mm (projected to the iso-center) and substantially higher X-ray power to provide sufficient signal-to-noise ratio. It will be a key consideration for the development of such scanners whether the related significant increase of radiation exposure can be justified by the additional diagnostic information.

Even with the maximum X-ray power of between 80 and 100 kW available in today's multi-slice CT scanners, signal-to-noise ratio may still be compromised in obese patients (Raff 2005) when protocols with the thinnest possible slices and shortest available rotation time are used (Fig. 8.6). While diagnostic image quality in obese patients can still be obtained by acquisition with slower rotation times and reconstruction with thicker slices, the availability of scanners with higher X-ray power would be beneficial to maintain the highest possible image resolution level. Of course, the related higher radiation exposure has to be taken into consideration and protocols have to be optimized to limit increased exposure to the minimum necessary level.

8.1.4 Radiation Exposure

Minimizing radiation exposure in retrospectively ECG-gated scanning of the heart and cardiothoracic vasculature is a key requirement for future technical developments in CT. With a radiation exposure of about 10 mSv for high-resolution scans of the heart using ECG-controlled dose modulation, radiation exposure is within acceptable limits but still higher than for invasive conventional diagnostic angiography. ECG-controlled dose modulation is a very important feature to limit radiation exposure; however, it cannot be regularly used if irregular beats are likely during the acquisition (Fig. 8.7). For this reason, some centers are not yet using ECG-controlled dose modulation on a regular basis, which results in radiation exposure values > 10 mSv for scans of the heart (Mollet 2005).

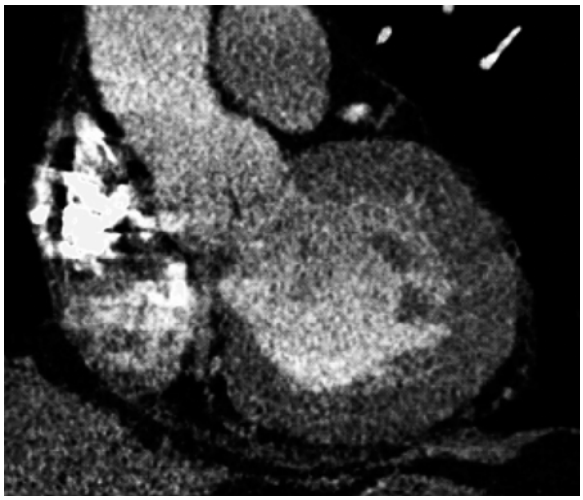

Fig. 8.6. Coronary CT angiography examination in an obese patient (130 kg body weight). The examination was carried out using a 64-slice CT scanner with 0.6-mm collimation and 0.33-s rotation time. Images are reconstructed with 0.75-mm slice width and a medium-smooth reconstruction filter kernel. Visualization of the cardiac anatomy and the coronary artery tree is compromised due to too high image noise. (Case courtesy of Klinikum Grosshadern, University of Munich, Germany)

The main opportunity to minimize radiation exposure in retrospectively ECG-gated multi-slice CT of the heart is to develop robust ECG-correlated dose modulation techniques that can be applied in every patient and that use maximum exposure only during very short time intervals of the cardiac cycle. Therefore, new scan and reconstruction techniques have to be evaluated that provide robust ECG-controlled dose modulation also in patients with irregular heart rates and limit ECG-gated reconstruction to shorter reconstruction intervals during the cardiac cycle.

8.2 A Future for Electron-Beam CT?

An alternative scanner concept that avoids any mechanically moving parts is electron-beam CT (EBCT), schematically shown in Figure 8.8. In EBCT, an electron beam is emitted from a powerful elec-

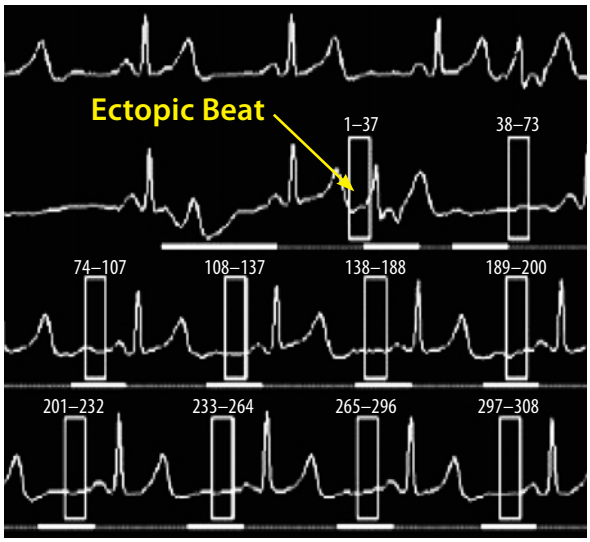

a

b

Fig. 8.7a,b. Coronary CT angiography examination using a 64-slice CT scanner with 0.6-mm collimation, 0.33-s rotation time, and ECG-controlled dose modulation. An ectopic beat during the acquisition (a) leads to misplacement of an interval of high exposure and subsequently to a noisy image slab during image reconstruction (b). It is desirable to develop intelligent ECG-controlled dose modulation techniques that identify ectopic beats and adjust the position of the window of high exposure within the cardiac cycle accordingly. (Case courtesy of Klinikum Grosshadern, University of Munich, Germany)

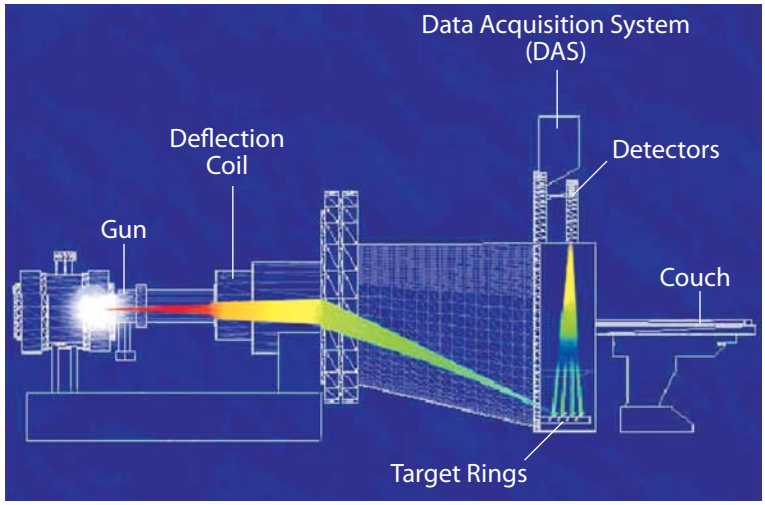

Fig. 8.8. The principle behind electron-beam CT (EBCT) principle. An electron beam is magnetically deflected to hit a semi-circular anode surrounding the patient (total angular coverage of 210° equals 180° plus the fan angle of the beam). The electron beam sweeps over the target in 50–100 ms, thus generating an X-ray source that virtually moves around the patient

tron gun and magnetically deflected to hit a semi-circular anode surrounding the patient. The magnetic deflection sweeps the electron beam over the target, thus generating an X-ray source that virtually rotates around the patient. Given the absence of mechanically moving parts, a sweep can be accomplished in as little as 50 ms.

EBCT systems were already introduced in 1982 as a non-invasive imaging modality for the diagnosis of coronary artery disease (Boyd 1982). The units that remain in operation today (C-150/C-300 or e-speed, Imatron, South San Francisco, California, USA) are equipped with two detector rings and four tungsten target rings, allowing for the acquisition of up to eight slices at different anatomical levels of the patient. The "volume mode" acquires eight images with 50- to 100-ms exposure time within 300–400 ms. For quantification of coronary calcification, coronary CT angiography, or evaluation of cardiac function, appropriate acquisition protocols are either the "cine mode" or the "flow mode", both of which are characterized by single-slice (C-150/C-300) or dual-slice (e-speed) acquisition using full-resolution detector rings and one target ring. The "cine mode" acquires a single scan with a 50-ms exposure time and at a rate of 17 scans per second for each anatomical level. The "flow mode" acquires a scan with a 50- to 100-ms exposure time at a specific phase of the cardiac cycle at different anatomical levels in subsequent or alternating heart beats. Due to the restriction to non-spiral sequential scanning, a single breath-hold scan of the heart is performed with a 3-mm slice-width using single-slice acquisition (C-150/C-300) and with a 1.5-mm slice-width using dual-slice acquisition. The resulting limited longitudinal resolution is sufficient for quantification of coronary calcification, but it is not adequate for 3D-visualization of the coronary arteries.

EBCT suffers from inherent disadvantages of the measurement principle, which have prevented a more wide-spread use of these systems in cardiology or general radiology. The technical principles have been discussed elsewhere (McCollough 1994a, McCollough 1994b, McCollough 1999). Due to the fourth-generation system geometry, the use of anti-scatter collimator blades on the detector is not possible. As a consequence, image quality is degraded by a large amount of scattered radiation and thus with typical artifacts, e.g., in the form of hypodense zones in the mediastinum. When quantitative evaluations are needed, such as in calcium scoring, any instability of the CT numbers due to scattered radiation, which depends on patient geometry and patient size, is a serious problem. Due to the ring collimator used to shape the beam in the z-direction (Fig. 8.9), the radiation profiles on the detector are "banana-shaped", resulting in a problematic geometric efficiency of the system. The

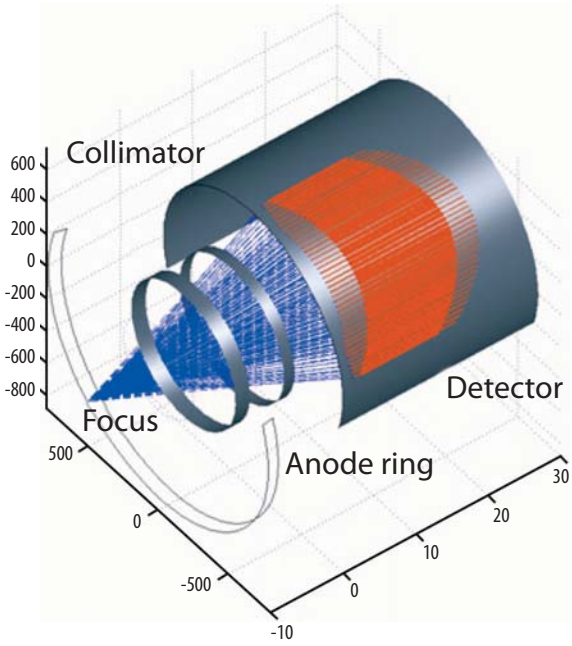

Fig. 8.9. Collimation principle of EBCT. Two collimator rings are used to shape the beam in the z-direction and to control slice width. Since an angular coverage of 210° is required, the anode ring and detector ring overlap and have to be displaced in the z-direction (longitudinal direction). The beam profile on the detector is banana-shaped as a consequence of both the collimation principle and the longitudinal displacement. This is problematic with regard to geometric efficiency and when it comes to introducing multi-row detectors into an EBCT gantry

banana-shaped profiles will be a serious drawback if a true multi-slice detector is to be incorporated into an EBCT system. The clinically most significant shortcoming of EBCT, however, is the fixed and limited electric power of the electron beam in the X-ray gun. The latest EBCT scanners (e-speed) can provide a fixed current of 1000 mA at 130 kV. While the resulting X-ray intensity is sufficient for small patients, it is at the limit for medium-sized patients and clearly inadequate for larger patients.

In summary, despite its inherent advantages in temporal resolution, the EBCT principle is currently not considered to be adequate for more advanced cardiac and general-purpose CT scanners.

8.3 Future Possibilities with Area Detector CT

A promising field of research is the development of area-detector technology and related cone-beam reconstruction techniques that may allow coverage of the entire coronary anatomy in a single heart beat without movement of the table (Ohnesorge 2005, Mori 2006). With area-detector CT scanners, high-resolution imaging of the heart morphology as well as dynamic and functional assessment by repeated scanning of the same scan range may become possible.

The first prototype systems, which use the CsI-aSi flat-panel detectors known from conventional angiography, are currently under evaluation in preclinical research settings. These systems can provide excellent in-plane and through-plane spatial resolution of 0.25 mm with up to 768 slices and up to 18 cm detector z-coverage (Knollmann 2003, Flohr 2005, Nikolaou 2005, Mahnken 2005) (Fig. 8.10). Studies with ex-vivo heart specimens and animal models have shown promising results in the visualization of very small cardiovascular features (Fig. 8.11). However, due to inherent limitations of the CsI-aSi flat-panel detectors and the corresponding read-out electronics, these systems can only be operated at gantry rotation times of 2 s and longer, which is a severe obstacle for in-vivo patient examinations. Moreover, CsI-aSi flat-panel detectors can provide no better low-contrast resolution than about 5–10 HU, which results in limited tissue differentiation compared to state-of-the-art multi-slice CT scanners that readily provide 2–3 HU low contrast resolution.

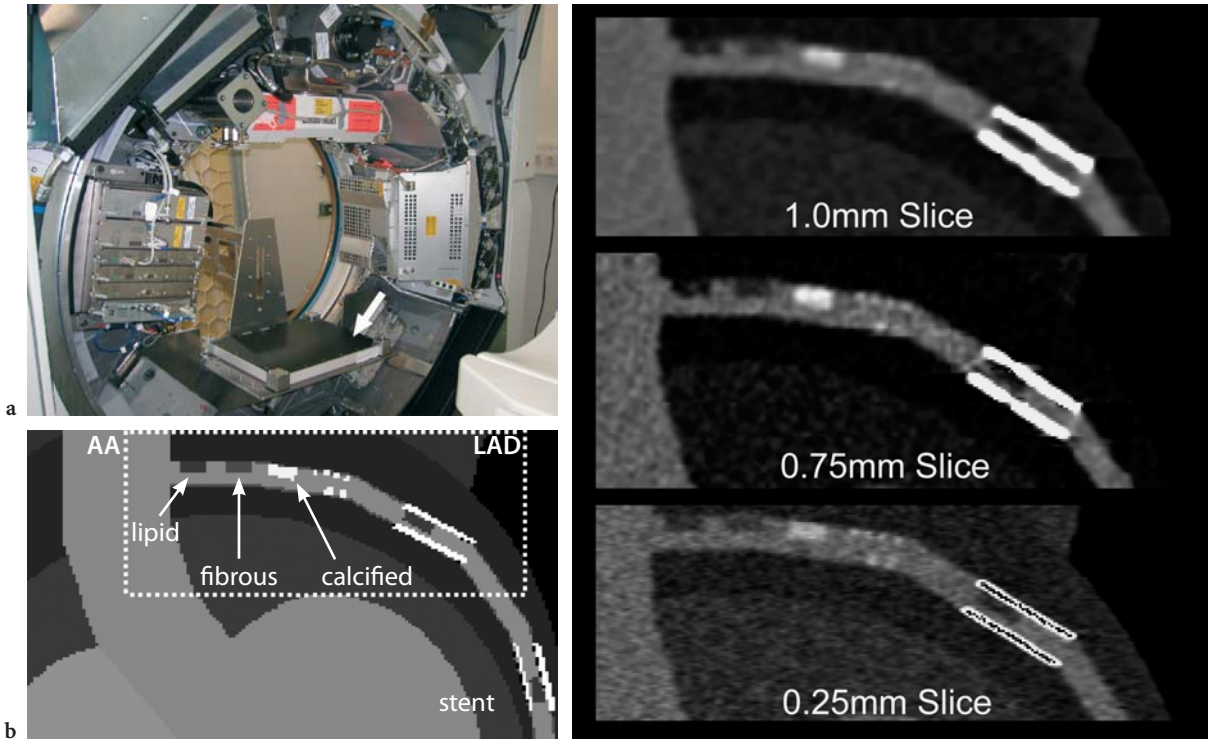

Fig. 8.10a–c. Principle of an area-detector CT prototype using a flat-panel detector with 768 × 0.25-mm slices. The flat-panel detector is mounted in a conventional multi-slice CT gantry system and can provide volume coverage up to 18 cm (**a**). Based on a phantom model of a coronary artery (**b**) substantially increased spatial resolution using the flat-panel CT prototype can be demonstrated (**c**)

Alternative prototype systems with large area-detectors based on conventional CT detector technology are capable of covering a scan range of about 12 cm by simultaneously acquiring 256 slices with 0.5-mm collimated slice width (Fig. 8.12). The first experimental patient studies, in which such prototype systems were used with a shortest gantry rotation time of 0.5 s, demonstrated their potential to visualize the cardiac anatomy and to assess cardiac function (Kondo 2005, Funabashi 2005a, Funabashi 2005b). Although the entire heart can be scanned within a single heart beat, image quality is inferior compared to today's 64-slice CT scanners due to limited temporal resolution and low-contrast resolution.

Initial experience has thus shown that today's area-detector CT prototypes are still too limited in temporal resolution and low-contrast resolution for regular in-vivo use. The high radiation dose that would be needed to provide adequate signal-to-noise ratio at 0.25-mm isotropic resolution, as is achieved with flat-panel CT systems, is problematic for human subjects in a clinical setting. Moreover, the huge scan data rates represent a challenge for currently available image reconstruction systems. Area-detector CT systems might become available for cardiac CT in 3–5 years. Until then, major technical challenges will have to be solved in order to increase temporal resolution, lower radiation dose, and reduce image reconstruction times.

8.4 New Frontiers with Dual-Source CT

A temporal resolution of < 100 ms at all heart rates is desirable to achieve full diagnostic quality in

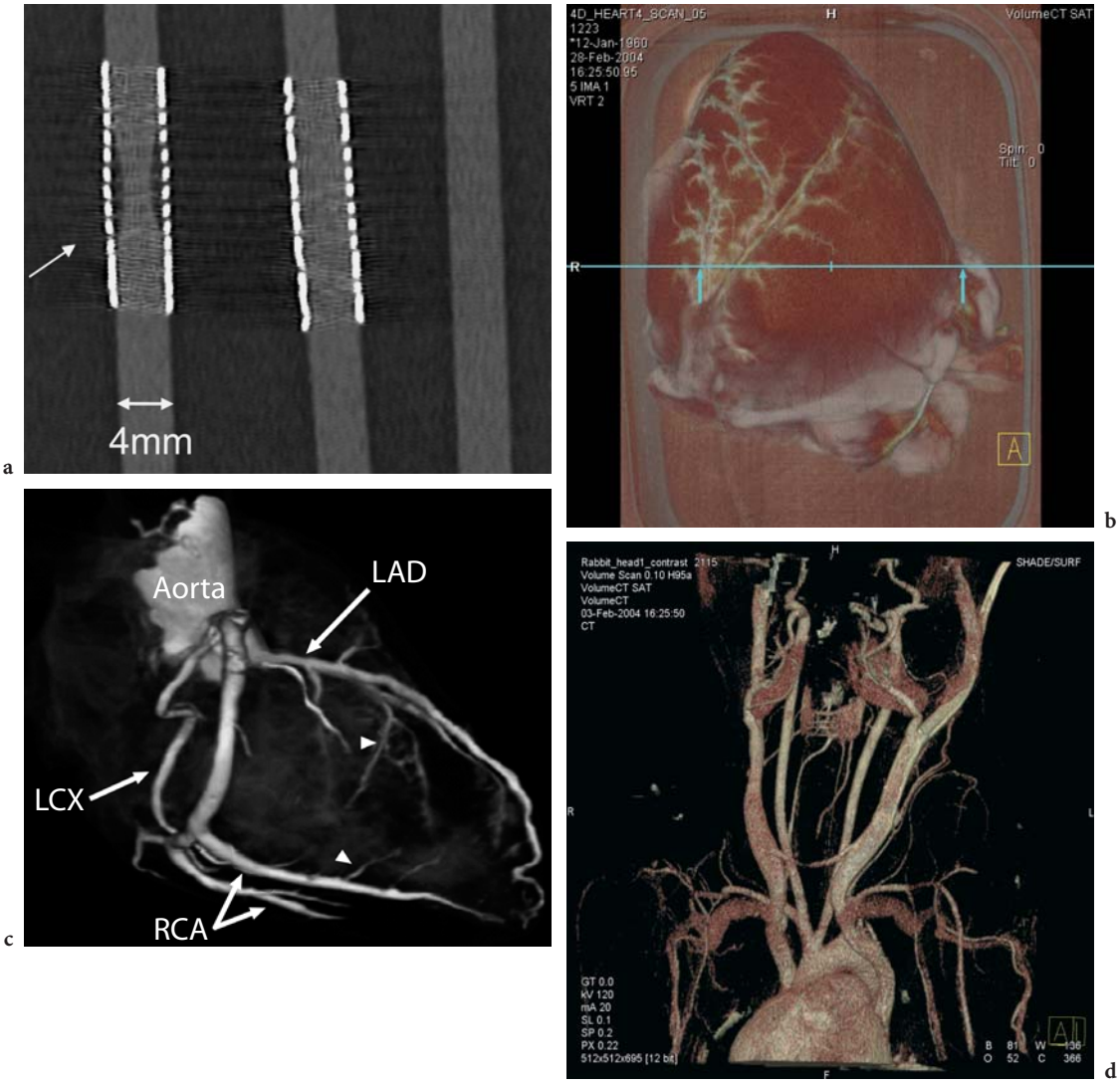

Fig. 8.11a–d. Preliminary results of an area-detector CT prototype using a flat-panel detector with 768 × 0.25-mm slices and a fastest rotation time of 2 s. The very high spatial resolution enables accurate assessment of the in-stent lumen in a coronary artery phantom (**a**). Very small coronary artery segments can be visualized in ex-vivo studies of contrast-enhanced heart specimen of a pig (**b**) and a human (**c**). Experimental in-vivo studies of vessels are feasible using animal models, as demonstrated in a CT angiography examination of the carotid arteries in a live rabbit (**d**). (Data courtesy of MGH Boston, USA)

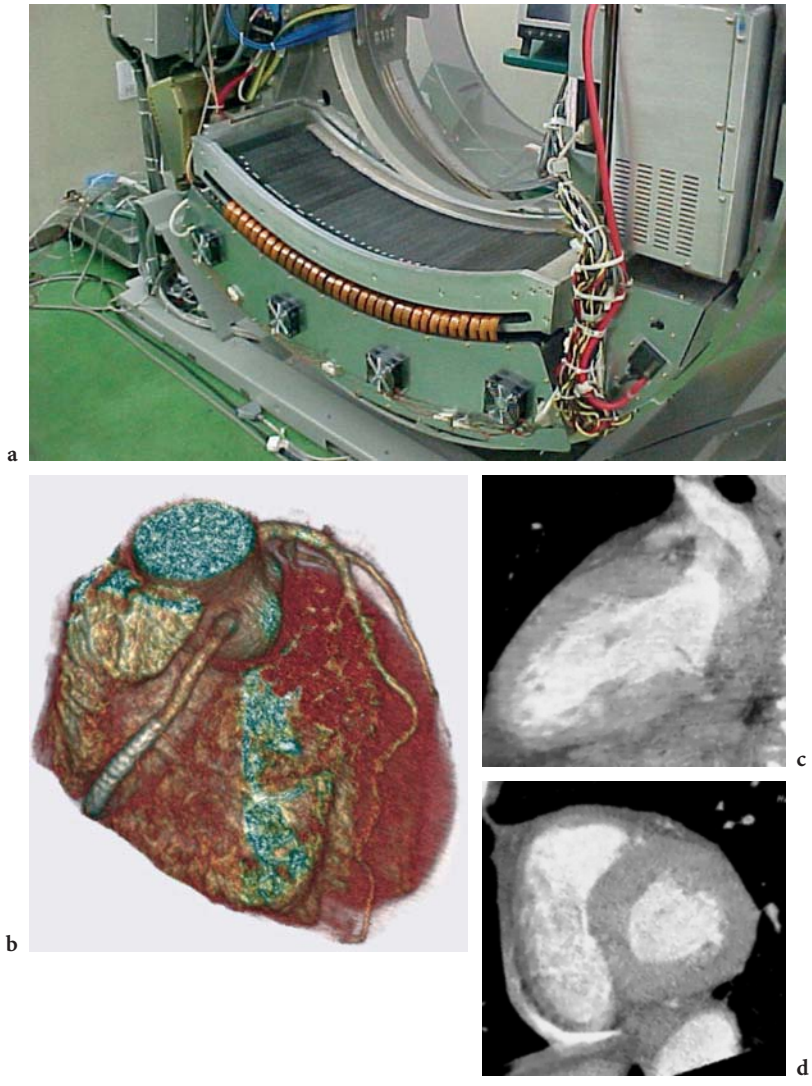

Fig. 8.12a–d. The principle of area-detector CT and preliminary, experimental, in-vivo patient results using a prototype with 256 × 0.5-mm slices and 0.5-s rotation time. **a** The area-detector prototype is mounted in a conventional multi-slice CT gantry system and provides volume coverage up to 12 cm. **b** A 4-dimensional data set of the heart and coronary arteries can be acquired from scans with one single rotation without table-feed. MPR display of the same data set allows for reconstruction of the left ventricle in the long (**c**) and short (**d**) axes. (Data courtesy of Ehime University, Japan)

cardiac CT examinations of patients with high and irregular heart rates and to completely eliminate the need to control heart rate. An alternative concept to improve temporal resolution for cardiac CT while maintaining the good general imaging capabilities of a modern multi-slice CT system is a scanner design with multiple X-ray sources and detectors, which was already described during the early days of CT (Robb 1979, Ritman 1980).

Recently, a new dual-source CT scanner generation has been introduced that will provide substantially improved scan speed and temporal resolution for CT scans of the heart compared to the most recent 64-slice CT scanners (Flohr 2006). In the following, we introduce the system concept of this new dual-source CT scanner and derive its consequences and potential benefits for ECG-gated cardiac CT applications (Flohr 2006, Bruder 2006). Also, preliminary results of the evaluation of temporal resolution, spatial resolution, and radiation exposure are presented (Flohr 2006, McCollough 2006) as well as the results of the first clinical patient examinations (Flohr 2006, Achenbach 2006, Johnson 2006).

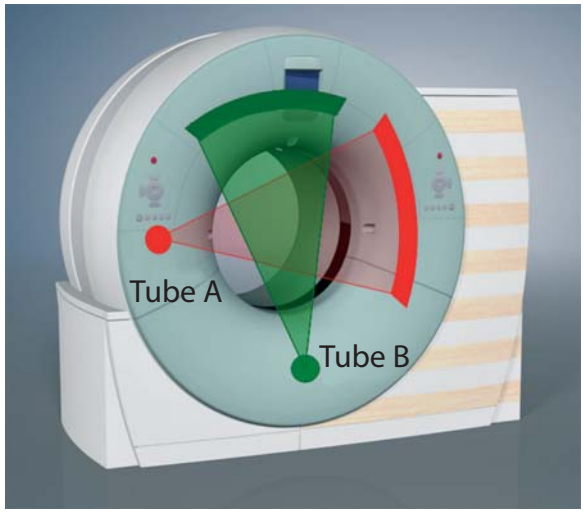

Fig. 8.13. A dual-source CT system with two tubes and two corresponding detectors offset by 90° (SOMATOM Definition, Siemens, Forchheim, Germany). A scanner of this type provides temporal resolution roughly equivalent to a quarter of the rotation time, independent of the patient's heart rate

8.4.1 Dual-Source CT: System Concept and Design

A dual-source CT system is equipped with two X-ray tubes and two corresponding detectors. The two acquisition systems are mounted on the rotating gantry with an angular offset of 90° (Fig. 8.13). One detector (A) covers the entire scan field of view (50 cm in diameter). The other detector (B) is restricted to a smaller, central field of view (26 cm in diameter) in order to maintain a compact system geometry with a short distance between the focal spot and the detector (Fig. 8.14). Each detector comprises 40 detector rows, the 32 central rows having a 0.6-mm collimated slice width and the four outer rows on both sides having a 1.2-mm collimated slice width. The total coverage in the longitudinal direction (z-direction) of each detector is 28.8 mm at isocenter. By proper combination of the signals of the individual detector rows, detector configurations of 32 × 0.6 mm or 24 × 1.2 mm can be realized. Using the z-flying focal spot technique introduced with 64-slice CT (Flohr 2004, Flohr 2005), two subse-

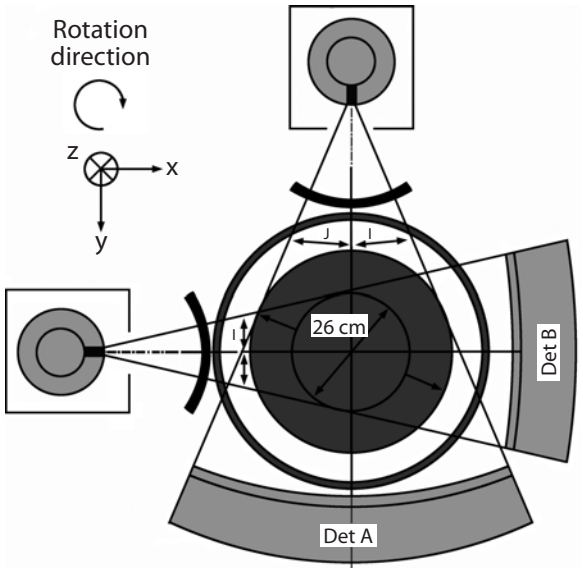

Fig. 8.14. Technical realization of a dual-source CT system (SOMATOM Definition, Siemens, Forchheim, Germany). One detector covers the entire scan field of view with a diameter of 50 cm, whereas the other detector is restricted to a smaller, central field of view with a diameter of 26 cm

quent 32-slice readings with 0.6-mm collimated slice width are combined to yield one 64-slice projection with a sampling distance of 0.3 mm at iso-center. In this way, each detector acquires 64 overlapping 0.6-mm slices per rotation. The shortest gantry rotation time is 0.33 s; other gantry rotation times are 0.5 and 1.0 s. Each of the two compact rotating-envelope X-ray tubes (Schardt 2004) allows up to 80 kW peak power from the two on-board generators. The tubes can be operated independently with regard to their kV and mA settings. The independent kV setting of 80, 100, 120, and 140 kV allows the acquisition of dual-energy data, e.g., with one tube being operated at 80 kV while the other is operated at 140 kV.

8.4.2 Dual-Source CT: Cardiac Scanning Principles and Techniques

The foremost benefit of dual-source CT for cardiac scanning is the improved temporal resolution. The temporal resolution of a multi-slice CT scanner with a single source is equivalent to half the gantry rotation time using single-segment half-scan image reconstruction. A dual-source CT scanner provides temporal resolution of approximately a quarter of the gantry rotation time, independent of the patient's heart rate and without the need for multi-segment reconstruction techniques.

In a dual-source CT scanner, a complete data set of 180° of parallel-beam projections can be generated from two 90° data sets ("quarter-scan segments") that are simultaneously acquired by the two independent measurement systems, which are offset by 90°. As both quarter-scan segments are acquired simultaneously within a quarter of a rotation, the total acquisition time and temporal resolution of the resulting half-scan data set are a quarter of the rotation time (Fig. 8.15). The two quarter-scan segments are appended with a smooth transition function to avoid streaking or other artifacts from potential discontinuities at the respective start- and end-projections. The use of a transition function with a transition angle of 30° does not affect temporal resolution. Since the second detector does not cover the entire scan field of view, its projections are truncated in objects that extend beyond the 26-cm field of view and have to be extrapolated by using data acquired with the first detector at the same projection angle

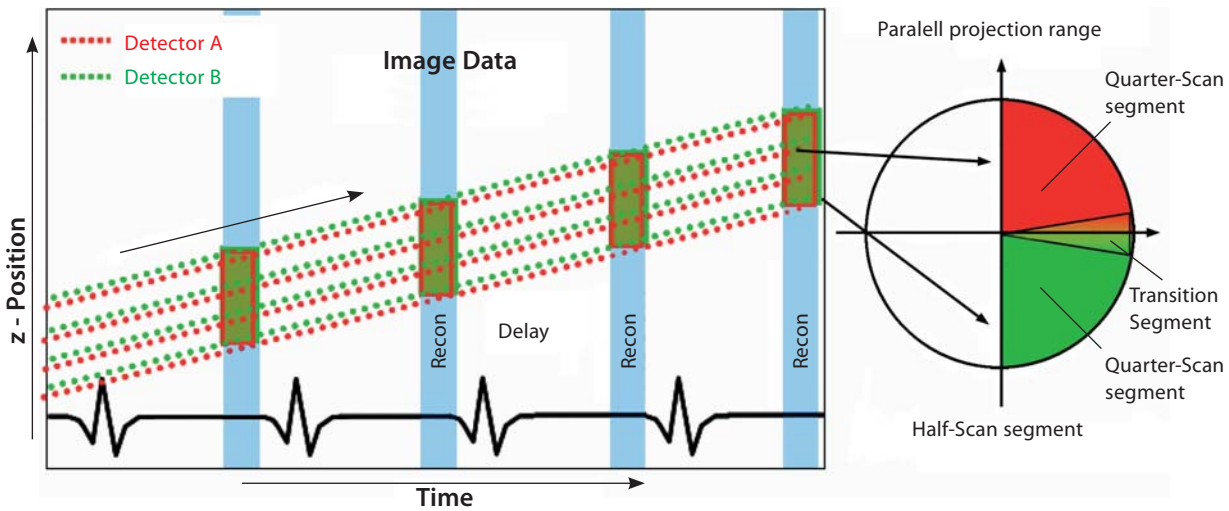

Fig. 8.15. Principle of ECG-gated spiral image reconstruction for a dual-source CT system. The positions of the detector slices of both measurement systems relative to the patient are indicated as a function of time. The patient's ECG signal is schematically indicated on the bottom. To simplify the drawing, only four detector slices are shown. Due to the 90° angle between both detectors, the 180° parallel projection data set can be split up into two 90° quarter-scan data sets. These are simultaneously acquired by the two acquisition systems in the same relative phase of the patient's cardiac cycle and at the same anatomical level

(i.e., a quarter rotation earlier). With this approach, constant temporal resolution equivalent to a quarter of the gantry rotation time $T_{rot}/4$ is achieved in a centered region of the scan field of view that is covered by both acquisition systems. For T_{rot} = 0.33 s, the temporal resolution is therefore 83 ms, independent of the patient's heart rate and with data used from one cardiac cycle only (Fig. 8.16). Thus, the basic mode of operation of a dual-source CT system corresponds to single-segment reconstruction. This is a major difference to conventional multi-slice CT systems, which can theoretically provide similar temporal resolution by means of multi-segment reconstruction approaches (Kachelriess 2000, Flohr 2001). With multi-segment reconstruction, however, temporal resolution strongly depends on the heart rate, and a stable and predictable heart rate and complete periodicity of the heart motion are required for adequate performance. Therefore, optimal temporal resolution can only be achieved at few heart rates, when the patient's heart beat and the gantry rotation of the scanner are properly de-synchronized (Fig. 8.16).

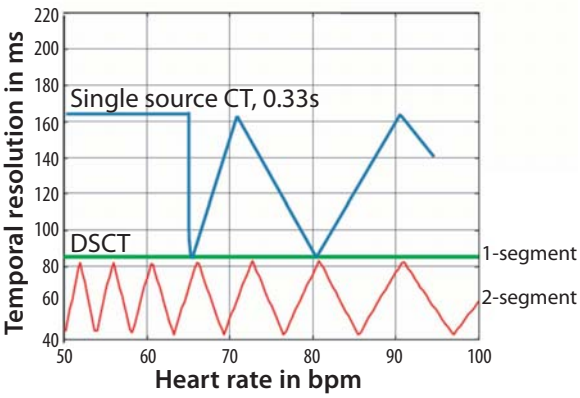

Fig. 8.16. Temporal resolution as a function of the patient's heart rate for a conventional multi-slice CT system with 0.33-s gantry rotation time, and for a dual-source CT scanner with 0.33-s gantry rotation time. While multi-slice CT reaches 83-ms temporal resolution only at the determined heart rates of 66, 81, and 104 bpm, dual-source CT provides 83-ms temporal resolution at all heart rates. Using 2-segment reconstruction with dual-source CT, temporal resolution varies as a function of the patient's heart rate, and a maximum temporal resolution of 42 ms and a mean temporal resolution of about 60 ms can be established for advanced functional evaluations

Nevertheless, multi-segment approaches can also be applied to dual-source CT to improve temporal resolution even further. In a two-segment reconstruction, the quarter-scan segments acquired by each of the two detectors are independently divided into smaller subsegments acquired in subsequent cardiac cycles of the patient – similar to two-segment reconstruction in conventional multi-slice CT (Fig. 8.16). Using a multi-segment approach, temporal resolution again varies as a function of the patient's heart rate, and a best temporal resolution of 42 ms can be established at certain heart rates based on a rotation time of 0.33 s. As temporal resolution varies strongly even for small changes in heart rate, it seems appropriate to define a mean temporal resolution of 60 ms. While the use of multi-segment reconstruction is not recommended for examinations of the coronary arteries, it may be beneficial for advanced evaluation of cardiac function, such as detection of wall motion abnormalities or determination of peak ejection fraction. For examinations of the coronary arteries and the assessment of global cardiac functional parameters, the single-segment mode should provide sufficient temporal resolution at clinically relevant heart rates.

It was shown in Chapter 5 that the patient's heart rate determines the maximum spiral pitch that can be used for gap-less coverage of the heart (Flohr 2001) and that the number of segments S used for multi-segment reconstruction demands a further reduction of the spiral pitch (Fig. 8.17):

$$pitch \leq \frac{1}{N}\left(\frac{N-1}{S}+1\right)\frac{T_{rot}}{T_{RR}} \qquad (8.1)$$

where N represents the number of simultaneously acquired detector rows, T_{rot} is the gantry rotation time, and T_{RR} the patient's heart cycle time. Since multi-segment reconstruction will usually not be required for cardiac CT examinations with dual-source CT (that means, S = 1 at all heart rates in Eq. 8.1), the pitch and thus the table-feed can be efficiently adapted to the patient's heart rate and significantly increased at elevated heart rates (Flohr 2006). Assuming a confidence interval of 10 bpm that the heart rate of the patient is allowed to drop during examination, the following pitch and table-feed settings may be used for the evaluated dual-source CT system with N = 32 and T_{rot} = 0.33 s (Table 8.1).

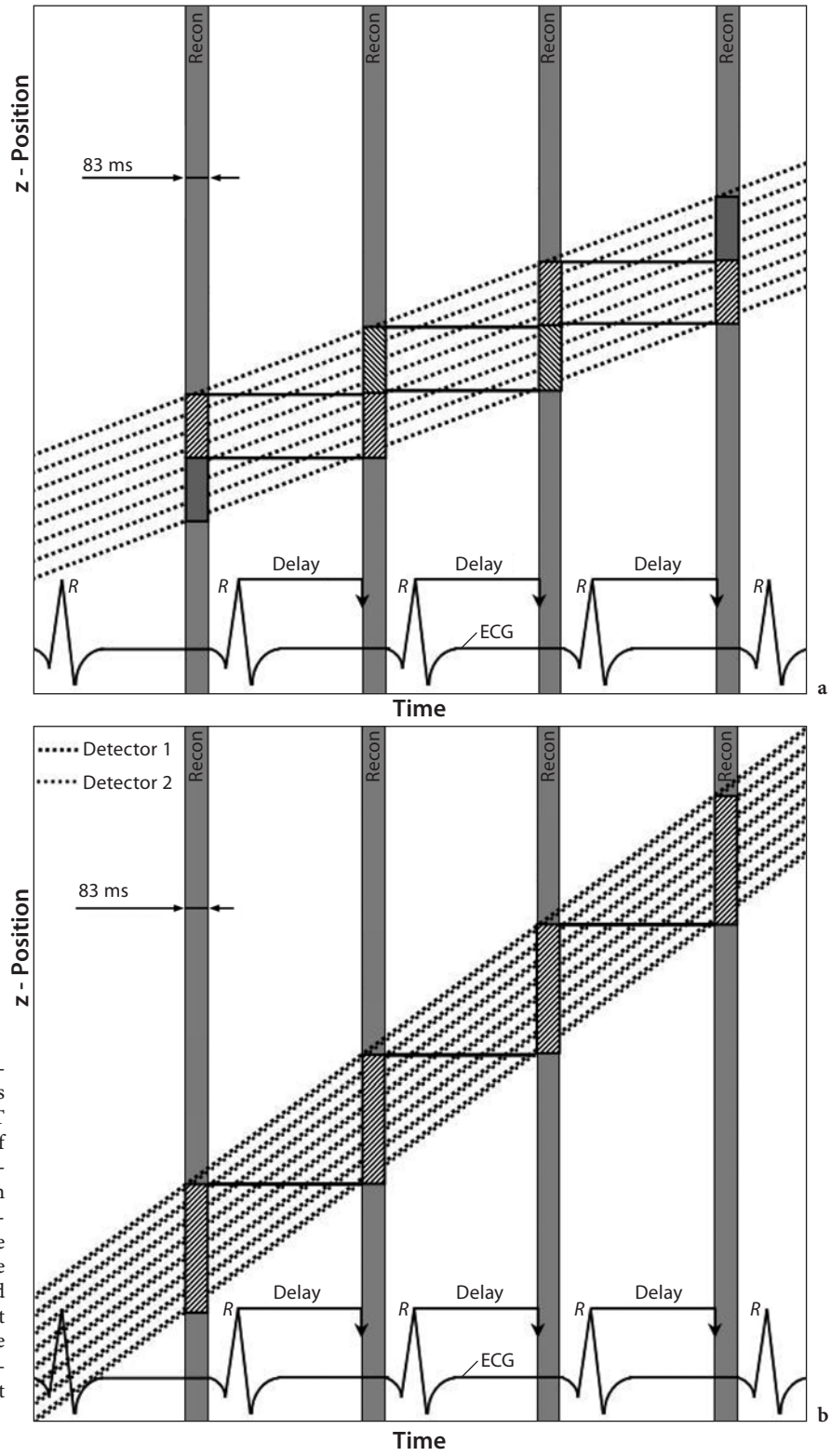

Fig. 8.17a,b. An ECG-gated spiral scan for high heart rates (> 65 bpm) with a multi-slice CT and b dual-source CT. The slope of the dotted lines (detector trajectories) is proportional to the pitch and is limited by the need for continuous volume coverage of the heart. Note the significant slope (pitch) difference due to the need to use 2-segment reconstruction at higher heart rates with multi-slice CT vs. the ability to use single-segment reconstruction at high heart rates with dual-source CT

Table 8.1. Heart-rate-dependent pitch and table-feed settings for the evaluated dual-source CT. The heart rate in brackets represents the minimum heart rate after subtraction of the confidence interval of 10 bpm

Heart rate (bpm)	Pitch	Table feed (mm/s)
55 (45)	0.20	11.6
70 (60)	0.27	15.4
80 (70)	0.36	21.0
90 (80)	0.46	26.8

The heart rate of the patient can be monitored before the examination so that the lowest heart rate can be determined. Evaluation of a variety of ECG signals has demonstrated that an additional confidence interval of 10 bpm should be subtracted before automatic adjustment of the pitch and the table-feed for the scan. The confidence interval of 10 bpm is already included in the values shown in Table 8.1. With the given pitch values, it becomes obvious that dual-source CT can provide faster volume coverage for comparable detector coverage than the latest 64-slice CT scanners, which usually employ pitch values between 0.20 and 0.26 (Sect. 6.2). Typical breath-hold times for ECG-gated spiral scans of the heart with dual-source CT are between 10 s for low heart rates and 5 s for high heart rates, assuming a scan range of 12 cm to cover the heart.

The increased pitch at higher heart rates not only reduces the examination time, but also the radiation dose to the patient (McCollough 2006). With single-source CT, the pitch cannot be increased at higher heart rates, because multi-segment reconstruction must be used to improve temporal resolution. This is not necessary for dual-source CT. An additional important technique to reduce patient dose is an intelligent ECG-controlled dose modulation that reacts to ectopic beats and variations in heart rate (Sect. 5.6.3). Due to the significantly higher temporal resolution of dual-source CT, the duration of full dose exposure during the cardiac cycle can be reduced compared to multi-slice CT; subsequently, the radiation exposure for the entire examination is also reduced (McCollough 2006) (Fig. 8.18).

8.4.3 Dual-Source CT: System Performance Evaluation

Temporal resolution during ECG-gated spiral scanning can be evaluated with a moving coronary-artery phantom to compare the performance of dual-source CT with a state-of-the-art 64-slice single-source CT scanner. The phantom consists of three contrast-filled Lucite tubes with a lumen of 4 mm. Coronary artery stents are inserted in two of the tubes. One of the stents contains an artificial 50% stenosis within the stent. The tubes are immersed in a water bath and moved in a periodic manner by a computer-controlled robot arm at an angle of 45° relative to the scan plane to simulate heart motion (Fig. 8.19). Motion patterns of moving

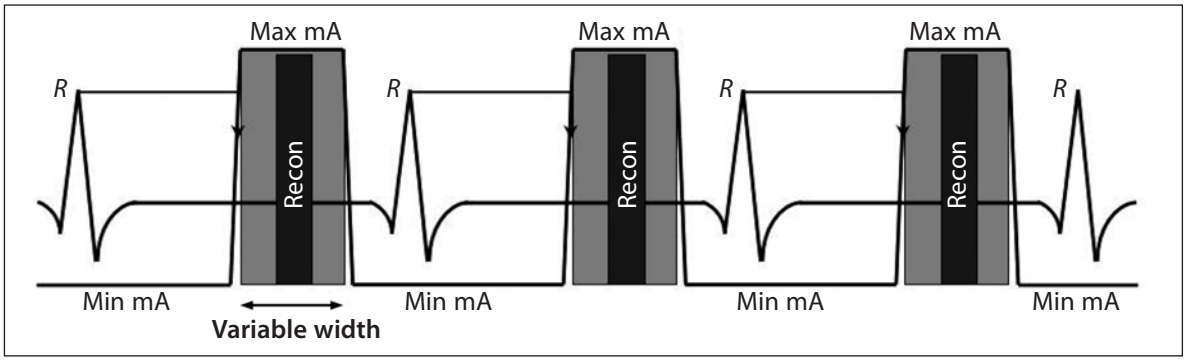

Fig. 8.18. ECG modulation of the tube current for a dual-source CT system. The width of the temporal window having the maximum tube current can be selected by the user, while the temporal width of the image reconstruction window is 83 ms. For full-quality images for coronary artery CT angiography, the reconstruction window should fall within the maximum mA window. Due to the higher temporal resolution independent of heart rate, this maximum mA window can be shorter than in multi-slice CT, thus lowering the patient's radiation dose during the examination

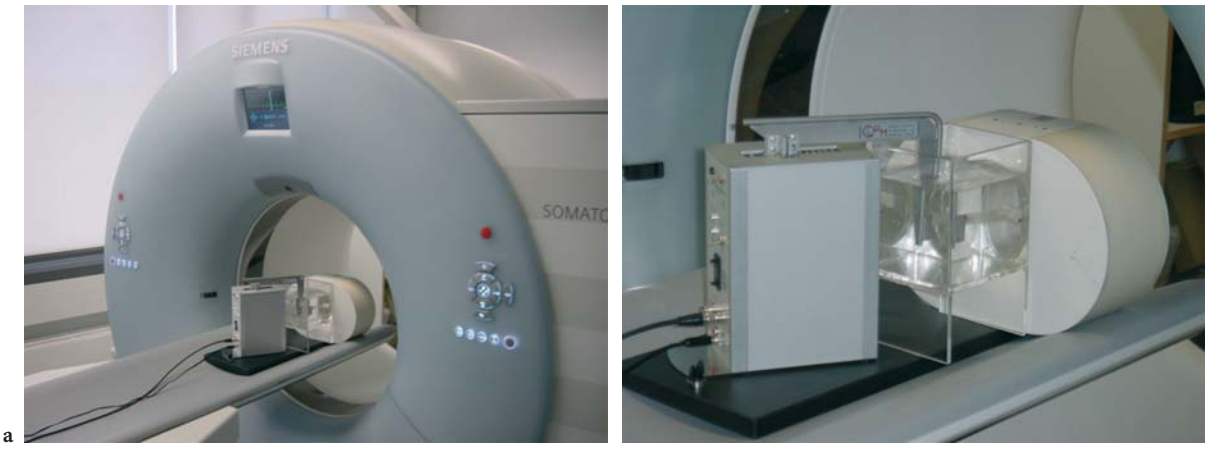

Fig. 8.19a,b. Computer-controlled robot arm that moves contrast-filled tubes ("coronary arteries") in a water tank. **a** Phantom set-up placed on the scanner table; **b** close-up of the phantom setup. The motion amplitudes and velocities of the robot arm can be adjusted to provide a realistic motion pattern of the coronary arteries

coronary arteries are implemented for heart rates of 70 and 90 bpm (Fig. 8.20). The motion amplitudes and velocities of the robot arm are based on published values for coronary artery motion (Achenbach 2000). Using dual-source CT with 83-ms temporal resolution, motion artifacts are considerably reduced compared to 64-slice single-source CT with 0.33-s rotation time (Fig. 8.21, 8.22). A computer-generated phantom model to simulate the motion of the cardiac chambers during the cardiac cycle with realistic motion patterns demonstrates the ability of dual-source CT to provide motion-free images also during the systolic phase of the cardiac cycle (Fig. 8.23).

To determine slice sensitivity profiles (SSPs) for ECG-gated spiral scanning with the dual-source CT system, a thin gold plate (40-µm thickness) embedded in a Lucite cylinder can be used. The gold plate is placed close to the iso-center of the scanner and highly overlapping images with an increment of 0.1 mm are reconstructed for the desired nominal slice widths. For each of the overlapping images, the mean CT value in a small region of interest within the gold plate is determined and the background CT value of the Lucite cylinder is subtracted. The maximum of these corrected mean values (with the gold plate fully in the reconstructed slice) was normalized to the value 1. The normalized mean values, plotted as a function of the z-positions of the

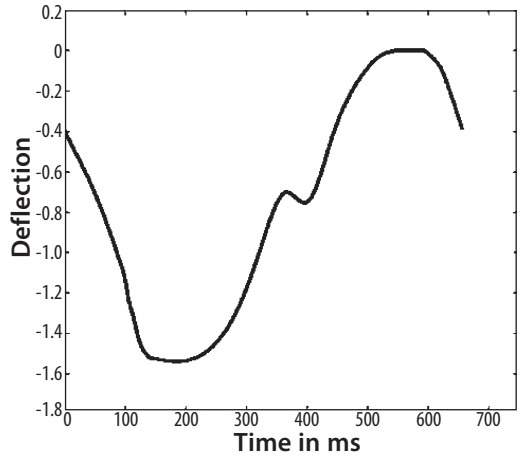

Fig. 8.20. Example of a motion curve for the computer-controlled robot arm, simulating a heart rate of 90 bpm. The motion pattern of a right coronary artery based on values given in the literature (Achenbach 2000) is shown

respective image slices, represent the measured SSP. The full-width at half maximum (FWHM) of this SSP is the measured slice width. Using an artificial ECG signal with 70 bpm, overlapping images with 0.6-, 0.75-, 1.0, 1.5-, and 2-mm nominal slice width and 0.1-mm increment are reconstructed. The SSPs are symmetrical bell-shaped curves without the far-reaching tails that would degrade longitudinal reso-

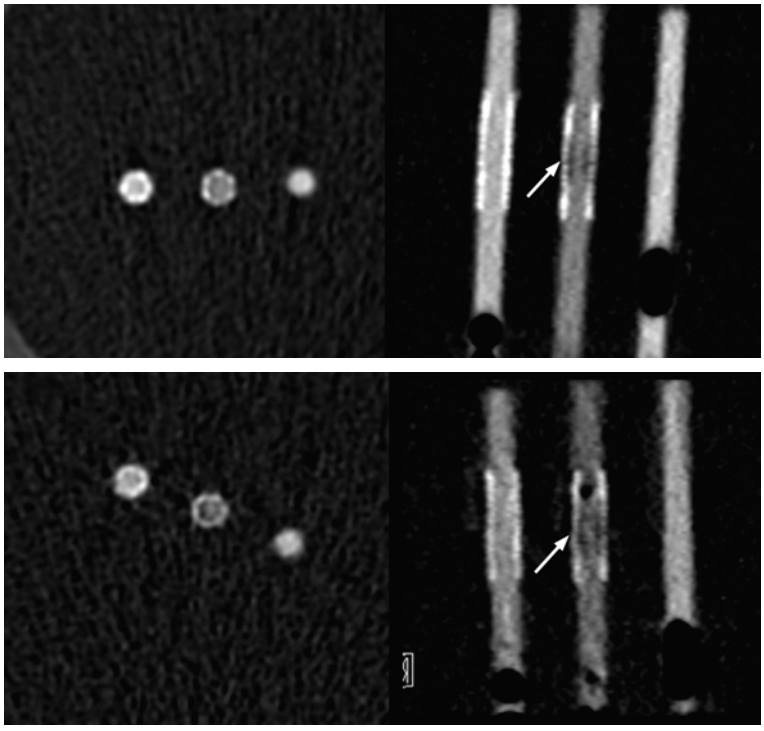

Fig. 8.21a,b. Axial slices and MPRs of the moving coronary-artery phantom at 70 bpm for the evaluated dual-source CT system (**a**) and for a comparable 64-slice single source CT system (**b**), both using 0.33-s gantry rotation time. The temporal resolution of the dual-source CT is 83 ms, while that of the 64-slice CT is 140 ms using 2-segment reconstruction at 70 bpm. **a** The in-stent stenosis (*arrow*) can be clearly delinated with the dual-source CT acquisition. **b** By contrast, despite the high temporal resolution provided by 2-segment reconstruction, the in-stent stenosis is blurred and overestimated with 64-slice CT acquisition

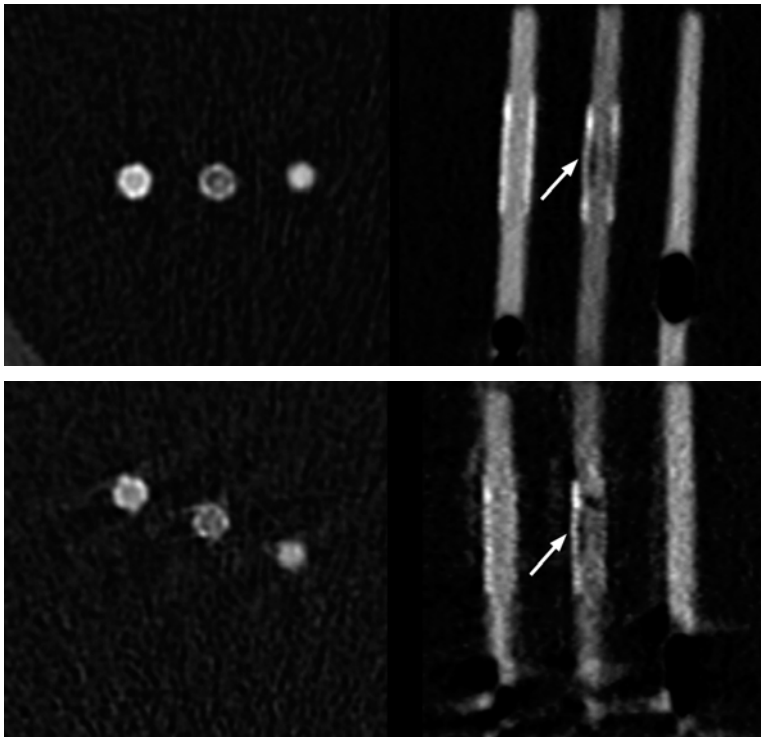

Fig. 8.22a,b. Axial slices and MPRs of the moving coronary-artery phantom at 90 bpm for the evaluated dual-source CT system (**a**) and for a comparable 64-slice single source CT system (**b**), both using 0.33-s gantry rotation time. The temporal resolution of the dual-source CT is 83 ms, while that of the 64-slice CT is 160 ms using 2-segment reconstruction at 90 bpm. **a** Despite the rapid movement of the coronary artery, the in-stent stenosis (*arrow*) can be clearly delineated with the dual-source CT acquisition. **b** Significant motion artifacts are present in the 64-slice CT acquisition and the in-stent stenosis is blurred and cannot be evaluated

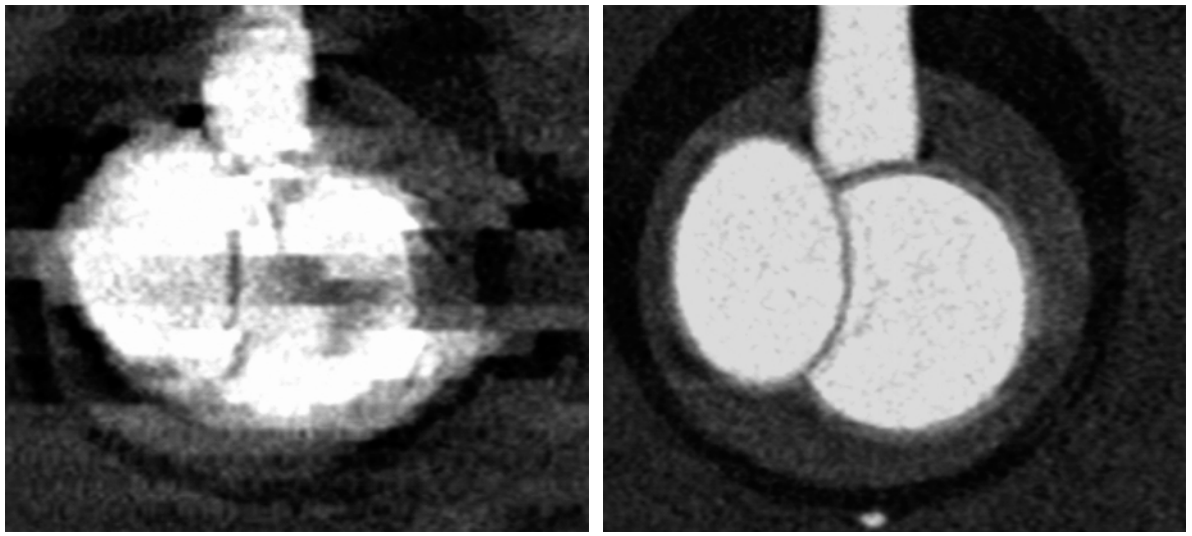

a b

Fig. 8.23a,b. MPRs of a moving heart phantom simulating the motion of the cardiac chambers at a heart rate of 75 bpm. Image data were generated for a conventional 64-slice single-source CT scanner and for a dual-source CT scanner, both using 0.33-s rotation time. Images were reconstructed during end-systole using single-segment reconstruction. a Due to the insufficient temporal resolution (165 ms) of the single-source CT scanner for a systolic reconstruction, image quality is severely degraded by step and band artifacts. b The temporal resolution of 83 ms of the dual-source CT scanner, however, is sufficient for adequate visualization of the heart in systole

lution. The measured FWHMs are 0.7, 0.83, 1.05, 1.5, and 2.05 mm, respectively, which is in good agreement with the nominal values (Fig. 8.24).

To investigate the maximum achievable longitudinal resolution of the dual-source CT system for ECG-gated spiral scanning, a z-resolution phantom can be used. This phantom consists of a Lucite plate with rows of cylindrical holes with diameters between 0.4 and 3 mm that are aligned in the z-direction. An artificial ECG signal is used for ECG-gated reconstruction of the non-moving object at virtual heart rates of 70 and 90 bpm. The spiral pitch of the scan is selected according to the virtual heart rate (pitch 0.32 for 70 bpm and pitch 0.43 for 90 bpm). Images are reconstructed with a 0.6-mm nominal slice width and 0.1-mm image increment. Multi-planar reconstruction (MPR) display in the z-direction is then used to determine the minimum diameter of the cylinders that can be resolved and to evaluate potential geometrical distortions. Dual-source CT with 0.6-mm slice width can resolve all cylinders down to 0.4 mm diameter for both heart rates, and the MPRs are free of geometric distor-

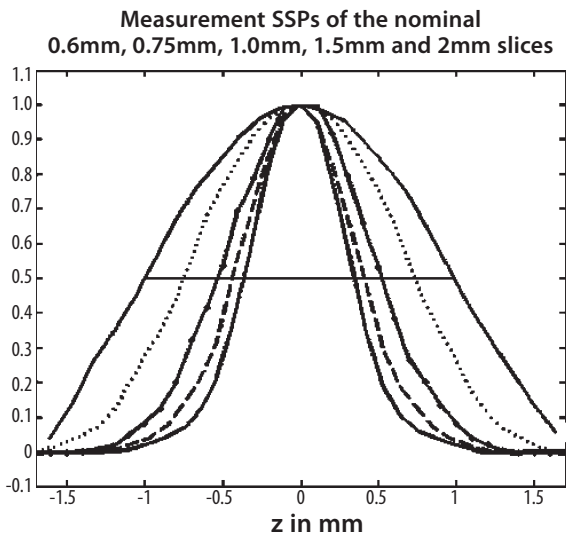

Fig. 8.24. Measured slice sensitivity profiles (SSPs) at iso-center of the nominal 0.6-, 0.75-, 1.0-, 1.5-, and 2.0-mm slices for the ECG-gated spiral scan mode of the evaluated dual-source CT system. The SSPs are well-defined and the measured full widths at half maximum (FWHMs) are 0.7, 0.83, 1.05, 1.5, and 2.05 mm

tions, thus proving the spatial integrity of the 3D image (Fig. 8.25). Heart-rate-independent spatial resolution is an important requirement for clinically reliable cardiac CT angiography. Using the thinnest slice width and sharp reconstruction filter kernels, up to 0.4 mm in-plane and 0.4 mm through-plane resolution can be achieved with dual-source CT in clinical routine with ECG-gated spiral scan modes.

Radiation exposure for retrospectively ECG-gated imaging of the heart can be measured using a standard CTDI body phantom to assess the $CTDI_w$ value in units of mGy. Widely available and validated software tools can then be used to translate the $CTDI_w$ values into effective organ dose in mSv (e.g., WinDose, Scanditronix, Germany). Dual-source CT uses double the X-ray power per time compared to single-source CT scanners. The restriction to single-segment reconstruction enables the pitch to be increased for scans at higher heart rates. This translates into dose reduction, as the radiation exposure is inversely proportional to the pitch in ECG-gated spiral CT scan protocols (Fig. 8.26). As a consequence of the substantially improved temporal resolution with dual-source CT, the interval of full exposure during the cardiac cycle in scans with ECG-controlled dose modulation can be reduced from around 400 ms with 64-slice single-source CT to about 200 ms with dual-source CT. As the ratio of the lengths of full-dose and low-dose intervals within the cardiac cycle is lower, the relative reduction of radiation exposure by ECG-controlled dose modulation is higher with dual-source CT (Fig. 8.26). Combining these dose reduction features (pitch adaptation and effective ECG pulsing) with an optimized beam pre-filtration that reduces the exposure in the periphery of the scan field of view (so-called cardiac-bowtie filter), radiation exposure in dual-source CT can be reduced by up to a factor of two compared to the latest 64-slice single-source CT scanners, while maintaining the same signal-to-noise ratio and spatial resolution (McCollough 2006). Deviating from single-source CT, radiation exposure decreases with increasing heart rate in dual-source CT due to the increased pitch at higher heart rates.

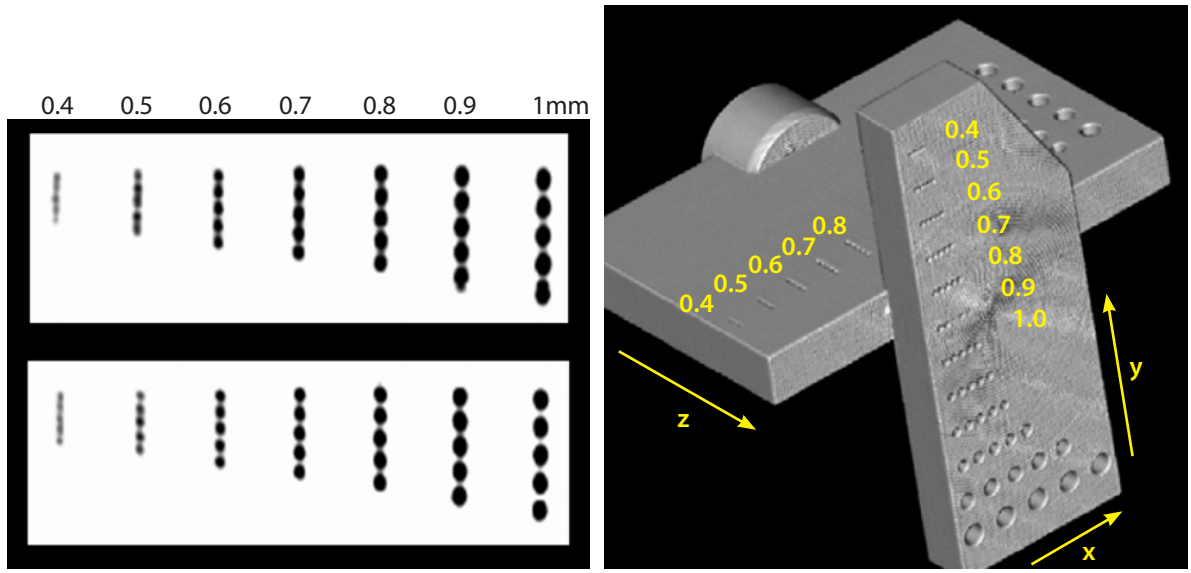

a b

Fig. 8.25a,b. Reconstruction of a resolution phantom (Lucite plate with cylindrical holes) in the iso-center of the evaluated dual-source CT scanner. The phantom was scanned using ECG-gated spiral mode and reconstructed with 0.6-mm slice-width, 0.1-mm image increment, and medium-sharp image reconstruction kernel. ECG-gated reconstruction was performed using artificial ECG signals with 70 and 90 bpm. **a** MPR in the z-direction shows that all cylinders down to 0.4 mm diameter can be resolved for heart rates of 70 bpm (top) and 90 bpm (bottom), and no significant geometrical distortions are visible. **b** 3D reconstruction of two resolution phantoms mounted perpendicular to each other demonstrates that all cylinders down to 0.4 mm in size can be resolved in both the x/y-direction and the z-direction, thus providing 0.4-mm isotropic resolution

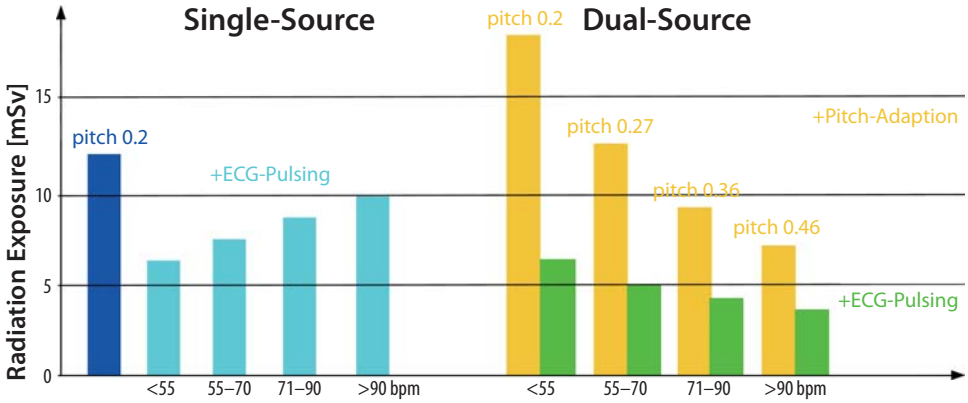

Fig. 8.26. Estimation of radiation exposure in male patients in relation to heart rate. Patients were examined by 64-slice single-source CT and dual-source CT using ECG-gated spiral scan protocols for cardiac CT angiography. In single-source CT (left), the spiral pitch is fixed for all heart rates and radiation exposure can be reduced by using ECG-controlled dose modulation with a temporal window of 400 ms of maximum exposure during the cardiac cycle. Radiation exposure increases with increasing heart rate, from about 6–7 mSv for a low heart rate of 55 bpm to about 9–10 mSv for a higher heart rate of 90 bpm. In dual-source CT (right), the temporal window of maximum exposure during the cardiac cycle for ECG-controlled dose modulation is reduced to 200 ms. In addition, the pitch is increased for increasing heart rate and radiation exposure decreases from 6–7 mSv for a low heart rate of 55 bpm to about 4 mSv for a higher heart rate of 90 bpm

8.4.4 Dual-Source CT: Clinical Scan Protocols and Preliminary Clinical Results

Cardiac CT examinations were used to assess the performance of dual-source CT in clinical practice. A series of consecutive patients who did not receive β-blocker medication to lower their heart rates prior to the examination were referred to coronary CT angiography with dual-source CT. All patients were scanned in the craniocaudal direction with 0.33-s rotation time, 0.6-mm collimation with z-flying focal spot for each detector, 120 kV, 550 mA for each X-ray tube, and a pitch between 0.27 and 0.36, depending on the patients' heart rate. In most cases, ECG-controlled dose modulation was used. ECG-gated reconstruction was carried out in diastole and systole with single-segment reconstruction, thus providing a temporal resolution of 83 ms independent of the heart rate. The patients received 80–100 ml contrast agent (300–400 mg Iodine per ml) at a flow rate of 4–5 ml/s, followed by a 50-ml saline bolus at the same flow rate.

These initial studies demonstrated that diagnostic image quality can be achieved in coronary CT angiography examinations in all patients irrespective of heart rate (Achenbach 2006, Johnson 2006). A substantial improvement of image quality compared to that obtained with the latest 64-slice CT scan acquisition can be demonstrated in patients with heart rates up to 100 bpm (Fig. 8.27). Cardiac images can be reconstructed free of motion artifacts in both diastole and systole (Fig. 8.28). Preliminary clinical experience indicates that robust image quality may also be achieved in patients with irregular heart rate during the scan (Figs. 8.29, 8.30). Diagnostic accuracy may also be improved in patients with low and normal heart rates due to the complete elimination of cardiac motion (Figs. 8.31–8.34). The high temporal resolution of dual-source CT enables global and regional cardiac function analysis, including myocardial wall motion and valve function (Fig. 8.35). In patients with higher heart rates, the spiral pitch can be increased, thus reducing radiation exposure and breath-hold time (Fig. 8.36).

Dual-source CT can also be used for general-purpose CT imaging by taking advantage of the high-

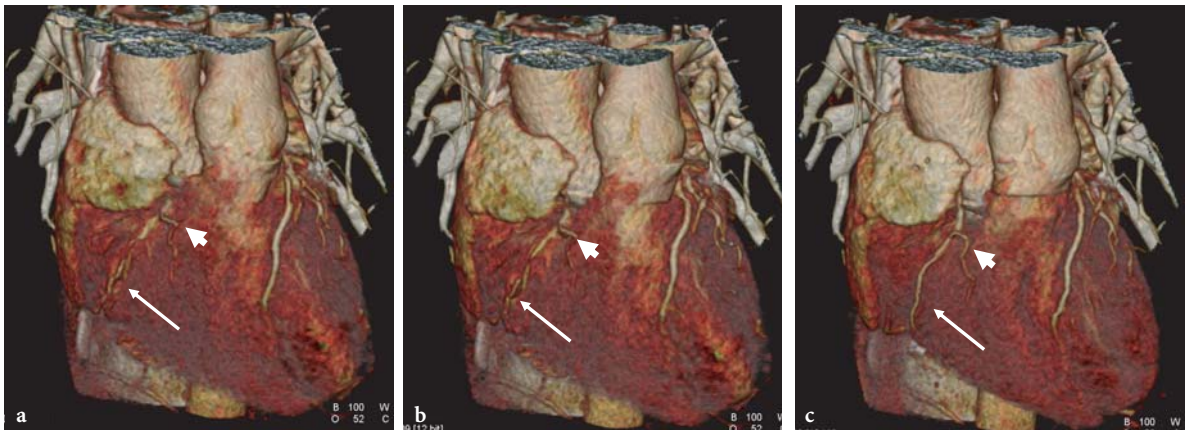

Fig. 8.27a–c. Coronary CT angiography examination using a dual-source CT scanner. No β-blocker was used for heart rate control and the patient had a variable heart rate between 86 and 122 bpm during the scan. The dual-source CT scan protocol with ECG-gated spiral acquisition consisted of 0.6-mm collimation, 0.33-s rotation time, pitch 0.2, 120 kV, and 550 mA tube current for each tube. The 12-cm scan range was covered in a 10-s breath-hold. A pitch of 0.2 was used to allow for simulation of a conventional 64-slice CT data acquisition by eliminating the data of the second tube-detector system during image reconstruction. Retrospectively ECG-gated image reconstruction was done during diastole (65%) using the data of one tube-detector system only with single-segment reconstruction and 165-ms temporal resolution (**a**) with 2-segment reconstruction providing 83 to 165ms temporal resolution (**b**) and utilizing the data of both tube-detector systems to achieve constant 83 ms temporal resolution (**c**). Volume-rendering (VRT) display of the data sets demonstrates presence of severe motion artifacts in the right coronary artery in the reconstruction with one tube-detector system only (*arrows* and *arrowheads* in **a** and **b**). Use of 2-segment reconstruction for data of one tube-detector system does not provide remarkable improvement of image quality (**b**). In the reconstruction with both tube-detector systems, motion artifacts are completely eliminated despite the high and irregular heart rate (*arrow* and *arrowhead* in **c**). (Case courtesy of University of Munich, Grosshadern Clinic, Germany)

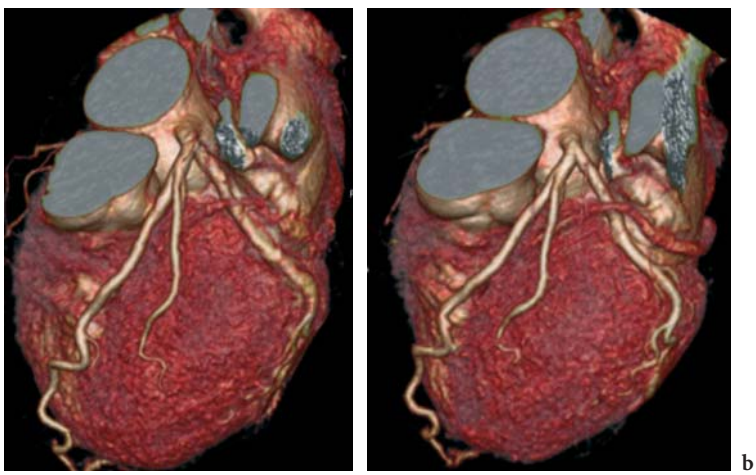

Fig. 8.28a,b. Coronary CT angiography examination to rule-out the presence of coronary artery disease in a patient with chest pain. The examination was carried out using a dual-source CT scanner. No β-blocker was used to control heart rate and the patient showed a stable heart rate of 85 bpm during the scan. The dual-source CT scan protocol with ECG-gated spiral acquisition consisted of 0.6-mm collimation, 0.33-s rotation time, pitch 0.36, 120 kV, and 550-mA tube current for each tube. The 12-cm scan range was covered in a 6-s breath-hold. Retrospectively ECG-gated image reconstruction was done during end-systole (30%) and during diastole (65%). VRT display of the data sets demonstrates motion-free reconstruction of the right and left coronary arteries in both end-systole (**a**) and diastole (**b**), despite the high heart rate. Based on the high image quality, the absence of coronary lumen narrowing could be confirmed with a high degree of confidence. (Case courtesy of Erlangen University, Germany)

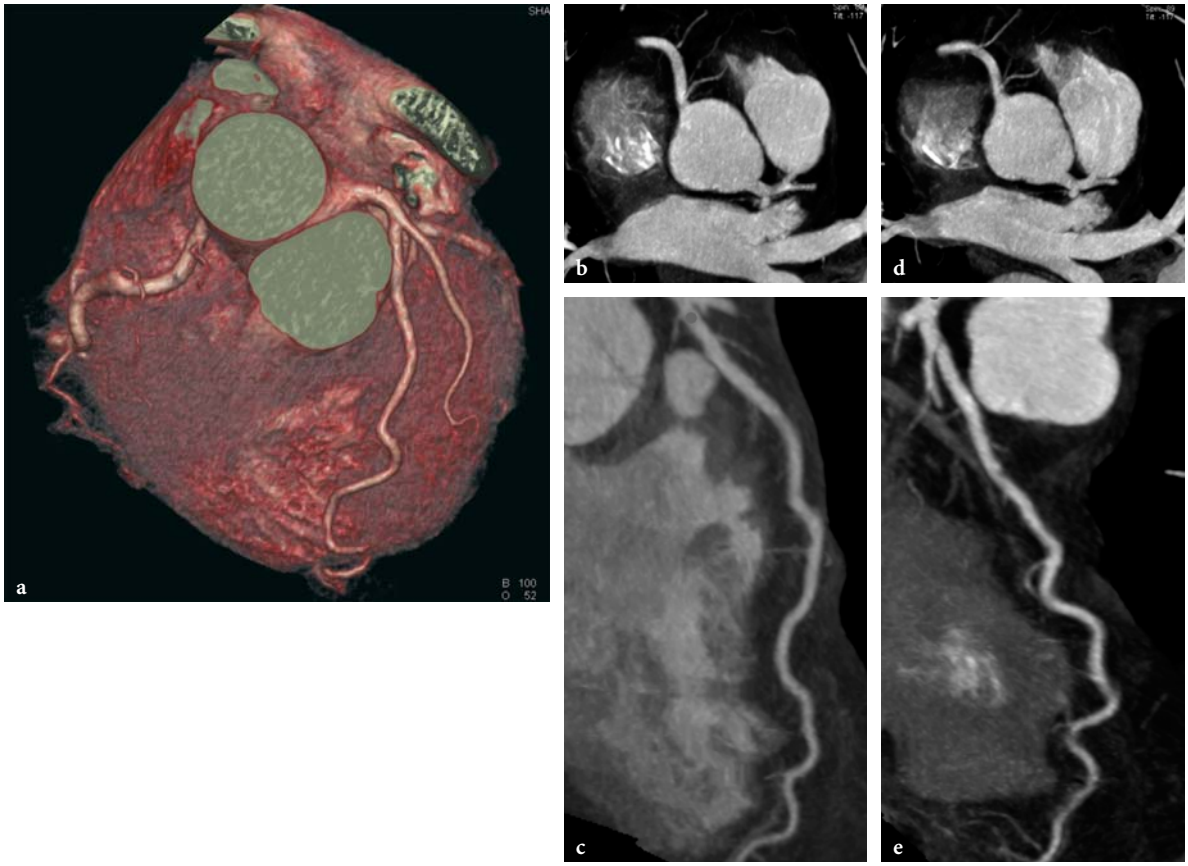

Fig. 8.29a–e. Coronary CT angiography examination in a patient with changing heart rate between 82 and 96 bpm during the scan. The examination was carried out using a dual-source CT scanner. The scan protocol, with ECG-gated spiral acquisition, consisted of 0.6-mm collimation, 0.33-s rotation time, pitch 0.36, 120 kV, and 550-mA tube current for each tube. The 12-cm scan range was covered in a 6-s breath-hold. Retrospectively ECG-gated image reconstruction was done during end-systole (30%) and during diastole (70%). VRT display of the data sets demonstrates motion-free reconstruction of the right and left coronary arteries in diastole (**a**) despite the high and irregular heart rate. MIP displays of the proximal right coronary artery and the left descending coronary artery in diastole (**b**, **c**) and in end-systole (**d**, **e**) reveal that the coronary arteries are free of motion artifacts in both phases. The absence of coronary artery disease could therefore be confirmed. (Case courtesy of Erlangen University, Germany)

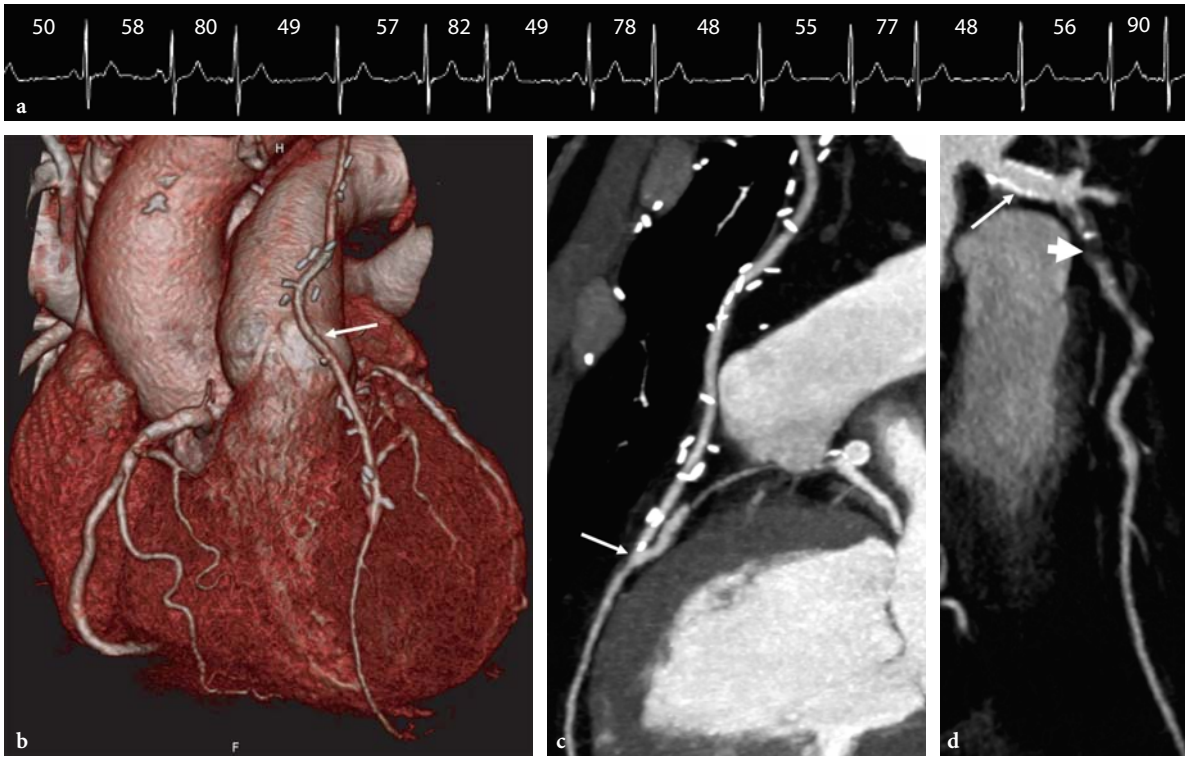

Fig. 8.30. a Cardiac CT angiography examination by dual-source CT in a patient with an internal mammary artery (IMA) bypass graft to the left coronary artery and a stent in the left main coronary artery. The patient suffered from atrial fibrillation and showed a changing heart rate between 48 and 90 bpm. The scan protocol, with ECG-gated spiral acquisition, consisted of 0.6-mm collimation, 0.33-s rotation time, pitch 0.27, 120 kV, and 550 mA tube current for each tube. The 12-cm scan range was covered in an 8-s breath-hold. Retrospectively ECG-gated image reconstruction was performed during diastole (70%). **b** VRT display demonstrates motion-free reconstruction of the coronary artery tree and the IMA graft (*arrow*) despite the high and irregular heart rate. **c** Curved MIP nicely delineates the open IMA graft, including a patent distal anastomosis (*arrow*). **d** Curved MPR allows assessment of the patent stent lumen in the left main coronary artery (*arrow*) and the occlusion in the left descending coronary artery (*arrowhead*). (Case courtesy of Erlangen University, Germany)

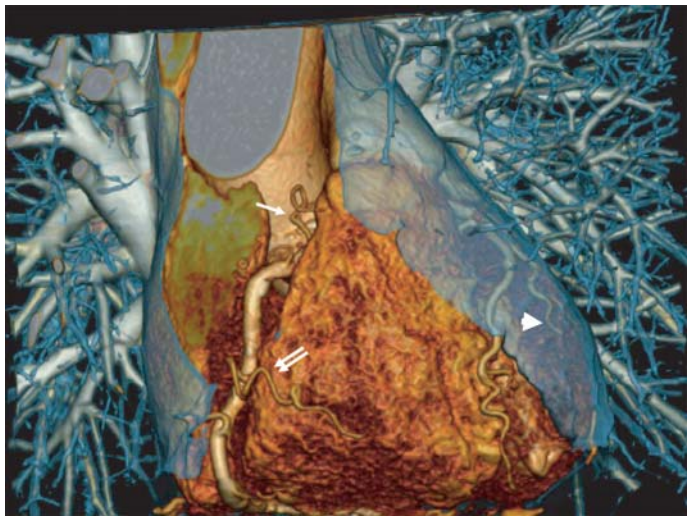

Fig. 8.31. Coronary CT angiography examination using a dual-source CT scanner. The patient had suspected coronary artery disease and stable heart rate of around 75 bpm during the scan (Johnson 2006). The scan protocol, with ECG-gated spiral acquisition, consisted of 0.6-mm collimation, 0.33-s rotation time, pitch 0.27, 120 kV, and 550 mA tube current for each tube. The 12-cm scan range was covered in an 8-s breath-hold. Retrospectively ECG-gated image reconstruction was done during diastole (70%). VRT display of the data sets demonstrates motion-free reconstruction of the left and right coronary artery tree and high-resolution reconstruction of the lung. The high temporal resolution enables clear depiction of subsegmental coronary branches, including the conus artery (*arrow*) and acute marginal branch (*double arrow*). Also, diagonal and obtuse marginal branches including 2nd-order branches can be visualized (*arrowhead*). (Case courtesy of University of Munich, Grosshadern Clinic, Germany)

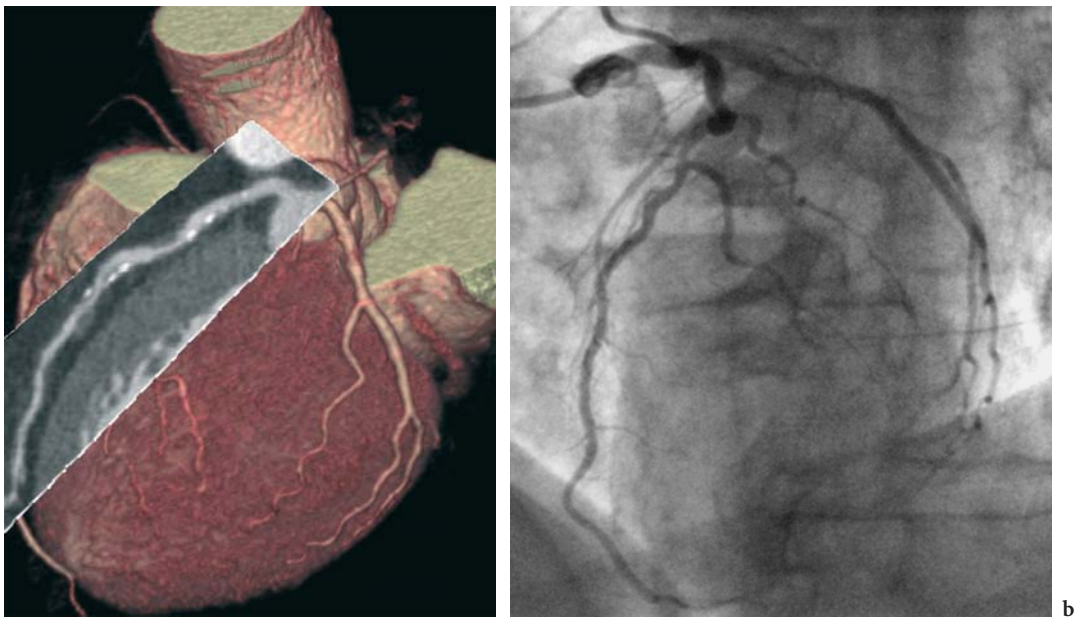

a b

Fig. 8.32a,b. Coronary CT angiography examination using a dual-source CT scanner. The patient had suspected coronary artery disease and a stable heart rate of around 70 bpm during the scan . The dual-source CT scan protocol with ECG-gated spiral acquisition consisted of 0.6-mm collimation, 0.33-s rotation time, pitch 0.27, 120 kV, and 550-mA tube current for each tube. The 12-cm scan range was covered in an 8-s breath-hold. Retrospectively ECG-gated image reconstruction was done during diastole (65%). **a** VRT display of the data sets demonstrates motion-free reconstruction of the left coronary artery tree in diastole. **b** MIP display of the left descending coronary artery in diastole can be overlapped with the 3DVRT reconstruction. A mixed coronary plaque, including moderate lumen narrowing, can be seen but the absence of high-grade stenosis was confirmed, consistent with the results of coronary angiography. (Case courtesy of Erlangen University, Germany)

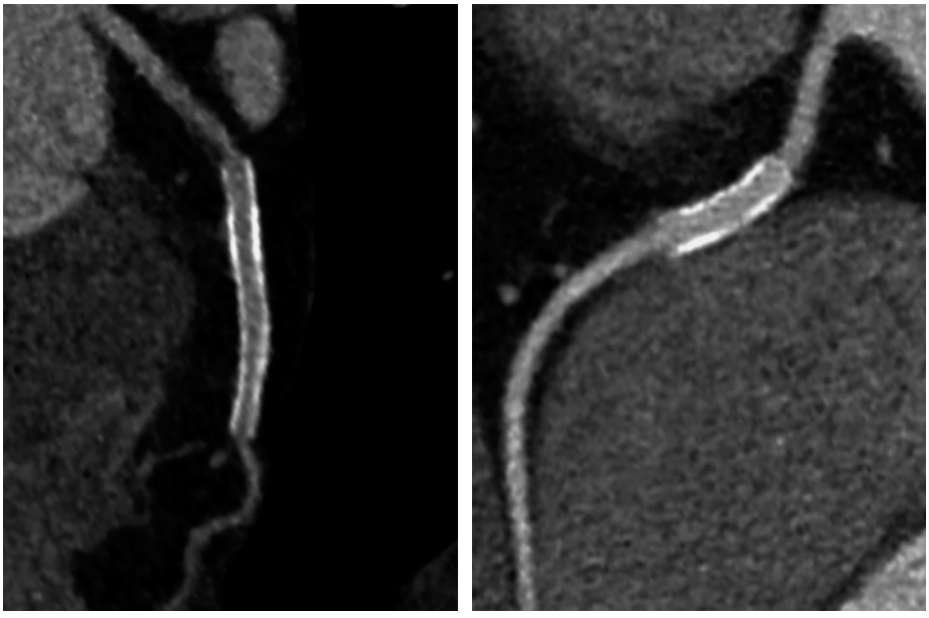

a b

Fig. 8.33a,b. Coronary CT angiography examination using a dual-source CT scanner. The patient had stent grafts in the left and right coronary artery and a stable heart rate of around 65 bpm during the scan. The dual-source CT scan protocol with ECG-gated spiral acquisition consisted of 0.6-mm collimation, 0.33-s rotation time, pitch 0.27, 120 kV, and 550-mA tube current for each tube. The 12-cm scan range was covered in an 8-s breath-hold. Retrospectively ECG-gated image reconstruction was done during diastole (65%). Curved MPR display reveals the patent lumen of both stents in the left descending coronary artery (**a**) and in the RCA (**b**). The high temporal resolution and the related absence of motion appear to reduce blooming artifacts in the presence of stents, thus improving in-stent visualization. (Case courtesy of University of Rotterdam, Netherlands)

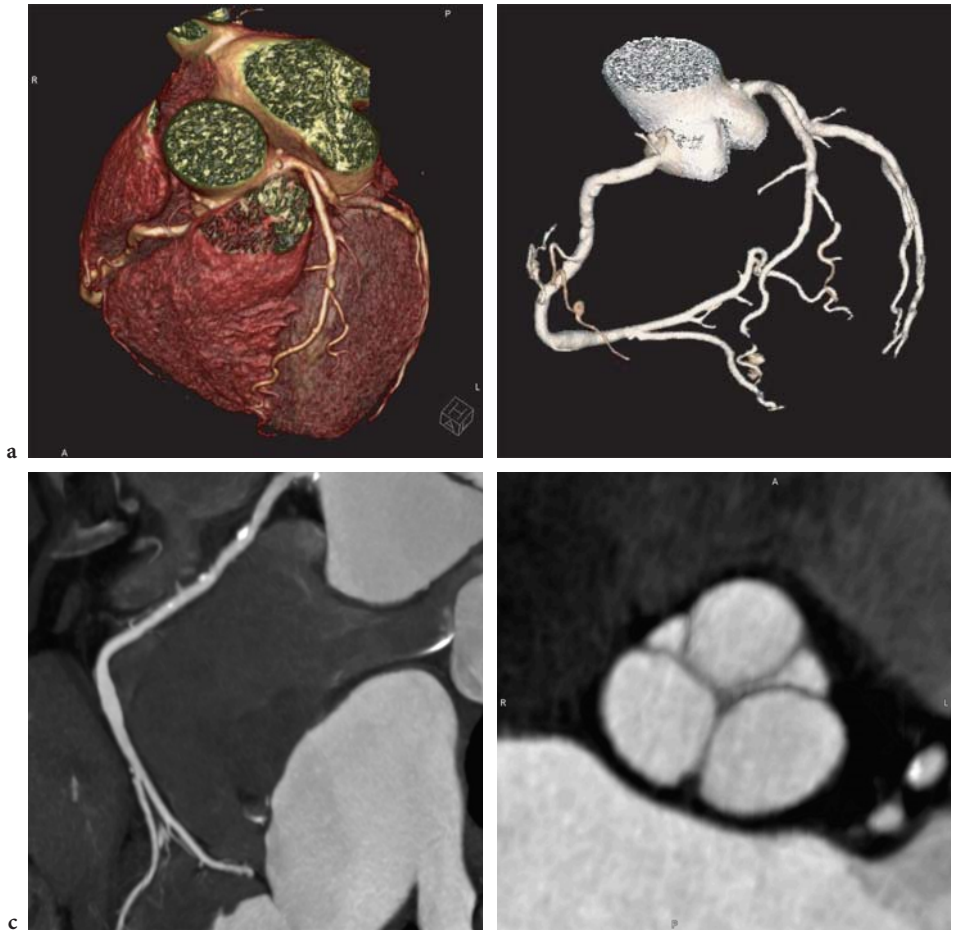

Fig. 8.34a–d. Coronary CT angiography examination using a dual-source CT scanner. The patient had a stable heart rate around 70 bpm during the scan. The dual-source CT scan protocol with ECG-gated spiral acquisition consisted of 0.6-mm collimation, 0.33-s rotation time, pitch 0.27, 120 kV, and 550-mA tube current for each tube. The 12-cm scan range was covered in an 8-s breath-hold. Retrospectively ECG-gated image reconstruction was done during diastole (70%). VRT display of the heart (**a**) and of the segmented coronary artery tree (**b**) allows significant coronary artery disease to be ruled-out. MIP of the RCA (**c**) reveals details of the vessel wall and presents outstanding image quality also of subsegmental branches. The high temporal resolution also allows for motion-free visualization of the closed aortic valve using MIP reconstruction (**d**). (Case courtesy of University of Munich, Grosshadern Clinic, Germany)

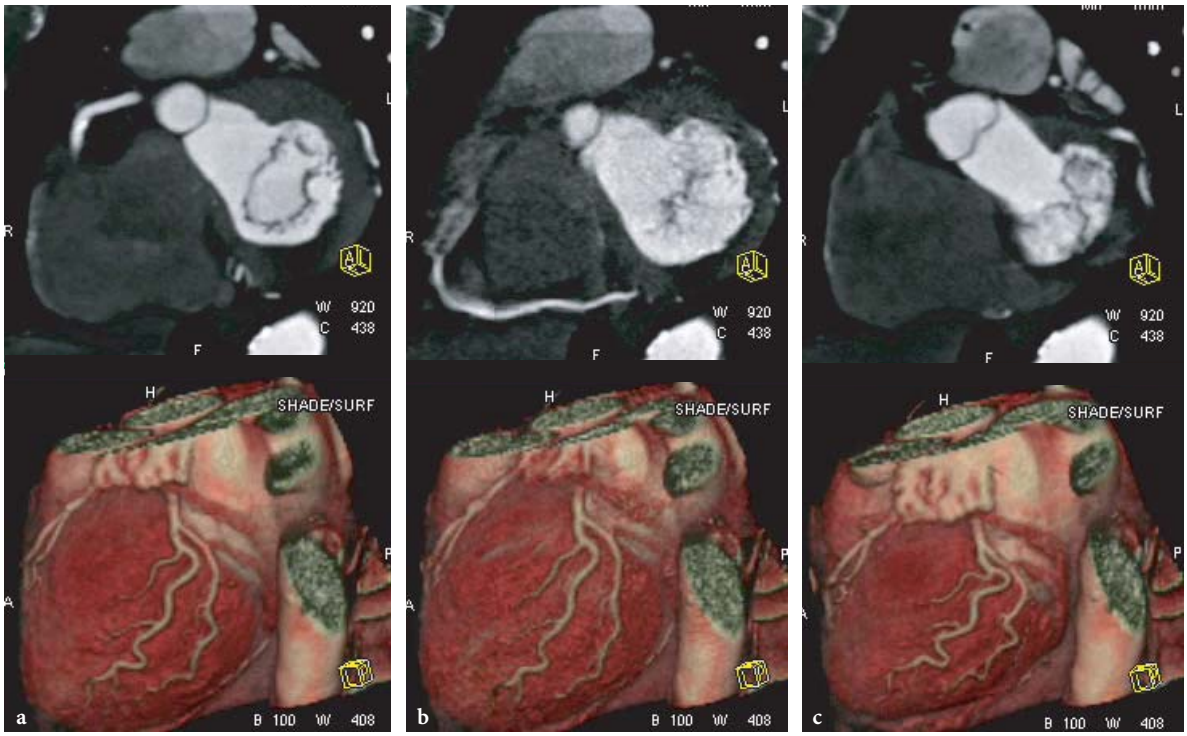

Fig. 8.35a–c. Cardiac CT angiography examination using a dual-source CT scanner. The patient had a stable heart rate of around 85 bpm during the scan. The dual-source CT scan protocol with ECG-gated spiral acquisition consisted of 0.6-mm collimation, 0.33-s rotation time, pitch 0.36, 120 kV, and 550-mA tube current for each tube. The 12-cm scan range was covered in a 6-s breath-hold. Retrospectively ECG-gated image reconstruction was done during: **a** mid-diastole (60%), **b** end-diastole (80%), and **c** end-systole (30%). MIP reconstruction (*top*) reveals the mitral valve open in mid-diastole, closed in end-diastole, and closed in end-systole. VRT display (*bottom*) demonstrates the different sizes of the left ventricle in the different phases of the cardiac cycle. (Case courtesy of University of Munich, Grosshadern Clinic, Germany)

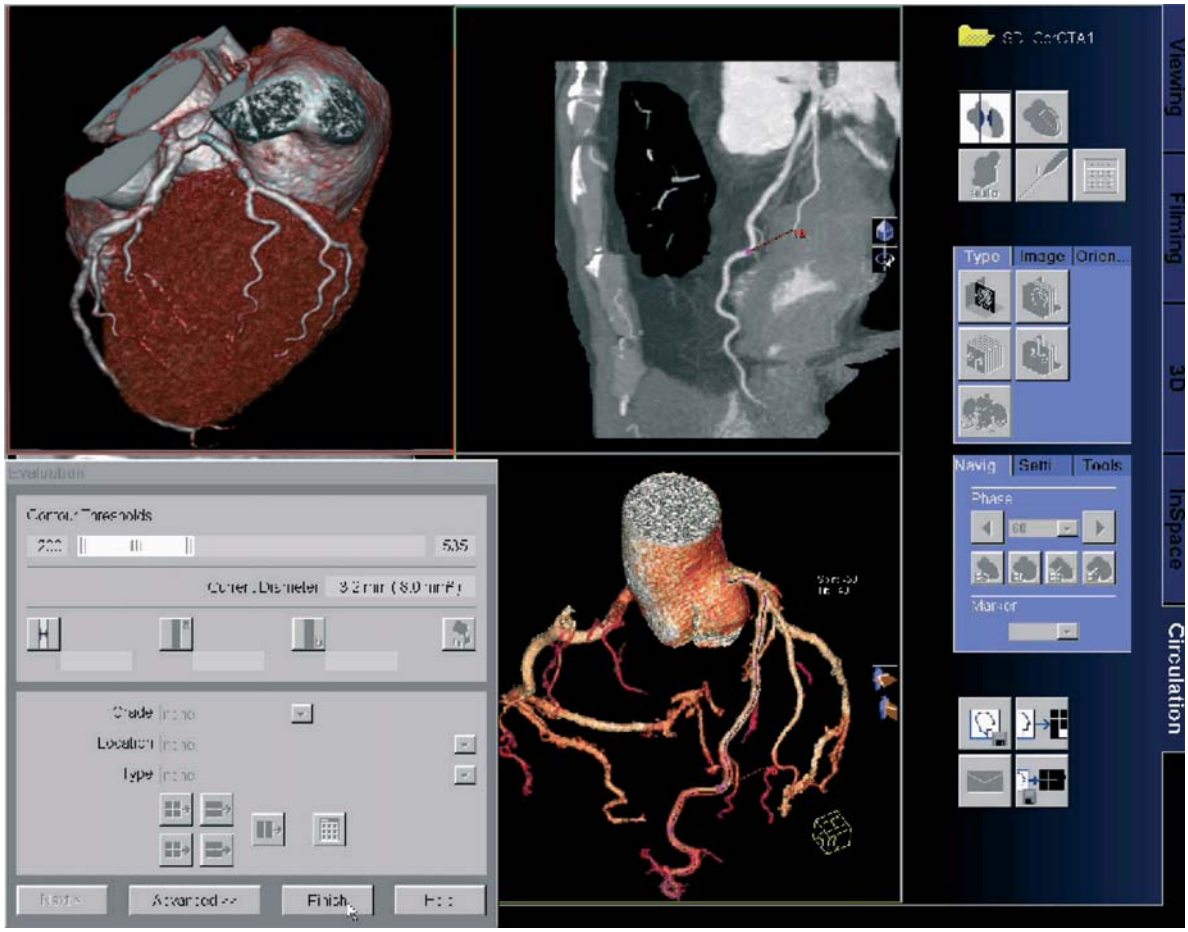

Fig. 8.36. Coronary CT angiography examination in a patient with suspected coronary artery disease and a stable heart rate of around 85 bpm during the scan. The examination was carried out using a dual-source CT scanner. The scan protocol, with ECG-gated spiral acquisition, consisted of 0.6-mm collimation, 0.33-s rotation time, pitch 0.36, 120 kV, and 550-mA tube current for each tube. The 12-cm scan range was covered in a 6-s breath-hold. Retrospectively ECG-gated image reconstruction was done during diastole (65%) and images were analyzed using modern automated segmentation and coronary analysis software. The fast pitch value of 0.36 and the ECG-controlled dose modulation with 200 ms of maximum exposure during the cardiac cycle allowed the scan to be acquired with a radiation exposure to the patient of only about 5–6 mSv. (Case courtesy of Erlangen University, Germany)

power reserves of 160 kW for long scan ranges and obese patients. The new possibility of dual-energy acquisition is likely to open an entirely new era of clinical applications. In cardiovascular CT applications, the high-power reserves enable whole-body CT angiographic studies with up to 200-cm scan range at sub-millimeter resolution (Fig. 8.37). Dual-energy acquisition can support the automatic differentiation of vessels and bone (Fig. 8.38) and may eventually become useful in differentiating vascular lesions.

The initial patient examinations also showed that dual-source CT has the potential to provide motion-free high-resolution CT images of the heart and the coronary arteries also in patients with high and irregular heart rates, thus avoiding the use of β-blocker pre-medication and the related workflow challenges. An improvement of diagnostic accuracy can also be expected in patients with lower heart rates, especially in the presence of stents or calcified lesions since any residual motion that might cause

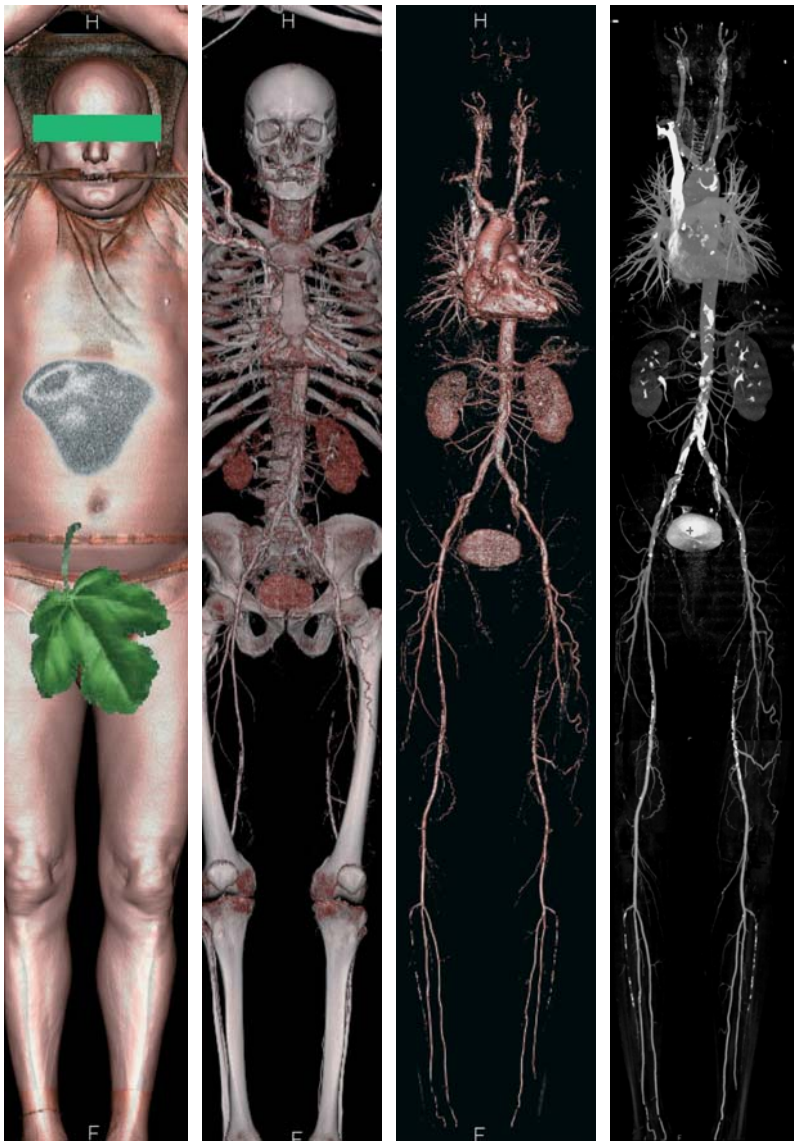

Fig. 8.37. Whole-body CT angiography examination using a dual-source CT scanner. A dual-source CT scan protocol without ECG-gating was applied. Scan parameters were 0.6-mm collimation, 0.33-s rotation time, pitch 1.5, 120 kV, and 550-mA tube current for each tube. The whole-body 200-cm scan range can be covered in a scan time of only 23 s and displayed with VRT and MIP. (Case courtesy of Erlangen University, Germany, and Grosshadern Clinic, University of Munich, Germany)

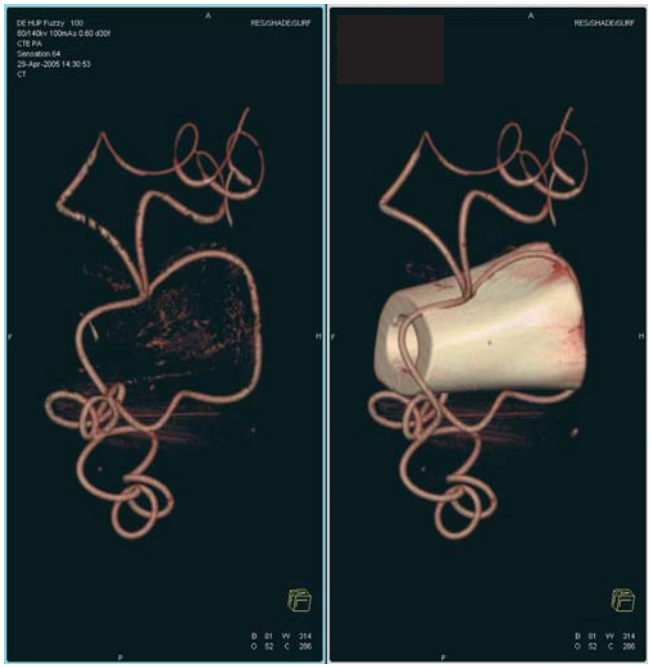

Fig. 8.38. Experimental CT angiography examination of a bone and vessel phantom using a dual-source CT scanner and a dual-energy CT scan protocol. Scan parameters were 0.6-mm collimation, 0.33-s rotation time, pitch 1.0, 140 kV/550 mA for tube 1, and 80 kV/550 mA for tube 2. A dual-energy reconstruction algorithm was used for segmentation of the bone and isolation of the vessel structures

blurring is substantially reduced. At the same time, volume coverage speed has been increased so that larger scan ranges, such as required for the chest, can be covered with ECG-gated scan protocols within comfortable breath-hold times. The dose reduction compared to today's 64-slice CT scanners will help the technology gain further and broader acceptance for regular clinical use. The combined benefits of higher temporal resolution, faster volume coverage, and lower dose may prove useful in pediatric cardiac CT applications. Due to the high temporal resolution and the ability of dual-energy acquisition, new applications are coming within reach, such as the evaluation of regional cardiac function, myocardial perfusion, and blood volume as well as the differentiation and quantification of arterial plaques.

References

Achenbach S, Ropers D, Holle J, et al (2000). In-Plane coronary arterial motion velocity: measurement with electron beam CT. Radiology 216:457–463

Achenbach S, Ropers D, Kuettner A, Flohr T, Ohnesorge B, Bruder H, Theesen H, Karakaya M, Daniela WG, Bautz W, Kalender WA, Anders K (2006). Contrast-enhanced coronary artery visualization by dual-source computed tomography – initial experience. Eur J Radiol 57: 331–335

Boyd DP, Lipton MJ (1982). Cardiac computed tomography. Proceedings of the IEEE 71:298–307

Bruder H, Stierstorfer K, McCollough C, Raupach R, Petersilka M, Grasruck M, Ohnesorge B, Flohr T (2006). Design considerations in cardiac CT. SPIE Proceedings 2006 (in press)

Ehara M, Surmely JF, Kawai M, Katoh O, Matsubara T, Terashima M, Tsuchikane E, Kinoshita Y, Suzuki T, Ito T, Takeda Y, Nasu K, Tanaka N, Murata A, Suzuki Y, Sato K, Suzuki T (2006). Diagnostic Accuracy of 64-Slice Computed Tomography for Detecting Angiographically Significant Coronary Artery Stenosis in an Unselected Consecutive Patient Population: Comparison With Conventional Invasive Angiography. Circ J 70: 564–571

Flohr T, Ohnesorge B (2001). Heart rate adaptive optimization of spatial and temporal resolution for ecg-gated multi-slice spiral CT of the heart. JCAT 25(6): 907–923

Flohr T, Stierstorfer K, Raupach R, Ulzheimer S, Bruder H. Performance evaluation of a 64-Slice CT-system with z-flying focal spot (2004). Röfo Fortschr Geb Rontgenstr Neuen Bildgeb Verfahr 176:1803–1810

Flohr TG, Stierstorfer K, Ulzheimer S, Bruder H, Primak AN, McCollough CH. Image reconstruction and image quality evaluation for a 64-slice CT scanner with z-flying focal spot (2005). Med Phys 32(8): 2536–2547

Flohr TG, McCollough C, Bruder H, Petersilka M, Gruber K, Süß C, Grasruck M, Stierstorfer K, Krauss B, Raupach R, Primak AN, Küttner A, Achenbach S, Becker C, Kopp A, Ohnesorge B (2006). First performance evaluation of a dual source CT (DSCT) system. Eur Radiol 16:256–268

Funabashi N, Yoshida K, Tadokoro H, Nakagawa K, Komiyama N, Odaka K, Tsunoo T, Mori S, Tanada S, Endo M, Komuro I (2005a). Cardiovascular circulation and hepatic perfusion of pigs in 4-dimensional films evaluated by 256-slice cone-beam computed tomography. Circ J 69(5):585–9

Funabashi N, Yoshida K, Tadokoro H, Nakagawa K, Komiyama N, Odaka K, Tsunoo T, Mori S, Endo M, Tanada S, Komuro I (2005b). Three dimensional segmented myocardial perfusion images by selective intracoronary injection of contrast using 256 slice cone beam computed tomography. Heart 91:1349–1351

Garcia MJ, Lessick J, Hoffmann MHK (2006). Accuracy of 16-Row Multidetector Computed Tomography for the Assessment of Coronary Artery Stenosis. JAMA 296:403–411

Haliburton SS, Stillman AE, Flohr T, Ohnesorge B, Obuchowski N, Lieber M, Karim W, Kuzmiak S, Kasper JM, White RD (2003). Do segmented reconstruction algorithms for cardiac multi-slice computed tomography improve image quality? Herz 28(1):20–31.

Johnson TRC, Nikolaou K, Wintersperger BJ, Leber AW, von Ziegler F, Rist C, Buhmann S, Knez A, Reiser MF, Becker CR (2006). Dual source CT cardiac imaging: initial experince. Eu Radiol (in press)

Kachelrieß M, Ulzheimer S, Kalender WA (2000). ECG-correlated image reconstruction from subsecond multi-row spiral CT scans of the heart. Med Phys 27:1881–1902

Knollmann F, Pfoh A (2003). Image in cardiovascular medicine. Coronary artery imaging with flat-panel computed tomography. Circulation 107(8):1209

Kondo C, Mori S, Endo M, et al (2005). Real-time volumetric imaging of human heart without electrocardiographic gating by 256-detector row computed tomography – initial experience. JCAT 29(5):694–698

Leber AW, Knez A, Ziegler F, Becker A, Nikolaou K, Paul S, Wintersperger B, Reiser MF, Becker CR, Steinbeck G, Boekstegers P (2005). Quantification of obstructive and nonobstructive coronary lesions by 64-slice computed tomography – a comparative study with quantitative coronary angiography and intravascular ultrasound. JACC 46(1):147–154

Leschka S, Wildermuth S, Boehm T, Desbiolles L, Plass A, Koepfli P, Schepis T, Marincek B, Kaufmann PA, Alkadhi H (2006). Non-Invasive Coronary Angiography with 64-Slice CT: Effect of the Average and the Variability of Heart Rate on Image Quality. Radiology in press

Mahnken AH, Seyfarth T, Flohr T, Herzog C, Stahl J, Stanzel S, Kuettner A, Wildberger JE, Guenther RW (2005). Flat-panel detector computed tomography for the assessment of coronary artery stents: phantom study in comparison with 16-slice spiral computed tomography. Invest Radiol 40(1):8–13

McCollough C H, Zink F E (1994a). The technical design and performance of ultrafast computed tomography. Radiol Clin North Am 32(3):521–36

McCollough C H, Zink F E, Morin R (1994b). Radiation dosimetry for electron beam CT. Radiology 192(3):637–43

McCollough C H, Kanal K M, Lanutti N, Ryan K J (1999). Experimental determination of section sensitivity profiles and image noise in electron beam computed tomography. Med Phys 26(2):287–95

McCollough CH, Primak AN, Saba O, Bruder H, Stierstorfer K, Raupach R, Süß C, Ohnesorge BM, Flohr TG (2006). Dose performance of a 64-channel dual source CT (DSCT) Scanner. Radiology (in press)

Mollet NR, Cademartiri F, van Mieghem CAG, Runza G, McFadden EP, Baks T, Serruys PW, Krestin GP, de Feyter PJ (2005b). High-resolution spiral computed tomography coronary angiography in patients referred for diagnostic conventional coronary angiography. Circulation 112:2318–2323.

Mori S, Endo M, Obata T, et al (2006). Properties of the Prototype 256-Detector Row (Cone Beam) CT Scanner. Eur Radiol (in press)

Nikolaou K, Flohr T, Stierstorfer K, Becker CR, Reiser MF (2005). Flat panel computed tomography of human ex vivo heart and bone specimens: initial experience. Eur Radiol 15:329–33

Ohnesorge BM, Westerman BR, Schoepf UJ (2005). Scan techniques for cardiac and coronary artery imaging with multislice CT. In: Schoepf UJ (ed) CT of the heart: principles and applications. Humana Press, Totowa, NJ, pp 23–43

Ong TK, Chin SP, Liew CK, Chan WL, Seyfarth TM, Liew HB, Rapaee A, Yip Y, Fong A, Ang CK, Sim KH (2006). Accuracy of 64-row multidetector computed tomography in detecting coronary artery disease in 134 symptomatic patients: Influence of calcification. Am Heart J 151:1323.e1–e6

Raff GL, Gallagher MJ, O'Neill WW, Goldstein JA (2005a). Diagnostic accuracy of noninvasive coronary angiography using 64-slice spiral computed tomography. JACC 46 (3): 552–557

Ritman E, Kinsey J, Robb R, Gilbert B, Harris L, Wood E (1980). Three-dimensional imaging of heart, lungs, and circulation. Science 210:273–80

Robb R, Ritman E (1979). High speed synchronous volume computed tomography of the heart. Radiology 1979; 133:655–61

Ropers D, Rixe J, Anders K, Küttner A, Baum U, Bautz W, Daniel WG, Achenbach S (2006). Usefulness of Multidetector Row Spiral Computed Tomography with 64 x 0.6-mm Collimation and 330-ms Rotation for the Noninvasive Detection of Significant Coronary Artery Stenoses. Am J Cardiol 97:343–348

Schardt P, Deuringer J, Freudenberger J, Hell E, Knuepfer W, Mattern D, Schild M (2004). New X-ray tube performance in computed tomography by introducing the rotating envelope tube technology. Med Phys 31(9):2699–2706

Wintersperger B, Rist C, Nikolaou K, Becker CR, et al (2006). Image quality, motion artifacts and reconstruction timing of 64-slice coronary CT angiography with 0.33 s rotation speed. Invest Radiology (in press)

Subject Index

A
absolute
– delay 106, 139
– reverse 106, 139
ACE inhibitor 226
acute
– chest pain 145, 320
– coronary syndrome 184, 185
– ischemia 214
– myocardial infarction 184, 219, 320
acute-care setting 189
adaptive
– axial interpolation 56
– cardiac volume (ACV) reconstruction 92
– multiple plane reconstruction (AMPR) 58
adaptive-segmented algorithm 92
Agatston score 131, 132, 171, 192, 207, 226, 229
akinesis 269
ALARA 259
Alderson phantom 116
algorithm
– adaptive segment 92
– Framingham 182, 214
– Kymogram 110
– motion-detection 110
– multi-segment 136
– PROCAM 182, 214
– region-growing 171
– single segment 92
– volumetric quantification 172
American Heart Association (AHA) 197
– classification 226
– – 17-segment classification 168
– segment model 269
aneurysm 14, 184
angiosarcoma 292, 294
animal model 336
anomalous
– course 245
– venous return 262
anterior papillary muscle 270
anthropomorphic
– calibration phantom 123
– chest phantom 174
aorta
– ascending 38, 317
– descending 5
– posterior displaced 261
– thoracic 38, 145
– – descending 38
– arch anomaly 261
– coarctation 261
– dissection 185, 317
– root 317
– valve 29, 35, 281
– – annulus 282
– – bicuspid 282
– – calcification 283
– – cusps 282
– – orifice 282
– – prosthesis 284
– – stenosis 282, 283
apex 24
area-detector CT 334
area-length method 267
array detector 50
– adaptive 50, 51
– fixed 50, 51
arrhythmia 108
arrhythmogenic right ventricular cardiomyopathy (ARVC) 277
artifact misregistration 109
ascending aorta 5, 38, 317
atherosclerosis
– plaque 211, 214
– risk factor 214
– subclinical 192
atrial
– fibrillation 13, 110, 289, 291, 296
– – acute 296
– – paroxysmal 296
– thrombus 288

atrium
– left 24, 33
– right 24, 33
automated bolus
– detection 233
– triggering 141
autosomal dominant syndrome 290
axial image 151
axis
– cardiac 23
– long 23
– – horizontal 29
– – vertical 24
– short 23, 29

B

balloon angioplasty 239
beam
– collimation 50
– pre-filtration 114
beam-hardening artifact 211, 239, 310
beta-blocker 136, 183, 206, 226, 233, 297, 327, 347, 356
bi-ventricular pacemaker 300
Bland–White–Garland syndrome 246
blood pool 170
blood-volume distribution 307
blooming artifact 184, 240, 352
body mass index 229
body phantom 114
breath-hold time 73, 133, 321
bronchogenic carcinoma 290
bulls-eye plot 34, 168
bypass graft 232
– occluded 232

C

CAD exclusion 230
calcification 129
calcified coronary segment 329
calcium
– accumulation 198
– mass 182, 193, 207, 227
– – calibration factor 174
– measurement reproducibility 129
– score 172, 200
– – interpretation 201
– – percentiles 202
calcium-channel blocker 297
calibration phantom 193
cardiac
– atria 14
– axes 23
– bowtie filter 346
– catheterization 179, 184
– cavity 290
– chambers 5, 13
– cone-beam reconstruction 98
– CT imaging protocol 127
– cycle 106
– enzyme test 320
– function 12, 72, 141, 189, 328, 340
– – defect 141
– – global 141
– magnetic resonance imaging (CMR) 8, 23, 141, 215, 307
– mass 189, 270, 288
– morphology 5, 133, 189
– motion 71
– myxoma 290
– neoplasm 290
– output 266, 268
– pulsation 101, 317
– sarcoma 292
– spiral reconstruction 55
– – multi-slice 81
– thrombus 290
– tumor 288
– valve 5, 13, 189, 281
– venous system 14, 189
cardiac-motion detection 110
cardiomyopathy 266
cardiothoracic vasculature 144, 189
cardiovascular risk factor 198, 225
Carney complex 290
catheter ventriculography 141
CATPHAN 64
center line 163
center of mass 110
central-airway compression 261
chest pain 225
– acute 320
– atypical 184
– equivocal 321
– protocol 144
chronic
– infarction 313
– stable angina 184
cine
– magnetic resonance imaging 268
– mode 333
– ventriculography 273

coated stent 239
collimated slice width 50, 81, 82
computed tomography (CT)
– 4-slice 43, 127
– 16-slice 43, 133
– 64-slice 44, 134
– angiography 41, 43, 65
– – 16-slice 67
– – 64-slice 67
– – ECG-correlated 144
– – of the chest 145
– – of the whole body 46, 66, 356
– contrast-enhanced
– dual source 338
– electron-beam (EBCT) 14, 180, 192, 332
– – multi-slice 16
– follow-up 302
– fourth generation 14
– mechanical 17
– multi-slice 2, 19, 42, 47, 192
– single-slice 1, 18
– spiral 18, 41, 79
– third generation 47
– thoracic 317
computerized tomographic dose index (CTDL) 113
cone angle 53
cone-beam
– artifact 53, 97
– geometry 58
– reconstruction 58, 97, 334
– – cardiac 98
congenital
– anomalies 245
– coronary artery disease 263
– heart disease 14, 258, 261
– – cyanotic 259
– vascular disease 146
congestive heart failure 298
continuous table-feed 81
contrast
– agent 141
– – protocol 127, 145
– bolus dynamic 308
– enhancement 73
– medium 180, 321
– timing 141
– ventriculography 313
contrast-enhanced cardiac CT 140
contrast-injection protocol 145
contrast-to-noise ratio 73
convolution kernel 152
coronary
– anatomical anomaly 184
– anatomy 24
– angiography (CA) 183, 205, 215
– – quantitative 212
– – selective 3, 7
– artery 205
– – aneurysm 254
– – anomalous 261
– – anomaly 254, 300
– – calcification (CAC) 127, 192
– – diagnosis 133
– – disease 11, 182, 209, 224, 321
– – dissection 254
– – fistula 246
– – left anterior descending (LAD) 24
– – left main (LM) 31
– – phantom 336
– – plaque 192
– – right (RCA) 24, 30
– – segments 30
– – stenosis 180, 183, 215
– – stent 140
– – tree 5
– – wall 182, 183
– atherosclerosis 11, 182, 192
– – plaque burden 241
– bypass 11
– – graft CTA 180
– calcification 12, 171, 214, 215
– – absence 201
– – progression 202
– – volumetric quantification 174
– calcium
– – mass 174
– – percentile 182
– – quantification 180
– – screening 179
– – standardized measurement 182
– – volume 174
– CT angiography (CTA) 180, 183
– – with dual source CT 347
– event 198
– – ten-year risk 198
– heart disease (CHD) 192, 197
– obstruction 205
– perfusion reserve 309
– plaque 12, 134
– – burden 198
– – differentiation 331
– restenosis 239
– segment 5, 205

coronary, segment *(continued)*
– – non-evaluable 183
– sinus 35
– stenosis 11, 205
– – quantitative measurement 212
– stent 134, 241, 329
– syndrome 320
– thrombus 185
– vasculitis 254
– vein 32
– venous anatomy 300
CTDI body phantom 346
culprit lesion 182, 204
curved MPR 240
cyanotic congenital heart disease 259

D

data transmission 49
descending aorta 5, 38
desynchronized heart rate 94
detection
– accuracy 129
– efficiency 49
detector
– ceramics 51
– coverage 329
– design 50
– module 52
– pitch 53
– rows 50
– types 50
– z-coverage 328
diastole 71
diastolic phase 269
DICOM-structured reporting 162
diffuse lung disease 317
dilatative cardiomyopathy 274
dilated pulmonary artery 216
direct volumetry 267
dissection 14, 184
distal anastomosis 236
dose
– adaptation 121
– measurement 114
– modulation
– – ECG-controlled 119, 130, 138, 145, 331, 346
– profile 58
– reduction 123
– reduction 346
double z sampling 44, 50, 62, 135
drug-eluting stent 239
dual-energy
– acquisition 356
– CT 357
dual-source CT 338
– scan protocol 348
dynamic imaging 307
dyskinesis 269

E

ECG
– analysis algorithm 121
– editing 136
– – tools 140, 329
– gating parameters 140
– prospective triggering 15, 127, 134, 196, 308
– pulsing 180, 233, 346
– retrospective gating 127, 134, 197, 269, 308, 317
– synchronized acquisition 75
ECG-controlled
– dose modulation 119, 130, 331, 342, 346
– tube output modulation 197
ECG-gated
– coverage of the chest 104, 144
– retrospective
– – reconstruction 83
– – spiral scanning 79, 80
ectopic beat 342
edge-enhancing weighting function 84
edge-preserving reconstruction kernel 240
Edwards syndrome 245
effective
– dose 116
– mAs 57, 116
– organ dose in mSv 346
– slice width 50
ejection fraction 141, 168, 266, 268
electrical stimulation 110
electron beam CT 180, 192, 332
electron-beam CT (EBCT) 14, 180, 192, 273, 332
– multi-slice 333
– perfusion measurement 308
– scanner
– – comparability of results 127
electrophysiological defect 14
emergency department 320
end-diastole 71, 107
end-diastolic volume 141, 168, 266, 268
endocardial contour 270
endocarditis 285
end-systole 71, 107

end-systolic volume 141, 168, 266, 268
enhancement curve 169
EP procedure 189
epicardial contour 270
epicardium 13
equivocal chest pain 321
exercise ECG 226
exposure reduction 119, 120
extracardiac shunt 246
extra-systole 110
extra-systolic beat 108, 109
– automatic detection 122
ex-vivo study 336

F

fan-beam
– data 74
– geometry 74
– projection 2, 75, 81
faster volume coverage 342
Feldkamp algorithm 58
fibroatheroma 198
fibroelastoma 294
fibroma 290, 294
field-of-view (FOV) 151
filtered back-projection 2
filtering
– mean 77
– median 77
first-line imaging 224
first-pass
– contrast enhancement 170
– perfusion 141
– – imaging 308
flat-panel detector 334
flow mode 333
focal saccular aneurysm 247
Framingham
– algorithm 182, 214
– risk index 198
full width at half maximum (FWHM) 50, 75, 343
functional imaging 107

G

gantry rotation
– speed 72
– time 114
general cardiac disease 189
global
– cardiac function 266, 340
– ventricular function 268
gold-plate phantom 82
graft
– bypass 232
– – occluded 232
– internal mammary artery (IMA) 234
– patency 232
– stenosis 232
– venous 232

H

half-scan reconstruction 74, 75
heart
– chamber 145
– cycle 78
– rate 71, 327
– – adaptive algorithm 90
– – control 136
– – high 356
– – irregular 108
heart-rate-dependent pitch 88, 342
hemodynamic steal phenomenon 247
high-power reserve 356
Hounsfield units 2
– peak value 172
hypertrophic cardiomyopathy 310
hypokinesis 269

I

image
– increment 81
– overlapping 81
– plane 151
– position 81
– post-processing 151
– reconstruction phase 139
– z positions 82
inconsistent heart plane 108
increased detector volume coverage 329
infarct
– area 310
– myocardium 310
– size 314
infarction
– chronic 313
– subendocardial 313
in-plane
– pixel size 151
– resolution 42

in-stent
– lumen 240
– restenosis 239
– stenosis 241, 242
intelligent ECG-controlled dose modulation 342
inter-/intra-observer variability 176
internal mammary artery (IMA) graft 234
International Commission on Radiation Protection (ICRP) 116
International Consortium of Standardization in Cardiac CT 123, 124, 182
interpolated projection 81
interpolation
– linear 81
– nearest neighbour 81
– weight 81
inter-scan
– reproducibility 182, 193
– variability 172, 176
intracardiac thrombus 291
intracavitary thrombus 313
intramural calcification 313
intravascular ultrasound (IVUS) 6, 8, 184, 216
intubated baby 259
ionization chamber 113
irregular heart rate 108, 327, 347
isotropic
– interpolation factor 173
– resolution 42

K

Kawasaki syndrome 254, 256
Klinefelter's syndrome 245
kV
– 100-kV tube voltage 123
– 80-kV scan protocol 123
– lower setting 123
Kymogram algorithm 110
Kymogram-gated image reconstruction 111

L

late enhancement 141, 171, 274, 312
leaflets of the mitral valve 270
left anterior descending coronary artery 24, 31
left atrium, 3D models 300
left circumflex artery 24, 31
left coronary artery 31
left main coronary artery (LM) 31
left ventricular
– aneurysm 313
– ejection fraction 168
– function 141, 143, 266
– hypertrophy 243, 297
– outflow tract 29
– stroke volume 141
– thombosis 313
– volume 168
– – curve 267
leimyosarcoma 294
linear interpolation 81
lipid-lowering medication 214
lipid-rich plaque 218
lipoma 290, 294
local ischemia 310
long scan range 356
long-axis reformation 270
longitudinal resolution 42, 62, 72
Lucite phantom 113
lung disease 317
lymphoma 294

M

magnetic resonance imaging (MRI) 8, 23, 141, 215, 307
major aorto-pulmonary collateral artery (MAPCA) 261
Marfan syndrome 254
mAs value 116
maximum intensity projection (MIP) 154, 208
– curved 157
– direct 159
– double-oblique 157
– thin-slab 156
mean filtering 77
mechanical
– force 328
– limit 328
median filtering 77
mediastinitis 263
metal artifact 236
mid-diastole 107
milli-Sievert (mSv) 116
minimizing radiation exposure 331
misregistration artifact 109
mitral valve 29, 35, 281
– annulus 283
– – calcification 285
– leaflets 283
– plane 270

modulation transfer function 133, 141
Monte Carlo calculation 116
Moore's Law 42
motion
– amplitude 72
– artifact 71, 328, 343, 347
motion-detection algorithm 110
motion-free imaging 107
moving coronary artery
– motion patterns 342
– phantom 342
multi-phase reconstruction 85
multi-planar reformation (MPR) 153, 208, 240
– curved 153
– direct 155
– double-oblique 153
– oblique 153
– slab-MPR 153
– stacks 153
– – in short and long heart axes 155
multi-segment
– algorithm 136
– reconstruction 144, 272, 328, 339
multi-slice
– cardiac spiral reconstruction 81
– cardiac volume reconstruction (MSCV) 81
– computed tomography (CT) 2, 19, 42, 47, 192
– – future development 327
– – pitfalls 327
– coronary CTA 207, 224
– linear interpolation (MLI) 54
– – spiral reconstruction 55
– spiral weighting 81
multi-vessel disease 206
myocardial
– blood flow 308
– bridging 251
– contrast enhancement 310
– coverage 308
– enhancement 170
– function 180
– infarction 11, 182, 184, 214, 312
– ischemia 182
– mass 168, 308
– morphology 180
– perfusion 168, 170, 307, 329
– – defect 189
– revascularization 274
– scar tissue 274
– segment 34
– viability 307
– wall motion 328, 347
– wall thickness 266
myocarditis 13
myocardium 13
– calcification 313
– infarcted 169, 310
myxoma 294

N

nearest-neighbour interpolation 81
neonate 258
non-assessability 205
non-cardiac thoracic structure 317
non-diagnostic segment 327
non-stenotic lesion 221
normalized score 172
normokinesis 269
nuclear imaging 8
nutating slice algorithm 58

O

obesity 331, 356
online reduction of the tube output 119
opposite parallel beam projection 110
optical coherence tomography 215
organ dose 116
osteosarcoma 294
outpatient clinic 225
overestimation of scores 133
overlapping
– acquisition 109
– images 81
– slice increments 108

P

P wave 107
pacemaker 14, 189, 291
– bi-ventricular 300
papillary
– fibroelastoma 290
– muscle 169, 283
parallel projection 75
parallel-beam
– geometry 74
– projection 2, 75, 101

partial
– rotation 74, 81
– scan 74
– voluming 211
– – averaging 197
patient
– dose 114
– pediatric 144, 146, 258
– pre-symptomatic 219
– size 121, 123
– vulnerable 12
– weight 121
– with chest pain 144
peak ejection fraction 340
percutaneous
– intervention (PCI) 239
– transluminal coronary angioplasty (PTCA) 6, 11
perfusion
– defect 310
– sequence 308
pericardial
– disease 189
– effusion 292, 313
pericarditis 13, 32
– constrictive 141
perivascular abscess 285
phantom calibration 176
pitch 52, 85, 101
– adaptation 346
– function of heart rate 92
– higher values for chest 145
pixel 151
plaque
– burden 166, 202
– – calcified 172
– calcified 164, 184
– characterization 220
– erosion 198
– evaluation 164
– fibrotic 218
– fibrous 164
– imaging 180
– lipid-rich 164, 218
– mixed 184
– non-calcified 184, 215, 226
– rupture 198, 214
– soft 218
– visualization 215
– volume 218
polar map 168
positron emission tomography (PET) 307
posterior displaced aorta 261
post-processing technique 208
post-stent stenosis 242
pre-ablation assessment 302
pre-stent stenosis 242
PROCAM
– algorithm 182, 214
– risk score 198
projection
– angle 81
– fan beam 2, 81
– filtered back-projection 2
– interpolated 81
– parallel beam 2, 101
prospective ECG triggering 76, 106
prosthetic valve 291
protocol
– contrast-agent 145
– contrast-injection 145
proximal anastomosis 236
PTCA, see percutaneous transluminal coronary angioplasty
pulmonary
– aneurysm 321
– artery 35, 145, 189, 317
– atresia 261
– CTA 317
– emboli 14, 185
– embolism 317
– emphysema 288
– metastasis 289
– sling 261
– trunk 298
– vein 14, 36, 189, 298, 300
– – 3D models 300
– – left inferior 298
– – left superior 298
– – mapping 302
– – measurement 299
– – ostial measurement 299
– – right inferior 298
– – right superior 298
– vessel 5
pulsation artifact 102
P-wave 110
– gating 110, 111

Q

quantification
– calcium mass 130
– calcium volume 130
quarter-scan segment 339

R

R peak editing 107
radiation
– dose reduction 123
– exposure 73, 110, 113, 259, 346
– – reduction 347
– – saving 119
– hazard 113
radiation-dose measurement 113
radiofrequency catheter ablation 298, 302
radionuclide ventriculography 272
rebinning 47, 75
reconstructed slice width 83
reconstruction
– adaptive cardiac volume (ACV) 92
– filter kernel 42, 133, 329
– – medium-smooth 140
– – sharp 141
– high-resolution 135
– increment 135
– multi-segment 144
– segmented 136
reducing radiation exposure 347
reference data bases 127, 195
– clinical 131
region wall motion 168
regional
– cardiac function 347
– function parameter 266
– wall function 268
region-growing algorithm 171
relative delay 106, 139
remodeling 12, 215
reproducibility of coronary calcium score 180
resolution
– cardiac 133
– in-plane 42, 72
– isotropic 42
– longitudinal 42, 62, 72
– low contrast 73
– spatial 42, 72
– temporal 71, 89, 90, 133
– z direction 42
respiratory artifact 258
restrictive cardiomyopathy 297
retrospective ECG-gating 106
revascularization 230
rhabdomyoma 290, 294
rhabdomyosarcoma 292, 294
right coronary artery (RCA) 24, 30
right ventricular
– disease 276
– enlargement 276
– function 142, 143
– volume 168
– wall motion 277
risk
– assessment 198
– stratification 202
ROI-based dynamic measurement 169
rotating-envelope tube 48, 62
rotation time 79, 85
RR interval time 77, 85, 106, 139
R-wave 76, 84, 106, 110
– gating 111

S

saline chaser bolus 141
scan
– field of view 74, 75, 339
– increased speed 145
– optimization of protocols 145
– protocol 127
scan-cycle time 77
scanner geometry 81, 114
scar tissue 268
sedation protocol 260
segmented reconstruction 89, 136
sequential
– coverage 77
– scan mode 77
– volume coverage 78
serum marker 321
shaded-surface display (SSD) 208
short-axis image 267, 270
signal-time curve 308
Simpson's method 267
single-photon emission computed tomography (SPECT) 272
single-segment
– algorithm 92
– reconstruction 340
single-slice CT 1, 18
single-vessel disease 206
slice
– collimation 50, 114
– sensitivity profile (SSP) 20, 57, 75, 81, 82, 343
– thickness 78
slice-broadening 83
solid-state detector 49

spatial resolution 41, 72, 133, 331
spiral
– computed tomography (CT) 18, 41, 79
– interpolation 53
– – artifacts 60, 64, 65
– – scheme 81
– – weights 81
– pitch 52, 85, 101, 340
– reconstruction 54
– table-feed 80
stable angina 184, 188, 207, 219
stable sinus rhythm 327
standard anatomic plane 23
statin 226
stenosis 164, 207
– measurement 164
stent 239
– coated 239
– coronary 241
– drug-eluting 239
– obstruction 240
– occlusion 242
– patency 242
– strut 239
stress
– perfusion scanning 309
– test 225
stroke volume 168, 266, 268
subendocardial infarction 313
sub-millimeter collimation 134
sub-segment 92
systemic arterial circulation 321
systole 71
systolic
– phase 269
– pulsation 101
– wall thickening 266, 268

T

T wave 107, 110
tachycardia 297
Takayasu arteritis 254
technical challenge 327
temporal
– data window 75
– resolution 71, 75, 89, 90, 133, 270, 339
– – high 347
– – improved 339
– – mean 340
– – of dual-source CT 342
– – spatially variable 76
tendinous cord 283
test-bolus injection 141
tetralogy of Fallot 261
thin-slab MPI 240
third-generation scanner 17
thoracic
– aorta 38, 145, 189
– CT 317
– vessel 14, 145
three-dimensional
– filtered back projection 58
– image volume 151
– image-processing 41
thromboembolic clot 317
time sensitivity profile 75, 94
tissue contrast 140
transaxial image slice 151
trans-esophageal echocardiography 285
transition weighting 75
transplanted heart 189
trans-thoracic echocardiography 272, 284
trapezoidal weighting function 83
tricuspid valve 29, 34
truncus arteriosus 261
tube current 114
– body-weight adapted 123
– reduction 121
tumor progression 289

U

ultrasound, intravascular 6, 8
unstable angina 185, 214, 320

V

Valsalva maneuver 108
valve
– aortic 29, 35
– function 286, 347
– mitral 29, 35
– tricuspid 29, 34
vascular lesion 356
vasculitis 184
vena cava 35
venous graft 232
ventricle
– left 24, 33, 34
– right 24, 33

ventricular
– septal defect 261
– thrombus 288
– volume measurement 266
– wall motion 168
– wall thickening 169
vertical long axis 24
vessel
– analysis 162
– probe 163
– segmentation 162
viability 266
viable myocardium 274
virtual endoscopy 162, 240
volume 132
– calcium score 193
– equivalent 172
– mode 333
– of interest punching 162
volume-rendering technique (VRT) 157, 208, 240
– brightness 158
– opacity 158
– slab 162
volumetric
– imaging 79
– quantification algorithm 172
voxel 41, 151
vulnerable
– lesion 198
– plaque 182

W

wall motion 141
– abnormality 269, 340
wall thinning 312
web-based database 182
weighted hyperplane reconstruction (WHR) 58
whole-body CT angiography 356
windmill artifact 60, 62
WinDose 116, 346

X

X-ray
– exposure 109
– tube 48
– – voltage 114, 123

Z

z filter reconstruction 56
z resolution 42, 65
– phantom 44, 57, 345
z-flying focal spot 44, 338

Printing and Binding: Stürtz GmbH, Würzburg